A Time-Resolved Infrared Spectroscopy Led Mechanistic Study into the Reactivity of Manganese Carbonyl Complexes: with a Focus on Routes of Precatalyst Activation Relating to Application in C–H Bond Functionalisation Reactions

Jonathan Benjamin Eastwood

PhD

University of York

Chemistry

September 2022

Abstract

This Thesis explores the mechanism by which ubiquitous manganese carbonyl precatalysts are activated, for their application in C−H bond functionalisation reactions. An additional focus was made to understand the underlying photochemistry of complexes that were examined *via* time-resolved infrared techniques. The structural information provided was crucial in determining key steps in chemical processes. Both *in situ* infrared spectroscopy, exploring reactions under catalytic conditions on a second to hour time scale, and Time-Resolved Multiple Probe Spectroscopy ($TR^{M}PS$), following events on a femtosecond to microsecond timescale, were employed herein.

An investigation using $TR^{M}PS$ explored the reactivity of catalytically relevant imine-derived 5-membered manganacycles. These were activated by excitation with a 355 nm pump wavelength. This resulted in photodissociation of a CO ligand, mimicking thermal loss of a CO ligand seen under catalytic conditions. The fundamental behaviour of photoproducts was established in a range of solvents, before studying the systematic addition of catalytically relevant compounds. *In situ* infrared spectroscopy was then employed to investigate how common manganese carbonyl precatalysts are activated. For the first time, evidence for how $[Mn_2(CO)_{10}]$ functions as a catalyst precursor was obtained. A novel mechanism of activation for $[MnBr(CO)_5]$ was then proposed, which was light dependant, and not seen in prior studies. The mechanism of action for lesser used manganese carbonyl precatalysts including $[BnMn(CO)_5]$ and $[Mn_2Br_2(CO)_8]$ were also explored.

Finally, the photochemistry of $[Mn_2(CO)_{10}]$ was established on a femtosecond to microsecond timescale, using $TR^{M}PS$. Initially, fundamental behaviour was determined. Then through excitation at selected wavelengths, the proportion of photochemically induced CO loss, and Mn−Mn bond cleavage could be controlled. The reactivity of subsequent photoproducts was then explored. $[Mn(CO)_5]^{\cdot}$ was observed to recombine under most conditions, but reactivity towards specific solvents, organohalides, and an imine ligand was revealed. The reactivity of the CO dissociative photoproduct $[Mn_2(CO)_9]$ was then linked back to *in situ* IR studies probing the activation of $[Mn_2(CO)_{10}]$ under catalytic conditions.

List of Contents

List of Tables

List of Figures

Acknowledgements

First and foremost, I would like to thank my supervisors Jason Lynam, Ian Fairlamb, and Charlotte Willans for their support, guidance, and supervision throughout my PhD. I feel that I have learnt a lot from them during my PhD, and have developed a lot as a chemist. I am also grateful for the University of York who funded me through a Teaching Studentship for the first three years of my PhD, and the Royal Society of Chemistry who funded me with a Research Enablement Grant during the fourth year of my PhD.

I would also like to thank all the staff that I have worked with at the ULTRA facility at the Rutherford Appleton Laboratory (Particularly Mike Towrie, Ian Clark, Igor Sazanovich, Gregory Greetham, Gabriel Karras, Emma Gozzard, and Marta Szynkiewicz) for support and scientific input running TR^{M}PS experiments. I thoroughly enjoyed my time working there as part of our collaboration. Highlights include Jason Lynam having to order Kopparberg cider, getting competitive running with Ian Fairlamb, making 3 am coffee underneath the smoke detector, and of course the cutting-edge science.

At the University of York I would like to thoroughly thank all the technical staff for their assistance, which without, I would not have been able to complete my PhD. Karl Heaton for the MS service, Heather Fish and Ryan Epton for the NMR service, Adrian Whitwood and Theo Tanner for X-ray crystallography service, and Barbara Procacci for running IR pump-probe experiments for me. Additional thanks to Charlotte Lee for technical support in E114.

Finally, I would like to thank all the members of the Fairlamb, Lynam and Slattery lab groups that I have worked with over the past four years. A special thanks to Anders Hammarback (who helped me find my feet when I started, taught me to be meticulous with my work, and for “David?”), Chris Goult (who trained me to use Schlenk lines and the glove box), Gayathri Athavan (for her great supply of cheesy jokes and top notch drawings), Neda Jeddi (for putting up with the fact that Mn > Pd and general lab shenanigans), Sara Bonfante (for keeping me company late in the lab while writing up my thesis, being wine buddies and introducing my to climbing), and finally Tom Burden (who was my team manganese partner in crime, helped me to thrive, not just survive and made my PhD experience thoroughly more enjoyable!).

Author's Declaration

I declare that this thesis is a presentation of original work and I am the sole author. The work was carried out at the University of York and the Rutherford Appleton Laboratory, Harwell between October 2018 and September 2022 and has not previously been presented for an award at this, or any other, University. All sources are acknowledged as references. Part of this work has been reproduced in a publication, a copy of which is attached as Appendix 1:

B. J. Aucott*, J. B. Eastwood*, L. A. Hammarback*, I. P. Clark, I. V. Sazanovich, M. Towrie, I. J. S. Fairlamb, and J. M. Lynam, *Dalton Trans.*, **2019**,*48*, 16426-16436.

J. Eastwood, L. A. Hammarback, M. T. McRobie, I. P. Clark, M. Towrie, I. J. S. Fairlamb, and J. M. Lynam, *Dalton Trans.*, **2020**,*49*, 5463-5470.

J. D. Firth, L. A. Hammarback, T. J. Burden, J. B. Eastwood, J. R. Donald, C. S. Horbaczewskyj, I. P. Clark, M. Towrie, A. Robinson, J. Krieger, I. J. S. Fairlamb, and J. M. Lynam, M. T. McRobie, A. Tramaseur, *Chem. Eur. J.*, **2021**, *27*, 3979.

L. A. Hammarback, A. L. Bishop, C. Jordan, G. Athavan, J. B. Eastwood, T. J. Burden, J. T. W. Bray, F. Clarke, A. Robinson, J. Krieger, A. Whitwood, I. P. Clark, M. Towrie, J. M. Lynam, and I. J. S. Fairlamb, *ACS Catalysis,* **2022**, *12*, 1532-1544.

L. A. Hammarback, J. B. Eastwood, T. J. Burden, C. J. Pearce, I. P. Clark, M. Towrie, A. Robinson, I. J. S. Fairlamb, and J. M. Lynam, *Chem. Sci.*, **2022**, *13*, 9902-9913.

*Equal author contributions.

Jonathan Benjamin Eastwood

September 2022

Chapter 1: Introduction

1.1 Manganese Carbonyl Catalysed C–H Bond Activation and Functionalisation Reactions

1.1.1 Early Examples of C–H Bond Activation and Functionalisation

C–H bond functionalisation reactions offer a low cost, highly chemo- and regio-selective method of achieving chemical transformations. [1,2] They enable the transformation of cheap hydrocarbon starting materials into valuable, versatile products. [3] Furthermore, by eliminating the need for reagent pre-functionalisation, transformations generate less by-product waste and possess higher atom efficiency than traditional cross-coupling reactions. [4]

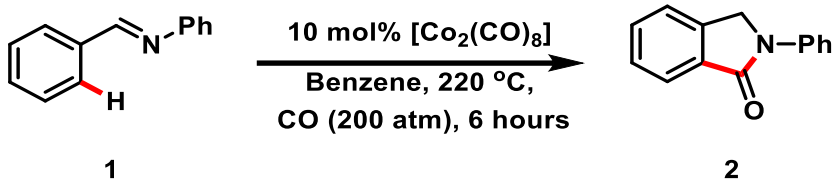

Figure 1. $[Co_2(CO)_8]$ catalysed insertion of CO into an aldimine.[5]

Early work by Murahashi demonstrated the ability to insertion a molecule of CO into aldimine **1**, in a reaction catalysed by $[Co_2(CO)_8]$ (see Figure 1).[5] Like many C–H bond functionalisation reactions, activation and subsequent activation of the *ortho* C–H bond was achieved *via* use of a directing group, in this instance the secondary imine nitrogen atom. Directing groups offer a simple solution to one of the key issues C–H bond functionalisation reactions face; the regioselective control over which C–H bond is activated.

Palladium catalysts are utilised in the majority of directed C–H bond functionalisation reactions.[6][7] However, in recent years, the potential of earth abundant first row transition metals has been widely explored in a variety of transition metal-mediated reactions, including C–H bond functionalisation reactions.[8] Most commonly, Mn, [9] Fe,[10] Cu, [11] Ni [12] and Co [13] have been employed as successful alternatives to platinum group metals.

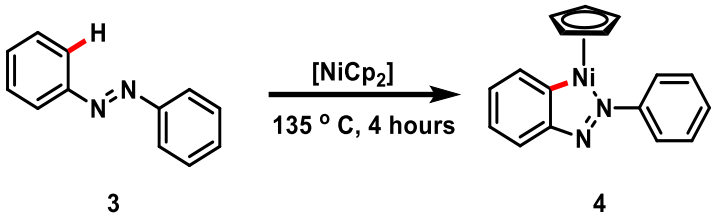

Figure 2. The first reported cyclometallation by Kleiman and Dubeck.[14]

The first metallacycle intermediate was illustrated by Kleiman and Dubeck in 1963 (see Figure 2).[14] The 5-membered metallacycle formed is typical of catalytic intermediates formed in manganese catalysed C–H bond functionalisation reactions. Usually, this is due to the thermodynamic stability offered through formation of the 5-, or 6-membered ringed system, in which the arene π system offers stability to the metal centre. The new C–M bond formed is more reactive than the pre-existing C–H bond, enabling the introduction of previously inert functionalities.[15]

1.1.2 C–H Bond Activation Using Manganese (I) Carbonyl Complexes

Evidence of $[Mn_2(CO)_{10}]$ was first provided in 1949 by Hurd and co-workers, where it was detected *via* mass spectrometry. [16] Five years later, in 1954, Brimm and co-workers isolated the compound, with a yield of 1 %. Since the discovery of manganese carbonyl, extensive studies have been conducted, covering a vast range of reactions. [17] Two reactions which were pivotal for early studies into C–H bond activation using Manganese (I) carbonyls, are the reduction of $[Mn_2(CO)_{10}]$ with H_2 to form $[HMn(CO)_5]$ **6**, and the subsequent reaction with diazomethane to form $[MeMn(CO)_5]$ **7** (see Figure 3). [18],[19] Methyl manganese pentacarbonyl was the precursor used by Stone and co-workers in the first reported direct C–H bond activation involving a manganese carbonyl. In this instance, $[MeMn(CO)_5]$ **7** reacted with azobenzene **3** in a similar manner to that with $[NiCp_2]$, activating the C–H bond *ortho* to the azo directing group.[14], [20] This was not the first time, the 5-membered metallacycle **9** was synthesised. Two years prior, Heck reported the synthesis of **9**, through the reaction of a palladacycle with a manganese anion. [21]

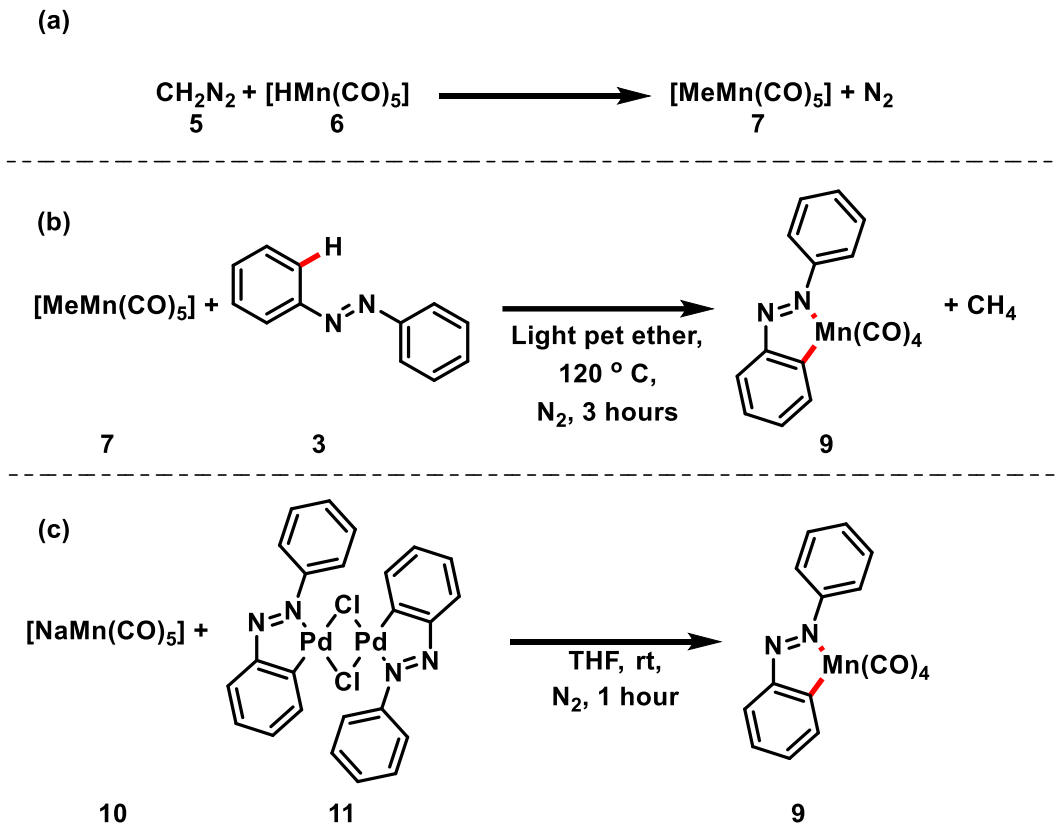

Figure 3.(**a**) Synthesis of [MeMn(CO)$_5$] **7**(**b**) The first reported direct cyclometallation using a manganese (I) carbonyl by Stone and co-workers in 1970. [20] (**c**) Alternative synthesis of **9** reported by Heck in 1968. [21]

In the decades following Stone and co-workers' initially report, analogous 5-membered metallacycles were reported using different heteroatom directing groups. These included *N*-containing amino[22] azo[23], imidazole[24] and pyridyl[25], *O*-containing ketone[23], aldehyde[26] and amide[27], *S*-containing thioether[22], *Se*-containing phosphoselenide [28] and even electron-poor *P*-containing phosphite[29] ligands (see Figure 4). Often these 5-membered metallacycles were then employed in subsequent functionalisation transformations.[30][31]

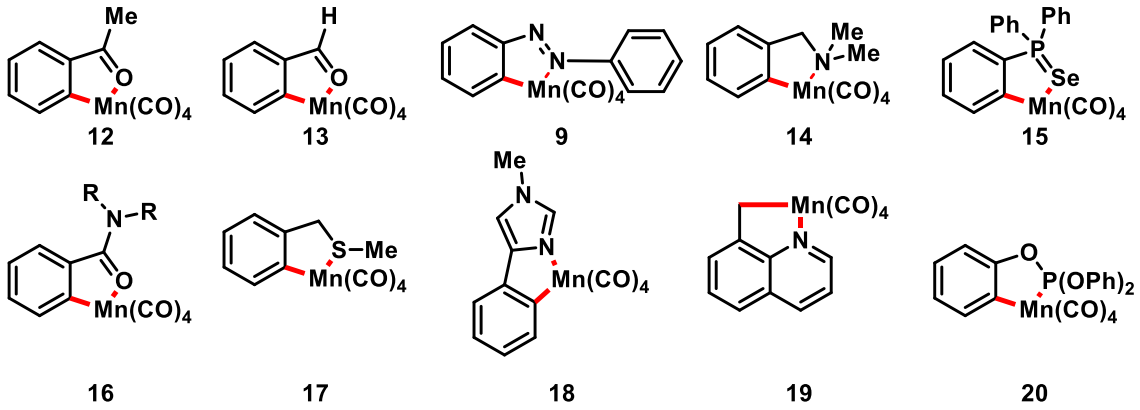

Figure 4. An array of literature C–H activated 5-membered manganacycle complexes.

1.1.3 Stoichiometric C–H Functionalisation Transformations involving Manganese (I) Carbonyl Complexes

The first functionalisation of C_{aryl}–Mn bonds , following stoichiometric activation of the C–H bond, were carried out by Gommans and co-workers.[32] Two reaction pathways were reported between methyl acrylate and 5-membered manganacycles **21** and **24**. By varying the manganacycle, either an arylated, or annulated product was preferred, when the reaction was conducted in the presence of a stoichiometric equivalency of $PdCl_2$ catalyst (see Figure 5).

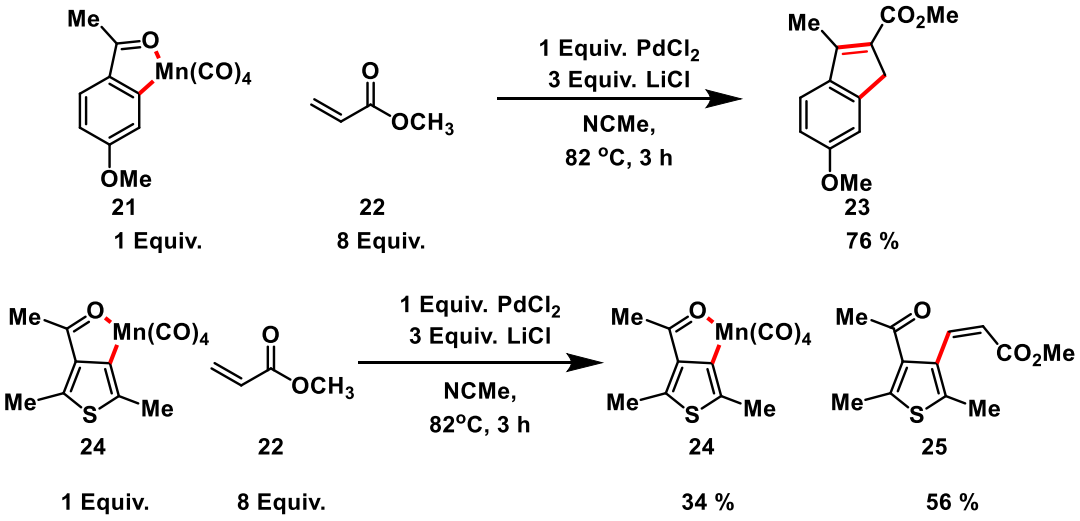

Figure 5. Pd-mediated stoichiometric functionalisation of 5-membered manganacycles reported by Gommmans and co-workers.[32]

Subsequent studies, including those by Cambie, Depree, and Liebeskind, successfully conducted Pd-free functionalisation of 5-membered manganacycle C_{aryl}–Mn bonds,

using a variety of alkene[28,33], acrylate[28,34], and alkyne[25,29,33,35–40] substrates (see Figure 6). These transformations mirrored the typical reactivity seen in catalytic transformations, which were conducted decades later. [1,41,42]

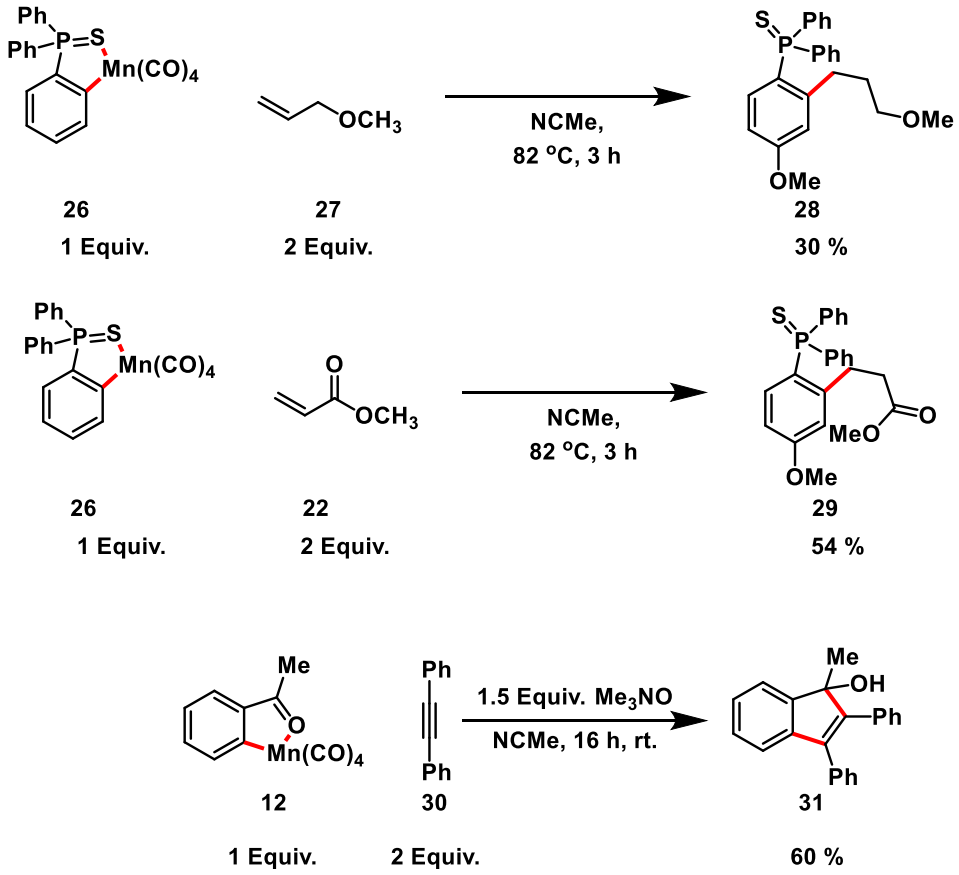

Figure 6. Early examples of Pd-free stoichiometric functionalisation of C_{aryl}–Mn bonds with acrylate,[28,34] alkene, and alkyne[33] substrates.

Liebeskind and co-workers proposed a mechanism by which the reaction with the manganacycle proceed. Initially, the substrate coordinates to the manganese centre prior to a migratory insertion of the respective unsaturated ligand, forming a 7-membered manganacycle motif. Following the formation of the 7-membered manganacycle, either a reductive elimination or protodemetallation step occurrs, forming the respective annulated or arylated/alkenylated products.[35] A photochemically activated reaction, between the triphenyl phosphite derived 5-membered manganacycle **20** and diphenyl acetylene, by Onaka and co-workers, resulted in evidence for the ligand coordinated complex **32**.[36] Uv light promoted the photochemical dissociation of one CO ligand, and a single crystal X-ray diffraction structure of the resultant π-bound diphenyl acetylene complex **32** was obtained. Grigsby

and co-workers probed the system further, but were unable to detect the intermediate complex **32**. Instead, they revealed additional products, which likely formed from **32** (see Figure 7). The expected 7-membered manganacycle product **34** was detected, formed *via* the insertion of the coordinated alkyne in complex **32**. Additionally side products were detected in which; a CO ligand inserted **33**, a second triphenyl phosphite ligand coordinated **35**, or the triphenyl phosphite ligand was alkenylated **36**.

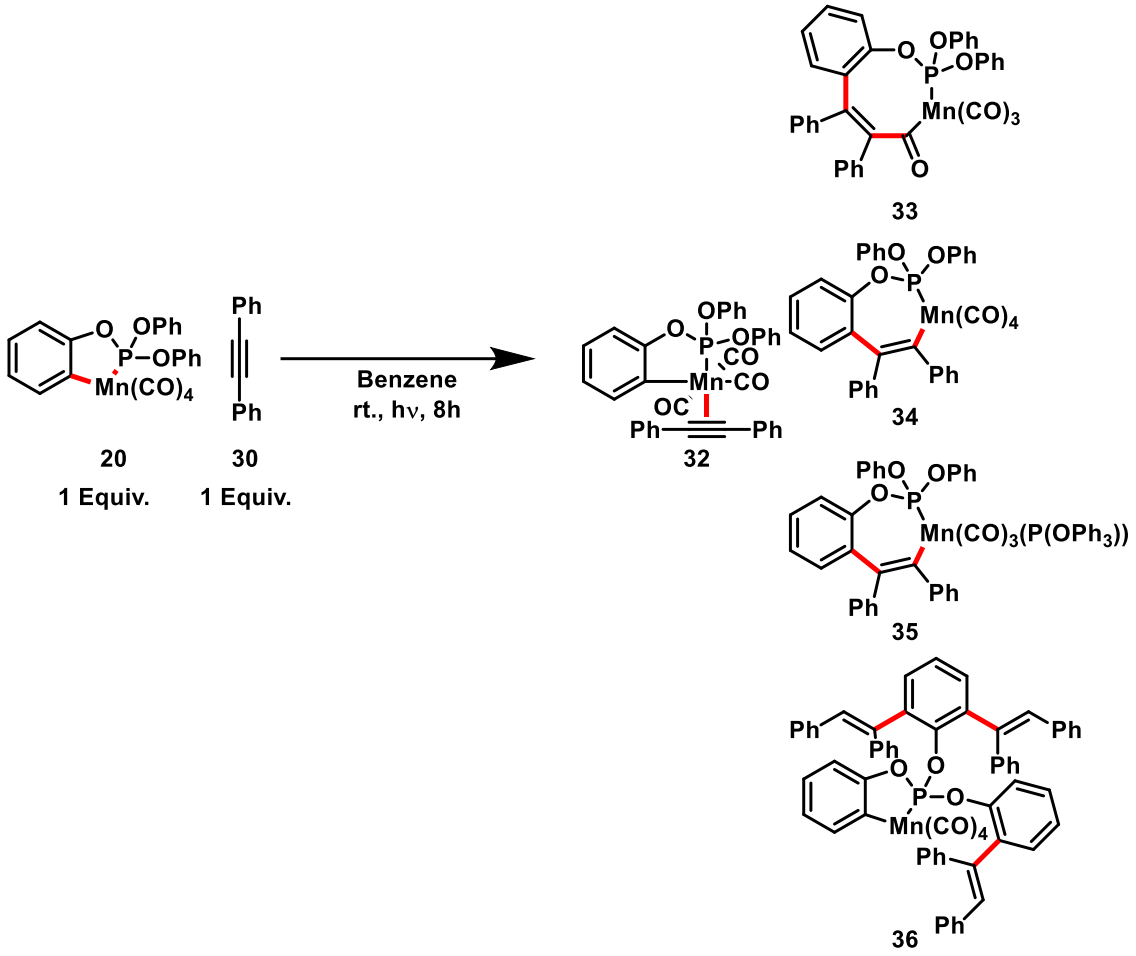

Figure 7. Products detected from the reaction between 5-membered manganacycle **20** and diphenyl acetylene.[35][36]

Assignment of the 7-membered manganacycle was later supported by Suárez and Tully.[39,40,43] Suárez and co-workers were able to successfully synthesise 7-membered manganacycles, in a moderate yield, inserting internal alkynes into phenylimidazole derived manganacycle **37**. While Tully and co-workers explored the reactivity of the 5-membered manganacycle **40**, isolating the subsequent reductive elimination product **41**, which possessed a coordinating [$Mn(CO)_3^-$] anion (see Figure 8).

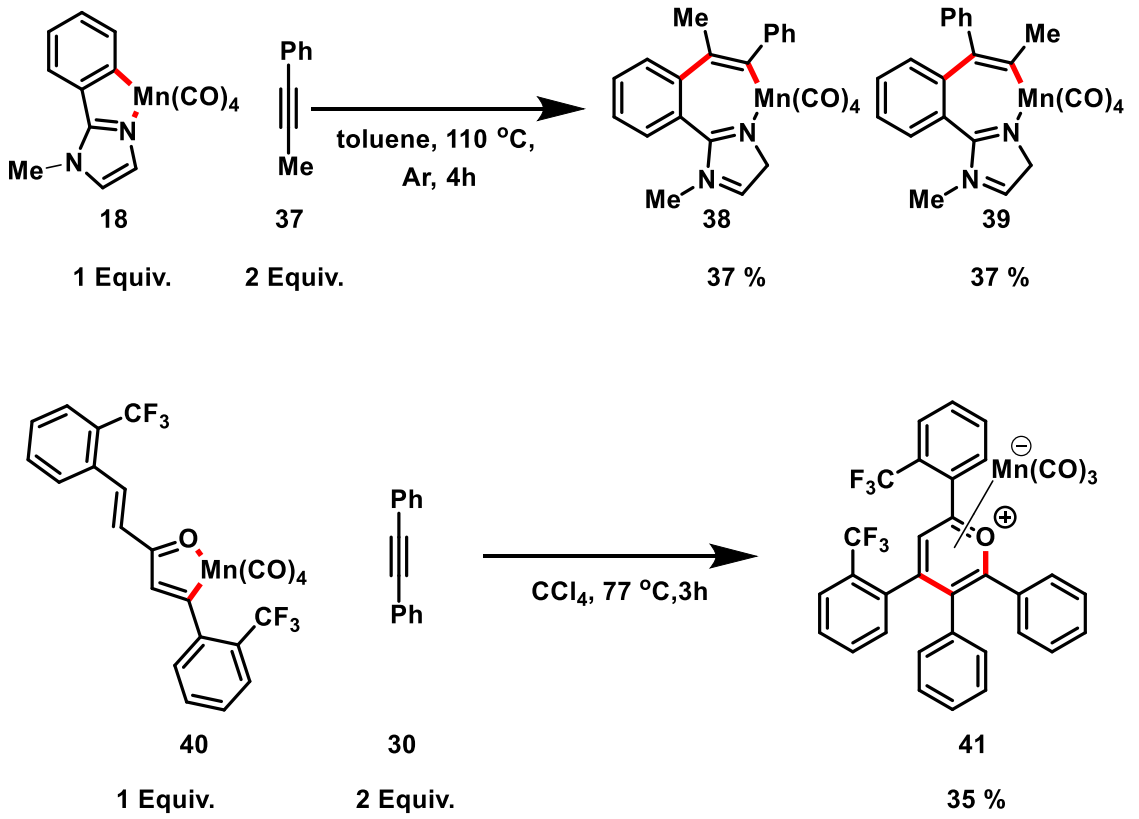

Figure 8. Top: First synthesis of a 7-membered manganacycle **38** and **39** by Suárez and co-workers.[43] Bottom: Stoichiometric synthesis of a the resulting reductive elimination product **41** by Tully and co-workers.[39,40]

Further mechanistic work, looking at the reactivity of 7-membered manganacycles, was carried out by Yahaya and co-workers (see Figure 9).[44] A 2-pyrone ring system containing a 2-pyridyl directing group was chosen as the model substrate, along with phenyl acetylene. The rational was that the 2-pyrone group would act as a hemilabile ligand stabilising the 7-membered manganacycle intermediate. Formation of the respective 5-memebred manganacycle was achieved through either a photochemical or thermal reaction between [$BnMn(CO)_5$] and the ligand of interest, **42** , activating the promoted C–H bond. Upon introduction of phenyl acetylene to the system, experimental $^{1}H/^{13}C$ NMR data supported the formation of the respective 7-membered manganacycle **43**. The subsequently reactivity of **43** was then highlighted. Warming up of the reaction mixture resulted in reductive elimination product **44** forming, while an excess of phenyl acetylene promoted formation of the alkenylated product **45**.

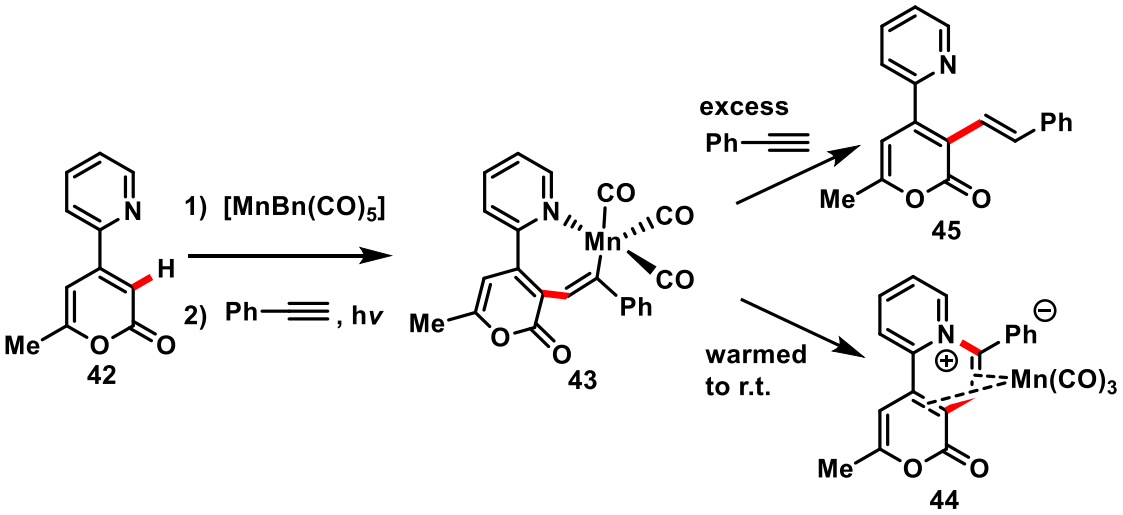

Figure 9.Mechanistic work by Yahaya and co-workers probing the reactivity of 7-membered manganacycles.[44]

1.1.4 Nitrogen Directed C–H Bond Functionalisation Reactions

Kuninobu and co-workers reported the first catalytic C–H bond functionalisation reaction using a manganese carbonyl catalyst (see Figure 10).[45] The transformation was initially stoichiometric, activating the *ortho* C–H bond of **46**, and subsequently alkylating the imidazoline. Through addition of two equivalents of triethylsilane, the precatalyst loading of $[MnBr(CO)_5]$ was reduced from 100 mol% to a loading of 5 mol%. Kuninobu and co-workers proposed that the silane aided catalyst regeneration, forming $[HMn(CO)_5]$, however this manganese complex was never detected *in situ*. Additional manganese complexes were tested as potential precatalysts, only $[Mn_2(CO)_{10}]$ was found to generate catalytically active species, reflecting many later works in the field. When a chiral non-racemic imidazoline was employed, asymmetric synthesis of the silyl ether was achieved, with diastereoselectivity of ~95% demonstrated.

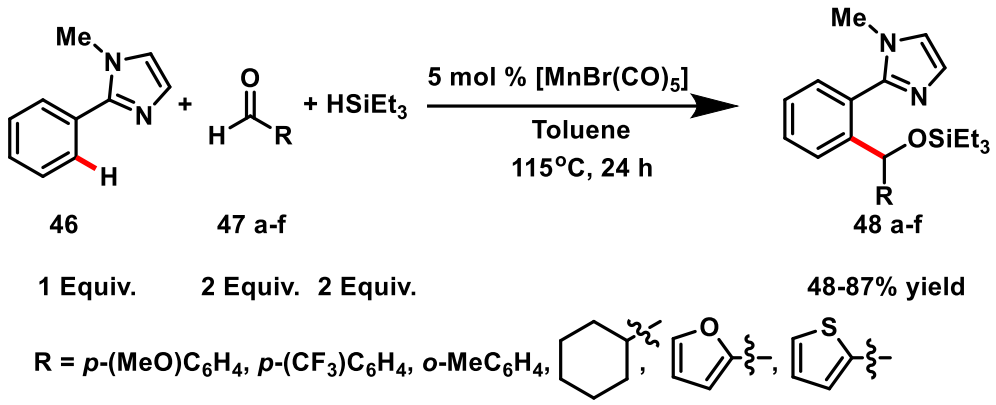

Figure 10. The first Manganese carbonyl catalysed C–H bond functionalisation reaction.[45]

Subsequently, Zhou and co-workers explored the alkenylation of phenylpyridines with terminal alkynes (see Figure 11).[46] $[MnBr(CO)_5]$ was found to be the optimal precatalyst (77%), while $[Mn_2(CO)_{10}]$, $[ReBr(CO)_5]$, and $[Ru_3(CO)_{12}]$ showed varying degrees of success (4-58%). A sub-stoichiometric quantity of dicyclohexylamine (0.1 equiv.) was used alongside the manganese precatalyst, enhancing the yield of alkenylated product further. This was rationalised with the hypothesis that the base lowers the activation energy for the activation of the C–H bond, aiding with the formation of 5-membered manganacycle.

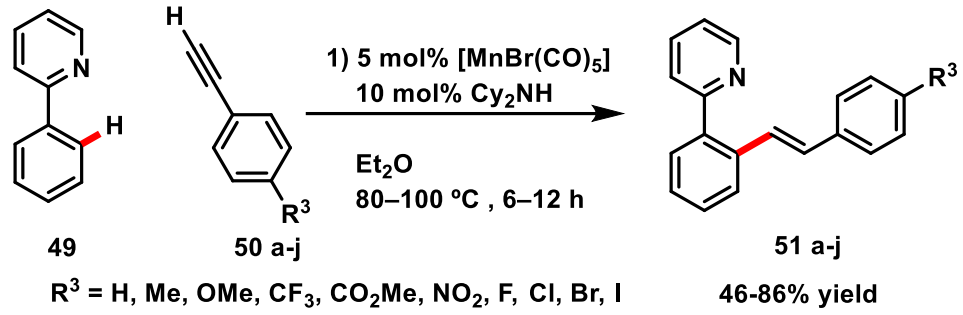

Figure 11. Manganese (I) catalysed alkenylation of phenylpyridines reported by Zhou and co-workers.[46]

Following the initially reported catalytic reactions by Kuninobu and co-workers[45], along with Zhou and co-workers[46], numerous manganese (I) catalysed C–H bond functionalisations have been carried out at the position *ortho* to a directing group. Indoles are an organic framework which utilise the C2 selectivity of manganese, as opposed the typical C3 directed activation achieved with palladium-based systems (see Figure 12).[47] Indoles have been successfully coupled with aryl isocyanates[48],

alkynes[49–51] ketones[52], alkenes[53,54], alkynyl bromides[55], allenes[56,57], imines[58], and maleimides.[59]

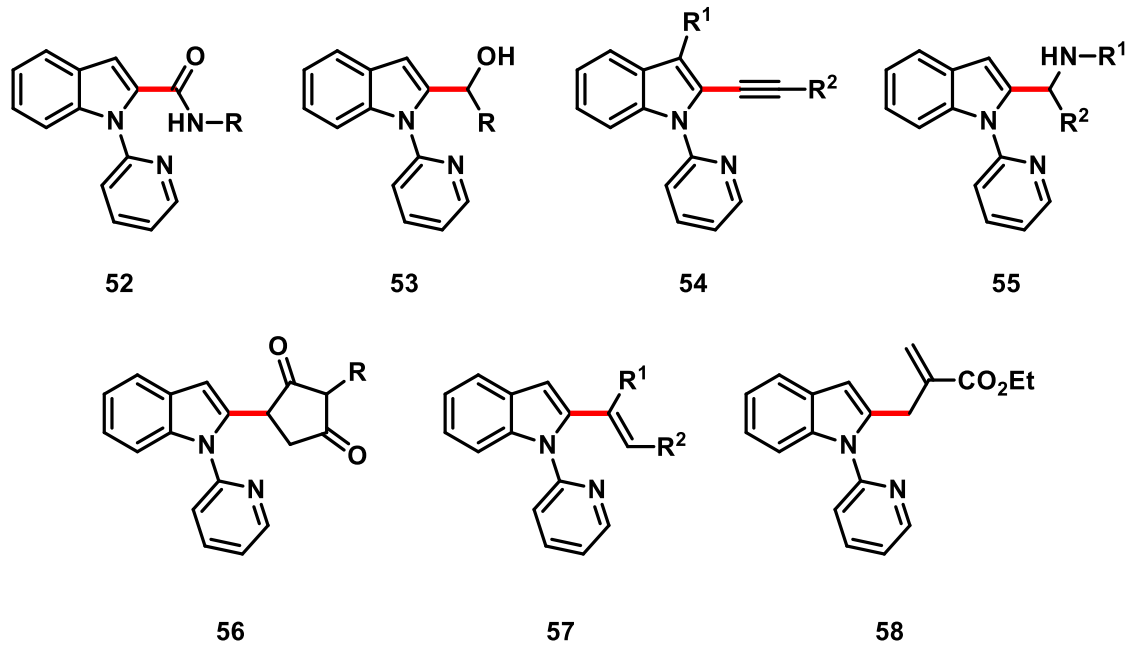

Figure 12. Indole derived products formed via directed manganese (I) catalysed C–H bond functionalisation reactions.

One example is that reported by Liu and co-workers, who carried out a manganese(I)-catalysed C-H aminocarbonylation of indoles (see Figure 13).[48] As with many other transformations, a 2-pyridyl directing group was used and the reaction was tolerant to a variety of electronically donating and withdrawing R groups. The reaction was proposed to proceed *via* the standard route forming 5- and 7- membered metallacycles. However, addition of a stoichiometric equivalency of 2,2,6,6-tetramethylpiperidine-*N*-oxide reduced the yield by 16% indicating that there is likely to be some radical involvement.

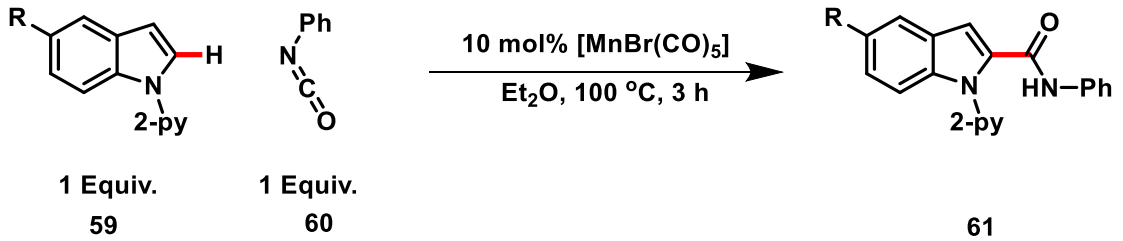

Figure 13. Directed activation at the C2 position, and subsequent aminocarbonylation reported by Liu and co-workers.[48]

Alternatively, imine motifs have been used as an N-containing directing groups. These typically possess a more readily activated *ortho* C−H bond than their oxygen containing carbonyl counterpart, due to their less electron withdrawing nature of nitrogen. Both annulation and alkenylation reactions have been reported with imines (see Figure 14). The former have been observed between both primary and secondary imines with alkynes, acrylates, and methylenecyclopropanes, while alkenylation and alkylation reactions have been demonstrated with alkynes and alkenes, respectively.[60–63]

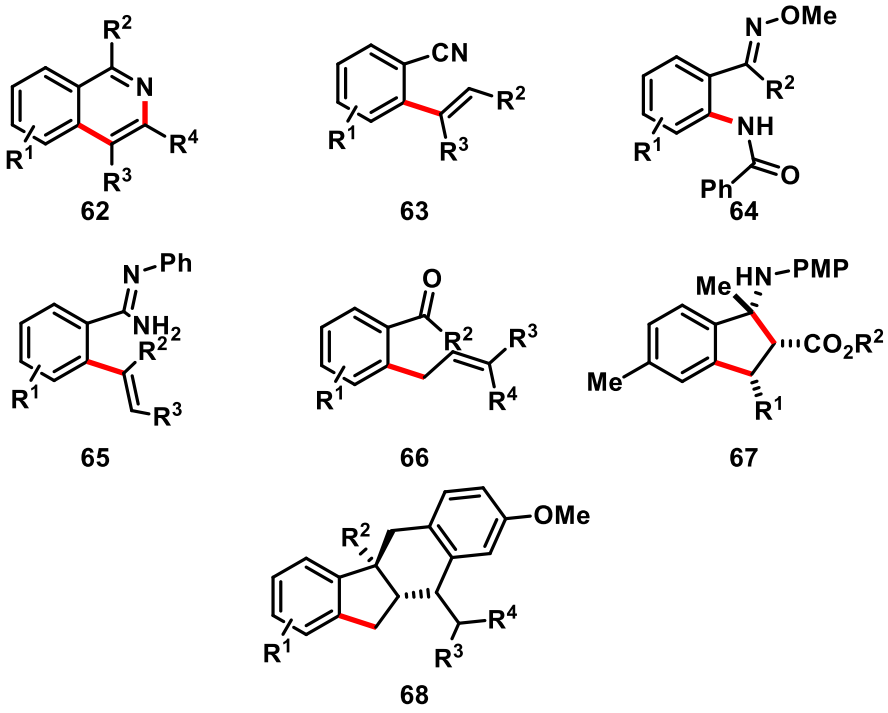

Figure 14. Imine derived products formed via directed manganese (I) catalysed C−H bond functionalisation reactions.[60–63]

He and co-workers reported the [4+2] annulation of N−H imines and alkynes, forming an isoquinoline motif (see Figure 15).[60] Both $[Mn_2(CO)_{10}]$ and $[MnBr(CO)_5]$ demonstrated similar catalytic activity, with yields of 92% and 87% reported respectively. This was the first instance of an additive free C–H bond functionalization reaction using a manganese(I) carbonyl catalyst, with many transformations requiring the addition of an additive such as $HNCy_2$[46], BPh_3[64,65], or $ZnMe_2$.[66] Furthermore, the system was tolerant towards internal alkynes, unlike many manganese catalysed transformations, which only proceeded with terminal alkynes.[46] Despite these nuances, the reaction was still proposed to proceed *via* typical 5-membered and 7-membered

metallacycle intermediates. Consequently, this reaction was used herein as a model system for mechanistic study, employing imines, alkynes, and isoquinolines used in the initial work by He and co-workers.

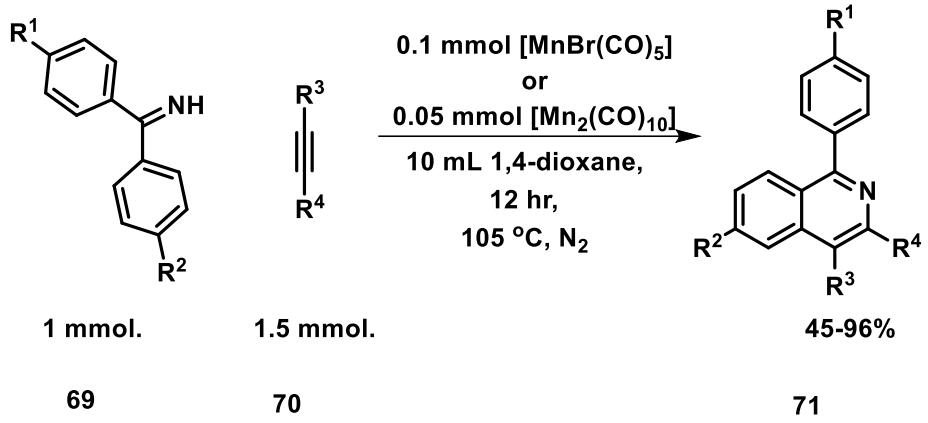

Figure 15. [4+2] annulation of N–H imines and alkynes by C–H/N–H activation.[60]

Xu and Kong explored the *ortho*- C–H amidation of oximines (**72**) with dioxazolones (**73**) using [MnBr(CO)$_5$] as their precatalyst (see Figure 16).[67] Uniquely, ionic liquids were employed as reaction solvents, as opposed to conventional solvents. [Hmim]OAc (1-hexyl-3-methylimidazolium acetate) was found to be optimal, with a yield of 89%. Whereas a yield of 66% was the highest reported in a traditional solvent (Et_2O). This difference in yield was attributed with the ability for [MnBr(CO)$_5$] to form the novel complex [MnOAc(CO)$_5$] in the ionic liquid. However, this species was never detected by Xu and Kong. Unlike other catalytic reactions, a lower catalyst loading of 2.5 mol% was used, and the authors demonstrated the ability to reuse the Mn-containing ionic liquid. After 5 repeat reactions, the yield had only decreased by 10%, to 79%.

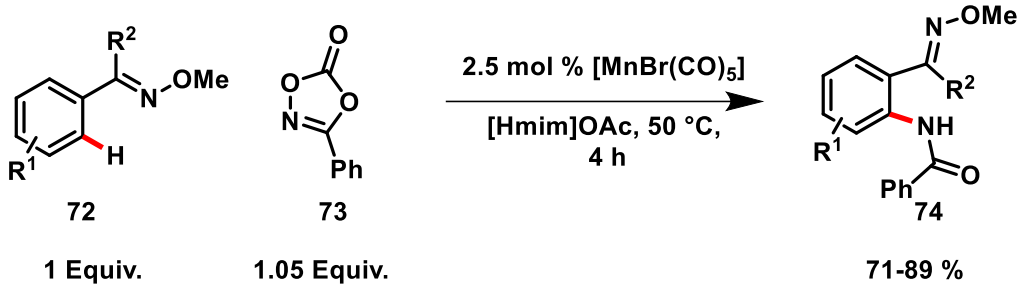

Figure 16. *Ortho*-C–H amidation of oximines **72** with dioxazolones **73** using [MnBr(CO)$_5$].[67]

1.1.5 Oxygen Directed C–H Bond Functionalisation Reactions

Compared to nitrogen derived directing groups, there are relatively few examples of manganese catalysed directed C–H bond functionalization reactions incorporating oxygen into cyclic products. Primary, this is due to the reduced activity of the C–H bond, and the weakly coordinating nature of oxygen containing directing groups to the manganese centre. Often additives have been employed to aid with the activation fo otherwise inert C–H bonds,[64,65] these include BPh_3, Me_2Zn, and $AlCl_3$ (see Figure 17). [65] [64] [66] [68]

Sueki and co-workers reported the synthesis of isobenzofuranones **77** from an ester **75** and oxirane **76**.[65] $[Mn_2(CO)_{10}]$, $[Re_2(CO)_{10}]$ and $[Pd(OAc)_2]$ were the only transition metal precatalysts capable of activating the transformation under the reaction conditions, with $[Mn_2(CO)_{10}]$ possessing the highest yield of 74%. A stoichiometric equivalency of triphenyborane was determined to be necessary in the reaction. The borane was proposed to aid with C–H bond activation, accelerating the formation of the proposed 5-membered manganacycle. Other additives which promote CO dissociation, such as trimethylamine N-oxide, were not explored.

Mechanistic work derived from the reaction between aromatic ketones and aldehydes, forming an isobenzofuran **79**, by Liu and co-workers, revealed two further roles that the borane plays. Firstly, $[PhMn(CO)_5]$ and $BrBPh_2$ were detected *in situ*, indicating that "transmetalation" can occur between $[MnBr(CO)_5]$ and the borane, forming highly reactive $[PhMn(CO)_5]$, promoting C–H bond activation. Furthermore, $BrBPh_2$ formed *in situ* was proposed to act as a Lewis acid, increasing the nucleophilicity of the aldehyde, aiding with the C–C bond forming step.

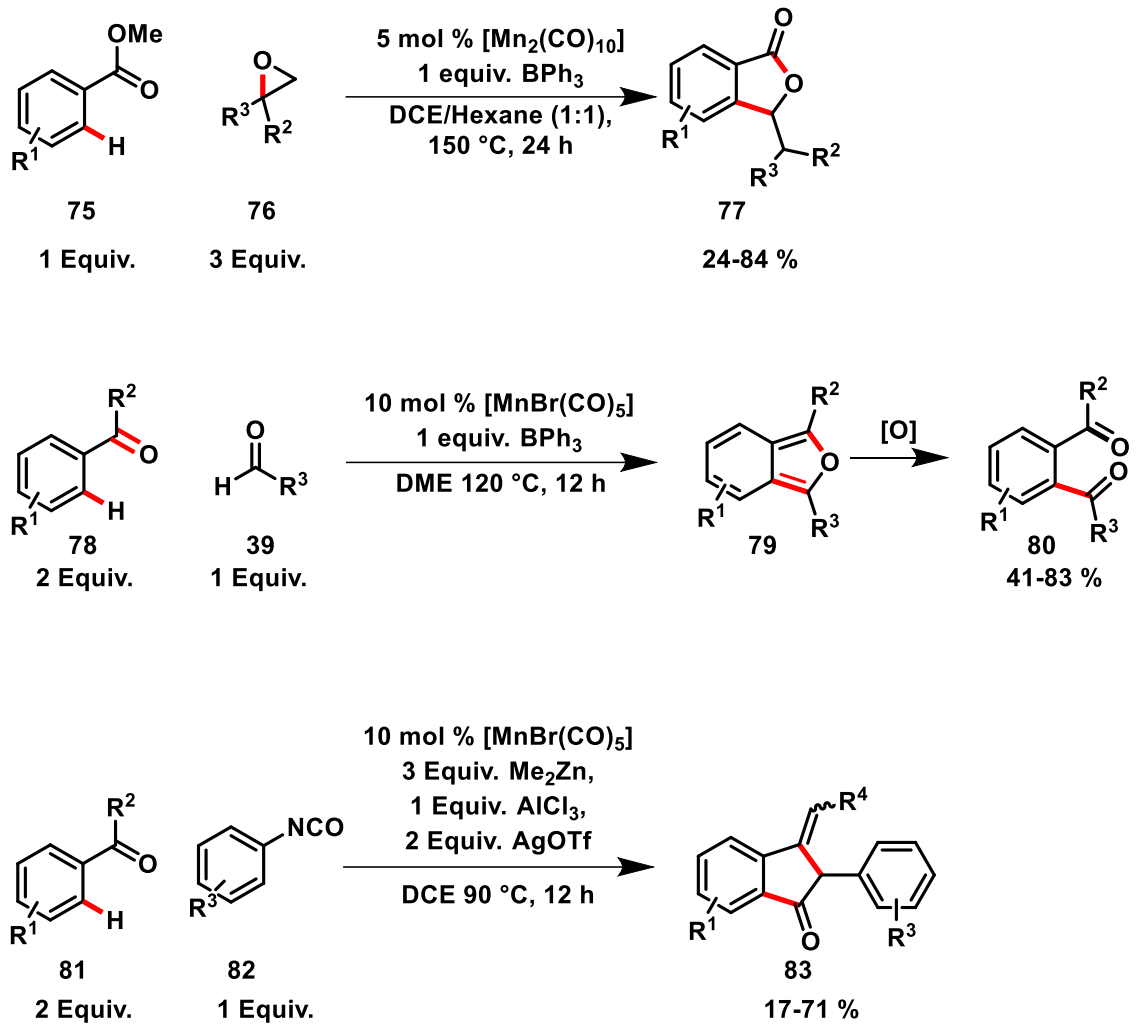

Figure 17. Top: Synthesis of isobenzofuranones **77** from an ester **75** and oxirane **76**. [65] Middle: synthesis of isobenofurans **79** and o-diacylbenzene products **80** from aromatic ketone **78** and aldehyde **39**. [64]Bottom: [3+2] cyclization of ketones **81** and isocyanates **82**, to form 3-alkylidene phthalimidines **83**. [66]

Dimethylzinc was observed to play a similar role.[66] Evidence was found by Huo and co-workers which indicated that transmetalation between $[MnBr(CO)_5]$ and $ZnMe_2$ generates $[MeMn(CO)_5]$ *in situ*, which is more active than $[MnBr(CO)_5]$, promoting initial C–H bond activation. This was reflected by an increase in yield from 0% to 50% upon inclusion of 3 equiv. of $ZnMe_2$. Additional inclusion of silver (I) triflate and $AlCl_3$ resulted in a further increase in yield to 70%. $AlCl_3$/AgOTf were proposed to act as a Lewis acid, increasing the nucleophilicity of the isocyanate, mirroring the role BPh_3 played in the prior reaction. [64]

1.1.6 Catalytic Manganese (I) C–H Aryl-Coupling

The piano-stool manganese (I) complex [$Mn(Cp)(CO)_3$] was found to be photoactivated upon irradiation with a blue LED , and competently catalyse the coupling of two aryl fragments, removing the need for preinstalled directing groups in this transformation (see Figure 18).[69] Unusually, in this instance [$Mn_2(CO)_{10}$] and [$MnBr(CO)_5$] were reported to give significantly reduced yields of 44% and 29% respectively. Yu-Feng and co-workers also demonstrated that the reaction could be carried out in flow and conducted on a gram scale.

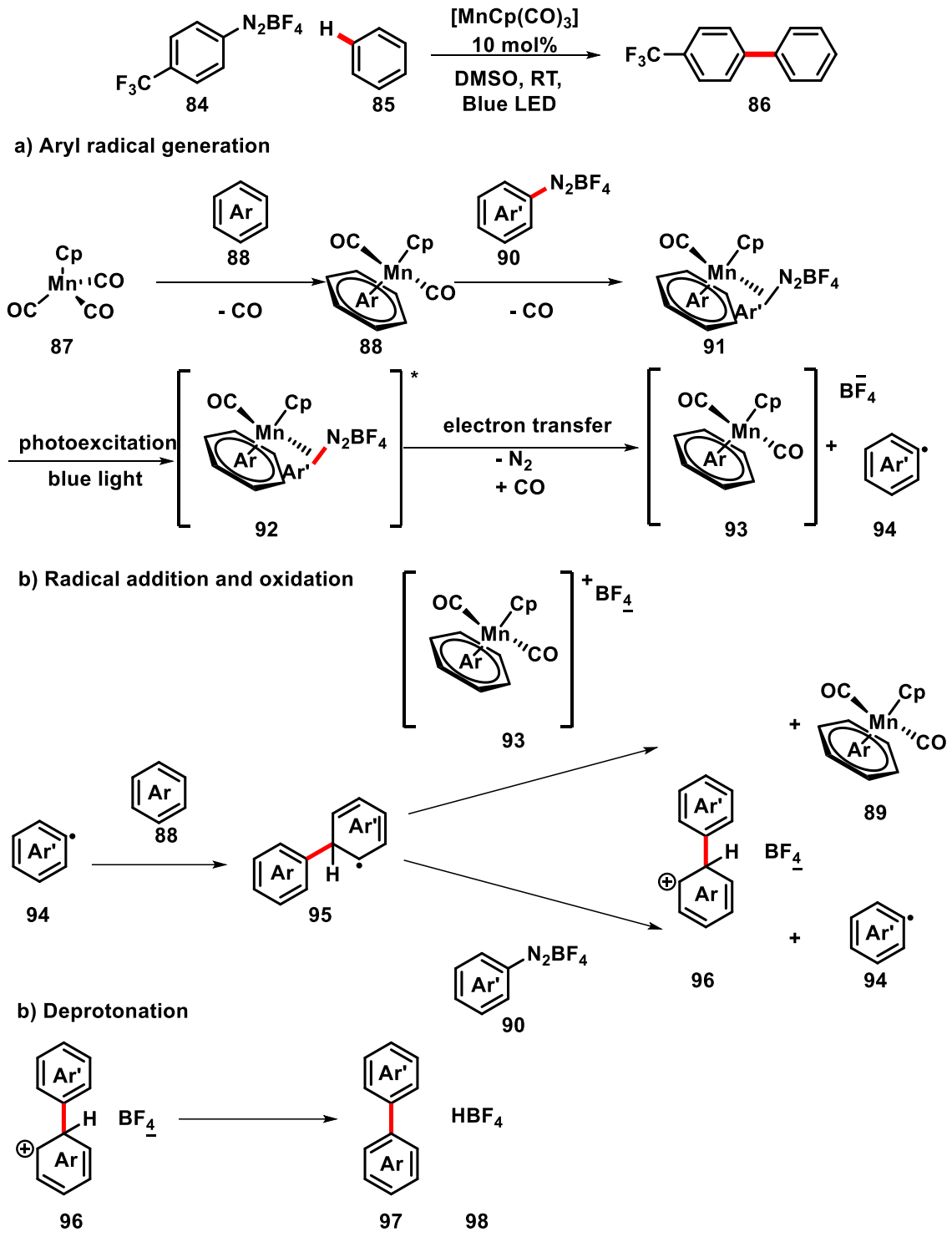

Figure 18. Photoinduced C–H arylation and proposed mechanism.[69]

The reaction also demonstrated a good degree of robustness, activating a variety of heteroarenes. A proposed mechanism was put forward by Yu-Feng and co-workers. This involved aryl radical generation **94** from photoexcitation of the photocatalyst **87**, followed by coupling with the arene substrate **85**, with re-aromatization to give the biaryl product **86**.

1.1.7 Manganese Aided Borylation of Aryl Diazonium Salts

Another example of manganese assisted functionalisations are the borylation of aryldiazonium salts, forming new C−B bonds (see Figure 19). These products themselves are important in Suzuki Miyaura reactions. Liang and co-workers first reported the transformation, using $[Mn_2(CO)_{10}]$ as their precatalyst.[69] This work was then built upon by Firth and co-workers, who optimised reaction conditions, conducted a thorough substrate scope, and probed the role of $[Mn_2(CO)_{10}]$ using time-resolved multiple probe spectroscopy.[70] Ultimately, $[Mn_2(CO)_{10}]$ was found to be a photoinitiator, rather than catalyst, as originally reported by Liang and co-workers.

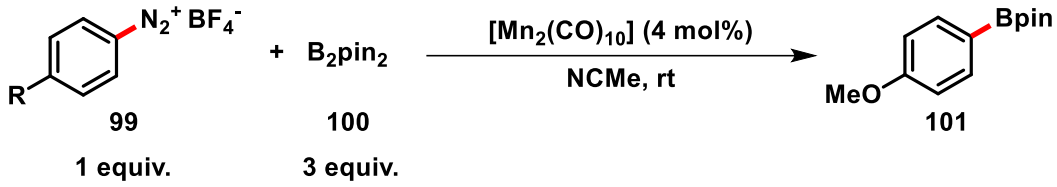

Figure 19. Manganese initiated borylation of aryl diazonium salts studied by Firth co-workers and Liang and co-workers.[70][69]

1.1.8 Radical Initiated Polymerisation Reactions

$[Mn_2(CO)_{10}]$ has also been reported numerous times as a radical initiator in polymerisation reactions.[71–76] The first example was reported by Bamford and co-workers, who used $[Mn_2(CO)_{10}]$ in the presence of carbon tetrachloride as a photochemical initiator (see Figure 1Figure 20). Photochemically generated $[Mn(CO)_5]^{\cdot}$ was proposed to abstract a halide atom, forming a CCl_3 radical, and subsequently polymerising methyl acrylate.[75] Alternatively, fluoro-olefins have been used in the presence of $[Mn_2(CO)_{10}]$, where addition of the $[Mn(CO)_5]^{\cdot}$ radical to the alkene was reported, rather than abstraction of a fluorine atom.[77]

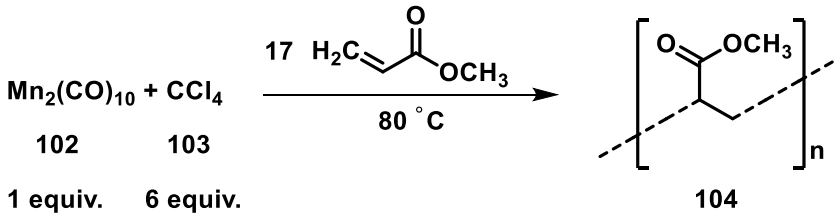

Figure 20. Polymerisation of methyl acrylate initiated by $[Mn_2(CO)_{10}]$.

1.1.9 Manganese (I) Catalysed Hydroarylation Reactions

The dimeric manganese (I) complex $[Mn_2Br_2(CO)_8]$ has been employed in several instances as a precatalyst in hydroarylation reactions (see Figure 21).[78–81] In all instances $[Mn_2Br_2(CO)_8]$ was proven to be significantly more efficient than $[Mn_2(CO)_{10}]$ and monomeric $[MnBr(CO)_5]$. The authors attributed this increased reactivity to the weakly coordinating manganese−bromide bonds, which readily break to form two reactive 16 electron $[MnBr(CO)_4]$ fragments. In contrast, $[MnBr(CO)_5]$ must first lose a CO ligand to form the 16 electron complex $[MnBr(CO)_4]$. Unlike almost all manganese (I) carbonyl catalysed reactions, these proceeded under oxygen rich conditions, and were not requiring of an atmosphere of dinitrogen or argon. This could also be attributed to the change in precatalyst from $[MnBr(CO)_5]$ and $[Mn_2(CO)_{10}]$, to $[Mn_2Br_2(CO)_8]$.

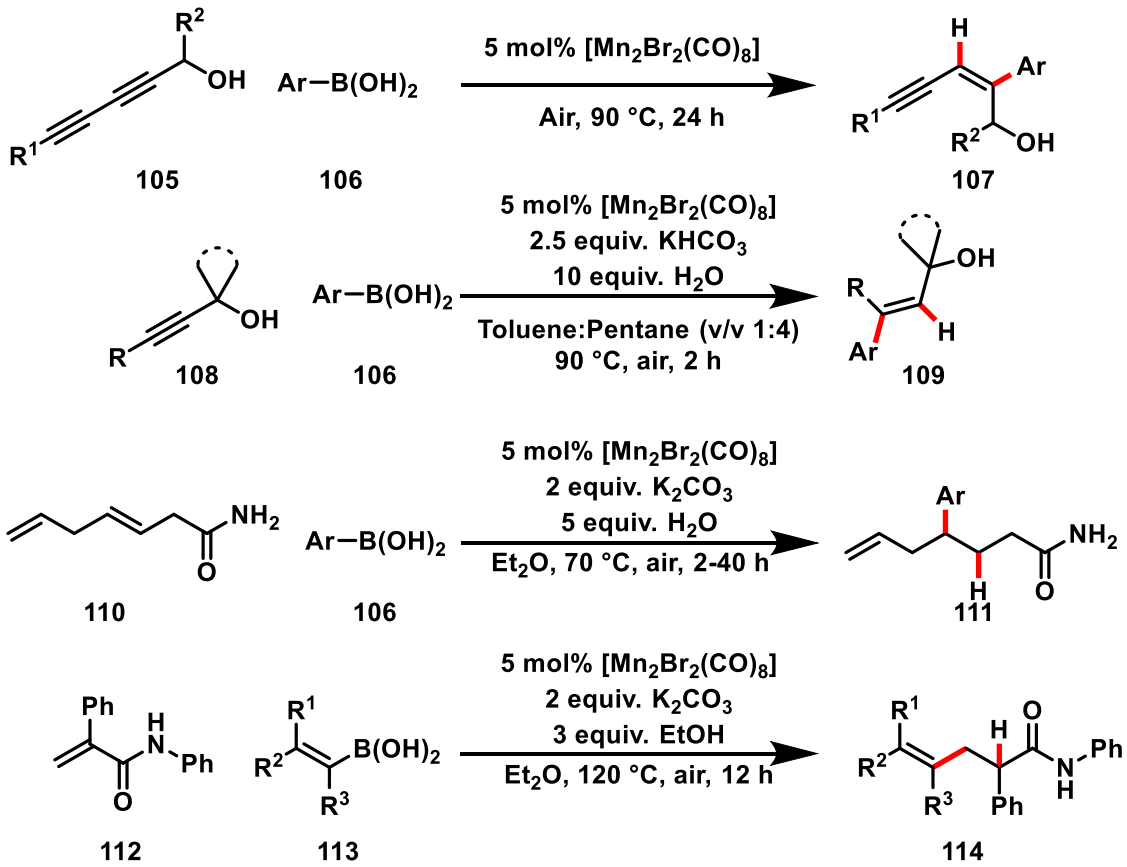

Figure 21. Hydroarylation reactions catalysed by $[Mn_2Br_2(CO)_8]$.[78–81]

1.1.10 Manganese (I) Catalysed Hydrogenation Reactions

Manganese (I) moieties possessing a $[MnBr(CO)_3(L)_2]$ structure have also been synthesised from $[MnBr(CO)_5]$, and used in hydrosilation,[82] hydrogenation[83] and

hydrogen auto transfer reactions.[84] Typically, either phosphorous or nitrogen coordinating ligands have been used in these transformations and the resulting complexes are less prone to deactivation, with catalyst loadings of as low as 0.5% reported.[83,85,86] However, no examples have been reported where these complexes have been reported as precatalysts in C−H bond functionalisation reactions. One example of a $[MnBr(CO)_3(L)_2]$ complex employed as a catalyst was that by Behera and co-workers, who used the $[MnBr(CO)_3(L)_2]$ complex in Figure 22 to selectively carry out the hydrosilylation of esters to alcohols (see Figure 22).[82,87] The reaction showed strong functional group tolerance towards aromatic, aliphatic, electron rich, and electron poor esters. Additionally, industrially relevant alcohols derived from esters present in palm and coconut oil were successfully synthesised in high yields.

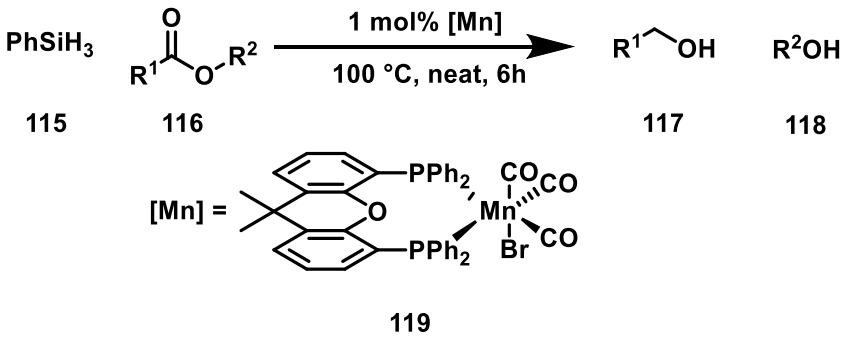

Figure 22. Hydrosilation with a manganese (I) carbonyl precatalyst.[82]

Azouzi and co-workers then demonstrated that by incorporating a chiral ligand, asymmetric hydrogenation of ketones to alcohols could be achieved with enantiomeric excess of up to 99% (see Figure 23).[83,85] These chiral alcohol products are important reagents in the synthesis of many pharmaceutical and agrochemical processes. A series of chiral bidentate aminophosphine ligands were synthesised, and the ligand depicted in Figure 23 was found to give the highest yield while retaining a respectable enantiomeric excess. A mechanism was proposed in which the complexes retain their three CO ligands and *fac* geometry, indicating that they could be suitable candidates for precatalysts in C−H bond functionalisation reactions.[88]

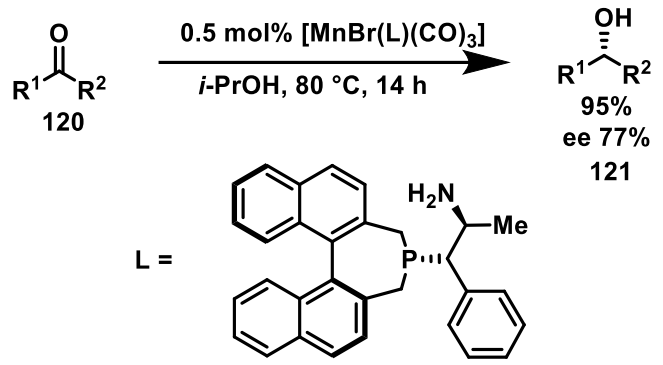

Figure 23. Asymmetric transfer hydrogenation of ketones promoted by manganese(I) pre-catalysts.[83]

The final transformation these $[MnBr(CO)_3(L)_2]$ complexes have been reported to catalyse are hydrogen auto transfer reactions. These provide another method of forming C−C bonds. Typically, an alcohol is dehydrogenated, forming an *in situ* aldehyde or ketone, the C−C bond forms with its coupling partner, and hydrogen reduces the product, in a redox neutral process. A phosphine free example is depicted in Figure 24, highlighting a pincer ligand which possessed both soft and hard hemilabile coordination modes. [84] The reaction by Jana and co-workers demonstrates an unusual example where both an intermolecular and intramolecular borrowing hydrogen reaction occur, producing cycloalkanes *via* a (n+1) annulation of methyl ketones with 1,n-diols).

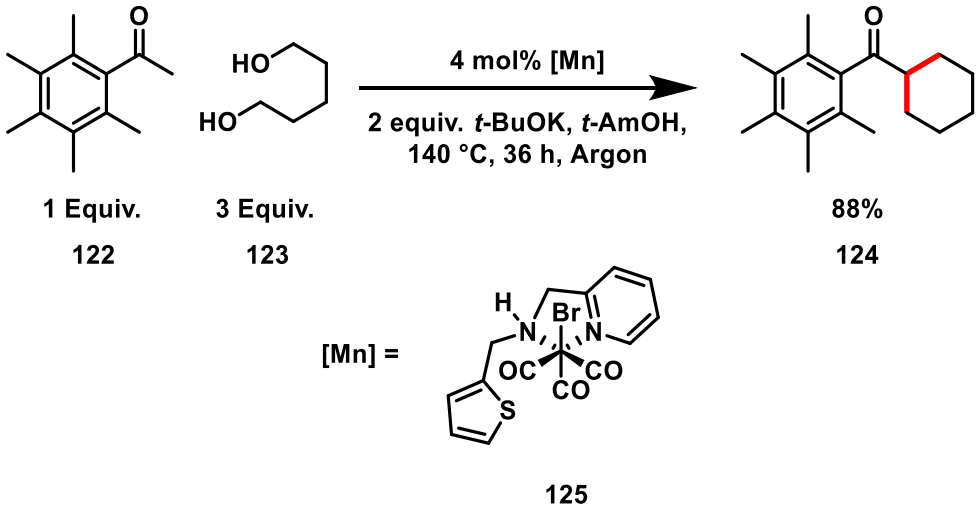

Figure 24. Synthesis of (1 + n)-Membered Cycloalkanes from Methyl Ketones and 1,n-Diols.[84]

In a final example by Schlagbauer and co-workers, a manganese (I) catalysed hydrogen auto transfer reaction where primary and secondary alcohols were methylated was

reported as shown in Figure 25. Here a catalyst loading of 0.1 mol% was used, significantly lower than loadings used in C−H bond functionalisation reactions, indicating that these complexes are less prone to deactivation, with the complex reported to be stable up to a temperature 140 °C.[86] This was surprising as the complex only possessed two CO ligands, which are usually required to stabilise low oxidation states of manganese, due to their strong π- accepting properties. Despite the low catalyst loading, the catalyst was highly tolerant towards challenging conditions in hydrogenation, such as C=C double bonds and iodides, and upscale up of the reaction, completing transformations in under three hours.

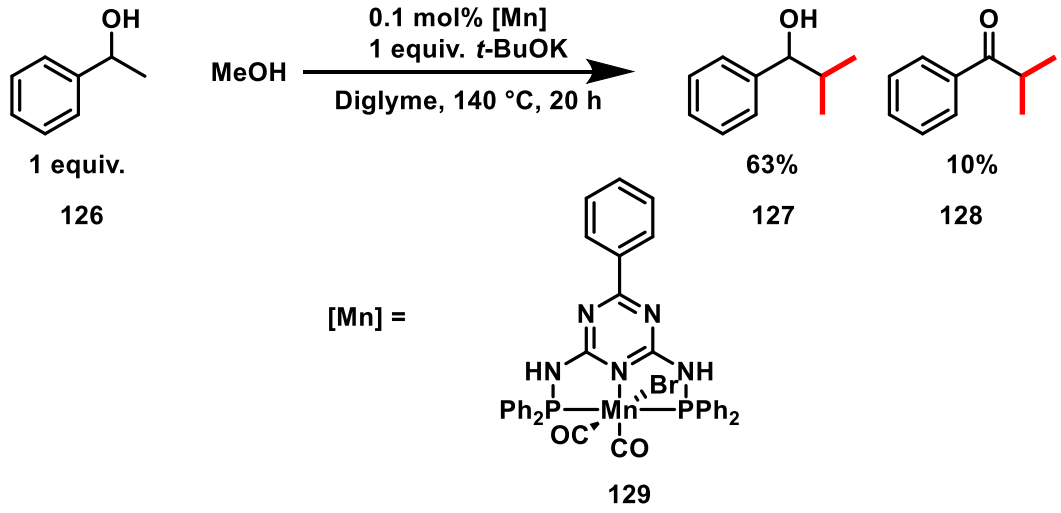

Figure 25. Manganese-Catalysed β-Methylation of Alcohols by Methanol.[86]

1.2 Aims and Objectives

Despite significant advances in the field of manganese carbonyl catalysed C−H bond functionalisation reactions, relatively little mechanistic work has been conducted. Of the work that has been carried out, the focus has been on the activation of $[MnBr(CO)_5]$, which has been conducted by Hammarback and co-workers.[51] The route of activation for $[Mn_2(CO)_{10}]$, a critical precatalyst in C−H bond functionalisation reactions, has never been explored. Furthermore, the behaviour of many other catalytically relevant manganese carbonyl complexes have never been probed.

The aims and objectives of the work in this thesis are:

- Study the reactivity of catalytically relevant 5-membered manganacycles, using the [4+2] annulation of biaryl imines and alkynes reported by He and co-workers as a model reaction (Chapter 2).[60]
    - Time resolved multiple probe spectroscopy will be used to monitor distinctive metal carbonyl bands on a picosecond through to microsecond time scale.
    - Thermal loss of a CO ligand will be mimicked by photochemical excitation with a wavelength of 355 nm.
    - Fundamental behaviour following CO dissociation will be established, before exploring speciation events upon addition of catalytically relevant additives.
- Investigate the methods of activation for commonly used precatalysts in manganese carbonyl catalysed C−H bond functionalisation reactions (Chapter 3).
    - The route of activation for $[Mn_2(CO)_{10}]$ will be established using *in situ* infrared spectroscopy.
    - Speciation leading to the activation of $[MnBr(CO)_5]$ will be compared to prior work by Hammarback and co-workers, establishing if the route of activation is consistent between catalytic systems.[51]
    - Activation of $[Mn_2Br_2(CO)_8]$ will be explored, comparing precatalyst behaviour to monomeric $[MnBr(CO)_5]$.

- The model reaction used herein, reported by He and co-workers, will be optimised further using mechanistic information gathered from the above points.[60]

- Explore the photochemistry of $[Mn_2(CO)_{10}]$ using time resolved multiple probe spectroscopy (Chapter 4).
  - The photochemistry of $[Mn_2(CO)_{10}]$ when excited at 310, 355, and 400 nm will be established and compared with literature data.
  - Ultrafast events between 500 femtoseconds and 25 picoseconds will be determined.
  - The reactivity between $[Mn(CO)_5]^{\cdot}$ and common solvents, organohalides, and catalytically relevant imines will be investigated.
  - The reactivity of $[Mn_2(CO)_9]$ will be established in common solvents and the subsequent reactivity toward catalytically relevant imines.

1.3 Commonly Referred to Compound Numbers

Figure 26 and Figure 27 show the compound numbers which belong to those referenced thoughout the Thesis.

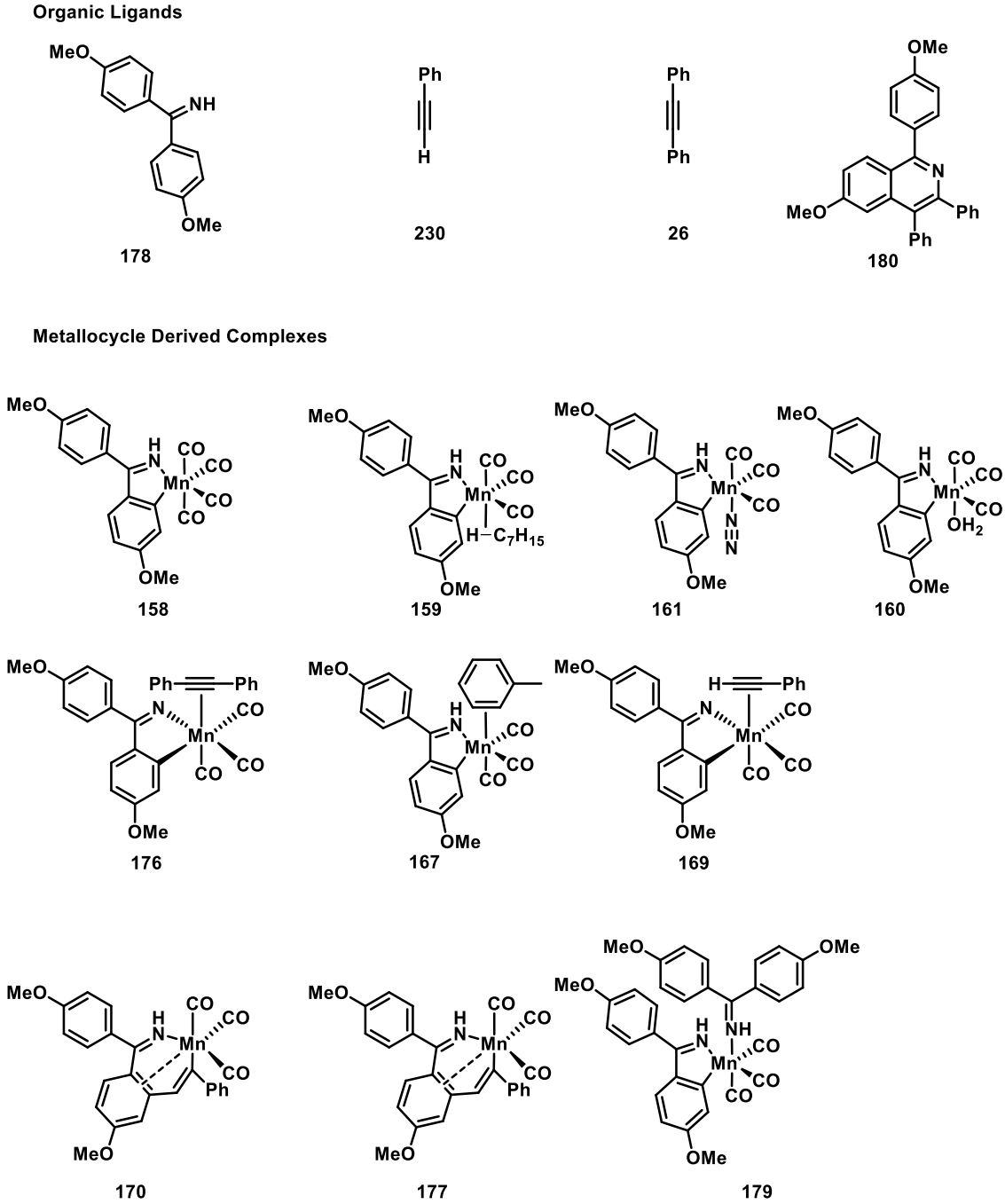

Figure 26. Commonly referred to compound numbers part 1.

[MnBr(CO)$_5$] Derived Complexes

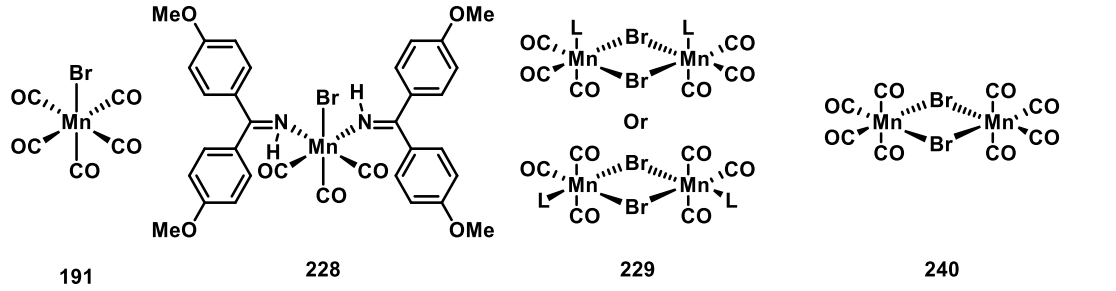

Further Pre-catalysts

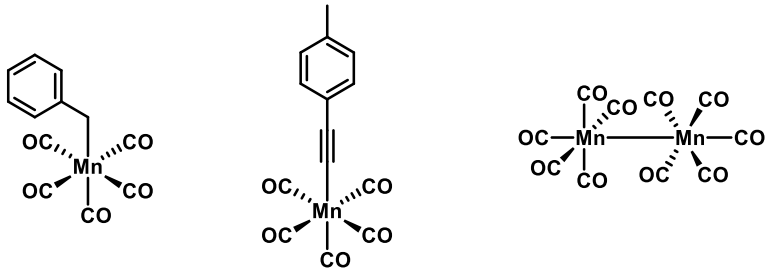

[Mn$_2$(CO)$_{10}$] Derived Complexes

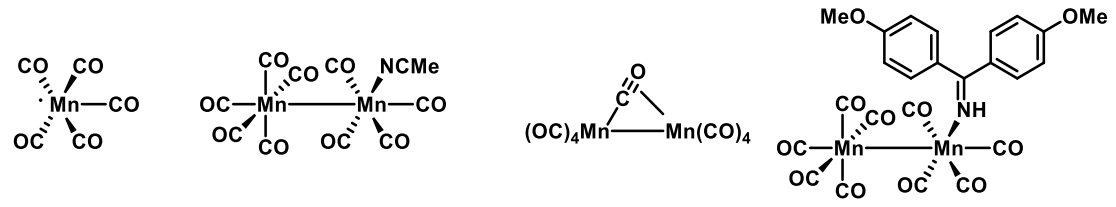

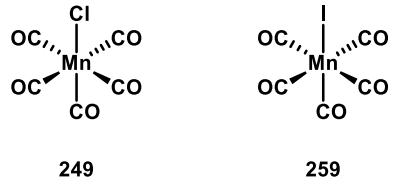

Figure 27. Commonly referred to compounds part 2.

Chapter 2: Ultrafast Time-Resolved Spectroscopy of [Mn(1,1-bis(4-methoxyphenyl)methanimine)$(CO)_4$]

2.1 Background

Metal carbonyl complexes typically have a high UV-visible extinction coefficient, and quantum yield for photochemical alteration.[89] This has made them ideal candidates for ultrafast time resolved studies. A pump-probe technique is often employed, where a UV-Visible pump pulse is used to photochemically alter the compound of interest. Then at a set delay time after the pump pulse, a probe pulse monitors change. Typically, either a UV-visible or infrared probe pulse are used. Transient absorption (TA) spectroscopy uses a UV-visible probe pulse. This enables the probing of sub-picosecond photochemically induced events such as ligand dissociation and geminate recombination, as the technique is not limited by vibrational relaxation of excited states. While time-resolved infrared (TRIR) spectroscopy used an infrared probe pulse and allows observation of photochemically induced events on a picosecond or slower timescale. This includes vibrational relaxation, relaxation of excited states and diffusion limited processes. Metal carbonyl (1800 to 2150 cm^{-1}) stretching frequencies are particularly informative in the infrared region for TRIR. Bands are typically sharp, and highly sensitive to small structural changes occurring at the metal centre, enabling distinction between chemically similar species. The electronic environment at the metal centre controls the energy of the vibrational modes. As this changes, the degree of backbonding into the antibonding orbitals of CO ligands change, weakening or strengthening the C≡O bond, shifting the stretching frequency to lower or higher wavenumber respectively. Additionally, the number of metal carbonyl stretching modes can be easily and accurately predicted though vibrational group theory analysis.

$[Cr(CO)_4$(2,2'-bipyridine)] is a compound that has been intensely probed by both TA and TRIR. Víchová and co-workers used TA to determine that formation of a ^{1}MLCT state causes dissociation of one of the mutually *trans* CO ligands.[90] Subsequent work by Farrell and co-workers used TRIR to follow coordination events after CO dissociation. The photoproduct was determined to be *fac*-$[Cr(CO)_3$(solvent)], with two broad weak

bands at 1791 cm^{-1} and high energy band at 1916 cm^{-1} .[91] Additionally, a non-dissociative ^{3}MLCT state was detected in both the TA and TRIR studies, which relaxed on a ps timescale.

The method of TRIR used in both this Chapter and Chapter 4 is Time-Resolved Multiple Probe Spectroscopy (TR^MPS), carried out at the ULTRA facility in Harwell Oxfordshire. The technique enables ps to ms dynamics to be monitored in a single experiment.[92,93] This is achieved by having the pump and probe laser synchronised at different frequencies, resulting in a pump-probe-probe-probe-…-pump- probe-probe-probe-… sequence (see Figure 28). Thus, a delay of 50 ns, with a probe repetition rate of 100 kHz, would result in spectra generated at 50 ns, 10050 ns, 20050 ns, 30050 ns, …, 990050 ns. This approach, as opposed to manually acquiring data for each time delay, significantly reduces the data acquisition time.

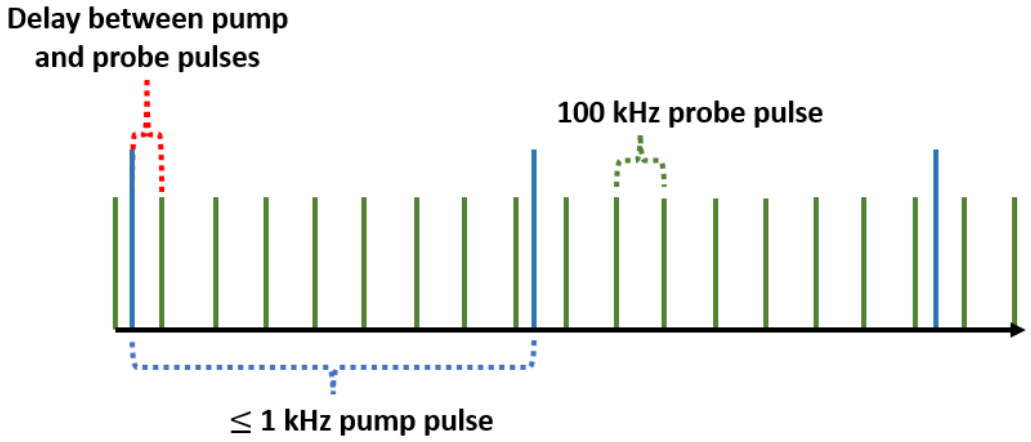

Figure 28. Schematic of the laser pump-probe delays.

Ytterbium potassium gadolinium tungstate (Yb:KGW) amplifiers are used as the pump and probe laser sources. The wavelength is then tuned using optical parametric amplifiers (OPA): 310, 355, or 400 nm for the pump pulses, 1500 to 2300 cm^{-1} for the probe pulses. The pump wavelength then proceeds through an optical delay line. Pump-probe delays of < 12.5 ns are achieved *via* the optical delay line, while longer delays are generated through a combination of the optical and electronic delay lines. The probe beam is the split in two. One beam acts as a reference for each probe beam pulse, accounting for variation in intensity between pulses. The second beam passes through

the Harrick cell containing the sample. The sample itself is pumped around an experimental setup composed of a Duran flask containing a sample reservoir, Harrick cell and peristaltic pump. Continuous flowing of the sample solution, combined with rastering of the Harrick cell, ensures that a build-up of photoproducts does not occur. The probe beam is then acquired on the detector and normalised difference spectra calculated by subtracting a 'pump off' spectrum. The schematic for this is depicted in Figure 29. This results in both positive and negative features in spectra. Negative (bleach) bands represent the loss of starting complex in an experiment. Positive (transient) bands represent the formation of new photoproducts.

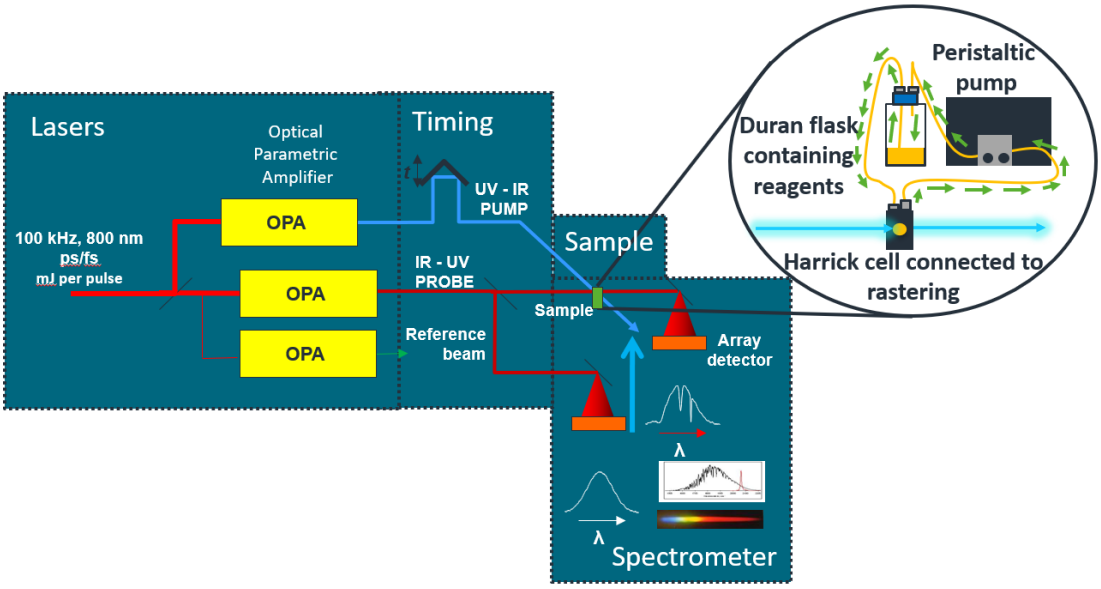

Figure 29. Laser schematic used in TR^{m}PS.

Several studies have used TR^{M}PS to explore ultrafast processes involving manganese (I) carbonyl complexes. In one of the earliest examples Hammarback and co-workers photochemically induced CO loss from [Mn(CO)$_4$(2-phenylpyridine)] **19** by excitation at 355 nm, simulating entry into the catalytic cycle for the alkylation and amidation of 2-phenylpyridine in the presence of *n*-butyl acrylate and 1-isocyanatohexane respectively (see Figure 30 and Figure 31).

When [Mn(CO)$_4$(2-phenylpyridine)] **19** underwent photolysis of a CO ligand in the presence of *n*-butyl acrylate, several binding modes were seen. At early pump-probe delays a σ-alkane complex **130** was observed. This underwent a competitive

rearrangement to form the η^1-(O) and the η^2- C=C coordinated acrylate complexes **131** and **132**. Subsequently, the η^2- C=C bound complex underwent a migratory insertion forming the 7−membered manganacycle **133**.[30]

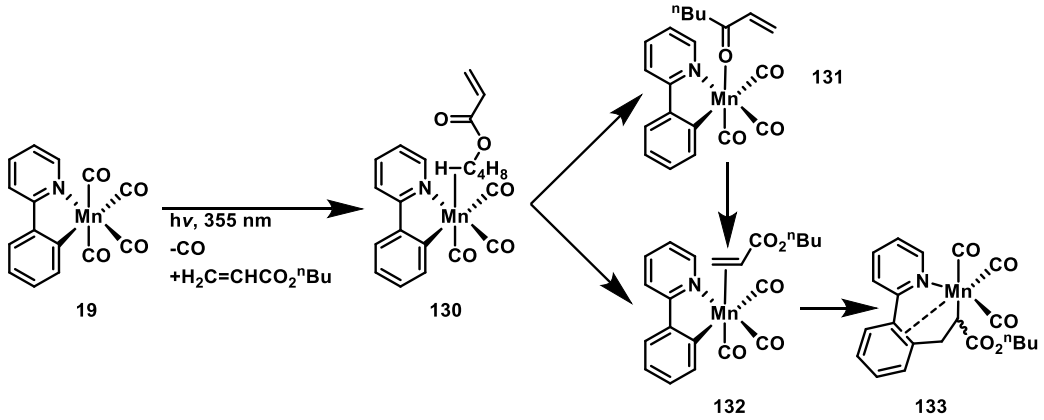

Figure 30. Speciation events reported by Hammarback and co-workers when **19** underwent CO loss in the presence of *n*-butyl acrylate.

Similar observations were also made when **19** underwent photo-induced CO loss in the presence of 1-isocyanatohexane. An initial σ-alkane complex **134** was observed. This rearranged to be η^1-(O) coordinated, and finally η^1-(N) coordinated modes, before inserting to form 7−membered manganacycle **137**. The formation of these complexes was also supported by kinetic analysis, demonstrating that the rate constant, k_{obs} for the loss of one complex corresponded to the formation of the next.

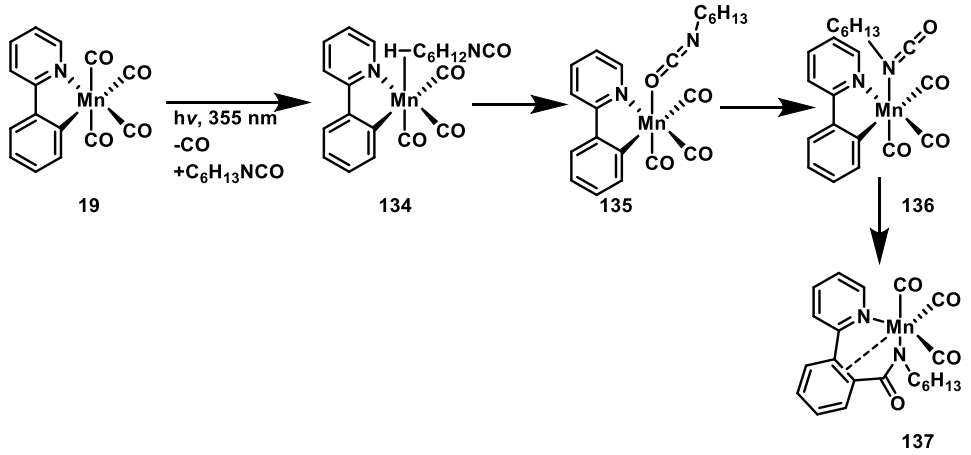

Figure 31. Speciation events reported by Hammarback and co-workers when **19** underwent CO loss in the presence of 1-isocyanatohexane.

TRIR, specifically TR^{M}PS was also used to directly observe the microscopic reverse of the concerted metalation deprotonation step in C−H bond activation (see Figure 32).[94] **19** was excited at 355 nm again, this time in the presence of acetic acid. As with their prior study, an initial σ-alkane coordination complex **138** was reported at early pump-probe delays (*ca*. 5 ps). This underwent rearrangement to a η^1-(O) coordinated complex **139** in *ca*. 50 ps. Over the course of *ca*. 500 ns, the acidic OH proton of acetic acid formed a hydrogen bond with the metal coordinated carbon of 2-phenylpyridine. This was followed by cleavage of the O−H bond and a κ^2-OAc coordinated acetate ligand to form the complex **141**. The cleavage of the O−H bond and formation of **141** was supported by a KIE of 5.8 ± 1.0, when deuterated acetic acid was used.

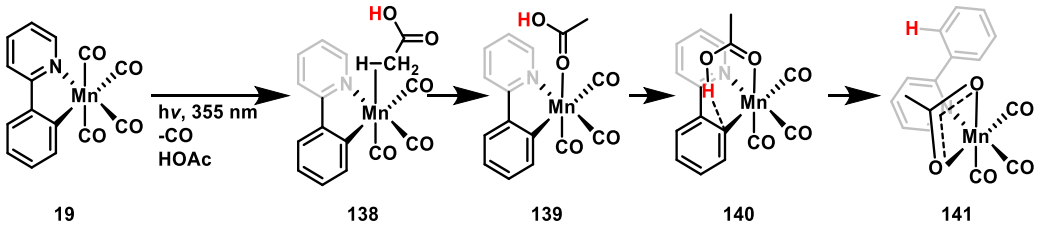

Figure 32. Speciation events reported by Hammarback and co-workers when **19** underwent CO loss in the presence of acetic acid, demonstrating the microscopic reverse of the concerted metalation deprotonation step in C−H bond activation.

Aucott and co-workers also used TR^{M}PS to investigate ultrafast metal−solvent interactions (see Figure 33). **19** underwent photochemical CO dissociation in an array of solvents: toluene, methylene chloride, NCMe, *n*-heptane, THF, 1,4-dioxane, *n*-Bu_2O, and DMSO. As observed by Hammarback, a kinetically favourable σ-C−H coordinated solvent complex was seen in early pump-probe delays for all solvents except NCMe and toluene. These coordinated through a η^1-(N) and η^2-arene coordination mode respectively. The σ-C−H coordinated solvent complexes then proceeded to rearrange to their heteroatom coordinated counterparts at later pump-probe delays. At early pump-probe delays ^{3}[**19**] was also observed with a lifetime, τ, of 4.1 ± 0.2 ps, red shifted from the ground state bands of **19** in *n*-heptane, THF and NCMe.

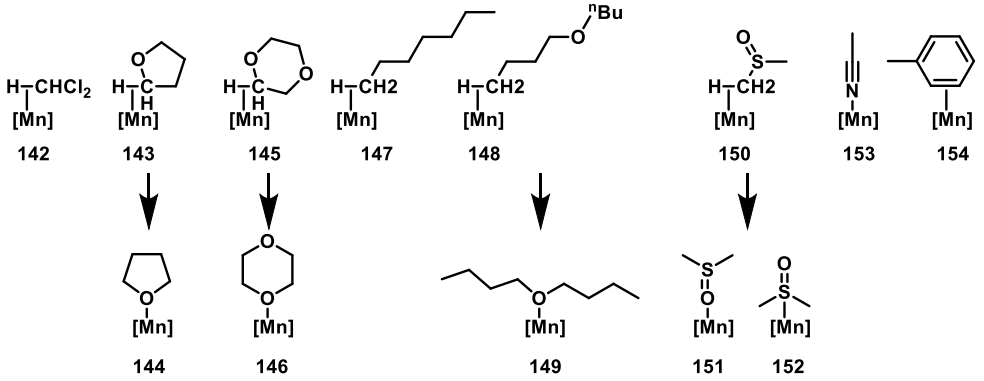

Figure 33. Coordination modes of solvents to **19** reported by Aucott and co-workers. [Mn] = *fac*-[Mn(2-phenylpyridine)$(CO)_3$].

The nature of photochemical release of CO from trypto-CORM (CO Releasing Molecule) **155**, another manganese (I) carbonyl complex, was probed by TR^{M}PS and DFT.[95] Ultimately, it was established that photolysis of trypto-CORM at 400 nm resulted in the formation of vibrationally 'hot' ^{3}[Mn(tryp)$(CO)_2$(NCMe)] **156**. Once in the ground electronic state (**156**), coordination of a NCMe ligand was observed by *ca*. 100 ps. The relaxation from a triplet to singlet excited state enabled the coordination of solvent. This formed *all-cis*-[Mn(tryp)$(CO)_2$$(NCMe)_2$] **157**, which remained for the duration of the experiment (see Figure 34).

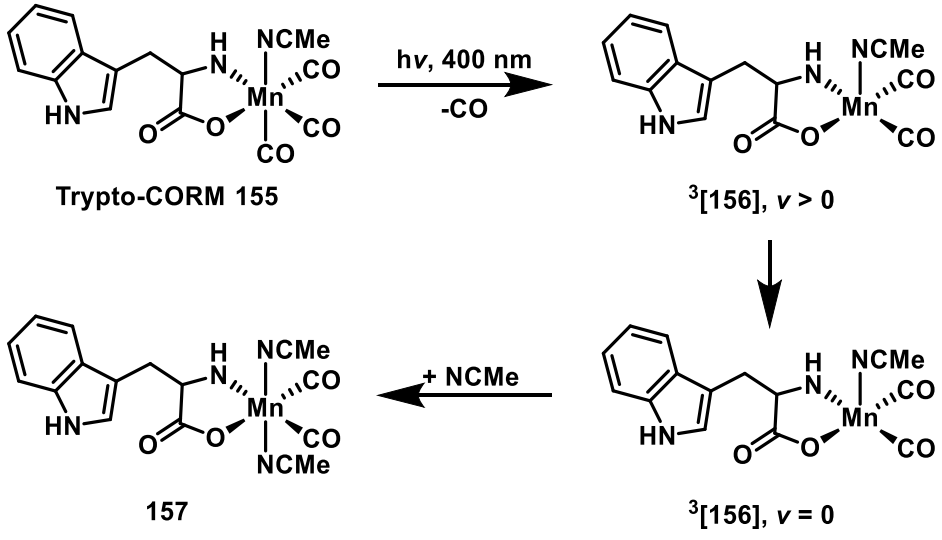

Figure 34. Mechanism for the photochemically induced loss of CO from trypto-CORM proposed by Aucott and co-workers. [95]

Thus, TR^{M}PS has been used to investigate several manganese (I) carbonyl complexes and their respective systems.[94,96] This has enabled the observation of both short and long-

lived photoproducts, and when combined with structural determination through carefully designed experiments, such studies have led to a greater understanding of the mechanistic nuances in these systems.

2.2 Aims and Objectives

The aims of this Chapter are to probe aspects of the mechanistic cycle proposed by He and co-workers for the [4+2] annulation of primary imines and alkynes forming an isoquinoline.[60] Time resolved multiple probe spectroscopy will be used as the primary methodology for exploring the system. As with the original synthetic methodology, 1,1-bis(4-methoxyphenyl)methanimine **178** and diphenyl acetylene were chosen as the model substrates for the system, along with the terminal alkyne phenyl acetylene. The 5-membered manganacycle derived from **178** enabled a controlled entry into the catalytic cycle. At room temperature the complex is thermally stable in solution. However, irradiation at 355 nm should photochemically dissociate a CO ligand, mimicking the thermal loss of a CO ligand. Which is proposed to occur in the catalyst pre-activation step.

The fundamental behaviour of the on cycle catalytic species will then be explored between 1 ps and 100 μs in *n*-heptane, a weakly coordinating solvent, which gives well defined peaks. Repeat experiments will then be conducted in toluene, a catalytically relevant solvent reported by He and co-workers.[60] Following this, catalytically relevant substrates (imines and alkynes) and isoquinoline product will be introduced and subsequent speciation followed. Finally, the less electronically rich 5-membered manganacycle **182** will be used to assess the impact of electronics on the observed processes, to aid with understanding how the electronics of the imine would likely impact the catalysis.

2.3 Ground state [Mn(1,1-bis(4-methoxyphenyl)methanimine)(CO)$_4$]

[Mn(1,1-bis(4-methoxyphenyl)methanimine)(CO)$_4$], **158**, is a proposed on cycle intermediate in the manganese (I)-catalysed [4+2] annulation of NH imines and alkynes reported by He and co-workers.[60] Previous mechanistic investigations also revealed 5−membered manganacycles to be key reaction intermediates within the catalytic cycle.[30,51,94]

158 possesses four bands in the metal carbonyl region (1850−2150 cm^{-1}), which are associated with various stretching modes. As shown in Figure 35, these are situated at 1940, 1980, 1990, and 2074 cm^{-1} in heptane solution.

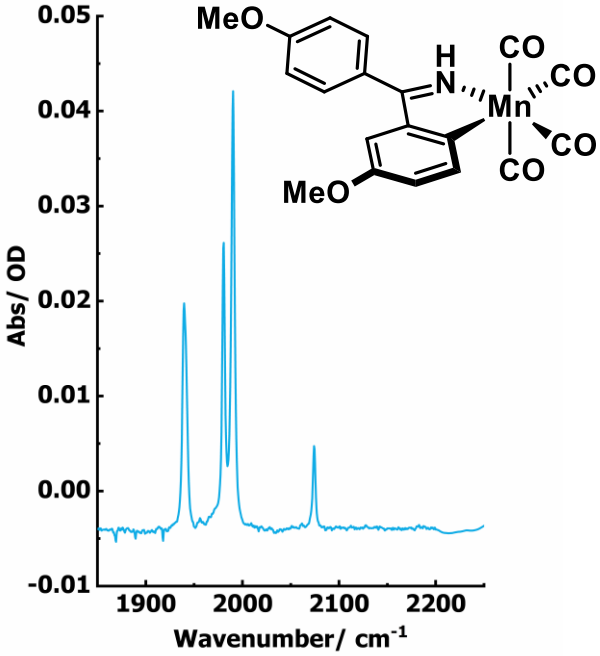

Figure 35. Ground state infrared spectrum of [Mn(1,1-bis(4-methoxyphenyl)methanimine)(CO)$_4$] **158** in heptane between 1850 and 2250 cm^{-1}.

The experimentally observed infrared active modes conform with those predicted though vibrational group theory analysis. **158** can be approximated to fit the *pseudo*-C_{2v} point group, following the assumption that the coordinated C and N atoms possess

similar mass, bond length and angles. If these requirements were not met, then **158** would belong to the C_s point group.

Table 1. Character table for the C_{2v} point group.

C_{2v}	E	$C_2(z)$	$\sigma_v(xz)$	$\sigma_v(yz)$	Linear functions
A_1	+1	+1	+1	+1	z
A_2	+1	+1	-1	-1	
B_1	+1	-1	+1	-1	x
B_2	+1	-1	-1	+1	y

The C_{2v} point group is composed of two mirror planes $\sigma_v(xz)$, $\sigma_v(yz)$, a $C_2(z)$ axis, and the identity E (see Table 1). Application of these symmetry elements to the CO ligands of **158** results in the reducible representation $\Gamma_{vib}(CO) = 4E + 2\sigma_v(xz) + 2\sigma_v(yz)$. Inspection of the point group table and application of Equation 1 reveals $2A_1 + B_1 + B_2$ to be the irreducible representation. Following the infrared active modes in Table 1, all of the stretching modes are predicted to be infrared active- reflecting the recorded infrared spectrum of **158**.

$$n = \frac{\sum N \times X_I \times X_R}{h}$$

Equation 1. N is the coefficient of a symmetry element, X_I the value in the character table, and X_R the value obtained from the reducible representation.

Prior work by Vlček and co-workers demonstrated that for a metal carbonyl complex [*cis*-$M(CO)_4L_2$]: the highest intensity band belongs to the B_1 asymmetric stretch of axial CO ligands; the lowest energy band being due to the B_2 asymmetric stretch of equatorial CO ligands; the highest energy band caused by one of the A_1 symmetric stretches; and the remaining band assigned as the final A_1 symmetric stretching mode (see Figure 36).[97] This rational was applied, and used in the assignment of metal carbonyl stretching modes of **158**.

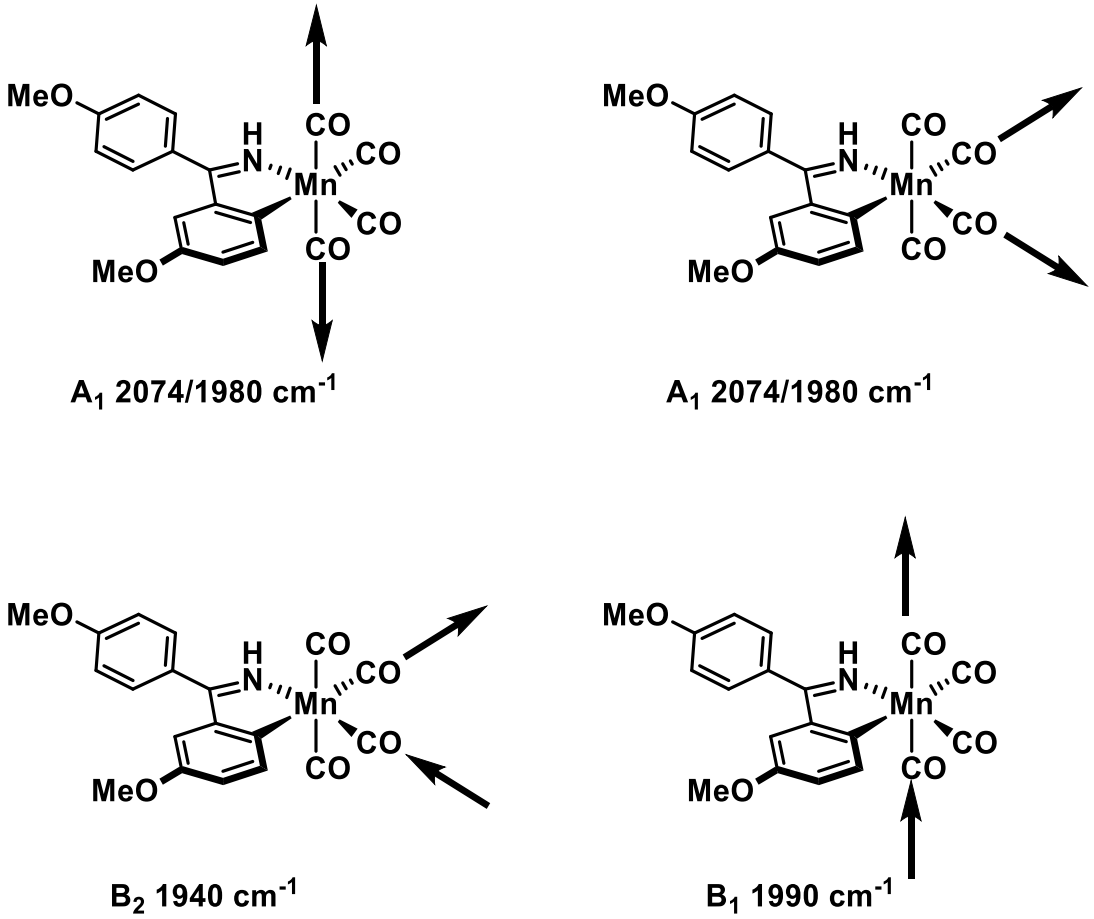

Figure 36. Assigned CO stretching modes of **158** in heptane solution from Figure 35 based on prior work by Vlček and co-workers. [97] A_1, B_1, and B_2 refer to the assigned IR active mode and XXXX cm^{-1} refers to the peak position in Figure 35.

To photochemically mimic the thermal activation of **158**, an electronic transition must occur which is CO dissociative. A UV-visible spectrum of **158** in toluene solution revealed a shoulder band at λ_{max} of 339 nm (see Figure 37). Studies by Aucott and co-workers on the similar complex [Mn(2-phenylpyridine)$(CO)_4$] **19** exhibited a shoulder band absorbing between 325−425 nm. Computational studies demonstrated that a component of the lowest energy allowed transition was the HOMO-1 → LUMO MLCT. This resulted in depopulation of the M−C bonding orbitals of the two mutually *trans* CO ligands, causing CO dissociation.[96] For the ultrafast time-resolved studies on **158**, a pump wavelength of 355 nm was chosen, enabling comparison to similar literature, while being close to the λ_{max}.[51,94–96]

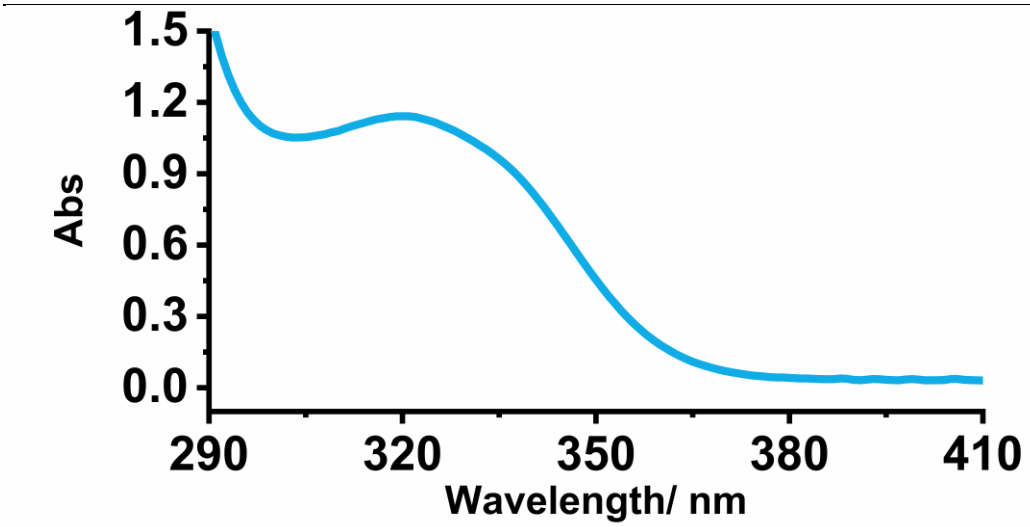

Figure 37. UV-Visible spectrum of **158** [Mn(1,1-bis(4-methoxyphenyl)methanimine)$(CO)_4$] in toluene.

2.4 Time-Resolved Multiple Probe Spectroscopy (TR^MPS)

Photochemical studies on [Mn(1,1-bis(4-methoxyphenyl)methanimine)$(CO)_4$] were conducted using a pump wavelength of 355 nm, and typically probed between 1850 and 2150 cm^{-1} (expanded to 2300 cm^{-1} where necessary). **158** (2 mmol dm^{-3}) in either anhydrous *n*-heptane or anhydrous toluene. *n*-Heptane has fewer solvent interactions with ground state **158** and photoproducts, resulting in sharper, well-defined bands. Weaker solvent coordination also enables the coordination and observation of weakly coordinating catalytically relevant ligands. Toluene gives an insight into the impact of a more strongly coordinating solvent; and enables comparison to catalytically relevant conditions.[60]

2.4.1 Solvents: *n*-Heptane

Initially, experiments were carried out in anhydrous *n*-heptane. This was to ensure that there were minimal interactions between the solvent and complexes, resulting in sharper, deconvoluted bands of photoproducts, to aid with assignment. Furthermore, by using a very weakly coordinating solvent, displacement of any bound solvent molecules is easy, allowing the possibility to observe complexes with poorly coordinating ligands.

Photolysis of [Mn(1,1-bis(4-methoxyphenyl)methanimine)$(CO)_4$] **158** in heptane solution at 355 nm was studied *via* TR^MPS, observing events between 1 ps and 998.5 µs post excitation. Following the general procedure for data analysis, as discussed in experimental Chapter 6.1.9, data are presented in the form of difference spectra. Consequently, spectra possess both positive and negative features. Positive bands represent photoproducts formed during an experiment, while the negative bands depict loss of the ground state complex **158**.

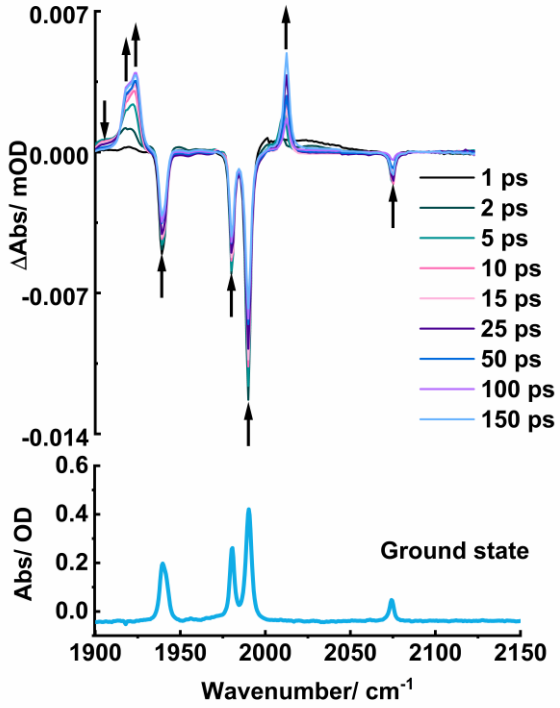

Figure 38. TRIR spectra of **158** in heptane solution under an atmosphere of N_2 at selected pump-probe delays between 1 and 150 ps. Arrows denote the change in band intensity.

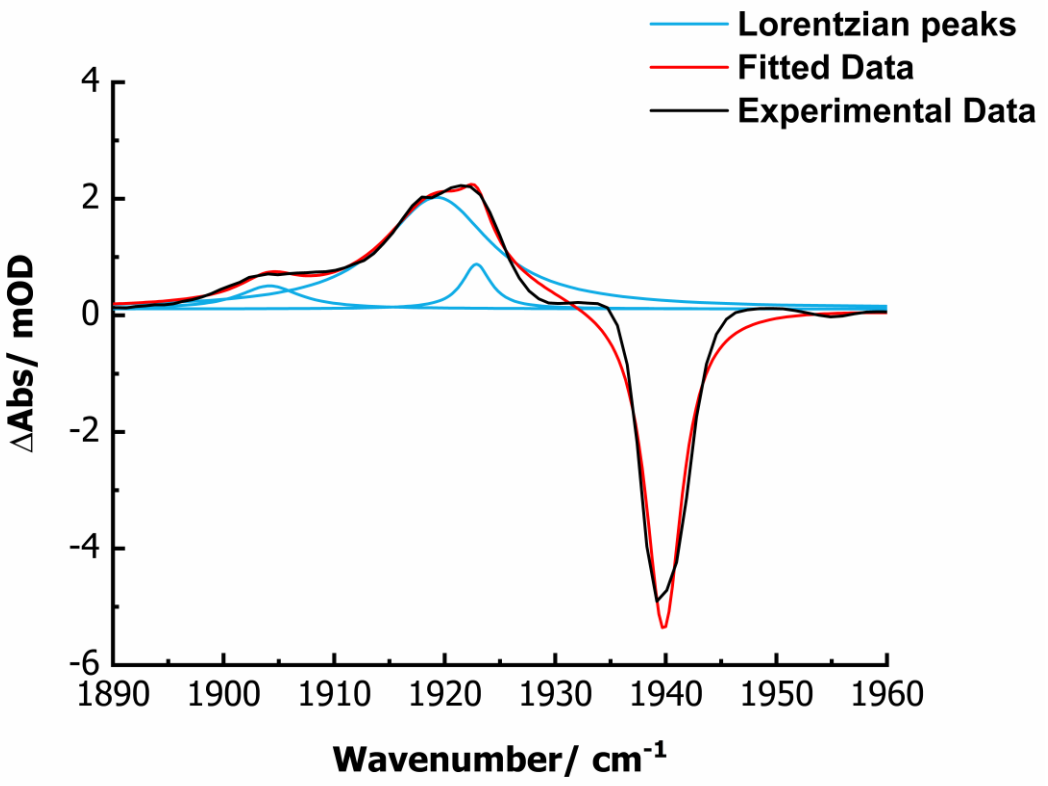

Figure 39. Zoomed in spectrum between 1890 and 1960 cm^{-1} of the spectrum in Figure 38. at 4 ps with fitted data using a Lorentzian peak functions. Black line depicts experimental data, red line depicts fitted data, and blue lines depict transient Lorentzian peaks used in the fitted data.

At the earliest pump-probe delay (1 ps), four transient and four bleach bands were observed (see Figure 38). The four bleach bands indicate loss of the starting complex **158**. The three major transient bands sharpen and shift to higher energy over the course of *ca*. 150 ps, resulting in stretching frequencies at 1917, 1923, and 2008 cm^{-1}. The four bleach bands and three major transient bands are indicative of photochemical CO loss. The changes in band shape and position are consistent with that of vibrational cooling of 'hot' photoproducts. Their presence is due to excess energy applied by the excitation wavelength of 355 nm, compared to that required to dissociate a CO ligand. This results in photoproducts initially populating vibrational energy levels greater than $v = 0$. Due to the anharmonic nature of the vibrational energy well, as relaxation occurs, the energy associated with Δv increases[98], causing the observed blue shift over *ca*. 150 ps as demonstrated in Figure 40. The fourth lower energy transient band situated at 1905 cm^{-1} was confirmed through the fitting of the spectrum obtained at 4 ps with Lorentzian peaks for the four transient and bleach bands, which resulted in the fitted data in Figure

39, confirming the presence of the fourth weaker transient band. This band was observed to decay with a lifetime, τ, of 26.4 ± 0.8 ps obtained through the modelling of an exponential fit (errors reported are the 95% confidence intervals). This was consistent with the partial recovery of the bleach bands for **158**, with a lifetime, τ, of (26.7 ± 2.6) ps, obtained through the same analysis (see Figure 40). This supports the assignment of the band at 1905 cm^{-1} as **158** in the vibrational energy level greater than v = 0, which relaxes to ground state **158**, accounting for the partial bleach recovery. A likely source of vibrationally excited **158** was from the partial recombination of the original CO ligand *via* geminate recombination (*ca.* < 1ps) , which still possesses excess energy from the photon it absorbed, accounting for the population of the v = 1 energy level.

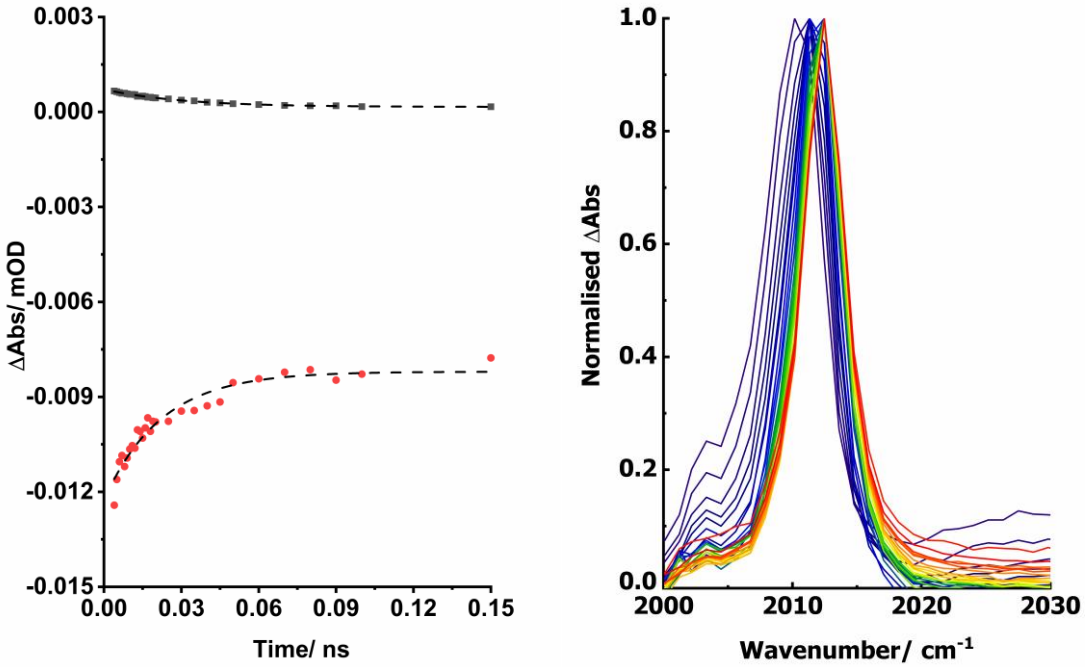

Figure 40. Left: Kinetics for the loss of the band at 1905 cm^{-1} (Black) and ground state recovery of **158** at 1990 cm^{-1} (Red). Right: Normalised spectra of the high energy band for **158** at 2008 cm^{-1} showing the shift in band position as vibrational relaxation occurs. Purple to blue to green to yellow to red depicts early to long (4-150 ps) pump-probe delays

In Figure 38 the long-lived transient bands are typical of a tricarbonyl species indicating that CO dissociation has occurred. The positioning of bands supports a *fac*-

[Mn(C^N)(X)(CO)$_3$] geometry, rather than the *mer*-[Mn(C^N)(X)(CO)$_3$] isomer. [91], [96] ((C^N) refers to the ligand bis-(4-methoxyphenyl)methanimine). For a *facially* orientated set of three metal carbonyl ligands, two broad bands at lower energy caused by asymmetric stretching of the metal carbonyls and one sharp band at higher energy due to the symmetric stretch are expected. [91], [96] Whereas the opposite pattern is expected for the *meridional* arrangement. [91], [96] Dissociation of one of the mutually *trans* CO ligands was expected, due to the mutually destabilising effect, supporting the assignment of the *facial* isomer.

The three bands at 1917, 1923, and 2008 cm^{-1} were assigned as the σ-coordinated heptane complex, *fac*-[Mn(C^N)(CO)$_3$(C$_7$H$_{16}$)] **159**. A long-lived excited state such as ^{3}[**158**] can be ruled out. Four stretching modes rather than three would be expected, and it is highly unlikely that ^{3}[**158**] would still exist after 1 μs. Another proposed possible candidate for the photoproduct was the 16 electron complex *fac*-[Mn(C^N)(CO)$_3$]. However, in prior work by Aucott and co-workers, instantaneous coordination of solvent was seen in all instances where analogous [Mn(CO)$_4$(ppy)] was photolysed at 355 nm. [96] This included *n*-heptane.[96] This is likely due to *fac*-[Mn(C^N)(CO)$_3$) possessing very high Lewis acidity. Perutz demonstrated this with [Cr(CO)$_5$] possessing Cr–Xe interactions when [Cr(CO)$_6$] lost a CO ligand in a xenon matrix.[99] Thus, coordination of the *n*-heptane ligand is highly likely. This is further supported by the diffusion limited rate, which is 2.35 × 10^{10} mol^{-1} dm^3 s^{-1} at 20 °C in *n*-heptane, implying that coordination of other ligand such as H_2O is highly unlikely to occur within 1 ps.[100]

Direct measurement of the extinction coefficients for short-lived species was not possible. At 150 ps only bleach bands for loss of ground state **158**, and transient bands associated with **159** are present. This enabled an approximation for the concentration of **159**, using the assumption that the concentration of **158** lost equals the concentration of **159** formed. Beer-Lambert plots were produced for **158** in *n*-heptane solution (see Chapter 6.4 Figure 220 to Figure 223), giving extinction coefficients for the four metal carbonyl stretching modes belonging to **158**.

Table 2. Extinction coefficients for the IR bands of **158** at 1940, 1980, 1990, and 2074 cm^{-1}.

	Metal carbonyl band of **158**/ cm^{-1}			
	1940	1980	1990	2074
Extinction coefficient ε / mol^{-1} dm μm^{-1}	0.67 ± 0.14	0.79 ± 0.11	1.2 ± 0.16	0.22 ± 0.03

Using the values of ε in Table 2 and the intensity of bleach bands at 150 ps in Figure 38, the concentration of long-lived photoproduct **159** was approximated to be between 4.5 and 5.8 $\times 10^{-5}$ mmol dm^{-3}.

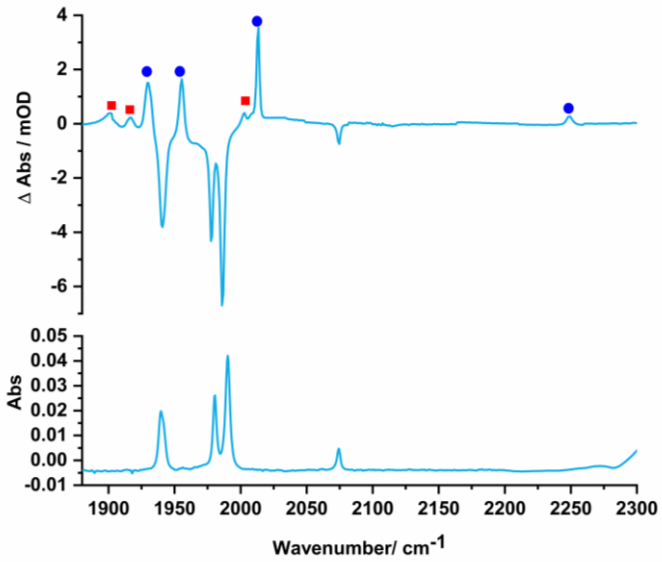

Figure 41. Top: TRIR spectrum of **158** in heptane solution under an N_2 atmosphere at 500 ns. The red square and blue dot denote the major and minor species formed. Bottom: Ground state FTIR spectrum of **158** in *n*-heptane.

Over the course of *ca*. 100 ns, the metal carbonyl bands assigned to *n*-heptane coordinated complex **159** depleted. Two sets of bands replaced **159**. The minor species formed with a rate constant, k_{obs}, of 4.8 ± 0.67 × 10^7 s^{-1} and the transient exhibited a red shift from **159**, with three bands at 1900, 1913, and 2002 cm^{-1}. Conversely, the bands of the major species underwent a blue shift to 1929, 1955, and 2013 cm^{-1} (see Figure 41). These formed with a rate constant, k_{obs}, of 3.2 ± 0.67 × 10^7 s^{-1}. At later pump-

probe delays, *ca*. 1.5 µs, equilibration resulted in loss of the minor species. Depletion of the minor species occurred with a rate constant, k_{obs}, of 4.1 ± 1.1 × 10^6 s^{-1} and further formation of the major species with a rate constant, k_{obs}, of 3.1 ± 0.67 × 10^6 s^{-1} (see Figure 42).

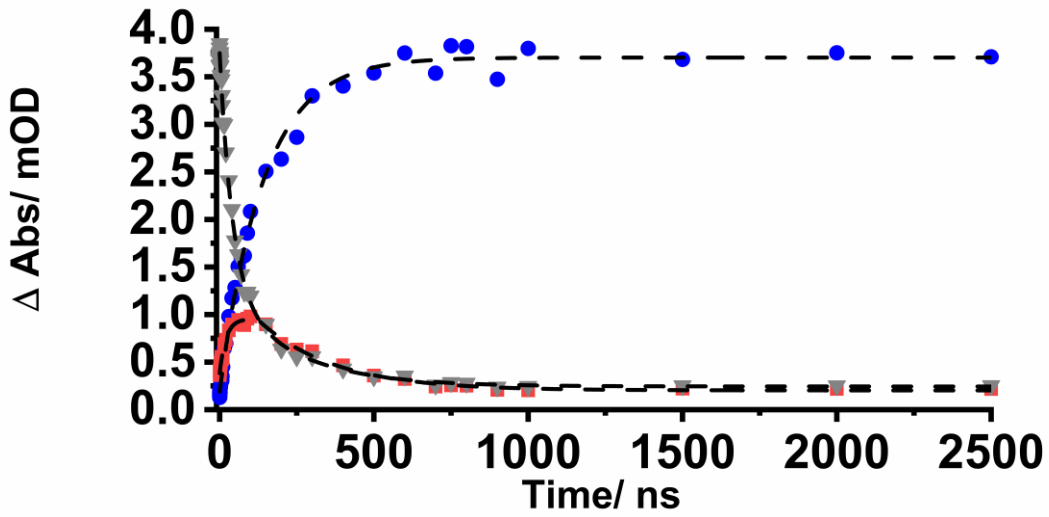

Figure 42. Kinetics for the loss of **159** and formation/ equilibration of **160** and **161**. **159** denoted by grey triangles, **160** denoted by red squares and **161** denoted by blue circles. Dotted lines denote exponential kinetics. Where appropriate a mono or biexponential fit was applied.

Both newly formed species still exhibited three metal carbonyl bands positioned to suggest *facial* tricarbonyl complexes, which would be expected if the poorly coordinating *n*-heptane ligand had undergone displacement. An additional band was observed at 2249 cm^{-1}, which was not assigned as a metal carbonyl stretching mode due to its high energy. The red shift in bands indicates coordination of an electron donating and/or poorly accepting π ligand. This ligand causes more electron density on the metal centre, which undergoes π-backbonding into the antibonding orbitals of the carbonyl ligands. This in turn reduces the bond order of the carbonyl ligands, shifting their vibrational frequencies to lower energy. Likewise, the blue shift in bands implies coordination of a less σ electron donating/ greater π-accepting ligand than *n*-heptane. This results in less π-backbonding to the coordinated carbonyl ligands, shifting their position to higher energy.

An initial hypothesis was put forth; the minor species had undergone coordination with an electron-rich water molecule, whereas the major species had undergone coordination with a π-accepting dinitrogen molecule.

In order to probe the coordination of OH_2, one drop (approx. 5 µL) of water was added to the system containing 20 mL of anhydrous *n*-heptane (see Figure 43). Under the assumption that 5 µL of water was added, a concentration of approx. 2000 ppm of water was present. The solubility of water in *n*-heptane is reported to be 82 ppm at 298 K, meaning that a saturated solution of water in *n*-heptane was achieved.[101]

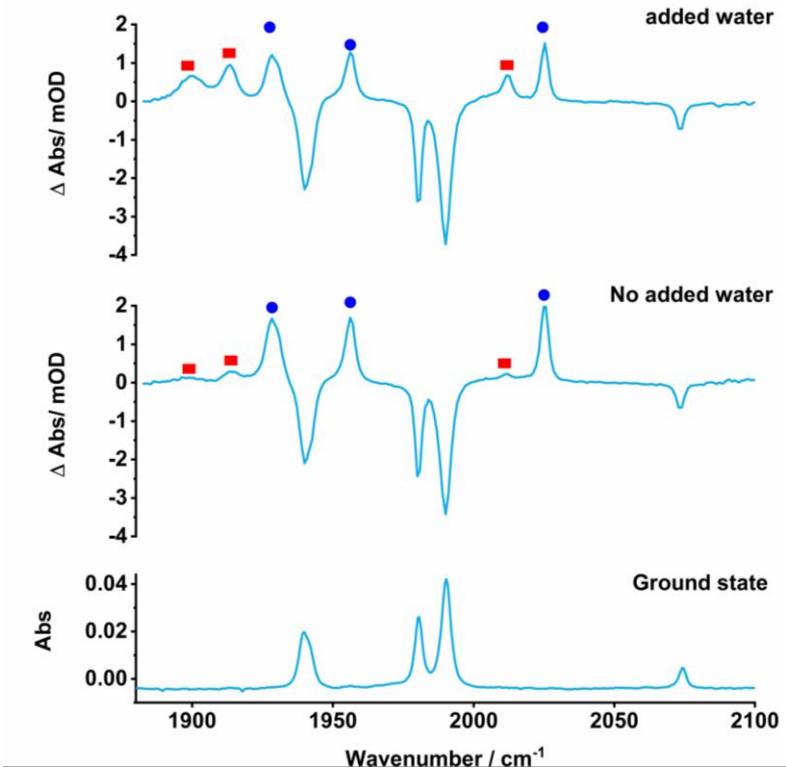

Figure 43. TRIR spectra of **158** in heptane solution with varied quantities of H_2O at a 500 ns pump-probe delay. Top) anhydrous *n*-heptane, Middle) saturated water in *n*-heptane solution, Bottom) ground state spectrum of **158**. Red square denotes **160**, and blue circle denotes **161**.

In this experiment, the proportion of **160** with respect to **161** (see Table 3) increased significantly, giving an insight into the nature of **160**. An increased intensity of bands assigned to **160** upon use of a saturated water in *n*-heptane solution supported the hypothesis that OH_2 had coordinated to Mn. **160** was thus proposed to be *fac*-$[Mn(C^N)(OH_2)(CO)_3]$.

Further repeats were conducted with varied sparge gasses, to aid with the elucidation of the structure of **161**, and provide further evidence for the coordination of OH_2 in **160**; $^{15}N_2$, Ar, and air were used in conjunction with anhydrous *n*-heptane. The impact of these sparge gasses is depicted in Figure 44.

Under an argon atmosphere, in which no N_2 was present, the metal carbonyl and high energy bands assigned to **161** were no longer detected. Instead, the intensity of the metal carbonyl stretches associated with **160** increased, due to the removal of competition with dinitrogen. The *n*-heptane bound complex **159** was also observed at the chosen pump-probe delay of 500 ns, being displaced by further water molecules at later pump-probe delays. This supported they hypothesis that **161** was a dinitrogen bound *fac*-tricarbonyl complex.

Further evidence was given when the system was sparged with $^{15}N_2$. The concentration of N_2 was assumed to be 9.54 mmol dm^{-3} based on literature values for the solubility of N_2 in heptane at 25 °C.[100] This ensured that there was a large excess of $^{15}N_2$ compared to the concentration of **159**. Using the assumption that the high energy stretching mode (2249 cm^{-1}) belonged to the N≡N stretch of bound dinitrogen, a shift in stretching frequency could be predicted using a basic harmonic oscillator model. Using the reduced mass of ^{14}N and ^{15}N, the stretching frequency for $^{15}N_2$ was predicted to be $2249 \times \frac{\sqrt[2]{14}}{\sqrt[2]{15}} = 2173$ cm^{-1}. An experimental frequency of 2174 cm^{-1} was seen, further securing our assignment of **161** as a *fac*-[Mn(C^N)$(CO)_3$ (N_2)]. Unsurprisingly, the metal carbonyl stretching frequencies remained unchanged when sparging with $^{15}N_2$ instead of $^{14}N_2$, no change in reduced mass for the CO ligand, or electronics in the complex occurred.

Finally, air was used as a sparge gas for the system. Again, this led to formation of the dinitrogen complex **161**. Under an atmosphere of air, the relative intensity of bands associated with the water bound complex **160** increased. This was likely due to additional water solubilised into the *n*-heptane *via* water vapour in the air. No evidence was seen to suggest coordination of a dioxygen complex under these conditions. The isoelectronic properties of N_2 with CO could explain the preferential binding of dinitrogen over dioxygen.

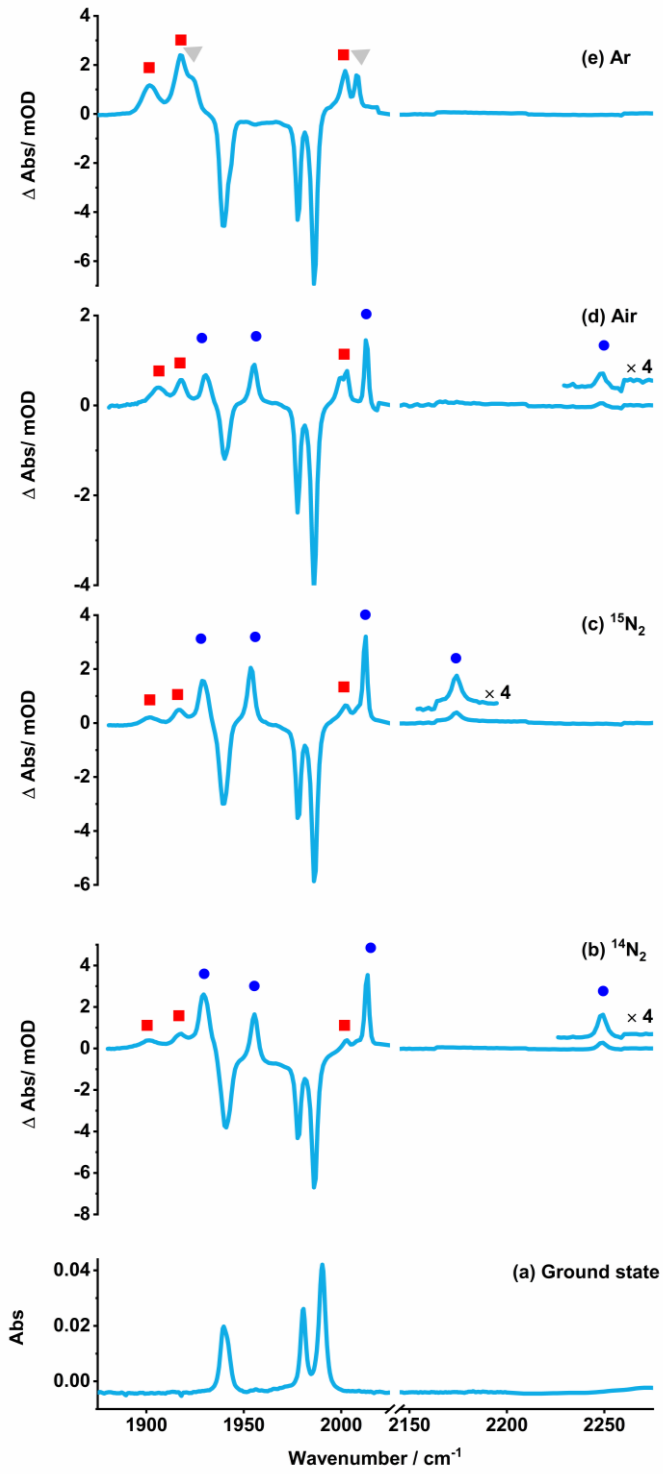

Figure 44. TRIR spectra of **158** in heptane solution using various sparge gasses at a pump-probe delay of 500 ns. Grey triangle denotes **159**, Red square denotes **160**, and blue circle denotes **161**.

Table 3. Ratio of **160** to **161** under various conditions.

Sparge gas	Additive	Ratio of [**161**]:[**160**]
Air	None	1.8 : 1
$^{14}N_2$	None	8.9 : 1
$^{15}N_2$	None	9.4 : 1
N_2	H_2O	2.2 : 1
Argon	None	0.0 : 1

Two binding modes of N_2 exist. End on (η^1) acting as a σ-donor and π-acceptor, or side on (η^2) where the ligand acts as a π-donor. The coordination mode in our system is highly likely to be end on coordination. Only a handful of manganese complexes exist with a coordinated N_2 ligand, these are depicted below in Figure 45, and all exist in the end-on coordination mode. The ligand in our system caused a blue shift when displacing σ-coordinated *n*-heptane, implying that the ligand caused a net decrease in electron density at the metal centre. This would only be possible in the end on binding mode, where π-backbonding into the antibonding orbitals of the dinitrogen ligand can occur. Finally, literature examples of dinitrogen complexes demonstrate that there is a large variety in stretching frequencies between (η^1) and (η^2) bound dinitrogen. Wang and co-workers reported the synthesis of both (η^1) and (η^2) [Ti(η^6-C_6H_6)(N_2)].[102] [Ti(η^6-C_6H_6)(η^2-N_2)] was reported to have a significantly lower stretching frequency at 1655 cm^{-1}, whereas Ti(η^6-C_6H_6)(η^1-NN)] possessed a N≡N stretching frequency of 1932 cm^{-1}. This further supports the N≡N stretch at 2249 cm^{-1} in **161** to be from an end on η^1-dinitrogen coordinated ligand.

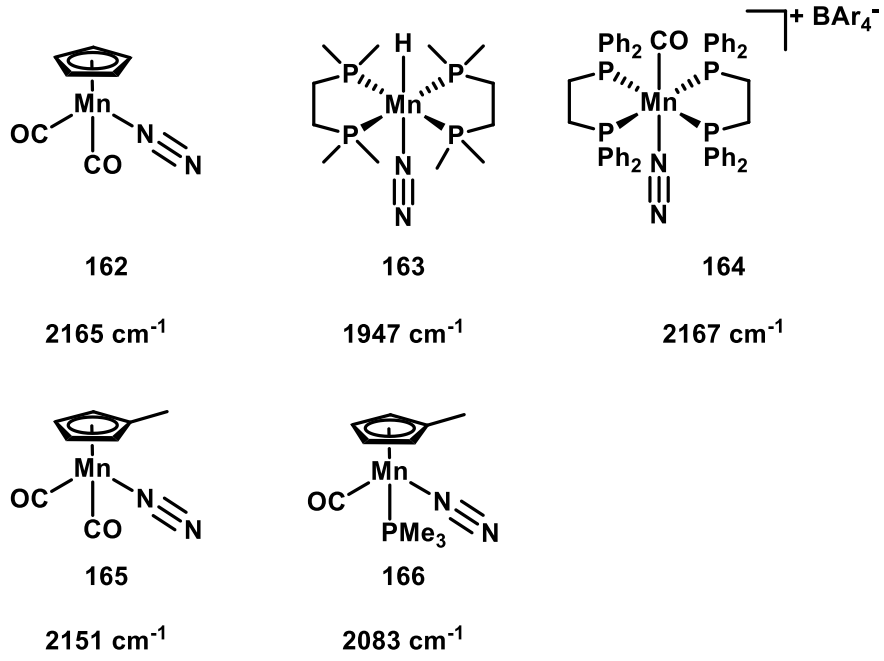

Figure 45. Literature Manganese dinitrogen complexes.[103–107]

Ultimately, upon excitation at 355 nm **158** undergoes photolysis, losing one of the two mutually *trans* CO ligands. The vacant coordination site is occupied by a σ-coordinated *n*-heptane molecule in sub 1 ps to form **159**. At later pump-probe delays (*ca*. 150 ns), diffusion limited processes are observed; *n*-heptane is kinetically displaced by water and dinitrogen, forming **160** and **161** respectively. Equilibration occurs over several microseconds, thermodynamically preferential dinitrogen displacing water, and **161** remains for the duration of the experiment.

An associative pathway was argued for the conversion of **160** to **161** (see Figure 46). Kinetic modelling in COPASI by Professor Jason M. Lynam distinguished that direct conversion between **160** and **161** gave a poor fit to experimental data, indicating that this was not the mechanistic pathway. Instead, conversion *via* **159** gave a good fit to experimental data.[108] Furthermore, a dissociative pathway cannot be argued as no evidence exists for the formally 16-electron *fac*-[Mn(C^N)$(CO)_3$) intermediate. TRIR studies discussed herein imply a sub-picosecond lifetime for this species, as it is not detected at early pump-probe delays in any experiments. Instantaneous coordination of solvent is seen in all experiments involving photolysis of **158**. This is likely due to *fac*-[Mn(C^N)$(CO)_3$) possessing very high Lewis acidity. Studies by Cowan and co-workers and Childs and co-workers demonstrate a number of [Mn(Cp)$(CO)_2$(alkane)] σ-

coordinated alkane complexes.[109,110] The longer chain alkanes including as *n*-pentane and *n*-heptane were shown to be stable for several minutes, before ultimately undergoing substitution with a CO ligand.[109] Thus, it could be expected that the σ-coordinated *n*-heptane observed here are similarly stable, and dissociation of the *n*-heptane ligand is highly unlikely.

To offer further support with assignments, DFT calculations were also performed by Professor Jason Lynam to predict the CO stretching modes for the complexes in Figure 46 and values were scaled using a correction factor previously applied to similar manganese carbonyl complexes.[30] These values are as follows: **159**: 1895, 1915, and 1999 cm^{-1}; **161**: 1999, 1929, and 2017 cm^{-1}; **160**: 1902, 1911, and 1998 cm^{-1}.

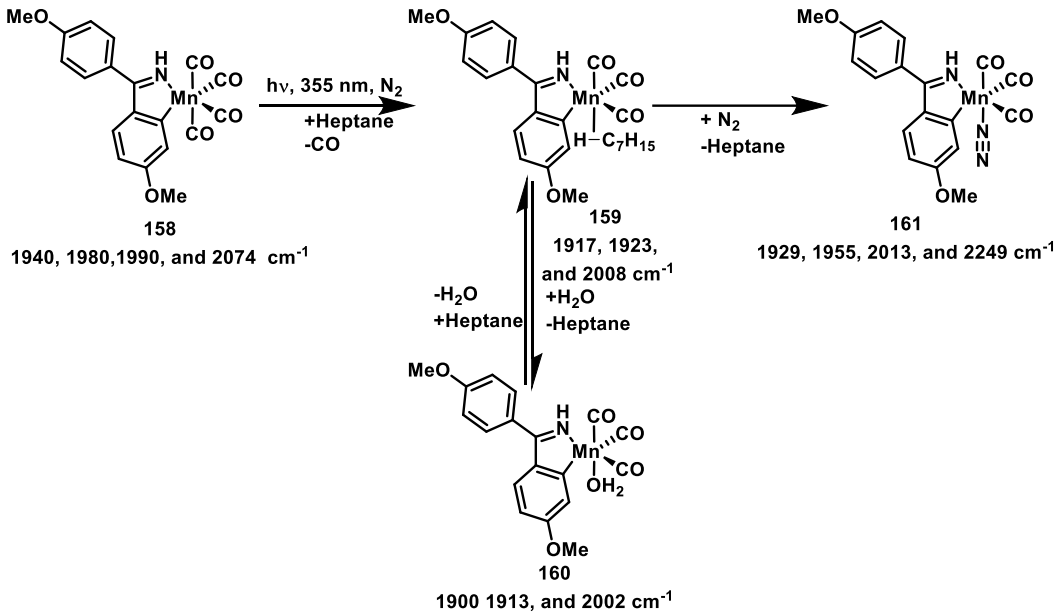

Figure 46. Summary of events observed by $TR^{M}PS$ following photolysis of **158** in anhydrous heptane solution at 355 nm under an atmosphere of N_2.

2.4.2 Solvents: Toluene

Having established speciation events in *n*-heptane, a similar set of experiments were conducted in toluene. The intention was to understand how **158** behaves in a catalytically relevant solvent, prior to adding imine, alkyne and isoquinoline substrates to the system.

Photolysis of [Mn(1,1-bis(4-methoxyphenyl)methanimine)$(CO)_4$] **158** was carried out in anhydrous toluene solution under an atmosphere of N_2 (see Figure 47). Similar

behaviour was seen to that in *n*-heptane. However, the peaks were broader and less resolved due to greater solvent-complex interactions in toluene, compared to *n*-heptane.

At early pump-probe delays, after relaxation of vibrationally 'hot' species (*ca.* 150 ps); a broad feature with two bands at 1910 and 1920 cm^{-1}, along with a higher energy band at 2011 cm^{-1} were observed. The early photoproduct was assigned as *fac*-[Mn(C^N)$(CO)_3$(Toluene)] **167**, with toluene coordination being the most likely coordination event following ultra-fast CO dissociation. The frequency of the metal carbonyl stretching modes also possessed similar frequencies to those of *fac*-[Mn(C^N)$(CO)_3(C_7H_{16})$], further supporting the assignment of the initial photoproduct as a solvent bound complex. Over the course of *ca*. 2 µs these three transient bands depleted with a rate constant, k_{obs}, of 1.7 ± 0.1× 10^6 s^{-1} obtained using an exponential fit. In their place, two sets of bands grew in. Three blue shifted bands at 1924, 1958, and 2024 cm^{-1} which grew in with a rate constant, k_{obs}, of 1.1 ± 0.2 × 10^6 s^{-1} were assigned as *fac*-[Mn(C^N)$(CO)_3$ (η^1-N_2)] **161**. While the three red shifted bands at 1898, 1909, and 2007 cm^{-1}, which grew in with a rate constant, k_{obs}, of 2.9 ± 1.3 × 10^6 s^{-1} were assigned as *fac*-[Mn(C^N)$(CO)_3$ (OH_2)] **160** mirroring that seen in *n*-heptane solution. The toluene bound solvent complex possessed a lifetime 42 times greater than that of *n*-heptane, highlighting how weakly *n*-heptane coordinated to the *fac*-[Mn(C^N)$(CO)_3$] moiety.

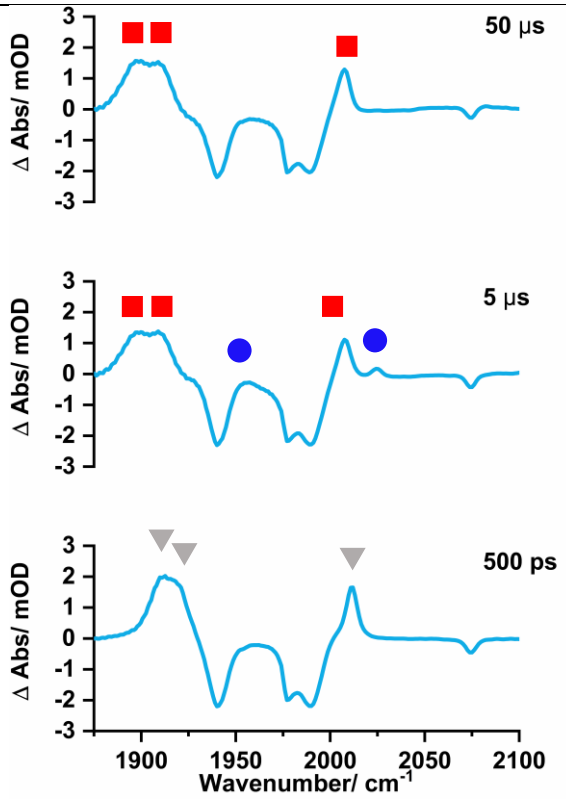

Figure 47. TRIR spectra of **158** in toluene solution under an N_2 atmosphere at selected pump-probe delays. Grey triangle denotes **167**, red square denotes **160**, and blue circle denotes **161**.

Unlike in *n*-heptane, at longer pump-probe delays (*ca*. 40 µs), preferential coordination of water over dinitrogen was observed. Toluene possess a similar solubility of N_2 at atmospheric pressure (4.7 mmol dm^{-3} of N_2 in toluene at 300 K[111]). However the solubility of water in toluene is significantly greater than that in *n*-heptane (5.1 mmol dm^{-3} of water in toluene at 298 K[101]), thus the additional water present in toluene shifts the equilibrium from favouring dinitrogen coordination, to that of water. Decay of the bands associated with **161** proceeded with a rate constant, k_{obs}, of 1.8 ± 0.2 × 10^5 s^{-1}. The k_{obs} for further growth of **160** was within 95% confidences limits at 2.1 ± 0.2 × 10^5 s^{-1} (see Figure 48 for kinetics and Figure 50 for speciation). Both the concentration of water and dinitrogen are several orders of magnitude greater than the concentration of photoproducts in these experiments (4.5 and 5.8 ×10^{-5} mmol dm^{-3}). Consequently, it is appropriate to treat the systems as *pseudo*-first order, and the assumption can be made that the concentration of water and dinitrogen remain constant for the duration of experiments.

For slower processes an artifact can be seen at 10000, 20000, 30000, … ns. This is due to the nature of TR^{M}PS. A consequence of ultrafast pump-probe delays is the high number of data points generated every 10000 ns (e.g., 10000.001 ns, 10000.002 ns, …, 11000 ns). These data points tend to possess a lot of noise and introduce a systematic artifact.

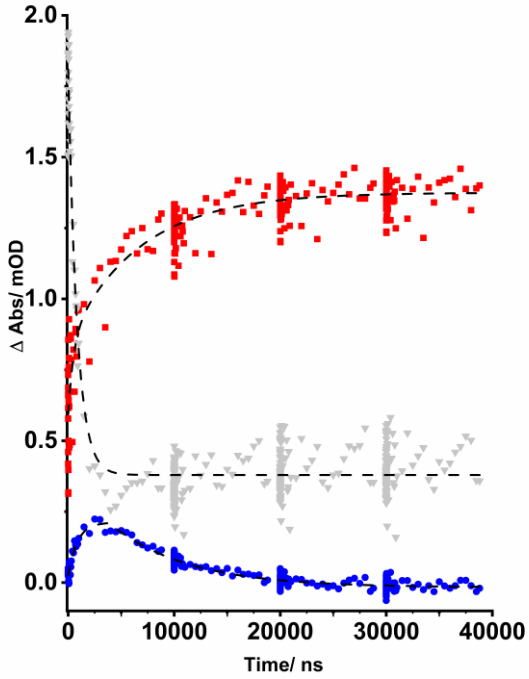

Figure 48. Kinetics for the loss of **167** and formation/ equilibration of **160** and **161**. **167** denoted by grey triangles, **160** denoted by red squares and **161** denoted by blue circles. Dotted lines denote exponential kinetics. Where appropriate a mono or biexponential fit was applied.

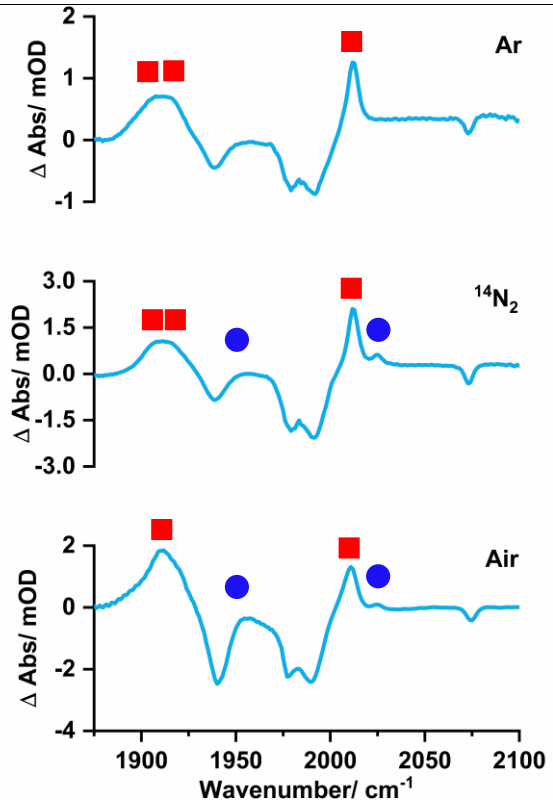

Figure 49. TRIR spectra of **158** in toluene solution using various sparge gasses at a pump-probe delay of 500 ns. Red square denotes **160** and blue circle denotes **161**.

Similar experiments to those conducted in *n*-heptane, to elucidate the nature of speciation, were conducted in toluene (see Figure 49). The results were almost identical at a 500 ns pump-probe delay. The highest proportion of **161** was observed when $^{14}N_2$ was used as sparge gas. The relative intensity of high energy band (2024 cm^{-1}) belonging **161** decreased upon sparging the system with air, and was not present when **158** was photolysed under an argon atmosphere. Despite toluene taking longer to initially displace than heptane, the toluene bound complex **167** was not detected at 500 ns, when argon was used as a sparge gas. Solely the water bound complex **160** was detected.

160 observed in these experiments is a candidate for an early species formed on route to forming hydroxy-bridged Mn carbonyl clusters. There are catalyst deactivation products formed in Mn(I) carbonyl catalysis.[51]

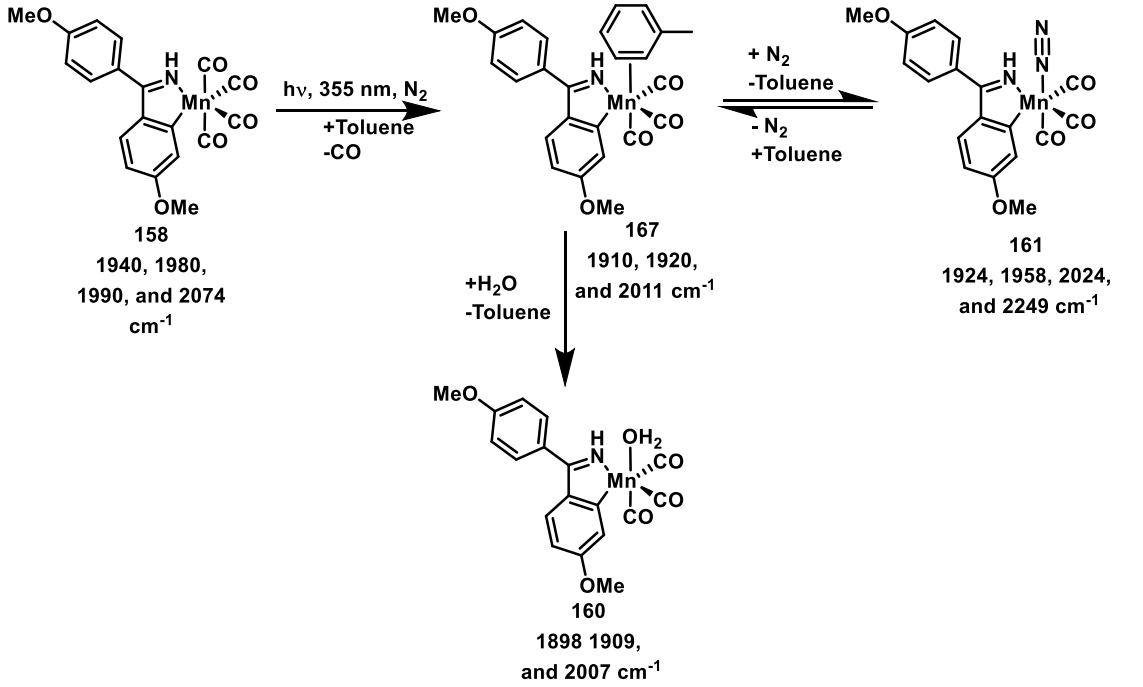

Figure 50. Summary of events observed by $TR^{M}PS$ following photolysis of **158** in anhydrous toluene solution at 355 nm under an atmosphere of N_2.

2.4.3 Catalytically relevant additives: Alkynes

Having established solvent dependant events in *n*-heptane and toluene, a variety of catalytically relevant additives were doped into the studied *n*-heptane and toluene systems: diphenyl acetylene, 6-methoxy-1-(4-methoxyphenyl)-3,4-diphenylisoquinoline and 1,1-bis(4-methoxyphenyl)methanimine, along with further alkynes.

Initially phenyl acetylene was explored. The objective here was to probe the carbon-carbon bond forming steps proposed by He and co-workers.[60] Following phenyl acetylene, the internal alkyne diphenyl acetylene used by He and co-workers in their optimisation, along with dec-5-yne were studied.

Unless stated otherwise approximately 20 mmol dm^{-3} of additive was introduced to the system (10 eq. wrt. **158**). As established prior, the concentration of photoproduct was determined to be approximately 5.0×10^{-5} mmol dm^{-3}, a 4×10^{5}-fold excess. This allowed us to treat the system as *pseudo* first order when carrying out kinetic analysis, as the concentration of additive remains effectively constant throughout.

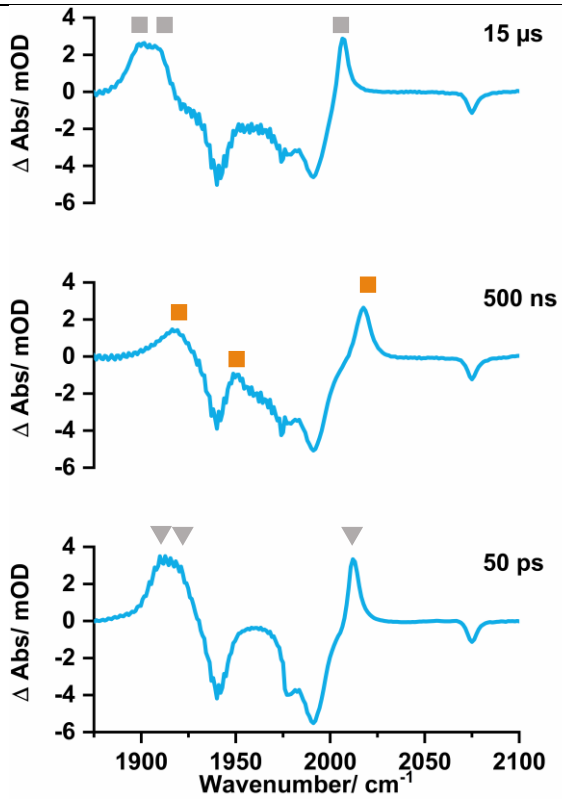

Figure 51. TRIR spectra of **158** in toluene solution with added phenyl acetylene under an N_2 atmosphere. **167** denoted by grey triangles, **169** denoted by orange squares, and **170** denoted by grey squares.

Initially, phenyl acetylene was doped into an anhydrous toluene solution containing **158** under an N_2 atmosphere. At early pump-probe delays *ca*. 50 ps, the bands associated with **167** were observed, which Indicates that the initial coordination event was still to toluene. Over the course of *ca*. 500 ns, water and dinitrogen did not coordinate to form **160** and **161** respectively. Instead, new blue-shifted transient bands were detected at 1917, 1950, and 2017 cm^{-1}, the rate constant for their formation being $7.5 \pm 1.2 \times 10^7$ s^{-1} (see Figure 51). These bands depleted with a rate constant, k_{obs}, of $3.7 \pm 0.2 \times 10^5$ s^{-1}, and three new bands with stretching frequencies of 1900, 1908, and 2006 cm^{-1} grew in with a rate constant, k_{obs}, of $3.8 \pm 0.4 \times 10^5$ s^{-1}. These bands lie within the detector resolution of ± 2 cm^{-1} of the water complex **160**. Thus, a definitive assignment cannot be made at this point.

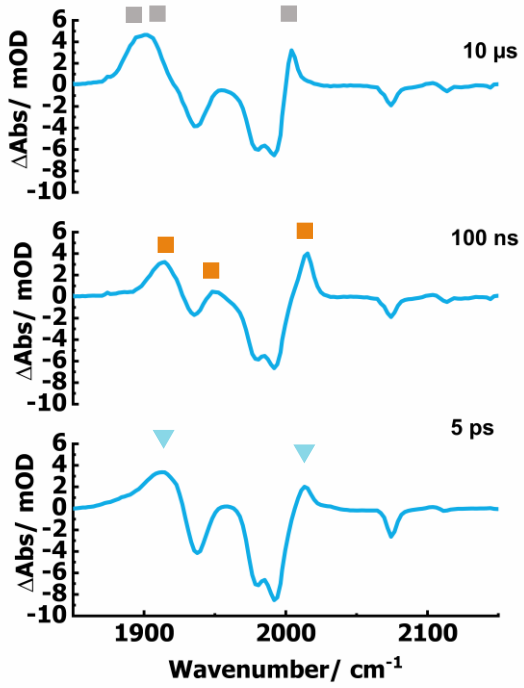

Figure 52. TRIR spectra of **158** in phenyl acetylene solution under an N_2 atmosphere at various pump-probe delays. **168** denoted by denoted by blue triangles, **169** denoted by orange squares, and **170** denoted by grey squares.

158 was then photolysed in neat phenyl acetylene, establishing the metal carbonyl stretching frequencies associated with alkyne coordinated complexes (see Figure 52). This removed the possibility of toluene-bound complexes forming at early pump-probe delays, forcing initial coordination with phenyl acetylene. Comparison could be made to the transient species formed when phenyl acetylene was doped into the toluene solution of **158**, being aware that minor shifts in wavenumber were possible due to changes in solvent interactions with photoproducts.

At very early pump-probe delays of *ca*. sub 50 ps a band at 2013 cm^{-1} and a broad band at 1912 cm^{-1} were observed. Over the course of 5 ns the depletion of these bands with a rate constant, k_{obs}, of 3.1 ± 0.3 × 10^9 s^{-1} was seen. In their place, three bands blue shifted, corresponding to those seen in toluene (*ca*. 500 ns) positioned at 1915, 1949, and 2015 cm^{-1} grew in with a rate constant, k_{obs}, of 3.3 ± 2.2 × 10^9 s^{-1} (see Figure 53). Then at later pump-probe delays, similar red shifted bands to those seen in toluene, with stretching frequencies at 1898, 1903, and 2004 cm^{-1} grew in. Application of an

exponential function gave a rate constant, k_{obs}, of 3.3 ± 0.2 × 10^5 s^{-1} for the formation of this complex, within 95% confidence limits of those seen for phenyl acetylene in toluene (see Figure 53).

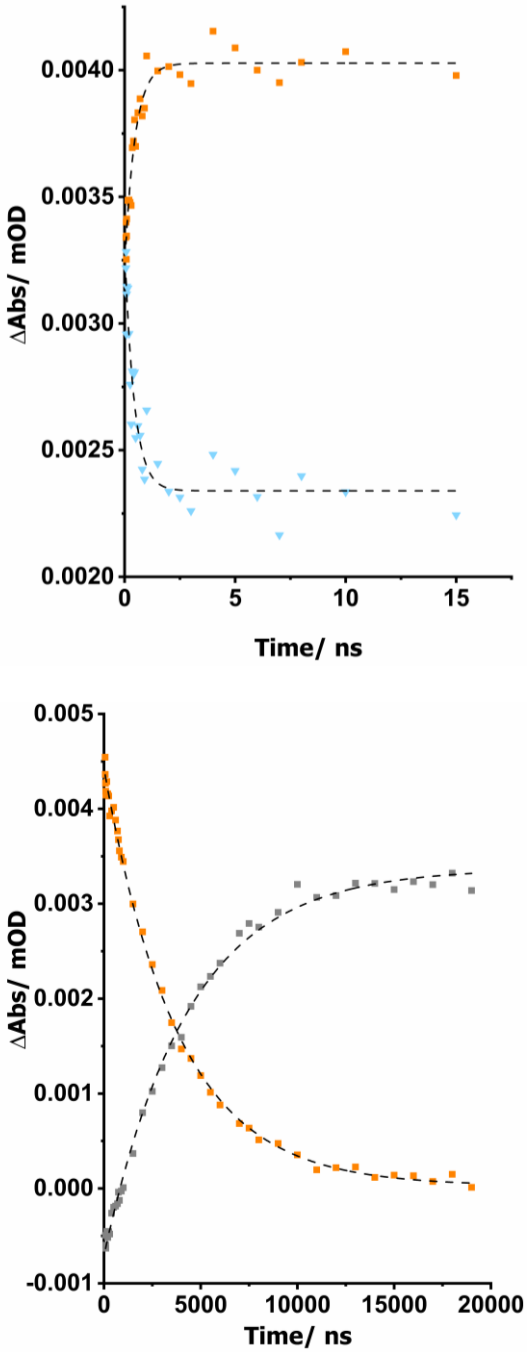

Figure 53. Kinetics for the loss of **168** and formation of **169**. The subsequent formation of **170** from **169**. Dotted lines denote exponential kinetics. Where appropriate a mono or biexponential fit was applied.

The bands at 1915, 1949, and 2015 cm^{-1} likely belong to *fac*-[Mn(C^N)$(CO)_3$ (η^2-HCCPh)], as these bands were seen in both neat phenyl acetylene, and toluene solution of phenyl acetylene. The most probably mode of coordination is η^2-bound phenyl acetylene through the C≡C bond. This reflects observation made by Hammarback and co-workers, who photolysed analogous complexes in the presence of phenyl acetylene (see Figure 54).[30] They reported three bands which displayed a distinctive blue shift from the solvated complex, which are similar to those seen herein. The red shifted bands (1912 and 2013 cm^{-1}) seen at very early pump-probe delays in neat phenyl acetylene give an insight into the coordination modes of the phenyl acetylene ligand. Following photodissociation of a CO ligand, the vacant coordination site was rapidly occupied, even in *n*-heptane solution. Thus, at early pump-probe delays phenyl acetylene is likely to bind through one of the multiple arene bonds of the phenyl ring, as opposed to the single η^2-bound alkyne mode. A picosecond rearrangement to the η^2-bound alkyne is then seen. This coordination mode is a greater π-acceptor, explaining the blue shift observed. The rapidness of this rearrangement also explains why the arene bound mode of phenyl acetylene was not seen in the toluene solution experiment, as the rate of phenyl acetylene coordination was less than that of ligand rearrangement.

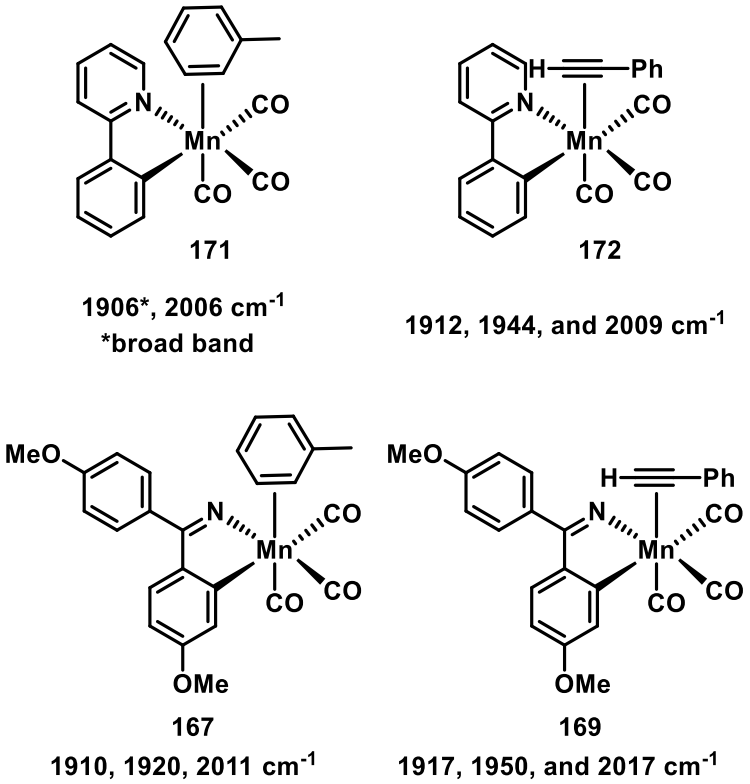

Figure 54. 2-phenylpyridine derived solvent and phenyl acetylene complexes compared to 1,1-bis(4-methoxyphenyl)methanimine derived complexes.[30,96]

The concentration of phenyl acetylene was varied between 23 and 464 mmol dm^{-3} and the observed rate constants for the formation of **169** (k_{1obs}) and **170** (k_{2obs}) were obtained from exponential fits applied to the data sets (see Table 4).

Table 4. Observed first order rate constants for formation of **169** and **170**.

$[PhC_2H]$/ mol dm^{-3}	Formation of **169** using the band at 2008 cm^{-1} k_{1obs} / s^{-1}	Formation of **170** using the band at 2006 cm^{-1} k_{2obs} / s^{-1}
0.023	$2.85 \pm 0.46 \times 10^6$	$2.35 \pm 0.18 \times 10^5$
0.046	$4.56 \pm 0.69 \times 10^6$	$2.30 \pm 0.68 \times 10^5$
0.116	$7.81 \pm 2.24 \times 10^6$	$1.87 \pm 0.23 \times 10^5$
0.232	$1.68 \pm 0.22 \times 10^7$	$2.36 \pm 0.15 \times 10^5$
0.464	$3.43 \pm 0.45 \times 10^7$	$2.19 \pm 0.17 \times 10^5$

Linear analysis of the plot of $[PhC_2H]$ versus k_{1obs} gave a fit of $Y = (6.8 \pm 0.97 \times 10^7)X + (1.3 \pm 0.63 \times 10^6)$ with an R^2 of 0.99 (see Figure 56). Using the gradient of the fit, the second order rate constant for formation of **169** by the substitution of the toluene ligand bound in **167** with phenyl acetylene was found to be $6.8 \pm 0.97 \times 10^7$ mol^{-1} dm^3 s^{-1}.

Further analysis on the logarithmic plot of ln([PhC_2H]) versus ln(k_{1obs}) gave a fit of Y = (0.83 ± 0.14)X + (17.9 ± 0.3), demonstrating the order with respect to phenyl acetylene for the conversion of **167** to **169** was 0.83 ± 0.14, approximately first order.

Linear analysis of the plot of [PhC_2H] versus k_{2obs} gave a fit of Y = (-9.1 ± 18.7 × 10^5)X + (2.3 ± 0.52 × 10^5). Using the intercept of the fit, the first order rate constant for the conversion of **169** to form **170** was found to be 2.3 ± 0.52 × 10^5 s^{-1}. Further analysis on the logarithmic plot of ln([PhC_2H]) versus ln(k_{2obs}) gave a fit of Y = (0.01 ± 0.11)X + (0.7 ± 0.25), demonstrating the order with respect to phenyl acetylene for the conversion of **169** to **170** was 0.01 ± 0.11, approximately zero order.

An approximately first order dependency on phenyl acetylene for the conversion of **161** to **169** supports the hypothesis that **169** is *fac*-[Mn(C^N)$(CO)_3$ (η^2-HCCPh)], with phenyl acetylene substituting out the toluene ligand. An order of zero with respect to phenyl acetylene for the loss of **169** disagrees with the displacement of phenyl acetylene by a molecule of water to form **160**. Instead, the order of zero implies that an intramolecular process occurred. It was anticipated that a migratory insertion of the alkyne ligand had occurred, forming a 7-membered manganacycle. A widely proposed intermediate in manganese (I) C−H bond transformations. The change in coordination of phenyl acetylene from η^2-HC≡CPh, to being incorporated into the metallacycle ring system explains the red shift in transient bands. Upon undergoing the migratory insertion, the degree of π-backbonding onto the phenyl acetylene moiety ligand would be significantly reduced. The tricarbonyl 7-membered manganacycle in Figure 55 is a more likely candidate that the tetracarbonyl species proposed by He and co-workers.[60] The three stretching modes are typical of a *fac* tricarbonyl complex, and bands positions reflect those observed by Hammarback and co-workers studying the analogous 2-phenyl pyridine derived manganacycle.[30]

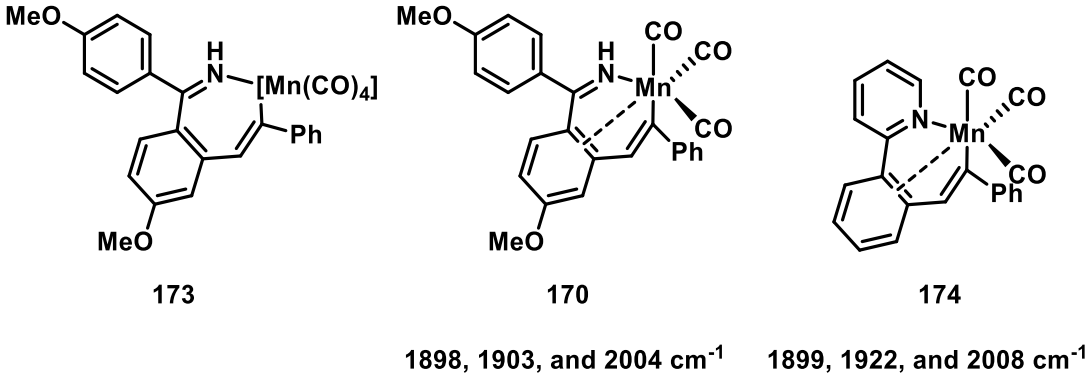

173 **170** **174**

1898, 1903, and 2004 cm^{-1} **1899, 1922, and 2008 cm^{-1}**

Figure 55. Left: proposed 7-membered manganacycle by He and co-workers.[60] Centre: *In situ* 7-membered manganacycle detected. Right: 7-membered manganacycle observed by Hammarback and co-workers.[30]

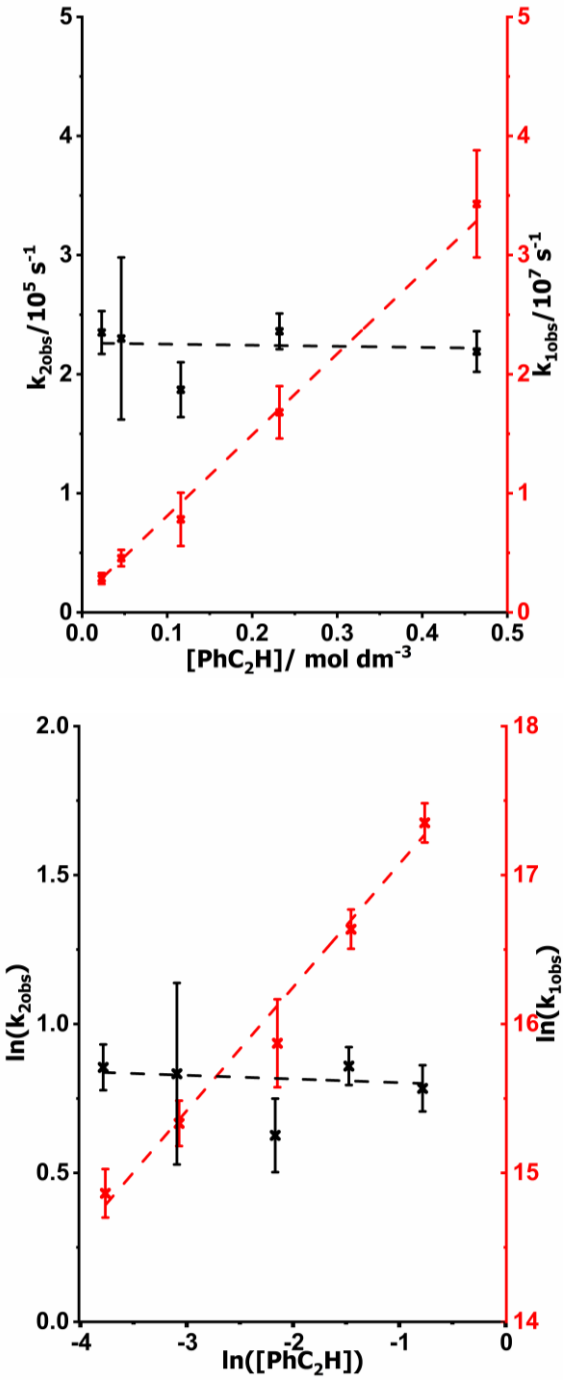

Figure 56. Top): Pseudo first order analysis for the conversion of **167** to **169** and **169** to **170** using the rate constants in Table 4. Bottom): Plots of $ln(k_{1obs})$ and $ln(k_{2obs})$ versus $ln([PhC_2H])$ to determine the order for the conversion of **167** to **169** and **169** to **170**. Data derived from the peak at 2008 cm^{-1}, **167** to **169** denoted by red X and **169** to **170** denoted by black X.

To offer further support with assignments, DFT calculations were also performed by Professor Jason Lynam to predict the CO stretching modes for the complexes in Figure 57. and values were scaled using a correction factor previously applied to similar manganese carbonyl complexes.[30] These values are as follows; **169**: 1913, 1942, and 2006 cm^{-1}; **170**: 1896, 1920, and 2001 cm^{-1}.

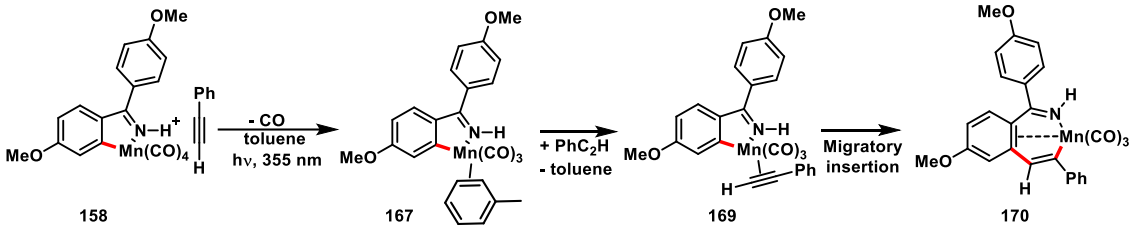

Figure 57. Coordination events following the photochemical dissociation of a CO ligand from **158** in toluene solution in the presence of phenyl acetylene.

A similar set of experiments were performed with diphenyl acetylene, to explore how an internal alkyne behaves (see Figure 58). The spectra indicate similar behaviour at early pump-probe delays. Upon photolysis a CO ligand dissociates from **158** and toluene initially coordinates. These bands depleted with an observed rate constant of $1.7 \pm 0.1 \times 10^6$ s^{-1}, an order of magnitude slower than that observed in the presence of phenyl acetylene. Five bands were detected at 1898, 1909, 2008, 1955 and 2025 cm^{-1}. The weak intensity high energy band at 2025 and 1955 cm^{-1} correlated with previously assigned *fac*-[Mn(C^N)$(CO)_3$ (η^1-N_2)], while the three remaining bands mirror those of *fac*-[Mn(C^N)$(CO)_3$ (OH_2)].

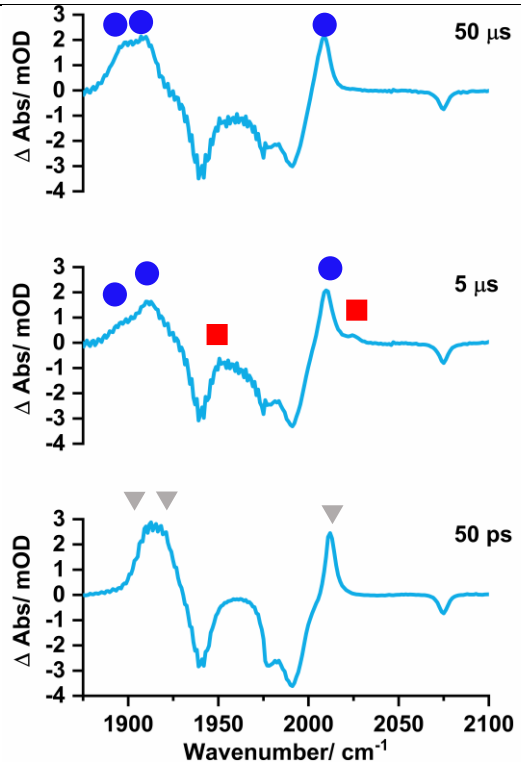

Figure 58. TRIR spectra of **158** in toluene solution with diphenyl acetylene additive under an atmosphere of N_2 at selected pump-probe delays. **167** denoted by denoted by grey triangles, **160** denoted by blue circles and **161** by red squares.

To ensure water coordination was outcompeting diphenyl acetylene, a set of experiments were carried out varying the concentration of diphenyl acetylene. A range of 25 to 250 mmol dm^{-3} were explored (see Table 5).

Table 5. Observed first order rate constants for loss of **167** with varying concentrations of Ph_2C_2.

$[Ph_2C_2]$/ mol dm^{-3}	Loss of **167** using the band at 2011 cm^{-1} k_{3obs} / s^{-1}
0.000	$12.3 \pm 2.90 \times 10^5$
0.025	$8.5 \pm 2.99 \times 10^5$
0.050	$8.4 \pm 2.3 \times 10^5$
0.075	$8.3 \pm 2.6 \times 10^5$
0.124	$10.1 \pm 3.0 \times 10^5$
0.249	$10.6 \pm 6.8 \times 10^5$

Addition of diphenyl acetylene to a toluene solution of **158** showed no significant impact upon the rate of loss of the solvent complex. Further analysis on the logarithmic plot of $\ln([Ph_2C_2])$ versus $\ln(k_{3obs})$ gave a fit of $Y = (0.08 \pm 0.15)X + (13.9 \pm 0.45)$, demonstrating

the order with respect to diphenyl acetylene for the loss of **167** was 0.08 ± 0.15, zero order (see Figure 59). Thus, both water and dinitrogen were outcompeting diphenyl acetylene in the substitution of toluene on **167**. This likely due to the additional steric bulk of the second phenyl moiety on diphenyl acetylene added, over phenyl acetylene.

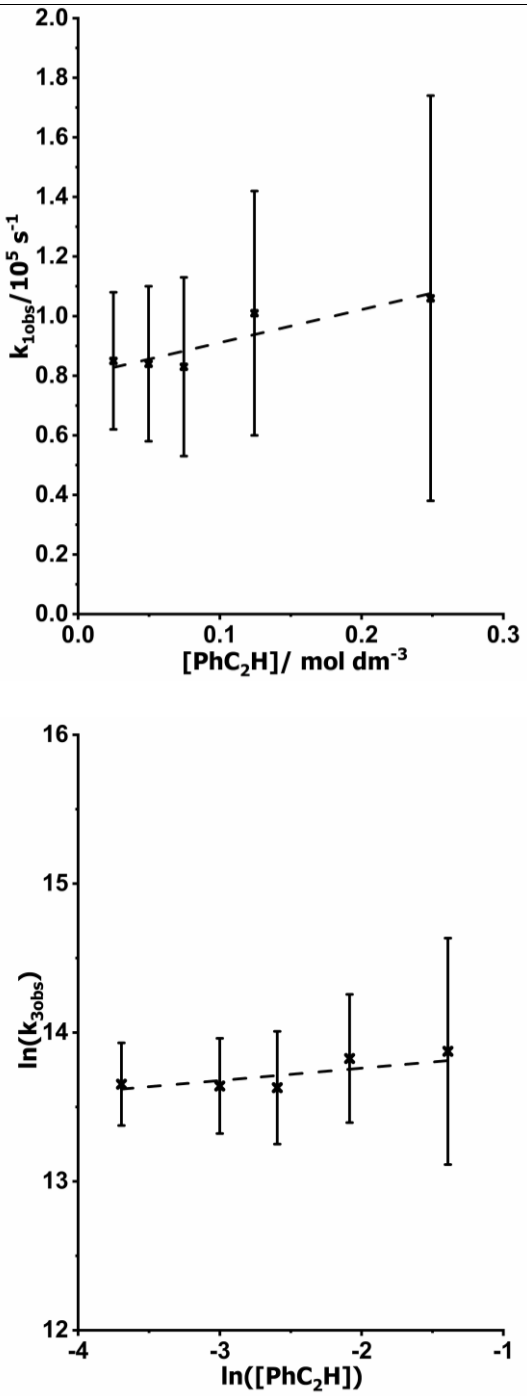

Figure 59. Top): Pseudo first order analysis for the loss of **167** using the rate constants in Table 5. Bottom): Plots of ln(k_{3obs}) versus ln([PhC_2H]) to determine the order for the of **167** with respect to [Ph_2C_2]. Data derived from the peak at 2011 cm^{-1}, loss of **167** denoted by black X.

The final alkyne investigated in this study was 5−decyne. This enabled study of a chemically different internal alkyne, to see if water also inhibited the coordination and

migratory insertion. **158** in anhydrous toluene solution with 5−decyne doped in, under a N_2 atmosphere, was excited at 335 nm and followed *via* TRIR (see Figure 60).

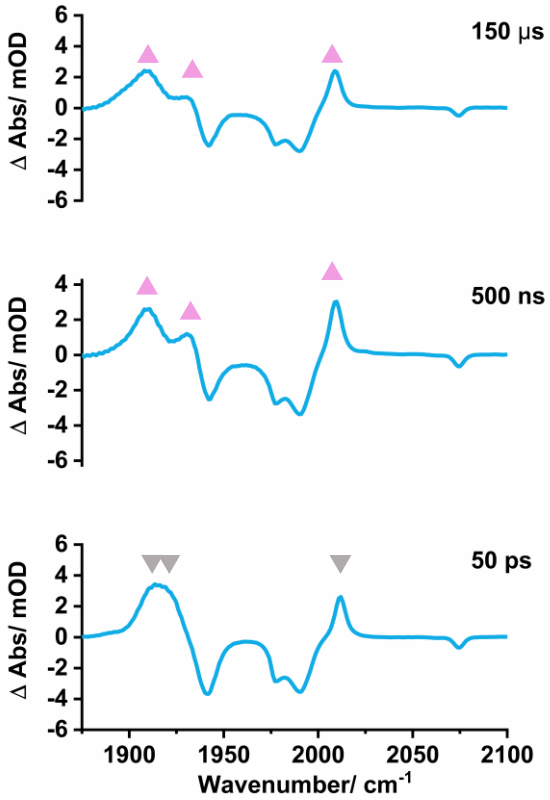

Figure 60. TRIR spectra of **158** in toluene solution with 5−decyne additive under an atmosphere of N_2 at selected pump-probe delays. **167** denoted by denoted by grey triangles and **175** denoted by pink triangle.

At early pump-probe delays, after vibrational relaxation, at *ca*. 50 ps, the bands associated with **167** were observed, indicating that the initial coordination event was expectedly that with toluene. The bands decayed with a rate constant, k_{obs}, of 6.8 ± 3.9× 10^6 s^{-1}, and three new bands at 1909, 1931, and 2010 cm^{-1} grew in with a rate constant, k_{obs}, of 8.9 ± 2.4× 10^6 s^{-1} (see Figure 61). These three transient bands then proceeded to remain for the duration of the experiment. The transient bands did not correlate to either *fac*-[Mn(C^N)$(CO)_3$ (η^1-N_2)], or *fac*-[Mn(C^N)$(CO)_3$ (OH_2)], but a blue shift similar to that seen when phenyl acetylene was doped in occurred. Thus, it was deduced that **175** was *fac*-[Mn(C^N)$(CO)_3$ (η^2-C≡C(C_4H_9)$_2$)].

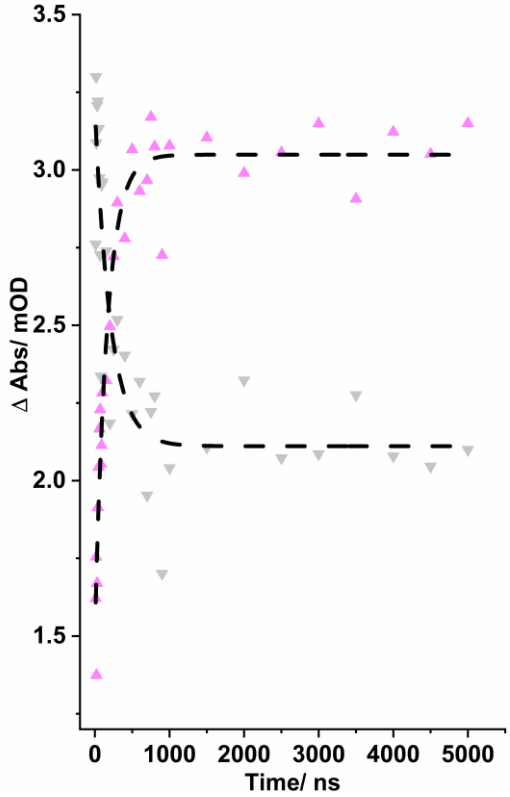

Figure 61. Kinetics for the loss of **167** and formation of **175**. **167** denoted by denoted by grey triangles and **175** denoted by pink triangle. Dotted lines denote exponential kinetics. Where appropriate a mono or biexponential fit was applied.

Returning to experiments with diphenyl acetylene, anhydrous *n*-heptane was used in lieu of anhydrous toluene because water possesses a significantly reduced solubility in heptane[111] compared to toluene[101]. The hypothesis was that in reducing the concentration of water, the coordination and subsequent migratory insertion of the alkyne would be promoted.

Following vibrational relaxation at *ca*. 50 ps, three sharp transient bands corresponding to *fac*-[Mn(C^N)(CO)$_3$(C_7H_{16})] **159** were detected (see Figure 62). The bands associated with **159** decayed over *ca*. 50 ns, and three new bands assigned to **176** situated at 1916, 1949, and 2000 grew in. These were slowly replaced by a third species (**177**) at *ca*. >100 µs, which remained for the duration of the experiment, with bands at 1899, 1908, and 1993 cm^{-1}. Neither of these sets of transient bands corresponds to dinitrogen, or water coordination, hinting at the coordination of diphenyl acetylene. However, a small amount of *fac*-[Mn(C^N)(CO)$_3$(OH_2)] was detected at long pump-probe delays, as depicted in Figure 62.

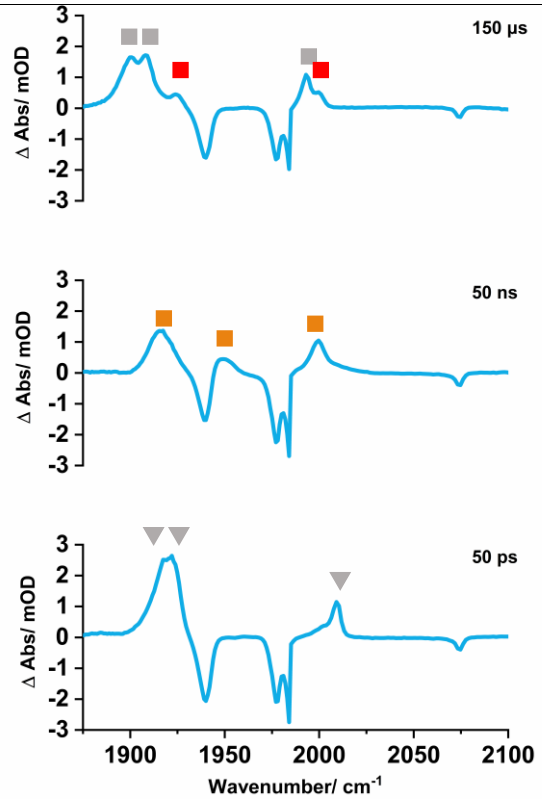

Figure 62. TRIR spectra of **158** in heptane solution with diphenyl acetylene additive under an atmosphere of N_2 at selected pump-probe delays. **167** denoted by denoted by grey triangles, **176** denoted by denoted by orange squares, **160** denoted by red squares and **177** denoted by pink triangle.

To validate the impact of the alteration in solvent, the order with respect to diphenyl acetylene was determined. A range of concentrations from 25 to 500 mmol dm^{-3} were used and the values for **167** to **176** (k_{4obs}) and **176** to **177** (k_{5obs}) were obtained from the metal carbonyl stretching mode of **176** at 2000 cm^{-1} (see Table 6).

Table 6. Observed first order rate constants for formation of **176** and **177**.

$[PhC_2H]$/ mol dm^{-3}	Formation of **176** using the band at 2000 cm^{-1} k_{4obs} / s^{-1}	Formation of **177** using the band at 2000 cm^{-1} k_{5obs} / s^{-1}
0.0246	$0.85 \pm 0.27 \times 10^8$	$2.53 \pm 0.31 \times 10^5$
0.0496	$1.50 \pm 0.42 \times 10^8$	$2.73 \pm 0.31 \times 10^5$
0.124	$4.17 \pm 0.58 \times 10^8$	$2.40 \pm 0.06 \times 10^5$
0.247	$8.19 \pm 1.76 \times 10^8$	$1.39 \pm 0.32 \times 10^5$
0.497	$17.66 \pm 4.01 \times 10^8$	$2.25 \pm 0.09 \times 10^5$

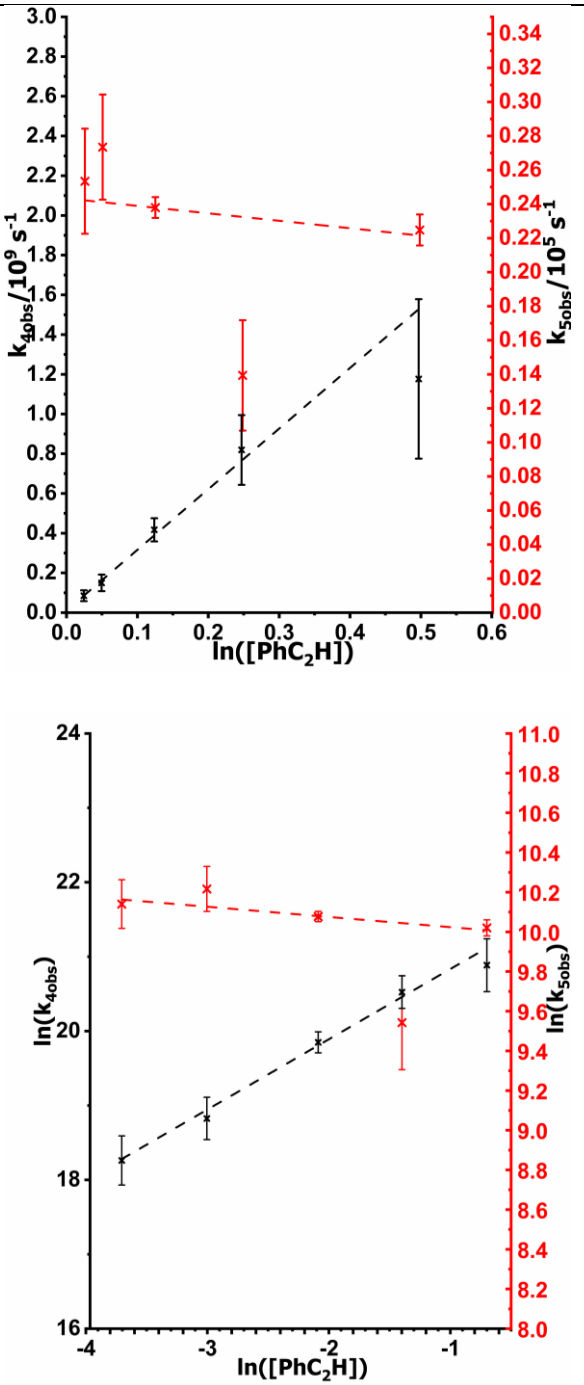

Figure 63. Top): Pseudo first order analysis for the conversion of **159** to **176** and **176** to **177** using the rate constants in Table 6. Bottom): Plots of ln(k_{4obs}) and ln(k_{5obs}) versus ln([PhC_2H]) to determine the order for the conversion of **159** to **176** and **176** to **177**. Data derived from the peak at 2000 cm^{-1}, **159** to **176** denoted by black X and **176** to **177** denoted by red X.

Linear analysis of the plot of [Ph_2C_2] versus k_{4obs} gave a fit of Y = (3.0 ± 0.89 × 10^9)X + (1.1 ± 6.00 × 10^7) with and R^2 of 0.97. Using the gradient of the fit, the second order rate

constant for the substitution of *n*-heptane ligand bound in **159** with diphenyl acetylene, to form **176** was found to be 3.0 ± 0.89 × 10^9 mol^{-1} dm^3 s^{-1}. Further analysis on the logarithmic plot of ln([PhC_2H]) versus ln(k_{1obs}) gave a fit of Y = (0.94 ± 0.21)X + (21.8 ± 0.47), demonstrating the order with respect to diphenyl acetylene for the conversion of **159** to **176** was 0.94 ± 0.47 and supported the argument that diphenyl acetylene coordinated to the to *fac*-[Mn(C^N)$(CO)_3$] moiety under more rigorously controlled anhydrous conditions (see Figure 63).

Linear analysis of the plot of [PhC_2H] versus k_{5obs} gave a fit of Y = (-4.4 ± 16.2 × 10^4)X + (2.4 ± 0.46 × 10^5). Using the intercept of the fit, the first order rate constant for the conversion of **176** to form **177** was found to be 2.4 ± 0.46 × 10^5 s^{-1}. Further analysis on the logarithmic plot of ln([PhC_2H]) versus ln(k_{2obs}) gave a fit of Y = (-0.05 ± 0.12)X + (9.97 ± 0.23), demonstrating zero order with respect to diphenyl acetylene for the conversion of **176** to **177**. As with phenyl acetylene, an order of zero supports the occurrence of an intramolecular process. Again, this was believed to be the migratory insertion the alkyne, forming a 7-membered manganacycle. The first order rate constants were found to be within 95% confidence limits of each other for migratory insertion of phenyl and diphenyl acetylene, despite the addition steric bulk of diphenyl acetylene.

To offer further support with assignments, DFT calculations were also performed by Professor Jason Lynam to predict the CO stretching modes for the complexes in Figure 64. and values were scaled using a correction factor previously applied to similar manganese carbonyl complexes.[30] These values are as follows; **177**: 1903, 1916, and 1995 cm^{-1}; **176**: 1907, 1939, and 2004 cm^{-1}.

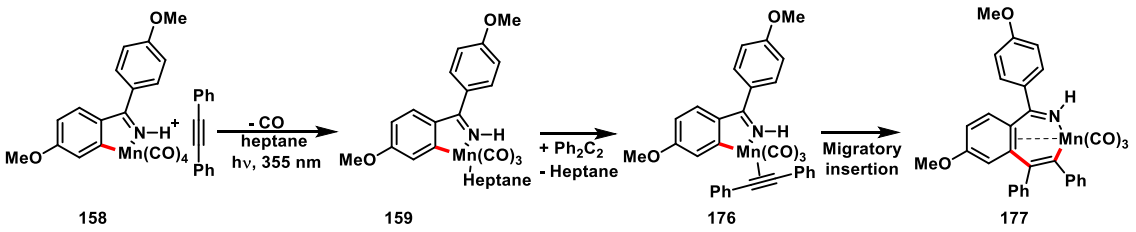

Figure 64. Coordination events following the photochemical dissociation of a CO ligand from **158** in *n*-heptane solution in the presence of diphenyl acetylene.

2.4.4 Catalytically relevant additives: Imine

The catalytically relevant imine, 1,1-bis(4-methoxyphenyl)methanimine **178** was introduced to an anhydrous toluene solution of **158** under an atmosphere of N_2, to assess its involvement with the catalytic intermediate **158** following loss of a CO ligand. After assessing how **178** interacts with solvent coordination events, **158** will be photolysed in the presence of both imine **178** and phenyl acetylene, in order to assess what are the kinetically and thermodynamically favourable products, while determining how the rate of migratory insertion is impacted.

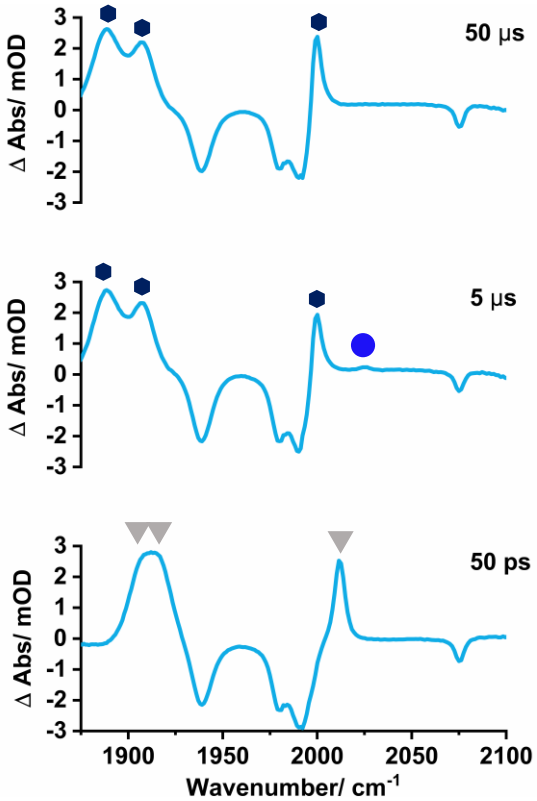

Figure 65. TRIR spectra of **158** in toluene solution with imine **178** additive under an atmosphere of N_2 at selected pump-probe delays. **167** denoted by denoted by grey triangles, **179** denoted by dark blue hexagons and **161** denoted by blue circles.

Depletion of initially formed bands belonging to *fac*-[Mn(C^N)$(CO)_3$(toluene)] **167** occurred by *ca*. 3 µs (see Figure 65). In their place, three highly red shifted bands with frequencies of 1888, 1907, and 2000 cm^{-1} grew in with a rate constant, k_{obs}, of 2.5 ± 0.2× 10^6 s^{-1}. This reflected the observed rate constant, k_{obs}, of 2.5 ± 0.3 × 10^6 s^{-1} for the loss of the toluene complex **167**, indicating that the new species formed directly from **167**

(see Figure 66). As the new transient bands did not correspond to those of the water complex **160**, it is likely that the new species is *fac*-[Mn(C^N)$(CO)_3$(1,1-bis(4-methoxyphenyl)methanimine)] **179**; coordinated through a lone pair of electrons on the imine nitrogen. Coordination of this electron rich ligand explains the significant red shift seen in CO stretching frequencies, as additional electron density donated to the metal centre reduces the CO bond order. Shortly after formation of **179**, very weak bands belonging to **161** were detected, indicating that N_2 was kinetically competitive. However, the weak band at 2025 cm^{-1} had depleted at longer pump-probe delays suggesting that imine coordination was thermodynamically favourable. To offer further support with assignments, DFT calculations were also performed by Professor Jason Lynam to predict the CO stretching modes for the complexes in Figure 65. and values were scaled using a correction factor previously applied to similar manganese carbonyl complexes.[30] These values for **179** are as follows **159**: 1879, 1906, and 1981 cm^{-1}.

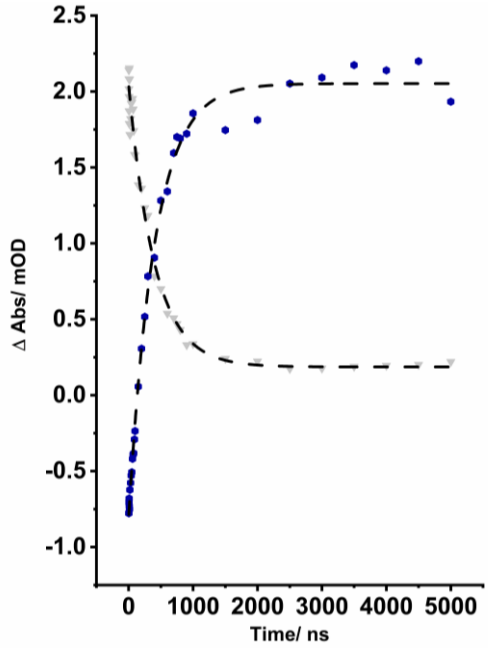

Figure 66. Kinetics for the loss of **167** and formation of **177**. **167** denoted by denoted by grey triangles and **179** denoted by dark blue hexagons. Dotted lines denote exponential kinetics. Where appropriate a mono or biexponential fit was applied.

Following these observations, 31 mmol dm^{-3} of phenyl acetylene were introduced alongside the 20 mmol dm^{-3} of imine to the system, replicating equivalencies seen in the catalytic system.[60] The aim was to probe whether imine or alkyne ligand coordination was preferential, and what impact was seen on the rate of alkyne migratory insertion (see Figure 67).

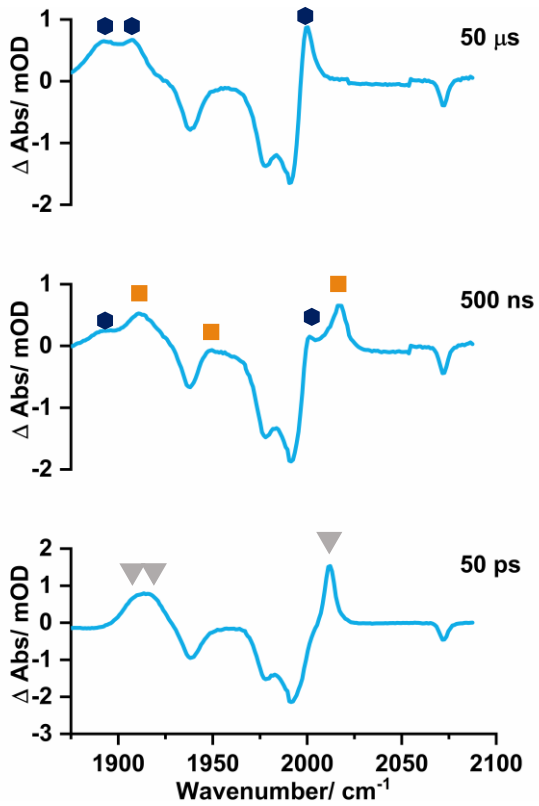

Figure 67. TRIR spectra of **158** in toluene solution with imine **178**and phenyl acetylene additives under an atmosphere of N_2 at selected pump-probe delays. **167** denoted by denoted by grey triangles, **179** denoted by dark blue hexagons and **169** denoted by orange squares.

Initially bands belonging to the toluene complex **167** were observed. At the pump-probe delay of 500 ns, high energy bands at 2000 and 2017 cm^{-1} corresponding to *fac*-[Mn(C^N)$(CO)_3$ (η^2-HCCPh)] **169** and *fac*-[Mn(C^N)$(CO)_3$(1,1-bis(4-methoxyphenyl)methanimine)] **179** respectively; multiple broad bands between 1900 and 1920 cm^{-1} caused by overlapping stretching modes; and a band at 1949 cm^{-1} belonging to *fac*-[Mn(C^N)$(CO)_3$ (η^2-HCCPh)] were observed. Application of a exponential fit to the band at 2013 belonging to **167** revealed the rate constant constant,

k_{obs}, of 7.0 ± 0.3 × 10^6 s^{-1} for the decay of the toluene bound complex. This aligned with the coordination of phenyl acetylene (k_{obs} = 9.7 ± 0.3 × 10^6 s^{-1}) (see Figure 68).

Depletion of **169** occurred with a rate constants, k_{obs}, of 3.5 ± 0.2 × 10^5 s^{-1}. However, the previously characterised bands at 1900, 1908, and 2006 cm^{-1} belonging to the migratory insertion product **170** were not detected. Instead, the bands belonging to **179** showed exponential growth in intensity, possessing a rate constants, k_{obs}, of 3.2 ± 0.2 × 10^5 s^{-1}, within 95% of the depletion of **169** (see figure 68).

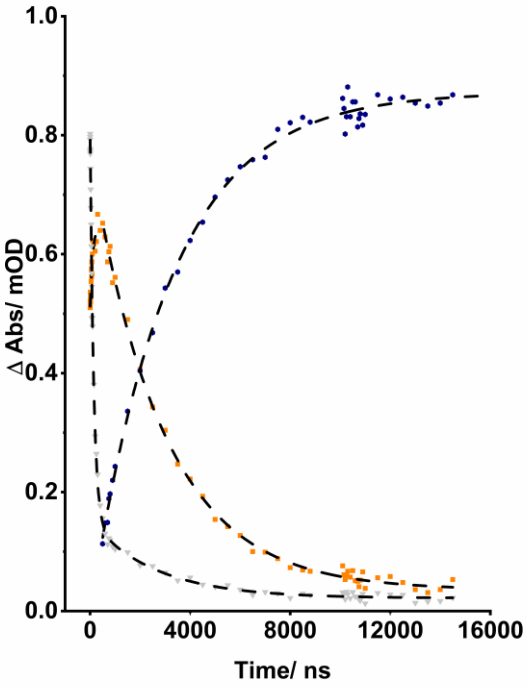

Figure 68. Kinetics for the loss of **159** and formation of **179** plus **169**, then subsequent conversion of **169** to **179**. **167** denoted by denoted by grey triangle, **169** denoted by orange squares, and **179** denoted by dark blue hexagons. Dotted lines denote exponential kinetics. Where appropriate a mono or biexponential fit was applied.

These observations indicate that phenyl acetylene coordination was kinetically favourable, substituting quicker with toluene. However, coordination of imine **178** was thermodynamically favourable, displacing the alkyne ligand (see Figure 69). Thus implying that if a *fac*-[Mn(C^N)(X)$(CO)_3$] species is the resting state of catalysis (as often proposed)[60], it is likely imine-bound rather than alkyne. This would also explain the

necessity for excess of alkyne in the original methodology reported by He and co-workers.[60] Additional alkyne would help sedate the formation of **179** from an alkyne bound complex, supporting the migratory insertion of the alkyne.

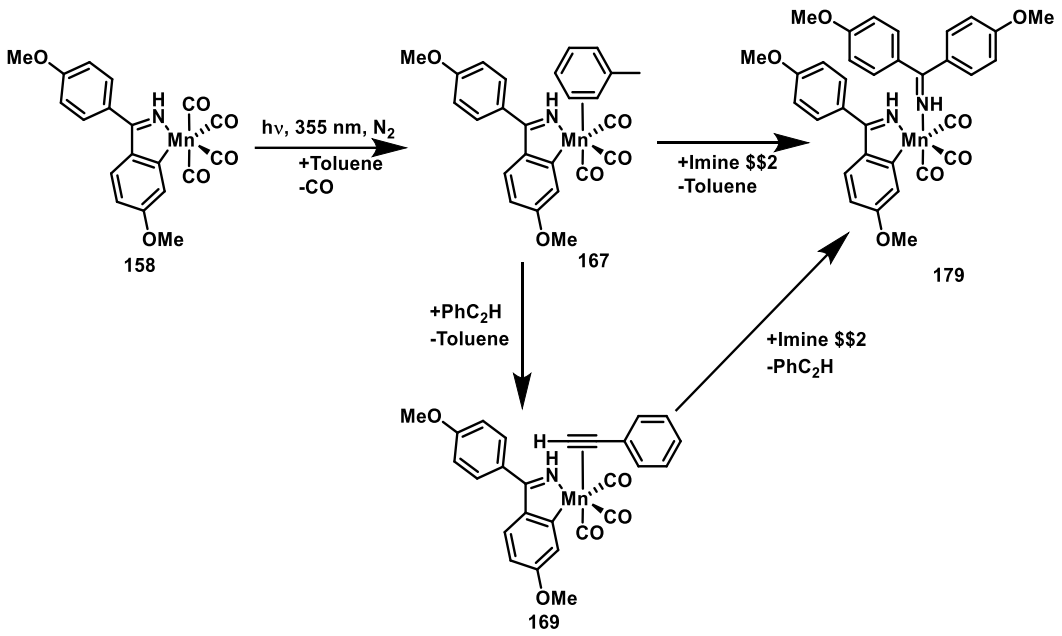

Figure 69. Summary of events observed by TR^{M}PS following photolysis of **158** in the presence of imine **178** and phenyl acetylene in anhydrous toluene solution excited at 355 nm under an atmosphere of N_2.

2.4.5 Catalytically relevant additives: Isoquinoline

Finally, a set of experiments like those conducted using imine **178** were carried out using the isoquinoline 6-methoxy-1-(4-methoxyphenyl)-3,4-diphenylisoquinoline **180**. The aim here was to probe product inhibition, and how the isoquinoline impacted speciation events.

Initially **158** in anhydrous toluene solution under an atmosphere of N_2 was probed by TR^{M}PS in the presence of just **180**, as a control experiment. Displacement of the initially bound toluene ligand from **167**, to form an isoquinoline bound transient **181** with bands at 1882, 1893, and 2001 cm^{-1} occurred with a rate constants, k_{obs}, of 7.4 ± 3.5 × 10^7 s^{-1}. Growth of the bands attributed to **181** grew in with a rate constants, k_{obs}, of 6.5 ± 3.1 × 10^7 s^{-1}. These bands then persisted for the duration of the experiment (see Figure 70 and Figure 71).

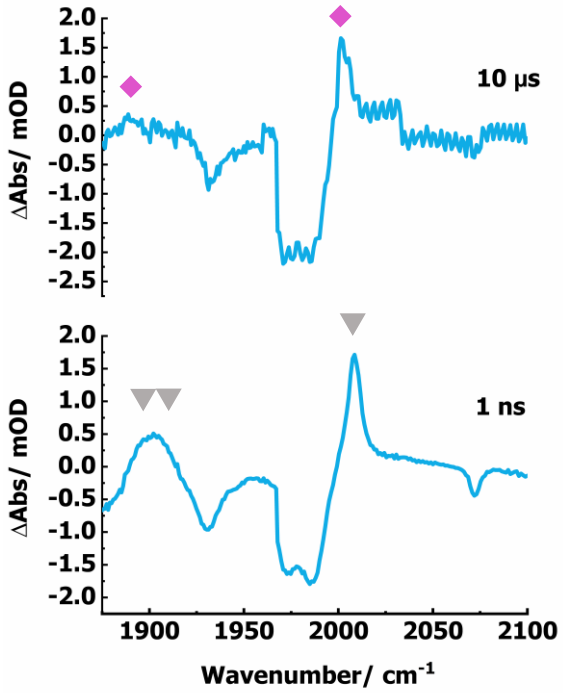

Figure 70. TRIR spectra of **158** in toluene solution with isoquinoline **180** additive under an atmosphere of N_2 at selected pump-probe delays. **167** denoted by denoted by grey triangles and **181** denoted by pink diamonds.*

*It should be noted that upon coordination of **180**, the TRIR spectra became substantially noisier, this was due to partial absorption of the pump laser pulses (355 nm) by the now bound isoquinoline.

Addition of a stoichiometric equivalency of either imine **178** or phenyl acetylene with respect to isoquinoline **180** had no statistical significance upon the lifetime of **167**, with values all within 95% confidence limits of eachother . In the presence of imine **178** and **180**, **167** decayed with a rate constant, k_{obs}, of 5.8 ± 1.5 × 10^7 s^{-1}. In the presence of **178**, **180**, and phenyl acetylene, **167** decayed with a rate constant, k_{obs}, of 6.5 ± 3.1 × 10^7 s^{-1}. Furthermore, at longer pump-probe delays *ca*. >100 µs, only the three transient bands at 2882, 1893, and 2001 cm^{-1} were detected. These observations indicate that coordination of isoquinoline **180** is both kinetically and thermodynamically favourable over phenyl acetylene and imine **178**. This infers that if the catalytic cycle proceeds through a *fac*-[Mn(C^N)(X)$(CO)_3$] intermediary species, product inhibition is likely to occur.

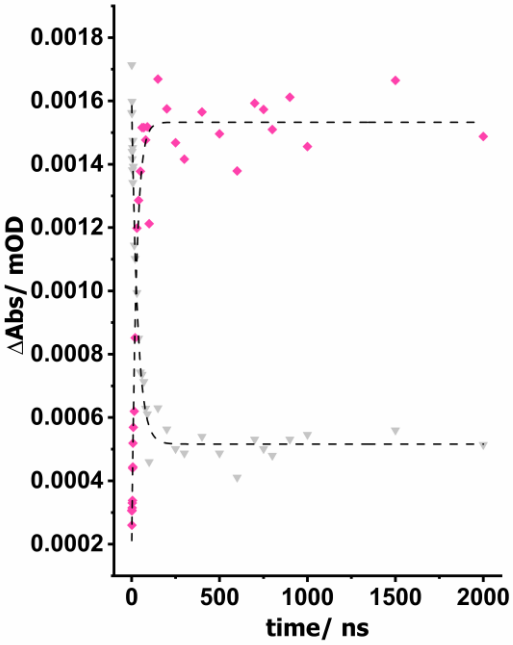

Figure 71. Kinetics for the loss of **167** and formation of **181**. **167** denoted by denoted by grey triangle, **181** denoted by pink diamonds. Dotted lines denote exponential kinetics. Where appropriate a mono or biexponential fit was applied.

2.4.6 Manganacycle 182

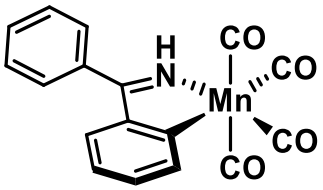

Figure 72. Structure of 5-membered manganacycle **182**.

To compliment the studies carried out on **158**, 5−membered manganacycle **182** was used (see Figure 72). Derived from the imine 1,1-diphenylmethanimine, the removal of the *para* methoxy groups compared to **178** decreases the electron density situated on the aromatic ring of the manganacycle, enabling us to probe the impact this has on alkyne coordination and subsequent migratory insertion.

182 possesses four bands in the metal carbonyl region, which are associated with various stretching modes. As shown in Figure 72, these are situated at 1944, 1983, 1991,

and 2075 cm^{-1} in toluene solution, which are assigned to the B_2, A_1, B_1, and A_1 CO stretching modes of **182** respectively. **182** also possesses a λ_{max} of 350 nm so a pump wavelength of 355 nm was used, as with experiment carried out on **158**.

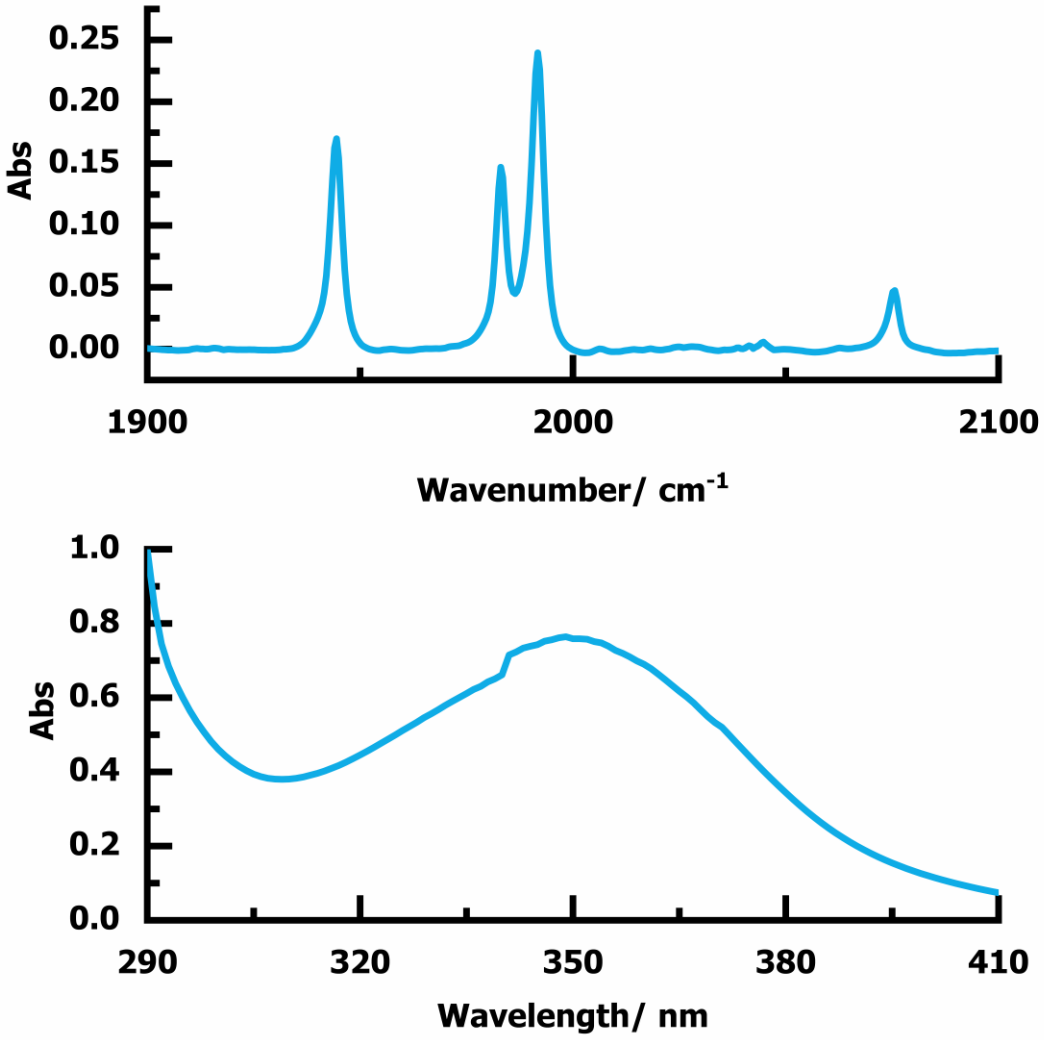

Figure 73. Top: FTIR spectrum of **182** in toluene solution. Bottom: UV/Vis spectrum of **182** in toluene solution with a λ_{max} of 350 nm.

An initial control was conducted, mirroring experiments using **158**, **182** in anhydrous toluene solution under an atmosphere of N_2 (see Figure 74). At early pump-probe delays *ca*. 100 ps, following the relaxation of vibrational hot photoproducts, a broad band

between 1904 and 1913 cm^{-1} and a sharper band at 1997 cm^{-1} were detected and assigned as the initially formed toluene complex *fac*-[Mn(C^N)$(CO)_3$(Toluene)] **183**, where (C^N) represents the imine 1,1-diphenylmethanimine. Over the course of 2 µs, these bands were replaced by a red shifted set of bands at 1893 to 1904 cm^{-1} and 1993 cm^{-1} which were assigned as *fac*-[Mn(C^N)$(CO)_3(OH_2)$] **184**. The second minor blue shifted bands at 1943 and 2013 cm^{-1} were attributed to *fac*-[Mn(C^N)$(CO)_3(\eta^1\text{-}N_2)$] **185**, with the third low energy band masked behind those of the water bound complex. As with **158**, in anhydrous toluene, the initially formed nitrogen complex underwent ligand substitution with water at long pump-probe delays.

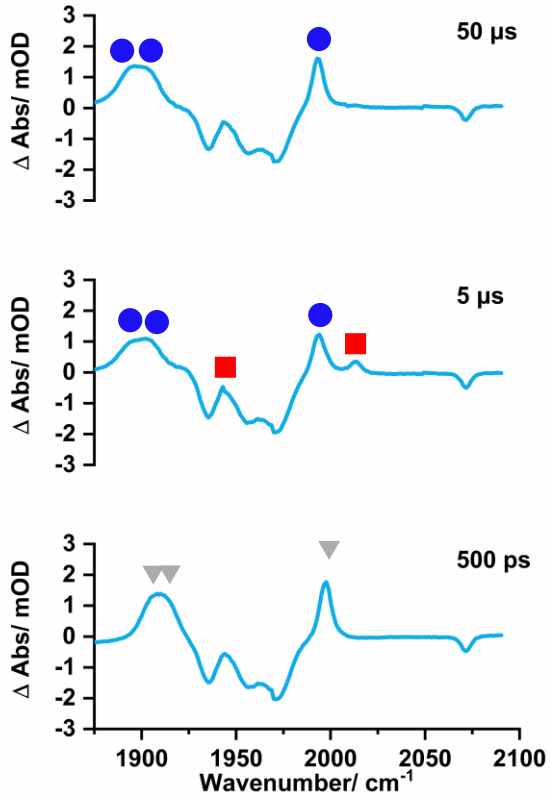

Figure 74. TRIR spectra of **182** in toluene solution under an N_2 atmosphere at selected pump-probe delays. Grey triangle denotes **183**, red square denotes **185**, and blue circle denotes **184**.

Phenyl acetylene was then introduced into the system, replicating the experiment conducted with **158** (see Figure 75). Displacement of toluene and coordination of phenyl acetylene occurred by *ca*. 300 ns. The rate constant, k_{obs}, for the depletion of **183** was 2.0 ± 0.8 × 10^7 s^{-1}, and 2.5 ± 0.4 × 10^7 s^{-1} for the formation of **186**, with bands blue shifted at 1916, 1942, and 2003 cm^{-1}. **186** was assigned to be the η^2-bound phenyl

acetylene complex *fac*-[Mn(C^N)(CO)$_3$(η^2-HCCPh)]. The rate constant, k_{obs}, for the migratory insertion of phenyl acetylene was then determined to be 6.1 ± 0.4 × 10^5 s^{-1} following the decay of **186**, forming red shifted bands at 1897, 1903 and 1992 cm^{-1} attributed to **187**. The complimentary rate constant, k_{obs}, was 5.6 ± 0.5 × 10^5 s^{-1} from an exponential fit applied to the band at 1992 cm^{-1}.

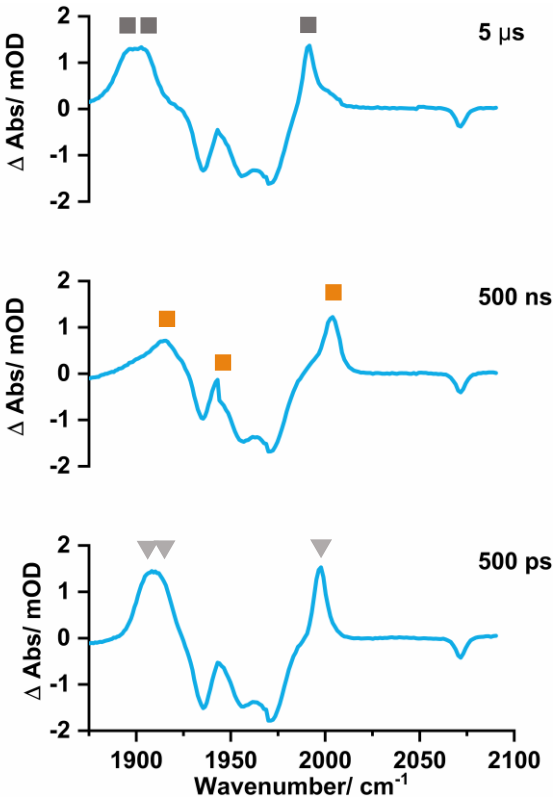

Figure 75. TRIR spectra of **182** in toluene solution with phenyl acetylene additive under an atmosphere of N_2 at selected pump-probe delays. **183** denoted by denoted by grey triangles, **186** denoted by denoted by orange squares, and **187** denoted by grey square.

For comparison, when under the same experimental conditions **158** was found to have a rate constant, k_{obs}, of 7.5 ± 0.1 × 10^7 and 3.7 ± 0.1 × 10^5 s^{-1} for the coordination and migratory insertion of phenyl acetylene (see Figure 76). Both of these values are statistically significant, lying outside of the 95% confidence limits determined for **182**. When the more electron rich 5−membered manganacycle **158** was excited, a faster rate constant was seen for the solvent bound complex, with the alkyne undergoing a more rapid displacement. Conversely, the less electron rich 5−membered manganacycle **186**

underwent a migratory insertion of its coordinated alkyne more rapidly, with the rate constant of the alkyne coordinated complex **186** over 50% less.

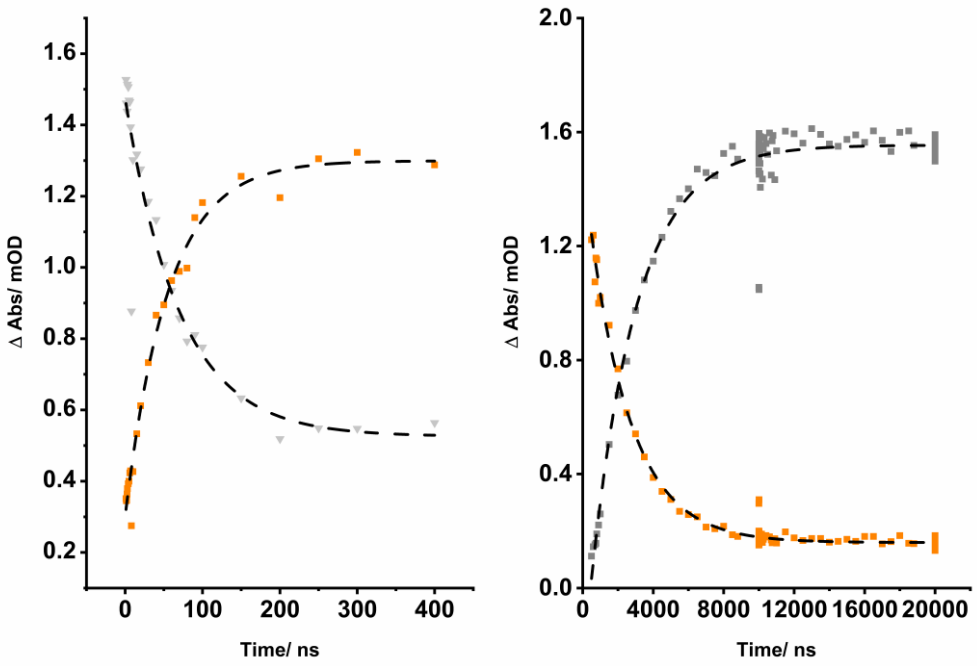

Figure 76. Left) Kinetics for the loss of **183** and formation of **186**. Right) Kinetics for the subsequent formation of **187** from **186**. **183** denoted by denoted by grey triangles, **186** denoted by denoted by orange squares, **187** denoted by grey squares. Dotted lines denote exponential kinetics. Where appropriate a mono or biexponential fit was applied.

2.5 Conclusions

Excitation of **158** and **182** at 355 nm successfully initiated photodissociation of one of the mutually *trans* CO ligands. This enabled the study of the ultrafast processes involving [Mn(C^N)(CO)$_4$] *via* time-resolved multiple probe spectroscopy. No evidence for the 16 electron complex *fac*-[Mn(C^N)(CO)$_3$] was seen. Instead, at the shortest pump-probe delay vibrationally 'hot' *fac*-[Mn(C^N)(CO)$_3$(solvent)] was observed. The solvent bound complexes proceeded to undergo ligand substitution (*ca*. 50-500 ns) with more favourable ligands, including residual water in 'anhydrous' solvent and dissolved dinitrogen- forming one of a handful of manganese dinitrogen complexes. The

dinitrogen bound complexes persited for the duration of experiments in anhydrous *n*-heptane, indicating a degree of stability. This stability could allow the study of alternative ways to activate dinitrogen.

Addition of catalytically relevant alkynes, imine, or isoquinoline resulted in their preferential coordination over N_2 and water in all instances, except for diphenyl acetylene in toluene solution. Phenyl acetylene displaced the coordinated solvent ligand, coordinating as η^2-HCCPh. In the absence of **178** or **180** the alkyne then underwent migratory insertion, forming a 7−membered manganacycle. The lifetime of the η^2-HCCPh bound alkyne complex was reduced when the less electron rich 5−membered manganacycle **182** was used, speeding up the rate of migratory insertion. Isoquinoline **180** was found to be the most thermodynamically favourable ligand coordinated in the vacant site generated though CO loss, implying that product inhibition is likely to occur in the system reported by He and co-workers.[60] To further distinguish between the water coordinated complex **160** and the 7-membered manganacycles formed, experiments could be conducted under an atmosphere of CO. If the water complex **160** had formed, then re-coordination of a CO ligand would be expected to ultimately occur. Conversely, if the alkyne has undergone a migratory insertion reaction to form a new carbon–carbon bond, then re-coordination of a CO ligand would not be expected.

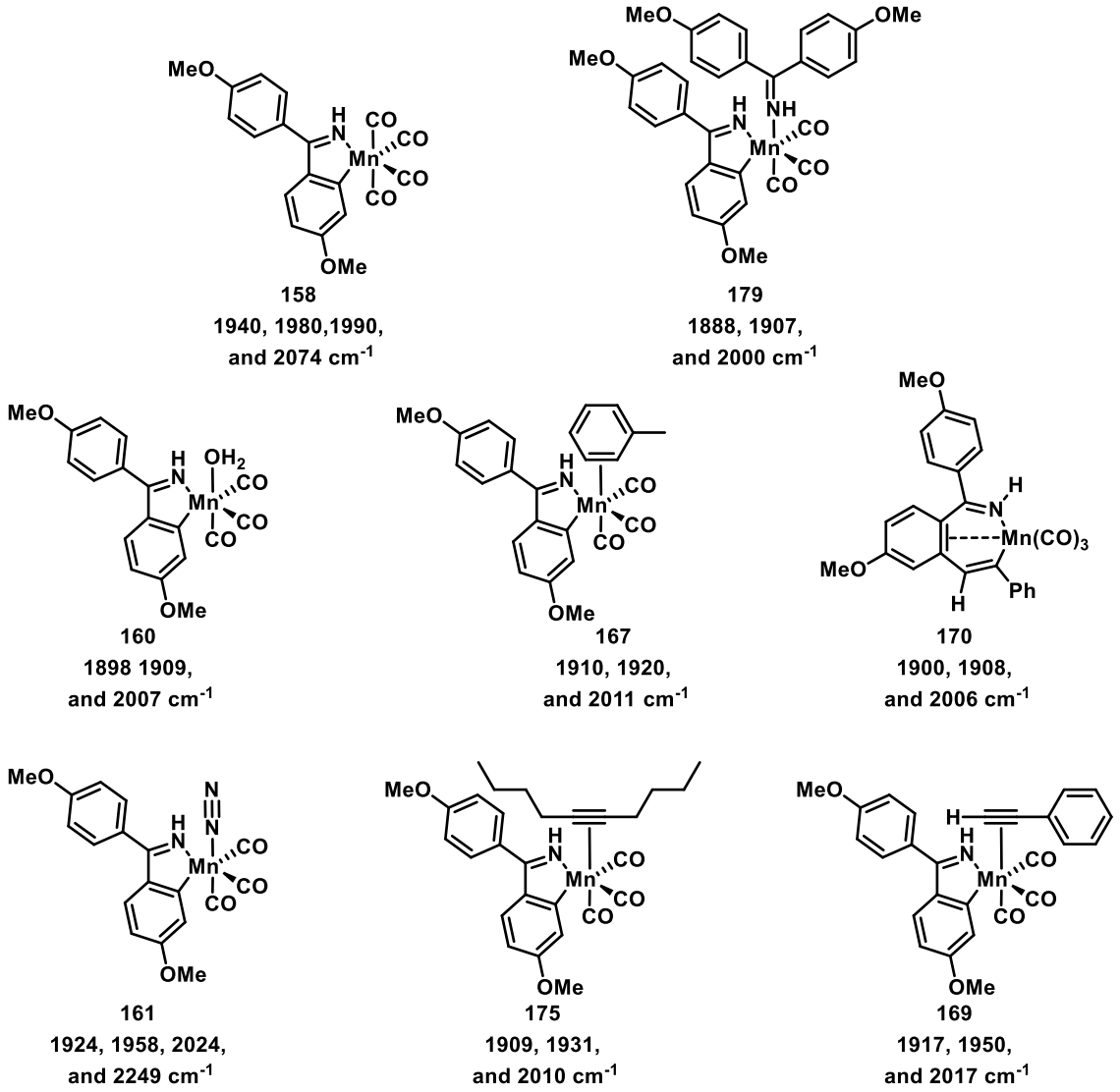

Figure 77. *fac*-[Mn(C^N)$(CO)_3$(X)] species observed during the TRIR studies conducted on **158** in toluene solution.

Compared to previous work by Hammarback and co-workers, who investigated the coordination and migratory insertion of phenyl acetylene to a 2-phenylpyridine derived manganacycle, phenyl acetylene undergoes substitution with toluene an order of magnitude faster ($3.43 \pm 0.45 \times 10^7$ s^{-1} compared to $3.85 \pm 1.24 \times 10^6$ s^{-1}).[30] This highlights the increased reactivity of the system, likely due to the moving of steric bulk an atom further from the heteroatom directing group. The rate of carbon-carbon bond formation through migratory insertion proceeded in neat phenyl acetylene with a rate constant, k_{obs}, of $3.3 \pm 0.2 \times 10^5$ s^{-1}, while a rate constant, k_{obs}, of $1.67 \pm 0.3 \times 10^5$ s^{-1}

was reported for the 2-phenyl pyridine derived analogue. Again, this highlights the increased reactivity with the imine ligand.

N_2 possesses a stronger affinity toward the imine derived tricarbonyl complex *fac*-[Mn(C^N)$(CO)_3$] than the 2-phenyl pyridine derivative. Prior work by Aucott and co-workers investigating 2-phenyl pyridine derived *fac*-[Mn(C^N)$(CO)_3$(Solvent)] complexes only reported formation of *fac*-[Mn(C^N)$(CO)_3(H_2O)$], not *fac*-[Mn(C^N)$(CO)_3(\eta^1\text{-}N_2)$] in a range of solvents including *n*-heptane and toluene. The dinitrogen complex was not reported in any experiments by Hammarback and co-workers who also worked with the 2-phenyl pyridine derived 5-membered manganacycle **19**.

Chapter 3: The Methods of Activation of Manganese Carbonyl Precatalysts used in C–H bond functionalisation reactions

3.1 Background

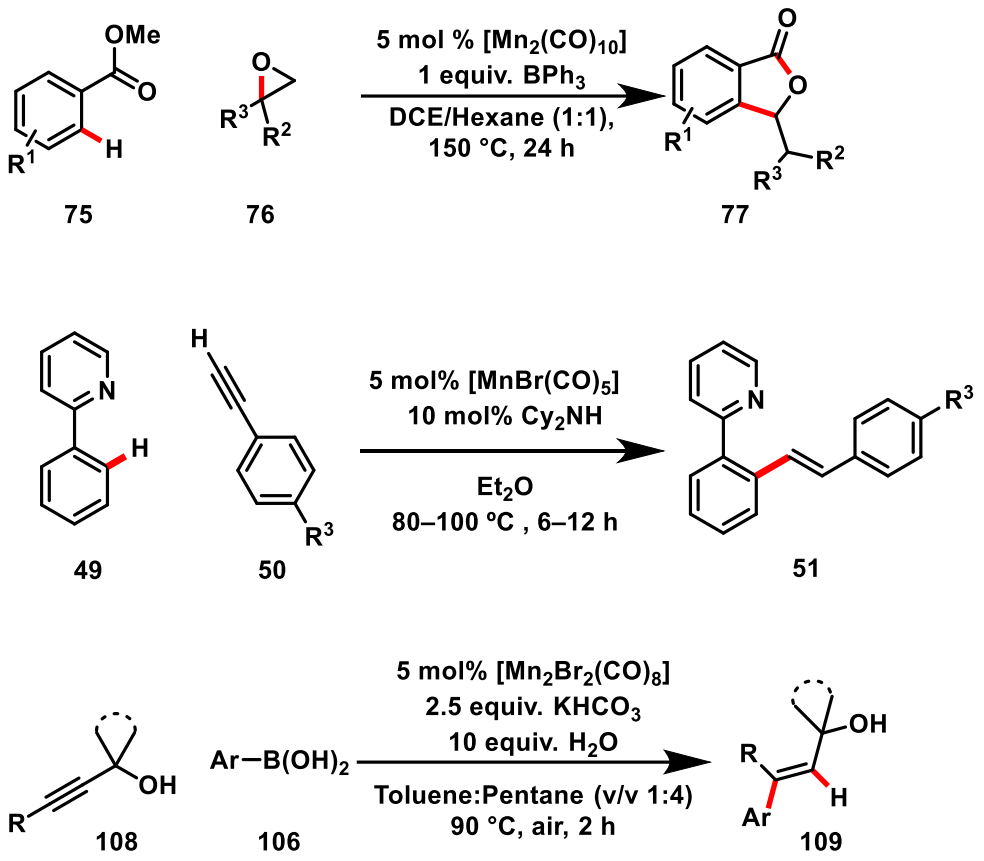

Figure 78. Examples of reactions catalysed by different manganese carbonyl precatalysts. Top: $[Mn_2(CO)_{10}]$ catalysed reaction reported by and Sueki co-workers.[65] Middle: $[MnBr(CO)_5]$ catalysed reaction reported by Zhou and co-workers.[46] Bottom: $[Mn_2Br_2(CO)_8]$ catalysed reaction reported by Yan and co-workers.[78]

As discussed in detail in Chapter 1, the last decade has seen a rapid evolution in the field of C–H bond functionalisation reactions catalysed by manganese carbonyl complexes, examples of the main precatalysts employed in these transformations are depicted in Figure 78.[1,2,41,42,46,65,78,112,113] Despite this, little attention has been given to precatalyst activation. This is highlighted by numerous publications where a proposed mechanism

has been given, yet the mechanism for precatalyst activation has been ignored in its entirety. Instead, the precatalyst is shown to form an on cycle 5-membered manganacycle directly.[58] Figure 79 highlights an example where the change in oxidation state was not addressed. $[Mn_2(CO)_{10}]$ possesses two manganese centres which are Mn^0, while both $[HMn(CO)_5]$ and the 5-membered manganacycle product are Mn^I. By having a greater understanding of the mechanism for pre-catalyst activation, reaction conditions can be optimised to address key issues in manganese (I) carbonyl catalysed reactions, such as the requirement for a high catalyst loading.

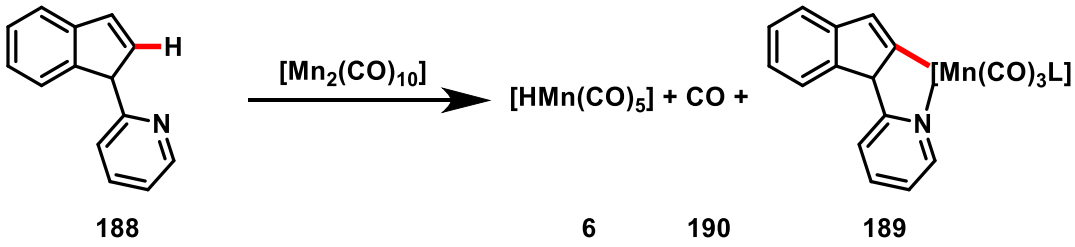

Figure 79. Proposed mechanism of activation for $[Mn_2(CO)_{10}]$ by Yu-Feng and co-workers.[58]

In the field of manganese carbonyl catalysed C–H functionalisation reactions a clear focus has been made on the development of synthetic methodologies. Research has been directed towards investigating what new bonds can be formed, rather than the underlying mechanisms that lie behind these reactions. This is highlighted by the overlooking of the route of precatalyst activation entirely, and numerous publications just proposing a catalytic cycle.[61][52]

Hammarback and co-workers explored the activation of $[MnBr(CO)_5]$ **191**, using the alkenylation of 2-phenylpyridine as a model reaction to probe precatalyst activation.[51] Two routes of precatalyst activation were discussed (see Figure 80). Following loss of a CO ligand and solvent coordination (**A**), the two routes diverge. The first route involves substitution of the solvent ligand with 2-phenylpyridine (**B**), activation of the 2-phenylpyridine C–H bond through a cyclometallation deprotonation (CMD) step (**C-D**), and substitution of a further CO ligand with phenyl acetylene (**E**). The second route involves substitution of the initially bound solvent ligand with phenyl acetylene (**F**), base-assisted deprotonation of phenyl acetylene to form an alkynyl complex (**G**), coordination of 2-phenylpyridene (**H**), and a proton rearrangement (**I**), reaching the same final

complex (**E**). It was found that direct activation of the C–H bond on 2-phenypyridine was slow, and that the second proposed route of activation was preferred. However, the route of activation for $[Mn_2(CO)_{10}]$ was not explored.

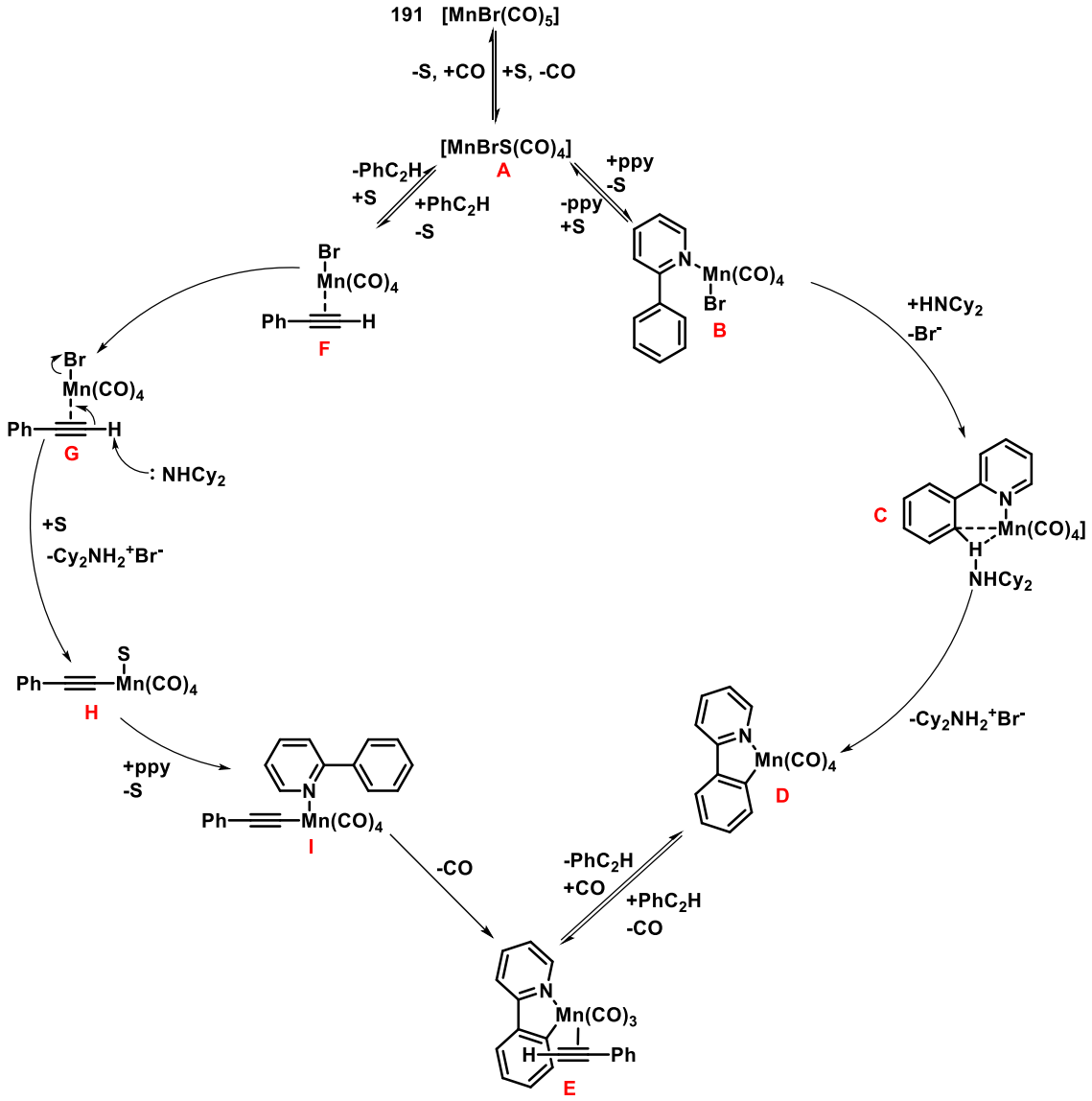

Figure 80. To possible routes of activation for $[MnBr(CO)_5]$ proposed by Hammarback and co-workers. Under conditions used by Hammarback and co-workers the left hand route was found to be favourable.[51]

Further work by Hammarback and co-workers explored the role acids play in manganese catalysed C–H bond functionalisation reactions.[114] In the presence of ethanoic acid 2-phenyl pyridine showed enhanced reactivity. This was demonstrated by the alkenylation of 2-phenyl pyridine with diphenyl acetylene. The reaction between 2-phenyl pyridine and diphenyl acetylene was unsuccessful in Zhou and co-workers initial

study, in which 2-phenyl pyridine was only alkenylated successfully by terminal alkynes (see Chapter 1, Figure 11).[46] It was hypothesised that ethanoic acid provided the additional source of "H" to form the desired product, which was previously unachievable.

Dicyclohexylamine-derived conjugate acids were then tested with a variety of substrates, including phenyl acetylene, propargyl benzoate, and butyl acrylate. The proton source had little impact on the alkenylation of 2-phenylpyridine with phenylacetylene, while a dramatic increase in yield was seen when a conjugate base was used to aid the reaction with propargyl benzoate. Conversely, conjugate acids had a negative impact upon the reaction between 2-phenylpyridine and n-butyl acrylate. Hammarback and co-workers rationalised these observations with two key points. Firstly, the conjugate base restricted formation of manganese hydroxyl clusters, which are known to be catalytically inactive. Secondly, the lifetime of the 5-membered manganacycles were increased. [51]

Herein, the [4+2] annulation of N–H imines and alkynes, forming an isoquinoline product was employed as a model reaction to probe routes of precatalyst activation (see Figure 81).[60] This particular manganese carbonyl catalysed reaction was chosen, as unlike many transformations, the addition of an additive such as $HNCy_2$[46], BPh_3[64,65], or $ZnMe_2$[66] was not required. Furthermore, this provides a platinum-group metal-free route towards an isoquinoline motif[115–117], which have medicinal applications due to anti-inflammatory and anti-malarial properties.[118],[1]

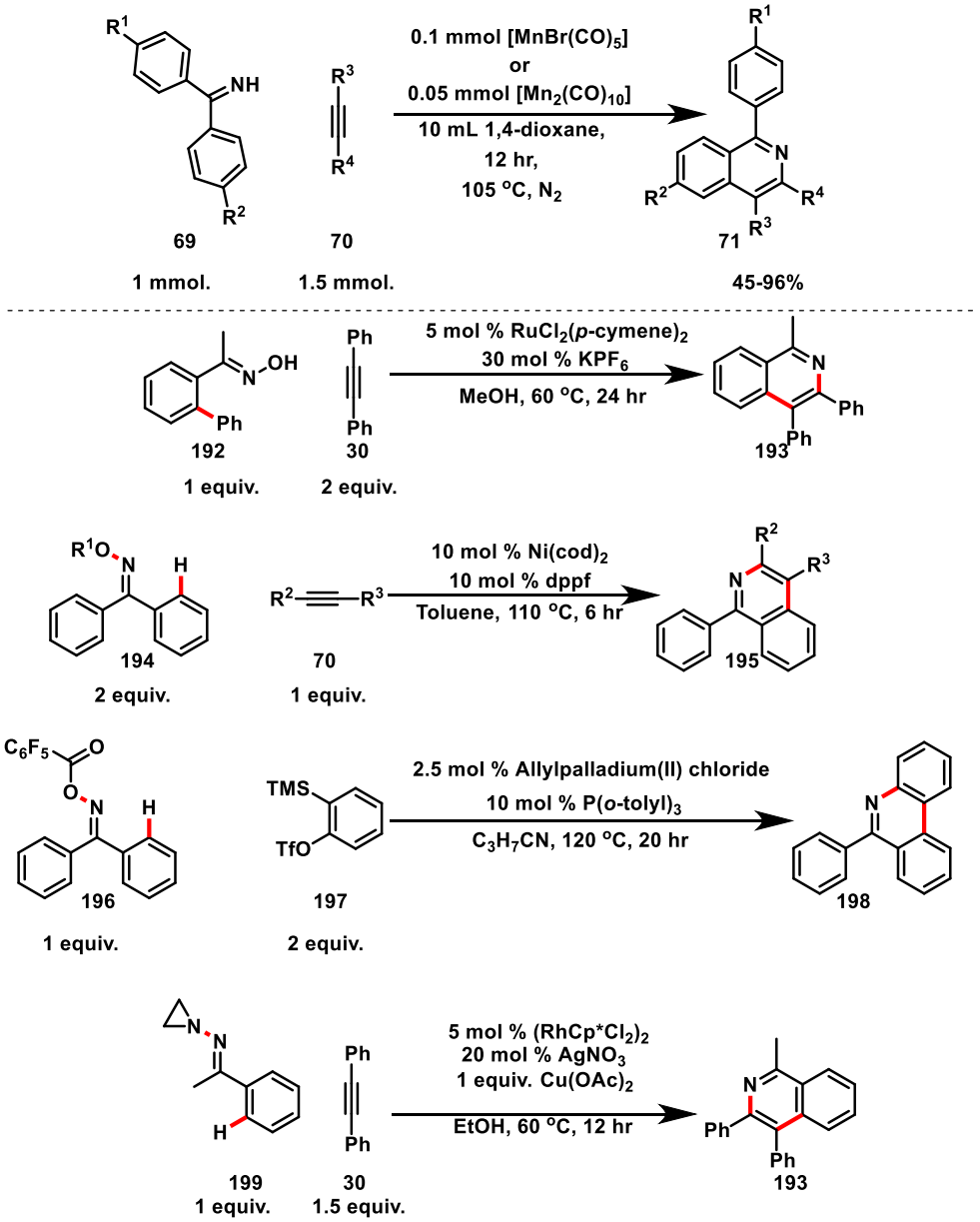

Figure 81. Top:[4+2] annulation of N–H imines and alkynes by C–H/N–H activation.[60] Bottom: alternative routes for synthesis of an isoquinoline motif Rh[115], Ru[116], Pd[117], and Ni[119].

He and co-workers first reported this reaction, which was shown to perform similarly using $[MnBr(CO)_5]$ and $[Mn_2(CO)_{10}]$ as a precatalyst, giving yields of 92% and 87% respectively.[60] Their substrate scope showed that the reaction proceeded with moderate to high yields for a range of electron-donating imines (varied R^1 and R^2 groups), however no electron withdrawing imines were reported. A more substantial substrate scope, changing R^3 and R^4 on the alkyne, showed that internal alkynes generally gave a higher yield than terminal alkynes, unlike many manganese carbonyl

catalysed reactions, which require the use of a terminal alkyne.[46] Steric bulk at R^3 and R^4 had a moderate impact on yields, with a decrease from 92% to 73% reported when changing from R = Ph to R = *n*-Pr. Similarly, a decreased yield of 63% was reported when a *p*-methyl benzoate functional group was incorporated.

A limited mechanistic study was also conducted, which revealed aspects of the mechanism (see Figure 82). First 2-styryl imine **200** was synthesised and probed under catalytic conditions (**A**), however cyclisation to form the respective isoquinoline product **201** did not occur. Instead, **200** remained mainly unreacted, with 3,4-dihydroisoquinoline **202** formed as a minor product. The reaction was then repeated in the presence of 1.5 equivalents of phenyl acetylene (**B**). A small amount of the isoquinoline product **203** was detected, most of **200** was involved in side reactions, forming **204** and **205**. This ruled out reaction progression *via* an alkenylation and subsequent cyclisation. The precatalyst $[MnBr(CO)_5]$ was then heated in the presence of imine **178**, under similar conditions to those used in catalysis, and formed the 5-membered manganacycle **158** in 30% yield (**C**). **158** reacted stoichiometrically with diphenyl acetylene to form the respective isoquinoline product **180** (84%) and *cis*-stilbene (15%) (**D**). The yield was similar to that achieved when $[MnBr(CO)_5]$ was used as a precatalyst, indicating that **158** is likely a catalytically relevant intermediate. Intramolecular, intermolecular, and parallel reactions were then conducted to determine KIE values (**E**-**G**). These were determined to be 1.9, 2.0 and 2.2 respectively, and from this the conclusion that irreversible C–H bond cleavage might be involved in the rate-determining step was made. Finally, GC analysis on the headspace of the catalytic system indicated that H_2 production occurred, and this was proposed to be part of the route for catalyst regeneration. Again, as with many other studies, no indication was given on how $[Mn_2(CO)_{10}]$ was activated.

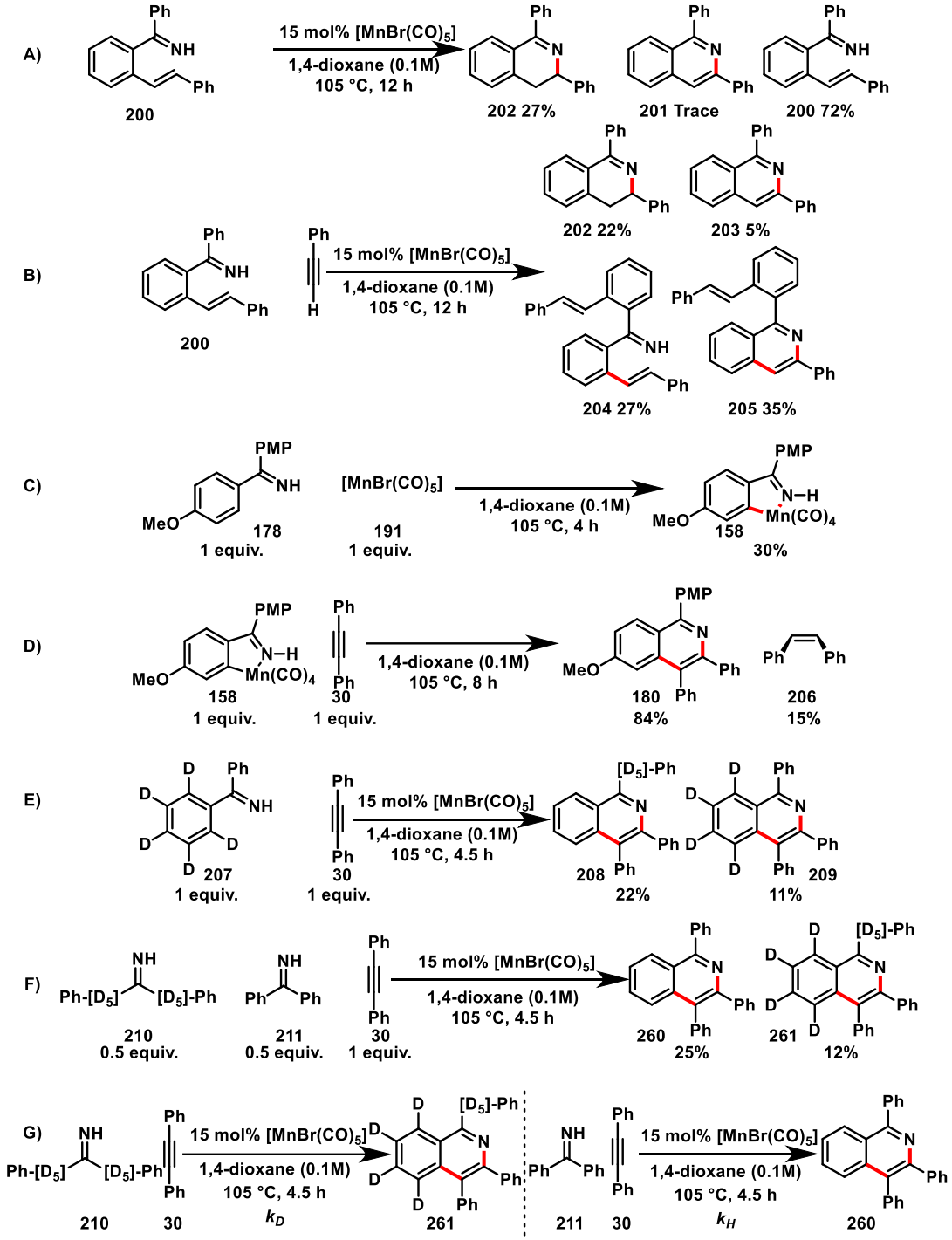

Figure 82. Mechanistic studies by He and co-workers.[60]

3.2 Aims and Objectives

The aims of the Chapter are to initially probe the various modes of activation for precatalysts used in manganese (I) catalysed C–H bond functionalisation reactions, then to optimise the light-dependant functionalisation of imine **178** using the precatalyst $[MnBr(CO)_5]$.

The [4+2] annulation of primary imines and alkynes, forming an isoquinoline, reported by He and co-workers has been chosen as the model reaction used to probe precatalysts.[60] [$MnBr(CO)_5$], [$Mn_2(CO)_{10}$], and [$Mn_2Br_2(CO)_8$] are precatalysts employed in the literature. [$Mn_2(CO)_9$(1,1-bis(4-methoxyphenyl)methanimine), [$BnMn(CO)_5$], [$Mn(CO)_5(NCMe)]^+$, and [Mn(*p*-tolylacetylide)$(CO)_5$] are alternative manganese precatalysts that will be explored.

3.3 Activation of Manganese (I) Precatalysts

Initially, commercially available [$MnBr(CO)_5$] **191** and [$Mn_2(CO)_{10}$] **102** from Insight Biotechnology and Strem Chemicals UK were used as precatalysts in the [4+2] annulation of primary imines and alkynes, forming an isoquinoline.[60] In almost all literature studies, one of these two have been reported as the optimum precatalyst for manganese (I) catalysed C–H bond functionalisation transformations. Mirroring the original study by He and co-workers, 1,1-bis(4-methoxyphenyl)methanimine **178** and diphenyl acetylene **26** were used as the model substrates.[60] Thus, the 5-membered manganacycle **158** was synthesised as an additional catalytically relevant species (see Figure 83), which was discussed by He and co-workers as an on-cycle intermediate.[60]

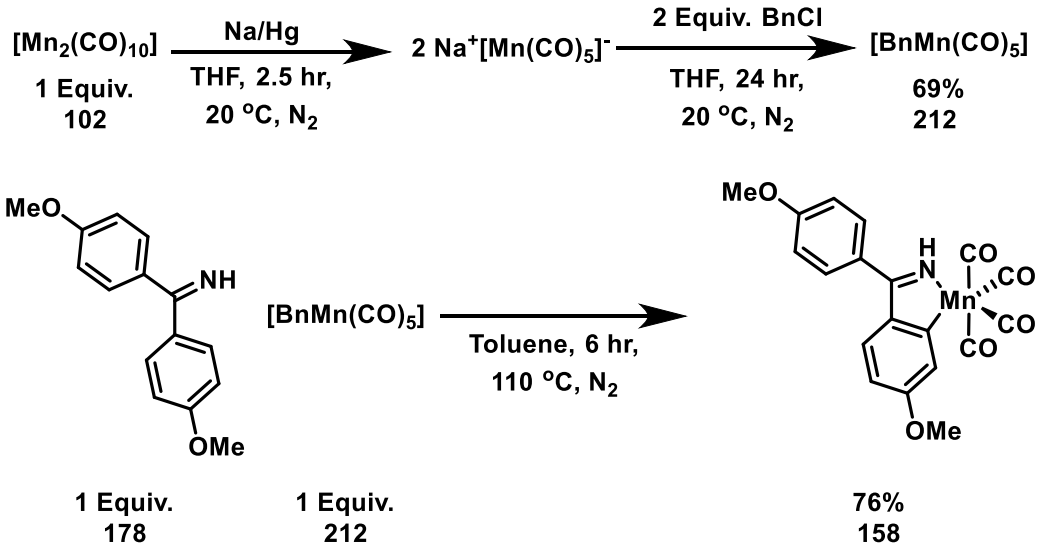

Figure 83. Synthetic route to **158.**

These complexes were then employed as precatalysts in the model reactions depicted in Figure 84. The system was excluded from light for the duration of reactions, as manganese (I) complexes typically possess a large extinction coefficient in the visible

region of the electromagnetic spectrum and have been shown to undergo light-induced CO loss.[96]

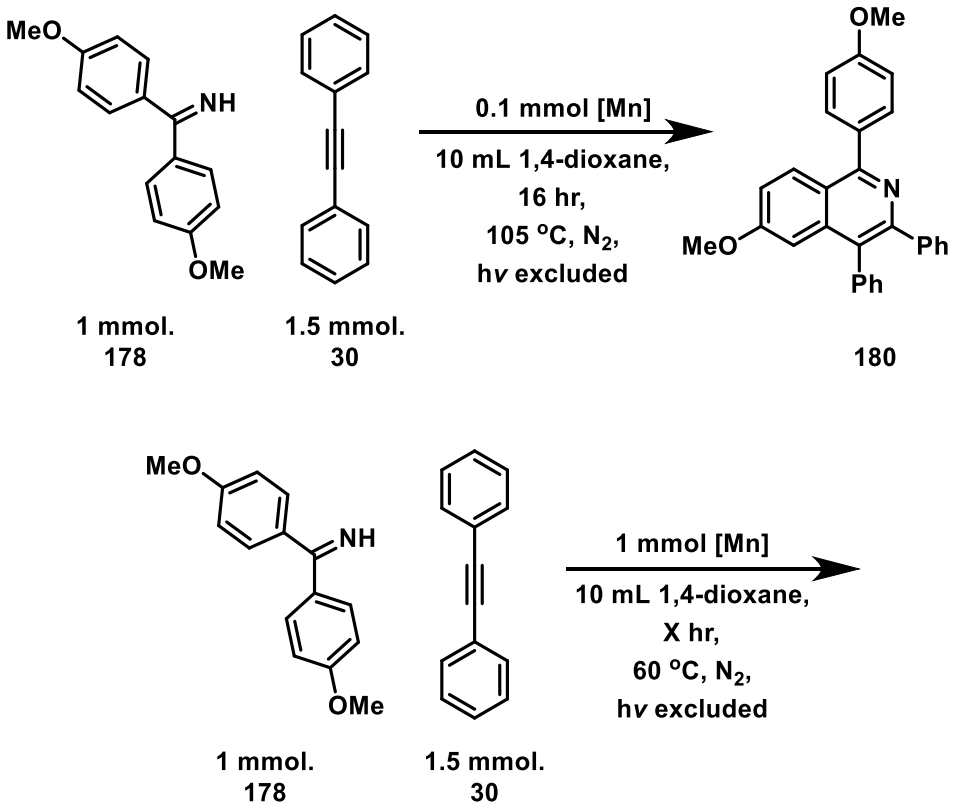

Figure 84. Model reactions used to probe precatalyst activation. Top: Catalytic reaction based on the model reaction used for optimisation by He and co-workers.[60] Bottom: stoichiometric conditions, when applicable 1 equiv. of imine, 1 equiv. of [Mn] and 1.5 equiv. of alkyne were used. Typically, a temperature of 60 °C was used. However, this was increased to 80 °C when necessary.

3.3.1 $[Mn_2(CO)_{10}]$

The route of activation for $[Mn_2(CO)_{10}]$ was initially explored. This was the most ambiguous precatalyst, as literature studies often assume that $[MnBr(CO)_5]$ and $[Mn_2(CO)_{10}]$ behave analogously, despite possessing different oxidation states. Even though the metal centres in $[Mn_2(CO)_{10}]$ are manganese (0), the active species generated is presumed to be manganese (I), hence the probing of this precatalyst.

An initial experiment was conducted under the catalytic conditions outlined in Figure 84 and 0.05 mmol of $[Mn_2(CO)_{10}]$ was used, due to two manganese centres present on the precatalyst. *In situ* IR spectroscopic measurements were made on a Mettler Toledo

ReactIR ic10 with a K6 conduit SiComp (silicon) probe and MCT detector using the general methodology outlined in Chapter 6.

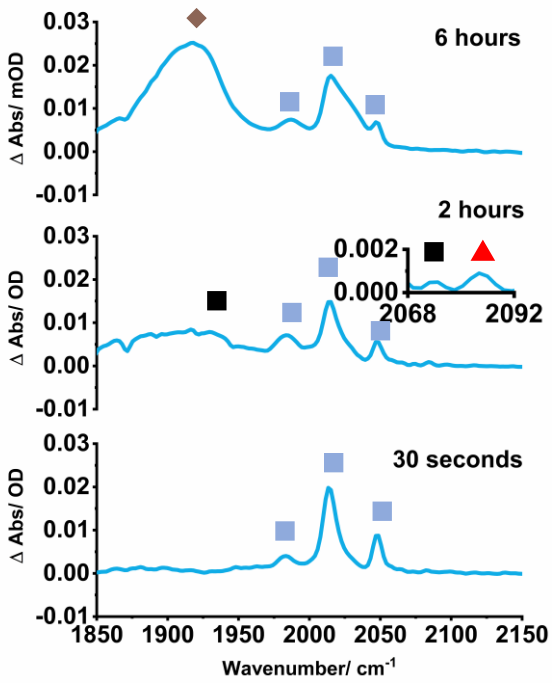

Figure 85. IR Spectroscopic changes over time for the reaction of **158** + **26** → **180** under conditions described in Figure 84. [Mn] = [$Mn_2(CO)_{10}$]. [$Mn_2(CO)_{10}$] denoted by blue square, **158** by black square, 2085 cm^{-1}(**216**) band by red triangle, and hydroxy-bridge clusters by brown diamond.

The three bands associated with [$Mn_2(CO)_{10}$] were seen throughout the experiment at 1982, 2014, and 2048 cm^{-1} (see Figure 85). Despite this, a yield of 83% (87% lit. yield of **180**[60]) was obtained for this experiment. This indicates that either [$Mn_2(CO)_{10}$] is reformed during the reaction, or only a small proportion of active catalyst is generated. As the reaction proceeded, two high energy stretching modes were detected at 2074 and 2085 cm^{-1}, along with a broad feature spanning 1870-1965 cm^{-1}. The band at 2085 cm^{-1} is assigned as an unknown species **216**, which will be discussed in greater detail in this section, and assigned in Chapter 4 based on additional evidence supporting the assignment of IR bands. The broad feature matches those assigned to manganese hydroxy and alkyne-bridged clusters reported by Hammarback and co-workers, who observed their formation under a similar experimental setup.[51] Hammarback and co-workers also reacted [$Mn_2(CO)_{10}$] with water, and were able to synthesise, isolate and characterise the manganese hydroxy-bridged cluster depicted in Figure 86.[51] This

included the growing of a single crystal and the crystallographic structure was determined to match that depicted in Figure 86, supporting the assignment of broad feature in Figure 85 spanning 1870-1965 cm^{-1}. The band at 2074, corresponds with the high energy A_1 stretching mode of **158**, as discussed in Chapter 2, but a definitive assignment cannot be made. Due to the weak intensity, bands at 1990, and 1980 cm^{-1} are potentially masked by the low energy band of $[Mn_2(CO)_{10}]$ (1982 cm^{-1}), while an argument can be made for a weak band at 1940 cm^{-1}, which would fit with the B_2 stretching mode of **158**.

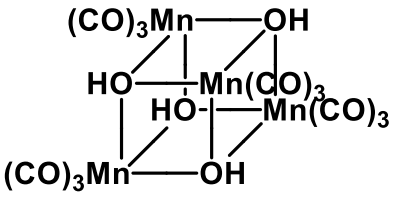

Figure 86. Manganese hydroxy-bridged cluster **213** reported by Hammarback and co-workers.[51]

The reaction was repeated with a stoichiometric quantity of imine **178**, alkyne **26** and $[Mn_2(CO)_{10}]$ at 60 °C (see Figure 84). However, $[Mn_2(CO)_{10}]$ remained unreacted. Upon increasing the reaction temperature to 80 °C, and repeating the experiment, the bands belonging to $[Mn_2(CO)_{10}]$ depleted, and formation of the isoquinoline product **180** was detected *via* ^{1}H NMR and MS aliquots. The formation and depletion of **216** and **158** could be followed by *in situ* IR spectroscopy. **216** and **158** were formed on similar timescales, as depicted in Figure 87. However, biexponential fits struggled to fit the data due to noise and observed rate constants could not be obtained.

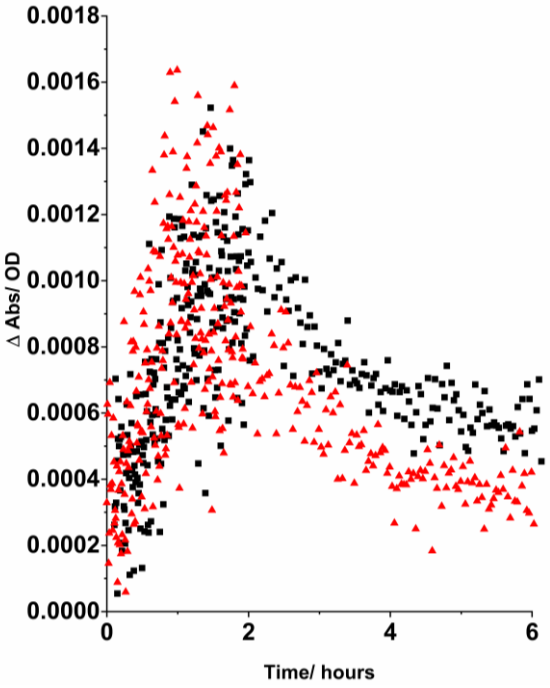

Figure 87. Kinetics for the formation and loss of 2085 cm^{-1} band and **158**. **158** denoted by black square, and 2085 cm^{-1} band by red triangle.

To gain further insight into the activation of $[Mn_2(CO)_{10}]$ in this reaction, the coordination of an imine molecule was investigated. Precatalyst activation must proceed through either the Mn−Mn bond, or one of the Mn-CO bonds being broken, as explored in detail within Chapter 4. Firth and co-workers also demonstrated that cleavage of the Mn−Mn bond ultimately forms either a *fac*-$[Mn(CO)_3(solvent)_3]^+$ or $[Mn(CO)_5(solvent)]^+$ cation.[70] $[Mn(CO)(NCMe)_3]^+PF_6^-$ was synthesised as analogue for *fac*-$[Mn(CO)_3(solvent)_3]^+$ (see Figure 88). CO-loss in the presence of a ligand is expected to give the complex $[Mn_2(CO)_9(L)]$, where L = a 2-electron donor ligand. Peng and Gao demonstrated that $[Mn_2(CO)_9(pyridine)]$ could be prepared by chemically inducing dissociation of a CO ligand from $[Mn_2(CO)_{10}]$, with trimethylamine *N*-oxide, in the presence of pyridine.[120] This was repeated in the presence of imine **178** to give $[Mn_2(CO)_9$(1,1-bis(4-methoxyphenyl)methanimine)] (see Figure 88).

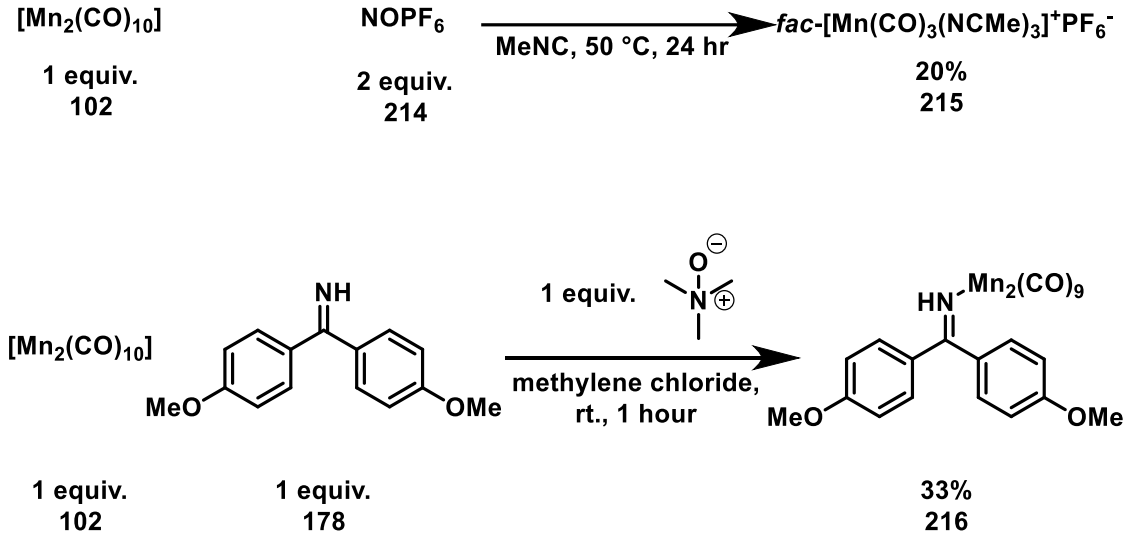

Figure 88. Top: synthetic route for $[Mn(CO)(NCMe)_3]^+PF_6^-$ **215**. Bottom: synthetic route for $[Mn_2(CO)_9$(1,1-bis(4-methoxyphenyl)methanimine)] **216**.

The structure of **216** was then confirmed *via* a single crystal isolated by recrystallisation from hot *n*-hexane. The structure demonstrated that one of the mutually *trans* CO ligands had dissociated, rather than the terminal CO ligand *trans* to the second manganese centre (see Figure 89).

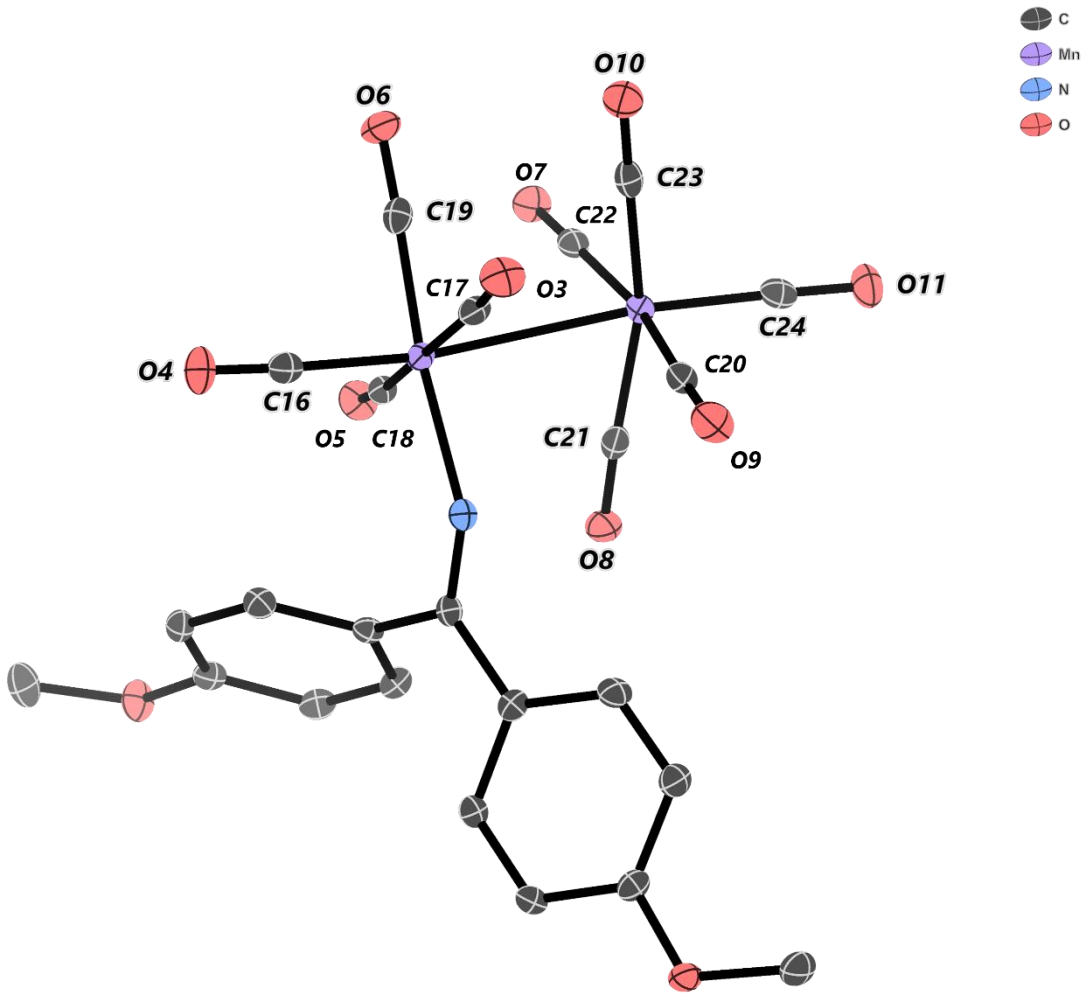

Figure 89. Crystallographic structure of the manganese complex $[Mn_2(CO)_9$(1,1-bis(4-methoxyphenyl)methanimine)] **216**.

215 and **216** were then employed in the catalytic model reaction shown in Figure 84, testing their catalytic relevance. The manganese cation **215** was found to be catalytically inert, not forming isoquinoline **180**. Whereas, when **216** was used as the precatalyst, a yield of 88% was recorded, reflecting observations when $[Mn_2(CO)_{10}]$ was used as a precatalyst. To further support the catalytic significance of **216**, the metal carbonyl stretching modes are positioned at 2084, 2019, 1998, 1980, 1958, and 1929 cm^{-1} in toluene, providing a potential candidate for the band at 2085 cm^{-1} in Figure 85. This assignment is supported further in Section 4.4.3 where TRIR studies clearly demonstrate the reaction between $[Mn_2(CO)_9]$ and the imine **178** to form **216**. Conversely **215** had bands positioned at 1975 and 2065 cm^{-1}, neither of which were observed in the initial experiment.

Table 7. Yield of **180** when $[Mn_2(CO)_{10}]$, **216**, and **215** were used in the model reaction depicted in Figure 84.

Precatalyst	Yield/ %
$[Mn_2(CO)_{10}]$	83
$[Mn(CO)(NCMe)_3]^+PF_6^-$	0
$[Mn_2(CO)_9$(1,1-bis(4-methoxyphenyl)methanimine)]	88

An experiment was then caried out using **216** as the manganese precatalyst in the model reaction, in which reaction progress was monitored *via in situ* IR spectroscopy, as with $[Mn_2(CO)_{10}]$ (see Figure 90). Initially only the precatalyst **216** was observed in solution. The bands associated with **216** decayed over the course of *ca*. 30 minutes. In their place bands associated with **158**, $[Mn_2(CO)_{10}]$, and finally features due to manganese hydroxy-bridged grew in intensity. Application of a mono exponential fit to the band at 2085 cm^{-1} for **216** gave a rate constant k_{obs} of 2.7 ± 0.6 × 10^{-3} s^{-1}, while the band at 2074 cm^{-1} associated with **158** grew in with a rate constant k_{obs} of 2.7 ± 0.3 × 10^{-3} s^{-1} indicating that **216** was converting into **158** (see Figure 91). Finally, a mono exponential fit applied to the $[Mn_2(CO)_{10}]$ band at 2048 cm^{-1} gave a rate constant k_{obs} of 1.9 ± 0.12 × 10^{-3} s^{-1}.

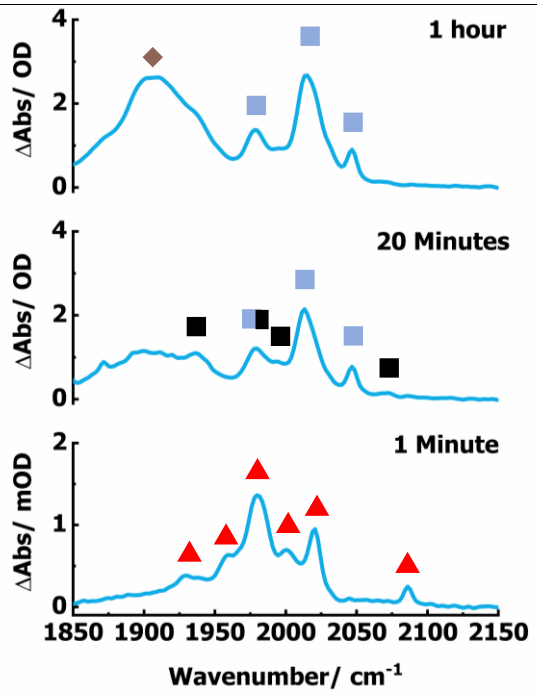

Figure 90. IR spectroscopic changes over time for the reaction of **178**+ **216** → **180** under conditions described in Figure 84. [Mn] = **216**. $[Mn_2(CO)_{10}]$ denoted by blue square, **158** by black square, **216** band by red triangle, and hydroxy-bridge clusters by brown diamond.

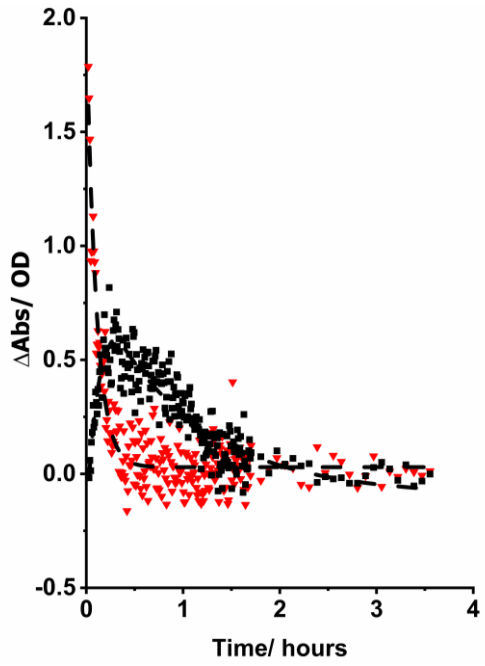

Figure 91. Kinetics for the loss of **216** and formation/loss of **158**. **216** denoted by red triangles and **158** denoted by black squares. Dotted lines denote exponential kinetics. Where appropriate a mono or biexponential fit was applied.

To further cement the hypothesis that **216** converts into **158**, a stoichiometric quantity (1 mmol dm^{-3}) of **216** and imine **178** were heated at 60 °C in the absence of alkyne **26**, preventing further reaction (see Figure 92). Reaction progress was followed *via in situ* IR spectroscopy. At 60 °C formation of **158** was not observed, only thermal decomposition of **216** occurred, forming manganese clusters. Upon heating the reaction mixture to 80 °C, **216** converted directly to **158** over the course of *ca*. 3 hours and remained for the duration of the reaction. Exponential fits gave a rate constant k_{obs} of $2.2 \pm 0.2 \times 10^{-4}$ s^{-1} and $2.0 \pm 0.1 \times 10^{-4}$ s^{-1} for the loss of **216** and formation of **158** respectively.

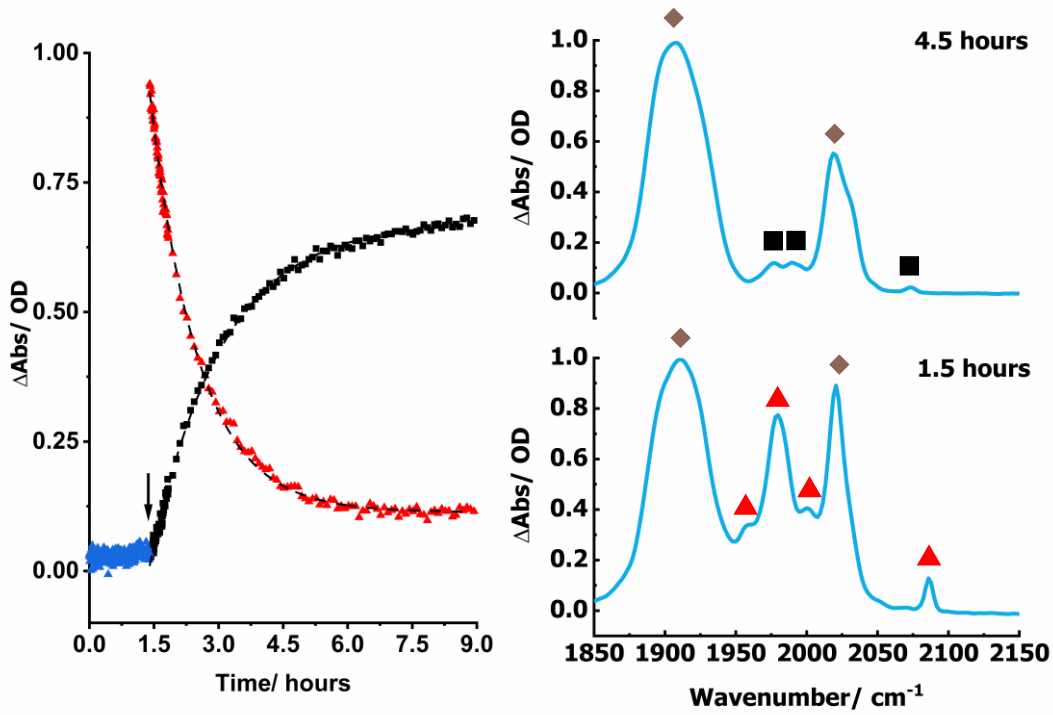

Figure 92. Left: Kinetics for the loss of **216** and formation **158**. Dotted lines denote exponential kinetics. Where appropriate a mono or biexponential fit was applied. Arrow denotes when the temperature was increased to 80 °C. Right: IR spectroscopic changes over time for the reaction of **178**+ **216** → **158**. **216** denoted by red triangles, **158** denoted by black squares, and hydroxy-bridge clusters by brown diamond.

Finally, a 1 mmol dm^{-3} solution of **216** in 1,4-dioxane was heated at 80 °C in the absence of imine **178** and alkyne **26**, while being followed *via in situ* IR spectroscopy (see Figure 94). The aim was to assess if further imine is required to active the precatalyst, or if

heating of **216** results in C–H bond activation of the bound imine molecule. The kinetics for the loss of **216** no longer abided to an exponential fit. Furthermore, $[Mn_2(CO)_{10}]$ was observed to form prior to the 5-membered manganacycle **158**. This implies that **216** was breaking down, forming $[Mn_2(CO)_{10}]$ plus free imine: **158** only formed at later times when free imine was present. To further cement this argument, a reaction aliquot was taken from a catalytic reaction, and analysed by ^1H nmr spectroscopy (see Figure 93). This sample had peaks associated with the reduced amine. These peaks were highlighted further by spiking in a sample of the amine to the aliquot (see Figure 93). This indicates that free imine is necessary for activation of the precatalyst **216**. The liberated imine has two potential roles. It can be sacrificially reduced to the respective amine, balancing the overall redox state, as manganese is oxidised to manganese (I). Secondly, the imine/amine side product can act as a base, aiding the C–H bond activation of the bound imine ligand.

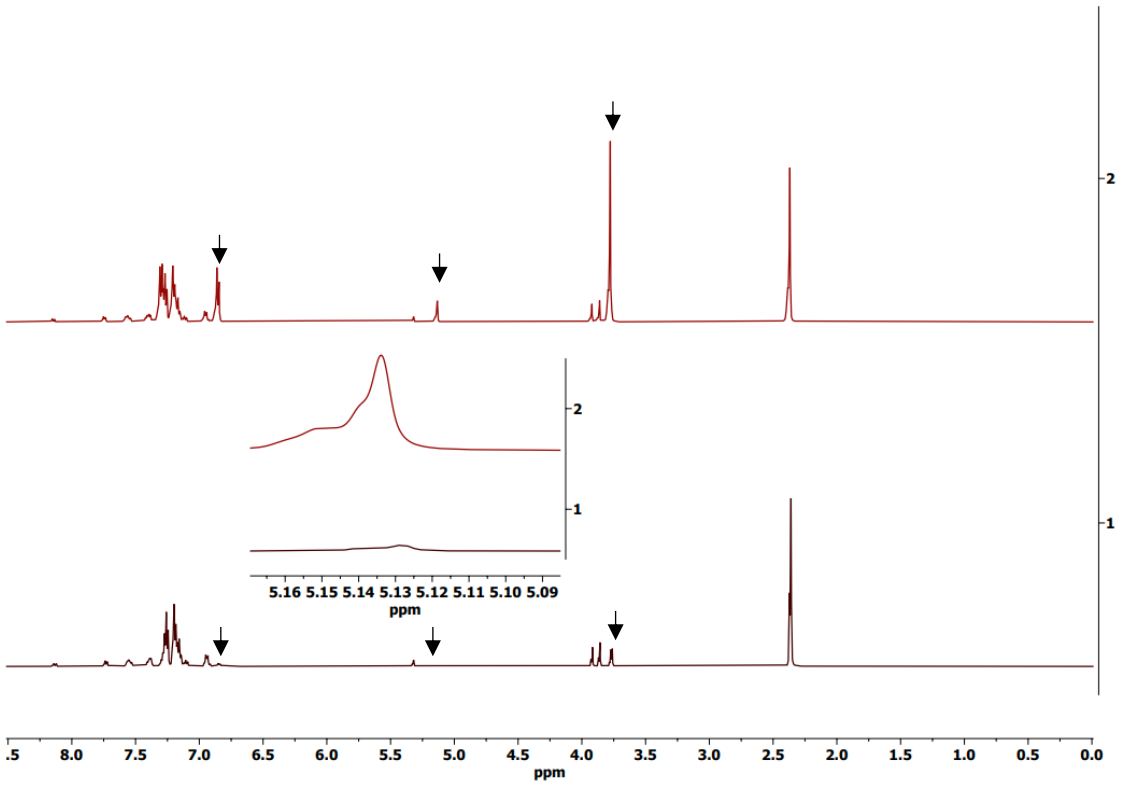

Figure 93. 1: Reaction aliquot. 2: Reaction aliquot spiked with 1,1-bis(4-methoxyphenyl)methanamine. 1,1-bis(4-methoxyphenyl)methanamine denoted by black arrow.

Alternatively, the 19-electron $[Mn(CO)_3(Solvent)_3]$ radical could be generated *in situ* (see Chapter 4), and reacts with **216** to form $[Mn(CO)_5]^-$, and **158** through heterolytic cleavage of the Mn–Mn bond, and free imine just acts as a base to aid with the CMD step.

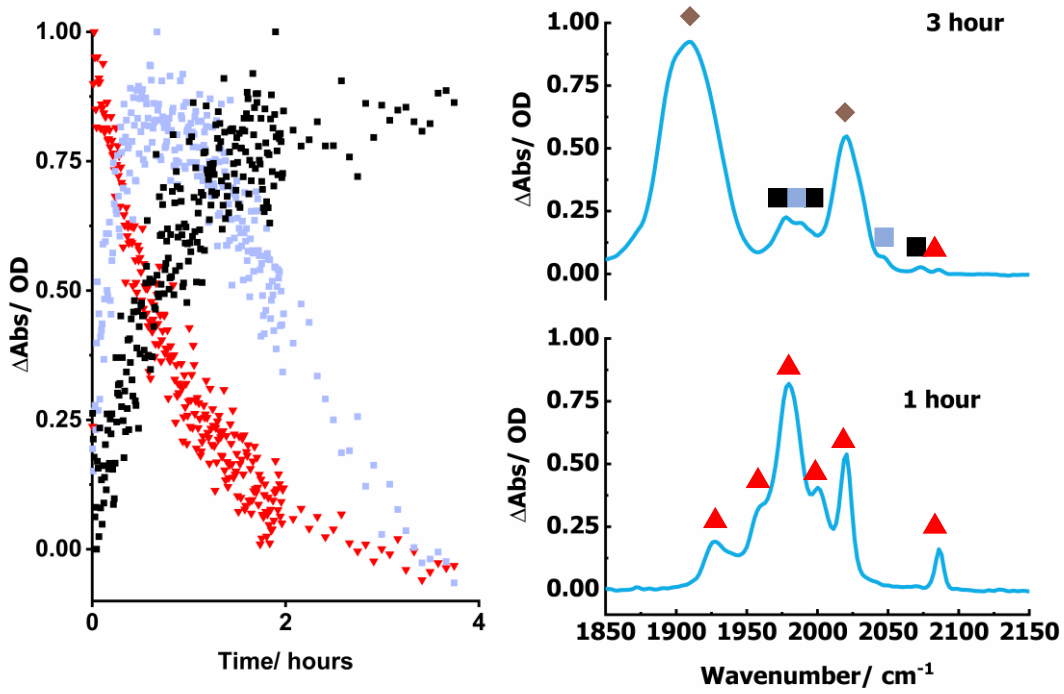

Figure 94. Left: Kinetics for the loss of **216** and formation **158**. Right: IR spectroscopic changes over time for the reaction of **178**+ **Δ** → **158**. **216** denoted by red triangles, **158** denoted by black squares, $[Mn_2(CO)_{10}]$ denoted by blue square, and hydroxy-bridge clusters by brown diamond.

In the [4+2] annulation of biaryl imines and alkynes, to form an isoquinoline product $[Mn_2(CO)_{10}]$ proceeds to be activated *via* thermal dissociation of a CO ligand at greater than 80 °C, subsequently imine **178** coordinates to form $[Mn_2(CO)_9$(1,1-bis(4-methoxyphenyl)methanimine)] **216**. **216** then requires free imine ligand to undergo C–H bond activation and form the 5-membered manganacycle **158**, that the subsequent reactivity of which was studied in Chapter 2 as an alkyne coordinates and undergoes a migratory insertion.

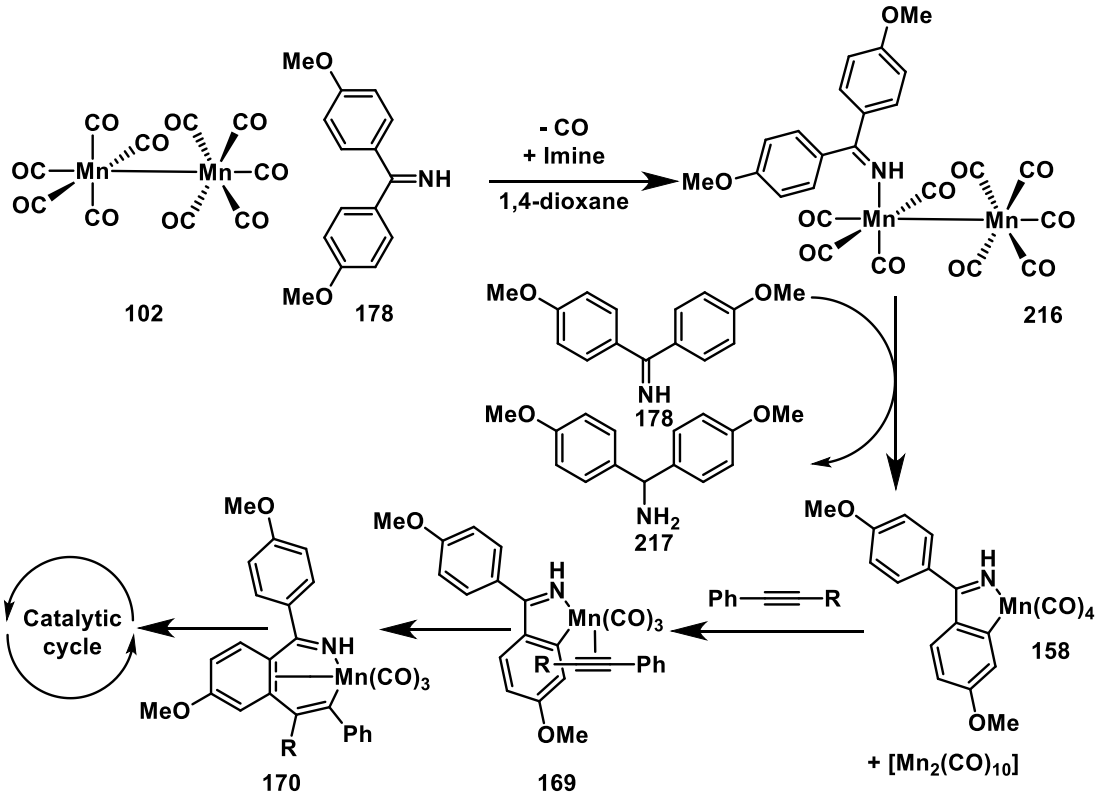

Figure 95. Route of activation for $[Mn_2(CO)_{10}]$ based on work in Chapter 2 and 3.

3.3.4 $[BnMn(CO)_5]$

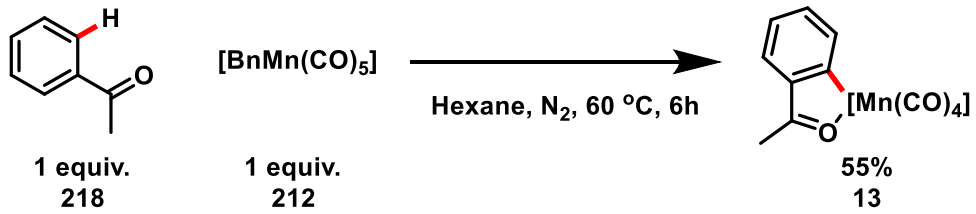

Figure 96. Literature example of $[BnMn(CO)_5]$ being used in the synthesis of a 5-membered manganacycle.[121]

The route of activation for $[BnMn(CO)_5]$ **212** was then explored, as this is a known precursor to 5-membered manganacycles, such as those discussed in Chapter 2 (see Figure 96 for an example).[121] Thus it is expected that $[BnMn(CO)_5]$ will undergo rapid C–H bond activation, making it an appropriate precatalyst.

Initially a stoichiometric reaction between 1 equiv. of $[BnMn(CO)_5]$ **212** and 1 equiv. of imine **178** was conducted following the reaction scheme in Figure 84 (see Figure 97). By *ca*. 1.5 hours bands associated with **212** had depleted, and in their place the bands

attributed to **158** grew in. Using the high energy band of **212** at 2108 cm^{-1}, kinetics were followed for the loss of **212** and a rate constant, k_{obs} of $8.8 \pm 0.4 \times 10^{-4}$ s^{-1} obtained from the mono exponential fit. Within 95% confidence limits, **158** grew in with a rate constant, k_{obs} of $8.3 \pm 0.4 \times 10^{-4}$ s^{-1}, indicating that **212** converted directly to **158**. As **212** was observed to convert directly into **158**, and no intermediates were detected, CO dissociation must be the rate determining state, and CMD occurs rapidly following the loss of CO and coordination of an imine ligand. At longer times, the degradation of manganese complexes were observed, with manganese clusters forming.

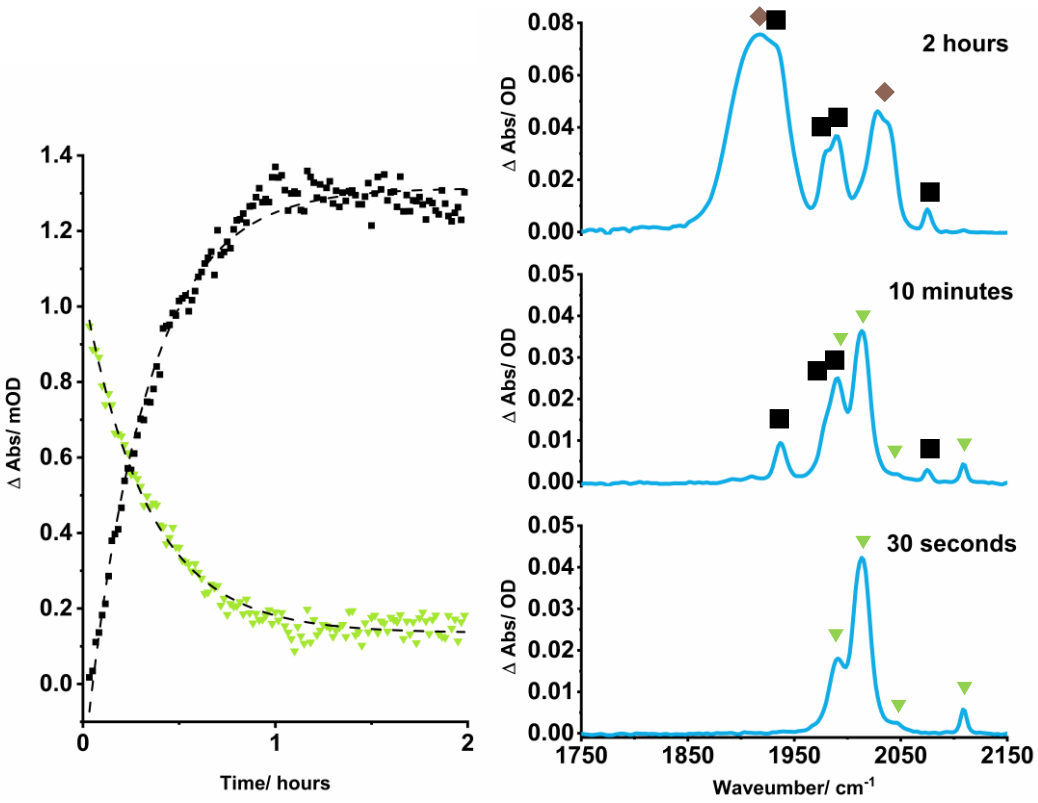

Figure 97. Left: Kinetics for the loss of **212** and formation of **158**. Dotted lines denote exponential kinetics. Where appropriate a mono or biexponential fit was applied. Right: IR spectroscopic changes over time for the reaction of **212** + **178**→ **158**. **212** denoted by green triangles, **158** denoted by black squares, and hydroxy-bridge clusters by brown diamond.

The experiment was then repeated with 1 equiv. of imine **178**, 1.5 equiv. of alkyne **26**, and 1 equiv. of manganese complex **212** (see Figure 98). The aim was to assess how the presence of alkyne impacts the formation of 5-membered manganacycle **158**. When in the presence of diphenyl acetylene, the 5-membered manganacycle **158** formed with a k_{obs} of 2.3 ± 0.3 × 10^{-4} s^{-1}, which was approximately four times slower than in the absence of diphenyl acetylene. **212** was not observed to convert directly into **158** in this instance. Instead, an intermediate with a band at 2050 cm^{-1} was observed after *ca.* 1 hour, which depleted with a rate k_{obs} of 2.7 ± 0.2 × 10^{-4} s^{-1}, corresponding to the formation of **158**. The band at 2050 cm^{-1} is proposed to correspond to the alkyne-bound complex [BnMn(CO)$_4$(η^2-Ph$_2$C$_2$), as this band was only observed in the presence of **26**. Again, at times > 1hour, bands attributed to manganese clusters were observed.

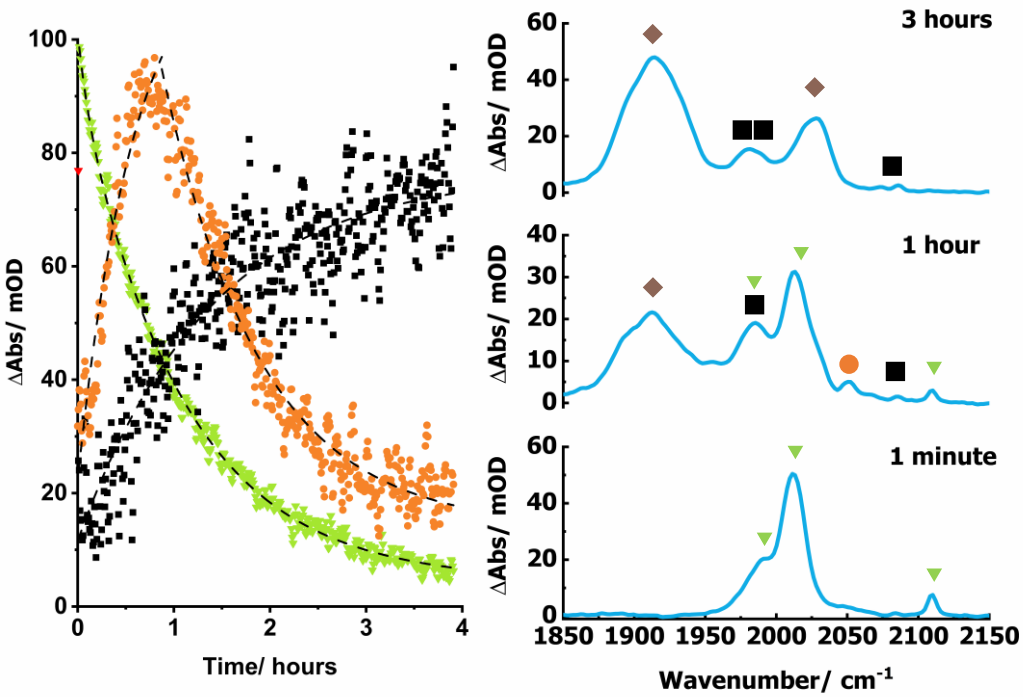

Figure 98. Left: Kinetics for the loss of **212** and formation of **158** in the presence of **26**. Dotted lines denote exponential kinetics. Where appropriate a mono or biexponential fit was applied. Right: IR spectroscopic changes over time for the reaction of **212** + **178**→ **158**. **212** denoted by green triangles, **158** denoted by black squares, **219** by orange circles, and hydroxy-bridge clusters by brown diamond.

This indicates that alkyne coordination is competitive with coordination of imine **178**, as seen in ultrafast studies in Chapter 2. The coordination of phenyl acetylene is likely thermodynamically favourable to coordination of imine **178**. But once an imine molecule coordinates, and undergoes a CMD reaction to form **158**, this is an irreversible process, and **219** cannot be reformed. Also, no evidence for a 5-membered manganacycle with an alkyne coordinated was seen. Only the bands for the tetracarbonyl complex **158**. This implies that C−H bond activation was not proceeding *via* formation of an alkynyl complex when [BnMn(CO)$_5$] was used as a precatalyst, as discussed in Section 3.3.5.

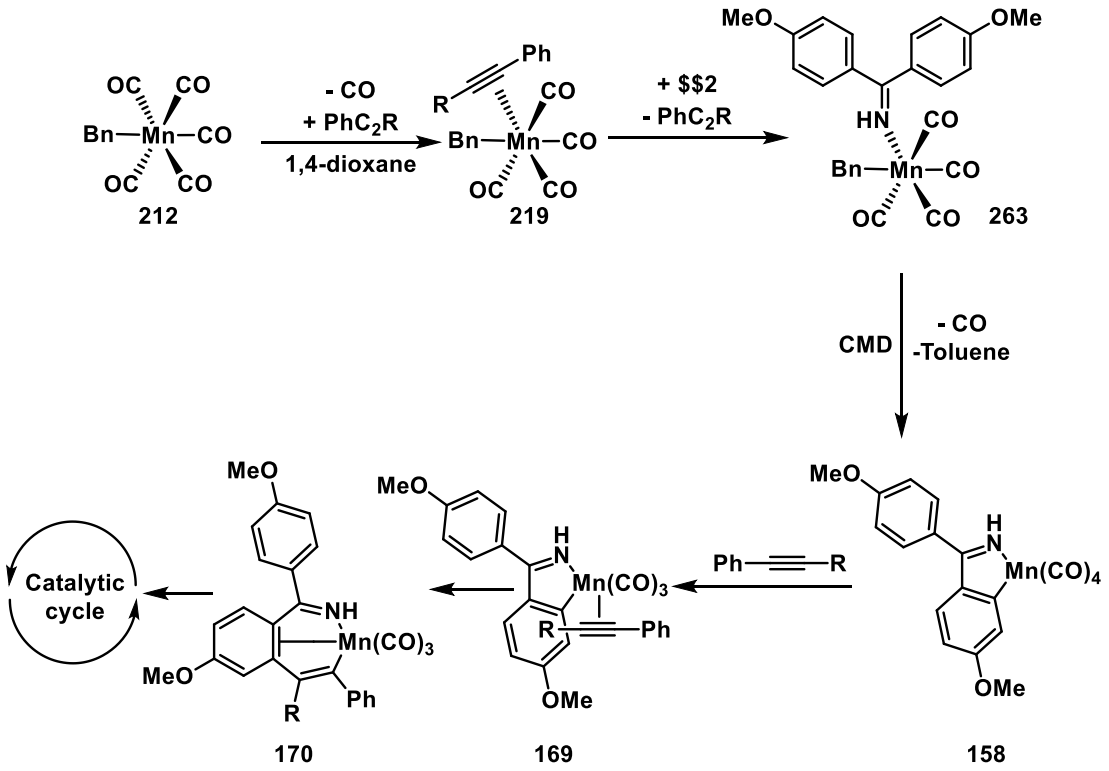

Figure 99. Route of activation for [BnMn(CO)$_5$] under catalytic conditions.

3.3.5 [Mn(CO)$_5$(*p*-tolylacetylide)]

Previous work by Hammarback and co-workers highlighted the role alkynyl manganese complexes play in the activation of C−H bonds (see Figure 100). Activation at the site of the terminal proton belonging to phenyl acetylene was preferential to C−H bond activation directly on 2-phenyl pyridine, as depicted in Figure 100.[51] The alkynyl

complex was then demonstrated to be able to react with 2-phenyl pyridine, activating the C–H bond and forming a *fac*-[Mn(C^N)(CO)$_3$(η^2-HCC*p*-tolyl)] complex.

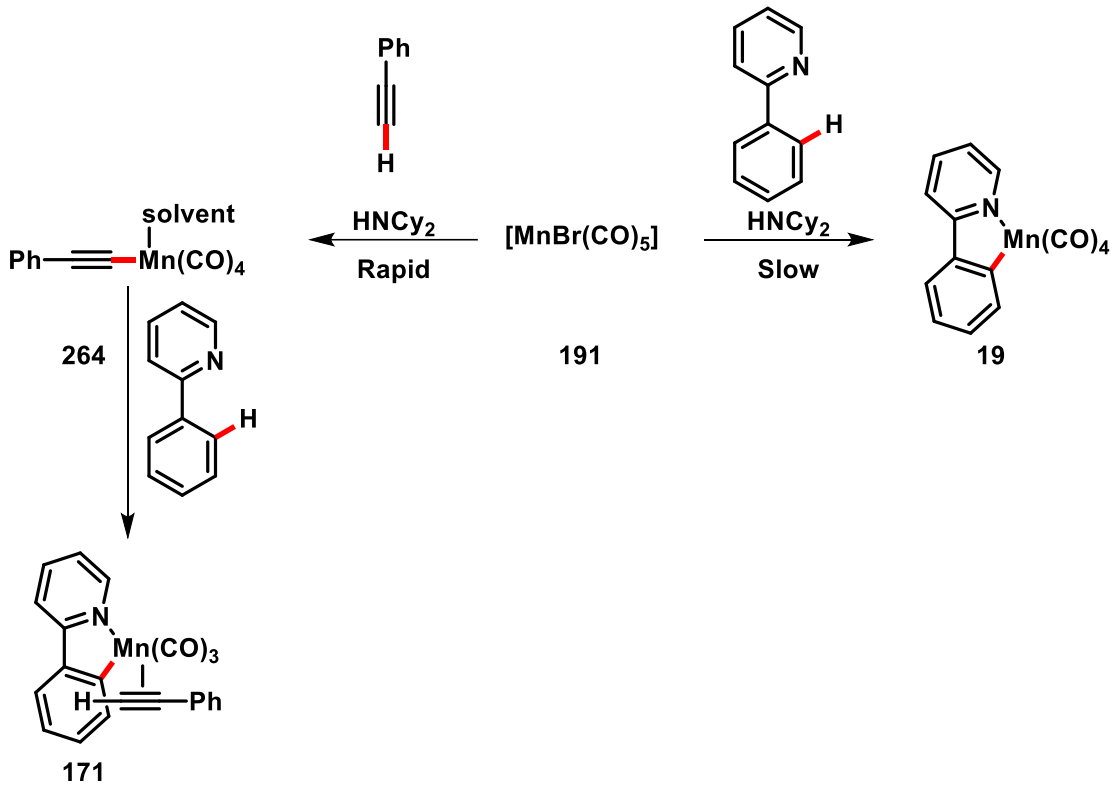

Figure 100. Initial modes of C–H bond activation explored by Hammarback and co-workers.[51]

The literature manganese (I) complex [Mn(CO)$_5$(*p*-tolylacetylide)] **223** was synthesised as shown in Figure 101, and subsequently used as precatalyst in both a stoichiometric and catalytic reaction. To test whether this is an alternative route of precatalyst activation in our system, **223** was heated in the presence of imine **178**.

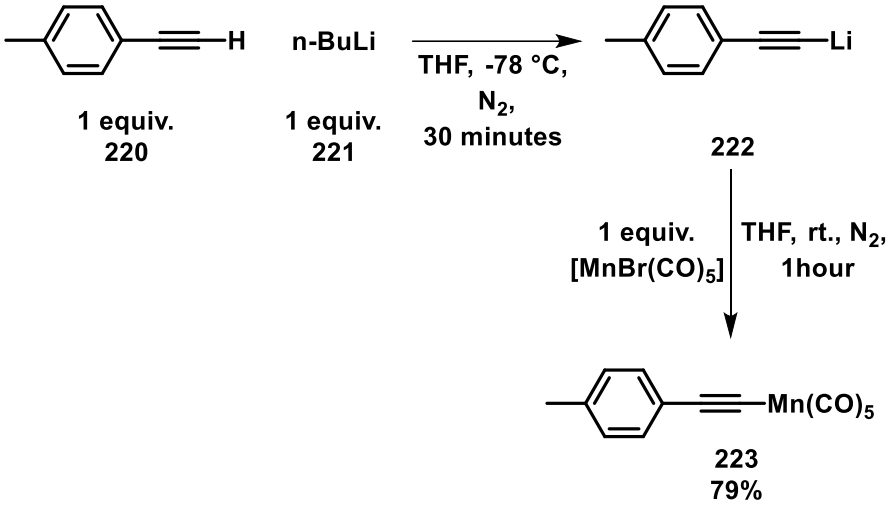

Figure 101. Synthetic route to **223**.

1 equiv. of **223** and imine **178** were reacted together stoichiometrically at 60 °C, and the reaction progress monitored by *in situ* IR spectroscopy (see Figure 102). Compound **223** was observed to deplete over the course of *ca*. 20 hours, and in its place two bands at 1914 and 1941 cm^{-1} initially grew in. These bands were masked by manganese clusters at later times, preventing kinetic analysis for the formation of **224**. The bands attributed to **223** were subtracted from the spectrum at 3 hours, revealing a third band position at *ca*. 2020 cm^{-1} for **224**. Based on the infrared spectrum indicating a tricarbonyl complex and the mechanism proposed by Hammerback and co-workers, a structure for **224** was tentatively proposed as depicted in Figure 103. This complex possesses similar metal carbonyl stretching frequencies to the analogous complex **169** which was discussed in Chapter 2. If **169** is the structure proposed in Figure 103, then C–H bond activation proceeding through an alkynyl complex is a plausible route when terminal alkynes are use.

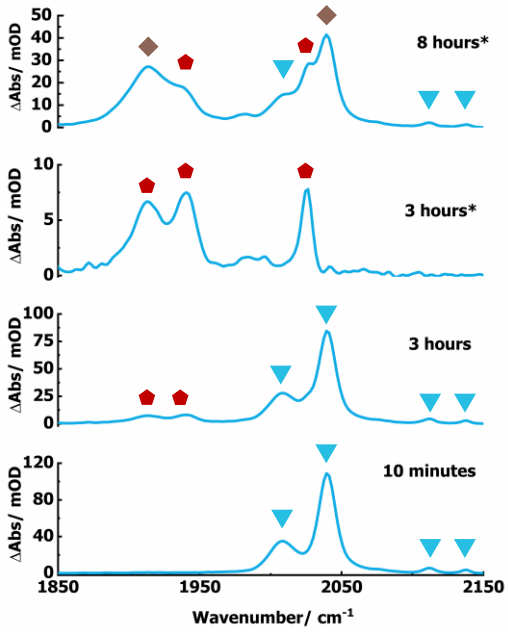

Figure 102. IR spectroscopic changes over time for the reaction of **223** + **178**. **223** denoted by blue triangles, **224** denoted by red pentagons, and hydroxy-bridge clusters by brown diamond.* Bands atributed to **223** subtracted from the spectrum at 3 hours.

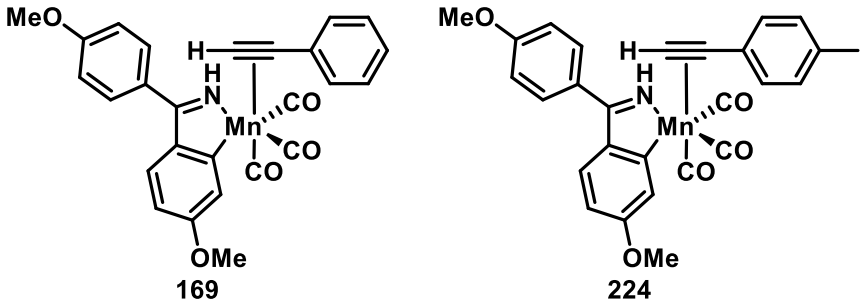

Figure 103. Structure of **169** and proposed structure for **224**.

Based on the observed intermediate in Figure 102, a mechanism for activation of the *ortho* C–H bond of **178** was proposed. This mimicked the previously proposed mechanism by Hammarback and co-workers, in which the proton of the activated C–H bond is transferred to the alkynyl complex, reforming the respective alkyne. Subsequently, it is expected that the alkyne will insert *via* a migratory insertion, forming

a 7-membered manganacycle, and then undergo a reductive elimination to form the respective isoquinoline product (see Figure 104). [51]

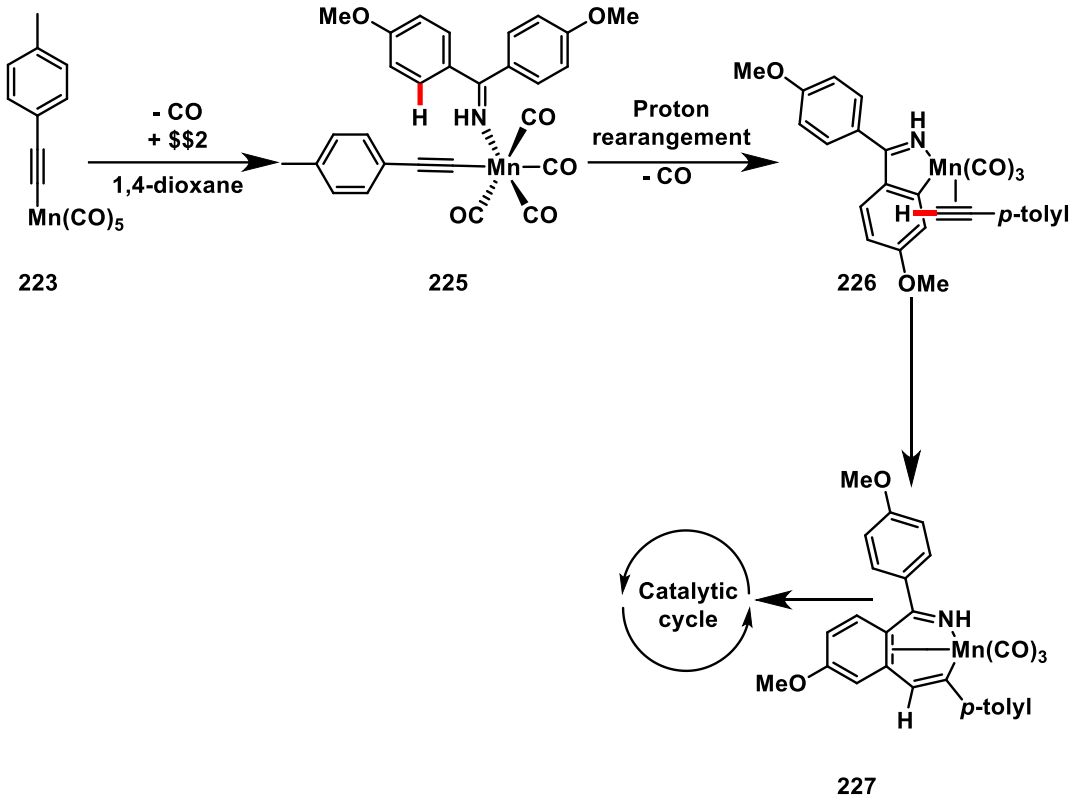

Figure 104. Proposed mechanism for the activation of **223**.

3.3.6 [MnBr(CO)$_5$] and [MnBr(1,1-bis(4-methoxyphenyl)methanimine)$_2$(CO)$_3$]

[MnBr(CO)$_5$] **191** was probed as the last major precatalyst. Initially a stoichiometric quantity of [MnBr(CO)$_5$] and imine **178** were reacted in 1,4-dioxane following the conditions outlined in Figure 84 (see Figure 105). An almost instantaneous reaction occurred, with a new species **228** possessing bands at 1914, 1942, and 2026 cm^{-1} forming by the first measurement at 30 seconds. By *ca*. 6 minutes, complete loss of [MnBr(CO)$_5$] had occurred, and the bands at 1914, 1942, and 2026 cm^{-1} were observed, along with four further bands at 1953, 2007, 2050, and 2095 cm^{-1} assigned to **229**. These bands then proceeded to remain for the duration of the reaction. When repeated in the presence of alkyne **26** no alteration in speciation was observed. Furthermore, when the experiment was conducted under the catalytic conditions outlined in Figure 84 the respective isoquinoline product **180** was not detected, despite He and co-workers

reporting a yield of 92% for the transformation under these exact conditions.[60] Instead **228** and **229** were observed as the sole metal carbonyl possessing species for the duration of the reaction.

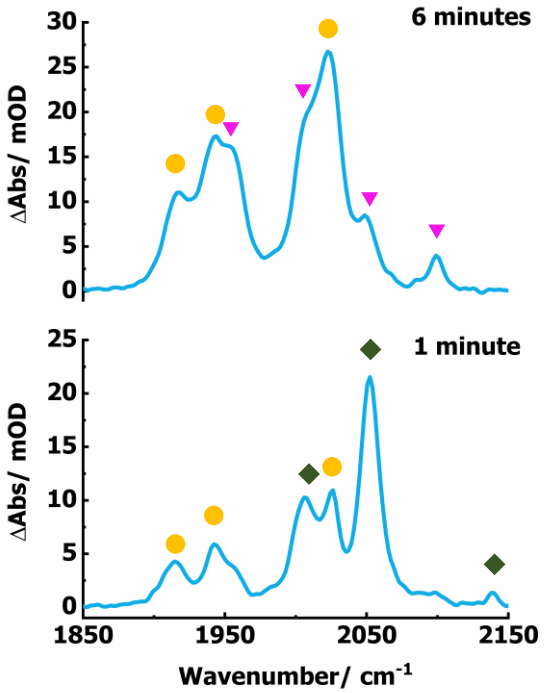

Figure 105. Spectroscopic changes over time for the reaction of **178** + **191**. **191** denoted by green diamonds, **228** denoted by yellow circle, and **229** by pink triangles.

Complex **228** was isolated from the reaction mixture associated with Figure 105 and single crystals obtained *via* a recrystallisation from methylene chloride/ *n*-pentane. The structure was then determined to be as depicted in Figure 106. To support the *in situ* assignment of metal carbonyl stretching modes, a solution phase IR spectrum of **228** was recorded in 1,4-dioxane, giving bands positioned at 1908, 1939, and 2026 cm^{-1}. The coordinated bromine and two N-coordinated imine ligands indicate that C–H bond activation had not occurred, explaining why the isoquinoline product was not detected. He and co-workers never reported this complex, instead they reported the reaction of **178** and [$MnBr(CO)_5$] to form the 5-membered manganacycle **158** with a yield of 30% (see Figure 82D).[60]

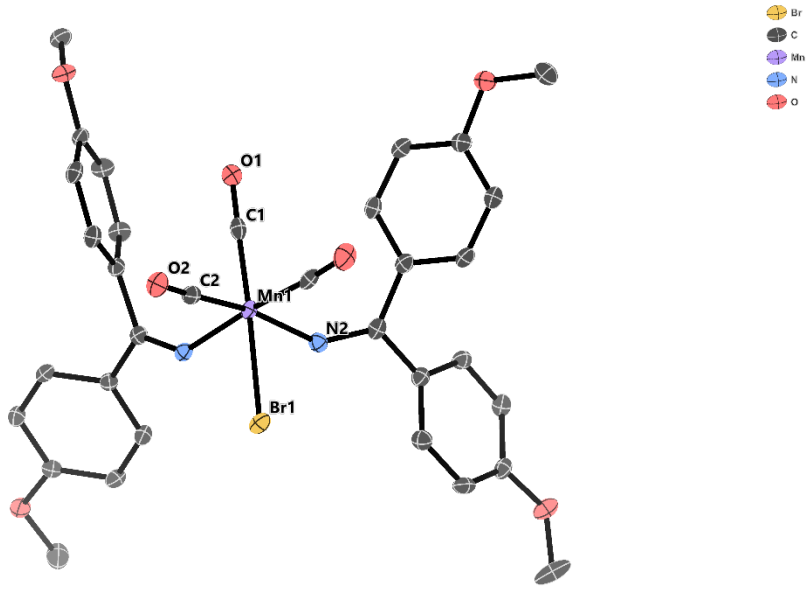

Figure 106. Crystallographic structure of the manganese complex *fac*-[MnBr(CO)$_3$(1,1-bis(4-methoxyphenyl)methanimine)$_2$] **228**.

Attempts were made to crystalise the second reaction component, complex **229**, however a single crystal was never successfully grown, **228** was always isolated as single crystals. Several experiments were conducted to aid with the elucidation of **229**. Initially a stoichiometric quantity of imine **178** and [MnBr(CO)$_5$] were reacted as in Figure 105, this time with a reduced temperature of 45 °C (see Figure 107). This resulted in partial reaction of [MnBr(CO)$_5$], which initially formed **228**, before an equilibrium between **228** and **229** was established at *ca*. 1 hour. Rate constants, k_{obs}, of 1.0 ± 0.6 × 10^{-3} s^{-1} and of 1.6 ± 0.1 × 10^{-3} s^{-1} were obtained for the initial loss of **228** and formation of **229**. The concentrations of **228**, **229**, and **191** then remained constant. A further equivalent of imine was added to the system, and this resulted in rapid depletion of **229** forming further **228** and consumption of the remaining precatalyst **229**. Rate constants, k_{obs}, of 5.1 ± 0.7 × 10^{-3} s^{-1} and of 4.3 ± 0.3 × 10^{-3} s^{-1} were obtained respectively for the loss of **229** and formation of **228**.

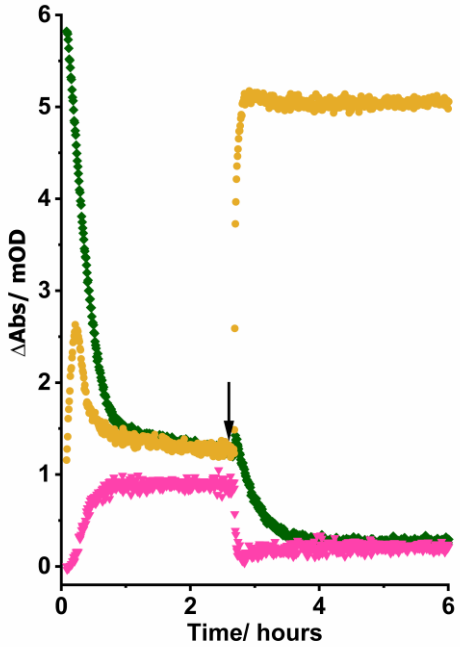

Figure 107. Kinetic profile for the stoichiometric reaction between **191** and **178** to form **228** and **229**. Arrow depicts when a second equivalent of imine **178** was introduced into the system. **191** denoted by green diamonds, **228** denoted by yellow circle, and **229** by pink triangles.

The experiment was then repeated with two equivalents of imine **178** initially in the system (see Figure 108). Conversion of **191** to **228** was observed, as in prior experiments. However, subsequent equilibration of **228** with **229** did not occur. Instead, a small proportion of **229** formed over the course of the reaction. These experiments indicate that the equilibrium between **228** and **229** is dependent on the concentration of **178**. When one equivalent of **178** is present formation of **229** is favoured, while two equivalents or greater of **178** drives the formation of **228**.

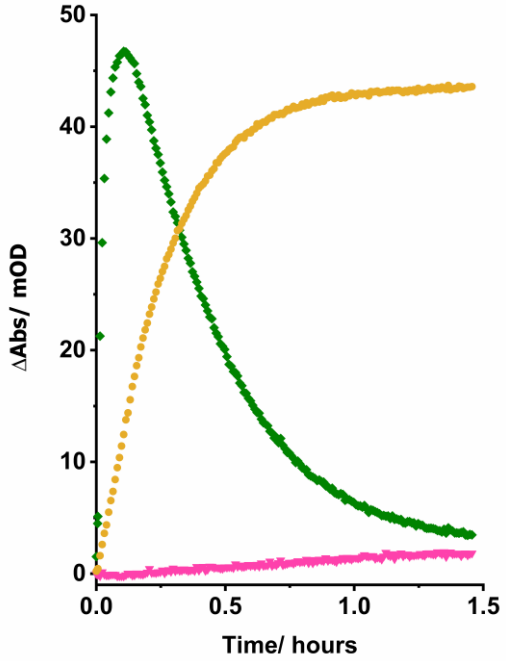

Figure 108. Kinetic profile for the stoichiometric reaction between **191** and two equiv. of **178** to form **228** and **229**.

LIFDI mass spectrometry spectra gave further evidence for the structure of **229**. A mass ion of 917.90432 *m/z* was detected, which corresponds to the molecular formula $C_{36}H_{30}N_2O_{10}Mn_2Br_2$, or [$Mn_2Br_2$(1,1-bis(4-methoxyphenyl)methanimine)$_2$(CO)$_6$]. From this formula the strutures in Figure 109 were proposed.

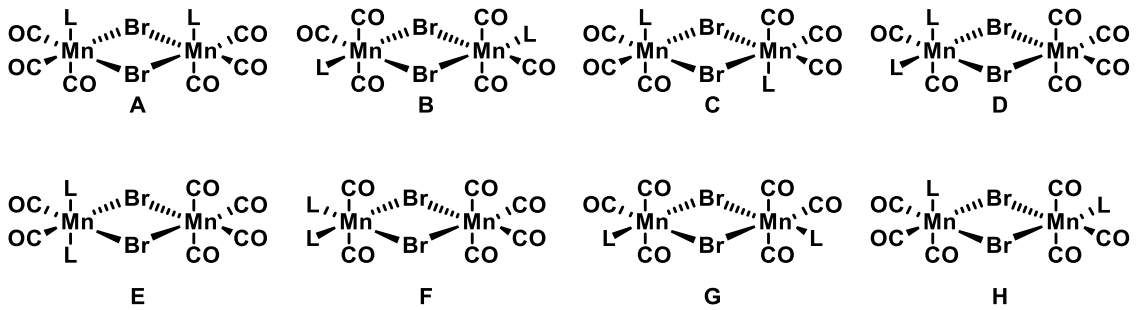

Figure 109. Proposed structures for **229** based on LIFDI mass spectrometry data.

NMR experiments gave additional information about the structure of **229**. Subtraction of the peaks associated with **228** from the NMR spectra of **229** (Figure 110) left distinctive ^{1}H peaks at 8.78, 3.88, and 3.84 ppm for the NH and OMe protons

respectively. The presence of one NH and two OMe environments indicates there are two chemically equivalent imine ligands. However, the two aromatic groups of the imine ligands are chemically inequivalent due to slow exchange at the C=N bond accounting for the two OMe environemnts. The ^{13}C NMR spectrum supports this assignment, with one enviroment for the C=N carbon, and two for the OMe carbons at 185.5, 56.0, and 55.9 ppm respectively, along with 8 aromatic carbon environments. This rules out complexes **229D** and **229H** in which the two imine ligands are chemically inequivalent. **229E** and **229F** are also unlikely complexes, as equilibriation between **228** and **229** would involve CO dissociation and association and no further intermediates were detected when **229** was in solution (see Figure 111).

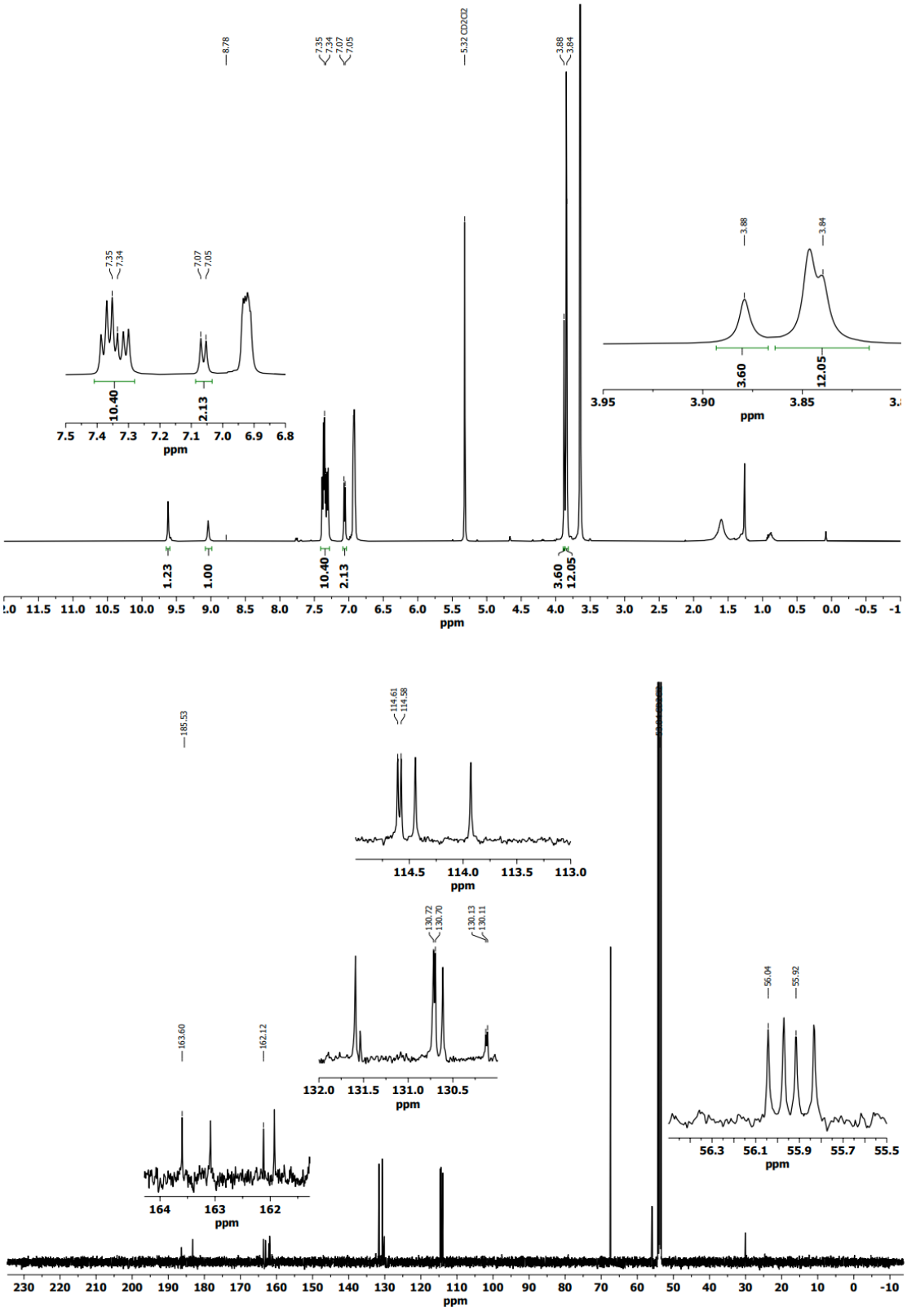

Figure 110. Top: ^{1}H NMR spectrum of **229**. Bottom: ^{13}C NMR spectrum of **229**. Peaks associated with **229** indicated by peak picking.

Finally to distinguish between **229A**, **229B**, **229C**, and **229G** the metal carbonyl stretching modes in Figure 109 were examined. Structures **229A** and **229G** possess the point group (C_{2v}), which explains the bands at 1953, 1978, 2007, 2050, and 2095 cm^{-1} (see Figure 111). The C_{2v} point group is composed of two mirror planes $\sigma_v(xz)$ and $\sigma_v(yz)$, a C_2, axis of rotation and the identity E. Application of these symmetry elements to **229A** and **229G** results in the reducible representation $\Gamma_{vib}(CO) = 8E+2\sigma_v(xz)$ and $8E+2\sigma_v(yz)$. Inspection of the point group table and application of equation 1 in Chapter 2 reveals $2A_1+B_1+A_2+2B_2$ and $2A_1+2B_1+A_2+B_2$ to be the irreducible representations for the CO ligands of **229A** and **229G**, respectively. Following the infrared active modes in Table 8, A_1, B_1, and B_2 stretching modes are predicted to be infrared active.

Conversely, only 3 metal carbonyl stretching modes were predicted for **229B** and **229C** which possess C_{2h} symmetry. The C_{2h} point group is composed of one σ_h mirror planes, a C_2, axis of rotation, centre of inversion, i, and the identity E. Application of these symmetry elements to **229B** and **229C** results in the reducible representation $\Gamma_{vib}(CO) = 8E+2\sigma_h$. Inspection of the point group table and application of equation 1 in Chapter 2 reveals $2A_g+B_g+A_u+2B_u$ to be the irreducible representations for **229B** and **229C**. Following the infrared active modes in Table 9, A_u and B_u stretching modes are predicted to be infrared active.

Based on the NMR, IR and LIFDI MS data discussed above, the structure of **229** is most likely either **229A** or **229G**, with the two structures being indistinguishable for each other with the data currently available. In order to determine which of these structures is correct, a single crystal would need to be grown and the structure solved.

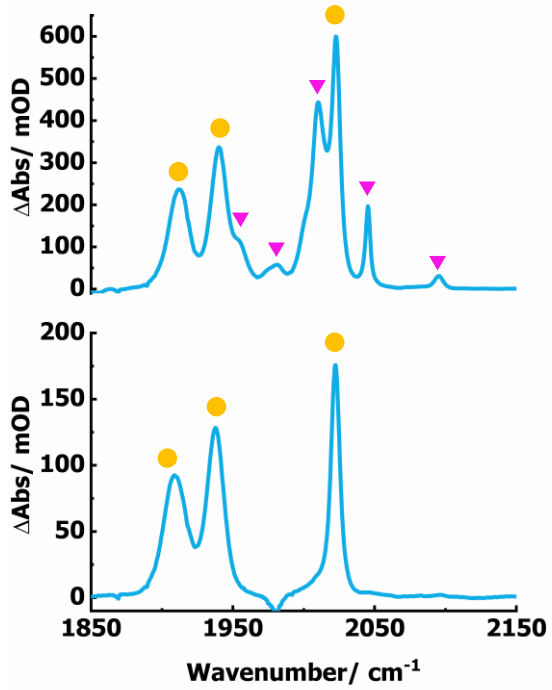

Figure 111. IR spectra of **228** and **229** in toluene. **228** denoted by yellow circle, and **229** by pink triangles.

Table 8. C_{2v} point group table.

C_{2v}	E	C_2	$\sigma_v(xz)$	$\sigma_v(yz)$	Linear functions
A_1	+1	+1	+1	+1	z
A_2	+1	+1	-1	-1	
B_1	+1	-1	+1	-1	x
B_2	+1	-1	-1	+1	Y

Table 9. C_{2h} point group table.

C_{2h}	E	C_2	i	σ_h	Linear functions
A_g	+1	+1	+1	+1	
B_g	+1	-1	+1	-1	
A_u	+1	+1	-1	-1	z
B_u	+1	-1	-1	+1	x, y

Table 10. Group theory analysis on candidate complexes for **229**.

Complex	Point group	Irreducible representation	IR active modes
229A	C_{2v}	$2A_1+B_1+A_2+2B_2$	$2A_1+B_1+2B_2$
229B	C_{2h}	$2A_g+B_g+A_u+2B_u$	A_u+2B_u
229C	C_{2h}	$2A_g+B_g+A_u+2B_u$	A_u+2B_u
229G	C_{2v}	$2A_1+2B_1+A_2+B_2$	$2A_1+2B_1+B_2$

No C–H bond activation had been observed at this point. So, the focus then returned to the activation of **228**. Several experiments were conducted, looking at alternative routes of promoting C–H bond activation of the bound imine ligands (Figure 112). Expectedly, **228** in the presence of two equivalents of alkyne **26** resulted in no reaction after 16 hours. The first approach to promote C–H bond activation was through the addition of dicyclohexylamine base, as was employed by Zhou and co-workers.[46] Addition of $HNCy_2$ successfully promoted activation of the bound imine, with **180** forming quantitively. The addition of base likely aids the deprotonation of the highlighted proton on the imine ligand, with $[H_2NCy_2]^+Br^-$ being favourable to HBr formation. Diphenyl acetylene was then substituted with phenyl acetylene **230**. The intention was to enable an alternative route of activation through formation of an alkynyl complex, as proposed by Hammarback and co-workers.[51] The use of a terminal alkyne resulted in isoquinoline **231** forming quantitively, indicating that precatalyst activation can proceed through an alkynyl complex. Finally, **228** and **26** were heated as in the initial control, this time while exposed to ambient laboratory light. Surprisingly the isoquinoline product **180** was detected**.** Through use of a "white" LED array, the conversion was increased to being quantitative. In all the examples where the respective isoquinoline product was formed, quantitative conversion was seen, rather than formation of one equivalent of isoquinoline. This indicates that once one imine ligand has undergone functionalisation, the remaining manganese complex is catalytically active and goes on to functionalise the remaining imine molecule.

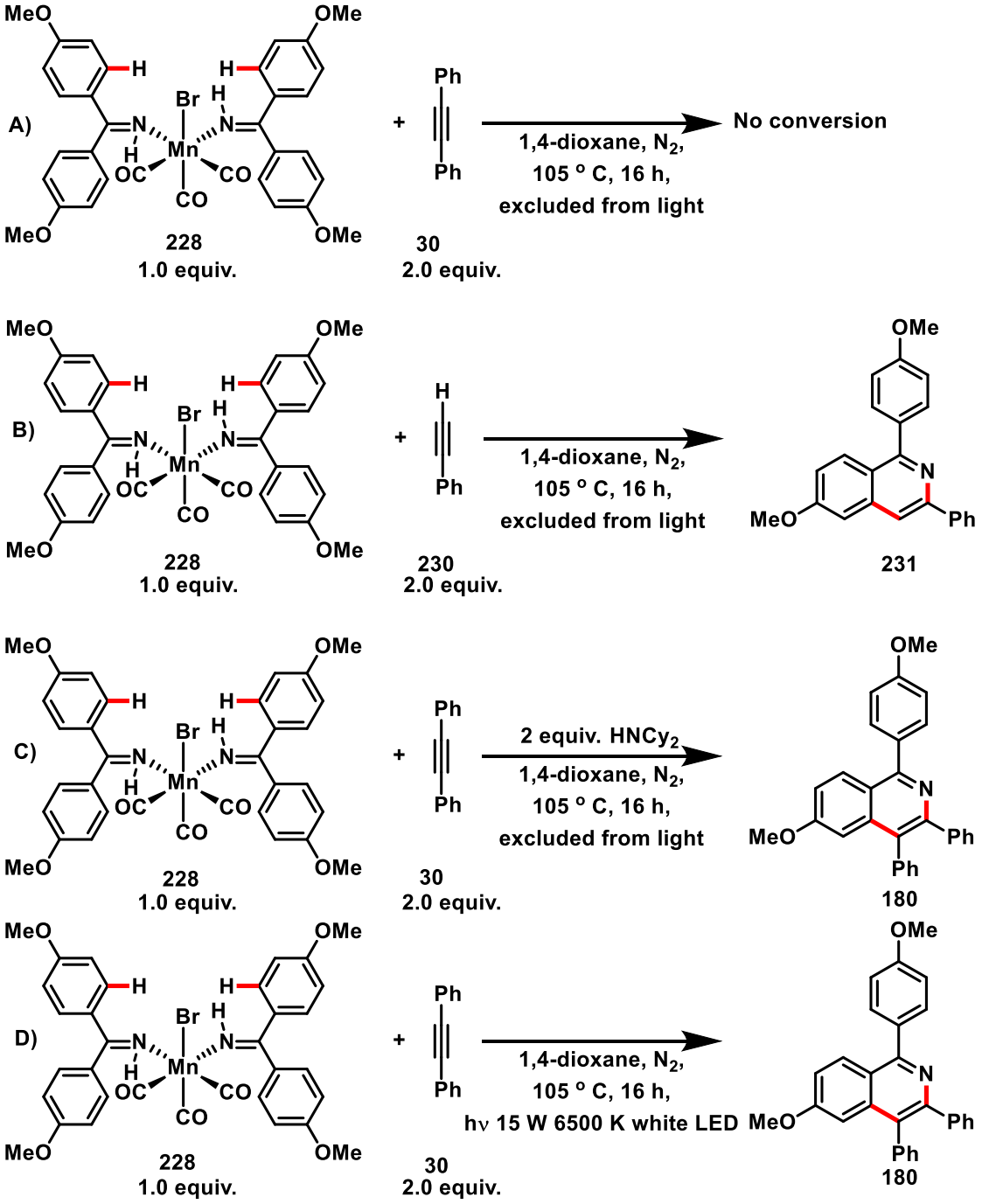

Figure 112. Stoichiometric reactions probing the activation of **228**. 0.1 mmol of **228**, 0.2 mmol of alkyne, 0.2 mmol of $HNCy_2$ where appropriate, and 10 mL of dry 1,4-dioxane. 6500 K white LED reference the spectrum of light emitted by a blackbody emitter heated to 6500 K.

3.3.6.1 Effect of Base

The role of $HNCy_2$ in the activation of $[MnBr(CO)_5]$ was next explored. A catalytic reaction following conditions in Figure 84, with 10 mol% $HNCy_2$ was monitored *via in*

situ infrared spectroscopy (see Figure 113). Within *ca*. 10 minutes, [$MnBr(CO)_5$] had converted into **228**, which proceeded to partially decompose as the reaction progressed. Between *ca*. 10 minutes and 2 hours, a band at 1981 cm^{-1} grew in and depleted, assigned to a new species **232**. The formation of **232** correlated with the initial formation of isoquinoline **180** product, while depletion of **232** occurred as the reaction reached completion. This indicates that the **232** was likely the resting state of catalysis. Figure 114 also implies that only a small proportion of **228** is activated and enters the catalytic cycle. An aliquot was taken and submitted for LIFDI mass spectrometry. From this, a mass-to-charge ratio of 735.17241 and 557.09202 *m/z* were detected, which corresponds to a formulae of $MnC_{46}H_{34}NO_5$ and $MnC_{32}H_{24}NO_5$. Likely structures based on these formulae are proposed in Figure 114.

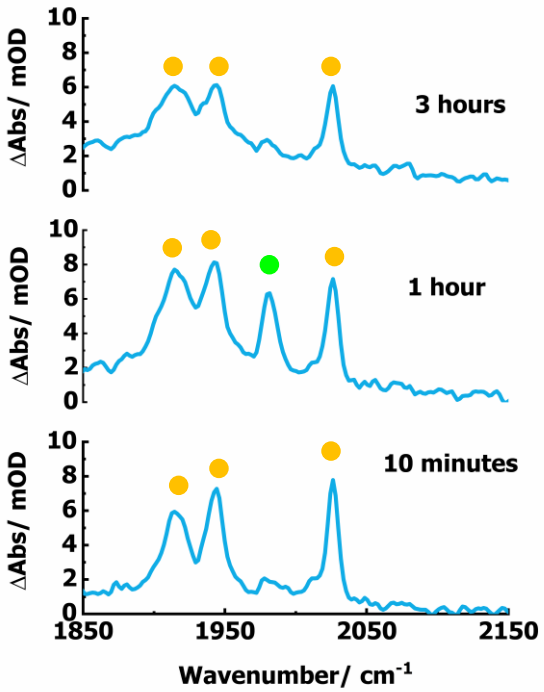

Figure 113. IR spectroscopic changes over time for the model catalytic reaction using [$MnBr(CO)_5$] as the precatalyst and 20 mol% $HNCy_2$ as a co-catalyst. **228** denoted by yellow circles and **232** denoted by green circles.

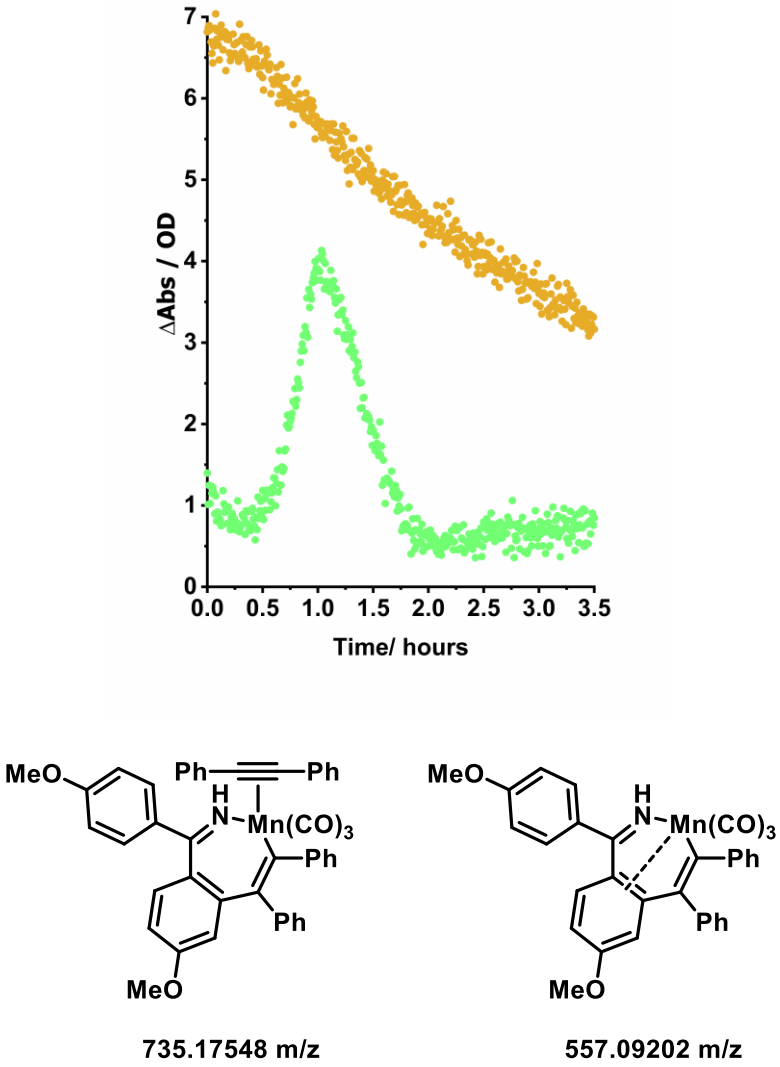

Figure 114. Top: Kinetic profile for **228** (yellow circles) and **232** (Green circles) in Figure 113 Bottom: Proposed structures for the intermediate **232**.

3.3.6.2 Effect of Terminal Alkynes

Next, the role terminal alkynes played in the activation of **228** was explored. A catalytic reaction following conditions in Figure 84 with phenyl acetylene was monitored *via in situ* infrared spectroscopy (see Figure 116). Again, initially **228** formed from $[MnBr(CO)_5]$. **228** was present for the duration of the reaction, with slight degradation, forming manganese clusters as the reaction progressed. The bands for the pentacarbonyl alkynyl manganese complex **223** were never observed, nor was a distinctive resting state of catalysis seen. Aliquots taken from the reaction associated with Figure 116 revealed an ion with a *m*/*z* of 584.0. This mass to charge ratio

corresponded to a formula of $C_{34}H_{26}MnNO_5$, **233A** and **233B** were proposed as likely structures (see Figure 115). DFT calculations by Zhou and co-workers illustrated that for the 2-phenylpyridine derivative, the alkynyl complex B was thermodynamically favourable.[46] Combined with the reactivity of [$Mn(CO)_5$(*p*-tolylacetylide)], this provides tentative evidence for C–H bond activation proceeding *via* the formation of an alkynyl complex when a terminal alkyne is used.

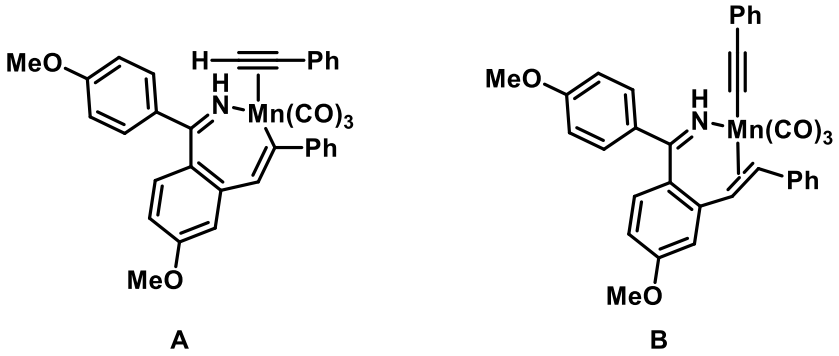

Figure 115. Proposed structures for **233A** and **233B**.

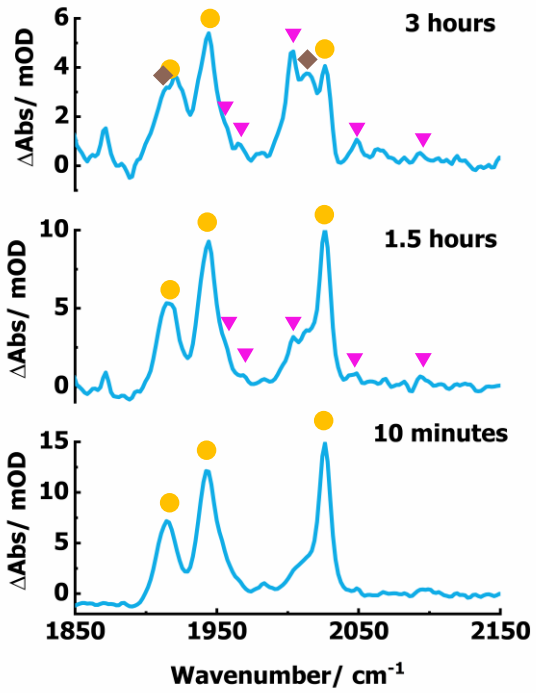

Figure 116. IR spectroscopic changes over time for the model catalytic reaction using $[MnBr(CO)_5]$ as the precatalyst and phenyl acetylene alkyne substrate. **228** denoted by yellow circles, **229** denoted by pink triangles, and manganese hydroxy-bridged clusters by brown diamonds.

3.3.6.3 The Role of Light

Finally, the photochemical activation of $[MnBr(CO)_5]$ was investigated. A catalytic reaction following a modified version of the conditions in Figure 84 where the sample was irradiated with a 6500 K white LED array and monitored *via in situ* infrared spectroscopy (see Figure 117). Rapid formation of **228** was observed at early times. As in previous experiments, **228** decayed as the reaction progressed. In the place of **228**, the band at 1981 assigned to **232** formed, similarly to when $HNCy_2$ additive was introduced. **232** remained until the reaction reacted completion, at which point the band also depleted, leaving no obvious metal carbonyl complex. No manganese hydroxy-bridged clusters were observed. This is possibly due to their photochemical decomposition in the presence of light.

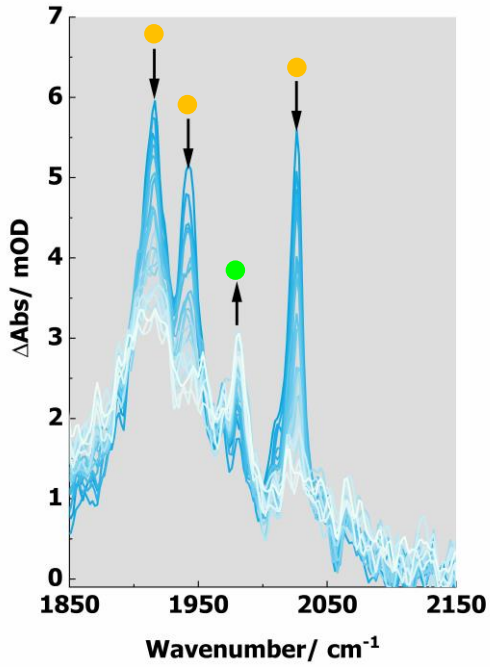

Figure 117. IR spectroscopic changes over time for the model catalytic reaction using [$MnBr(CO)_5$] while being irradiated with a 6500 K white LED array. **228** denoted by yellow circles and **232** denoted by green circles.

To gain further insight into the role light plays in the activation of [$MnBr(CO)_5$] and **228**, 1,4-dioxane solutions of **228** were prepared at catalytic concentrations in the presence of varying equivalents of imine, and irradiated with the white LED array (see Figure 118). When a 0.1 mol dm^{-3} 1,4-dioxane solution of **228** in a solution phase IR cell was irradiated with the white LED array, **229** was observed in the first IR spectrum at 10 minutes. The bands associated with **229** then remained for the duration that the sample was irradiated. After being covered with foil to exclude light and left overnight, the bands for **229** depleted, and the bands for **228** increased in intensity, indicating reformation of **228**. When the experiment was repeated in the presence of imine ligand **178**, the intensity of **229** decreased as the concentration of **178** increased. At a catalytic equivalency of imine **178** (10 equiv.), **229** was not detected. This is due to the equilibrium existing between **228** and **229**. When the experiment was conducted with 10 equiv. of imine **178**, the equilibrium will have been shifted further towards strongly favouring **228** over **229**. Consequently, in the time between irradiation ending and the

IR spectrum being recorded which takes *ca*. 2 minutes any photochemically formed **229** had converted back to **228**. These findings indicate that irradiation of **228** with the white LED promotes dissociation of one of the imine ligands, and consequently enables dimerisation to form **229**.

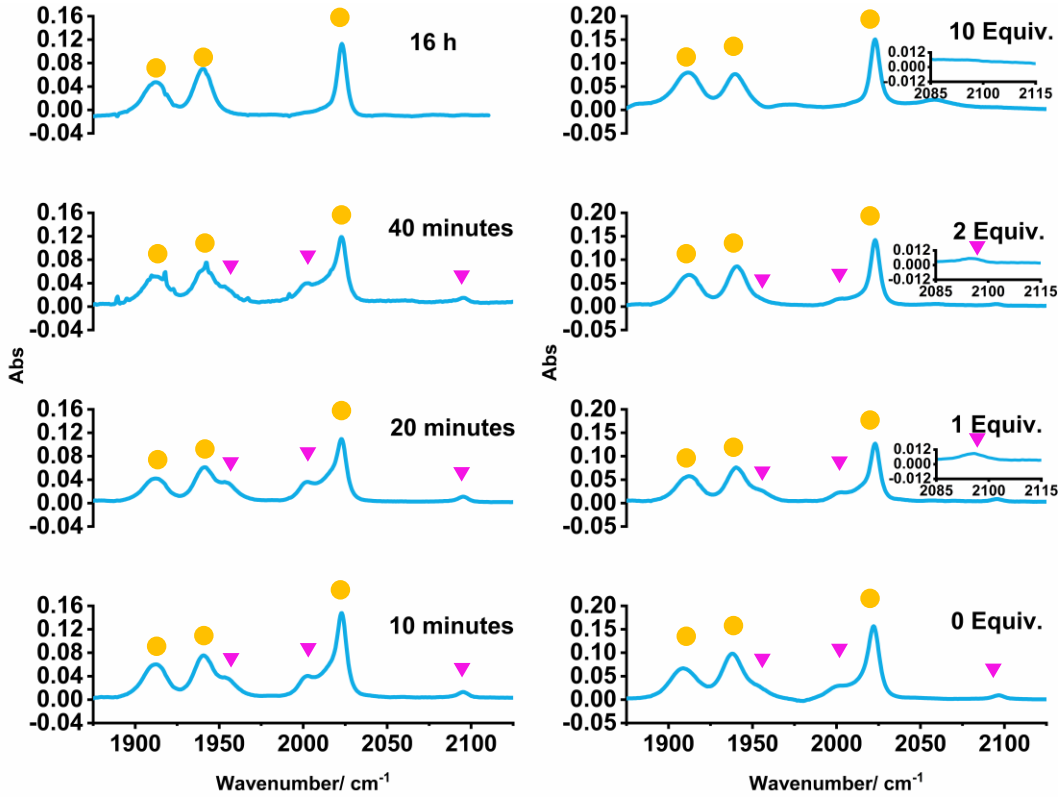

Figure 118. Left: Spectroscopic changes over time for the irradiation of a 0.1 mmol dm^{-3} 1,4-dioxane solution of **228**. Right: IR spectra at time = 40 minutes for the irradiation of a 0.1 mmol dm^{-3} 1,4-dioxane solution of **228** containing varying equivalents of imine **178**. **228** denoted by yellow circles and **229** denoted by pink triangles.

To provide further evidence that visible light promotes loss of an imine ligand, the fluorinated analogue of **228** was synthesised, as outlined in Figure 119. Due to the addition of a fluorine atom on the aromatic ring of the imine, ^{19}F NMR spectroscopy could be used to follow the reactivity of **234**. Ligand exchange experiments were conducted on **234**. As a control experiment, a 0.05 mmol dm^{-3} 1,4-dioxane solution of **234** and 1 equivalent complex **228** were left in an amberised J Youngs NMR tube. Meanwhile an equivalent solution was irradiated with the white LED array in a non-amberised J Youngs NMR tube.

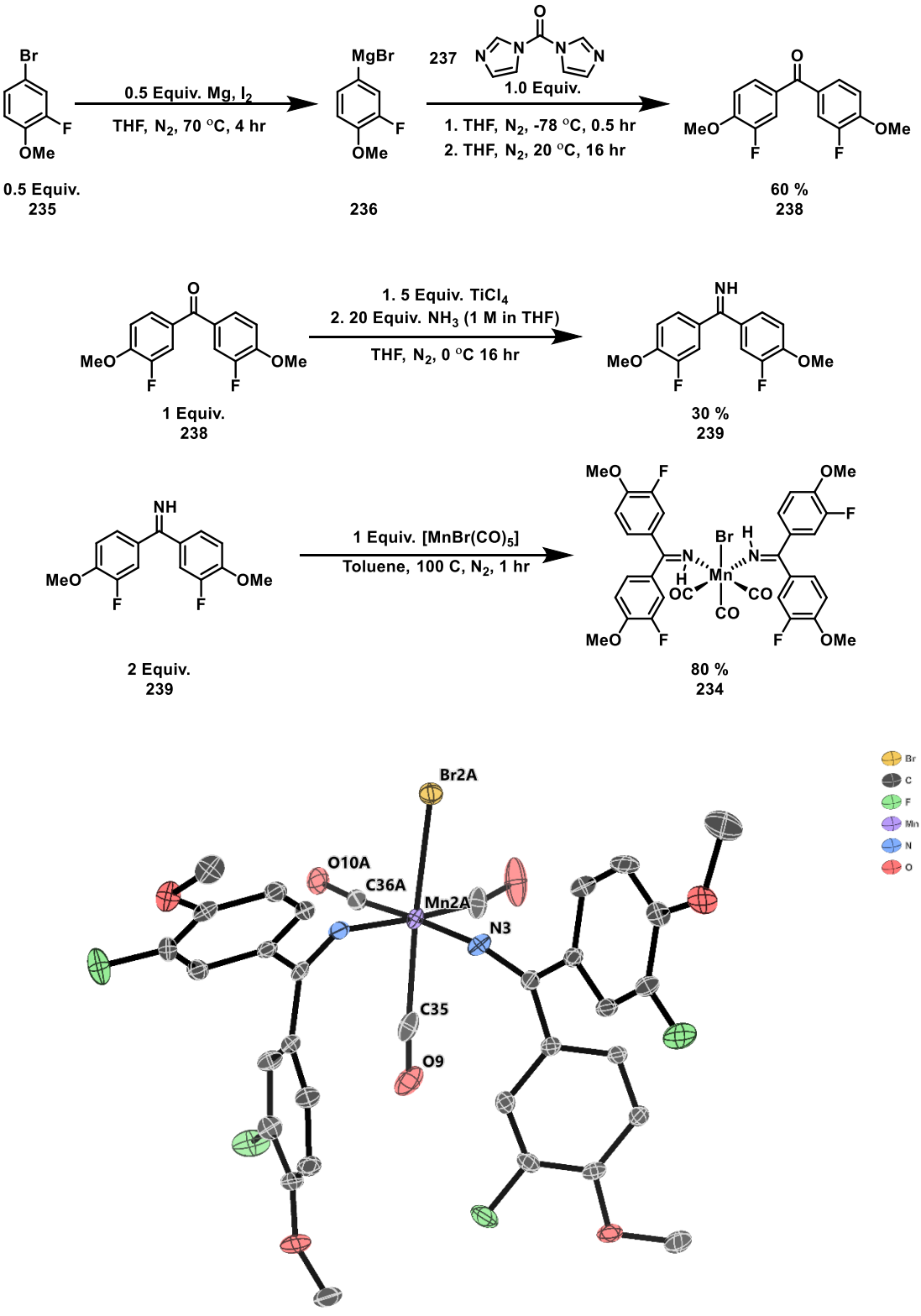

Figure 119. Synthetic route to, and crystal structure of **234**.

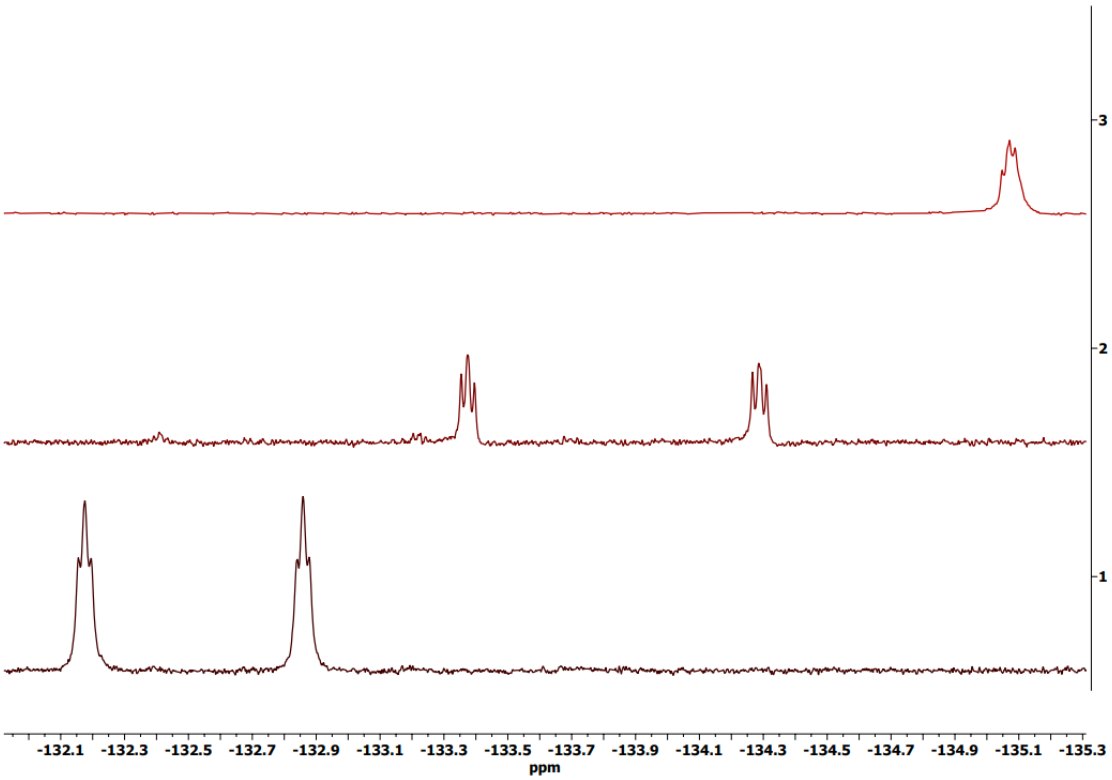

Figure 120. Top: ^{19}F NMR spectrum of imine **239**. Middle: ^{19}F NMR spectrum of **228** and **234** irradiated with the white LED array for 1 hour. Bottom: ^{19}F NMR spectrum of **228** and **234** excluded from light in an amberised J Youngs NMR tube.

The control experiment in the amberised J Youngs NMR tube only showed peaks associated with the complex **234**. Conversely, the solution which was irradiated showed two new peaks. These did not correspond to **234**, nor was the peak associated with the free imine **239** present (see Figure 120). This indicated that scrambling of the imine ligands bound to **228** and **234** had occurred, providing further evidence that visible light aids with loss of an imine ligand. Loss of an imine ligand provides a vacant coordination site, which is required for CMD to occur, activating one of C–H bonds of an imine ligand.

Finally, to gain a greater understanding of how the wavelength of light impacted the reaction, the wavelength of light was controlled. This was achieved through the application of visible light filters to the LED array, as shown in Figure 121 and results are displayed in Table 11. Specific UV/ visible light spectra for the filters are shown in Chapter 6.6. A control experiment with no filter present gave a reduced yield of 10.5%, due to the reduction in light intensity with the modified LED array. The filter at 412 nm gave a low yield, likely due to the LED array not producing a high intensity of light at this

wavelength. > 435 and > 458 nm filters gave the highest yield of 7.5%, which supports the observation that ambient laboratory light activated the precatalyst. While the filters at > 495 and > 520 nm gave reduced yields as the filter wavelength moved further away from the λ_{max} of **228**.

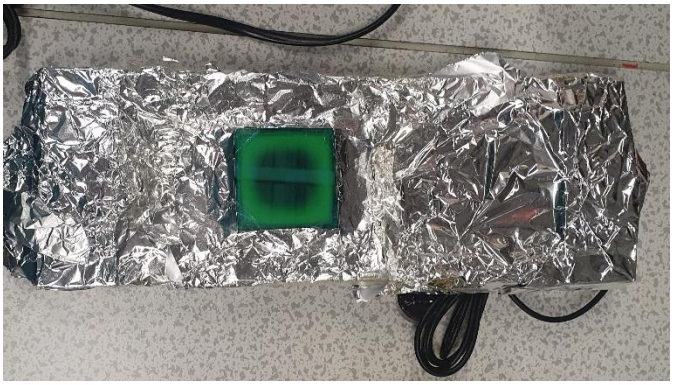

Figure 121. Alteration to the LED array for cut-off and windowed filters.

Table 11. The impact of wavelength on yield of **180**.

Filter λ/ nm	Type of filter	Yield when excluded from light/ %
None	n/a	10.5
412	Windowed	1.1
435	Cut-off	7.5
458	Cut-off	7.5
493	Windowed	1.9
495	Cut-off	0.5
520	Cut-off	0.2

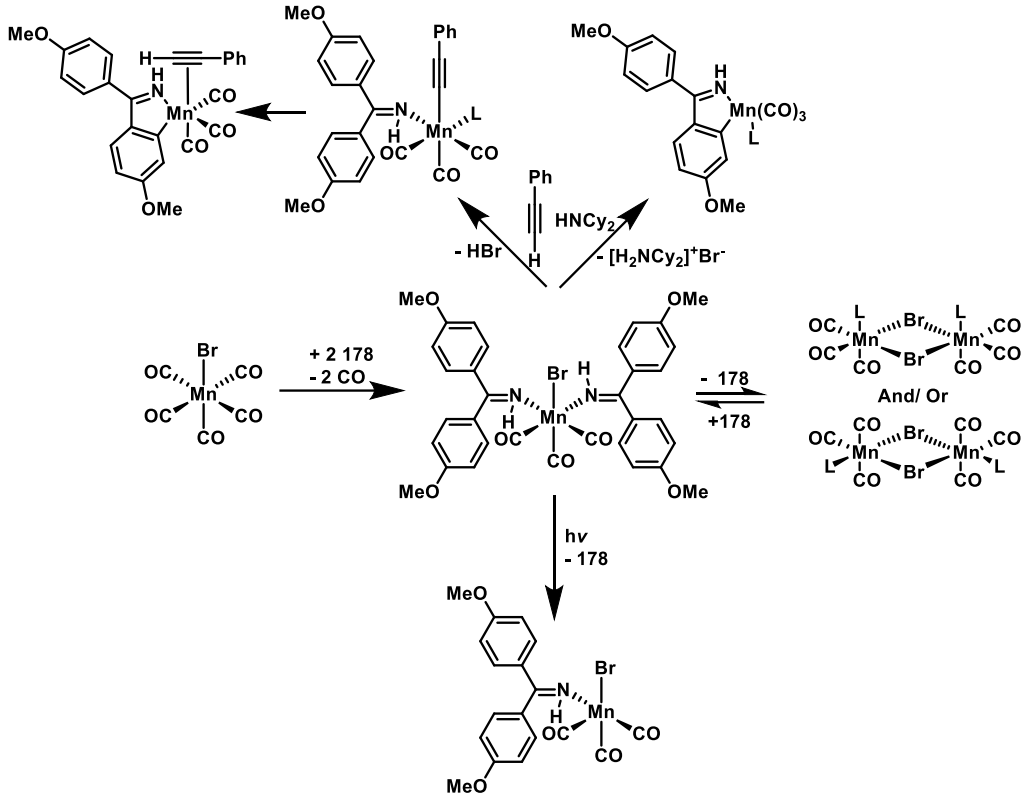

Figure 122. Proposed reactivity for $[MnBr(CO)_5]$, including routes of activation.

3.3.8 $[Mn_2Br_2(CO)_8]$

Finally, activation of the lesser used precatalyst $[Mn_2Br_2(CO)_8]$ **240** was investigated. Xie and co-workers used this precatalyst as an alternative to $[MnBr(CO)_5]$ in several studies.[78,80,81] Control experiments indicated that heating **240** to 105 °C in 1,4-dioxane resulted in rapid formation of $[Mn_2(CO)_{10}]$ within *ca*. 20 minutes (Figure 123). Heating of **240** to 105 °C in the presence of imine **178** resulted in formation of **228** as with $[MnBr(CO)_5]$ (Figure 123). From these control experiments, it could be postulated that **240** acts as a source of $[MnBr(CO)_5]$ or $[Mn_2(CO)_{10}]$ depending on conditions, rather than possessing its own route of activation and unique reactivity.

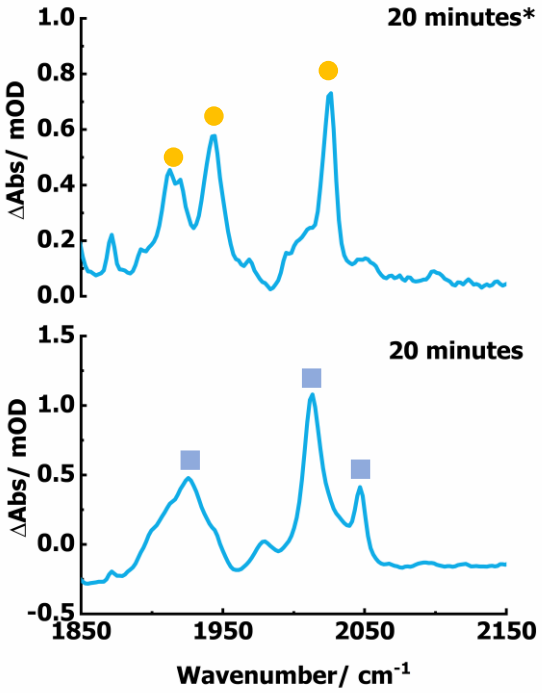

Figure 123. Top: $[Mn_2Br_2(CO)_8]$ heated in the presence of imine **178**. Bottom: $[Mn_2Br_2(CO)_8]$ heated in 1,4-dioxane. **228** denoted by yellow circles, and **102** denoted by blue squares.

3.4 Optimisation of the Reaction Conditions for the [4+2] Annulation of Primary Imines and Alkynes

Having established the modes of activation for relevant manganese carbonyl precatalysts, the reaction used for probing the mechanism, the [4+2] annulation of primary imines and alkynes was optimised further. Reaction aliquots for the $[MnBr(CO)_5]$, $[BnMn(CO)_5]$, $[Mn_2(CO)_{10}]$, and $[Mn(C^N)(CO)_4]$ catalysed reaction revealed that the rection had reached completion by 4 hours (Figure 125). The kinetic profiles for $[Mn_2(CO)_{10}]$ and $[Mn(C^N)(CO)_4]$ use the same conditions as reported by He and co-workers. However, only $[MnBr(CO)_5]$ had a reported kinetic profile for the formation of isoquinoline **180**. This highlights the importance of fully screening potential precatalysts, as $[Mn(C^N)(CO)_4]$ achieved a comparable yield to $[MnBr(CO)_5]$ in $1/12^{th}$ of the time. Further screening with $[BnMn(CO)_5]$, the precursor to $[Mn(C^N)(CO)_4]$, showed that a comparable catalyst performance could be achieved, while requiring less

precatalyst functionalisation. Finally, the formation of **180** was followed when $[MnBr(CO)_5]$ was irradiated with the white LED array. Under these conditions, the reaction reached completion by *ca*. 3 hours, a significant decrease in time from that reported by He and co-workers (12 hours).[60]

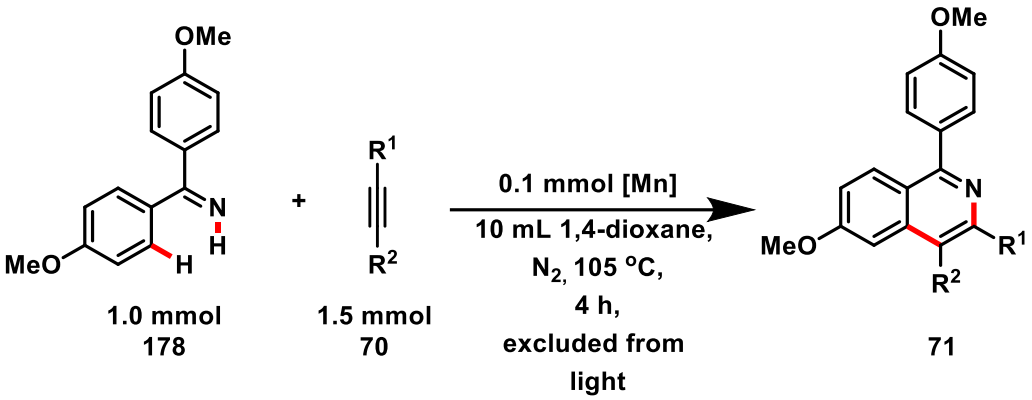

Figure 124. Updated model reaction.

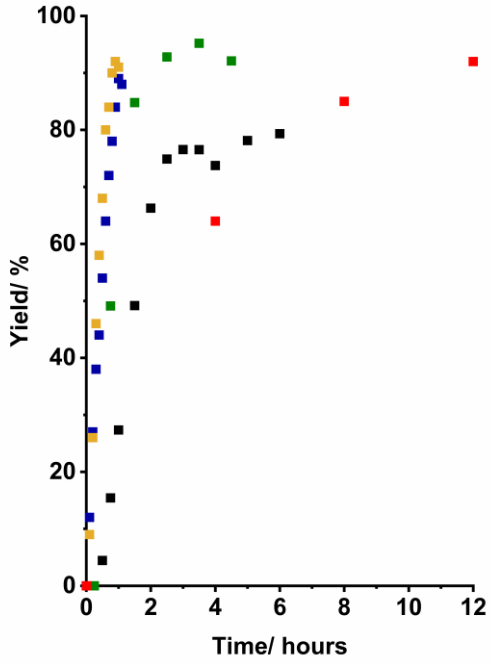

Figure 125. Reaction kinetics for the formation of isoquinoline **180** using the conditions in Figure 124 yellow square denotes $[Mn(C^N)(CO)_4]$, blue square denotes $[BnMn(CO)_5]$, green square denotes $[MnBr(CO)_5]$ irradiated with a white LED array, black squares denote $[Mn_2(CO)_{10}]$,a and red squares denote literature date for $[MnBr(CO)_5]$ precatalyst.[60]

Out of all of the conditions screened, $[MnBr(CO)_5]$ gave the highest yield of 95% (entry L), followed closely by $[BnMn(CO)_5]$ (entry C) and [Mn(C^N)(CO)$_4$] (entry F). $[MnCl(CO)_5]$ and $[MnI(CO)_5]$ were subsequently tested as analogues of $[MnBr(CO)_5]$, but performed significantly worse with yields of 0 and 29% respectively. Additon of $HNCy_2$ gave a similarly high yield of 90% (entry J), while activation of $[MnBr(CO)_5]$ with the terminal alkyne phenyl acetylene gave a lower yield of 82%. Isoquinoline formation was further inhibited by the irradiation of the reaction mixture with the white LED array, reducing the yield to 29% (entry I). Several further terminal alkynes were tested (see Table 13). In each instance a yield reflecting the literature transformation was recorded in the absence of light. Upon repeating the reactions while irradiating the reaction solution with the white LED array a significant decrease in yield was observed. Conversely, isoquinoline product was only detected for the internal alkynes used when the reaction was conducted in the presence of light. This highlights the differences in precatalyst activation. Terminal alkynes proceed through an alkynyl complex, and this species is likely prone to photodecomposition, hence the reduction in yield when irradiated. In contrast, irradiation is a necessity for precatalyst activation when an internal alkyne is used.

Finally, due to the rapid product formation in Figure 125, $[BnMn(CO)_5]$ was tested as a precatalyst in more challenging conditions for manganese (I) catalysed C−H bond functionalisation reactions. The literature precedent for catalyst loading is 10 mol% precatalyst when $[Mn_2(CO)_{10}]$ or $[MnBr(CO)_5]$ are used. When catalyst loading was dropped from the typical loading of 10 to 1% a yield of 33% was recorded. A reduction in temperature to 60 °C, still resulted in isoquinoline formation, with a yield of 35%. These observations indicate that $[BnMn(CO)_5]$ is a more readily activated precatalyst, and less prone to deactivation.

Table 12. Precatalyst condition scope using the reaction outlined in Figure 124. R^1 and R^2 are Ph unless stated otherwise.

Entry	Precatalyst	Mol %	Notes	yield
A	$[BnMn(CO)_5]$	1		33
B	$[BnMn(CO)_5]$	10	60 °C	35
C	$[BnMn(CO)_5]$	10		91
D	$[Mn_2(CO)_{10}]$	5		83
E	$[Mn_2(CO)_9$(1,1-bis(4-methoxyphenyl)methanimine)]	10		88
F	[Mn(C^N)$(CO)_4$]	10		94
G	[Mn$(CO)_5$(*p*-tolylacetylide)]	10	1-Ethynyl-4-methylbenzene	80
H	$[MnBr(CO)_5]$	10	Phenyl acetylene	82
I	$[MnBr(CO)_5]$	10	Phenyl acetylene, White LED array	29
J	$[MnBr(CO)_5]$	10	$HNCy_2$	90
K	$[MnBr(CO)_5]$	10	Ambient laboratory light	8
L	$[MnBr(CO)_5]$	10	White LED array	95
M	$[MnBr(CO)_5]$	10		0
N	[MnBr(1,1-bis(4-methoxyphenyl)methanimine)$_2(CO)_3$]	10	White LED array	87
O	[MnBr(1,1-bis(4-methoxyphenyl)methanimine)$_2(CO)_3$]	10		0
P	$[MnI(CO)_5]$	10	White LED array	29
Q	$[MnCl(CO)_5]$	10	White LED array	0
R	$[Mn(CO)_3(NCMe)_3]^+PF_6^-$	10		0

Table 13. Yield when internal and terminal alkynes were used as the alkyne substrate in Figure 124 and $[MnBr(CO)_5]$ as the precatalyst.

R groups		Lit. Yield/ % [60]	Yield when irradiated with white LED array/ %	Yield when excluded from light/ %
R^1 = Ph	R^2 = H	87	29	87
R^1 = 3-thienyl	R^2 = H	45	14	34
R^1 = *c*-Pr	R^2 = H	56	32	55
R^1 = *n*-Pr	R^2 =*n*-Pr	73	95	0
R^1 = PMP	R^2 = PMP	92	95	0
R^1 =*p*-fluorobenzene	R^2 = *p*-fluorobenzene	79	79	0

3.5 Conclusions

The mode of activation for a range of precatalysts used in manganese (I) catalysed C−H bond functionalisation were determined. For the first time, the route of precatalyst activation for $[Mn_2(CO)_{10}]$ was observed. In this reaction, initially loss of a CO ligand occurred, as opposed to cleavage of the Mn−Mn bond. An imine ligand then coordinated in the vacant coordination site, forming $[Mn_2$(1,1-bis(4-methoxyphenyl)methanimine)$(CO)_9]$. In the presence of free imine, activation of the C−H bond activation then occurred, forming the 5-membered manganacycle **158**. $[Mn_2(CO)_{10}]$ reformed from the $[Mn(CO)_5]^{\cdot}$ fragment of $[Mn_2$(1,1-bis(4-methoxyphenyl)methanimine)$(CO)_9]$. Potential roles of the imine are that an imine molecule was sacrificially reduced to the amine as the manganese centre was oxidised to manganese(I). Alternatively, imine could be reacting to form $[Mn(CO)_3(L)_3]$ 19-electron complex, and reacting with **216** to form $[Mn(CO)_5]^-$ and **158**. Following formation of the 5-membered manganacycle **158**, it was assumed that events reported in Chapter 2 occur. $[BnMn(CO)_5]$ was observed to directly form **158**, presumably through a concerted metalation deprotonation (CMD) pathway, with CO loss being rate-determining. In the presence of alkyne ligands, an intermediate with a η^2- coordinated alkyne was detected prior to formation of **158**. $[Mn(CO)_5$(*p*-tolylacetylide)] reacted with free imine **178** in a similar manner to 2-phenyl pyridine, activating the C−H bond of the imine ligand, and protonating the alkynyl complex. Finally, $[MnBr(CO)_5]$ was observed to

undergo activation through a novel route. Under no circumstances was the 5-membered manganacycle **158** detected. Instead, [MnBr(1,1-bis(4-methoxyphenyl)methanimine)$_2$(CO)$_3$] initially formed under all conditions. This complex was then found to be catalytically competent when either a terminal alkyne was used, $HNCy_2$ additive was introduced, or the reaction solution was irradiated with a white LED array. The terminal alkyne likely provided an alternative pathway for activation through formation of an alkynyl complex. The addition of $HNCy_2$ likely aids the deprotonation of the imine ligand, with $[H_2NCy_2]^+Br^-$ being favourable to HBr formation. Finally, irradiation of the reaction solution promoted the dissociation of an imine ligand, creating an available coordination site for C–H bond activation to proceed *via* a CMD style mechanism.

Chapter 4: Ultrafast Time-Resolved Spectroscopy of Decacarbonyl Dimanganese(0)

4.1 Background

The photochemistry of decacarbonyldimanganese(0) ($[Mn_2(CO)_{10}]$) has long been a topic of great interest due to the suitability of metal carbonyl complexes for time-resolved spectroscopic studies.[17,122,123] Early works were focused on the determination and characterisation of the radical photoproduct $[Mn(CO)_5]^{\cdot}$. This was due to applications of $[Mn_2(CO)_{10}]$ such as those reported by Bamford and co-workers, where it was used as an initiator in the polymerisation of acrylates in the presence carbon tetrachloride (see Figure 126).[75] Here, initiation was proposed to proceed through halogen atom transfer from carbon tetrachloride to $[Mn(CO)_5]^{\cdot}$, forming $[MnCl(CO)_5]$ in the process. [73]

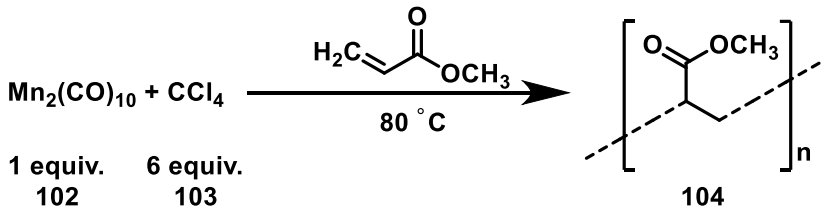

Figure 126. Polymerisation of methyl acrylate initiated by $[Mn_2(CO)_{10}]$ reported by Bamford and co-workers.

The first evidence for $[Mn(CO)_5]^{\cdot}$ was reported by Bidinosti and McIntyre, where several mass spectrometry experiments established that $[Mn(CO)_5]^{\cdot}$ was generated *via* pyrolysis, as opposed to $[Mn(CO)_5]^{+}$.[124] Following this, several attempts to isolate and observe photochemically generated $[Mn(CO)_5]^{\cdot}$ were made in the 1970s using electron paramagnetic (EPR) spectroscopy. [125], [126], [127] These reports of $[Mn(CO)_5]^{\cdot}$ were later disproven, and assigned as $[Mn(CO)_5(O_2)]$, along with several Mn(II) complexes.[128][129] Observation of $[Mn(CO)_5]^{\cdot}$ was not made by EPR spectroscopy until 1981, at which point other methods had been used to synthesise and characterise the complex. [130][131]

Transient absorption (TA) spectroscopy provided *in situ* evidence for the formation of $[Mn(CO)_5]^{\cdot}$. Hughey and co-workers used a broad pump wavelength of 310 nm < λ < 385 nm to photochemically excite $[Mn_2(CO)_{10}]$ ($\sigma \rightarrow \sigma^*$)[132] in THF and obtained kinetics for

the recovery of the ground state bleach band at 343 nm.[133] Recombination of the ground state bleach band was observed to occur *via* a second order process with a rate constate, $k = 1.9 \times 10^9$ s^{-1} mol^{-1} dm^3 in THF. This supported their hypothesis that the recombination of $[Mn(CO)_5]^{\cdot}$ occurred to form $[Mn_2(CO)_{10}]$. However, they reported no transient bands assigned for $[Mn(CO)_5]^{\cdot}$. Further TA studies by Waltz and co-workers revealed $[Mn(CO)_5]^{\cdot}$ to have a λ_{max} of 830 nm in THF. [134] This transient band was reported to decay with a second order rate constant of 9.5×10^8 s^{-1} mol^{-1} dm^3, consistent with the value reported by Hughey and co-workers, supporting their assignment.[133]

To establish the infrared stretching modes of $[Mn(CO)_5]^{\cdot}$, matrix isolation was initially used. Using an argon matrix, Huber and co-workers first reported carbonyl stretching modes at 2060, 1965 and 1911 cm^{-1} using a CO/Ar matrix. These fit with the predicted number of stretching modes for a C_{4v} square pyramidal pentacarbonyl complex.[135] This assignment was later proved incorrect in work conducted by Church and co-workers, who established the bands for $[Mn(CO)_5]^{\cdot}$ to be positioned at 1988 (E) and 1978 (A_1). Here $[Mn(CO)_5]^{\cdot}$ was synthesised from $[HMn(CO)_5]$ deposited on a solid CO matrix at 20 K *via* irradiation at $\lambda > 375$ nm.[131] Bands for $[Mn(^{12}CO)_5]$ were reported at 1987 cm^{-1} (E) and 1978 cm^{-1} (A_1). Further spectroscopic characterisation was conducted in this instance, with evidence provided in the form of Uv/Vis spectra. A λ_{max} of 798 nm was reported, which reflected the previously reported solution-phase λ_{max} of 830 nm in THF.[133] A further band was observed at $\lambda < 340$ nm, this was missed in prior solution-phase Uv/Vis spectra due to the dominant absorption band of ground-state $[Mn_2(CO)_{10}]$ at 343 nm. Due to the nature of matrix isolation limiting diffusion, kinetic data were not obtained during this work on $[Mn(CO)_5]^{\cdot}$, unlike in TA spectroscopic studies.

Table 14. Literature values for the UV/vis and infrared bands of $[Mn(CO)_5]^{\cdot}$.

Medium	UV/Vis $\lambda_{max\ A}$/ nm	UV/Vis $\lambda_{max\ B}$/ nm	IR active bands/ cm^{-1}	reference
THF	830	n/a	n/a	[134]
Propan-2-ol	830	n/a	n/a	[136]
CCl_4	827	n/a	n/a	[137]
Cyclohexane	n/a	n/a	1985	[138]
Propan-2-ol	n/a	n/a	1985	[138]
Heptane	n/a	n/a	1988	[139]
NCMe	n/a	n/a	1985	[140]
CO matrix	798	< 340	1987, 1978	[131]
CO/ Ar matrix	n/a	n/a	2060, 1965, 1911	[135]
Gas phase	n/a	n/a	2000	[141]

Hughey and co-workers hinted towards a second species forming in their TA spectroscopy studies.[133] They postulated that formation of $[Mn(CO)_5L]$ occurred, where L was a coordinating ligand. This was based on recovery of the ground state bleach band for $[Mn_2(CO)_{10}]$ through a slower first order process on a second timescale. A transient band with a λ_{max} at 490 nm was reported for this complex in THF. Further evidence for a second photoproduct was obtained *via* TA spectroscopy. Studies by Yesaka and co-workers, alongside Rothberg and co-workers both clearly demonstrated an additional transient band when $[Mn_2(CO)_{10}]$ was irradiated in cyclohexane and ethanol solutions at $\lambda < 355$ nm ($\sigma \rightarrow d\ \pi^*$ and $d\ \pi \rightarrow d\ \pi^*$).[142]Values for λ_{max} of 500 and 480 nm were reported respectively. [143], [144] Both authors proposed the formation of a $[Mn_2(CO)_9(S)]$ complex, where S is the relevant solvent ligand coordinated.

Research by Hepp and co-workers, demonstrated that photoexcitation at 355 nm of $[Mn_2(CO)_{10}]$ immobilised in a 3-methylpentane matrix at 77 K resulted in several new

transient infrared active stretching modes.[145] Free CO was detected and indicated that 20-30 % of $[Mn_2(CO)_{10}]$ had undergoing photochemical dissociation of a CO ligand, as opposed to Mn–Mn bond cleavage. A new band at approx. 1760 cm^{-1} was also observed, along with several bands in the typical metal carbonyl region (2055, 2017 and 1986 cm^{-1}). Incorporation of ^{13}C labelled CO resulted in a band shift from 1760 cm^{-1} to 1717 cm^{-1}, which aided in band assignment as a bridging CO ligand. Warming of the matrix to 298 K resulted in reformation of $[Mn_2(CO)_{10}]$, while addition of PPh_3 prior to warming resulted in formation of $[Mn_2(CO)_9(PPh_3)]$, aiding in assignment of the new transient species as $[Mn_2(CO)_9]$. Further work by Church and co-workers complimented Hepp's study. Church and co-workers conducted kinetic analysis on the solution-phase recombination of CO with $[Mn_2(CO)_9]$, to form $[Mn_2(CO)_{10}]$, through the use of time-resolved infrared (TRIR) spectroscopy.[139] In heptane, a rate constant, *k* was reported to be 1.2×10^6 mol^{-1} dm^3 s^{-1}. Unfortunately, Hughey and co-workers did not report the rate constant for the "slow" reformation of $[Mn_2(CO)_{10}]$, so a comparison cannot be made.

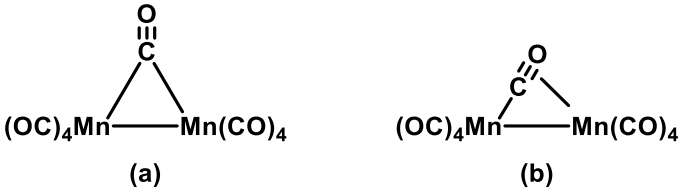

Figure 127. Proposed structures of $[Mn_2(CO)_9]$ (**a**) ketonic CO, (**b**) semibridged bridged CO.

To elucidate the structure of $[Mn_2(CO)_9]$, observed by Hepp and co-workers, experiments using plane-polarised photolysis of matrix isolated $[Mn_2(CO)_{10}]$ were employed to reveal information about the bridging CO ligand.[146] Dunkin and co-workers were able to differentiate between the two rationalised bridging modes for $[Mn_2(CO)_9]$. One structure included a ketonic bridging CO ligand, while the second was with a semibridging CO ligand (Figure 127). Their results revealed that the stretching mode at 1764 cm^{-1} exhibited no dichroism. This observation was satisfied by the semi-bridged $[Mn_2(CO)_9]$ structure; in which the stretching mode was at 45 ° from the photoactive transition of $[Mn_2(CO)_{10}]$, accounting for the lack of dichroism between photolsying parallel and perpendicular planes of polarisation.

Table 15. Literature values for the Uv/vis and infrared bands of $[Mn_2(CO)_9]$.

Medium	Uv/vis $\lambda_{max\ A}$/ nm	IR active bands/ cm^{-1}	reference
THF	490	n/a	[134]
EtOH	480	n/a	[144]
Cyclohexane	500	n/a	[143]
3-methyl pentane matrix	n/a	1760, 1986, 2017, 2055	[145]
Argon matrix	n/a	1764, 1977, 1993, 2037, 2058	[146]
Heptane	480	1760, 1968, 1996, 2008, 2022, 2058	[139]
Cyclohexane	n/a	1760, 1985, 2015, 2052	[138]
Gas Phase	n/a	1745, 1980, 2014, 2050	[141]

Several investigations were also conducted where the photochemical behaviour of $[Mn_2(CO)_{10}]$ was observed in the gas-phase. Research by Seder and co-workers followed transient complexes formed *via* irradiation at 193, 248 and 351 nm, mirroring solution-phase and matrix isolation studies conducted prior.[141],[147] Unsurprisingly, similar ratios of Mn–Mn bond cleavage to Mn–C were observed with the changing excitation wavelength. The rate of $[Mn(CO)_5]^{\cdot}$ recombination was an order of magnitude faster than solution-phase studies, with the rate constant k = 2.7×10^{10} mol^{-1} dm^3 s^{-1}, which was close to the limit for gas-phase radical-radical recombination processes (*ca.* 1×10^{10} mol^{-1} dm^3 s^{-1}). Re-coordination of CO to $[Mn_2(CO)_9]$ was reported with a rate constant of 2.4×10^{10} mol^{-1} dm^3 s^{-1}, reflecting rate constants reported in solution-phase studies. [139] Interestingly, these gas-phase studies reported several additional transient bands at ~1850, 1900, and 2048 cm^{-1}. Tentatively the authors assigned these to $[Mn(CO)_4]$ and $[Mn_2(CO)_y]$ where y < 9. The additional loss of CO was justified by excess

vibrational energy, in which relaxation was greatly reduced, due to fewer collisions occurring in the gas phase, as opposed to solution-phase. In a separate gas-phase study by Prinslow and Vaida, which used quadrupole mass spectrometry as their primary method of detection, fragment ions for $[Mn_2(CO)_y]^+$ where $5 < y < 9$ and $[Mn(CO)_4]^+$ were detected, supporting Seder and co-workers assignment.[148]

Table 16. Bridging ratios of $[{\cdot}Mn(CO)_5]$ to $[Mn_2(CO)_9]$ at varying excitation wavelengths.

Excitation wavelength/ nm	Solvent	Bridging ratio of $[Mn(CO)_5]^{\cdot}$: $[Mn_2(CO)_9]$	Reference
266	Cyclohexane	0.16 : 0.84	[137]
337	Cyclohexane	0.30 : 0.70	[144]
347	Ethanol	0.33 : 0.67	[137]
355	Cyclohexane	0.49 : 0.44	[137]
400	Cyclohexane/ Propan-2-ol	> 0.72 : 0.28	[149]

Following the aforementioned studies on the photochemistry $[Mn_2(CO)_{10}]$, research focused on the wavelength dependency and the kinetics of ultrafast events. Kobayashi and co-workers clearly demonstrated the wavelength dependence for the ratio of homolytic Mn–Mn bond cleavage to Mn–C bond cleavage. This was explored between excitation wavelengths of 266-355 nm, through the use of TA spectroscopy.[137] A clear trend for preferential Mn–C bond cleavage ($\sigma \rightarrow d\,\pi^*$ and $d\,\pi \rightarrow d\,\pi^*$) was observed at a lower excitation wavelength(266 nm), while Mn–Mn bond cleavage ($\sigma \rightarrow \sigma^*$) became the dominant process as excitation wavelength tended towards 355 nm. Their results are summarised in Table 16, along with other values reported in the literature. By conducting double-pump TA experiments, several photoproducts from excitation of $[Mn_2(CO)_9]$ at 532 nm were also characterised (Figure 128). As with $[Mn_2(CO)_{10}]$, both homolytic Mn–Mn bond cleavage and Mn–C bond cleavage were observed, with $[Mn(CO)_5]^{\cdot}$ + $[Mn(CO)_4]$ and $[Mn_2(CO)_8]$ formed respectively.

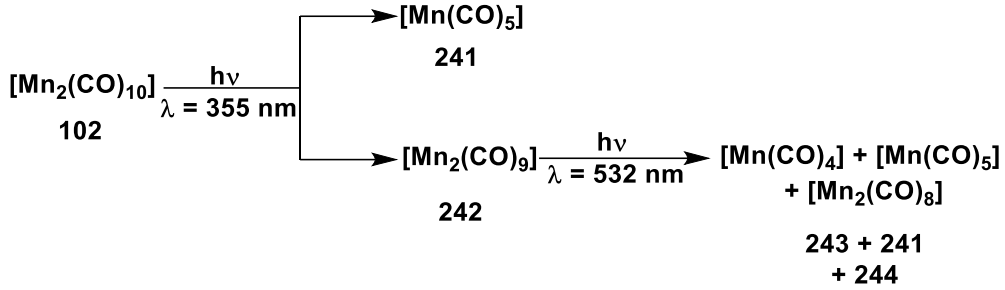

Figure 128. Secondary photoproducts formed *via* excitation of $[Mn_2(CO)_9]$ at 532 nm. [137]

Ultra-fast studies (< 250 ps) were conducted using time of flight (TOF) mass spectrometry, TA and TRIR spectroscopy, exploring speciation when $[Mn_2(CO)_{10}]$ was photolysed with pump wavelengths of 295< λ < 310 nm. Waldman and co-workers were able to follow intricate events occurring during the first 10 ps following excitation, *via* the use of TA.[150] Using the transient bands at 310, 460 and 520 nm in ethanol, initially coherent effects were observed. Breakage of both the Mn–Mn and Mn–C bond occurred within 500 fs, rotation and possible bridging of a CO ligand in $[Mn_2(CO)_9]$ by 2 ps, and solvent rearrangement by 7 ps. Work by Kim and co-workers also explored this timeframe for bond cleavage following excitation, in this instance TOF spectrometry was used to follow speciation.[151] Formation of $[Mn(CO)_5]^{\cdot}$ was followed by the formation of Mn^+, and formation of $[Mn_2(CO)_9]$ by the detection of Mn_2^+. An ultrashort lifetime of <85 fs was observed for excited $[Mn_2(CO)_{10}]$ through the detection of $[Mn_2(CO)_{10}]^+$. Formation of Mn_2^+ and Mn^+ were detected from 20 and 40 fs respectively, with the difference attributed to impact that the change in reduced mass between Mn–Mn and Mn–CO has on bond cleavage.

A study into the photodissociation dynamics of $[Mn_2(CO)_{10}]$ by Zhang and Harris gave contradictory results.[136] Using TA spectroscopy, they reported dissociation at approx. 2-3 ps after excitation with a 295 nm pump wavelength. Further analysis of their data revealed an interesting insight into the vibrational relaxation dynamics for both $[Mn(CO)_5]^{\cdot}$ and $[Mn_2(CO)_9]$ photoproducts. Examination of the band at 582 nm for $[Mn_2(CO)_9]$ in cyclohexane revealed biexponential kinetics. Fast decay of 15 ps, followed by a slow decay of 176 ps was reported. These were attributed to vibrational relaxation through low frequency stretching modes and CO stretching modes respectively. Typically, fast vibrational relaxation (< 100 ps) is associated with low frequency

vibrational modes, while "slow" relaxation (> 100 ps) is typical for CO stretching modes. A solvent dependency was then demonstrated, following the relaxation of $[Mn_2(CO)_9]$ in propan-2-ol solution, faster decay of 10 and 145 ps were reported. Finally, Zhang and Harris monitored the vibrational relaxation of $[Mn(CO)_5]^{\cdot}$ using the absorption at 740-830 nm. A single exponential decay was observed, with a lifetime of 3-10 ps, indicating relaxation of $[Mn(CO)_5]^{\cdot}$ occurs through low frequency vibrational modes, rather than CO vibrational modes.

The final study probing the photodissociation and ultra-fast event when $[Mn_2(CO)_{10}]$ was excited at ≤ 310nm was conducted by Owrutsky and Baronavski.[138] Unlike prior studies observing subpicosecond events, TRIR spectroscopy was used. This limited pump-probe delays to a picosecond timescale (1-500 ps), as species are too vibrationally hot at subpicosecond times. Vibrational coherence was observed prior to the 0 ps and at the shortest pump-probe delays (<5 ps), evidence for sub-picosecond processes were observed. Beyond this, vibrational relaxation occurred, resulting in sharpening of transient bands (<100 ps), along with partial ground state bleach band recovery (50 %) by 38 ps. Both the possibility of geminate recombination and relaxation of vibrationally excited $[Mn_2(CO)_{10}]$ were discussed as explanations for bleach recovery; but conclusive evidence was not provided either way. In cyclohexane the band associated with the semi-bridged CO ligand of $[Mn_2(CO)_9]$ (1760, 1985, 2015, and 2052 cm^{-1}) formed within 31 ps, giving an upper limit to the formation of the bridged bond. Formation of this band occurred before sharpening of the terminal band of $[Mn_2(CO)_9]$ finished (54 ps), indicating that formation of the semi-bridged band occurred before vibrational relaxation was complete.

A follow up publication was written by Owrutski, Baronavski and Steinhurst 6 years later.[149] In this study, similar TRIR spectroscopy experiments were conducted to their prior work, using a pump-wavelength of 400 nm instead.[138] Again vibrational coherence was observed prior to the 0 ps pump-probe delay. At early pump-probe delays a new transient band was observed at low energy (*ca.* 1977 cm^{-1}), no comments were made about the origin of this band, due to the weak intensity it possessed. Vibrational relaxation of $[Mn(CO)_5]^{\cdot}$ was found to be complete by 58 ps, resulting in a transient band at 1985 cm^{-1} in both cyclohexane and propan-2-ol. This value was comparable to their

previous work, but significantly longer than times reported in TA studies by Zhang and Harris.[138], [136] The mono exponential relaxation of $[Mn(CO)_5]^{\cdot}$ implied that relaxation was occurring through either low frequency modes, or CO stretching modes, not both. As with prior studies exciting at 295 nm, vibrational relaxation was attributed to relaxation through low frequency vibrational modes, rather than CO stretching modes, due to the observed timespan.[136] Bands for $[Mn_2(CO)_9]$ were not reported at 400 nm, this was justified by a branching ratio of ≥ 2.5 for the ratio of $[Mn(CO)_5]^{\cdot}$ to $[Mn_2(CO)_9]$, thus times for vibrational relaxation were not reported.

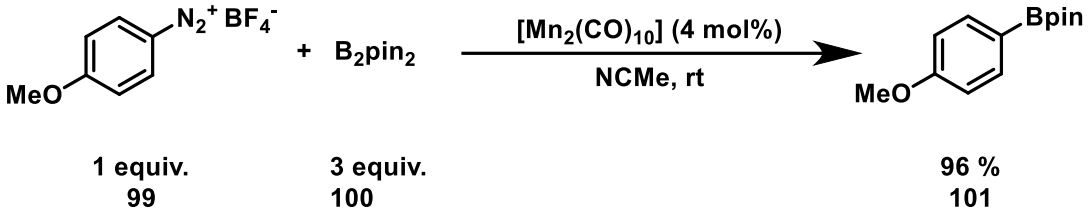

Figure 129. Manganese initiated borylation of aryl diazonium salts studied by Firth co-workers. [140]

Recently, work was published Firth and co-workers used ultrafast TRIR spectroscopy to aid mechanistic insight into the role $[Mn_2(CO)_{10}]$ plays in borylation of aryl diazonium salts (Figure 129).[140] Time-resolved multiple probe spectroscopy (TR^MPS) enabled probing of events following photo dissociation on a picosecond to microsecond timescale in a single experiment. [92], [93] As in prior work, excitation of $[Mn_2(CO)_{10}]$ at a pump wavelength of 400 nm resulted in generation of vibrationally relaxed $[Mn(CO)_5]^{\cdot}$ within *ca*. 100 ps.[149] Photolysis of $[Mn_2(CO)_{10}]$ was conducted in acetonitrile, which resulted in $[Mn(CO)_5]^{\cdot}$ exhibiting previously unobserved reactivity. Second order recombination of $[Mn(CO)_5]^{\cdot}$ was observed through bleach band recovery, reflecting prior studies, although no comparison to rates of recombination was made. A second previously undetected, long-lived photoproduct formed, possessing a transient band at 2055 cm^{-1} was observed within 8.8 µs. This transient band was attributed to the cationic complex $[Mn(CO)_3(NCMe)_3]^+$, with assignment based on a prior synthesis of the complex from $[MnCl(CO)_5]$ (Figure 130).[152] A route for formation of this complex was proposed; initial CO ligand substitution with NCMe forming the 19-electron complex $[{\cdot}Mn(CO)_3(NCMe)_3]$, followed by oxidation, reacting with $[Mn_2(CO)_{10}]$ to generate $[Mn(CO)_3(NCMe)_3]^+$. Formation of $[Mn(CO)_3(NCMe)_3]^+$ was amplified *via* addition of

B_2pin_2, which was justified by B_2pin_2 acting as an oxidising agent for the 19-electron complex. A second long-lived photoproduct was observed in the presence of a diazonium, with a transient band at 2071 cm^{-1}. The reaction of $[Mn(CO)_5]^{\cdot}$ reducing PhN_2BF_4 to form N_2, a phenyl radical and $[Mn(CO)_5(NCMe)]^+BF_4^-$ was put forward as a viable explanation for this transient band.

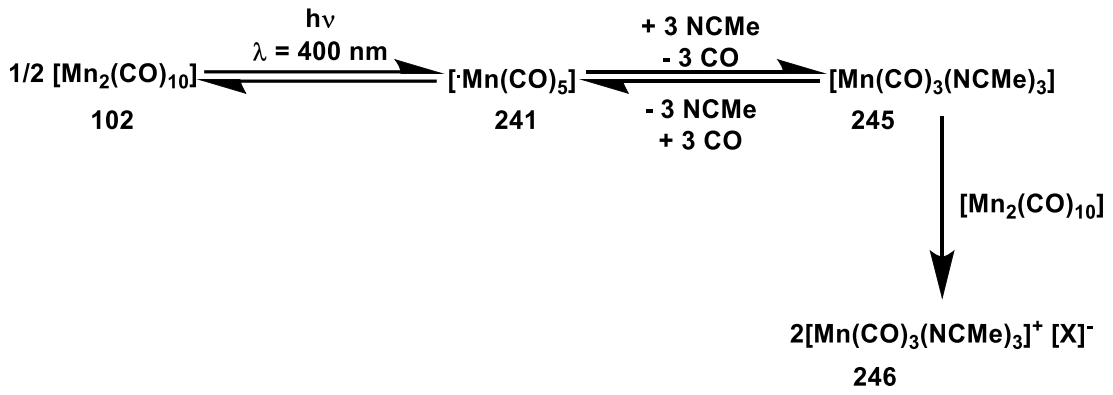

Figure 130. Speciation following photochemical excitation of $[Mn_2(CO)_{10}]$ in NCMe solution with a pump wavelength of 400 nm. [140]

4.2 Aims and Objectives

The aims of this Chapter are to probe photochemically induced events following speciation derived from $[Mn_2(CO)_{10}]$. The reactivity of these photoproducts has been studied in little detail, and have not been related back to catalytic systems, such as those seen in C–H bond functionalisation reactions. Events will be followed on a picosecond to microsecond timescale using TR^MPS, as described in Chapter 2.1. A UV pump, IR probe setup will be used. Pump wavelengths of 310 to 400 nm are used to excited $[Mn_2(CO)_{10}]$, and a region of 1500 to 2150 cm^{-1} will be probed in the infrared region of the electromagnetic spectrum. Pump wavelengths of 310 – 400 nm will be chosen, as literature studies suggest that as the wavelength changes, different electronic transitions occur. [138]

Once fundamental photochemistry of $[Mn_2(CO)_{10}]$ has been established with our setup, and compared to literature studies, the impact of solvent on speciation will be probed. Solvents with a variety of coordination modes, and varying degrees of interactions with $[Mn_2(CO)_{10}]$ and subsequent photoproducts will be examined. Toluene, acetonitrile, *n*-

heptane, THF, methylene chloride, 1,4-dioxane, acetone, DMSO, styrene, butyl acrylate, and cyclohexane were chosen.

Finally, the reactivity of the imine 1,1-bis(4-methoxyphenyl)methanimine **178** with photoproducts will be investigated. This is to look at how different photoproducts react with **178**, providing further evidence for the route of activation of $[Mn_2(CO)_{10}]$ and tying the study back to catalytic work conducted by He and co-workers.[60]

4.3 Ground state $[Mn_2(CO)_{10}]$

$[Mn_2(CO)_{10}]$ in solution possesses three bands in the metal carbonyl region (1850-2200 cm^{-1}), which are associated with various stretching modes. These are situated at 1983, 2014, and 2046 cm^{-1} in *n*-heptane solution (Figure 131).

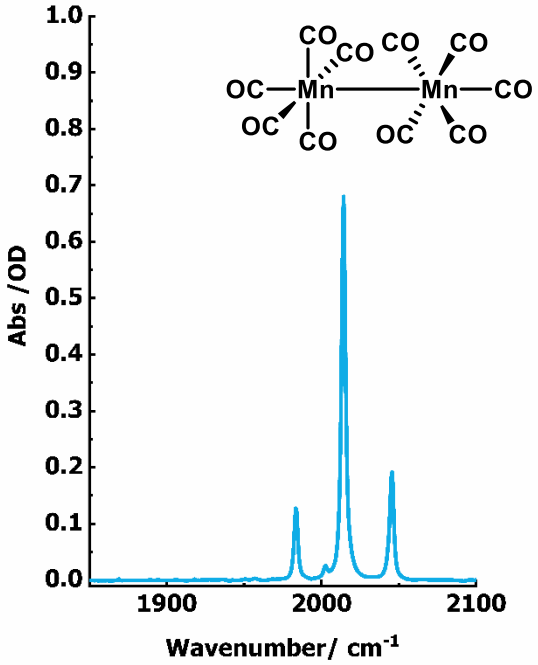

Figure 131. Ground state infrared spectrum of $[Mn_2(CO)_{10}]$ in *n*-heptane between 1850 and 2150 cm^{-1}.

The experimentally observed infrared active modes conform with those predicted though vibrational group theory analysis. $[Mn_2(CO)_{10}]$ can be represented by the D_{4d} point group.

Table 17. Character table for the D_{4d} point group.

D_{4d}	E	$2S_8$	$2C_4$	$2S_8^3$	C_2	$4C_2'$	$4\sigma_d$	Linear functions
A_1	+1	+1	+1	+1	+1	+1	+1	
A_2	+1	+1	+1	+1	+1	-1	-1	
B_1	+1	-1	+1	-1	+1	+1	-1	
B_2	+1	-1	+1	-1	+1	-1	+1	z
E_1	+2	$+\sqrt{2}$	0	$-\sqrt{2}$	-2	0	0	x, y
E_2	+2	0	-2	0	0	0	0	
E_3	+2	$-\sqrt{2}$	0	$+\sqrt{2}$	-2	0	0	

The D_{4d} point group is composed of four mirror planes σ_d, a C_2, two C_4, and four C_2' axis of rotation, two S_8 and S_8^3 improper axis of rotation, and the identity E. Application of these symmetry elements to $[Mn_2(CO)_{10}]$ results in the reducible representation $\Gamma_{vib}(CO) = 10E + 2C_4 + 2C_2 + 4\sigma_d$ for the CO ligands. Inspection of the point group table and application of equation 1 in Chapter 2 reveals $2A_1 + 2B_2 + E_1 + E_2 + E_3$ to be the irreducible representation. Following the infrared active modes in Table 17, B_2 and E_1 stretching modes are predicted to be infrared active, reflecting the recorded infrared spectrum of $[Mn_2(CO)_{10}]$ (Figure 132).

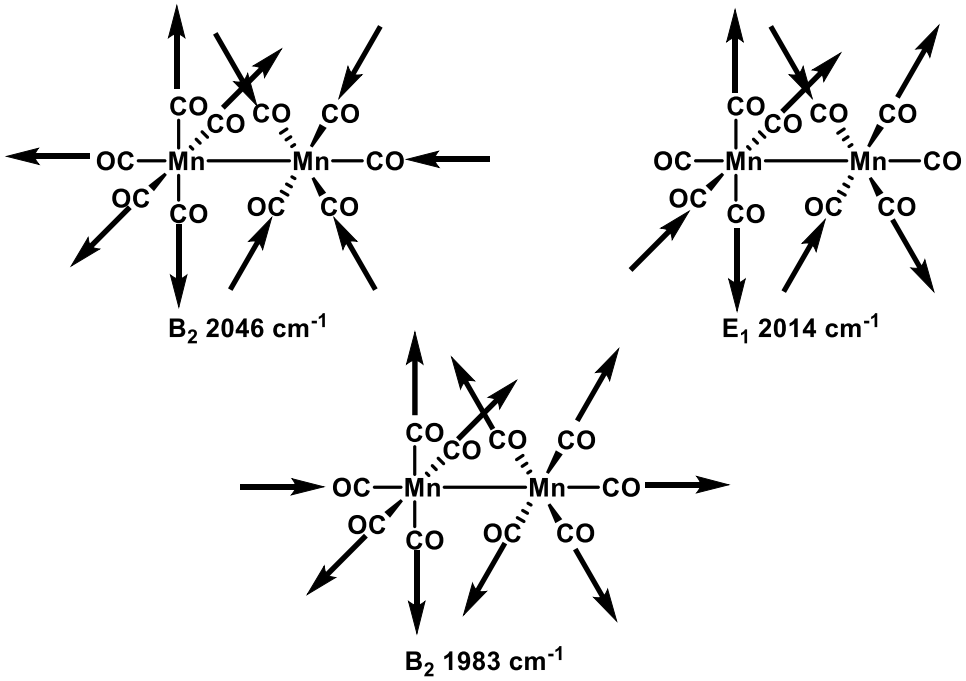

Figure 132. Assigned stretching modes of $[Mn_2(CO)_{10}]$.

$[Mn_2(CO)_{10}]$ possesses several electronic transitions in the region of 300 to 400 nm, as depicted in Figure 133. A CO dissociative ($\sigma \rightarrow \pi^*$) transition occurs with a band at approximately 313 nm in *n*-heptane. While the peak with a λ_{max} of 343 nm due to a ($\sigma \rightarrow \sigma^*$) and shoulder peak at approximately 374 nm caused by a ($d\,\pi \rightarrow \sigma^*$) transition results in cleavage of the Mn−Mn bond.[137], [153] Based on the UV-visible spectrum of $[Mn_2(CO)_{10}]$, three pump wavelengths were chosen: 310 nm, which should favour dissociation of a CO ligand; 355 nm, where Mn−Mn bond and Mn−C cleavage should occur; and 400 nm, where Mn−Mn bond cleavage should be preferential.

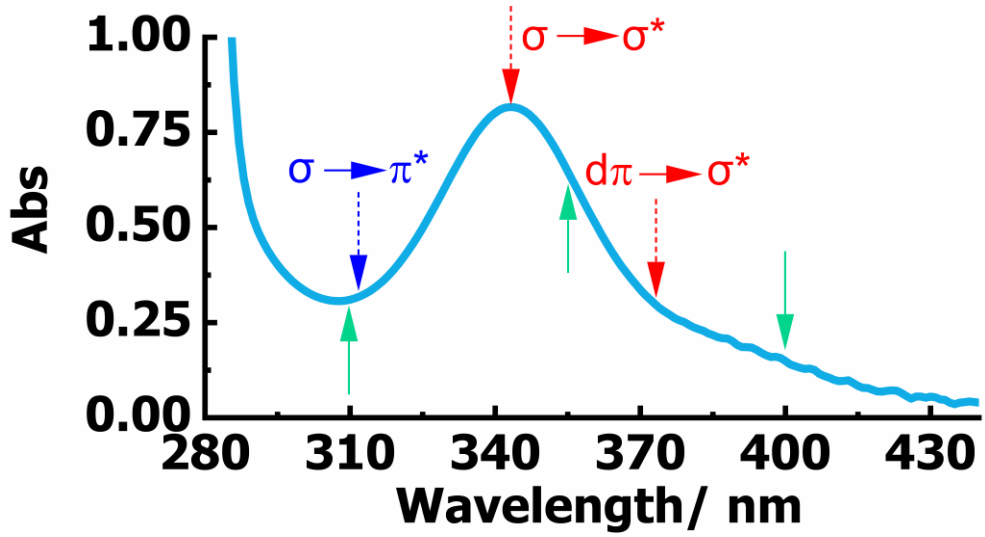

Figure 133. UV/Visible spectrum of $[Mn_2(CO)_{10}]$ in *n*-heptane. Green arrows depict experiment pump wavelengths of 310, 355, and 400 nm. The blue arrow depicts an electronic transition which is CO dissociative and the red arrows depict electronic transitions which cleave the Mn–Mn bond.

The UV/Visible spectrum of $[Mn_2(CO)_{10}]$ was then recorded in a range of 'typical' solvents to assess the degree of solvatochromism that occurs. As Figure 134 shows, the UV/Visible spectra of $[Mn_2(CO)_{10}]$ shows little solvent dependence for the $\sigma \rightarrow \sigma^*$ and $d\,\pi \rightarrow \sigma^*$ transitions. Whereas the higher energy $\sigma \rightarrow \pi^*$ transition shows greater solvent dependency.

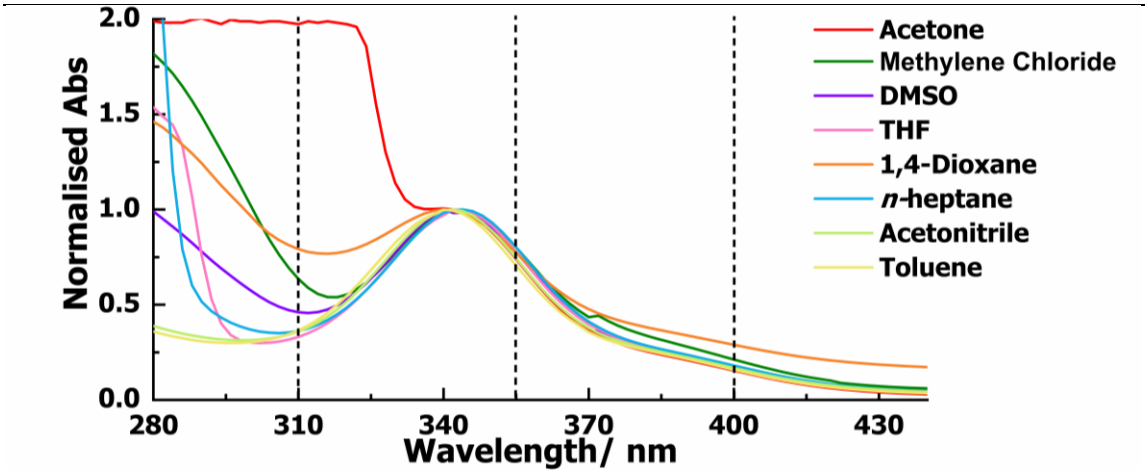

Figure 134. Solvent dependency of the UV/Vis spectrum for $[Mn_2(CO)_{10}]$. Red line denotes acetone (solvent cutoff at 330 nm), green line denotes methylene chloride, purple line denotes DMSO, pink line denoted THF, orange line denotes 1,4-dioxane, blue line denote *n*-heptane, light green line denotes acetonitrile, and yellow line denotes toluene. Black dotted lines denote the UV pump wavelengths of 310, 355, and 400 nm that were used.

4.4 Time-Resolved Multiple Probe Spectroscopy (TR^MPS)

Photochemically induced events involving $[Mn_2(CO)_{10}]$ were followed *via* TR^MPS, as in Chapter 2, enabling monitoring between 1 ps and 998.5 µs. Following the general procedure for data analysis, as discussed in experimental Chapter 6.1.9, data are presented in the form of difference spectra. Consequently, spectra possess both positive and negative features. Positive bands represent photoproducts formed during an experiment, while the negative bands depict loss of the ground state $[Mn_2(CO)_{10}]$.

Experiments were carried out in anhydrous *n*-heptane, toluene, and acetonitrile. *n*-heptane has few interactions with ground state $[Mn_2(CO)_{10}]$ and photoproducts. This ensures that peaks are well defined, and coordination of weakly coordinating ligands can be observed in solution phase samples. Acetonitrile was chosen as a second solvent due to the highly coordinating nature of the solvent. This enables confident assignment of solvent bound complexes at early pump-probe delays. However, spectra often possess broad bleach and transient bands, due to increased complex-solvent interactions. Finally, toluene was chosen as a third solvent. Toluene is catalytically relevant in many manganese carbonyl catalysed C–H bond functionalisation reaction. This includes the [4+2] annulation of primary imines and alkynes, which was used as a

basis for studies in Chapter 2 and 3.[60] *Ca*. 6 mg of $[Mn_2(CO)_{10}]$ was dissolved in 10 mL of anhydrous solution, resulting in a concentration of approximately 1.56 mmol dm^{-3} for ground state $[Mn_2(CO)_{10}]$ in all experiments. All experiments were carried out under a positive atmosphere of N_2 gas, to ensure that the experimental system was oxygen-free.

4.4.1 Ultrafast Photochemically Induced Events

Initially, ultrafast studies (0.5-1000 ps) on $[Mn_2(CO)_{10}]$ were conducted in *n*-heptane using a 310, 355, and 400 nm pump wavelength. *n*-heptane was chosen as the solvent because bands are sharp and well defined due to the limited solvent-complex interactions. This aids with determination of transient speciation, as bands are broader at these early pump probe delays due to the occupation of vibrationally excited states. At 400 nm, where predominantly Mn−Mn bond cleavage was expected, additional experiments were conducted in both perfluoro(methylcyclohexane) and acetonitrile.[137] Experiments in perfluoro(methylcyclohexane) and acetonitrile enable the probing of how a highly non-interactive and interactive solvent impact the lifetime of photoproducts and excited states.

Furthermore, to aid with the assignment of vibrationally excited states of $[Mn_2(CO)_{10}]$, an experiment was carried out in which both an IR pump and probe wavelength was undertaken (Figure 135). This enabled the determination of the bands due to the first and second vibrationally excited states of $[Mn_2(CO)_{10}]$. The ground state bleach bands of $[Mn_2(CO)_{10}]$ in Figure 135 correspond to the transition from v = 0 to v = 1. The dominant transient features at 1971, 2008, and 2040 cm^{-1}, which are red shifted from the ground state bleach bands belong to the first vibrationally excited state of $[Mn_2(CO)_{10}]$. These transient bands correspond to the transition v = 1 to v = 2. A set of three weaker transient bands at 1938, 1990, and 2024 cm^{-1} were assigned to the second vibrationally excited state of $[Mn_2(CO)_{10}]$ due to their increased red shift from the ground state bands of $[Mn_2(CO)_{10}]$.

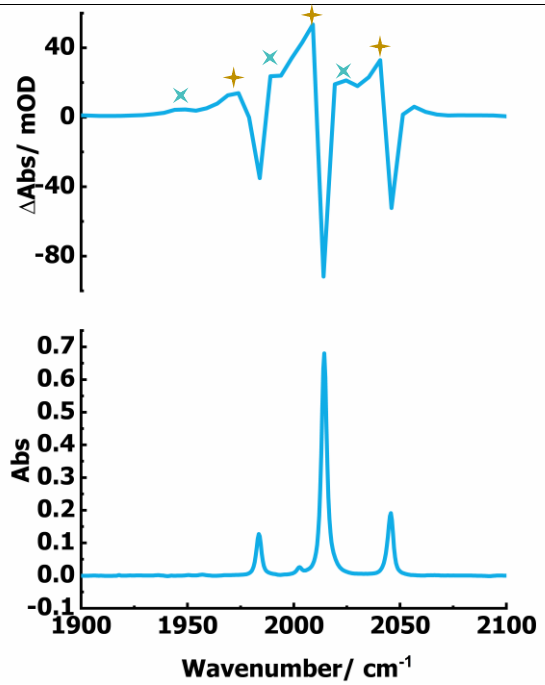

Figure 135. Top: TRIR spectra of $[Mn_2(CO)_{10}]$ in anhydrous *n*-heptane solution exciting with an IR pump wavelength at selected pump-probe delay of 500 fs. Bottom: Ground state spectrum of $[Mn_2(CO)_{10}]$ in anhydrous *n*-heptane. $[Mn_2(CO)_{10}]$ in the excited state $v = 1 \rightarrow 2$ transition denoted by yellow star and $[Mn_2(CO)_{10}]$ in the excited state $v = 2 \rightarrow 3$ transition denoted by turquoise star.

The lifetime for each of the bands associated with vibrational relaxation of $[Mn_2(CO)_{10}]$, from v=2 to v=1 were determined through the application of mono exponential fits to the appropriate bands at 1938, 1990, and 2024 cm^{-1} (see Figure 136 and Table 18). Hereafter, transitions will be denoted as $B_{2_1}^2$ and E_1^2 for specific bands. Slight variations in lifetime for vibrational relaxation were observed between the different vibrational modes of $[Mn_2(CO)_{10}]$. This was due to the differences in interactions between the vibrational modes of $[Mn_2(CO)_{10}]$ and solvent, which impact the rate of vibrational relaxation. Determination of the lifetime, τ, for vibrational relaxation undergoing the transition v=1 to v=0, returning to ground state $[Mn_2(CO)_{10}]$ was not as simple. Both relaxation from v=2 to v=1 and v=1 to v=0 proceed on the same timescale. Thus, the application of a mono exponential to the bands at 1971, 2008, and 2040 cm^{-1} is inappropriate and a kinetic model was required. The lifetime, τ, was approximated using a simple kinetic model In COPASI ($v = 2 \xrightarrow{k_1} v = 1 \xrightarrow{k_2} v = 0$) (Figure 137). This used the experimentally determined rate constants for $v = 2$ to $v = 1$ and the experimental data for the vibrational relaxation from v=2 to v=1 and v=1 to v=0. The modelled lifetimes, τ,

for v=1 to v=0 are reported in Table 18, along with the experimental values determined for v=2 to v=1.

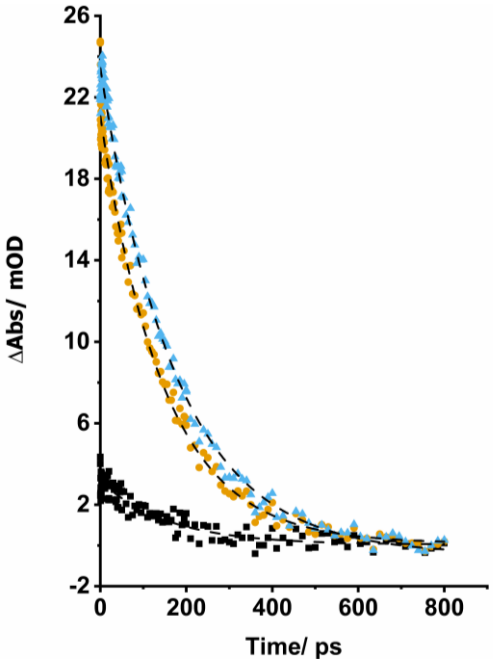

Figure 136. Experimentally observed vibrational relaxation from v=2 to v=1 for the bands positioned at 1938, 1990, and 2024 cm^{-1} in Figure 135 with mono exponential fits applied to determine the lifetime, τ, for each of the vibrational modes of $[Mn_2(CO)_{10}]$. B_2 band at 1938 cm^{-1} denoted by black squares, E band at 1990 cm^{-1} denoted by orange circles, and B_2 band at 2024 cm^{-1} denoted by blue triangles. Lifetimes in Table 18.

Table 18. Lifetime, τ, for relaxation of vibrationally excited $[Mn_2(CO)_{10}]$.

Transition	v=2 to v=1			v=1 to v=0		
Band/ cm^{-1}	1938	1990	2025	1971	2008	2040
τ/ ps	109 ± 20	102 ± 5	122 ± 4	152 ± 10	176 ± 34	122 ± 18

The bands belonging to ground state $[Mn_2(CO)_{10}]$ were not included in the COPASI model, and were not used to determine the lifetime, τ, for the relaxation of v=1 to v=0. This was due to the overlap of excited states with the ground state bleach bands, which meant that the intensity of the bands changed with both the decrease in intensity of overlapping excited states and recovery of the ground state $[Mn_2(CO)_{10}]$, complicating any kinetic modelling.

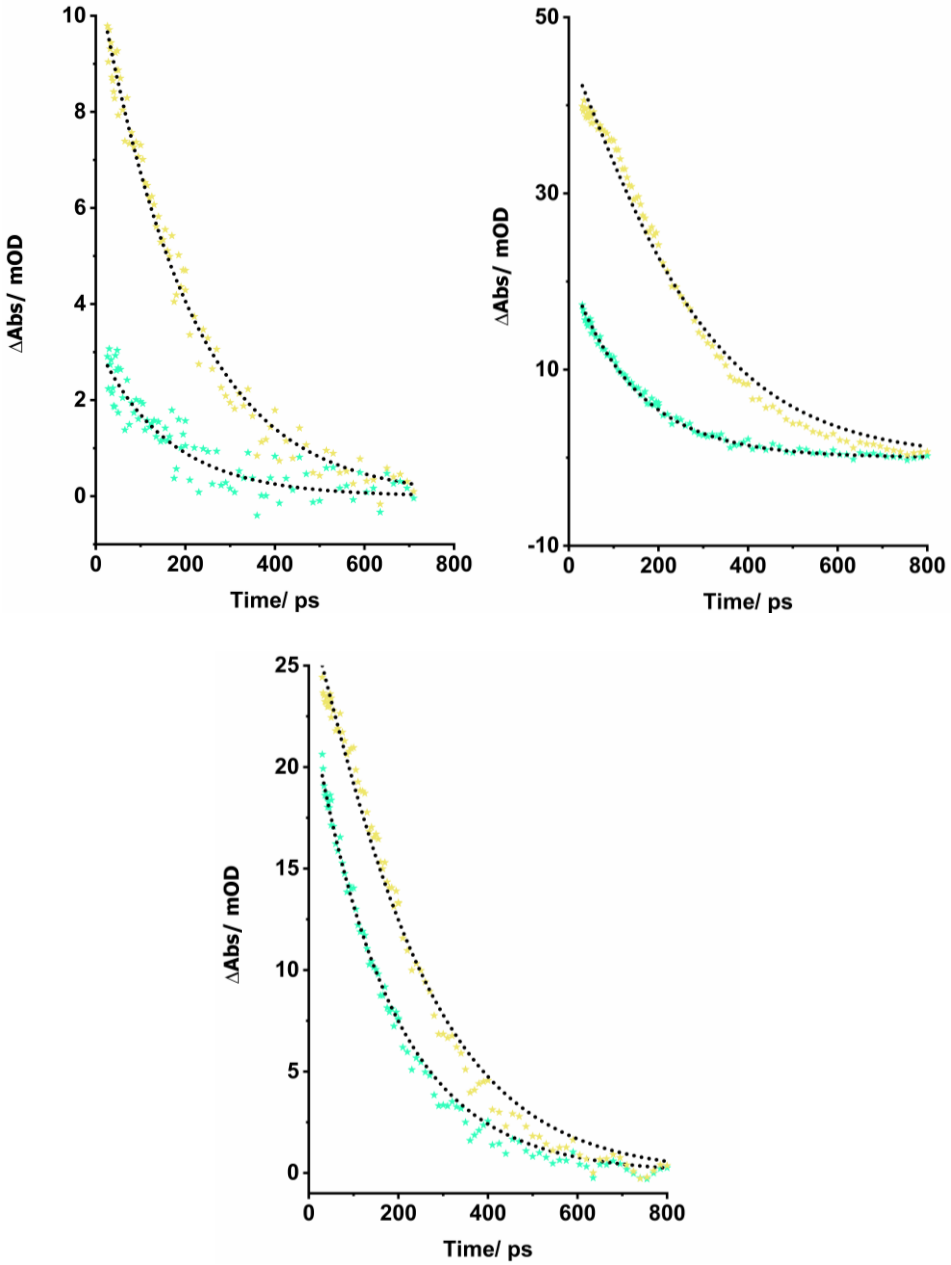

Figure 137. Top left: Experimental and modelled kinetics for the $B_{2_2}^{1}$ band at 1938 cm^{-1} and $B_{2_1}^{0}$ band at 1971 cm^{-1}. Top right: Experimental and modelled kinetics for the E_2^1 band at 1990 cm^{-1} and E_1^0 band at 2008 cm^{-1}. Bottom: Experimental and modelled kinetics for the $B_{2_2}^{1}$ band at 2025 cm^{-1} and $B_{2_1}^{0}$ band at 2040 cm^{-1}. Experimental *v*=2 to *v*=1 kinetic data denoted by turquoise stars, experimental *v*=1 to *v*=0 kinetic data denoted by yellow star, and modelled kinetics denoted by black dotted line.

Following this IR pump-probe experiment, a 1.5 mmol dm^{-3} anhydrous *n*-heptane solution of [$Mn_2(CO)_{10}$] was excited with varying pump wavelengths of 310, 355, and 400 nm, to observed ultrafast photochemical events. Initially, [$Mn_2(CO)_{10}$] was excited

at 310 nm, where CO dissociation was expected to result in the major photoproduct (Figure138).[137] Bleach bands were observed at 1984, 2014, and 2046 cm^{-1}, which indicate the loss of ground state [$Mn_2(CO)_{10}$]. Multiple photoproducts were also detected, as depicted in Figure 138. Three transient bands at 1970, 2008, and 2040 cm^{-1} decayed with lifetimes, τ, of 130 ± 55, 90 ± 45, and 110 ± 60 ps. The band position for each of these corresponded with vibrationally excited [$Mn_2(CO)_{10}$] undergoing the transition $B_{2_1}^2$, E_1^2, and $B_{2_1}^2$ respectively. The lifetime, τ, for each of these bands are in accordance with modelled lifetimes from the IR pump-probe experiment in Table 18. This assignment to vibrational relaxation was further supported by kinetic analysis of the ground state bleach band for [$Mn_2(CO)_{10}$], which underwent recovery with a lifetime, τ, of 132 ± 75 (Figure 139). Further transient bands at 1975, 1997, 2016, 2039, and 2054 cm^{-1} were assigned to [$Mn_2(CO)_9$], which is discussed later in this Chapter (4.4.4). While a final bands at 1980 and 1987 cm^{-1} overlapping with the bleach band (Figure 139), was assigned as the minor photoproduct, [$Mn(CO)_5$]$^{\cdot}$, also discussed in detail later in this Chapter (4.4.2).

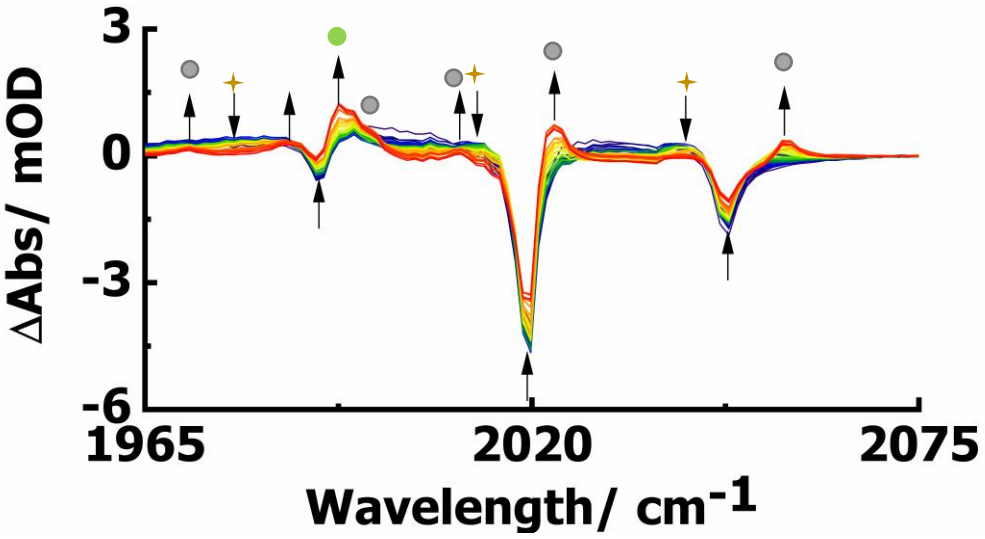

Figure 138. TRIR spectra of [$Mn_2(CO)_{10}$] in anhydrous *n*-heptane solution exciting with a 310 nm pump wavelength under an atmosphere of N_2 at selected pump-probe delays between 1 ps and 500 ps. Arrows denote the respective increases and decreases in intensity of bands. Colour change from purple to blue green to yellow to orange and finally to red denotes the procession from fast to longer pump-probe delays. Yellow star denotes [$Mn_2(CO)_{10}$] in the v = 1 vibrationally excited state, grey circle [$Mn_2(CO)_9$], and green circle [$^{\cdot}Mn(CO)_5$].

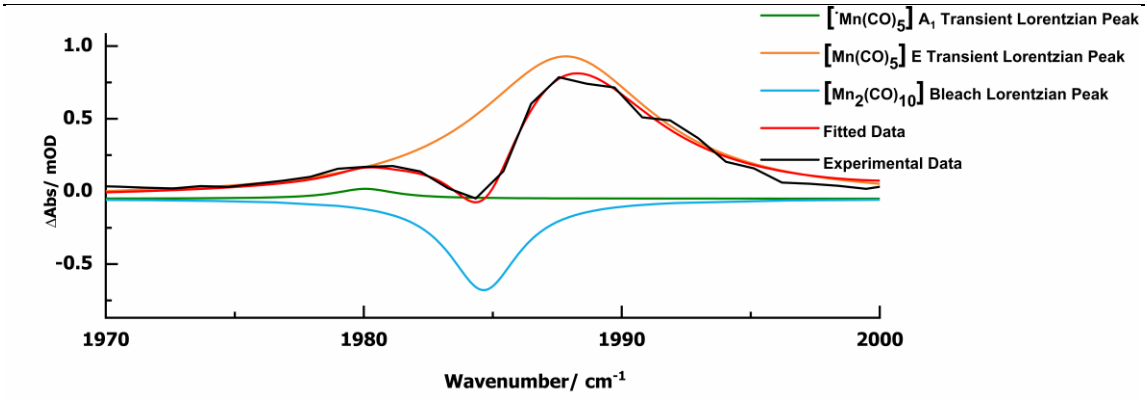

Figure 139. Experimental TRIR spectrum at 500 ps from Figure 138 fitted with Lorentzian peaks to deconvolute peak positions. Black line denotes experimental data, red line denotes fitted data, blue line denotes $[Mn_2(CO)_{10}]$ Lorentzian peak, green line denotes A_1 band of $[\cdot Mn(CO)_5]$ Lorentian peak, and orange line denotes E band of $[\cdot Mn(CO)_5]$ Lorentian peak.

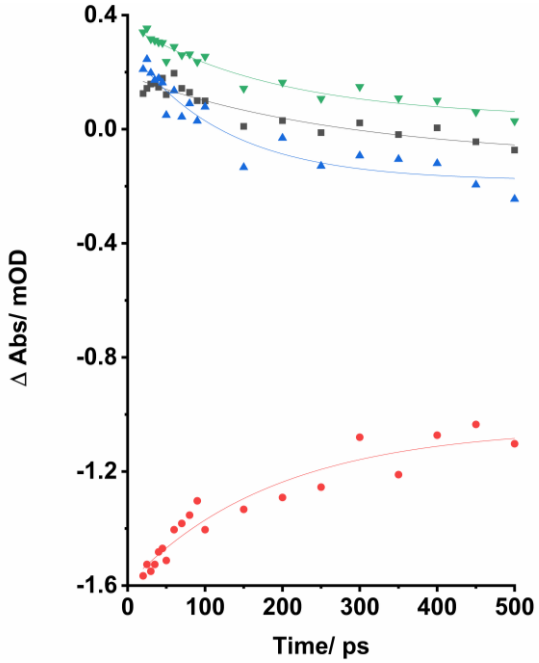

Figure 140. Kinetics obtained for the vibrational relaxation $v = 1$ to $v = 0$ for $[Mn_2(CO)_{10}]$ in anhydrous *n*-heptane solution, when excited with a 310 nm pump wavelength. Red denotes ground state $[Mn_2(CO)_{10}]$ recovery, green denotes vibrational relaxation of the B_2 band at 1970 cm^{-1}, blue denotes vibrational relaxation of the E band at 2008 cm^{-1}, and black denotes vibrational relaxation of the B_2 band at 2040 cm^{-1}.

The experiment was then repeated using an excitation wavelength of 355 nm (Figure 141). Again, bleach bands were observed at 1984, 2014, and 2046 cm^{-1}, which indicate the loss of ground state $[Mn_2(CO)_{10}]$. The three transient bands at 1970, 2008, and 2040

cm^{-1} corresponding to vibrationally excited $[Mn_2(CO)_{10}]$, $B_{2_1}^2$, E_1^2, and $B_{2_1}^2$ respectively. These decayed with lifetimes, τ, of 105 ± 10, 104 ± 14, and 104 ± 9 ps. While a lifetime, τ, of 91 ± 26 ps was observed for the recovery of ground state $[Mn_2(CO)_{10}]$ using the change in intensity of the bleach band at 2046 cm^{-1} (Figure 142). Finally, the bands at 1975, 1984, 1997, 2016, 2039, and 2054 cm^{-1} belonging to $[Mn_2(CO)_9]$ and $[Mn(CO)_5]^{\cdot}$ were detected, however the proportion of each species differed from excitation at 310 nm, reflecting the change in proportion reported in literature. [137]

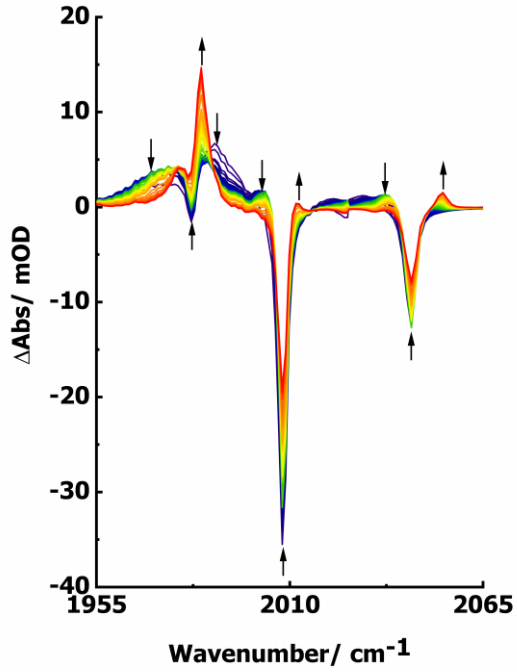

Figure 141. TRIR spectra of $[Mn_2(CO)_{10}]$ in anhydrous heptane solution exciting with a 355 nm pump wavelength under an atmosphere of N_2 at selected pump-probe delays between 5 ps and 150 ps. Arrows denote the respective increases and decreases in intensity of bands. Colour change from purple to blue to green to yellow to orange and finally to red denotes the procession from fast to longer pump-probe delays.

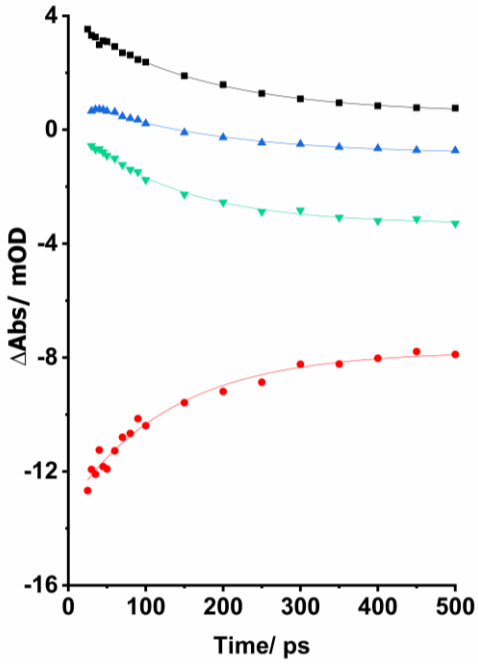

Figure 142. Kinetics obtained for the vibrational relaxation v = 1 to v = 0 for $[Mn_2(CO)_{10}]$ in anhydrous *n*-heptane solution, when excited with a 355 nm pump wavelength. Red denotes ground state $[Mn_2(CO)_{10}]$ recovery, green denotes vibrational relaxation of the B_2 band at 1970 cm^{-1}, blue denotes vibrational relaxation of the E band at 2008 cm^{-1}, and black denotes vibrational relaxation of the B_2 band at 2040 cm^{-1}.

Finally, the experiment was conducted using a pump wavelength of 400 nm, which predominantly favours Mn−Mn bond cleavage, to form $[Mn(CO)_5]^{\cdot}$ (Figure 143). As with prior wavelengths, both the ground state bleach bands at 1984, 2014, and 2046 cm^{-1}, and vibrationally excited $[Mn_2(CO)_{10}]$ with bands at 1970, 2008, and 2040 cm^{-1} were observed. The lifetime, τ, for the loss of $[Mn_2(CO)_{10}]$ in the v = 1 vibrationally excited state was measured to be 70 ± 7, 60 ± 5, and 67 ± 16 ps, while the lifetime, τ, for the recovery of ground state $[Mn_2(CO)_{10}]$ was found to be 68 ± 14 ps (Figure 144). These values are statistically different from those recorded at 310, 355 nm, and the IR pump-probe experiment, lying just outside the 95% confidence limits, but are roughly concordant. This difference in values indicates that vibrationally excited $[Mn_2(CO)_{10}]$ could be formed through a different route when excited at 400 nm, which if occurring on a different timescale, is impacting the lifetimes determined for vibrationally excited $[Mn_2(CO)_{10}]$.

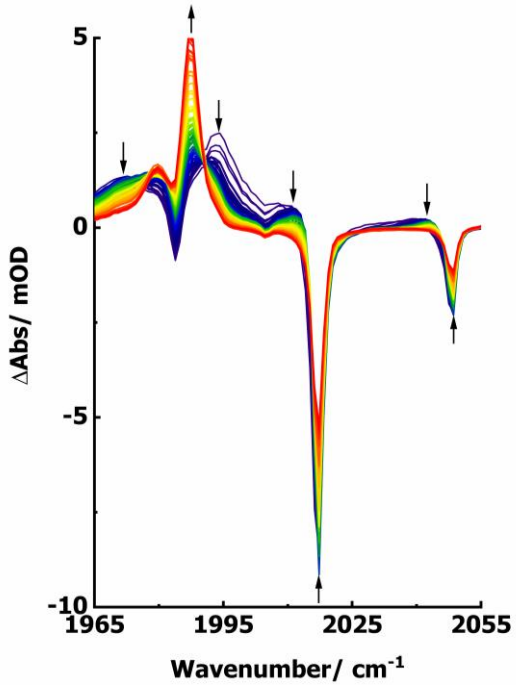

Figure 143. TRIR spectra of $[Mn_2(CO)_{10}]$ in anhydrous heptane solution exciting with a 400 nm pump wavelength under an atmosphere of N_2 at selected pump-probe delays between 1 ps and 500 ps. Arrows denote the respective increases and decreases in intensity of bands. Colour change from purple to blue to green to yellow to orange and finally to red denotes the procession from fast to longer pump-probe delays.

Table 19. Lifetime, τ, for the vibrational relaxation $v = 1$ to $v = 0$ of $[Mn_2(CO)_{10}]$ at various pump wavelengths.

	Lifetime, τ/ ps			
Pump wavelength	B_2 1970 cm^{-1}	E 2008 cm^{-1}	B_2 2040 cm^{-1}	B_2 ground state 2046 cm^{-1}
310	130 ± 55	90 ± 45	110 ± 60	132 ± 75
355	105 ± 10	104 ± 14	104 ± 9	91 ± 26
400	70 ± 7	60 ± 5	67 ± 16	68 ± 14
Broad IR	152 ± 10	176 ± 34	122 ± 18	-

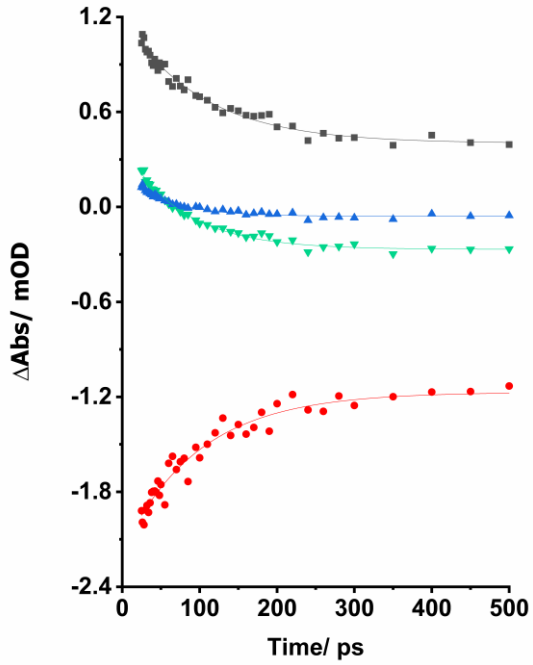

Figure 144. Kinetics obtained for the vibrational relaxation v = 1 to v = 0 for $[Mn_2(CO)_{10}]$ in anhydrous *n*-heptane solution, when excited with a 400 nm pump wavelength. Red denotes ground state $[Mn_2(CO)_{10}]$ recovery, green denotes vibrational relaxation of the B_2 band at 1970 cm^{-1}, blue denotes vibrational relaxation of the E band at 2008 cm^{-1}, and black denotes vibrational relaxation of the B_2 band at 2040 cm^{-1}.

An additional feature was observed in both the spectra at 355 nm, and 400 nm, positioned at 1993 cm^{-1}. This band was observed to decay with a lifetime, τ, 3.8 ± 0.6 ps (Figure 145). This band was hypothesised to be $[Mn(CO)_5]\cdot$ formed from cleavage of the Mn−Mn bond belonging to $[Mn_2(CO)_{10}]$, which was still in the ground state solvent cage of $[Mn_2(CO)_{10}]$. The depletion of this band thus correlates with the rearrangement of the solvent cage, and separation of the $[Mn(CO)_5]\cdot$ fragments. The hypothesis was based on the observation that the band lies close in wavenumber to $[Mn(CO)_5]\cdot$ (1983 cm^{-1}). Furthermore, the band at 1993 cm^{-1} depleted by *ca*. 20 ps in *n*-heptane, which correspond with the increase in intensity of the band at 1983 cm^{-1} belonging to $[Mn(CO)_5]\cdot$. Kinetic analysis of the band at 1983 cm^{-1} belonging to $[Mn(CO)_5]\cdot$ revealed a lifetime, τ, of 52 ± 4 ps, an order of magnitude longer than the lifetime for the band at

1993 cm^{-1}, ruling out vibrational cooling of $[Mn(CO)_5]^{\cdot}$. This lifetime closely reflected the value reported by Steinhurst and co-workers, who reported a lifetime, τ, of 58 ps.[149]

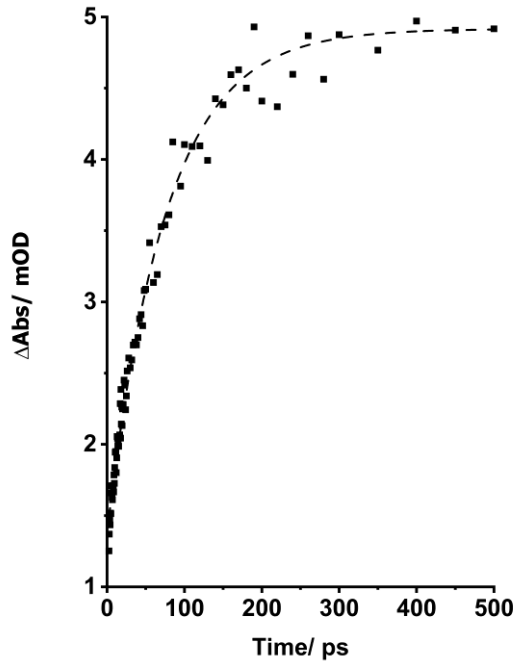

Figure 145. Kinetics for the vibrational relaxation of the band at 1983 cm^{-1} belonging to $[Mn(CO)_5]^{\cdot}$ in *n*-heptane solution.

To further support the hypothesis, the experiment was repeated in a highly interacting solvent, acetonitrile, alongside perfluoro(methylcyclohexane), which possesses very little metal-solvent interactions (Figure 147 an Figure 148). The lifetime, τ, was found to be solvent dependant, with a shorter lifetime observed in the more highly interacting solvent (see Table 20). Whereas, in perfluoro(methylcyclohexane), a lifetime similar to that in *n*-heptane, another weakly interacting solvent, was observed. Two further experiments in anhydrous THF and methylene chloride gave lifetimes in-between those of acetonitrile and cyclohexane, reflecting the change in solvent polarity. This supported the hypothesis that the solvent cage was rearranging at short pump-probe delays, and the $[Mn(CO)_5]^{\cdot}$ fragments were drifting apart.

Table 20. Solvent dependency for the lifetime, τ, of the band at 1993 cm^{-1}.

Solvent	lifetime, τ/ ps	Relative solvent polarity/ a.u.[154]
Perfluoro(methylcyclohexane)	3.4 ± 0.6	-
Cyclohexane	4.3 ± 0.6	0.006
n-heptane	3.8 ± 0.6	0.009
THF	3.3 ± 0.5*	0.207
Methylene chloride	2.2 ± 0.5*	0.309
Acetonitrile	1.1 ± 0.5*	0.46

* Error from mono exponential fits were smaller than the smallest instrumental measurement of 0.5 ps.

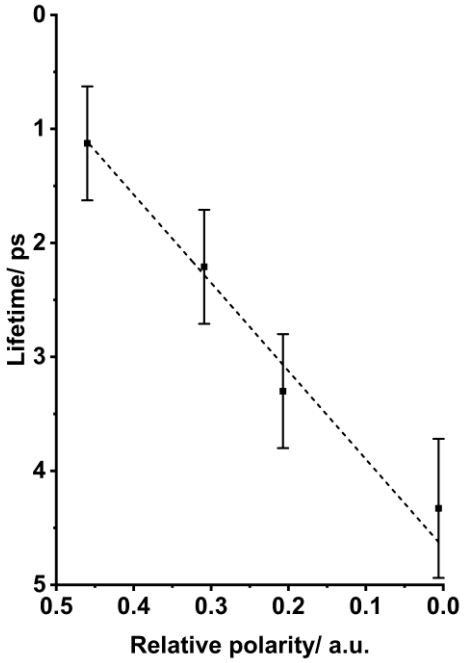

Figure 146. Relationship between relative solvent polarity and the lifetime, τ, of the band at 1993 cm^{-1}. A linear fit was plotted with the equation $y = (-4.7 \pm 0.3)x + (7.7 \pm 0.8)$.

The inverse relationship between solvent polarity and the lifetime of the band at 1993 cm^{-1} indicates that the solvent interactions with $[Mn(CO)_5]^{\cdot}$ are dictating the lifetime (Figure 146). A more polar solvent, which possesses greater solvent−complex interactions, stabilises the $[Mn(CO)_5]^{\cdot}$ radical, favouring its formation.

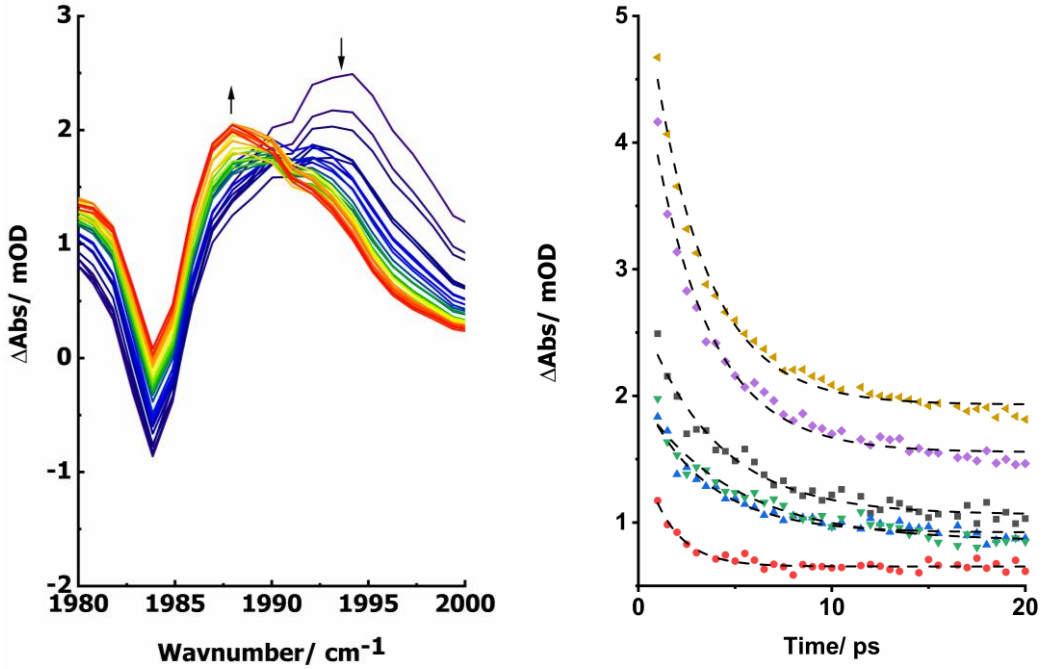

Figure 147. Left: TRIR spectra of $[Mn_2(CO)_{10}]$ in anhydrous *n*-heptane solution exciting with a 400 nm pump wavelength under an atmosphere of N_2 at selected pump-probe delays between 0.5 ps and 25 ps. Arrows denote the respective increases and decreases in intensity of bands. Colour change from purple to blue to green to yellow to orange and finally to red denotes the procession from fast to longer pump-probe delays. Right: Kinetics for the loss of the band at 1993 cm^{-1}. Black denotes *n*-heptane, blue denotes perfluoro(methylcyclohexane), red denotes acetonitrile, purple denotes THF, and yellow denotes methyl chloride.

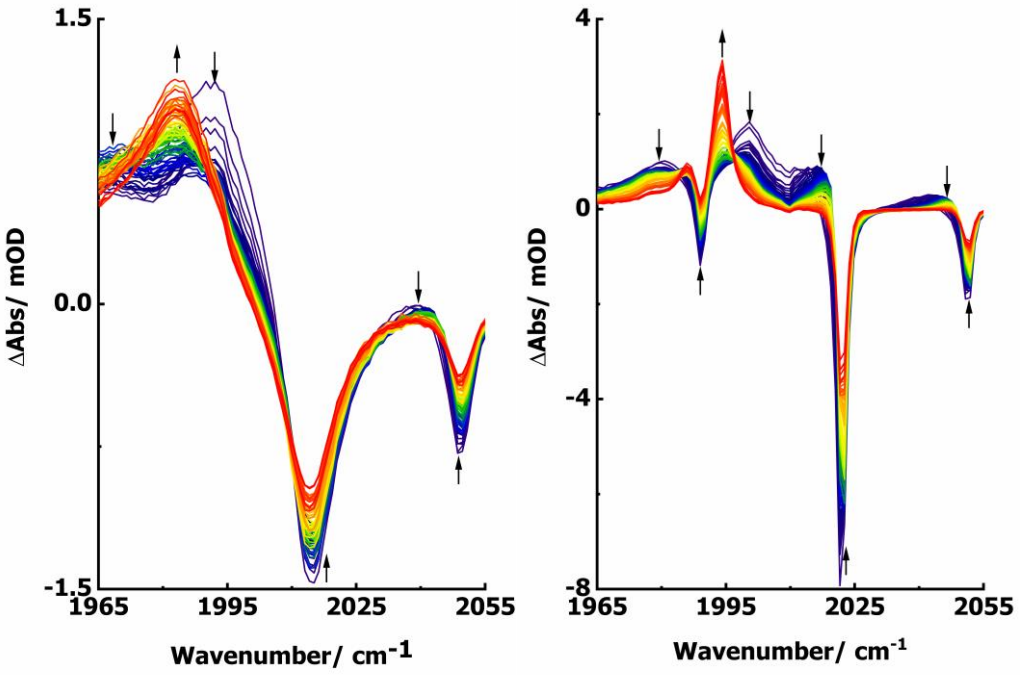

Figure 148. Left: TRIR spectra of $[Mn_2(CO)_{10}]$ in anhydrous acetonitrile solution exciting with a 400 nm pump wavelength under an atmosphere of N_2 at selected pump-probe delays between 1 ps and 500 ps. Right: TRIR spectra of $[Mn_2(CO)_{10}]$ in anhydrous perfluoro(methylcyclohexane) solution exciting with a 400 nm pump wavelength under an atmosphere of N_2 at selected pump-probe delays between 0.5 ps and 500 ps. Arrows denote the respective increases and decreases in intensity of bands. Colour change from purple to blue to green to yellow to orange and finally to red denotes the procession from fast to longer pump-probe delays.

Finally, a control experiment was conducted in anhydrous *n*-heptane, varying the temperature (Figure 149). This was to assess whether there was a temperature dependence on the FTIR spectrum of $[Mn_2(CO)_{10}]$. If no temperature dependence was observed, then the possibility that the band at 1993 cm^{-1} is due to localised heating from the pump laser pulse can be excluded. Thus, the temperature dependant changes in the solvent interactions with non-photochemically activated $[Mn_2(CO)_{10}]$ are not inducing a shift in band position. $[Mn_2(CO)_{10}]$ was heated in anhydrous *n*-heptane solution between 25 °C and 80 °C, spectra were recorded *via in situ* infrared spectroscopy on a Mettler Toledo ReactIR ic10, while the temperature was monitored *in situ* with a temperature probe. The resultant spectra are depicted in Figure 149. Between 25 °C and 80 °C there

was no shift in band position for the B_2 stretching mode of $[Mn_2(CO)_{10}]$, indicating that the band at 1993 cm^{-1} is not due to a shift in band position involving non-photochemically activated $[Mn_2(CO)_{10}]$ interacting with hot solvent molecules.

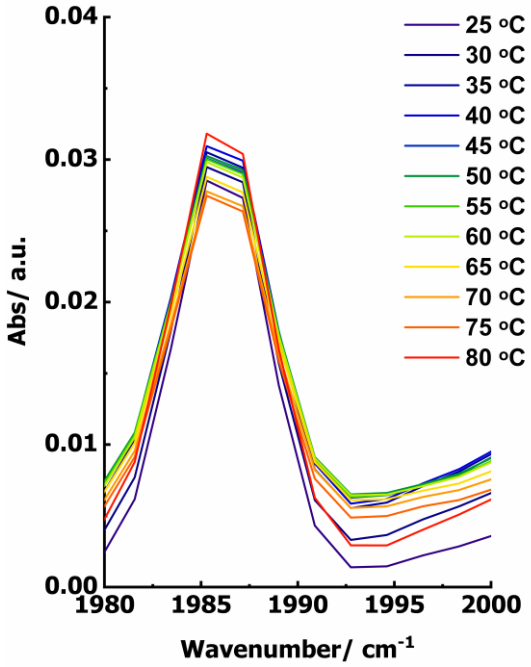

Figure 149. Low energy B_2 stretching mode of $[Mn_2(CO)_{10}]$ at 1985 cm^{-1} in anhydrous *n*-heptane solution, with varied temperatures between 25 °C and 80 °C.

4.4.2 Reactivity of Photochemically Formed $[Mn(CO)_5]\cdot$

The first UV pump wavelength used was at 400 nm. Predominantly, a 400 nm pump wavelength promotes a ($\sigma \rightarrow \sigma^*$) transition, which should result in Mn−Mn bond cleavage, according to literature studies.[137] This enables the determination of photoproducts formed from Mn−Mn bond cleavage, and to establish their subsequent chemical behaviour.

Photolysis of $[Mn_2(CO)_{10}]$ in anhydrous *n*-heptane solution resulted in a broad transient band at 1983 cm^{-1} following relaxation of excited states (Figure 150). This species corresponded to the $[Mn(CO)_5]\cdot$ Radical **241**, which possessed a literature position of 1988 cm^{-1} in heptane for a strong E band and weak A_1 stretching mode.[139] No further bands were observed for the CO dissociative product $[Mn_2(CO)_9]$ **242** at early pump-probe delays. Over the course of *ca*. 200 µs, the broad band at 1983 cm^{-1} depleted and

the bleach bands for ground state $[Mn_2(CO)_{10}]$ recovered. In *n*-heptane, 76% of the bleach band recovered. This indicated that CO dissociation is the minor photochemically induced pathway when a pump wavelength of 400 nm is used. This is in line with the literature values of >72% $[Mn(CO)_5]^{\cdot}$ Radical formation and <28% CO dissociation to form $[Mn_2(CO)_9]$ when $[Mn_2(CO)_{10}]$ is photochemically excited at 400 nm .[149] The remaining bleach bands are likely due to the formation of $[Mn_2(CO)_9]$, through the dissociation of a CO ligand, which is unable to undergo recombination with a free CO ligand on this timescale. The weak band positioned at 2032 cm^{-1} on the spectrum at 200 µs in Figure 150 is potentially one of the stretching modes belonging to $[Mn_2(CO)_9]$. $[Mn(CO)_5]^+$ and $[Mn(CO)_5]^-$ can be ruled out as long lived photoproducts, with highly solvent dependant stretching frequencies reported at 2065 and 1830 cm^{-1} respectively. [140,155]

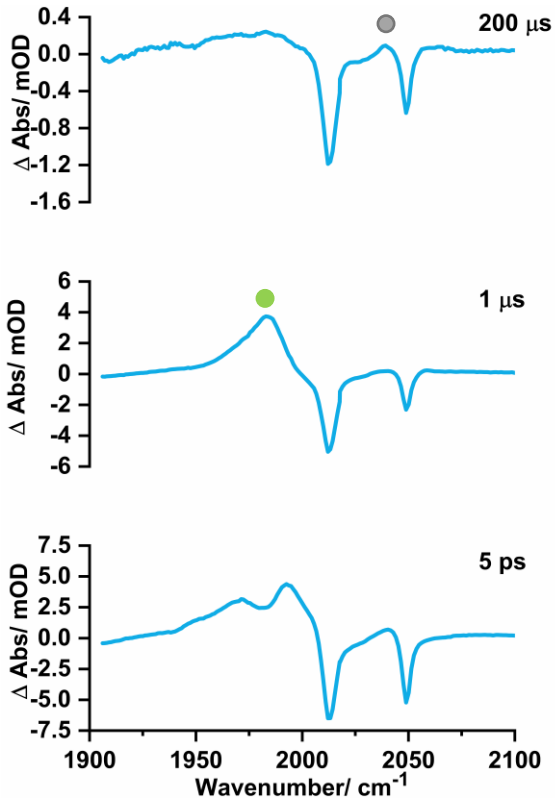

Figure 150. TRIR spectra of $[Mn_2(CO)_{10}]$ in anhydrous heptane solution exciting with a 400 nm pump wavelength under an atmosphere of N_2 at selected pump-probe delays. **242** denoted by grey circles and **241** denoted by denoted by green circles.

The recombination of $[Mn(CO)_5]^{\cdot}$ To form $[Mn_2(CO)_{10}]$ must be a bimolecular process. Consequently, a simple mono exponential model is inadequate. Instead, the kinetic data were treated as second order. Using the gradient from a plot of time (x axis) versus 1/ concentration (y axis), a second order rate constant can be determined. The concentration of $[Mn(CO)_5]^{\cdot}$ Is unknown, and the species is short-lived. Consequently, an extinction coefficient could not be measured. Instead, the concentration of $[Mn(CO)_5]^{\cdot}$ Can be approximated from the bleach bands of $[Mn_2(CO)_{10}]$. The assumption was made that all recovery of ground state $[Mn_2(CO)_{10}]$ bleach bands was due to radical recombination. Thus, the change in $[Mn_2(CO)_{10}]$ concentration is proportional to the concentration change of $[Mn(CO)_5]^{\cdot}$. To determine the concentration of $[Mn_2(CO)_{10}]$, Beer-Lambert plots were produced at relevant concentrations (see Chapter 6.4), and the extinction coefficients established for each of the three infrared active modes of $[Mn_2(CO)_{10}]$.

Table 21. Extinction coefficients established for $[Mn_2(CO)_{10}]$ infrared active modes in *n*-heptane.

Band Position	ε/ mol^{-1} dm^3 μm^{-1}
1984	1.1 ± 0.1
2014	5.7 ± 0.8
2046	1.6 ± 0.2

A modified plot of time (x axis) versus 1/ (Δ absorption- Δ $absorption_{inf}$) (y axis), with a gradient equal to the second order rate constant × pathlength × molar absorption coefficient was produced. Δ $absorption_{inf}$ is the value for Δ absorption that the ground state bleach band recovered to. From this, the gradient was determined to be $9.1 \pm 1.1 \times 10^{10}$ s^{-1} (Figure 151). Using the value of ε in Table 21 for the band at 2046 cm^{-1}, and pathlength of 100 µm, a second order rate constant, *k*, was calculated to be $5.7 \pm 0.7 \times 10^{8}$ mol^{-1} dm^3 s^{-1} for the recovery of the ground state bleach of $[Mn_2(CO)_{10}]$ at 2046 cm^{-1}.

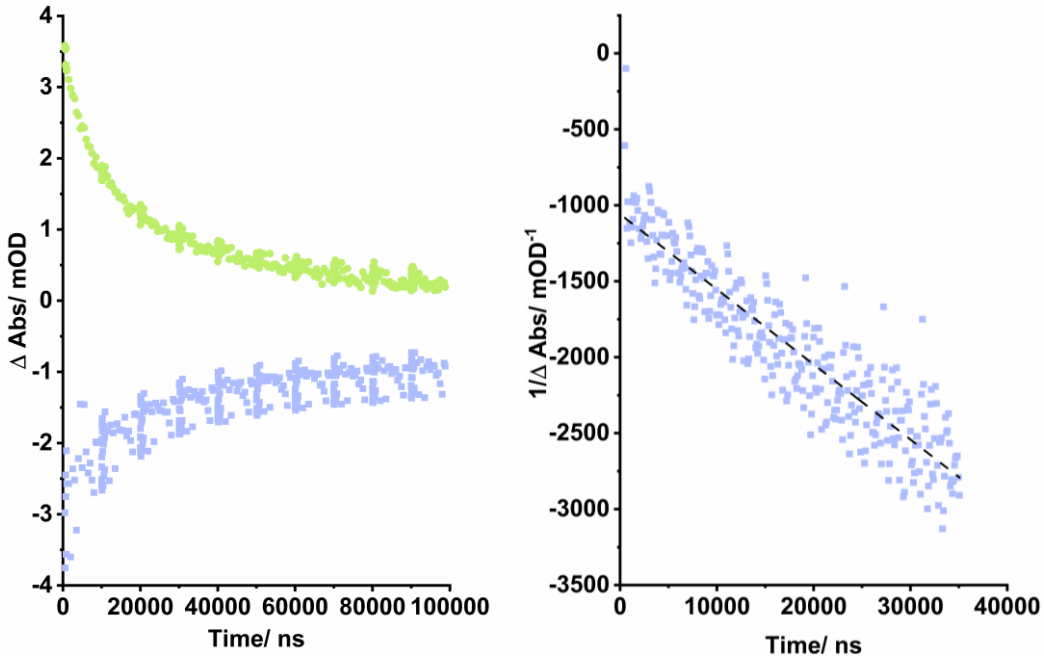

Figure 151. Left: First order kinetic plot to show the loss of $[Mn(CO)_5]^{\cdot}$ **241** and recombination of $[Mn_2(CO)_{10}]$. Right: Plot of time (x axis) versus 1/ Δ absorption (y axis) to determine the second order rate constant for the recovery of the ground state bleach of $[Mn_2(CO)_{10}]$ at 2046 cm^{-1}.

A similar experiment was then conducted in both anhydrous toluene and acetonitrile (Figure 152). Following relaxation of vibrationally excited states, the broad band for $[Mn(CO)_5]^{\cdot}$ **241** was observed at 1985 and 1987 cm^{-1} in toluene and acetonitrile respectively. Over *ca*. 200 µs, **241** depleted, and the ground state bleach bands of $[Mn_2(CO)_{10}]$ recovered. Recovery of 72% and 66% were observed in toluene and acetonitrile respectively. From the recovery of ground state $[Mn_2(CO)_{10}]$, the second order rate constant, *k*, of $5.2 \pm 0.8 \times 10^8$ and $3.0 \pm 0.5 \times 10^9$ mol^{-1} dm^3 s^{-1} was determined in toluene and acetonitrile respectively. [133][134] Other than changes in line broadening due to changes in solvent-complex interaction, no difference in speciation was detected between experiments conducted in anhydrous *n*-heptane, toluene, and acetonitrile.

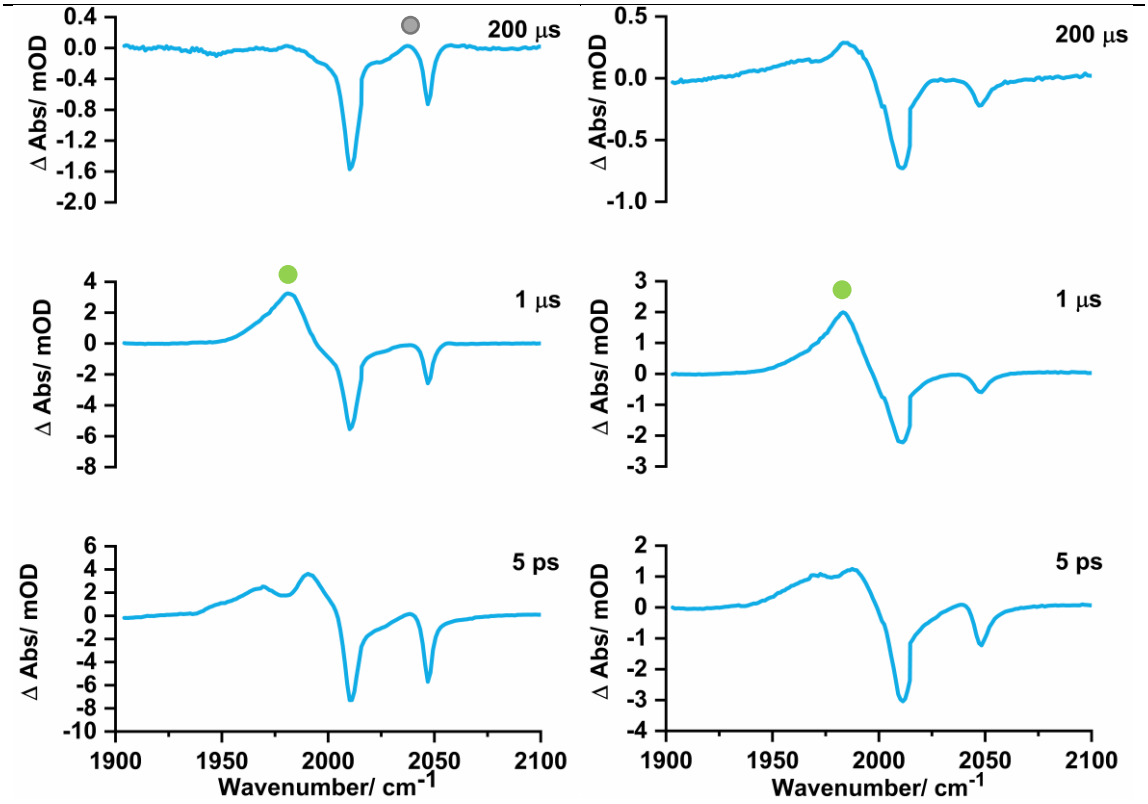

Figure 152. Left: TRIR spectra of $[Mn_2(CO)_{10}]$ in anhydrous toluene solution exciting with a 400 nm pump wavelength under an atmosphere of N_2 at selected pump-probe delays. Right: TRIR spectra of $[Mn_2(CO)_{10}]$ in anhydrous acetonitrile solution exciting with a 400 nm pump wavelength under an atmosphere of N_2 at selected pump-probe delays. **242** denoted by grey circles and **241** denoted by denoted by green circles.

Table 22. Extinction coefficients for the infrared active modes of $[Mn_2(CO)_{10}]$ in various solvents.

Solvent	Band Position	ε/ mol^{-1} dm^3 μm^{-1}	Solvent	Band Position	ε/ mol^{-1} dm^3 μm^{-1}
	1984	1.1 ± 0.1		1975	0.2 ± 0.04
Heptane	2014	5.7 ± 0.8	Dioxane	2009	1.4 ± 0.02
	2046	1.6 ± 0.2		2045	0.7 ± 0.09
	1980	0.2 ± 0.04		1979	0.2 ± 0.03
Toluene	2010	1.7 ± 0.1	THF	2008	1.4 ± 0.08
	2045	1.0 ± 0.7		2044	0.8 ± 0.04
	1979	0.2 ± 0.02		1979	0.07 ± 0.01
Acetonitrile	2011	1.2 ± 0.06	DMSO	2006	0.6 ± 0.3
	2046	0.6 ± 0.04		2044	0.3 ± 0.03
	1982	0.2 ± 0.01		1981	0.2 ± 0.02
Acetone	2010	1.2 ± 0.04	*n*-butyl acrylate	2010	1.3 ± 0.07
	2046	0.6 ± 0.04		2046	0.7 ± 0.05
	1978	0.2 ± 0.01		1981	0.18^*
Methylene chloride	2011	1.2 ± 0.04	Styrene	2009	1.3^*
	2046	0.7 ± 0.02		2045	0.83^*
	1982	1.3			
Cyclohexane	2013	7.6			
	2045	2.0			

Further experiments were then conducted in anhydrous methylene chloride, acetone, THF, 1,4-dioxane, dimethyl sulfoxide, styrene, butyl acrylate, and cyclohexane to assess the reactivity of the $[Mn(CO)_5]\cdot$ radical. The extinction coefficient, ε, was determined for each of the metal carbonyl stretching modes of $[Mn_2(CO)_{10}]$ in each of the aforementioned solvents, and are displayed in Table 22. In THF, 1,4-dioxane, DMSO, styrene, and cyclohexane $[Mn(CO)_5]\cdot$ recombined to reform $[Mn_2(CO)_{10}]$, as was observed in *n*-heptane, toluene and acetonitrile. The second order rate constants for radical recombination in each of these solvents are reported in Table 23. In THF, literature values of 1.9×10^9 and 9.5×10^8 s^{-1} mol^{-1} dm^3 were reported for the second order rate constant for the recombination of $[Mn(CO)_5]\cdot$, in good agreement with the experimental value of 1.1×10^9 s^{-1} mol^{-1} dm^3 measured here. [133] [134]

Table 23. Second order rate constant for the reformation of $[Mn_2(CO)_{10}]$ in various solvents.

Solvent	Second order rate constant, *k*, for reformation of $[Mn_2(CO)_{10}]$ / mol^{-1} dm^3 s^{-1}	Relative solvent polarity/ a.u.[154]
Heptane	$5.7 \pm 0.7 \times 10^8$	0.009
Toluene	$5.2 \pm 0.9 \times 10^8$	0.099
Acetonitrile	$3.0 \pm 0.5 \times 10^9$	0.46
Methylene chloride	*n/a*	0.309
Acetone	*n/a*	0.355
Tetrahydrofuran	$1.10 \pm 0.03 \times 10^9$	0.207
1,4-dioxane	$1.04 \pm 0.03 \times 10^9$	0.164
Dimethyl sulfoxide	$4.0 \pm 0.3 \times 10^9$	0.444
Styrene	$1.07 \pm 0.02 \times 10^9$	*n/a*
Butyl acrylate	*n/a*	*n/a*
Cyclohexane	$2.8 \pm 0.7 \times 10^8$	0.006

In acetone, methylene chloride and *n*-butyl acrylate, recombination of the $[Mn(CO)_5]\cdot$ radical was not observed. This was reflected by 34, 14, and 8.4% bleach band recovery in each of these solvents respectively. This minor "recovery" of bleach bands was

attributed to partial overlap between new transient bands and the ground state bleach bands of $[Mn_2(CO)_{10}]$.

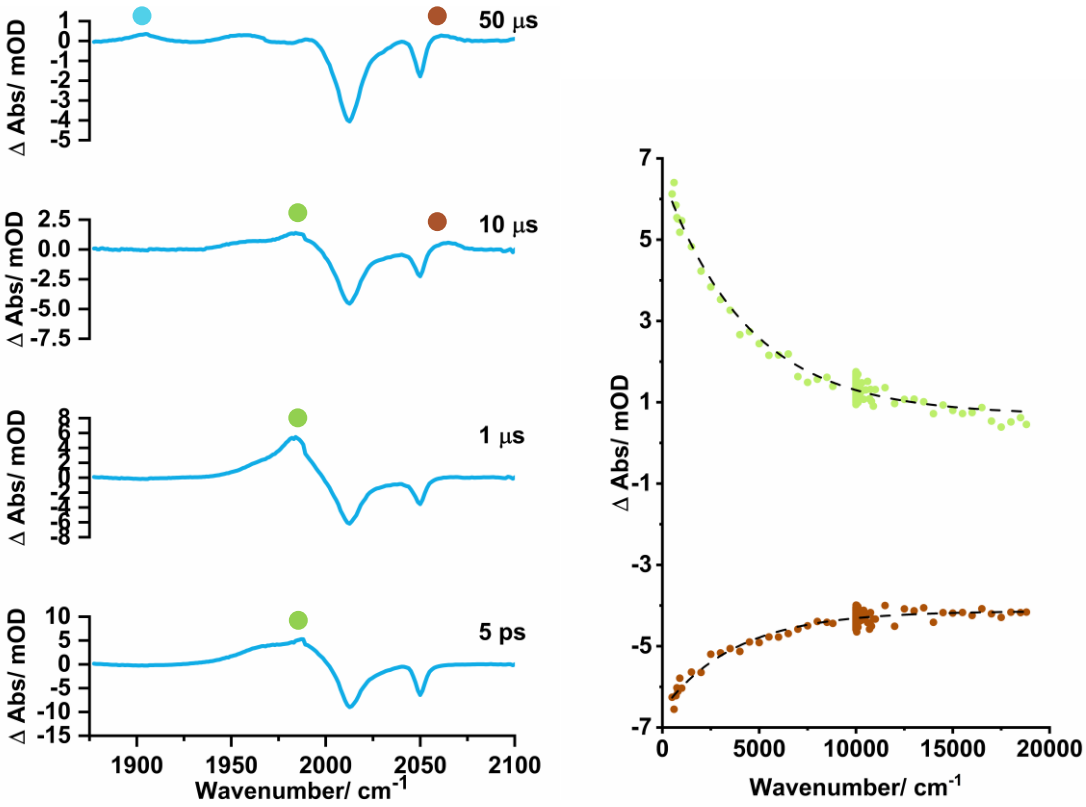

Figure 153. Left: TRIR spectra of $[Mn_2(CO)_{10}]$ in anhydrous acetone solution exciting with a 400 nm pump wavelength under an atmosphere of N_2 at selected pump-probe delays. Right: Kinetics for the loss of **241** and formation of **247**. **241** denoted by denoted by green circles, **247** denoted by brown circles, and **1823** by cyan circles.

Photolysis of $[Mn_2(CO)_{10}]$ in anhydrous acetone solution resulted in a broad band at 1983 cm^{-1}, which belonged to $[Mn(CO)_5]^{\cdot}$ **241** (Figure 153). This band depleted over the course of *ca*. 15 µs. Unlike prior solvents, recovery of the bleach band was minor, and the loss of **241** abided to a mono exponential fit, with a rate constant, k_{obs}, of $2.3 \pm 0.2 \times 10^5$ mol^{-1} dm^3 s^{-1}. A new band positioned at 2064 cm^{-1} grew in with a rate constant, k_{obs}, of $2.6 \pm 0.5 \times 10^5$ mol^{-1} dm^3 s^{-1}, supporting the hypothesis that **241** was reacting before radical recombination could occur. A similar observation was made when anhydrous *n*-butyl acrylate was used as a solvent (Figure 154). The broad band at 1986 cm^{-1} belonging to **241** depleted with a rate constant, k_{obs}, of $3.6 \pm 0.5 \times 10^5$ mol^{-1} dm^3 s^{-1} and a band at 2052 cm^{-1} grew in with a rate constant, k_{obs}, of $4.6 \pm 1.1 \times 10^5$ mol^{-1} dm^3 s^{-1}. In a study by Firth and co-workers, $[Mn_2(CO)_{10}]$ was photolysed in

anhydrous acetonitrile solution.[140] Here they reported the reaction of **241** with B_2pin_2 or PhN_2BF_4 to form *fac*-$[Mn(CO)_3(NCMe)_3]^+$ and $[Mn(CO)_5(NCMe)]^+$ cations which possessed a strong band at 2057 cm^{-1} and 2071 cm^{-1}. These formed over the course of *ca*. 8.8 μs. Based on Firth and co-workers assignment, the band at 2064 and 2052 in acetone and *n*-butyl acrylate respectively were tentatively assigned to the complex, $[Mn(CO)_5(acetone)]^+$ $[Mn(CO)_3(n\text{-butyl acrylate})_3]^+$. Furthermore, literature values for the complexes *fac*-$[Mn(CO)_3(Acetone)_3]^+$ and $[Mn(CO)_5(acetone)]^+$ are 1935, 2023 and 2012, 2049, and 2139 respectively.[156] The band at 2049 cm^{-1} for $[Mn(CO)_5(acetone)]^+$ is in rough concordance with the broad band at 2064 cm^{-1}, which is partially obscured by the bleach band of $[Mn_2(CO)_{10}]$, while the band at 2012 cm^{-1} is covered by a bleach band. The *n*-butyl acrylate bound complex could be either the tri- or pentacarbonyl complex, and tentative assignment was based on the lower energy of the band. However, a large shift in band position would be expected between acetonitrile, acetone, and *n*-butyl acrylate due to differences in the nature of bound solvent electronics donating and accepting electron density, along with solvent- complex interactions.

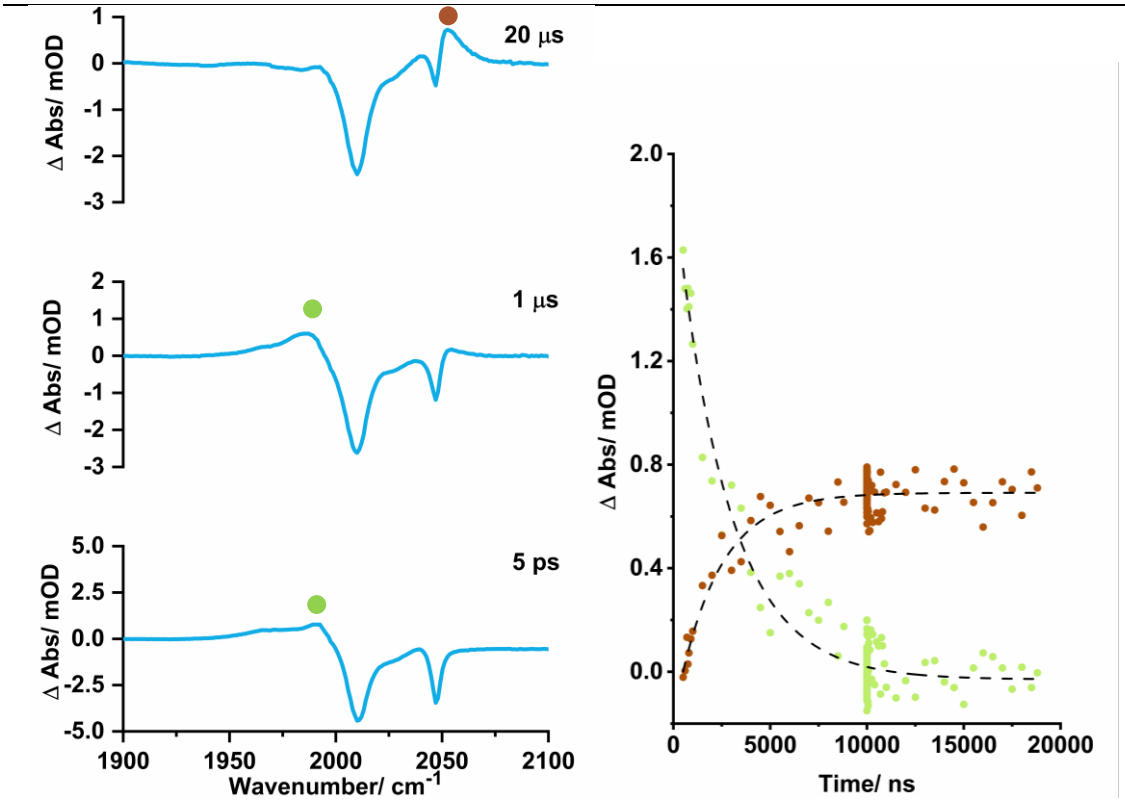

Figure 154. Left: TRIR spectra of $[Mn_2(CO)_{10}]$ in anhydrous *n*-butyl acrylate solution exciting with a 400 nm pump wavelength under an atmosphere of N_2 at selected pump-probe delays. Right: Kinetics for the loss of **241** and formation of **247**. **241** denoted by denoted by green circles and **247** denoted by brown circles.

Finally, photolysis of $[Mn_2(CO)_{10}]$ in methylene chloride solution resulted in formation of the bands for **241** at 1981 cm^{-1}, as in prior experiments (Figure 155). However, **241** decayed with kinetics fitting a mono exponential profile, an order of magnitude faster than in acetone and *n*-butyl acrylate. A rate constant, k_{obs}, of $1.5 \pm 0.1 \times 10^6$ mol^{-1} dm^3 s^{-1} was obtained for the decay of **241**. Within 95% confidence limits, bands at 2144 and 2055 grew in with a rate constant, k_{obs}, of $1.6 \pm 0.1 \times 10^6$ mol^{-1} dm^3 s^{-1}. It was proposed that the $[Mn(CO)_5]^{\cdot}$ radical **241** was abstracting a halogen atom from methylene chloride, to form $[MnCl(CO)_5]$ **249**. To corroborate this hypothesis, a sample of $[MnCl(CO)_5]$ was synthesised. This possessed metal carbonyl stretching modes at 1977, 2011, 2057, and 2142 cm^{-1} in methylene chloride solution. The experimental transient bands at 2055 and 2144 cm^{-1} are within experimental error (± 2 cm^{-1}) of the synthesised sample of $[MnCl(CO)_5]$. The expected bands at 1977 and 2011 cm^{-1} lie directly under $[Mn_2(CO)_{10}]$ ground state bleach bands, and are likely obscured. The observation of the high energy band at 2144 cm^{-1} does provide evidence that halide abstraction occurs in

methylene chloride solution, as opposed to formation of the complex *fac*-$[Mn(CO)_3(\text{methylene chloride})_3]^+$.

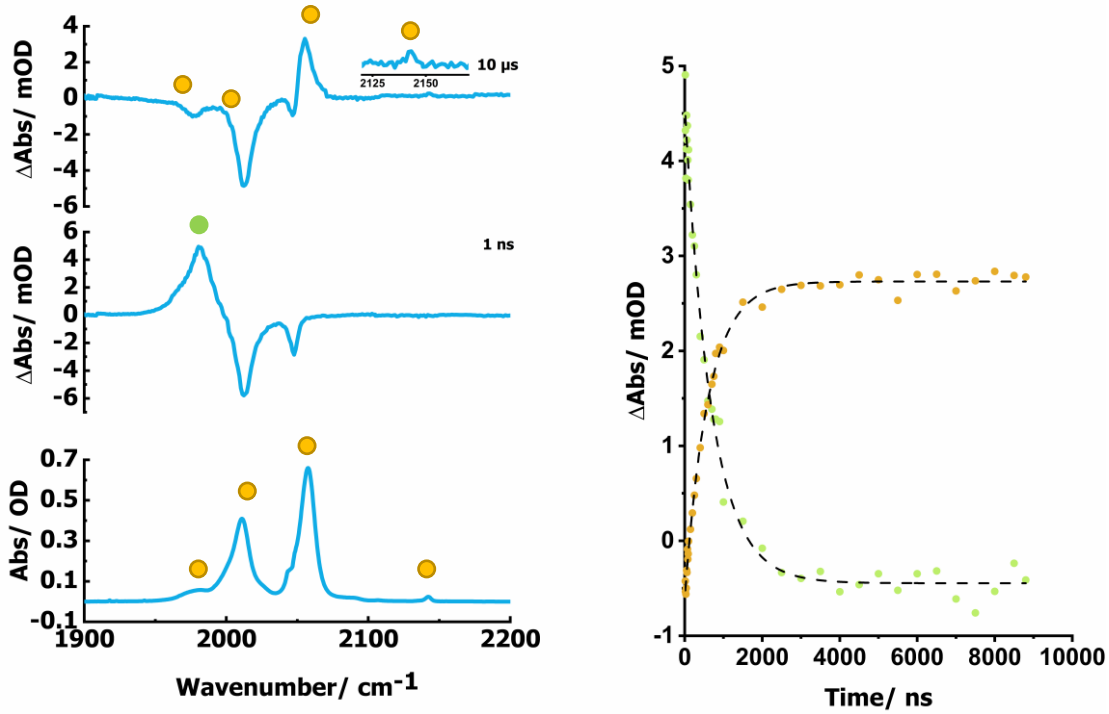

Figure 155. Left: TRIR spectra of $[Mn_2(CO)_{10}]$ in anhydrous methylene chloride solution exciting with a 400 nm pump wavelength under an atmosphere of N_2 at selected pump-probe delays. Right: Kinetics for the loss of **241** and formation of $[MnCl(CO)_5]$ **249**. **241** denoted by denoted by green circles and **249** denoted by yellow circles.

Following the observed chlorine atom abstraction from methylene chloride by **241**, the ability for $[Mn(CO)_5]^{\cdot}$ radical **241** to abstract halogen atoms was probed further. $[Mn_2(CO)_{10}]$ was photolysed in a variety of halogenated solvents at 400nm, with the same concentration of $[Mn_2(CO)_{10}]$. Chloroform, chlorobenzene, bromobenzene, iodobenzene, chlorohexane, bromohexane, iodohexane, ethyl 4-chlorobenzoate, ethyl 4-bromobenzoate, ethyl 4-iodobenzoate were all selected as alternative halogenated solvents.

In iodobenzene, ethyl 4-clorobenzoate, ethyl 4-bromobenzoate, ethyl 4-iodobenzoate, bromohexane, and iodohexane abstraction of the respective halogen atom occurred. The rate constant, k_{obs}, for each of these solvents are reported in Table 24. Whereas no

further reactivity with **241** was observed in chloroform, chlorobenzene, or bromobenzene. Instead, **241** recombined to form $[Mn_2(CO)_{10}]$. In all instances the iodine atom was abstracted, likely due to the weakness of C−I bonds. Bromine was abstracted from all the brominated solvents other than bromobenzene. In bromobenzene the resulting phenyl radical is unstable, due to the radical lying outside the aromaticity of the phenyl ring. Finally, chlorine atom abstraction was only exhibited in dichloromethane and ethyl 4-chlorobenzoate. This was likely because of both the increased number of chlorine atoms and weaker C−Cl bonds in methylene chloride, along with a stabilised radical upon abstraction from ethyl 4-chlorobenzoate.

Table 24. Observed rate constant, k_{obs} for the abstraction of a halogen atom from various halogenated solvents.

Solvent	Rate constant of halogen abstraction, k_{obs}/ s^{-1}	Carbon−Halide bond dissociation energy/ kJ mol^{-1} [157]
Chlorobenzene	*n/a*	399
Bromobenzene	*n/a*	336
Iodobenzene	$2.7 \pm 0.7 \times 10^5$	268
Ethyl 4- chlorobenzoate	$1.0 \pm 0.3 \times 10^6$	-
Ethyl 4- bromobenzoate	$5.7 \pm 1.7 \times 10^5$	-
Ethyl 4-iodobenzoate	$1.5 \pm 0.4 \times 10^5$	-
Methylene chloride	$1.6 \pm 0.1 \times 10^6$	310
Chloroform	*n/a*	350
Bromohexane	$1.3 \pm 0.1 \times 10^6$	296
Iodohexane	$9.1 \pm 2.6 \times 10^5$	236

The experiments in unreactive solvents were then repeated. The experimental procedure was modified so that $[Mn_2(CO)_{10}]$ was dissolved in a solution of 0.2 mL of halogenated solvent and 9.8 mL of anhydrous acetonitrile (Figure 157). The initial intent was to test if there was a concentration dependence. In all instances, **241** now reacted, rather than reforming $[Mn_2(CO)_{10}]$. A peak at *ca*. 2055 cm^{-1} was detected, but not the high energy band associated with $[MnX(CO)_5]$ compounds. Thus, the transient band formed at 10 μs in Figure 157 was as assigned as *fac*-$[Mn(CO)_3(NCMe)_3]^+$ (see Table 25 for the the rate constant, k_{obs}, in each of these solvents, and the acetonitrile control). Comparatively, when $[Mn_2(CO)_{10}]$ was photolysed at 400 nm in either neat halogenated solvent (chlorobenzene, bromobenzene, or chloroform), or acetonitrile, **241** did not react, instead radical recombination occurred. From this, it is hypothesised that **241** reacts with acetonitrile to form a 19-electron radical $[Mn(CO)_3(NCMe)_3]$. This species

would be expected to be both a highly reducing and reactive species.[158] This is then able to activate the previously inert C−Cl and C−Br bonds, forming $[Mn(CO)_3(NCMe)_3]^+[X]^-$, where X is the respective halide counter anion. The 19-electron radical $[Mn(CO)_3(NCMe)_3]$ has previously been proposed by Stiegman and Tyler (Figure 156), when exploring the quantum yield of disproportionation of $[Mn_2(CO)_{10}]$ in the presence of mono, bi, and tri-dentate N coordinating ligands.[158] A radical chain mechanism was proposed, where the 19-electron complex $[Mn(CO)_3(L)_3]$ played a crucial role in the cleavage of $[Mn_2(CO)_{10}]$, forming $[Mn(CO)_3(L)_3]^+$ as a side product. This is possible due to the highly reducing properties of the 19-electron radical, with a reduction potential of > 3.0 V reported.[158]

Table 25. Rate of $[Mn(CO)_3(NCMe)_3]^+$ formation from $[Mn(CO)_5]^{\cdot}$.

Solvent	Rate of $[Mn(CO)_3(NCMe)_3]^+$ formation , k_{obs}/ s^{-1}
Chlorobenzene	$4.0 \pm 0.1 \times 10^6$
Bromobenzene	$1.1 \pm 0.1 \times 10^6$
Chloroform	$1.2 \pm 0.1 \times 10^6$
Acetonitrile	*n/a*

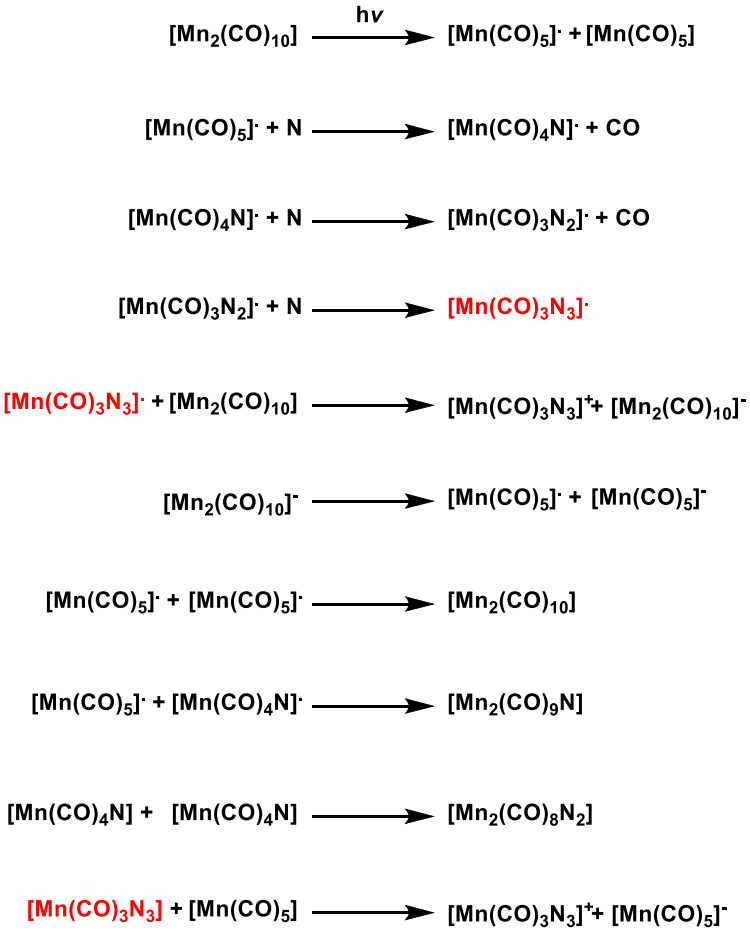

Figure 156. Radical chain reaction proposed by Siegman and Tyler, with the 19-electron species highlighted in red. N denotes the coordination of a nitrogen-containing ligand.[158]

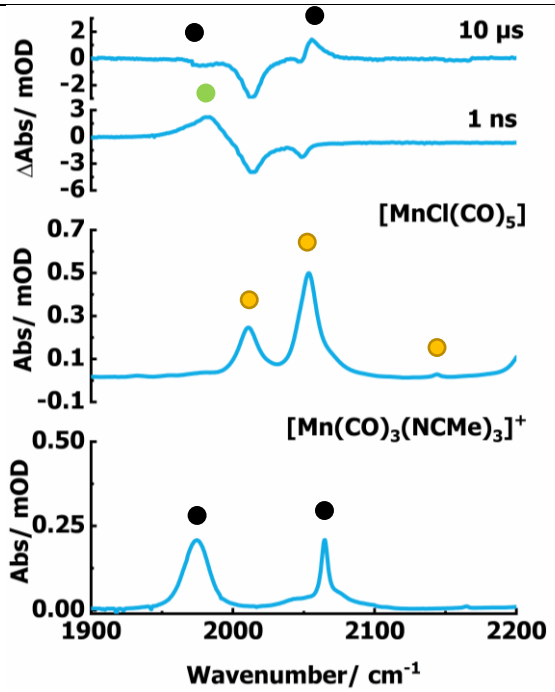

Figure 157. Top: TRIR spectra of $[Mn_2(CO)_{10}]$ in 0.2 mL chloroform and 9.8 mL anhydrous acetonitrile solution exciting with a 400 nm pump wavelength under an atmosphere of N_2 at selected pump-probe delays. Middle: FTIR spectrum of **249**. Bottom: FTIR spectrum of **215**. **241** denoted by green circles, **249** denoted by yellow circles, and **215** denoted by black circles.

To further reinforce the hypothesis, the reaction with 0.2mL of chloroform and 9.8 mL of anhydrous acetonitrile was repeated. This time, $[Mn_2(CO)_{10}]$ was dissolved in 0.2 mL of chloroform and 9.8 mL of anhydrous *n*-heptane (Figure 158). The rational being that *n*-heptane is a poorer ligand than acetonitrile, thus the 19-electron complex will be less favourable, and radical recombination will be preferred, rather than activation of the carbon−halogen bond. When $[Mn_2(CO)_{10}]$ was photolysed at 400 nm in chloroform + *n*-heptane solution, no reaction with the halide was observed. Instead, **241** recombined (42%), as was observed in neat *n*-heptane, supporting the hypothesis that in chloroform acetonitrile solution, a highly reactive 19-electron is formed and activates the C−Cl bond. The experiment was then repeated with both 0.2 mL of bromobenzene and 0.2 mL of chlorobenzene. In both cases, loss of **241**, and recovery of the ground state bleach bands occurred over the course of *ca*. 100 µs. Ground state bleach band recovery of 45% and 50% was observed in bromobenzene and chlorobenzene respectively.

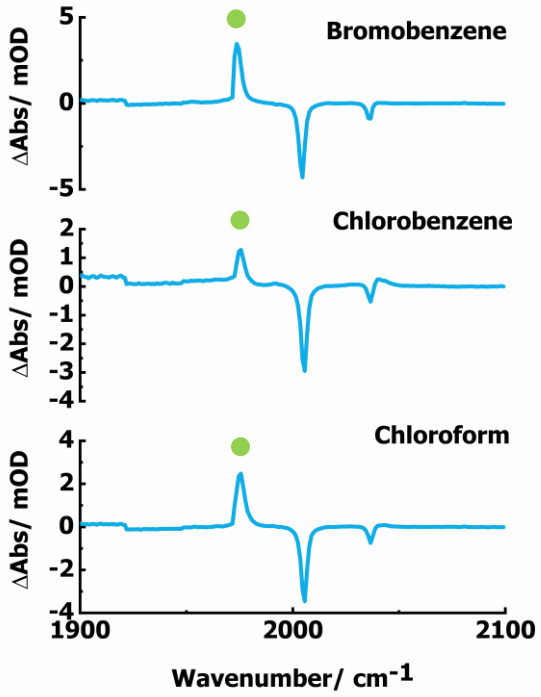

Figure 158. Top: TRIR spectra of $[Mn_2(CO)_{10}]$ in 0.2 mL bromobenzene and 9.8 mL anhydrous *n*-heptane solution exciting with a 400 nm pump wavelength under an atmosphere of N_2 at a selected pump-probe delay of 20 µs. Middle: TRIR spectra of $[Mn_2(CO)_{10}]$ in 0.2 mL chlorobenzene and 9.8 mL anhydrous *n*-heptane solution exciting with a 400 nm pump wavelength under an atmosphere of N_2 at a selected pump-probe delay of 20 µs. Bottom: TRIR spectra of $[Mn_2(CO)_{10}]$ in 0.2 mL chloroform and 9.8 mL anhydrous *n*-heptane solution exciting with a 400 nm pump wavelength under an atmosphere of N_2 at a selected pump-probe delay of 20 µs. **241** denoted by green circles.

Finally, $[Mn_2(CO)_{10}]$ was photolysed in anhydrous toluene solution in the presence of 1,1-bis(4-methoxyphenyl)methanimine **178** (13.8 mmol dm^{-3}) (Figure 159). The aim was to assess how the $[Mn(CO)_5]^{\cdot}$ **241** radical reacts with catalytically relevant imine **178**. In the absence of imine **178**, **241** recombines to form $[Mn_2(CO)_{10}]$ when in anhydrous toluene solution. When in the presence of imine **178**, recombination of **241** to form $[Mn_2(CO)_{10}]$ did not occur. Instead, **241** decayed over the course of *ca*. 20 µs with a kinetic profile fitting a first order exponential fit. From this the rate constant, k_{obs}, of 2.0 ± 0.2 × 10^5 mol^{-1} dm^3 s^{-1} was obtained. A band belonging to a new species **250** at 2055 cm^{-1} grew in as **241** depleted with a rate constant, k_{obs}, of 2.6 ± 0.5 × 10^5 mol^{-1} dm^3 s^{-1}.

Based on the assignment of previously discussed bands at *ca*. 2055 cm^{-1} forming from **241** being *fac*-$[Mn(CO)_3(solvent)_3]^+$ complexes, **250** has been assigned as the imine coordinated complex, *fac*-$[Mn(CO)_3(1,1\text{-bis}(4\text{-methoxyphenyl})methanimine)_3]^+$.

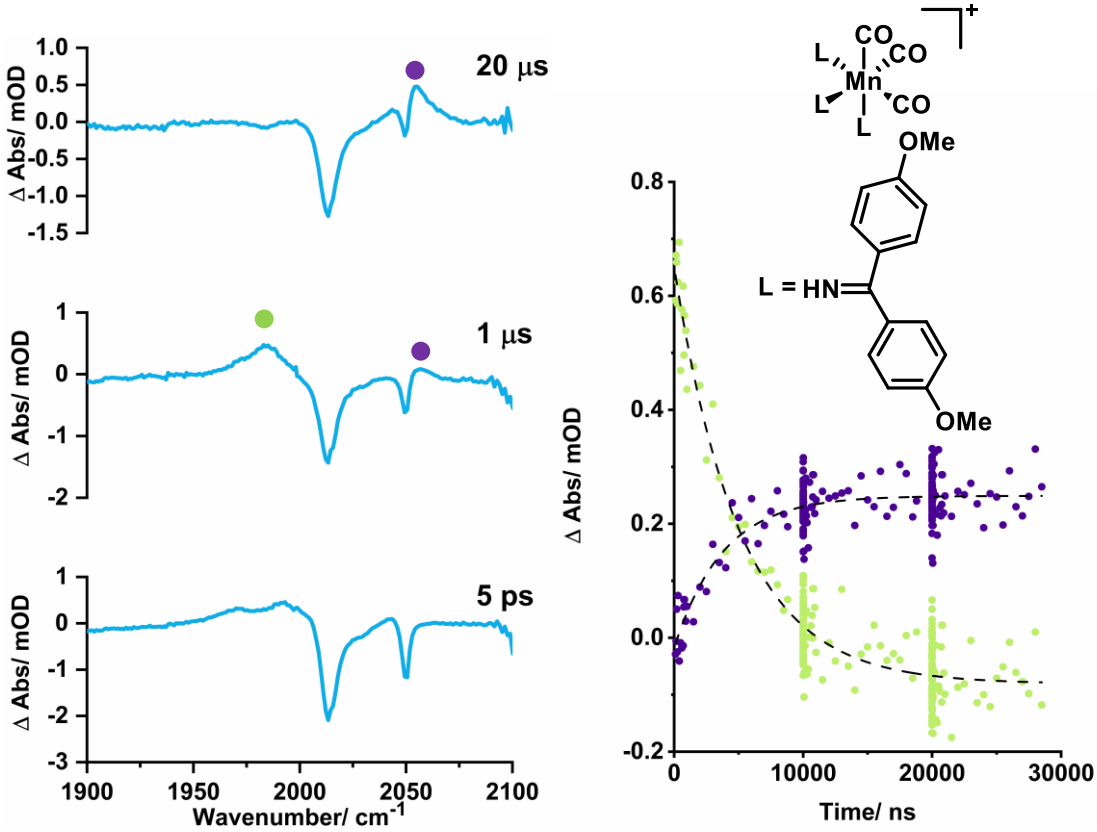

Figure 159. Left: TRIR spectra of $[Mn_2(CO)_{10}]$ in anhydrous toluene solution in the presence of imine **178**, exciting with a 400 nm pump wavelength under an atmosphere of N_2 at selected pump-probe delays. Right: Kinetics for the loss of **241** and formation of **250**. **241** denoted by denoted by green circles and **250** denoted by purple circles.

4.4.3 Reactivity of Photochemically Formed $[Mn_2(CO)_9]$

The next aim was to form the other major photoproduct formed from photolysis $[Mn_2(CO)_{10}]$, $[Mn_2(CO)_9]$. A higher energy pump wavelength of 310 nm was used. Predominantly, a 310 nm pump wavelength should promote ($\sigma \rightarrow d\,\pi^*$ and $d\,\pi \rightarrow d\,\pi^*$) electronic transitions, which are CO dissociative, according to literature studies.[137] This enabled the probing of the reactivity of photochemically formed $[Mn_2(CO)_9]$.

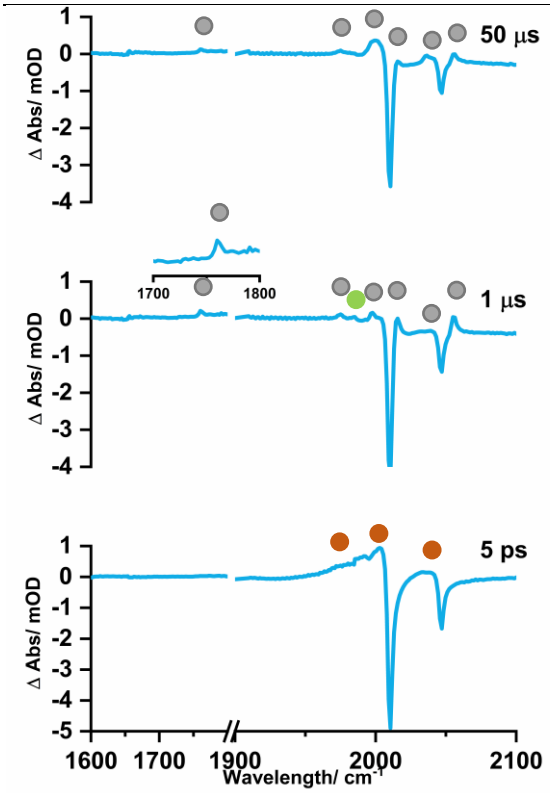

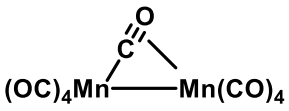

Figure 160. Left: TRIR spectra of $[Mn_2(CO)_{10}]$ in heptane solution exciting with a 310 nm pump wavelength under an atmosphere of N_2 at selected pump-probe delays. **242** denoted by denoted by grey circles, **241** denoted by denoted by green circle, and vibrationally hot $[Mn_2(CO)_{10}]$ denoted by orange circles. Right: The structure of $[Mn_2(CO)_9]$ **242**.

Photolysis of $[Mn_2(CO)_{10}]$ in *n*-heptane at 310 nm resulted in two distinct bleach bands at 2014 and 2046 cm^{-1}, while the third bleach band at 1983 cm^{-1} was obscured by both ground state bleach bands and transient bands of $[Mn(CO)_5]^{\cdot}$ (Figure 160). These negative bands indicate loss of ground state $[Mn_2(CO)_{10}]$. Within *ca*. 200 ps, transient bands at 1975, 1997, 2016, 2039, and 2054 cm^{-1} were observed. These then proceeded to remain for the duration of the experiment. Additional bands at 1759 and 1984 cm^{-1} were also detected. The band at 1984 cm^{-1} was the $[Mn(CO)_5]^{\cdot}$ radical **241**, which was observed when a 400 nm pump wavelength was used. The remaining transient bands correlated with the literature values for semibridged $[Mn_2(CO)_9]$ **242**, as depicted in Figure 127. This possesses bands at 1760, 1968, 1996, 2008, 2022 and 2058 cm^{-1} in heptane solution.[139] Over the course of *ca*. 500 ps, a band belonging to **242** at 1759 cm^{-1} formed with a rate constant, k_{obs}, of $29.1 \pm 5.3 \times 10^9$ s^{-1}, this apparent formation was attributed to vibrational relaxation of $[Mn_2(CO)_9]$.

At longer pump-probe delays the bands for **242** were present and remained for the duration of the experiment. This indicated that coordination of the semibridged CO ligand was preferential to coordination of *n*-heptane solvent. By 200 µs, the bleach band at 2045 cm^{-1} for ground state $[Mn_2(CO)_{10}]$ had undergone 39% recovery, providing further evidence that the band at 1984 cm^{-1} was the $[Mn(CO)_5]\cdot$ radical **241**.

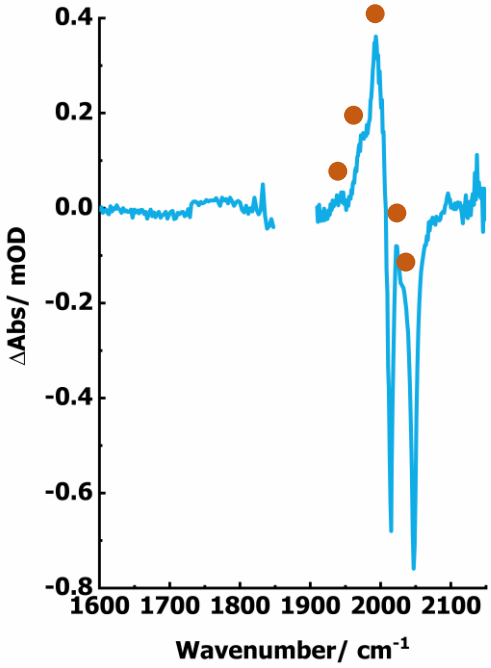

Figure 161. TRIR spectra of $[Mn_2(CO)_{10}]$ in acetonitrile solution exciting with a 310 nm pump wavelength under an atmosphere of N_2 at a selected pump-probe delay of 60 ns. **251** denoted by orange circles.

The experiment was then repeated in anhydrous acetonitrile solution to establish bands for the solvated complex **251** in anhydrous acetonitrile solution (Figure 161). Upon the relaxation of vibrationally excited states, distinct bands at 1938, 1972, 1993, 2023, and 2032 cm^{-1} were observed for the duration of the experiment. No low energy band around 1760 cm^{-1} was detected, indicating that the semibridged CO ligand was preferentially displaced by a NCMe ligand. Consequently, these were proposed to be the bands for $[Mn_2(CO)_9(solvent)]$ **251**, where the solvent is a bound ligand NCMe. Bleach band recovery of 32% was calculated, indicating again that $[Mn(CO)_5]\cdot$ was formed and undergoing recombination at longer pump-probe delays.

Finally, $[Mn_2(CO)_{10}]$ was photolysed at 310 nm in anhydrous toluene solution (Figure 162). Following vibrational relaxation, transient bands were detected at at 1755, 1964, 1984, 2022, 2038, and 2055 cm^{-1} and attributed to **242**. These underwent vibrational relaxation with a rate constant, k_{obs}, of 38.0 ± 12.9 × 10^9 s^{-1}, reflecting observations made in *n*-heptane. Unlike in *n*-heptane, **242** did not remain for the duration of the experiment. The bands depleted over *ca*. 100 µs with a rate constant, k_{obs}, of 2.8 ± 1.0 × 10^4 s^{-1}, forming a distinctive new transient band at 1926 cm^{-1}. Due to the significant red shift of the new band, even compared to $[Mn_2(CO)_9(NCMe)]$ which possessed a band at 2038 cm^{-1}, this species was proposed to be $[Mn_2(CO)_9(OH_2)]$ **252**. The increased solubility of water in toluene, compared to *n*-heptane would explain why the species was only seen in this case. [101]

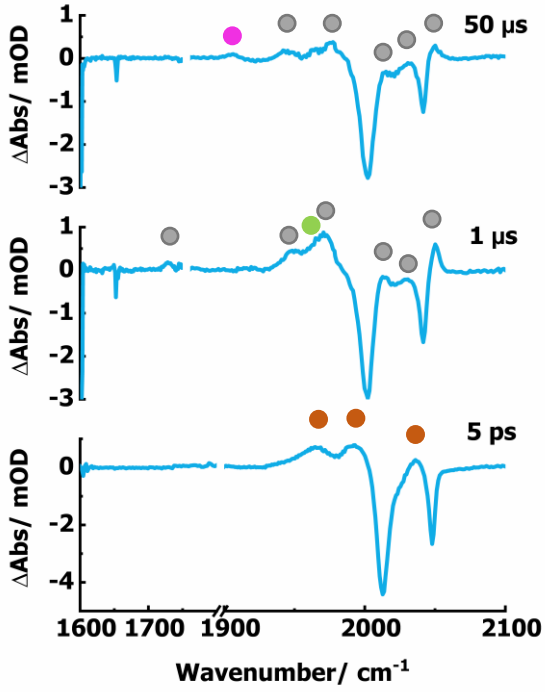

Figure 162. TRIR spectra of $[Mn_2(CO)_{10}]$ in anhydrous toluene solution exciting with a 310 nm pump wavelength under an atmosphere of N_2 at selected pump-probe delays. **242** denoted by denoted by grey circles, **241** denoted by denoted by green circle, vibrationally hot $[Mn_2(CO)_{10}]$ denoted by orange circles, and **252** denoted by pink circles

Recombination of **241** to form $[Mn_2(CO)_{10}]$ resulted in bleach band recover of 33% using the band at 2046 cm^{-1}. This was in line with values determined in *n*-heptane (39%) and acetonitrile solution (32%) when using a 310 nm pump wavelength. This gives an approximation of 30-39% Mn−Mn bond cleavage and 61-70% CO dissociation when $[Mn_2(CO)_{10}]$ is photolysed at 310 nm. The closest literature value was 30% Mn−Mn bond cleavage when $[Mn_2(CO)_{10}]$ was excited at 337 nm in cyclohexane.[144]

To validate the assignment of **252** as $[Mn_2(CO)_9(OH_2)]$, the experiment was repeated in anhydrous toluene with one drop of water added (220pprox.. 5 µL) under an atmosphere of N_2 (Figure 163). Under the assumption that 5 µL of water was added, a concentration of approx. 2000 ppm of water was present, and thus in a large excess compared to $[Mn_2(CO)_{10}]$. However, the band at 1926 cm^{-1} did not form by *ca*. 50 µs, disproving the hypothesis that **252** is the water coordinated complex $[Mn_2(CO)_9(OH_2)]$.

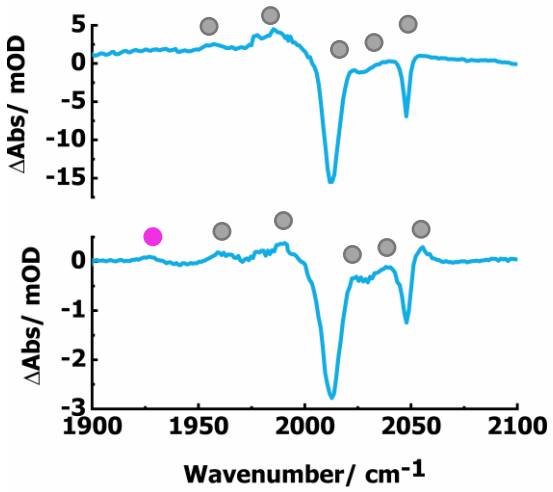

Figure 163. Top: TRIR spectra of $[Mn_2(CO)_{10}]$ in wet toluene solution exciting with a 310 nm pump wavelength under an atmosphere of N_2 at a selected pump-probe delay of 50 µs. Botton: TRIR spectra of $[Mn_2(CO)_{10}]$ in anhydrous toluene solution exciting with a 310 nm pump wavelength under an atmosphere of N_2 at a selected pump-probe delay of 50 µs. **242** denoted by denoted by grey circles and **252** denoted by pink circles.

Following the photolysis of $[Mn_2(CO)_{10}]$ in anhydrous toluene solution, catalytically relevant primary imine 1,1-bis(4-methoxyphenyl)methanimine **178** was added (Figure 164). 6.4 mg of imine **178** was dissolved in toluene solution to give a concentration of 3 mmol dm^{-3}. This imine was introduced into the system to explore how $[Mn_2(CO)_9]$

interacts with the substrate, as a potential route for C–H bond activation. This specific imine was chosen as it was the substrate used in both Chapter 2 and 3 herein, and used by He and co-workers in catalytic transformations.[60]

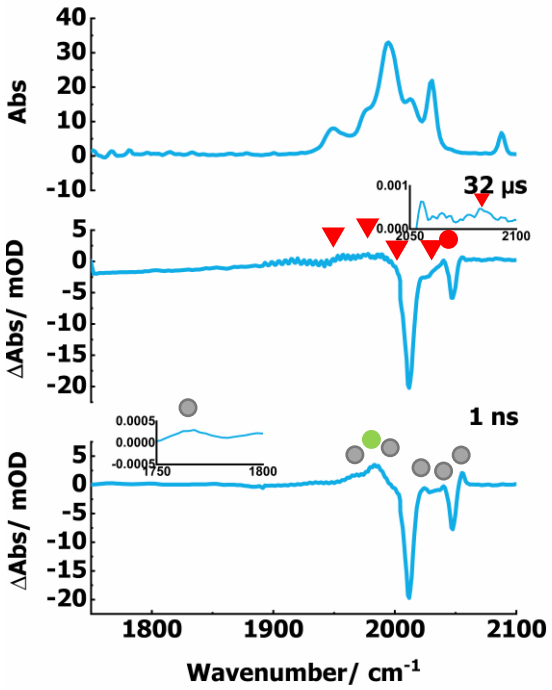

Figure 164. Top: FTIR spectrum of complex **216** in toluene. Bottom: TRIR spectra of $[Mn_2(CO)_{10}]$ and imine **178**in anhydrous toluene solution exciting with a 310 nm pump wavelength under an atmosphere of N_2 at selected pump-probe delays. **242** denoted by denoted by grey circles, **241** denoted by denoted by green circle, **250** denoted by red circles, and **216** denoted by red triangles.

At early pump-probe delays, after relaxation of vibrationally 'hot' species (*ca*. 200 ps) the bands for $[Mn_2(CO)_9]$ **242** and $[Mn(CO)_5]^{\cdot}$ **241** were observed at 1758, 1965, 1985, 2022, 2038, and 2055 cm^{-1}. **241** reacted with the imine **178**, as at a pump wavelength of 400 nm. **241** depleted by *ca*, 4 µs with a rate constant, k_{obs}, of 7.0 ± 1.8 × 10^5 s^{-1}, and the band at 2052 cm^{-1} assigned to **250** grew in with a rate constant, k_{obs}, of 7.0 ± 1.7 × 10^5 s^{-1} (Figure 165). This indicates that the highly reactive 19-electron species is being formed *in situ* and has the potential to react with other manganese complexes in the experiment. The band at 1760 cm^{-1} for semibridged $[Mn_2(CO)_9]$ also depleted over the course of *ca*. 30 µs with a rate constant, k_{obs}, of 1.1 ± 0.1 × 10^5 s^{-1}. In their place, the bands attributed to the imine bound complex described in Chapter 3.3.1, $[Mn_2(CO)_9$(1,1-

bis(4-methoxyphenyl)methanimine)] **216**, at 2086 cm^{-1} grew in with a rate constant k_{obs}, of 2.1 ± 0.7× 10^5 s^{-1} (Figure 166). These values are slightly outside of 95% confidence limits of each other. This was attributed to the weak intensity of the band at 2086 cm^{-1}, which introduced a significant degree of noise into the data.

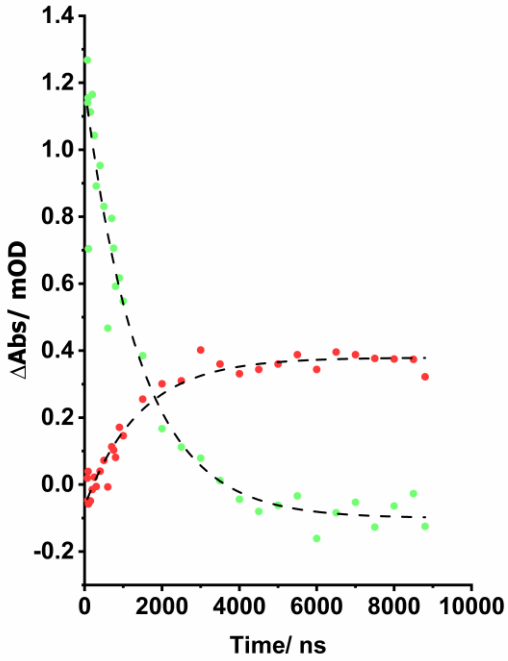

Figure 165. Kinetics for the loss of **241** and formation of **250**. **241** denoted by denoted by green circles and **250** denoted red circles. Dotted lines denote exponential kinetics. Where appropriate a mono or biexponential fit was applied.

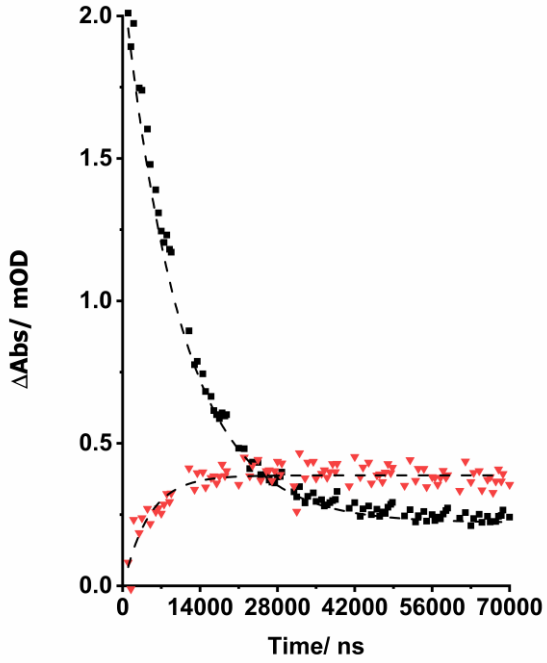

Figure 166. Kinetics for the loss of **242** and formation of **216**. **242** denoted by denoted by orange circles and **216** denoted red triangles. Dotted lines denote exponential kinetics. Where appropriate a mono or biexponential fit was applied.

4.4.4 Intermediate 355 nm Pump Wavelength

Finally, photochemical studies on $[Mn_2(CO)_{10}]$ were conducted using a pump wavelength of 355 nm. This intermediate wavelength was chosen to compare our data with prior studies which had been conducted at 355 nm. The proportion of Mn−Mn and Mn−CO bond cleavage should differ from what was observed at 310 and 400 nm. While the second order rate constant for $[Mn(CO)_5]^{\cdot}$ radical recombination should remain constant. As with prior pump wavelengths, anhydrous *n*-heptane, acetonitrile, and toluene were used as solvents.

Initially, $[Mn_2(CO)_{10}]$ was excited with a 355 nm pump wavelength in anhydrous toluene solution (Figure 167). Following ultrafast events, bands belonging to both $[Mn(CO)_5]^{\cdot}$ **241** and $[Mn_2(CO)_9]$ **242** were detected. A much smaller transient band belonging **241** was observed at *ca*. 1 µs when a 355 nm pump wavelength was used, which was almost entirely masked by the ground state bleach band of $[Mn_2(CO)_{10}]$ at 1983 cm^{-1}. This was reflected by a reduced recovery of 63% for the ground state bleach bands of

$[Mn_2(CO)_{10}]$, supporting the observation that less Mn−Mn bond cleavage had occurred. Similar degrees of bleach band recovery were seen in both anhydrous *n*-heptane and acetonitrile solution, at 64 and 57% respectively. This is slightly higher than expected at a pump wavelength of 355 nm, with 49% Mn−Mn bond cleavage reported for $[Mn_2(CO)_{10}]$ in cyclohexane solution. [137] Partial overlap of transient bands, with the ground state bleach band accounts for this discrepancy in ratio of bond cleavage. Kinetic analysis of the ground state bleach bands of $[Mn_2(CO)_{10}]$ using the same approach discussed in Section 4.4.2 resulted in a second order rate constant, *k*, of $6.5 \pm 0.4 \times 10^8$ mol^{-1} dm^3 s^{-1}. Additional experiments conducted in anhydrous *n*-heptane and acetonitrile yielded second order rate constants $2.7 \pm 0.1 \times 10^8$ and $3.0 \pm 1.0 \times 10^9$ of mol^{-1} dm^3 s^{-1}. As expected, the recovery of $[Mn_2(CO)_{10}]$ in anhydrous toluene and acetonitrile exhibited second order rate constants that were statistically the same when a pump wavelength of 355 or 400 nm was used. However, the values obtained in *n*-heptane were statistically different. The rate constant was greater by a factor of two when a pump wavelength of 400 nm was used. The values of the second order rate constant were expected to be the same, and this error is likely due to error introduced by the approximations in the calculation.

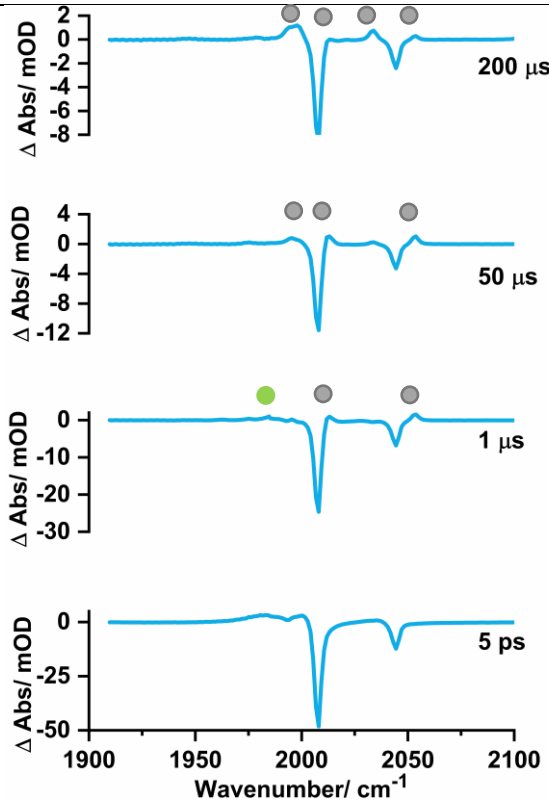

Figure 167. TRIR spectra of $[Mn_2(CO)_{10}]$ in anhydrous toluene solution exciting with a 355 nm pump wavelength under an atmosphere of N_2 at selected pump-probe delays. **241** denoted by green circles and **242** denoted by grey circles.

Table 26. Second order rate constants determined for the recombination of $[Mn(CO)_5]^{\cdot}$ at a pump wavelength of 355 and 400 nm.

Solvent	Rate constant, *k*, using a 355 nm pump wavelength/ mol^{-1} dm^3 s^{-1}	Rate constant, *k*, using a 400 nm pump wavelength/ mol^{-1} dm^3 s^{-1}
n-heptane	$2.7 \pm 0.1 \times 10^8$	$5.7 \pm 0.7 \times 10^8$
Toluene	$6.5 \pm 0.4 \times 10^8$	$5.2 \pm 0.9 \times 10^8$
Acetonitrile	$3.0 \pm 1.0 \times 10^9$	$3.0 \pm 0.5 \times 10^9$

4.5 Conclusions

Excitation of $[Mn_2(CO)_{10}]$ at wavelengths of 310, 355, and 400 nm resulted in the formation of vibrationally excited $[Mn_2(CO)_{10}]$, $[Mn_2(CO)_9]$, and $[Mn(CO)_5]^{\cdot}$. The proportion of $[Mn_2(CO)_9]$ and $[Mn(CO)_5]^{\cdot}$ was found to vary with excitation wavelength. Higher energy pump wavelengths favoured cleavage of the Mn−C bond, to form $[Mn_2(CO)_9]$. Lower energy pump wavelengths resulted in Mn−Mn bond cleavage being the major photochemically induced event.

Ultrafast studies showed that at all wavelengths, vibrationally excited $[Mn_2(CO)_{10}]$ in the $v = 1$ state was formed. Vibrational cooling was observed to then proceed with a lifetime of *ca*. 100 ps. Additionally, at a pump wavelength of 355 and 400 nm, there was evidence for the rearrangement of the solvent cage around $[Mn(CO)_5]^{\cdot}$, and the drifting apart of two $[Mn(CO)_5]^{\cdot}$ fragments. This proceeded with a lifetime of *ca*. 4 ps in weakly interacting solvents. This lifetime was further reduced to *ca*. 1 ps in the highly interacting solvent acetonitrile. This ultrafast rearrangement explains events reported in the literature on the 10s of picosecond timescale involving $[Mn(CO)_5]^{\cdot}$, which were previously attributed to vibrational relaxation. [136][150] [151]

Upon formation of $[Mn(CO)_5]^{\cdot}$, predominantly at 355 and 400 nm, recombination to reform $[Mn_2(CO)_{10}]$ was the most common fate. This occurred in the majority of solvents: *n*-heptane, THF, DMSO, toluene, acetonitrile, 1,4-dioxane, styrene and cyclohexane. A second order rate constant, *k*, was determined to be 1.1×10^9 s^{-1} mol^{-1} dm^3 in THF, which reflected literature values of 1.9×10^9 and 9.5×10^8 s^{-1} mol^{-1} dm^3 obtained from transient absorption spectroscopy studies. [133][134] In acetone and butyl acrylate, $[Mn(CO)_5]^{\cdot}$ instead reacted with the solvent to form *fac*-$[Mn(CO)_3(solvent)_3]^+$ complexes, as was observed by Firth and co-workers. They irradiated at 400 nm $[Mn_2(CO)_{10}]$ in acetonitrile solution in the presence of diazonium or B_2pin_2 additives to form *fac*-$[Mn(CO)_3(NCMe)_3]^+$. A similar fate was observed when $[Mn(CO)_5]^{\cdot}$ was formed in the presence of imine **178** in anhydrous toluene solution. Instead of the radical undergoing recombination, the complex *fac*-$[Mn(CO)_3(Imine)_3]^+$ was formed.

In the presence of halogenated solvents, specifically: methylene chloride, iodobenzene, ethyl 4-chlorobenzoate, ethyl 4-bromobenzoate, ethyl 4-iodobenzoate, bromohexane, and iodohexane, the halogen atom was abstracted to form $[Mn(halide)(CO)_5]$. However, $[Mn(CO)_5]^{\cdot}$ was unable to abstract the halogen atom from bromobenzene, chlorobenzene or chloroform. When replicated in an acetonitrile solution containing bromobenzene, chlorobenzene or chloroform, $[Mn(CO)_5]^{\cdot}$ was observed to react. Again, formation of *fac*-$[Mn(CO)_3(NCMe)_3]^+[Halide]^-$ was seen. This supported the formation of a highly reacting 19-electron radical intermediate, proposed prior by Stiegman and Tyler, which activated the previously insert C−Halide bonds.[158]

Cleavage of the Mn−C bond at higher energies resulted in formation of $[Mn_2(CO)_9(Solvent)]$. When a poorly coordinating solvent (toluene or *n*-heptane) was used, the solvent ligand was substituted by a semi-bridging CO ligand which possessed a distinctive band at 1760 cm^{-1}. In acetonitrile, solvent coordination was found to be favourable to formation of the semi-bridging CO ligand. Furthermore, addition of imine **178** in toluene solution resulted in substitution of the semi-bridging CO ligand with the imine, forming $[Mn_2(CO)_9$(1,1-bis(4-methoxyphenyl)methanimine)] **216**, a catalytically relevant intermediate discussed in Chapter 3.

Chapter 5: Conclusions and Future Work

5.1 Conclusions

The work described in this Thesis has focused on the exploring the mechanism of activation for ubiquitous manganese(I) carbonyl complexes in C−H bond functionalisation reactions. The reaction between a biaryl primary imine and substituted alkyne, initially reported in 2014 by He and co-workers, was used as the model reaction to probe the pathway for precatalyst activation.[60]

In Chapter 2, a focus was placed on gaining a greater understanding of the reactivity of 5-membered manganacycles, which are a common reaction intermediate in manganese catalysed C−H bond functionalisation reactions (Figure 168). The imine-derived manganacycle **158** was synthesised, and thermal activation of the complex was mimicked, by photolysis at 355 nm, releasing a CO ligand in the process. Subsequent steps were then followed *via* time-resolved multiple probe spectroscopy. As in prior studies by Aucott and co-workers, solvent bound complexes were detected from the earliest pump-probe delay (1 ps), and no evidence was found for a 16-electron *fac*-$[Mn(C\hat{}N)(CO)_3]$ complex.[96] Solvent coordinated manganese complexes were then observed to undergo ligand substitution with either a water or dinitrogen molecule, where an equilibrium was established. This was based on the solubility of water and dinitrogen in the respective solvent. The water coordinated complex *fac*-$[Mn(C\hat{}N)(CO)_3(H_2O)]$ highlights a potential route towards catalytically- inert manganese(I) hydroxy bridged cluster **213**. These were previously reported by

Hammarback and co-workers, and observed spectroscopically in catalytic studies in Chapter 3, where anhydrous 1,4-dioxane containing 20 ppm of water was used.[51] Unlike prior studies on 5-membered manganacycles, favourable coordination of dinitrogen was observed in *n*-heptane, and the novel complex *fac*-[Mn(C^N)(CO)$_3$(η^1-N$_2$)] was detected, which possessed a distinctive N≡N stretching mode with a band at 2249 cm^{-1}. This example represents one of only a handful of literature manganese(I) dinitrogen complexes. [103–107]

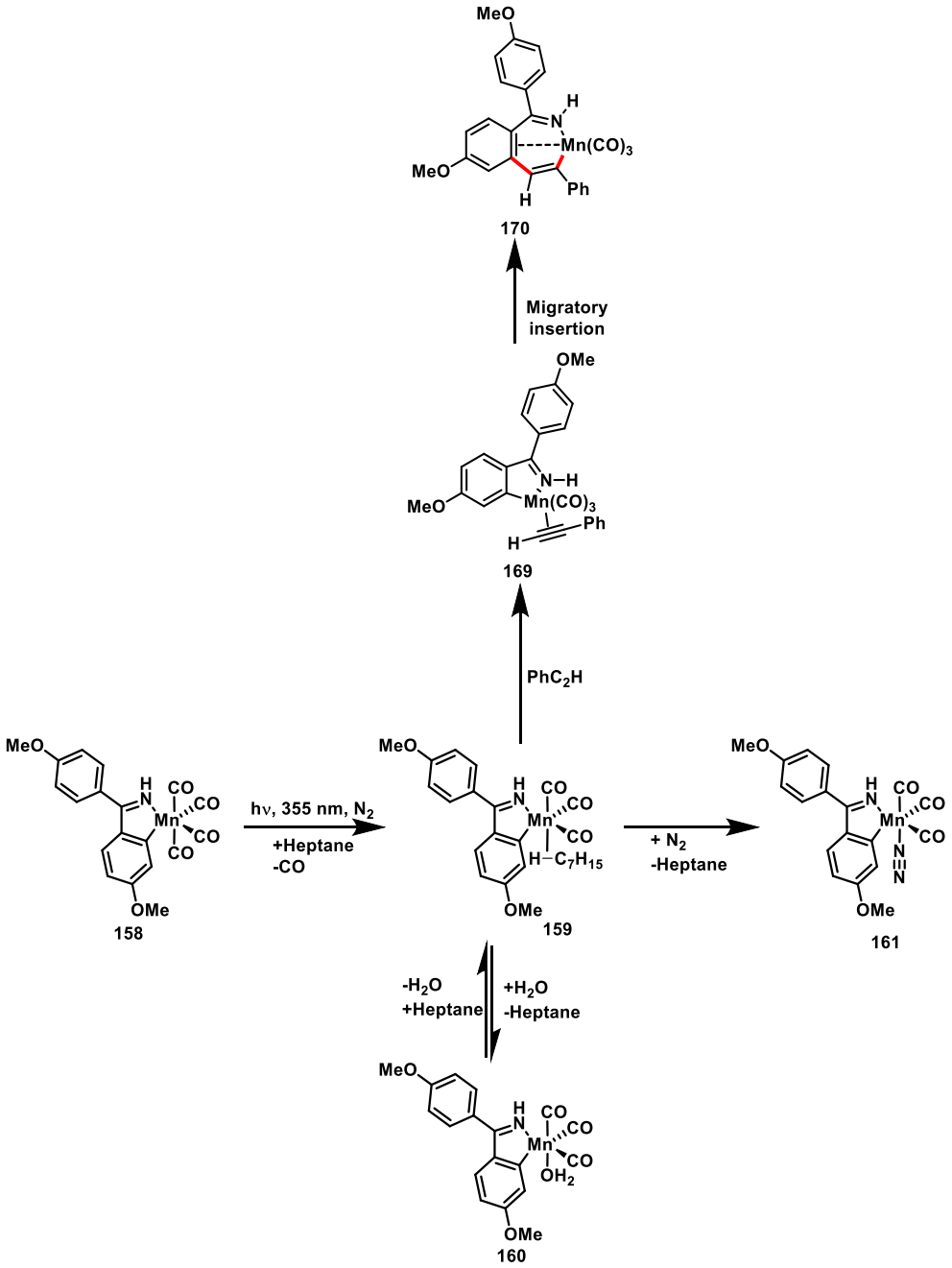

Figure 168. Reactivity of the 5-membered manganacycle **158** discussed in Chapter 2.

Catalytically-relevant additives were then introduced into the system. These included imine **178**, alkynes, and the isoquinoline product **180**. Phenyl acetylene displaced the coordinated solvent ligand, coordinating to manganese in a η^2-HCCPh fashion. In the absence of imine **178** (or isoquinoline **180**) the terminal alkyne then underwent migratory insertion, forming a 7−membered manganacycle containing a new C−C bond. When imine **178** or isoquinoline **180** were present, the migratory insertion step was inhibited and coordination of **178** or **180** was favoured, indicating that product inhibition is likely to occur as the catalytic reaction proceeds. The 7-membered manganacycle also reflected similar manganese complexes detected in Chapter 3, where *in situ* IR spectroscopy combined with LIFDI MS gave information related to plausible catalyst resting states.

Chapter 3 presented the pathways of activation for common manganese(I) carbonyl precatalysts. For the first time, a mechanism was proposed for the activation of $[Mn_2(CO)_{10}]$, which ultimately formed the 5-membered manganacycle discussed in Chapter 2. When $[Mn_2(CO)_{10}]$ was used as a precatalyst, the complex $[Mn_2(CO)_9$(1,1-bis(4-methoxyphenyl)methanimine)] was detected *in situ* under catalytic conditions and subsequently isolated. $[Mn_2(CO)_9$(1,1-bis(4-methoxyphenyl)methanimine)] in the presence of imine **178** then underwent a C−H bond activation step to form the 5-membered manganacycle **158**. Either the imine **178** or a 19-eletron manganese tricarbonyl radical discussed in Chapter 4 were proposed to aid with the formation of **158**. Ultimately, these results provide evidence that under these conditions $[Mn_2(CO)_{10}]$ forms 5-membered manganacycles, supporting proposals made in various synthetic methodologies (Figure 169).[2,42]

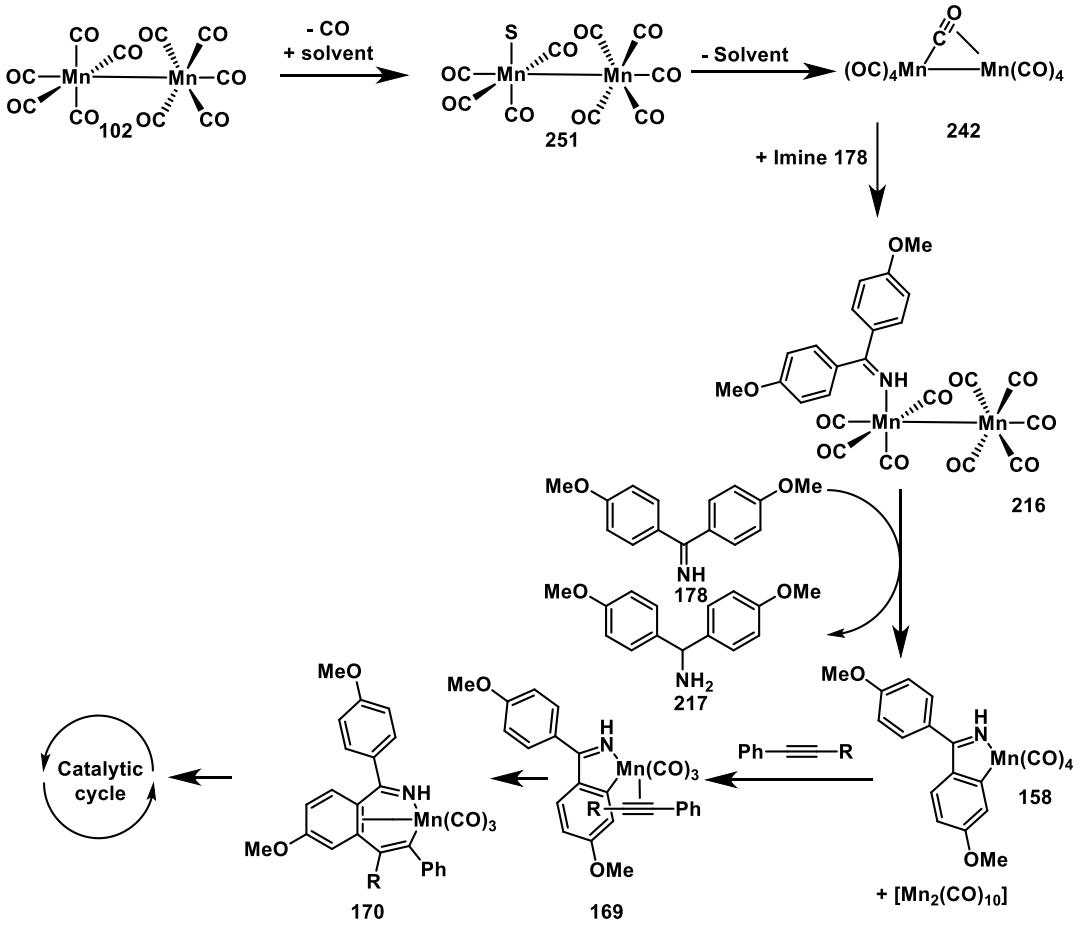

Figure 169. Proposed mechanism of activation for $[Mn_2(CO)_{10}]$ based on results in Chapters 2,3, and 4.

The activation of $[MnBr(CO)_5]$ was further probed (Figure 170). Previously this was studied in detail by Hammarback and co-workers.[30] Under the conditions described herein, $[MnBr(CO)_5]$ activated *via* a different mechanism to that proposed in the literature. Instead of forming the 5-membered manganacycle **158**, the complex *fac*-[MnBr(1,1-bis-(4-methoxyphenyl)methanimine$)_2(CO)_3$] **228** was exclusively detected. Under literature conditions, this complex was catalytically non-functional. However, through application of either base, irradiation with visible light, or the use of a terminal alkyne, the respective isoquinoline product was detected. Once activated, *in situ* IR spectroscopy, supported by LIFDI MS, provided evidence for a 7-membered manganacycle with a further alkyne π-bound as the resting state of catalysis. $[MnBr(CO)_5]$ not forming a 5-membered manganacycle on route to the catalytic cycle emphasises that manganese carbonyl precatalysts do not all exhibit the same reactivity under the same conditions. This explains the differences in reactivity in literature

studies, where some transformations only work with $[Mn_2(CO)_{10}]$ or $[MnBr(CO)_5]$, while other transformations exhibit similar reactivity with both precatalysts.[65,159,160]

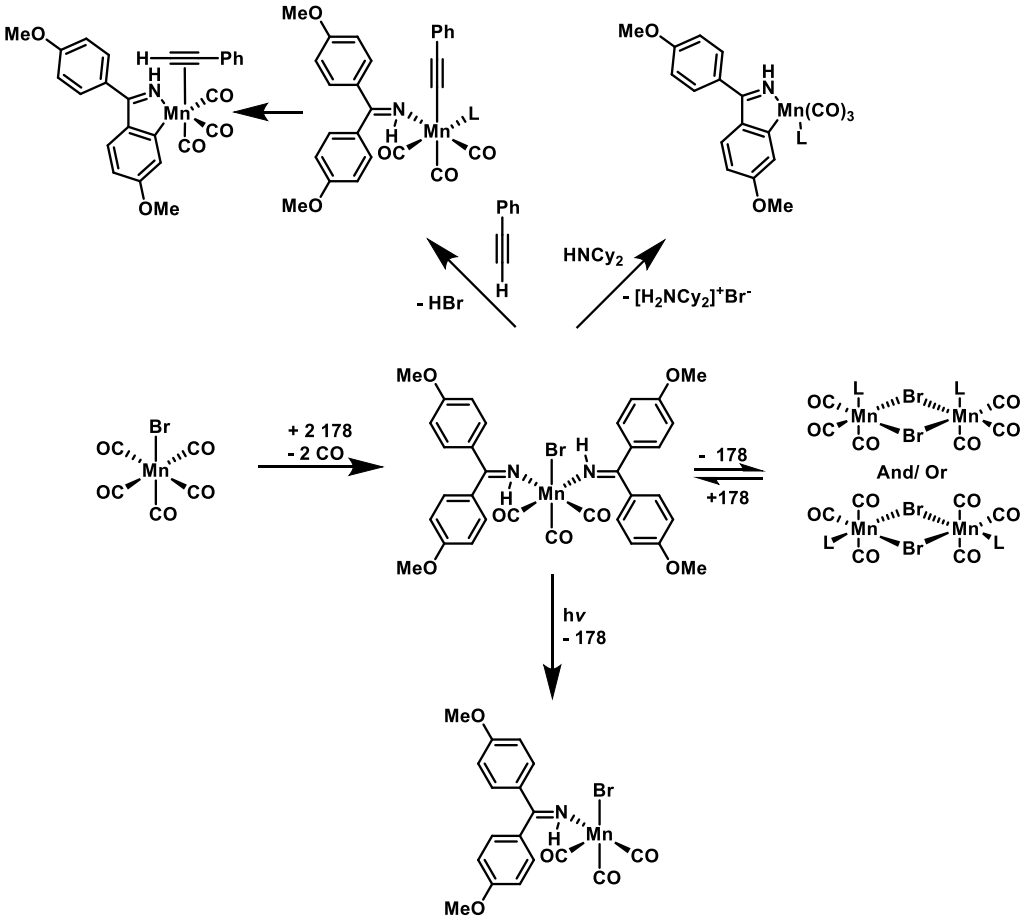

Figure 170. Reactivity of $[MnBr(CO)_5]$ discussed in Chapter 3.

Finally, the fundamental photochemistry of $[Mn_2(CO)_{10}]$ was studied using time-resolved multiple probe spectroscopy (Figure 171). The reactivity of the subsequently formed photoproducts was also explored. Fundamental reactivity mirrored observations previously made in the literature.[138,149] As the excitation wavelength shifted from lower to higher energy, a preference for Mn−CO bond cleavage over Mn−Mn bond cleavage was seen. Mn−Mn bond cleavage resulted in formation of a $[Mn(CO)_5]^{\cdot}$ radical, which under most conditions recombined. In comparison, no recoordination of CO was observed when Mn−CO bond cleavage occurred. Instead, solvent coordination and then formation of a semi bridging CO $[Mn_2(CO)_9]$ complex was observed (See Figure 127). In addition to these previously reported photoproducts, advances in technology allowed the observation of previously unseen events. Within *ca*. 5 ps, when the Mn−Mn bond of $[Mn_2(CO)_{10}]$ was cleaved, the rearrangement of the

solvent cage, and drifting apart of the $[Mn(CO)_5]^{\cdot}$ radical to form two independent entities was clearly observed. Through the use of more polar solvents, the lifetime, τ, could be reduced to *ca*. 1 ps. This demonstrates how the capability of TRIR has evolved, revealing mechanistic intricacies which 20 years ago were undetectable.

The $[Mn(CO)_5]^{\cdot}$ radical was observed to react with acetone and *n*-butyl acrylate to form cationic solvent manganese(I) complexes. Additionally, the radical successfully abstracted the halogen atom from numerous organohalides to form $[Mn(X)(CO)_5]$, where X is the respective halogen atom. Interestingly, in instances where the halogen atom was not abstracted, repetition of the reaction in acetonitrile solvent resulted in activation of previously inert C–X bonds, and formation of $[Mn(CO)_3(NCMe)_3]^+$. This provided evidence that a highly reactive 19-electron radical $[Mn(CO)_3(NCMe)_3]$ was formed, which was proposed by Stiegman and Tyler, and was able even activate strong organohalide bonds such as the C–Cl bond of chlorobenzene. [158]

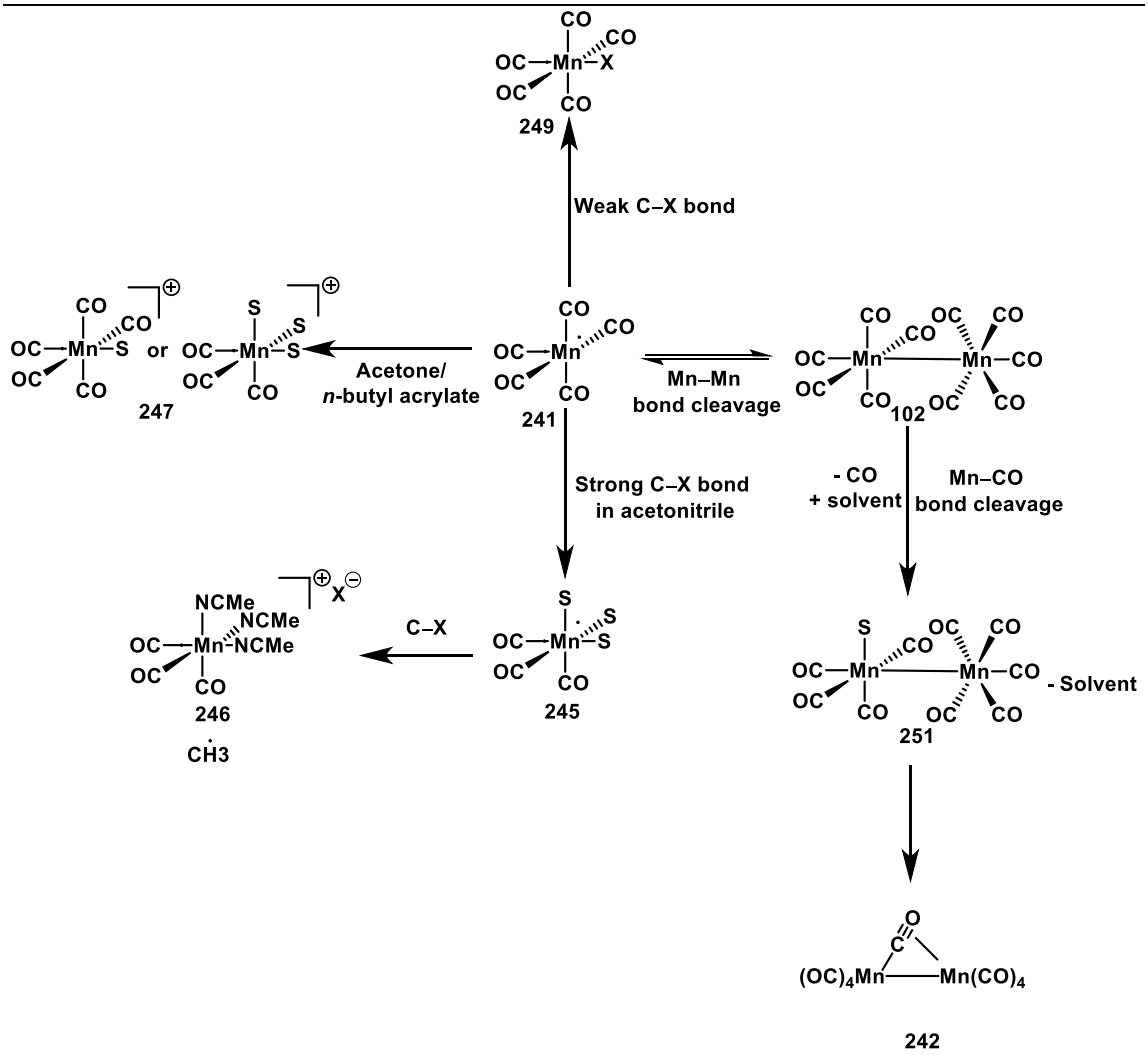

Figure 171. Reactivity of $[Mn_2(CO)_{10}]$ following either Mn−Mn or Mn−CO bond cleavage discussed in Chapter 4.

Lastly, $[Mn_2(CO)_9]$ was observed to react with imine **178** to form $[Mn_2(CO)_9$(1,1-bis(4-methoxyphenyl)methanimine)], which was isolated from catalytic studies discussed in Chapter 3, giving greater detail on the process of precatalyst activation for $[Mn_2(CO)_{10}]$.

5.2 Future Work

A crucial limitation in the field of manganese carbonyl catalysed C−H bond functionalisation reactions is the synthesis of the precatalysts. $[Mn_2(CO)_{10}]$ is synthesised from $MnCl_2$ under 200 atm of CO at high temperatures.[17] Subsequent precatalysts are then made by reacting $[Mn_2(CO)_{10}]$ with either methyl iodide, bromine, or sodium mercury amalgam ($[MeMn(CO)_5]$, $[MnBr(CO)_5]$, and $[BnMn(CO)_5]$ respectively). These reactions are unsustainable, and often employ toxic or highly carcinogenic reagents.

To improve the sustainability of manganese carbonyl catalysed reactions, alternative ligands to CO could be designed, removing the need for these conditions. *N*-heterocyclic carbenes are one potential alternative to CO ligands. A tripodal NHC ligand could be employed to enforce a *fac* geometry, which was observed in many complexes herein. Alternatively, more efficient active catalyst species could be designed. $[BnMn(CO)_5]$ offered catalytic activity at the lowest temperature. Thus, a complex could be designed based on $[BnMn(CO)_5]$, which has further functionality on the benzyl group. Once the initial C−H bond activation step has occurred, liberating the benzyl group, there is a *N*-coordinating functionality attached which could coordinate to the active catalyst over H_2O, to reduce formation of manganese hydroxy bridged deactivation products, lowering the catalyst loading .

Finally, the application of TRIR techniques could be expanded. The mechanistic work carried out using time-resolved multiple probe spectroscopy, especially on $[Mn_2(CO)_{10}]$ highlights how TRIR techniques have evolved over the last two decades. As the sensitivity of these techniques has increased, it will enables the exploration of systems beyond those containing metal carbonyl complexes, opening up the potential for exploring systems which are currently difficult to study by traditional mechanistic techniques.

Chapter 6: Experimental

6.1 General Experimental Information

6.1.1 Solvents and Reagents

Commercial chemicals were purchased from Acros Organics, Alpha Aesar, Apollo Scientific, Fisher Scientific, Fluorochem, Insight Biotechnology, Merck Life Science, Sigma-Aldrich, Strem Chemicals UK, or Tokyo Chemical Industry UK and were used without further purification unless otherwise stated. Dry MeOH, heptane and 1,4-dioxane were purchased from Acros Organics, stored over 4 Å molecular sieves and under an atmosphere of N_2. Dry Et_2O, hexane, MeCN, methylene chloride, THF and toluene were collected from a Pure Solv MD-7 solvent system and stored in oven dried ampoules under an atmosphere of N_2.

Petroleum ether (pet ether) in following experimental procedures refers to the distillate with a boiling point of 40−60 °C.

Room-temperature (RT) typically refers to 21 °C, with an upper and lower limit of 16−23 °C recorded.

6.1.2 Chromatography

Thin-layer chromatography (TLC) was conducted using Merck aluminium-backed 5554 silica plates. Visualisation of spots was achieved *via* irradiation (254 nm), or sequential staining with potassium permanganate followed by heating. Flash column chromatography was carried out following the procedure reported by Still *et al*.,[161] using Fluorochem silica gel 60 (particle size 40−63 µm), with the solvent system stated in the specific procedure.

6.1.3 Melting Points

Melting points were recorded on a Stuart digital SMP3 machine, with a temperature ramp of 2 °C min^{-1} used.

6.1.4 Infrared Spectroscopy

Infrared spectra for characterisation were obtained using a Unicam Research Series FTIR (KBr IR) or a Bruker APLHA-Platinum FTIR Spectrometer with a platinum−diamond ATR sampling module.

Extinction coefficients (ε) were calculated by fitting measured concentrations to the Beer-Lambert Law, using five concentrations, repeating the experiments in triplicate.

In situ IR spectroscopic measurements were made on a Mettler Toledo ReactIR ic10 with a K6 conduit SiComp (silicon) probe and MCT detector. An oven dried 3-necked round-bottom flask equipped with a stirrer bar was attached to the ReactIR ic10 probe. One neck was sealed with a septum, and the other connected to a Schlenk line. The system was evacuated and subsequently backfilled with N_2 five times. Following this a background spectrum was recorded under an N_2 atmosphere. An internal thermocouple and dry deoxygenated solvent were introduced *via* the septum. The system was heated using a stirrer hotplate until thermocouple was giving steady readings at the desired temperature.

Sample measurements were then started at 30 second intervals, and reagents added in a sequential order. First any imine reagents were added, followed by unsaturated reagents, additives and finally any manganese containing compounds. Liquids were injected through the septum, whereas solids required rapid removal of the septum under a positive flow of N_2, addition, and replacement of the septum. After each addition, a comment was added to the experimental run, and at least 2 minutes were given for the IR signal/ reaction temperature to stabilise. Where solubility of a reagent was an issue, long was give as appropriate. A sampling interval of 30 seconds was maintained for the initial 2 hours of an experiment. This was extended to 5-minute intervals beyond the first 2 hours.

Peaks of interest between ∼1800−2200 cm^{-1} with a resolution of ± 4 cm^{-1} were individually monitored on an experiment-by-experiment basis. A solvent subtraction, one- or two-point baseline and baseline offset were applied to all peaks. Where multiple peaks were convoluted, second derivative function was finally applied. Following this, peak data was exported into a Microsoft Excel document, and subsequent analysis conducted in OriginPro 2019b (64-bit) 9.6.5.169 (Academic) software.

IR Pump- Probe experiments were performed using one third of the output of a Ti-sapphire femtosecond laser (Spectra-Physics Solstice Ace, 800-nm, 6 W, 90-fs, 1 kHz pulse repetition rate) to pump an optical parametric amplifier (OPA, Spectra-Physics TOPAS Prime) equipped with noncollinear difference frequency generation. The resulting mid-IR laser pulses had a duration of ~150 fs and a bandwidth of ~200 cm^{-1}. The central frequency was set on resonance with modes for the studied sample (2014 cm^{-1} for $Mn_2(CO)_{10}$). The mid-IR laser pulse was split by a 95:5 CaF_2 beam splitter to generate the pump and probe beams respectively. A parabolic gold mirror was used to focus the beams onto the sample. The transmitted probe beam was refocused using a second parabolic mirror, prior to frequency-dispersion and detection using a spectrograph (Horiba Jobin Yvon Ltd, Triax) and liquid nitrogen-cooled mercury cadmium telluride (MCT) detector (Infrared Associates Inc, MCT-6-64).

6.1.5 UV−Visible spectroscopy

UV−Visible spectra were recorded with a Jasco V−560 spectrometer using Quartz cuvettes.

6.1.6 Nuclear Magnetic Resonance Spectroscopy

Solution phase ^{1}H, ^{13}C and ^{19}F NMR analysis were carried out on a Brucker AV500 spectrometer (500, 125, 470 MHz for ^{1}H, ^{13}C and ^{19}F respectively) at 298 K (295 K for methylene chloride). ^{13}C NMR spectra were recorded with ^{1}H decoupling. Spectra were processed in MestReNova software version 14.0.0-23239. In ^{1}H spectra, coupling constants were quoted with ± 0.5 Hz. Chemical shifts are reported in ppm and referenced to the residual non-deuterated solvent.

Residual $CDHCl_2$ in methylene chloride-d_2: ^{1}H: 5.32 ppm, ^{13}C: 53.49 ppm

Residual $CHCl_3$l in chloroform-d: ^{1}H: $CHCl_3$ 7.26 ppm, ^{13}C: $CHCl_3$ 77.36 ppm

^{1}H NMR peaks are reported to two decimal places, whereas ^{13}C and ^{19}F NMR peaks are reported to one decimal place.

6.1.7 Mass Spectrometry

MS spectra were measured using a Bruker Daltronics micrOTOF MS, Agilent series 1200LC with electrospray ionization (ESI). Liquid Injection Field Desorbtion Ionisation

(LIFDI) mass spectrometry was carried out using a Waters GCT Premier MS Agilent 7890A GC. Data were quoted as a mass to charge ratio (m/z) in Daltons and relative intensity in parenthesis. High resolution mass spectra (HRMS) are reported within 5 ppm error of the theoretical value unless stated otherwise.

6.1.8 Single Crystal X-Ray Diffraction

Single crystals were crystalised from a suitable solvent system. An appropirate crystal was selected and [oil on 200 micrometre micromount] on a SuperNova, Dual, Cu at home/near, Eos diffractometer. The crystal was kept at 110.00(10) K during data collection. Using Olex2[162] , the structure was solved with the SHELXT[163] structure solution program using Intrinsic Phasing and refined with the SHELXL[164] refinement package using Least Squares minimisation.

6.1.9 Time-Resolved Multiple Probe Spectroscopy (TR^MPS)

TRIR measurements were carried out at the LIFEtime facility using TR^MPS technique at the Central Laser Facility (Science and Technology Facility Council Rutherford Appleton Laboratories).[92,93] The experiments were driven by a 100 kHz repetition rate Yb:KGW amplifier (Pharos) as a pump source, producing 15 W, 260 fs pulses at 1030 nm. The laser output was used to drive a BBO-based 515 nm pumped optical parametric amplifier (OPA). The pump beam was collimated, travelled along an programable optical delay line (0-16 ns 1200 mm long double pass), then focused onto the sample. The probe beam sources from a 100 kHz repetition rate YB:KGW amplifier(Pharos) producing 6W, 180 fs pulses at 1030 nm, driving two 3 W BBO/KTA based OPAs. The two Pharos sources shared a 80 MHz oscillator, allowing pump-probe delay steps f 12.5 ns. The probe beam was split to provide probe and reference pulses. The probe beams were collimated, synchronised by a fixed optical delay, and focused by a gold parabolic mirror onto the sample. The three beams were overlapped on the sample using a 50 µm pinhole. The probe beams were measured by two separate 128-element detectors. To go beyond 12.5 ns, subsequent seed pulses can be selected from the 80 MHz oscillator. Data were collected using pump-probe delays ranging from 1 ps to 988.5 µs.

Samples were prepared as follows. To an oven dried Duran bottle approx. 15 mg of manganese complex were added and dissolved in 20 mL of anhydrous solvent from a newly opened sure-seal bottle. The system was then sparged (N_2, Ar, or air) for 10

minutes with solution pumping around the system. For the duration of the experiment, the Duran flask was sealed while under a positive pressure of sparge gas. The Duran bottle was connected *via* PTFE tubing to a Harrick cell with a spacer (100 μm unless stated otherwise), with solvent being pumped round the system using a peristaltic pump. During experiments, the Harrick cell was attached to rastering, to prevent excitation of photoproducts. Following an experiment all solution was pumped from the system, 3×10 mL of new solvent pumped around to clean the kit, and dried using a positive pressure of N_2 for 10 minutes.

Initially spectra were processed in ULTRA_VIEW_v2 where negative times were subtracted, and a polynomial second order baseline correction was applied, and data exported as a text file. The resulting data were then analysed in OriginPro 2019b (64-bit) 9.6.5.169 (Academic) software. For data which extended beyond 50 μs a root mean square correction was applied to account for flow of solution out of the probe beam. Where data sets were particularly noisy, early time points after the first trump were deleted and up to a 12-point average of data points applied. Kinetic fits were performed with appropriate ExpGro, ExpDec and ExpGroDec functions and values were quoted with in the format of XX ± XX indicating the 95% confidence limits of values obtained from exponential fits. The suitability of kinetic fits were then assessed using the built in residual plots produced by OriginPro software.

6.1.10 DFT Calculations

DFT calculations were performed using the TURBOMOLE V6.4 package using the resolution of identity (RI) approximation.[165–171] Initial optimisations were performed at the (RI-)BP86/SV(P) level, followed by frequency calculations at the same level. All minima were confirmed as such by the absence of imaginary frequencies. Single-point calculations on the (RI-)BP86/SV(P) optimised geometries were performed using the hybrid PBE0 functional and the def2-TZVPP basis set. The (RI-)PBE0/def2-TZVPP SCF energies were corrected for their zero-point energies, thermal energies and entropies (obtained from the (RI-)BP86/SV(P)-level frequency calculations). No symmetry constraints were applied during optimisations. Solvent corrections were applied with the COSMO[172] dielectric continuum model and dispersion effects modelled with Grimme's D3 method.[173,174]

6.2 Compound Synthesis and Characterisation

Where a compound was synthesised following a literature procedure, the reference for the synthesis has been included. Following the synthetic procedure, a lab book reference has been given, which corresponds to the characterisation data.

Benzyl pentacarbonyl manganese(I) (212)

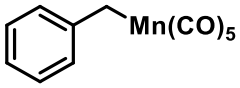

To an oven dried Schlenk tube equipped with a magnetic stirrer bar, under nitrogen, was added mercury (18 mL). Sodium metal (4 eq., 64.2 mmol, 1.78 g) was added in small pieces with high stirring to allow dissolution. In a separate Schlenk tube under nitrogen was added $Mn_2(CO)_{10}$ (1eq., 16.08 mmol, 6.24 g), followed by anhydrous, deoxygenated THF (100 mL). The THF solution was then transferred by cannula on to the sodium amalgam and was stirred for 3 hours. In a separate Schlenk tube equipped with a magnetic stirrer under nitrogen was added benzyl chloride (2 eq., 32.1 mmol, 3.7 mL). The Schlenk tube containing benzyl chloride was placed in a bath of ice and water and was put under vacuum with stirring for 60 seconds, before being backfilled with N_2. At ambient temperature, the THF solution of $NaMn(CO)_5$ was transferred by cannula into the benzyl chloride. The mixture was stirred at ambient temperature for 20 hours. The solution was then filtered through a bed of Celite®, and was washed with diethyl ether (5 × 40 mL). The contents were then loaded on to silica gel and this was added onto a pad of silica (5 cm). The pad was washed with pet ether (3 × 80 mL). The solvent was removed to yield the product containing benzyl chloride. Benzyl chloride was removed at 35 °C under vacuum. The product must be broken up with a spatula and put back under vacuum. A slightly yellow crystalline product was obtained (6.4 g, 69 %).

m.p. = 38.2-38.6 °C. ^{1}H NMR ($CDCl_3$, 500 MHz)δ (ppm) 2.42 (2H, s), 6.98 (1H, m), 7.19 (4H, m); ^{13}C NMR ($CDCl_3$, 125 MHz) δ 12.25, 123.61, 125.98, 127.74, 128.77, and 151.95, 212.46. R_f 0.37 (pet ether). LIFDI-MS m/z (ion, %): 285.96677($[M]^+$, 100).IR (Hexane, cm^{-1}): 2106, 2042, 2010, 1989, 1598, 1465, 1379, 1261 and 1220.

The analytical data were obtained in accordance with the literature.[51]

Lab book reference number: jbe-2-002

1,1-Bis(4-methoxyphenyl)methanimine (178)

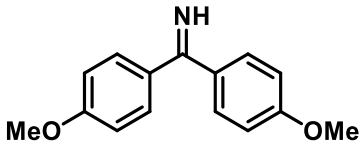

To an oven dried Schlenk equipped with a magnetic stirrer, under an N_2 atmosphere, was added 0.5 M 4-methoxyphenylmagnesium bromide (1 eq., 16.6 mL, 8.3 mmol). In a separate oven dried Schlenk, 4-methoxybenzonitrile (1 equ., 1.1 g, 8.3 mmol) was added and dissolved in anhydrous deoxygenated THF (6 mL). The 4-methoxybenzonitrile solution was added dropwise to the Grignard solution and heated to reflux overnight. The reaction mixture was cooled in an ice bath, quenched with anhydrous methanol (3 mL) and stirred for 30 minutes. The solution was diluted with 20 mL of hexane and filtered through a Celite® plug. The Celite® plug was washed with toluene (3×10 mL) and the filtrate reduced in *vacuo*. The pale yellow solid was recrystalised from methylene chloride/pentane to give a white crystalline solid being 1,1-bis(4- methoxyphenyl) methanimine (1.75 g, 88 %).

m.p. = 132.8-133.2 ^{o}C. ^{1}H NMR ($CDCl_3$, 500 MHz)δ 7.56 (4H, d, J= 8.6 Hz), 6.93 (4H, d, J= 8.6 Hz), 3.85 (6H, s). ^{13}C NMR ($CDCl_3$, 125 MHz) δ 177.3, 161.7, 131.4, 130.7, 113.6, 55.5. ESI-MS m/z (ion, %): 242.1176 ($[M+H]^+$, 100). IR (hexane, cm^{-1}): 2969, 2963, 2995, 2940, 2926, 2901, 2888, 2878, 2845, 2360, 2341, 1607, 1514, 1476, 1390, 1360, 1295, 1250, 1172 and 1038.

The analytical data were obtained in accordance with the literature.[60]

Lab book reference number: jbe-2-003

Tetracarbonyl (η^2-2-(*p*-anisylC=NH)-5-methoxyphenyl) manganese(I) (158)

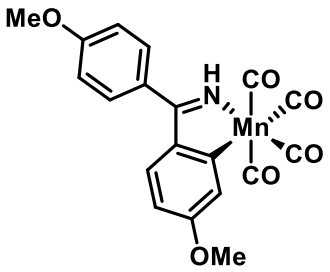

To an Oven dried Schlenk tube equipped with a magnetic stirrer, under an atmosphere of N_2 was added $BnMn(CO)_5$ (1 eq., 1.8 mmol, 510 mg) and 1,1-bis(4- methoxyphenyl) methanimine (1 eq., 1.8 mmol, 430 mg). The Schlenk tube was evacuated and backfilled with N_2 five times, then anhydrous, deoxygenated toluene was added. The solution was then heated to reflux for 6 hr and the Schlenk tube was covered in aluminium foil to exclude light. Reaction progress was monitored by solution phase IR, Looking at the metal carbonyl stretching bands. When the reaction was complete, the reaction mixture was allowed to cool to room temperature and solvent removed in *vacuo*. The crude solid underwent purification using flash column chromatography on silica gel (4:1 v/v pet ether: methylene chloride to yield a pale yellow powder (560 mg, 76%).

^1H NMR (CD_2Cl_2, 500 MHz) δ (ppm) = 7.74 (1H, s), 7.61 (1H, s, J = 2.5 Hz), 7.48 (1H, d, J = 8.5 Hz), 7.41 (2H, m), 7.00 (2H, m), 6.62 (1H, dd, J = 1, 8.5 Hz), 3.92 (3H, s), 3.88 (3H, s). ^{13}C NMR (CD_2Cl_2, 125 MHz) δ (ppm) = 188.55, 161.50, 159.02, 132.12, 129.95, 129.21, 123.19, 114.32, 109.93, 55.63, 55.37. R_f 0.2 (4:1 *v*/*v* pet ether: methylene chloride). LIFDI-MS m/z (ion, %): 407.01860 (100%, $[M]^+$). IR (Hexane, cm^{-1}): 3320, 3098, 3076, 3040, 3028, 3012, 2636, 2882, 2746, 2340, 2360, 2072, 1986, 1978, 1932, 1606, 1577, 1536, 1505, 1495, 1456, 1420, 1390, 1296, 1238, 1176, 1072 and 1037. Uv/Vis λmax(toluene)/ nm 339.

The analytical data were obtained in accordance with the literature.[60]

Lab book reference number: jbe-2-045

6-Methoxy-1-(4-methoxyphenyl)-3,4-diphenylisoquinoline (180)

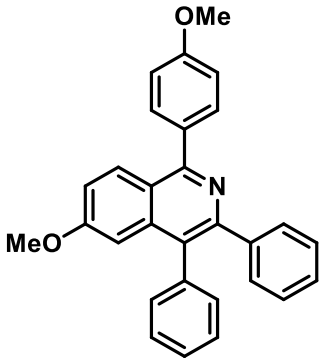

To an oven dried Schlenk that was evacuated, backfilled with N_2 five times and equipped with a magnetic stirrer, 1,1-bis-(4-methoxyphenyl) methanimine (1 eq., 1 mmol, 241 mg), diphenyl acetylene (1.5 eq., 1.5 mmol, 267 mg) and [$MnBr(CO)_5$] (0.1 eq., 0.1 mmol, 27.5 mg) were added. Anhydrous deoxygenated dioxane (10 mL) was added and the reaction stirred at 105 ^oC for 3hr, while being irradiated with a white LED array (15 W, 6500K). Once complete, solvent was removed in *vacuo* and the product purified by flash column chromatography (94:6 *v*/*v* pet ether: diethyl ether). to give a white powder (383 mg, 92 %).

^1H NMR (500 MHz, $CDCl_3$) δ 8.13 (1H, d, J = 8.6 Hz), 7.77 (2H, m), 7.44-7.34 (5H, m), 7.32-7.28 (2H, m), 7.22-7.14 (4H, m), 7.10-7.06 (2H, m), 6.97, (1H, d , J = 8.6 Hz), 3.91, (3H, s), 3.74 (3H, s). ^{13}C NMR ($CDCl_3$, 125 MHz) δ 160.62,160.10, 158.95, 150.34, 141.25, 139.23, 138.04, 132.60, 131.64, 131.38, 129.65, 128.84, 128.52, 127.60, 127.34, 127.03, 121.31, 118.88, 113.88, 104.31, 55.55, 55.35. R_f 0.25 (94:6 *v*/*v* pet ether: diethyl ether). ESI- MS m/z (ion, %) 418 ($[M+H]^+$, 100 %). IR (Hexane, cm^{-1}): 3097, 3077, 3041, 3029, 2933, 2921, 2886, 2835, 1615, 1578, 1567, 1542, 1513, 1497, 1487, 1454, 1441, 1410, 1381, 1339, 1291, 1263, 1247, 1222, 1175, 1117, 1087, 1071, 1034 and 980. Uv/Vis λMax(Toluene)/nm 320.

The analytical data were obtained in accordance with the literature.[60]

Lab book reference number: jbe-2-018

6-Methoxy-1-(4-methoxyphenyl)-3-phenylisoquinoline (231)

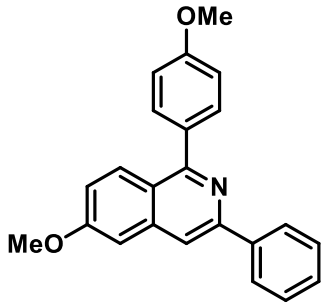

To an oven dried Schlenk that was evacuated, backfilled with N_2 five times and equipped with a magnetic stirrer, 1,1-bis-(4-methoxyphenyl) methanimine (1 eq., 1 mmol, 241 mg), phenyl acetylene (1.5 eq, 1.5 mmol, 142 µL) and [$MnBr(CO)_5$] (0.1 eq., 0.1 mmol, 27.5 mg) were added. Anhydrous deoxygenated dioxane (10 mL) was added and the reaction stirred at 105 ^oC for 3hr, while excluded from ambient light with aluminium foil. Once complete, solvent removed in *vacuo* and the product purified by flash column chromatography (30:1 *v*/*v* pet ether: diethyl ether) to give a colourless oil (297 mg, 87 %).

^1H NMR (500 MHz, $CDCl_3$) δ 8.20 (2H, d, J = 7.6 Hz), 8.06 (1H, d, J = 9.2), 7.97-7.93 (1H, m), 7.76 (2H, d, J = 8.1), 7.49 (2H, t, J = 7.4 Hz), 7.41 (1H, d, J = 7.3), 7.18 (1H, d , J = 2.5 Hz), 7.13 (1H, dd, J = 9.2, 2.5 Hz), 7.08 (2H, d, J = 8.1 Hz) 3.98 (3H, s), 3.91 (3H, s). ^{13}C NMR ($CDCl_3$, 125 MHz) δ 160.76, 160.19, 159.56, 150.76, 140.10, 139.83, 131.65, 129.61, 128.77, 128.54, 127.23, 121.62, 119.73, 115.01, 113.86, 105.08, 55.62, 55.56. R_f 0.24 (10:1 pet ether: diethyl ether) ESI- MS m/z (ion, %) 342 ($[M+H]^+$, 100). IR (Et_2O, cm^{-1}): 3060, 3034, 3001, 2959, 2931, 2933, 2883, 1610, 1565, 1513, 1495, 1456, 1402, 1360, 1293, 1240, 1171, 1121, 1028, 973, 877, 838, 767, 692, 594, 562, 464.Uv/Vis λMax(Toluene)/nm 317.

The analytical data were obtained in accordance with the literature.[60]

Lab book reference number: jbe-4-196

3,4-Bis(4-fluorophenyl)-6-methoxy-1-(4-methoxyphenyl)isoquinoline (253)

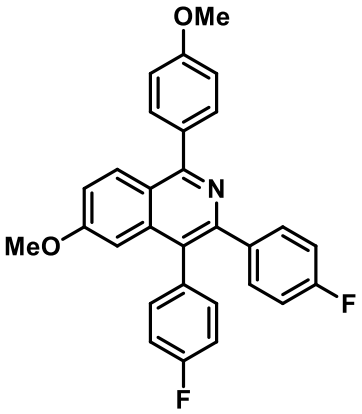

To an oven dried Schlenk that was evacuated, backfilled with N_2 five times and equipped with a stirrer bar, 1,1-bis-(4-methoxyphenyl) methanimine (1 eq., 1 mmol, 241 mg), 4,4'-difluorodiphenyl acetylene (1.5 eq, 1.5 mmol, 321 mg) and $[MnBr(CO)_5]$ (0.1 eq., 0.1 mmol, 27.5 mg) were added. Anhydrous deoxygenated dioxane (10 mL) was added and the reaction stirred at 105 ^oC for 3hr, while being irradiated with a white LED array (15 W, 6500K). Once complete, solvent removed in *vacuo* and the product purified by flash column chromatography (200:1 *v*/*v* Toluene: diethyl ether) to give a white powder (358 mg, 79%).

m.p. = 216.3-218.1 ^oC .^1H NMR (500 MHz, $CDCl_3$) δ 8.15 (1H, d, J = 12.0 Hz), 7.77 (2H, m), 7.39 (2H, m), 7.28 (2H, m), 7.18 (1H, dd, J = 2.3, 9.2 Hz), 7.17-7.08 (4H, m), 6.95- 6.88, (3H, m), 3.93, (3H, s), 3.79 (3H, s). ^{13}C NMR ($CDCl_3$, 125 MHz) δ 162.20 (d, J = 246 Hz), 162.12 (d, J = 245 Hz) , 160.84, 160.21, 159.27, 149.59, 139.27, 137.20 (d, J = 3 Hz), 133.86 (d, J = 3 Hz), 132.95 (d, J = 9 Hz), 132.41, 132.21 (d, J = 9 Hz), 131.59, 129.82, 127.67, 121.33, 121.31, 119.05, 115.83 (d, J = 21 Hz), 114.69 (d, J = 21 Hz), 55.56, 55.40. ^{19}F NMR (470 MHz, $CDCl_3$)) δ -114.33 (1F, s), -115.14 (1F, s) . R_f 0.25 (200:1 *v*/*v* toluene: diethyl ether). ESI- MS m/z (ion, %) 454($[M+H]^+$, 100). IR (Et_2O, cm^{-1}): 3009, 2972, 2838, 2156, 2002, 1614, 1576, 1504, 1463, 1404, 1334, 1296, 1256, 1218, 1155, 1115, 1034, 980, 884, 819, 786, 760, 733, 693, 663, 616, 568, 546, 529, 503. Uv/Vis λMax(Toluene)/nm 321.

The analytical data were obtained in accordance with the literature.[60]

Lab book reference number: jbe-4-199

6-Methoxy-1-(4-methoxyphenyl)-3,4-dipropylisoquinoline (254)

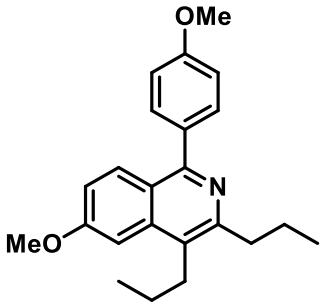

To an oven dried Schlenk that was evacuated, backfilled with N_2 five times and equipped with a magnetic stirrer, 1,1-bis-(4-methoxyphenyl) methanimine (1 eq., 1 mmol, 241 mg), 4-octyne 1.5 eq, 1.5 mmol, 220 µL) and [$MnBr(CO)_5$] (0.1 equiv., 0.1 mmol, 27.5 mg) were added. Anhydrous deoxygenated dioxane (10 mL) was added and the reaction stirred at 105 ^oC for 3hr, while being irradiated with a white LED array (15 W, 6500K). Once complete, solvent removed in *vacuo* and the product purified by flash column chromatography (20:1 *v*/*v* pet ether: diethyl ether) to give a colourless oil (332 mg, 95 %).

^1H NMR (500 MHz, $CDCl_3$) δ 7.96 (1H, d, J = 9.2 Hz), 7.60 (2H, m), 7.25-7.22 (1H, d, J = 2.5 Hz), 7.09-7.05 (1H, dd, J = 9.2, 2.5 Hz), 7.05-7.01 (2H, m), 3.97 (3H, s), 3.88, (3H, s), 3.04-2.95, (4H, m), 1.89-1.79 (2H, m), 1.79-1.69 (2H, m), 1.17-1.10 (3H, m), 1.08-1.02 (3H, m). ^{13}C NMR ($CDCl_3$, 125 MHz) δ 160.36, 159.85, 157.32, 152.86, 138.25, 132.36, 131.41, 130.22, 126.03, 121.14, 117.42, 113.86, 102.06, 55.53, 55.43, 37.61, 30.25, 23.77, 23.72 14.87, 14.51. R_f 0.20 (5:1 *v*/*v* pet ether: diethyl ether) ESI- MS m/z (ion, %) 350 ($[M+H]^+$, 100). IR (Et_2O, cm^{-1}): 2963, 2934, 2870, 1615, 1581, 1557, 1512, 1463, 1416, 1378, 1346, 1286, 1247, 1117, 1031, 836, 735, 583. Uv/Vis λMax(Toluene)/nm 312.

The analytical data were obtained in accordance with the literature.[60]

Lab book reference number: jbe-4-190

3-Cyclopropyl-6-methoxy-1-(4-methoxyphenyl)isoquinoline (255)

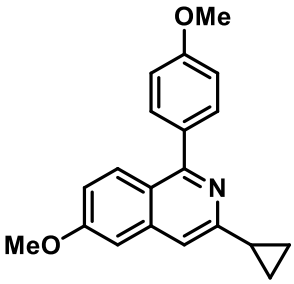

To an oven dried Schlenk that was evacuated, backfilled with N_2 five times and equipped with a magnetic stirrer, 1,1-bis-(4-methoxyphenyl) methanimine (1 eq., 1 mmol, 241 mg), cyclopropylacetylene (1.5 eq, 1.5 mmol, 128 µL) and $[MnBr(CO)_5]$ (0.1 equiv., 0.1 mmol, 27.5 mg) were added. Anhydrous deoxygenated dioxane (10 mL) was added and the reaction stirred at 105 ^oC for 3hr, while excluded from ambient light with aluminium foil. Once complete, solvent removed in *vacuo* and the product purified by flash column chromatography (30:1 *v*/*v* pet ether: diethyl ether) to give a yellow oil (190 mg, 59%).

^1H NMR (500 MHz, $CDCl_3$) δ 7.94 (1H, d, J = 9.1 Hz), 7.66-7.60 (2H, m), 7.28 (1H, s), 7.06-6.98 (4H, m), 3.94 (3H, s), 3.89 (3H, s), 2.29-2.14 (1H, m), 1.13-1.07 (2H, m), 1.03-0.97 (2H, m). ^{13}C NMR ($CDCl_3$, 125 MHz) δ 160.43, 159.88, 159.02, 155.89, 139.66, 131.35, 129.39, 120.81, 118.43, 114.27, 113.64, 103.79, 55.39, 17.15, 9.23. R_f 0.25 (10:1 *v*/*v* pet ether: diethyl ether). ESI- MS m/z (ion, %) 306 ($[M+H]^+$, 100). IR (Et_2O, cm^{-1}): 3002, 2960, 2932, 2837, 1621, 1561, 1512, 1463, 1408, 1250, 1224, 1170, 1123, 1023, 990, 903, 861, 840, 585. Uv/Vis λMax(Toluene)/nm 330.

The analytical data were obtained in accordance with the literature.[60]

Lab book reference number: jbe-4-191

6-Methoxy-1-(4-methoxyphenyl)-3-(thiophen-3-yl)isoquinoline (256)

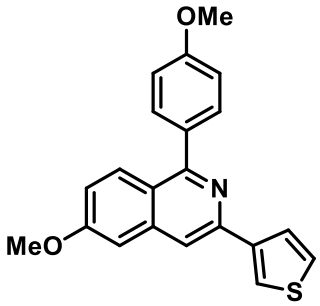

To an oven dried Schlenk that was evacuated, backfilled with N_2 five times and equipped with a magnetic stirrer, 1,1-bis-(4-methoxyphenyl) methanimine (1 eq., 1 mmol, 241 mg), 3-ethynylthiophene (1.5 eq, 1.5 mmol, 148 µL) and [$MnBr(CO)_5$] (0.1 eq., 0.1 mmol, 27.5 mg) were added. Anhydrous deoxygenated dioxane was added and the reaction stirred at 105 ^oC for 3hr, while excluded from ambient light with aluminium foil. Once complete, solvent removed in *vacuo* and the product purified by flash column chromatography (30:1 *v*/*v* pet ether: diethyl ether). to give a colourless oil (156 mg, 34%)

^1H NMR (500 MHz, $CDCl_3$) δ 8.09 (1H, s), 8.02 (1H, d, J = 9.2 Hz), 7.81 (1H, s), 7.79-7.75 (1H, d, J = 5 Hz), 7.75-7.70 (2H, d, J = 5 Hz), 7.43-7.38 (1H, s), 7.15-7.04 (5H, m), 3.97, (3H, s), 3.91 (3H, s). ^{13}C NMR ($CDCl_3$, 125 MHz) δ 60.67, 160.08, 159.54, 131.53, 129.58, 126.23, 126.05, 123.47, 121.39, 119.33, 114.31, 113.71, 55.49, 55.44. R_f 0.25 (10:1 *v*/*v* pet ether: diethyl ether) ESI- MS m/z (ion, %) 348 ($[M+H]^+$, 100). IR (Et_2O, cm^{-1}): 3108, 3003, 2960, 2930, 2834, 1621, 1563, 1521, 1494, 1462, 1405, 1361, 1296, 1241, 1174, 1122, 1032, 983, 875, 838, 779, 723, 691, 602. Uv/Vis λMax(Toluene)/nm 315.

The analytical data were obtained in accordance with the literature.[60]

Lab book reference number: jbe-4-193

6-Methoxy-1-(4-methoxyphenyl)-3-o-tolyllisoquinoline (257)

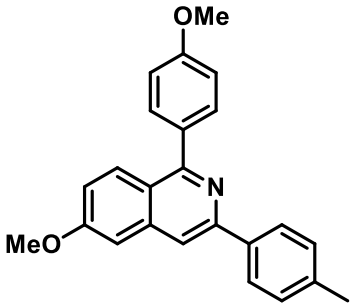

To an oven dried Schlenk that was evacuated, backfilled with N_2 five times and equipped with a magnetic stirrer, 1,1-bis-(4-methoxyphenyl) methanimine (1 eq., 1 mmol, 241 mg), 4-ethynyltoluene (1.5 eq, 1.5 mmol, 190 µL) and [$MnBr(CO)_5$] (0.1 eq., 0.1 mmol, 27.5 mg) were added. Anhydrous deoxygenated dioxane was added and the reaction stirred at 105 ^oC for 3hr, while excluded from ambient light with aluminium foil. Once complete, solvent removed in *vacuo* and the product purified by flash column chromatography (90:10 *v*/*v* pet EtOAc: hexane). to give a colourless oil (80 mg, 22%)

^1H NMR (500 MHz, $CDCl_3$) δ 8.10 (2H, d, J = 7.5 Hz), 8.04 (1H, d, J = 9.0 Hz), 7.92 (1H, s), 7.75 (2H, d, J = 8.0 Hz), 7.29 (2H, d, J = 7.0 Hz), 7.16 (1H, s), 7.09 (3H, m), 3.98 (3H, s), 3.91 (3H, s), 2.42 (3H, s). ^{13}C NMR ($CDCl_3$, 125 MHz) δ 160.63, 160.13, 159.43, 150.83, 140.09, 138.37, 137.11, 132.77, 131.63, 129.51, 129.47, 127.04, 121.50, 119.45, 114.41, 113.83, 105.00, 55.54, 21.40. R_f 0.1 (90:10 *v*/*v* pet EtOAc: hexane). ESI- MS m/z (ion, %) 356 ($[M+H]^+$, 100). IR (ATR, cm^{-1}): 3011, 2972, 2938, 2913, 2853, 1690, 1575, 1516, 1505, 1494, 1461, 1436, 1408, 1398, 1380, 1335, 1296, 1252, 1235, 1216, 1183, 1174, 1157, 1115, 1107, 1095, 1078, 1036, 1025, 1014, 983, 958, 943, 909, 845, 819, 811, 761, 738. Uv/Vis λMax(Toluene)/nm 324.

Lab book reference number: jbe-6-379

fac-[MnBr(1,1-bis-(4-methoxyphenyl)methanimine)$_2$(CO)$_3$] (228)

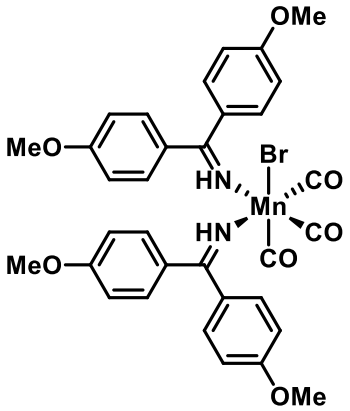

To an Oven dried Schlenk tube under N_2 equipped with a magnetic stirrer, $MnBr(CO)_5$ (1 eq., 0.9 mmol, 274 mg) and 1,1-bis-(4- methoxyphenyl) methanimine (2 eq., 1.8 mmol, 430 mg) were added, evacuated and backfilled with N_2 five times. Then anhydrous deoxygenated 1,4-dioxane was added. The solution was then heated to reflux for 1 hr and the Schlenk tube was covered in aluminium foil to exclude ambient light. Reaction progress was monitored by IR Looking at the metal carbonyl stretching bands. When the reaction was complete, the reaction mixture was allowed to cool to room temperature and solvent removed in *vaccuo*. The crude solid underwent purification by recrystallisation, dissolving the solid in anhydrous deoxygenated methylene chloride and adding the solution to ampule which was evacuated and backfilled with nitrogen. Anhydrous deoxygenated pentane was layered on top of the methylene chloride, the ampule, sealed and excluded from light for several days. This resulted in formation of orange crystals (0.5 g, 80%).

^{1}H NMR (500 MHz, $CDCl_3$) δ 9.62 (2H, s), 7.38 (4H, s), 7.31 (4H, s), 6.92 (8H, m), 3.85 (6H, s), 3.84 (6H, s) .^{13}C NMR ($CDCl_3$, 125 MHz) δ 183.44, 183.19, 163.25, 162.09, 131.76, 131.71, 130.78, 130. 75, 130.37, 130.28, 114.61, 114.10, 56.14, 56.00. LIFDI- MS m/z (ion, %) 700 (M^+, 100). IR (1,4-dioxane, cm^{-1}): 3241, 2757, 2695, 2026, 1939, 1908, 1610, 1589, 1519, 1510, 1422. Uv/Vis λMax(Toluene)/nm 374 and 351sh.

Lab book reference number: jbe-6-379

Nonacarbonyl (1,1-bis-(4-methoxyphenyl)methanimine) dimanganese(0) (216)

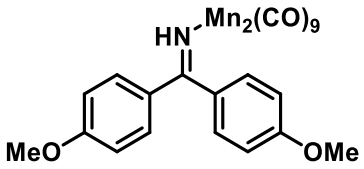

To a round-bottom flask equipped with a magnetic stirrer was added 1,1-bis(4-methoxyphenyl) methanimine (1 eq., 1 mmol, 241 mg), [$Mn_2(CO)_{10}$] (1 eq., 1 mmol, 389 mg) and methylene chloride (40 mL). Trimethylamine N-oxide (1 eq., 1 mmol, 80 mg) was added 5 mg at a time. The solution was left stirring at ambient temperature for 1 hour, before being filtered through an alumina plug. The plug was washed with hexane (50 mL), then Et_2O (50 mL). The Et_2O fraction was reduced in *vacuo* and the resulting solid was recrystalised from boiling hexane, giving orange crystals (201 mg, 33%).

^1H NMR (500 MHz, CD_2Cl_2) δ 7.27 (2H, m), 7.05 (2H, m), 6.99 (2H, m), 6.81 (2H, m), 3.89 (3H, s), 3.81 (3H, s). ^{13}C NMR (CD_2Cl_2, 125 MHz) δ 186.01, 161.75, 160.61, 130.38, 10.33, 128.77, 128.47, 113.25, 112.98, 52.66, 52.23. LIFDI- MS m/z (ion, %): 602.96135 ($[M]^+$, 100). IR (toluene, cm^{-1}): 3087, 3063, 2084, 2019, 1998, 1980, 1958, 1929, 1717, 1603, 1360, 1218, 1082, 1030. Uv/Vis λMax(Toluene)/nm 348 and 440sh.

Lab book reference number: jbe-5-344

1,1-bis-(3-fluoro-4-methoxyphenyl)methanone (238)

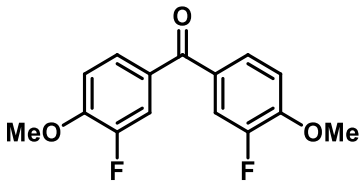

To an oven dried Schlenk flask equipped with a magnetic stirrer was added oven dried Mg turnings (2.5 eq., 20 mmol, 486 mg). The flask was evacuated and backfilled with N_2 five times, anhydrous deoxygenated THF (20 mL) added and a crystal of I_2. 3-fluoro-4-bromo anisole (2.5 eq., 20 mmol, 20 mL) was added dropwise while the solution was heated with a heat gun. Once the colour of iodine had gone, the solution was heated at reflux for 3 hours. Upon completion, the solution was cooled to -78 °C with a dry ice acetone bath.

To a second oven dried Schlenk flask equipped with a magnetic stirrer was added 1,1'-Carbonyldiimidazole (1 eq., 8 mmol, 1.29 g). The flask was evacuated and backfilled with N_2 five times, anhydrous deoxygenated THF (20 mL) added and the solution cooled down to -78 °C with a dry ice acetone bath. The Grignard solution was added dropwise and stirred at -78 °C for 15 minutes, before being warmed to ambient temperature and stirred overnight. The reaction mixture was quenched with saturated ammonium chloride (30 mL), extracted with EtOAc (3×30 mL), washed with $NaHCO_3$ (30 mL), dried with Na_2SO_4 and the solvent removed in *vacuo*. The crude material was recrystalised from methylene chloride/hexane to yield a white powder (1.6 g, 72%).

M.p 163.3-163.8 °C. ^{1}H NMR (500 MHz, $CDCl_3$) δ 7.62-7.50 (4H, m), 7.03 (2H, dd, J = 8.0, 8.0 Hz), 3.98 (6H, s). ^{13}C NMR (125 MHz, $CDCl_3$) δ 151.9 (d, J = 246.0 Hz), 151.5 (d, J = 10.0 Hz), 130.5 (d, J = 5.0 Hz), 127.4 (d, J = 2.5 Hz), 117.7 (d, J = 19.0 Hz), 112.4 (d, J = 2.5 Hz), 56.4. ^{19}F NMR (470 MHz, $CDCl_3$) δ -134.12 (m). R_f 0.4 (60:40 *v*/*v* hexane: EtOAc). IR (ATR, cm^{-1}): 3075, 2963, 2601, 1637, 1611, 1575, 1514, 1447, 1430, 1326, 1287, 1271, 1236, 1211, 1192, 1179, 1129, 1015, 920, 823, 803, 762, 749, 711, 617 564.

Lab book reference number: jbe-5-291

1,1-bis-(3-fluoro-4-methoxyphenyl)methanimine (239)

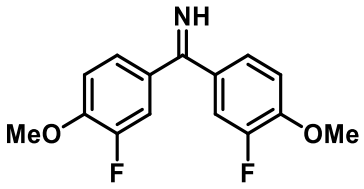

To an oven dried Schlenk equipped with a magnetic stirrer was added 1,1-bis-(3fluoro-4methoxyphenyl)methanone (1 eq., 4 mmol, 1.1 g). The flask was evacuated and backfilled with N_2 five times and anhydrous deoxygenated THF (20 mL) added. The solution was cooled to 0 °C with a salt ice bath and $TiCl_4$ (1.25 eq., 5 mmol, 0.55 mL) added dropwise. Subsequently 0.5 M NH_3 in THF (4 eq., 16 mmol, 16 mL) was added dropwise, the reaction mixture allowed to warm to room temperature, and stirred at ambient temperature overnight. The reaction mixture was stirred over Na_2CO_3 (50 mL) for 10 minutes, the organic layer washed with $Na_2(CO)_3$ (25 mL), brine (25 mL), dried with Na_2SO_4 and solvent removed in *vacuo*. The crude material was used immediately in the synthesis of (**234**).

^{1}H NMR (500 MHz, CD_2Cl_2) δ 7.35-7.29 (4H, m), 7.05-7.00 (2H, m), 3.93 (6H, s). ^{13}C NMR (125 MHz, CD_2Cl_2) δ 175.1, 151.9 (d, J = 245.0 Hz), 149.6 (d, J = 11.0 Hz), 132.0 (d, J = 5.0 Hz), 125.1 (d, J = 4.0 Hz), 116.0 (d, J = 20.0 Hz), 112.8 (d, J = 2.5 Hz), 56.3. ^{19}F NMR (470 MHz, CD_2Cl_2) δ -135.32 (m). R_f 0.3 (30:70 *v*/*v* pet ether: hexane).* LIFDI- MS m/z (ion, %): 277.08811 ($[M]^+$, 100).

*Slight degradation on the TLC plate.

Lab book reference number: jbe-5-295

fac-[MnBr(1,1-bis-(3-fluoro-4-methoxyphenyl)methanimine)$_2$(CO)$_3$] (234)

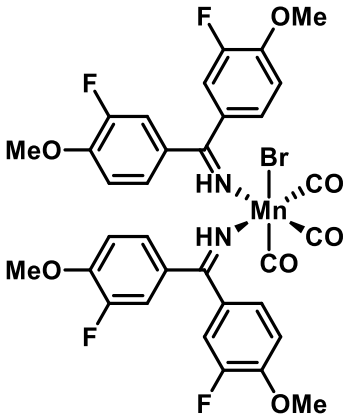

To an oven dried Schlenk equipped with a magnetic stirrer was added 1,1-bis-(3fluoro-4methoxyphenyl)methanimine (2 eq., 0.46 mmol, 130 mg) and [MnBr(CO)$_5$] (1 eq., 0.23 mmol, 65 mg). The flask was evacuated and backfilled with N_2 five times and anhydrous degassed toluene (20 mL) added. The reaction mixture was heated at 60 °C for 2 hours and reaction progress followed *via* IR aliquots. Upon completion, the solvent was removed in *vacuo* and the product crystalised from methylene chloride/pentane to afford the title compound as orange crystals (31 mg, 18%).

^{1}H NMR (500 MHz, CD_2Cl_2) δ 9.90 (2H, s), 7.32-7.02 (12H, m), 3.94 (12H, s). ^{13}C NMR (125 MHz, CD_2Cl_2) δ 181.6, 152.7(d, J = 13.5 Hz), 151.3 (d, J = 11.5 Hz), 150.9 (d, J = 15.0 Hz), 150.1 (d, J = 10.0 Hz), 130.5 (d, J = 6.5 Hz), 129.2 (d, J = 7.0 Hz), 126.2, 125.4, 117.2 (d, J = 20.0 Hz), 116.0 (d, J = 20.0 Hz), 113.2, 113.2, 56.5, 56.4. ^{19}F NMR (470 MHz, CD_2Cl_2) δ -133.70 (1F, s), 134.46 (1F, s). LIFDI- MS m/z (ion, %): ([M]$^+$, 100). IR (toluene, cm^{-1}): 2025, 1946, 1916, 1526, 1280.

Lab book reference number: jbe-5-296

fac-[MnBr(1,1-bis-(3-fluoro-4methoxyphenyl)methanimine)(1,1-bis-(4-methoxyphenyl)methanimine)$(CO)_3$] (258)

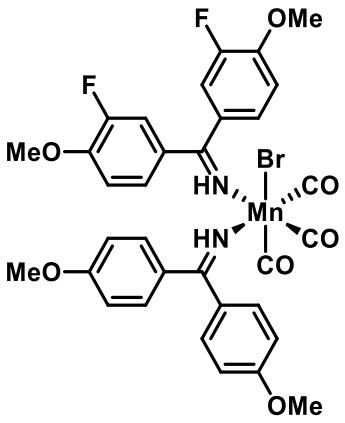

To an oven dried J Youngs NMR tube was added compound 228 (1 eq., 0.1 mmol, 1.5 mg) and compound 234 (1 eq., 0.1 mmol, 1.5 mg). The tube was evacuated and backfilled with N_2 five times, anhydrous deoxygenated toluene (0.4 mL) added and heated at 105 °C for 30 minutes. The crude reaction mixture was analysed *via* ^{19}F NMR, IR spectroscopy.

^{19}F NMR (470 MHz, CD_2Cl_2) δ -133.38, -134.27. IR (toluene, cm^{-1}): 2023, 1941, 1911, 1608, 1460, 1255.

Lab book reference number: jbe-5-316

Tetracarbonyl [η^2-2-(phenyl C=NH)-5-phenyl manganese(I) (182)

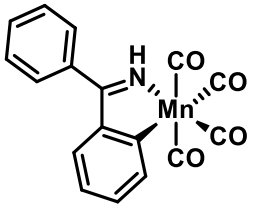

An oven dried Schlenk flask equipped with a magnetic stirrer was evacuated and backfilled with N_2 five times. Anhydrous deoxygenated THF (40 mL), benzonitrile (1 eq., 30 mmol, 4.2 mL) and 1 M phenyl magnesium bromide in THF (1.1 eq., 33 mmol, 33 mL) were added. The reaction mixture was heated at reflux overnight, then cooled to 0 °C with a salt ice bath. Anhydrous deoxygenated methanol (5 mL) was added dropwise, and the reaction mixture stirred for 30 minutes. The solution was diluted with Et_2O (50 mL), filtered through a celite® plug and solvent removed in *vacuo* to give a yellow oil.

Crude 1,1-diphenylmethanimine (1 eq., 0.65 mmol, 130 µL), pentacarbonyl benzylmanganese(I) (1 eq., 0.65 mmol, 150 mg) and anhydrous deoxygenated toluene (30 mL) were added to a second oven dried Schlenk flask equipped with a magnetic stirrer that was evacuated and backfilled with N_2 five times. The reaction mixture was heated at 100 °C for 1 hour, with reaction progress monitored *via* IR aliquots. Upon completion solvent was removed and the crude material purified *via* flash column chromatography (70:30 *v*/*v* hexane: EtOAc) to afford a yellow solid (105 mg, 47 %).

^{1}H NMR (500 MHz, CD_2Cl_2) δ 8.38 (1H, s), 8.10 (1H, dd, 7.5, 1.5 Hz), 7.62-7.50 (4H, m), 7.50-7.45 (2H, m), 7.34 (1H, ddd, 7.5, 7.5, 1.5 Hz), 7.14 (1H, ddd, 7.5, 7.5, 1.5 Hz). ^{13}C NMR (125 MHz, CD_2Cl_2) δ 220.3, 215.6, 213.8, 190.9, 183.4, 146.7, 141.5, 136.8, 131.6, 131.3, 131.1, 129.3, 127.9, 123.8. R_f 0.43 (70:30 *v*/*v* hexane: EtOAc) LIFDI- MS m/z (ion, %) 246.99846 ([M]$^+$, 100). IR (hexane, cm^{-1}): 2076, 1992, 1982, 1944, 1749, 1384, 1373, 1292, 1246, 1239, 1224, 1065. Uv/Vis λMax(Toluene)/nm 350.

Lab book reference number: jbe-6-402

Pentacarbonyl (*p*-tolylacetylide) manganese(I) (223)

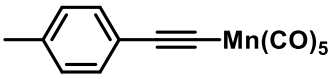

An oven dried Schlenk flask equipped with a magnetic stirrer was evacuated and backfilled with N_2 five times. 1-ethynyl-4-methylbenzene (1 eq., 4.5 mmol, 0.57 mL) and anhydrous deoxygenated THF (30 mL) were added, and the solution cooled to -78 °C with a dry ice acetone bath. 2.5 M n-butyllithium in hexane (1 eq., 4.5 mmol, 1.8 mL) was added dropwise, the solution stirred at -78 °C for 30 minutes, then warmed up to ambient temperature. In a separate oven dried Schlenk flask equipped with a magnetic stirrer was added [$MnBr(CO)_5$] (1 eq., 4.5 mmol, 1.2 g). The flask was evacuated and backfilled five times with N_2, and anhydrous deoxygenated THF (45 mL) added. The [$MnBr(CO)_5$] solution was added slowly to the initial Schlenk flask, and the reaction mixture stirred for 1 hour. H_2O (45 mL) was added and extracted with methylene chloride (3×30 mL), organic layers combined, dried over $MgSO_4$, and solvent removed in *vacuo*. The crude material was purified by flash column chromatography (99:1 *v*/*v* hexane: EtOAc), fractions combined, stirred over activated carbon, filtered and solvent removed in *vacuo* to afford the title compound as a pale-yellow solid (1.1g, 79%).

Mp 110−113 °C. ^{1}H NMR (500 MHz, CD_2Cl_2) δ 7.23 (2H, d, J = 7.5 Hz), 7.06 (2H, d, J = 7.5 Hz), 2.31 (3H, s). ^{13}C NMR (125 MHz, CD_2Cl_2) δ 208.2, 207.5, 136.5, 131.5, 129.1, 124.6, 116.9, 89.0, 21.4. R_f 0.2 (99:1 *v*/*v* hexane: EtOAc). LIFDI- MS m/z (ion, %) 309.96685 ($[M]^+$, 100). IR (methylene chloride, cm^{-1}): 3005, 2135, 2110, 2041, 2010, 1740, 1436, 1273. Uv/Vis λMax(Toluene)/nm 293.

The analytical data were obtained in accordance with the literature.[51]

Lab book reference number: jbe-6-405

Pentacarbonyl manganese(I) Iodide (259)

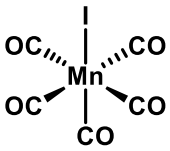

An oven dried Schlenk flask equipped with a magnetic stirrer was evacuated and backfilled with N_2 five times. $[Mn_2(CO)_{10}]$ (1 eq., 2 mmol, 760 mg), I_2 (1 eq., 2mmol, 504 mg) and anhydrous deoxygenated methylene chloride (50 mL) were added, and the solution was stirred at 25 °C for 6 hours. Reaction progress was followed *via* IR aliquots and upon completion solvent, $[Mn_2(CO)_{10}]$ and I_2 removed in *vacuo*. The remaining solid was washed with cold hexane (100 mL) to give an orange solid (512 mg, 79%)

LIFDI- MS m/z (ion, %) 321 ($[M]^+$, 100). IR (MeCN, cm^{-1}): 2132, 2046, 2011, 1980. Uv/Vis λMax(Toluene)/nm 344.

The analytical data were obtained in accordance with the literature.[175]

Lab book reference number: jbe-6-394

Pentacarbonyl manganese(I) Chloride (249)

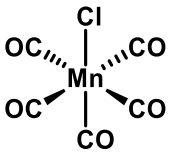

An oven dried Schlenk flask equipped with a magnetic stirrer was evacuated and backfilled with N_2 five times. [$Mn_2(CO)_{10}$] (1 eq., 2.76 mmol, 1 g), sulfuryl chloride (17.4 eq., 48 mmol, 4 mL) and anhydrous deoxygenated methylene chloride (75 mL) were added. The reaction mixture was stirred at ambient temperature for 8 days and reaction progress followed *via* IR aliquots. Upon completion the solvent was removed and the crude material washed with cold ethanol to afford a yellow solid (274, 54%).

IR (MeCN, cm^{-1}): 2143, 2053, 2011, 1977. Uv/Vis λMax(Toluene)/nm 345.*

The analytical data were obtained in accordance with the literature.[176]

Lab book reference number: jbe-6-395

*Did not fly by LIFDI MS.

fac-Tricarbonyl triacentonitrile manganese(I) hexafluorophosphate (215)

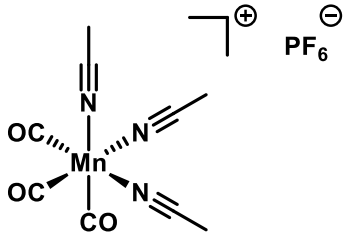

An oven dried Schlenk flask equipped with a magnetic stirrer was evacuated and backfilled with N_2 five times. $[Mn_2(CO)_{10}]$ (1 eq., 10 mmol, 3.9 g) was dissolved in anhydrous deoxygenated MeCN (90 mL) and $NOPF_6$ (2 eq., 20 mmol, 5 g) was added. The reaction mixture was stirred at ambient temperature for 1 hour, reduced to approx. 30 mL, heated at 50 °C for 24 hr and solvent removed to afford a pale-yellow solid (1.1 g, 20%). Crude material was used immediately in the subsequent React IR^{TM} experiment.

IR (MeCN, cm^{-1}): 1975, 2065.*

The analytical data were obtained in accordance with the literature.[177]

Lab book reference number: jbe-6-343

*Did not fly by LIFDI MS.

Octacarbonyl dimanganese(I) μ_2-dibromide (240)

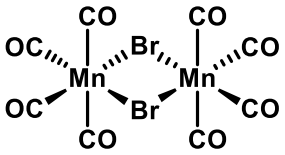

To an oven dried Schlenk flask equipped with a magnetic stirrer was added $[MnBr(CO)_5]$ (1 eq., 2 mmol, 560 mg). The flask was evacuated and backfilled five times with N_2, and anhydrous deoxygenated hexane (40 mL) added. The hexane solution of $[MnBr(CO)_5]$ was heat at 60 °C overnight, then filtered to yield red crystals of title compound (400 mg, 81%).

LIFDI- MS m/z (ion, %) 309.96685 ($[M]^+$, 100). IR (methylene chloride, cm^{-1}): 3028, 2102, 2045, 2012, 1976, 1603, 1496, 1082, 1029. Uv/Vis λMax(Toluene)/nm 430.

Lab book reference number: jbe-5-337

6.3 NMR Spectra of Compounds

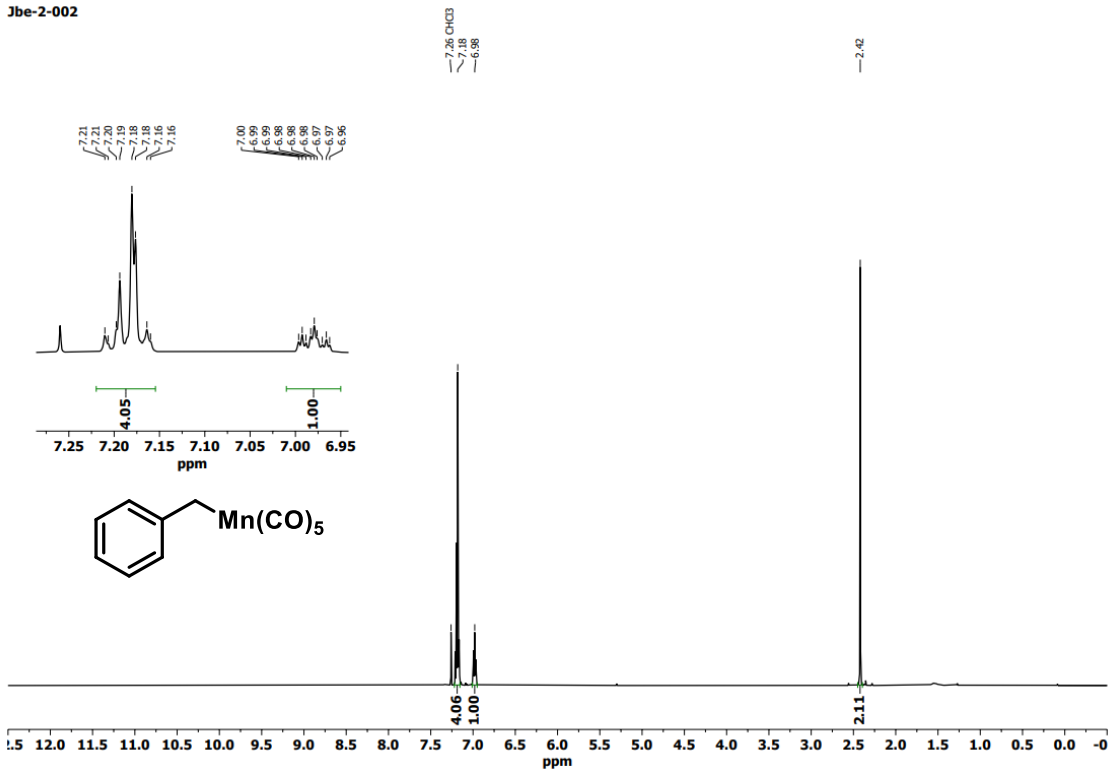

Figure 172. ^{1}H NMR spectrum of compound **212** in deuterated chloroform.

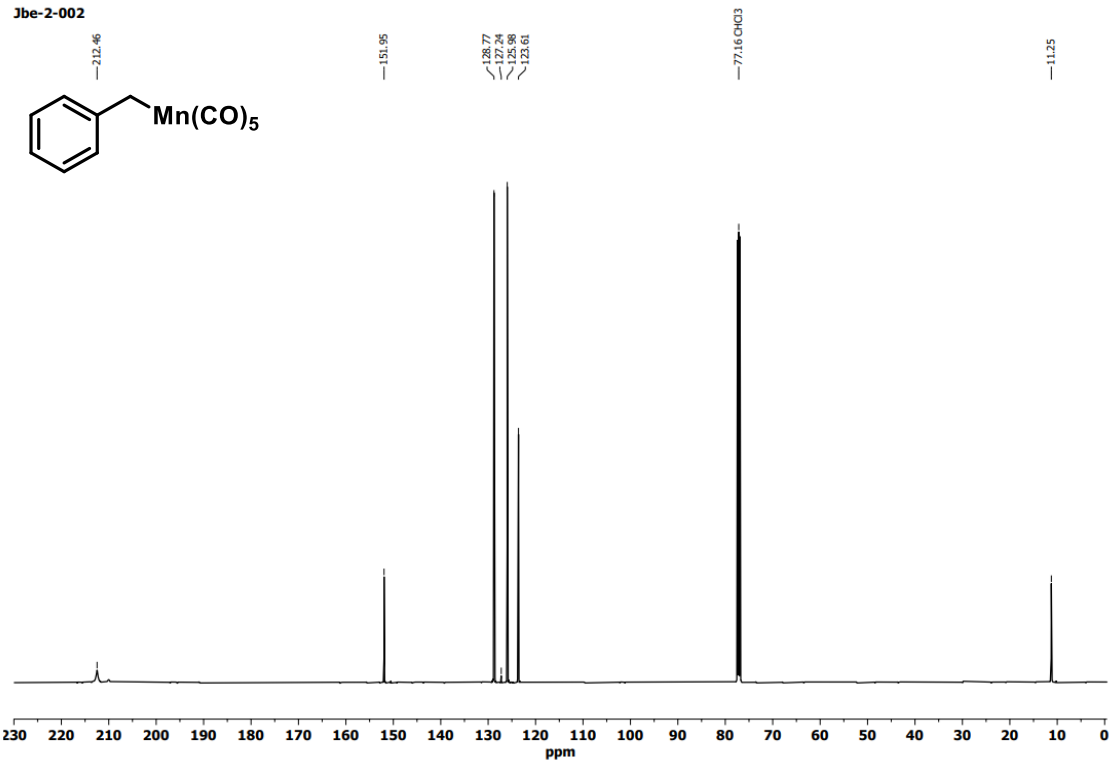

Figure 173. ^{13}C NMR spectrum of compound **212** in deuterated chloroform.

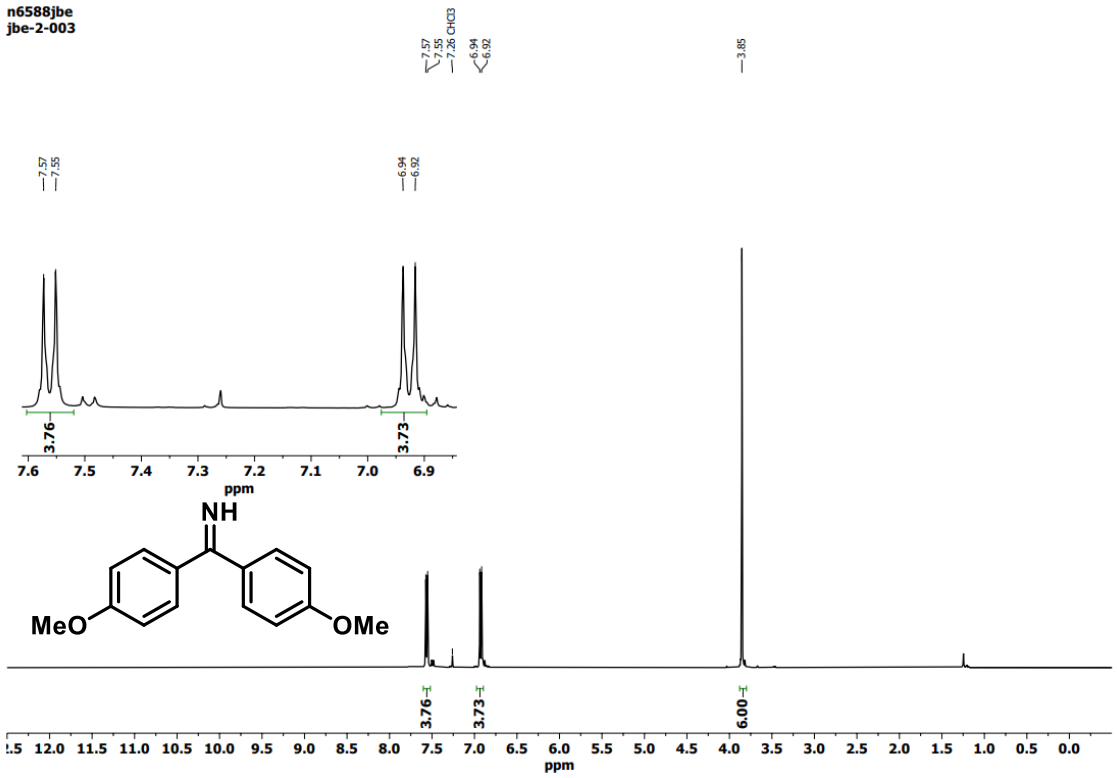

Figure 174. ^{1}H NMR spectrum of compound **178** in deuterated chloroform.

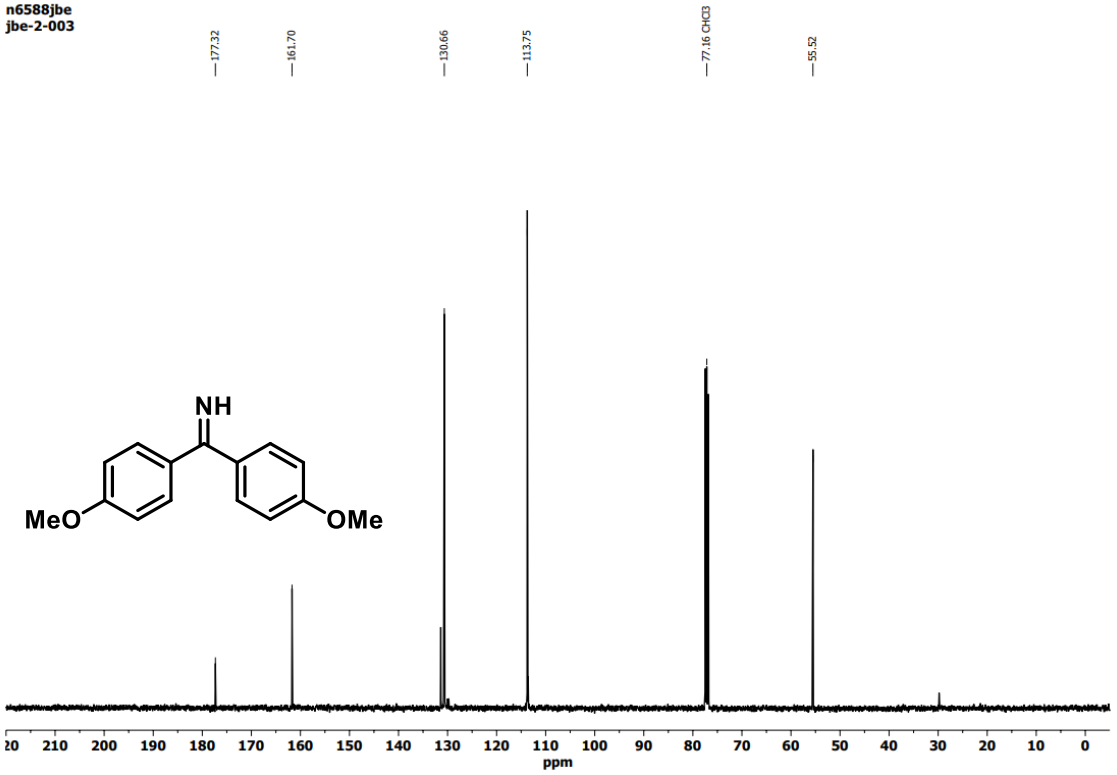

Figure 175. ^{13}C NMR spectrum of compound **178** in deuterated chloroform.

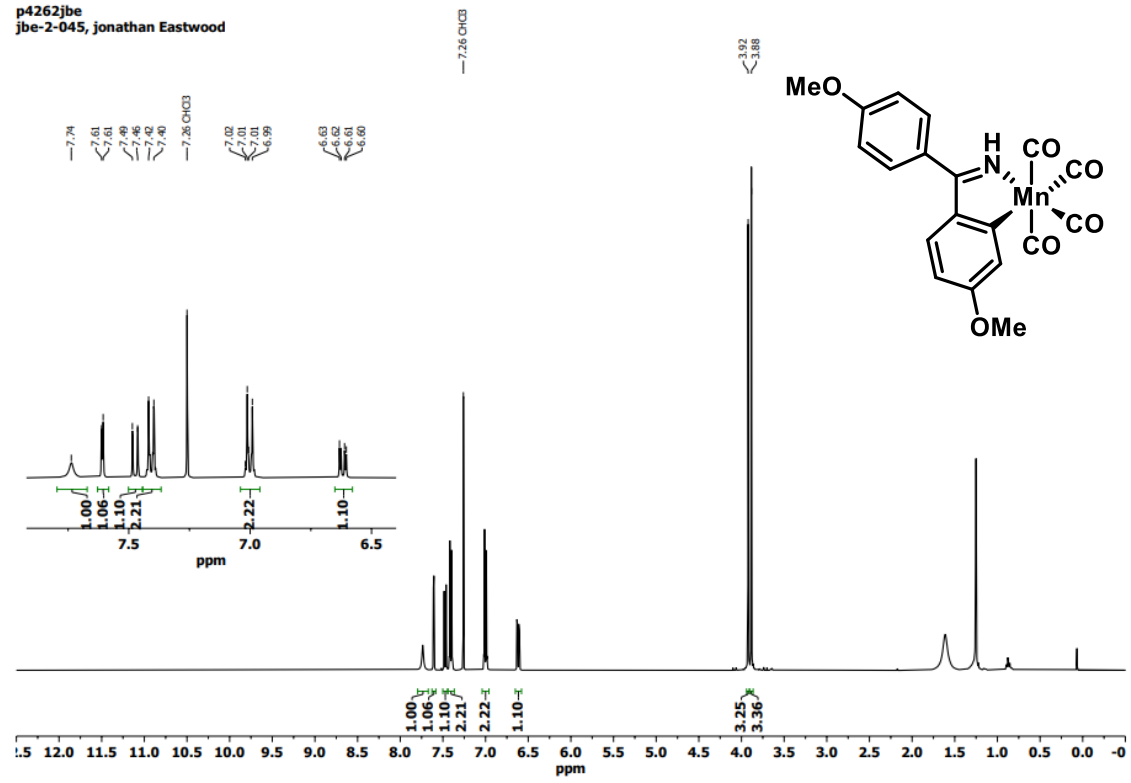

Figure 176. ^{1}H NMR spectrum of compound **158** in deuterated chloroform.

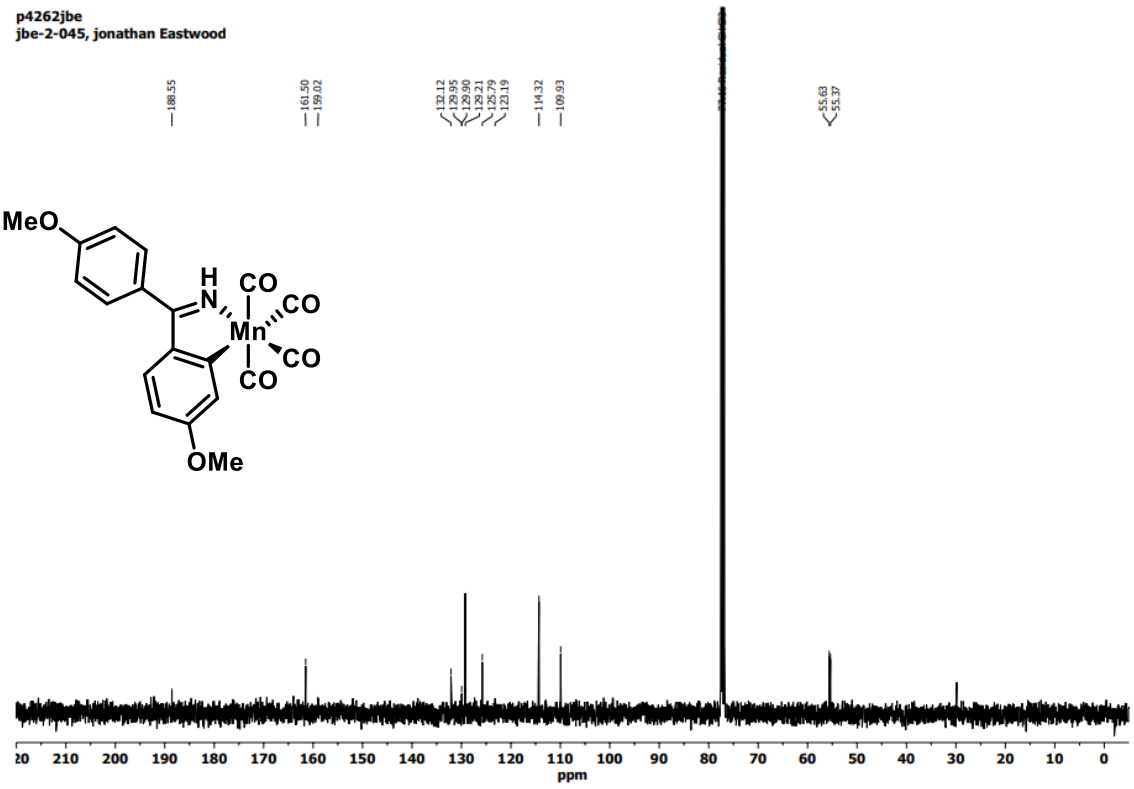

Figure 177. ^{13}C NMR spectrum of compound **158** in deuterated chloroform.

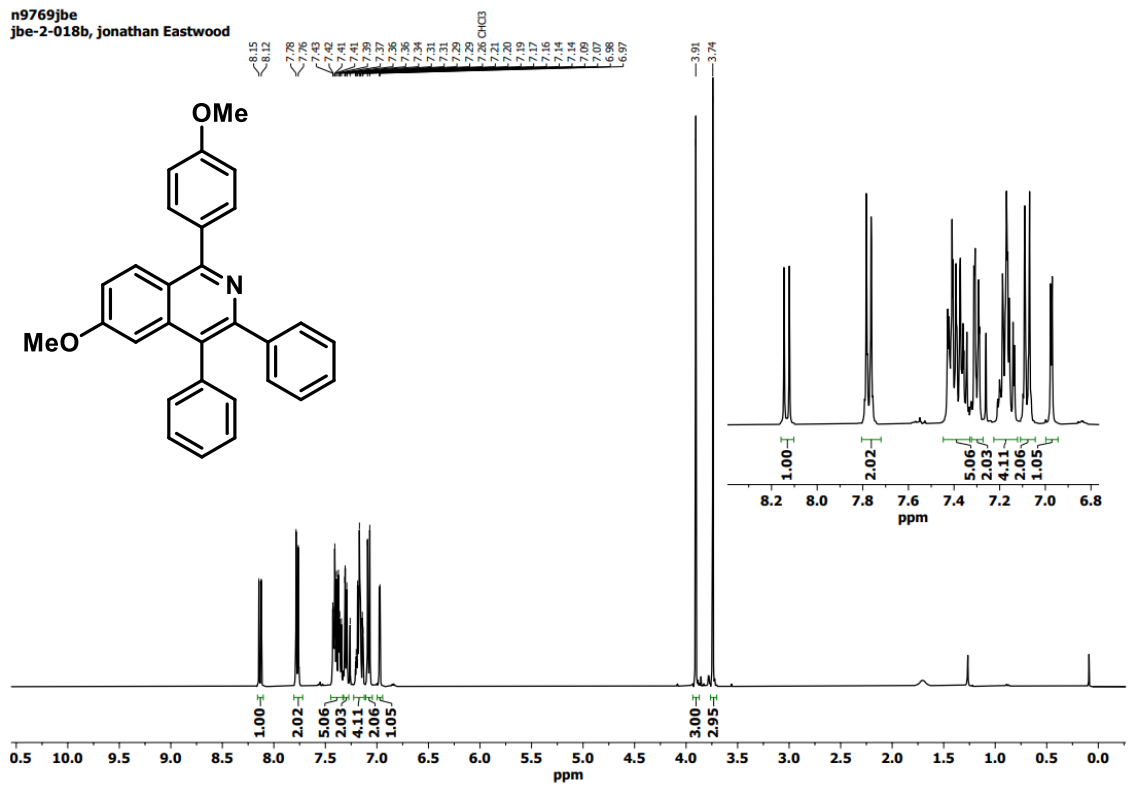

Figure 178. ^{1}H NMR spectrum of compound **180** in deuterated chloroform.

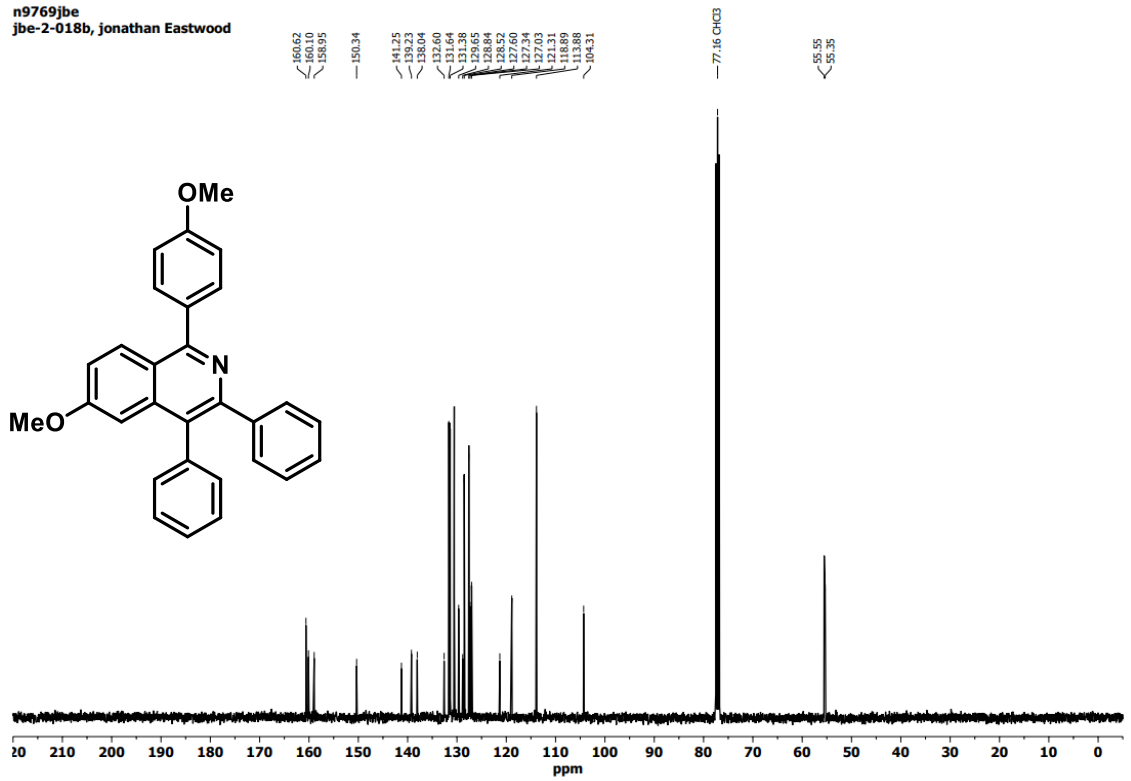

Figure 179. ^{13}C NMR spectrum of compound **180** in deuterated chloroform.

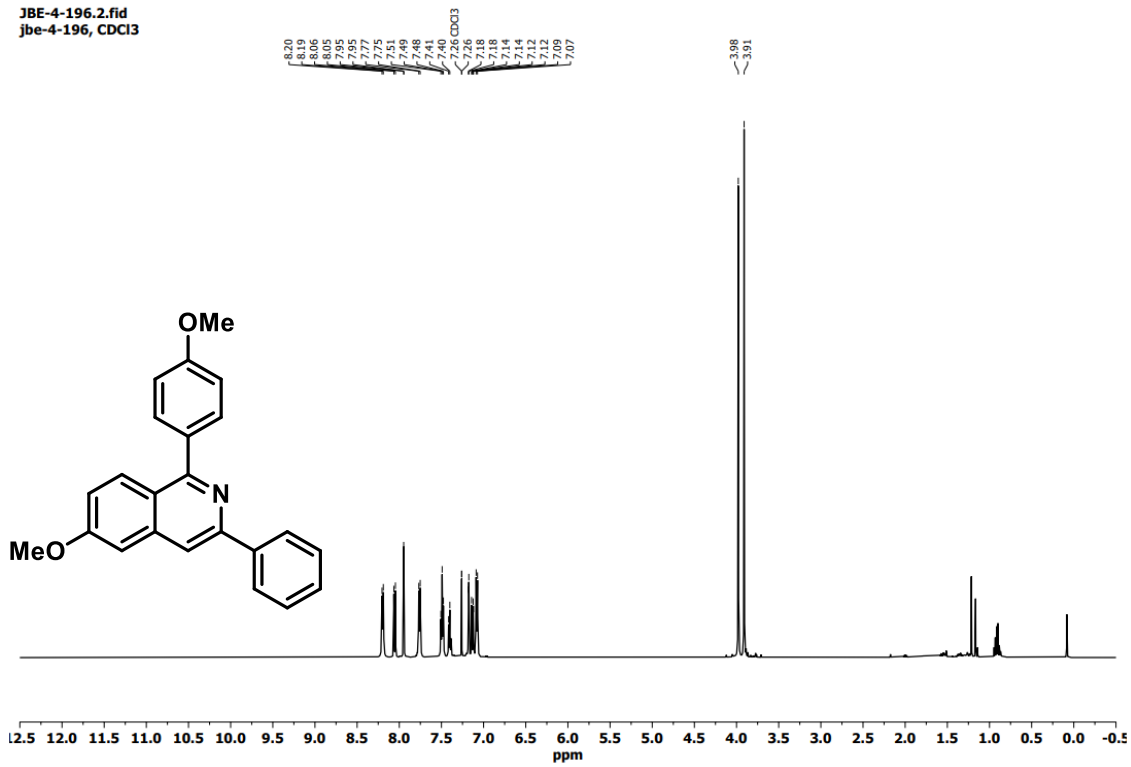

Figure 180. ^{1}H NMR spectrum of compound **231** in deuterated chloroform.

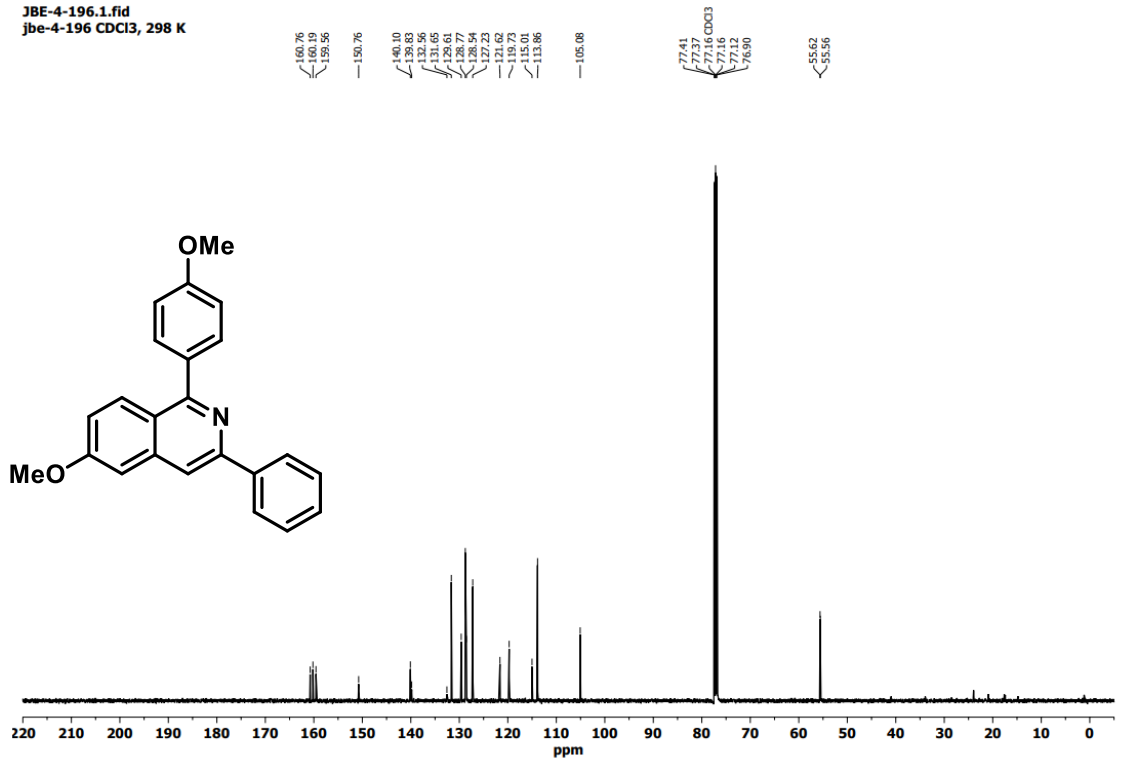

Figure 181. ^{13}C NMR spectrum of compound **231** in deuterated chloroform.

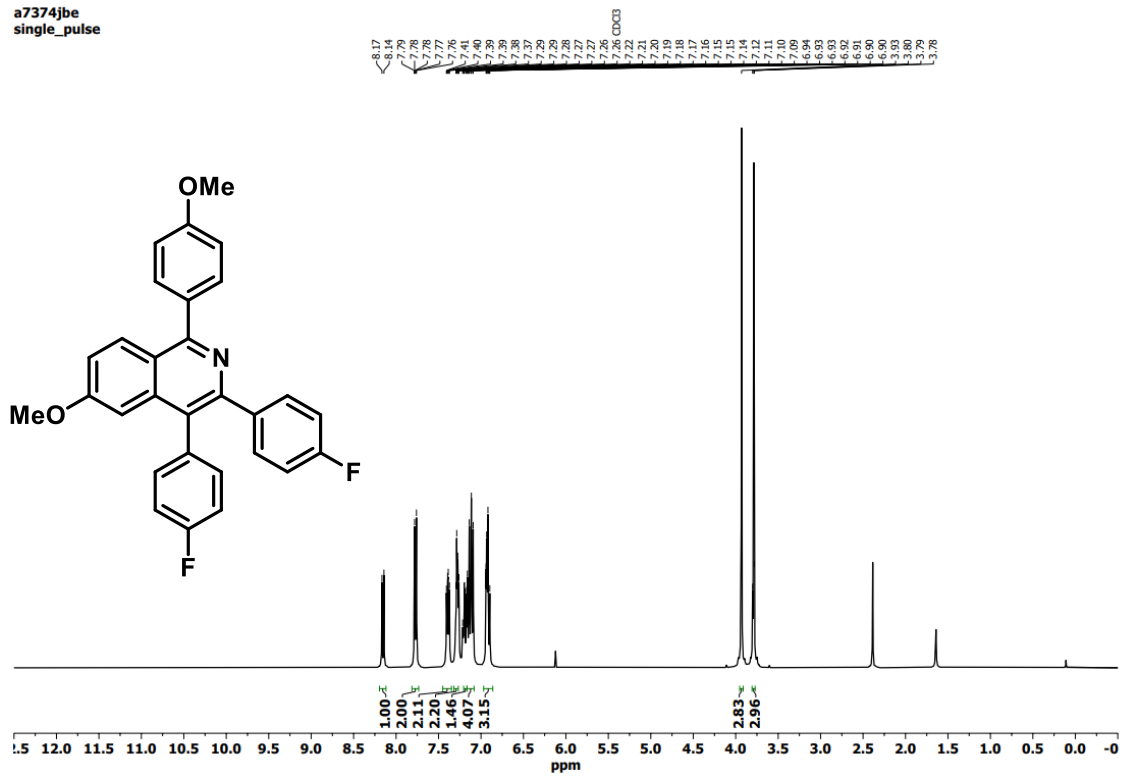

Figure 182. ^{1}H NMR spectrum of compound **253** in deuterated chloroform.

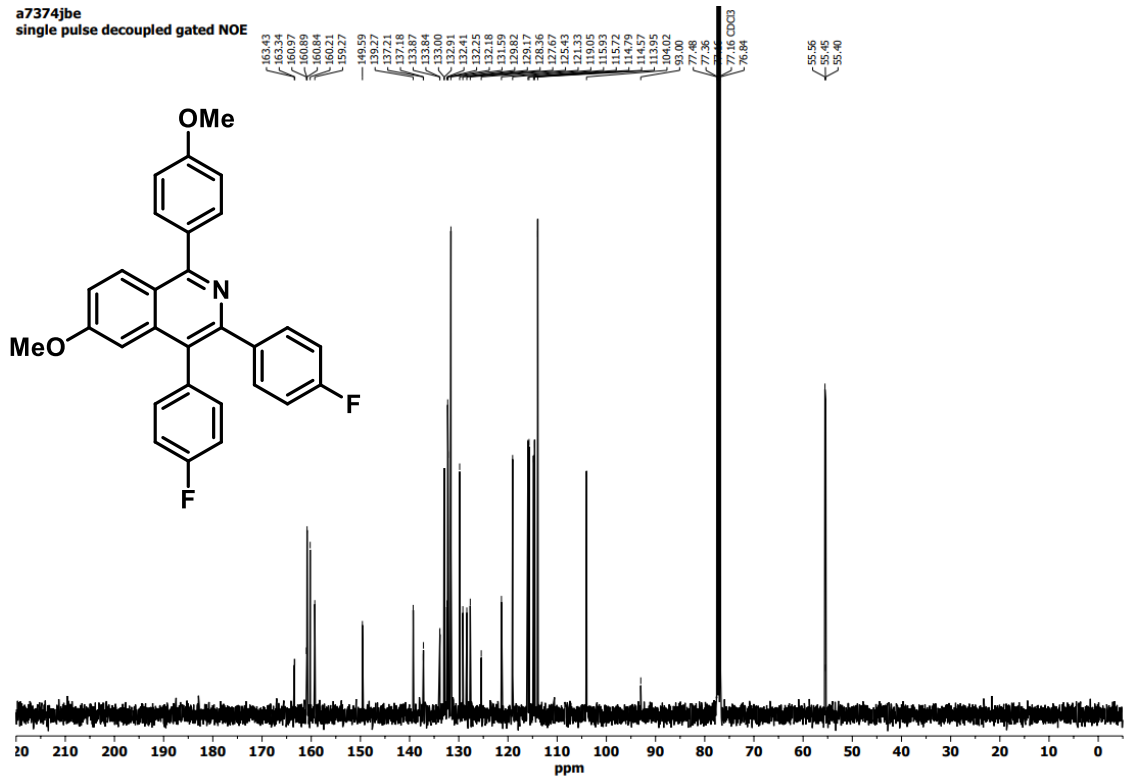

Figure 183. ^{13}C NMR spectrum of compound **253** in deuterated chloroform.

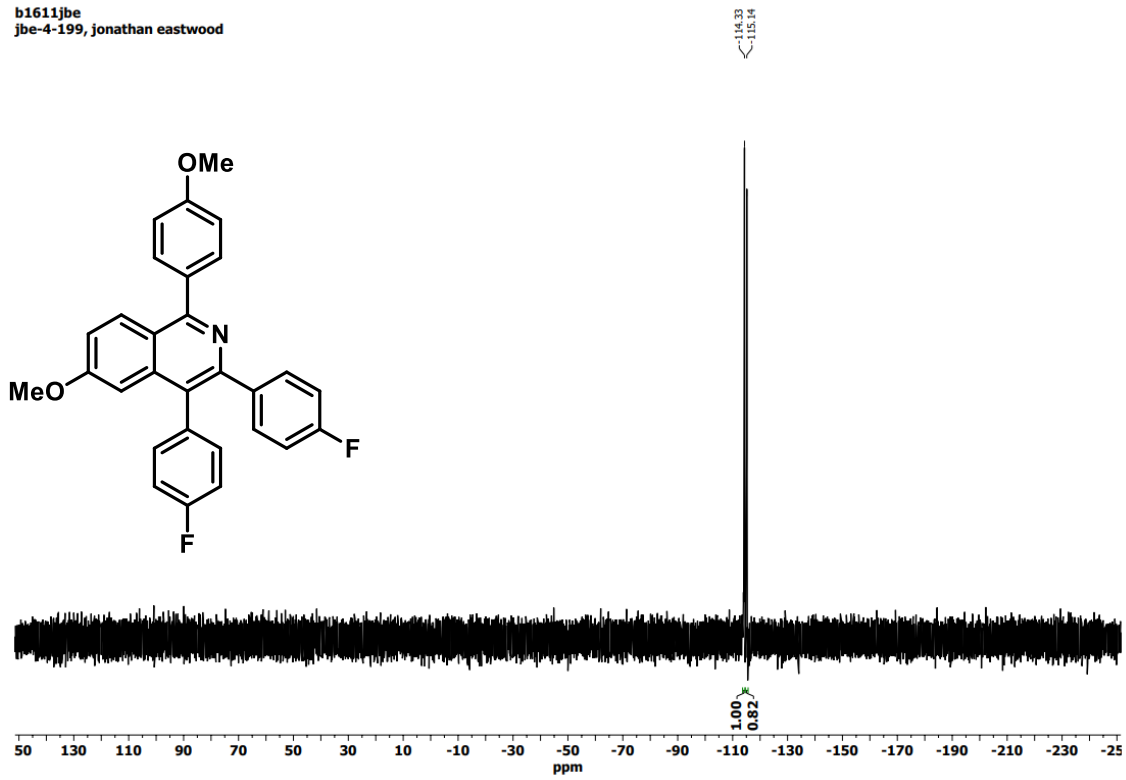

Figure 184. ^{19}F NMR spectrum of compound **253** in deuterated chloroform.

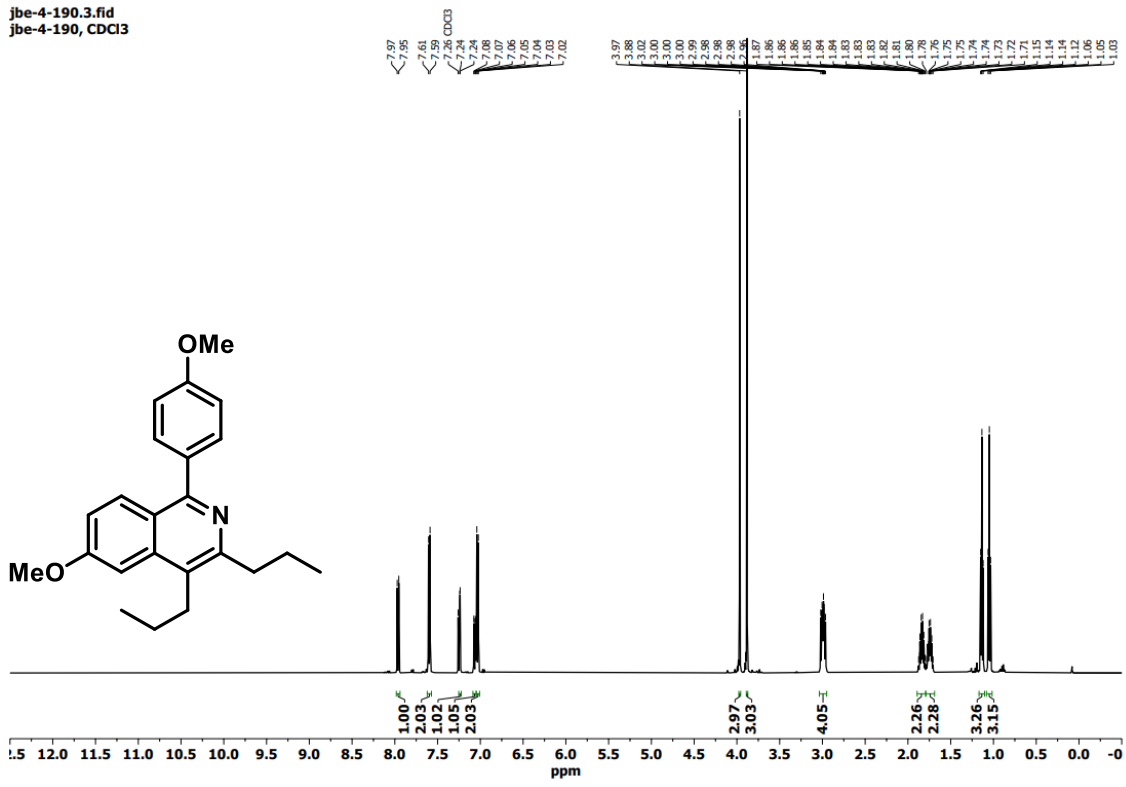

Figure 185. ^{1}H NMR spectrum of compound **254** in deuterated chloroform.

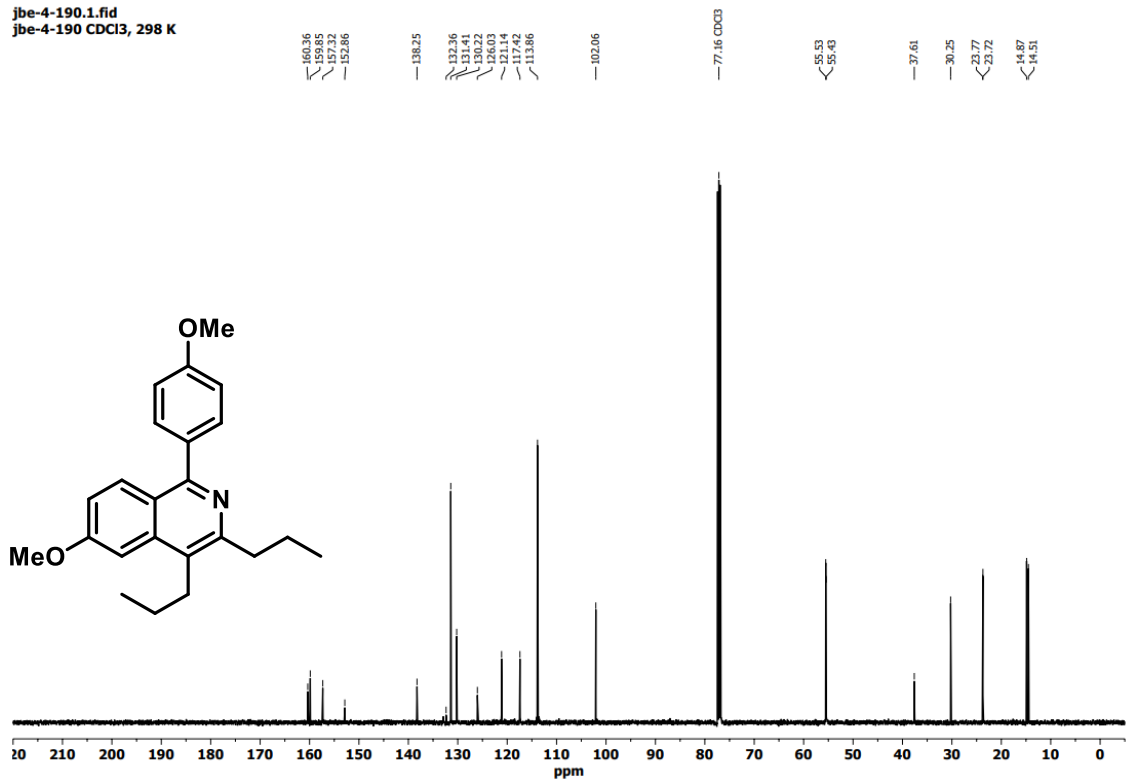

Figure 186. ^{13}C NMR spectrum of compound **254** in deuterated chloroform.

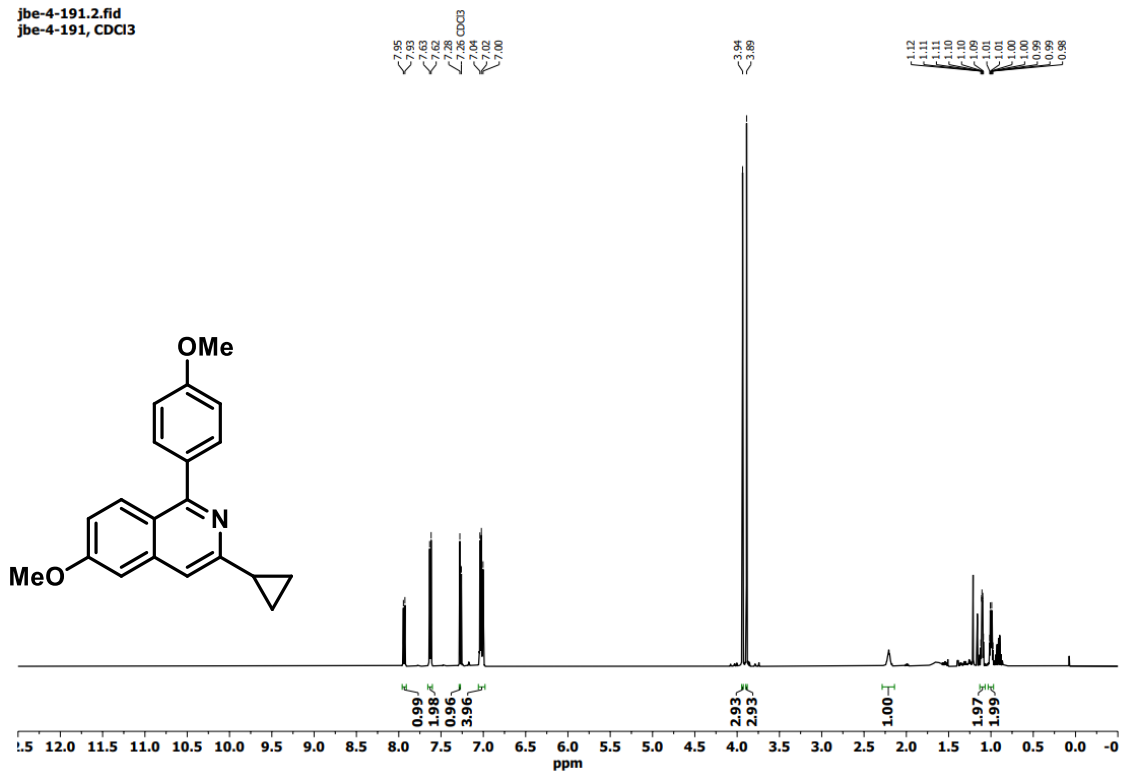

Figure 187. ^{1}H NMR spectrum of compound **255** in deuterated chloroform.

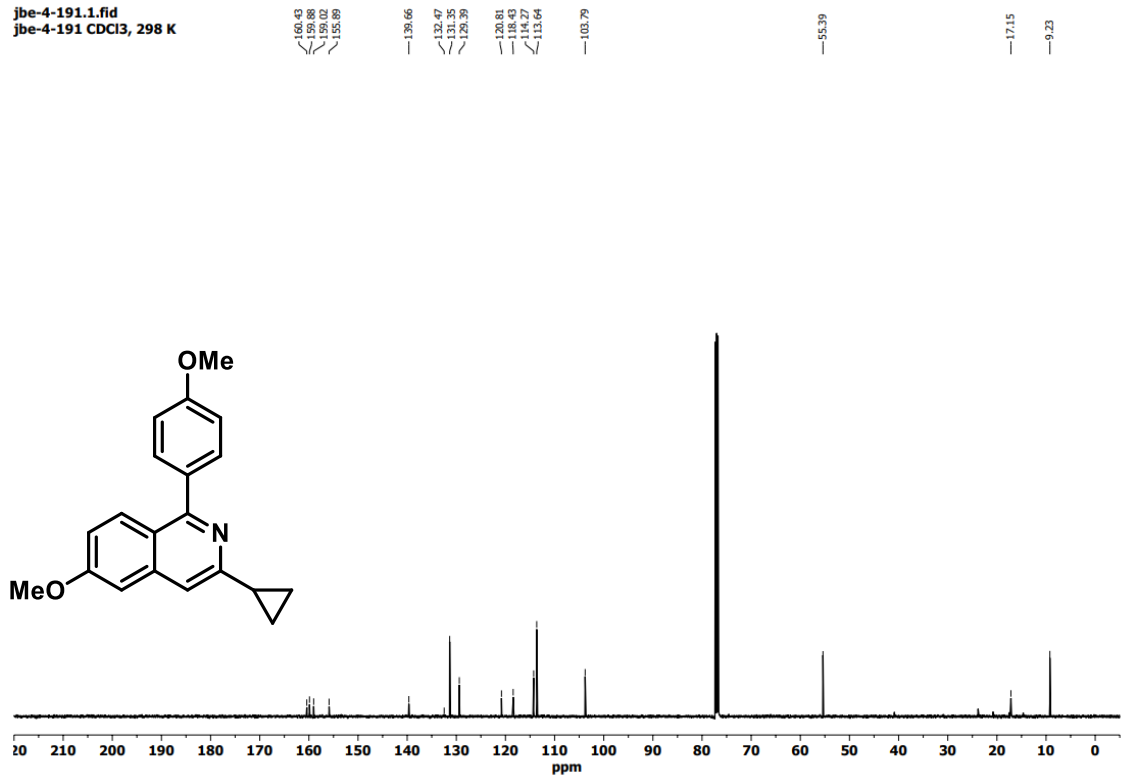

Figure 188. ^{13}C NMR spectrum of compound **255** in deuterated chloroform.

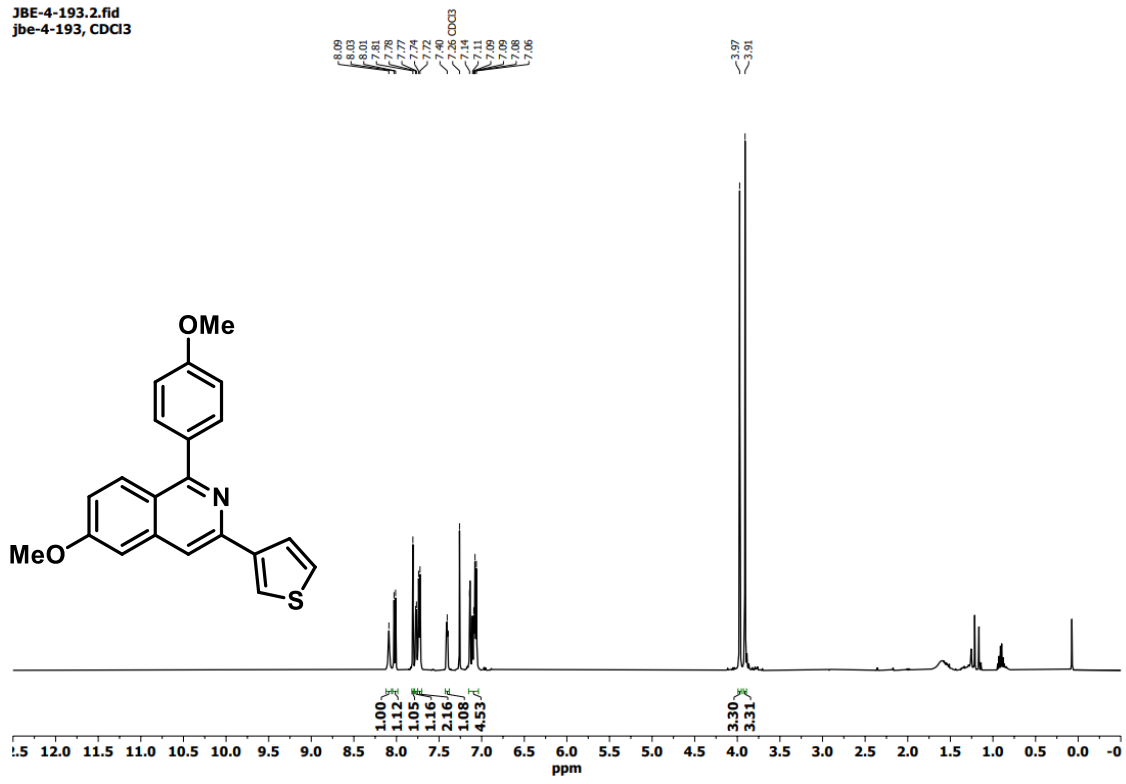

Figure 189. ^{1}H NMR spectrum of compound **256** in deuterated chloroform.

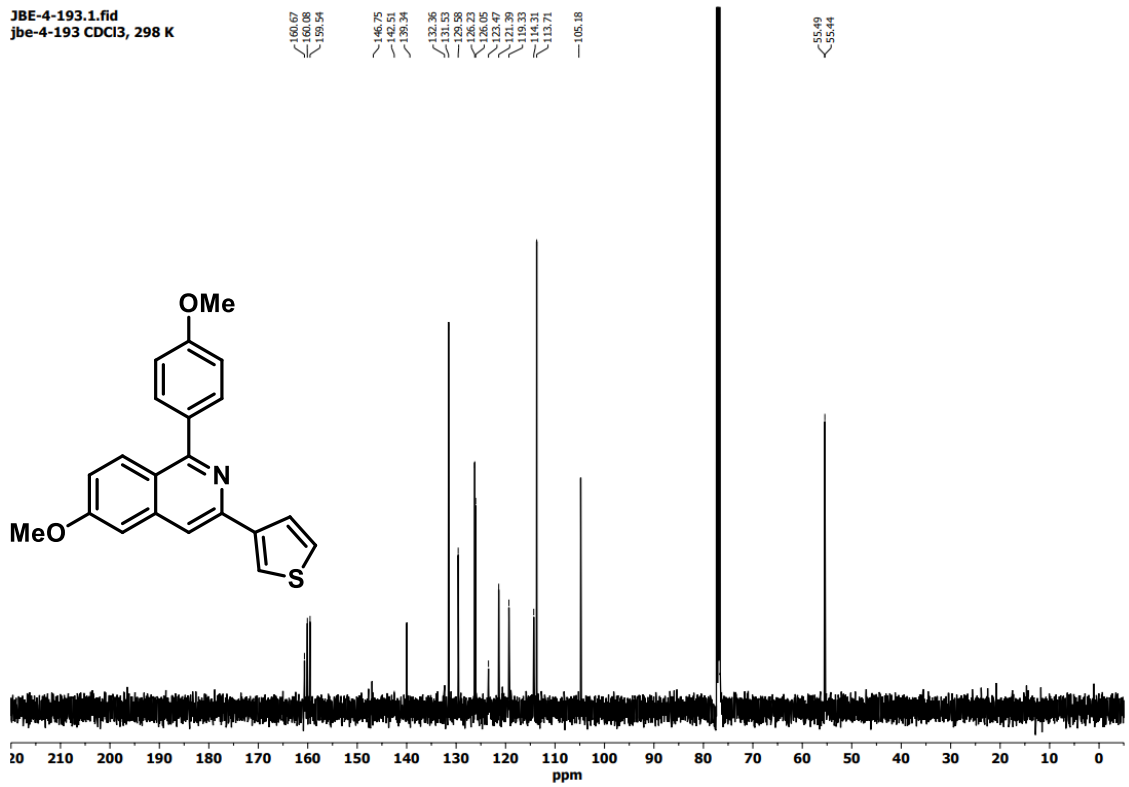

Figure 190. ^{13}C NMR spectrum of compound **256** in deuterated chloroform.

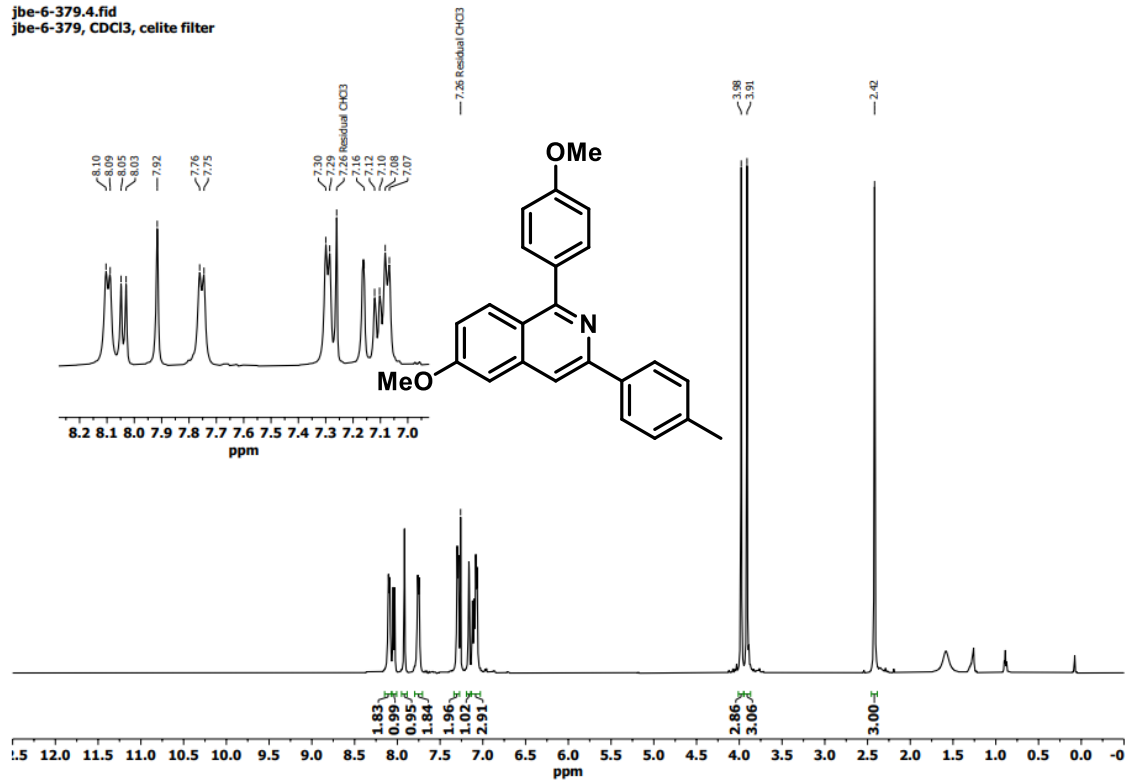

Figure 191. ^{1}H NMR spectrum of compound **257** in deuterated chloroform.

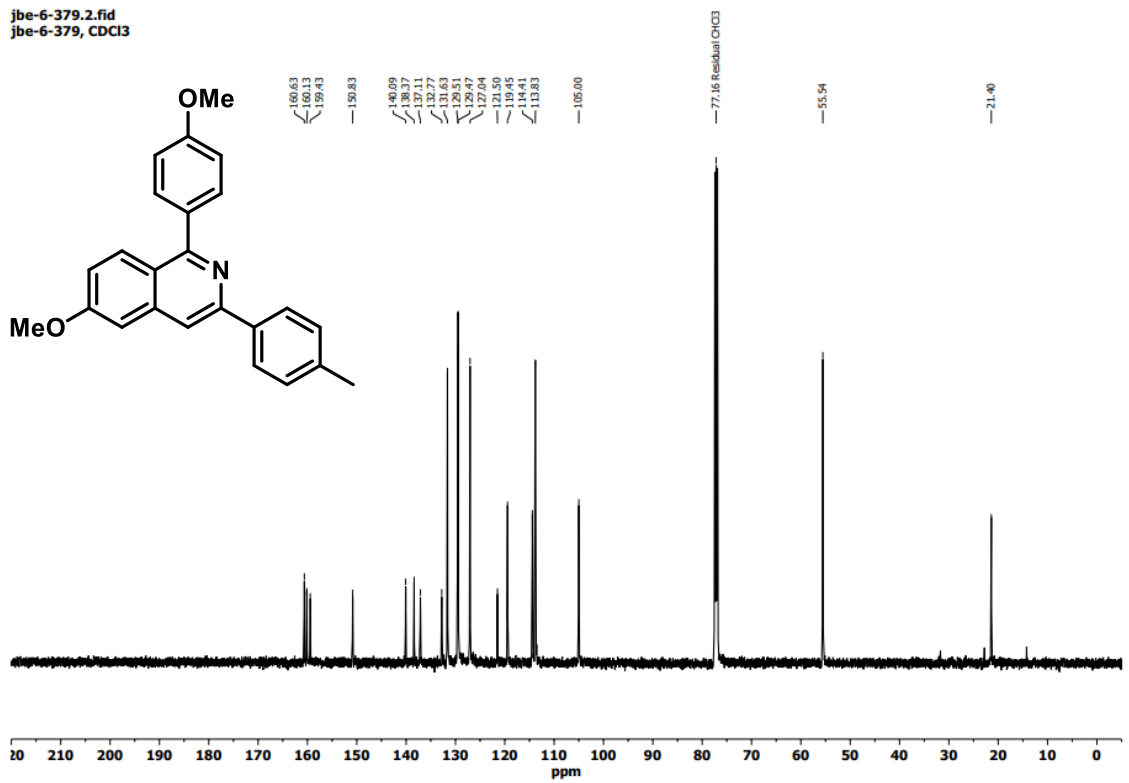

Figure 192. ^{13}C NMR spectrum of compound **257** in deuterated chloroform.

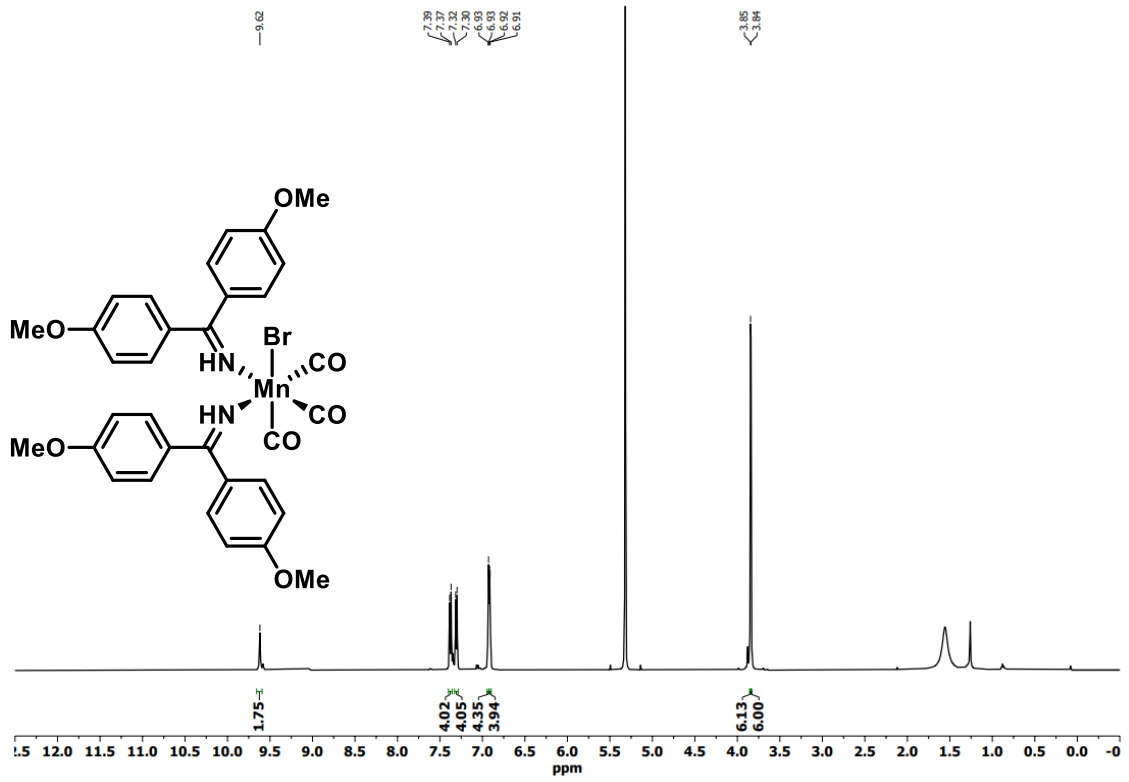

Figure 193. ^{1}H NMR spectrum of compound **228** in deuterated chloroform.

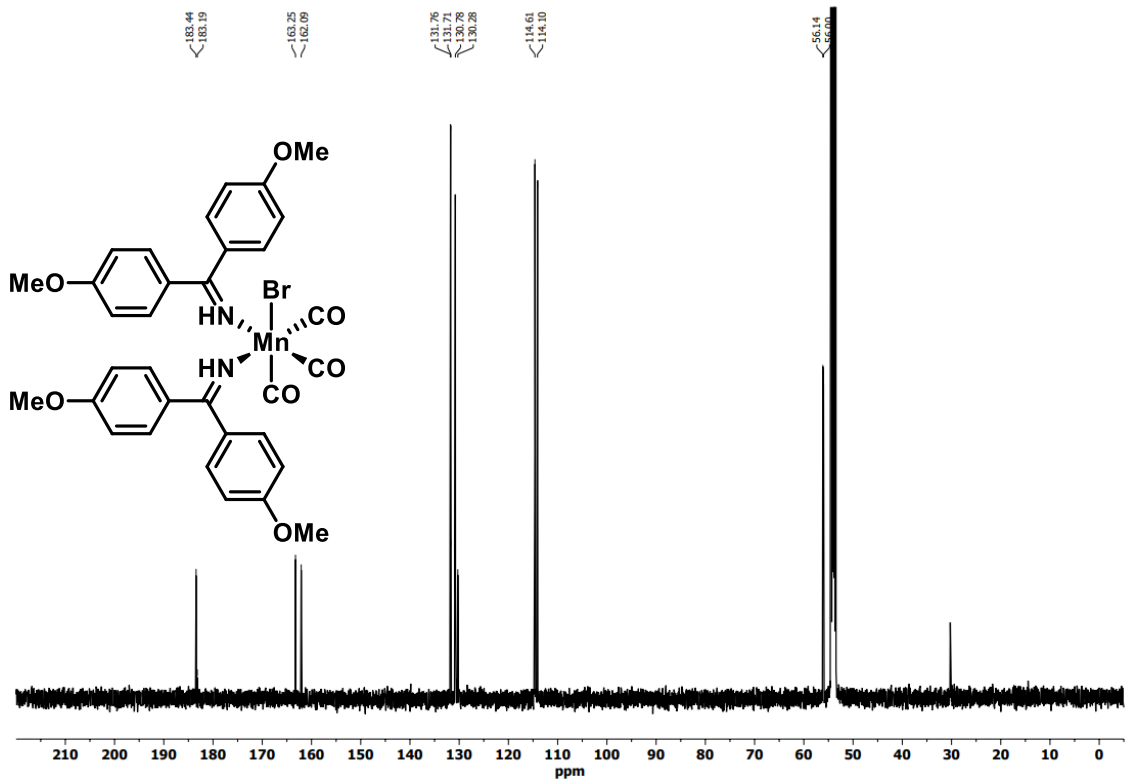

Figure 194. ^{13}C NMR spectrum of compound **228** in deuterated chloroform.

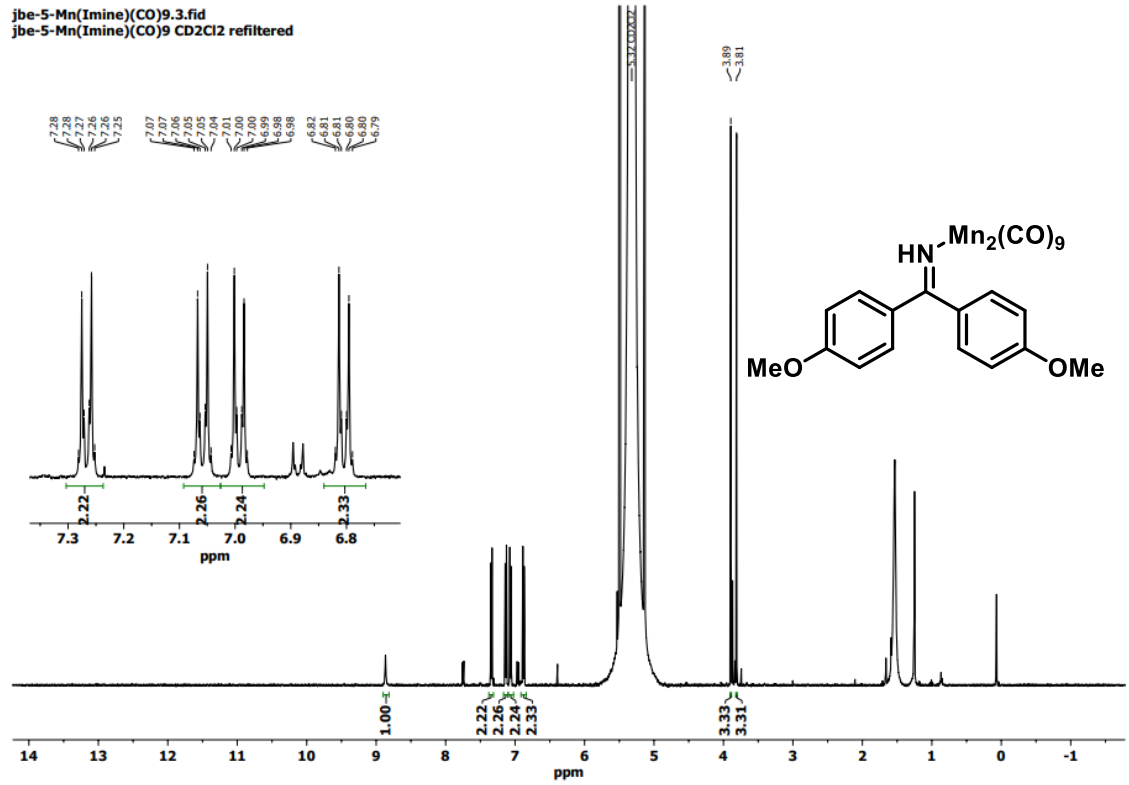

Figure 195. ^{1}H NMR spectrum of compound **216** in deuterated methylene chloride.

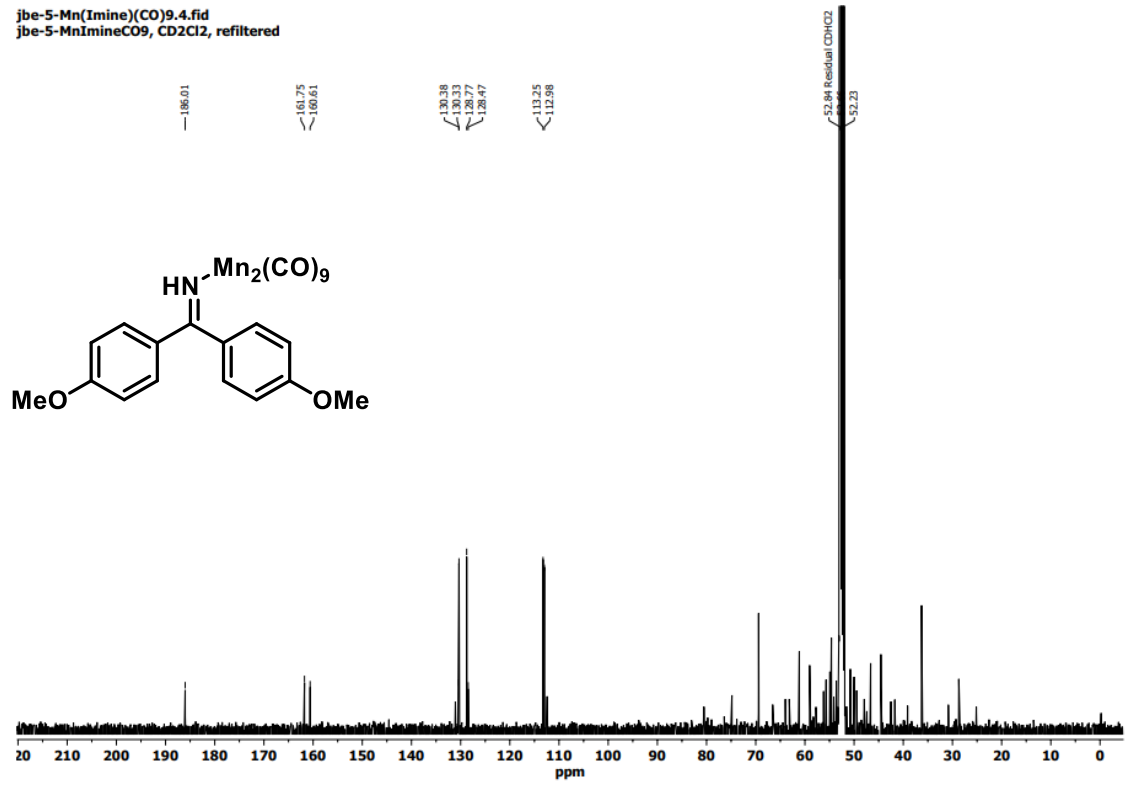

Figure 196. ^{13}C NMR spectrum of compound **216** in deuterated methylene chloride.

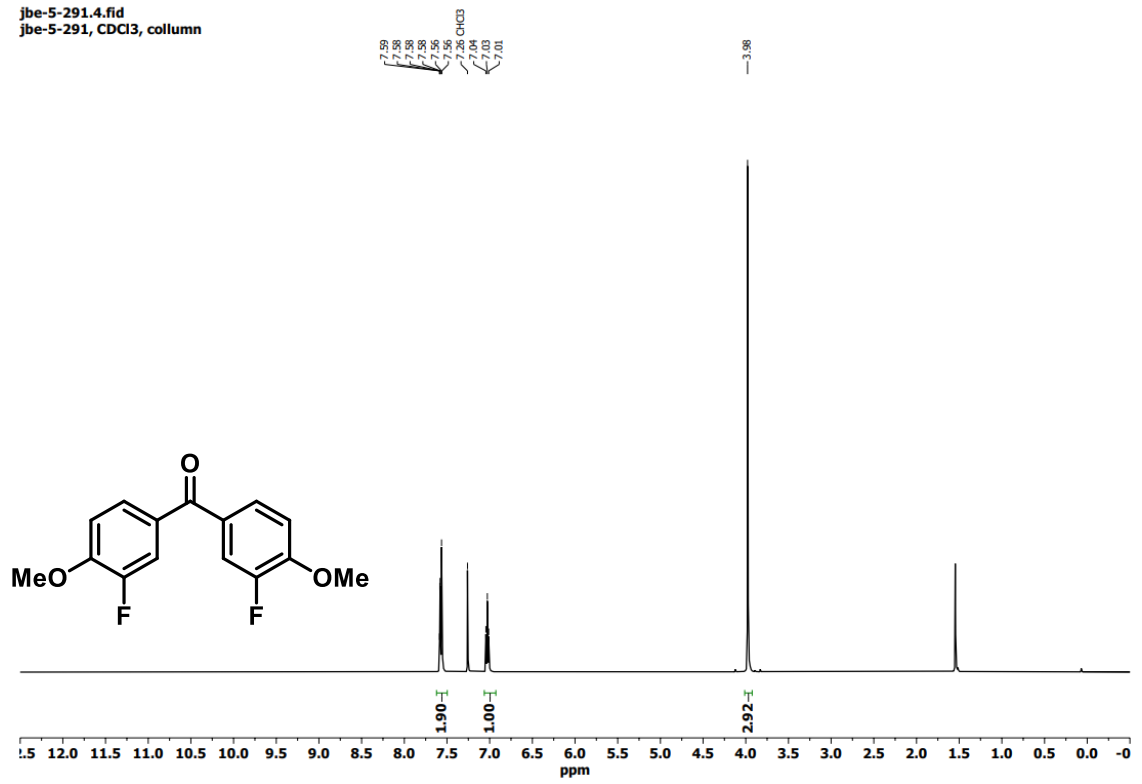

Figure 197. ^{1}H NMR spectrum of compound **238** in deuterated chloroform.

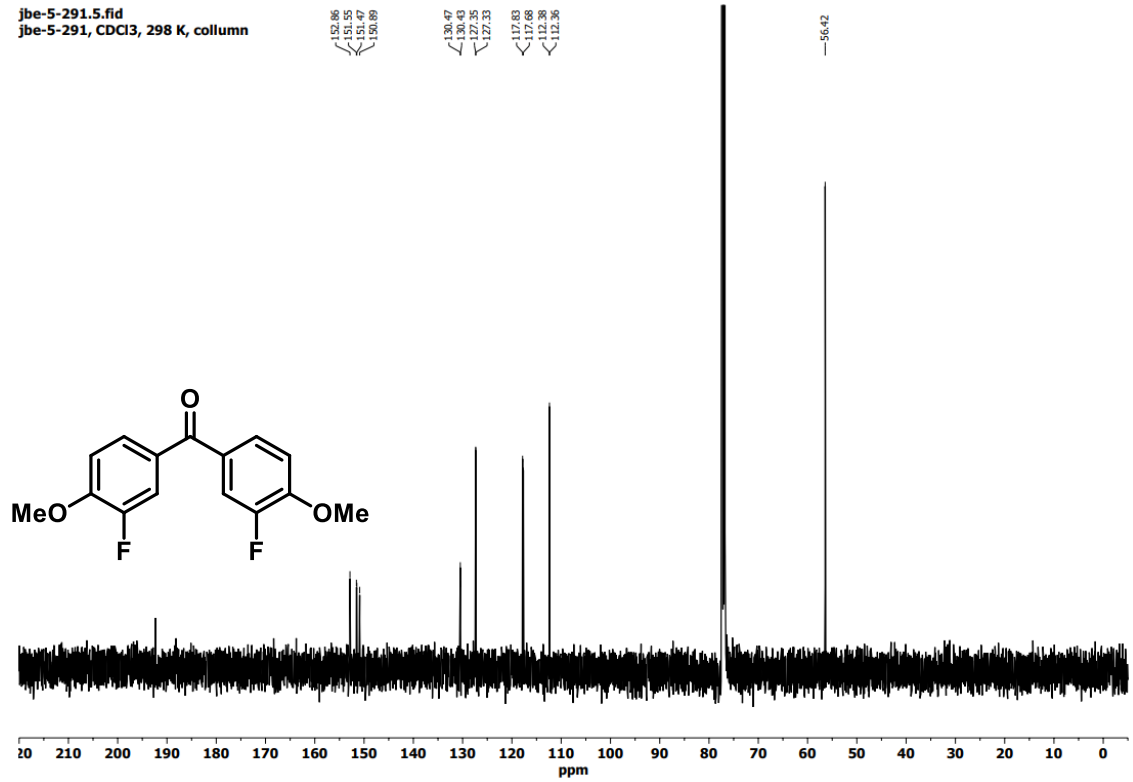

Figure 198. ^{13}C NMR spectrum of compound **238** in deuterated chloroform.

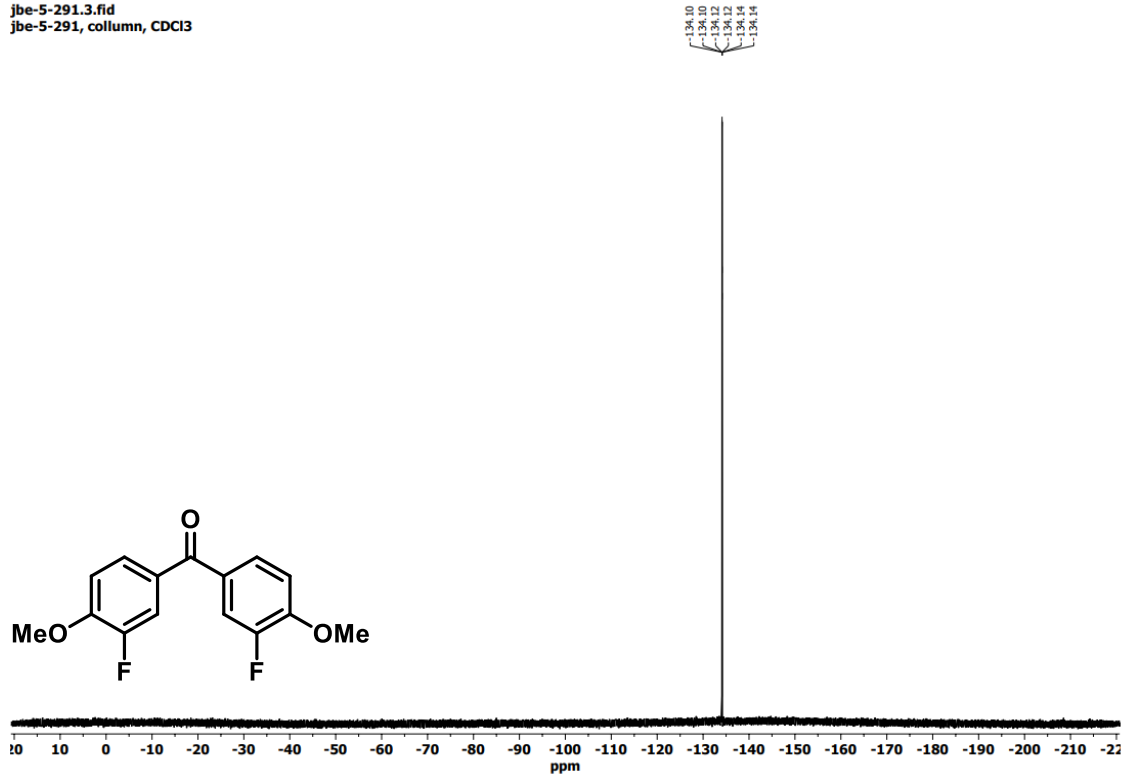

Figure 199. ^{19}F NMR spectrum of compound **238** in deuterated chloroform.

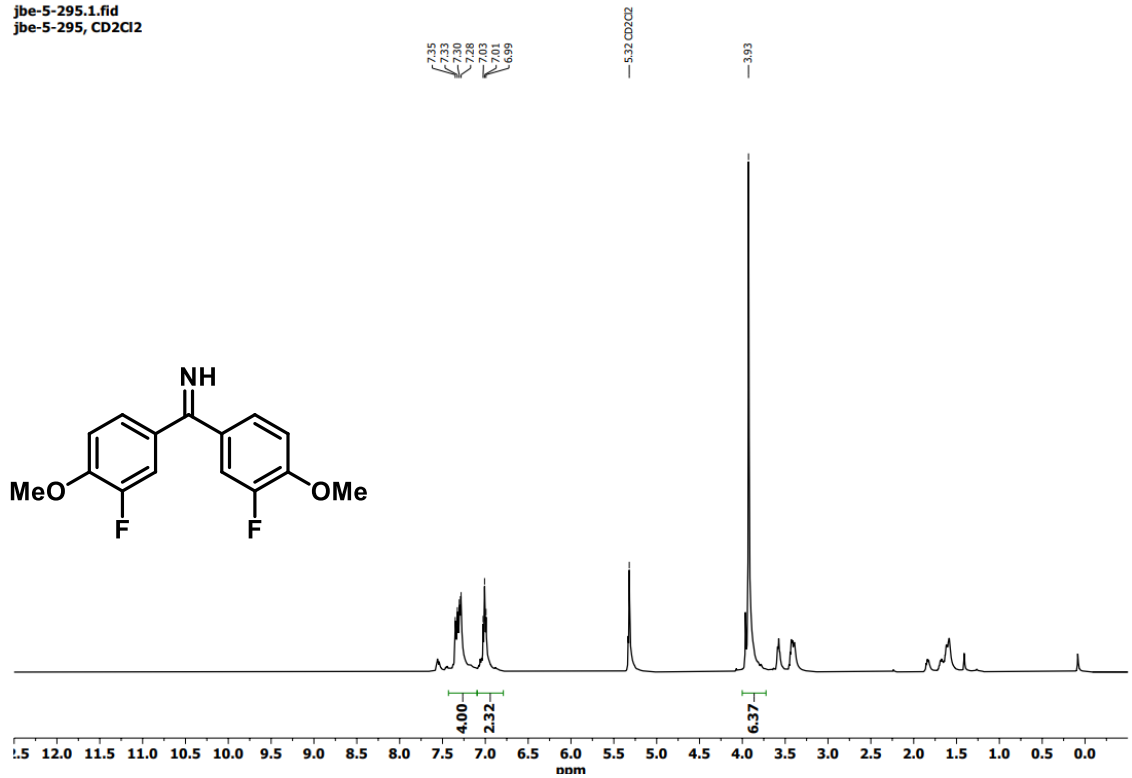

Figure 200. ^{1}H NMR spectrum of compound **239** in deuterated methylene chloride.

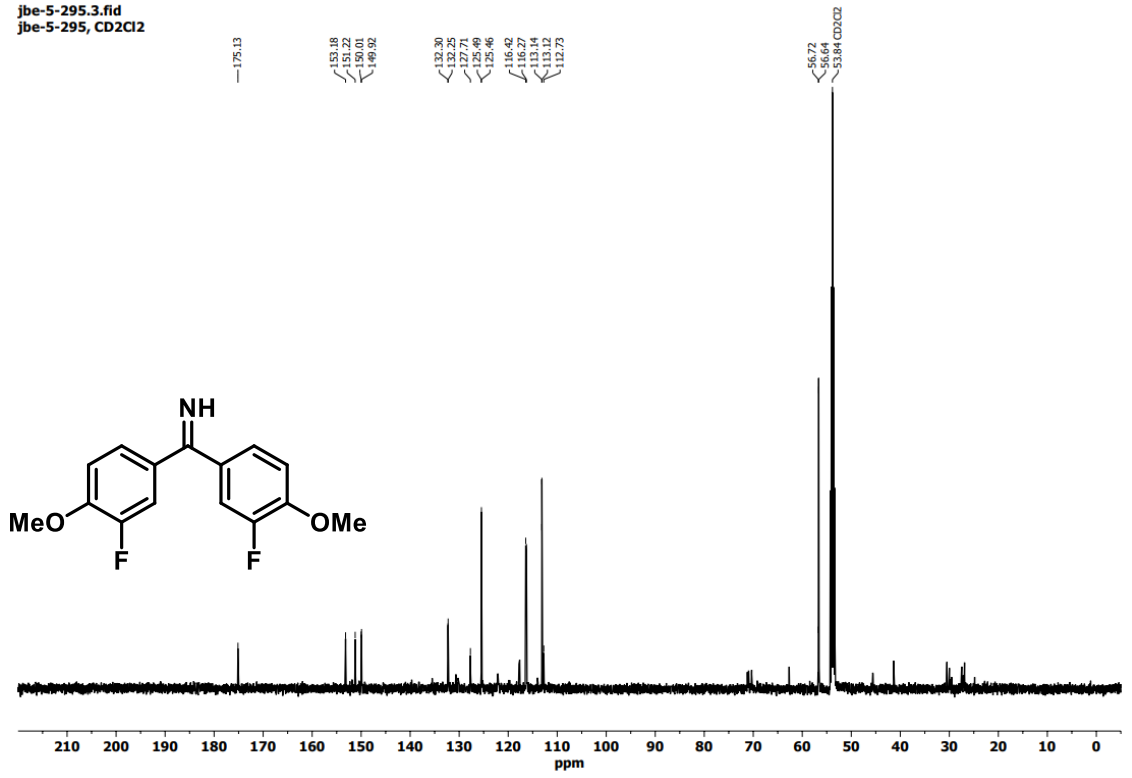

Figure 201. ^{13}C NMR spectrum of compound **239** in deuterated methylene chloride.

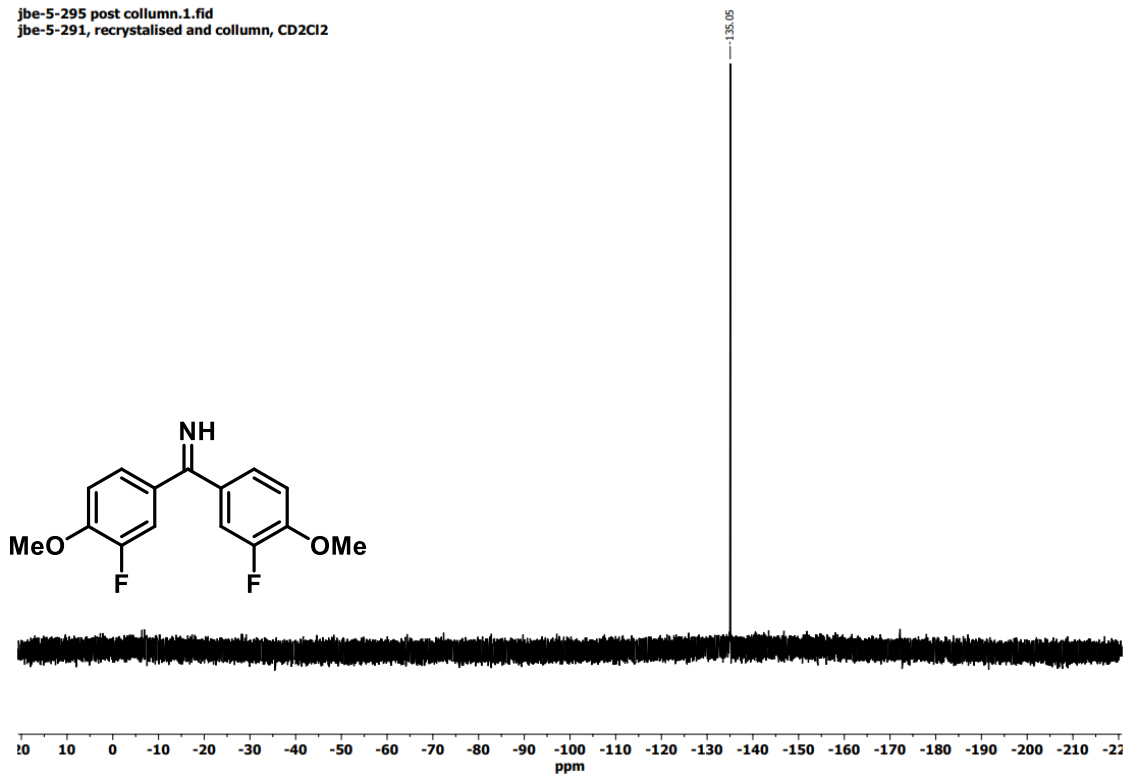

Figure 202. ^{19}F NMR spectrum of compound **239** in deuterated methylene chloride.

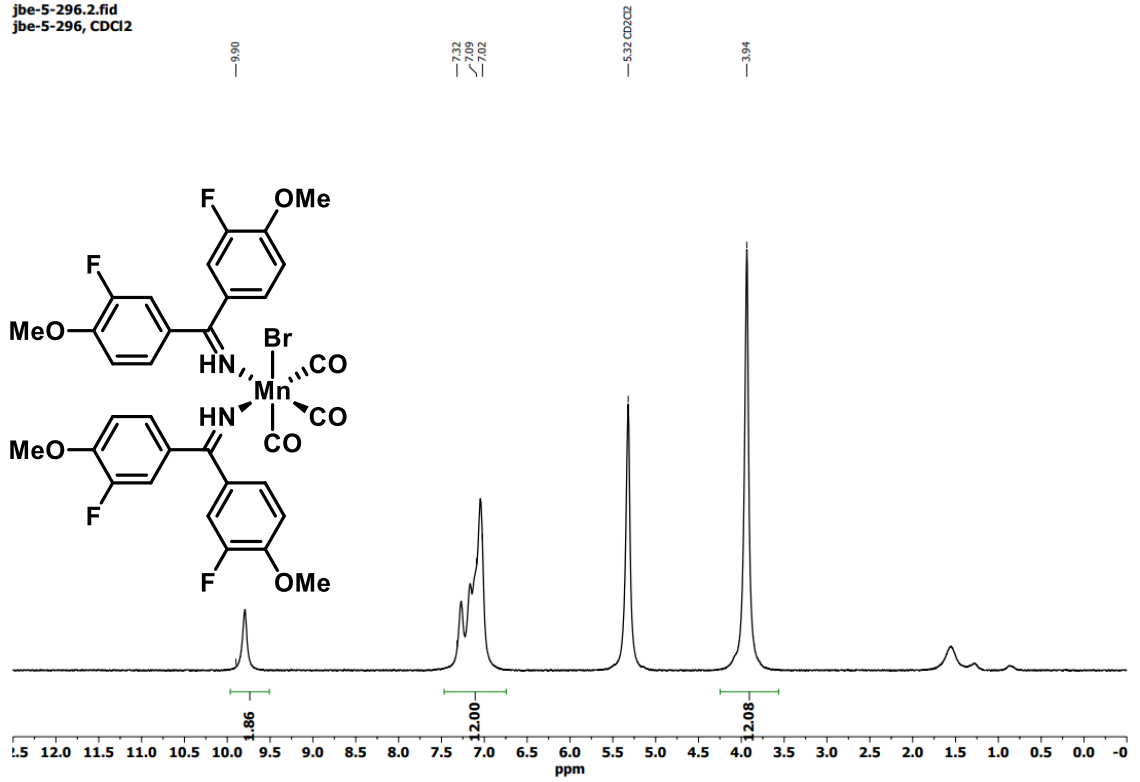

Figure 203. ^{1}H NMR spectrum of compound **234** in deuterated methylene chloride.

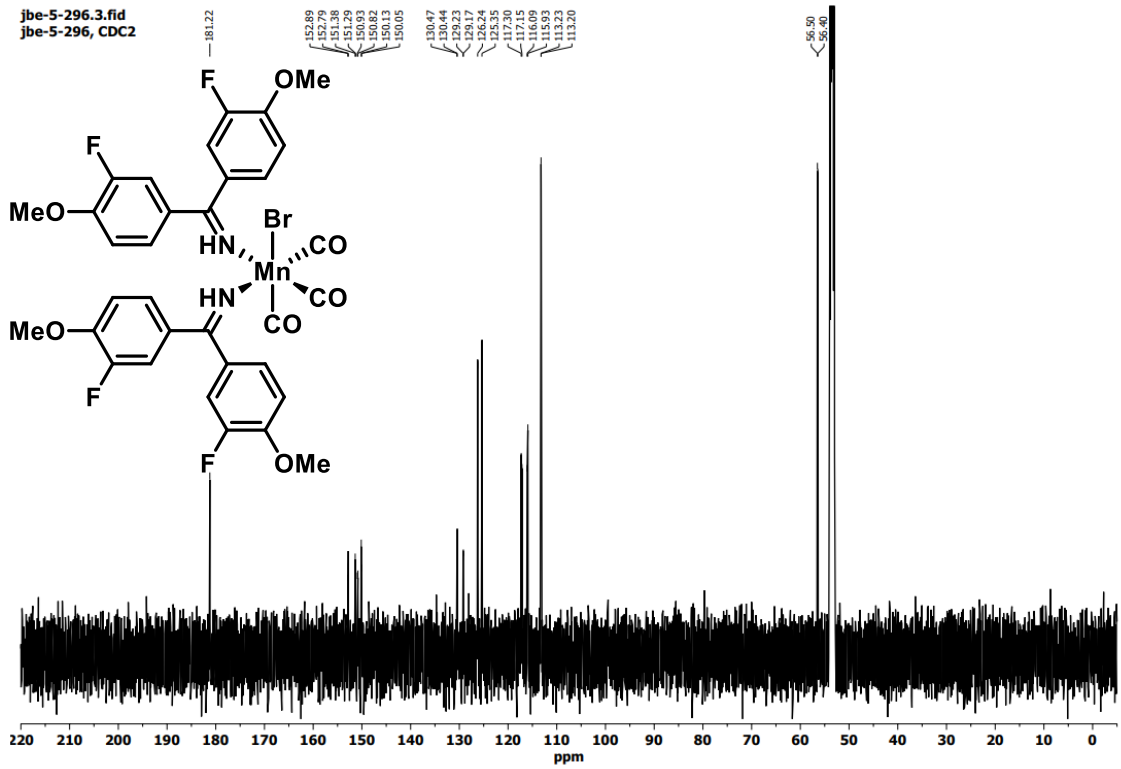

Figure 204. ^{13}C NMR spectrum of compound **234** in deuterated methylene chloride.

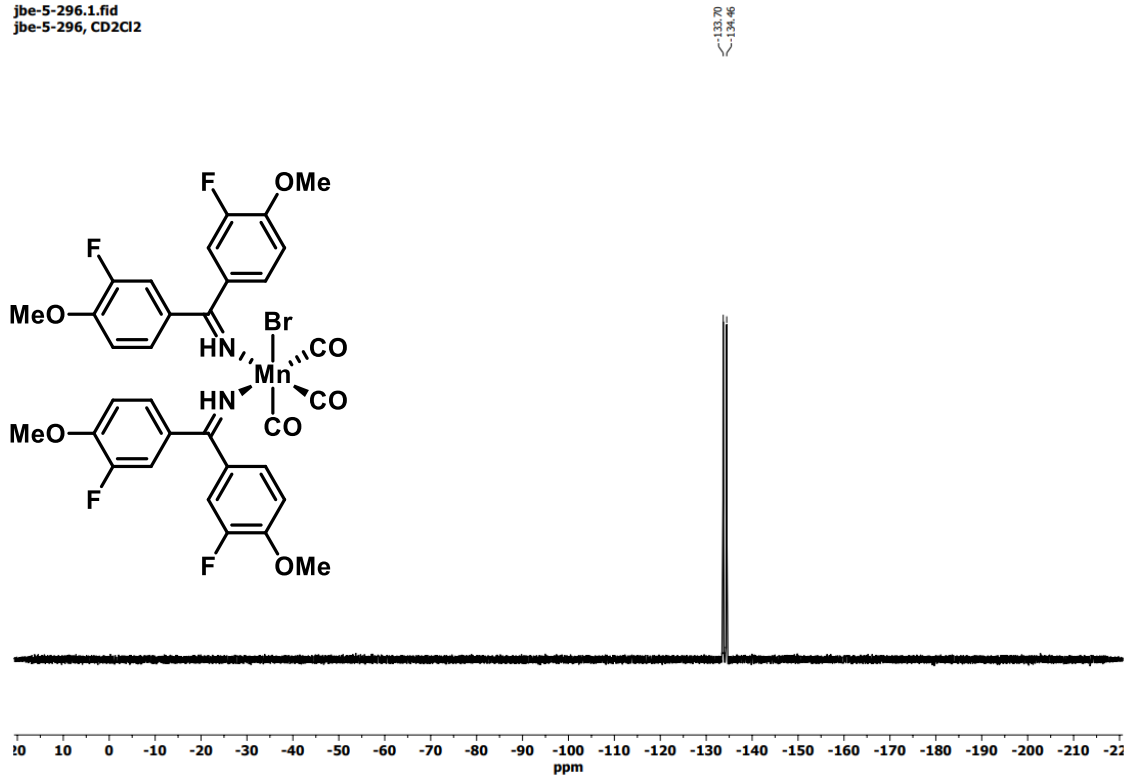

Figure 205. ^{19}F NMR spectrum of compound **234** in deuterated methylene chloride.

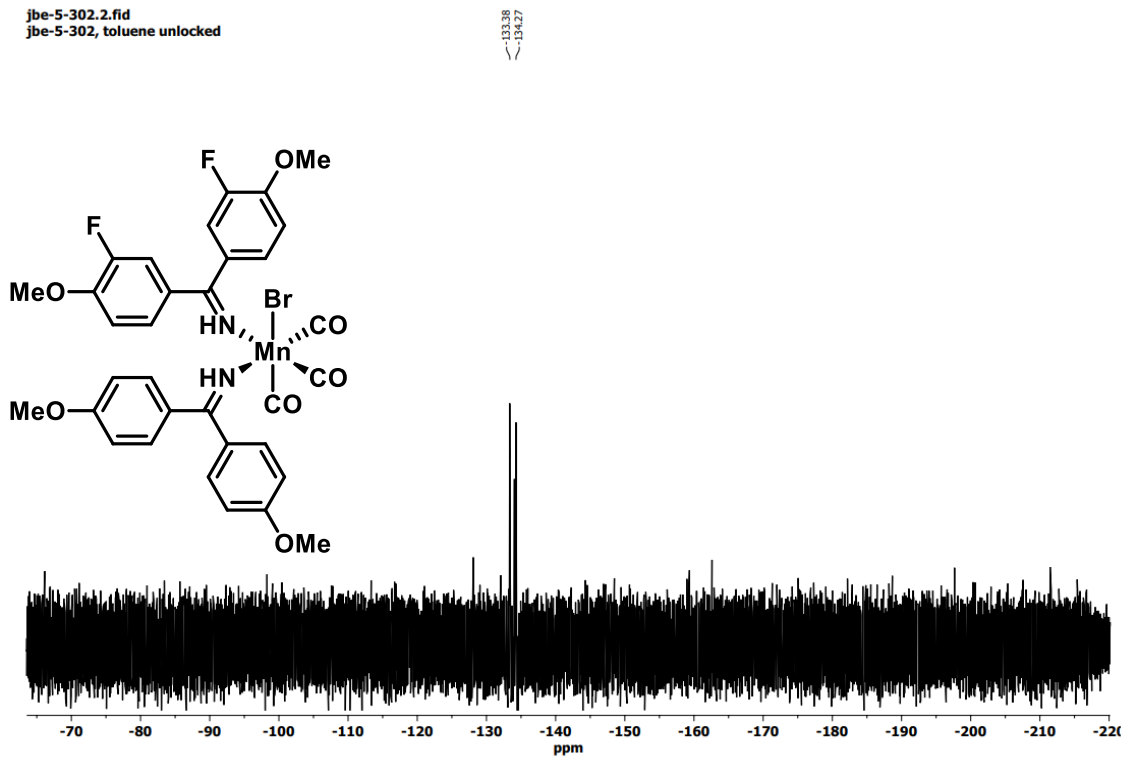

Figure 206. ^{19}F NMR spectrum of compound **258** in toluene.

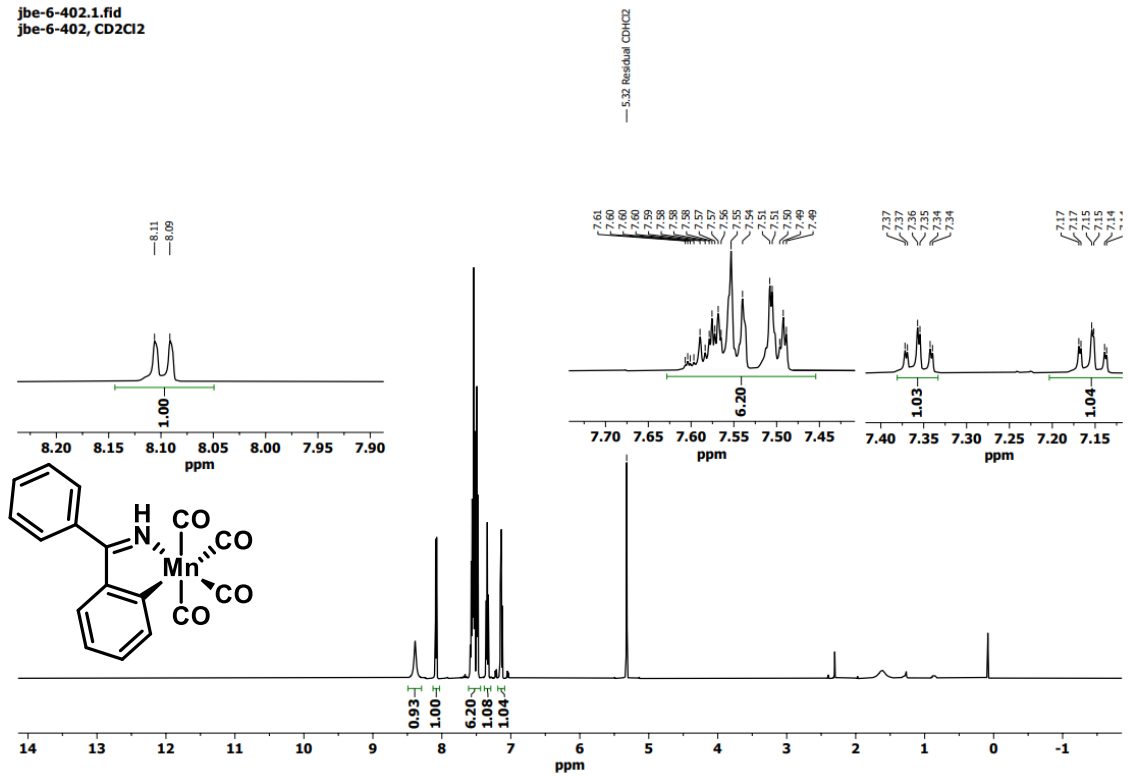

Figure 207. ^{1}H NMR spectrum of compound **182** in deuterated methylene chloride.

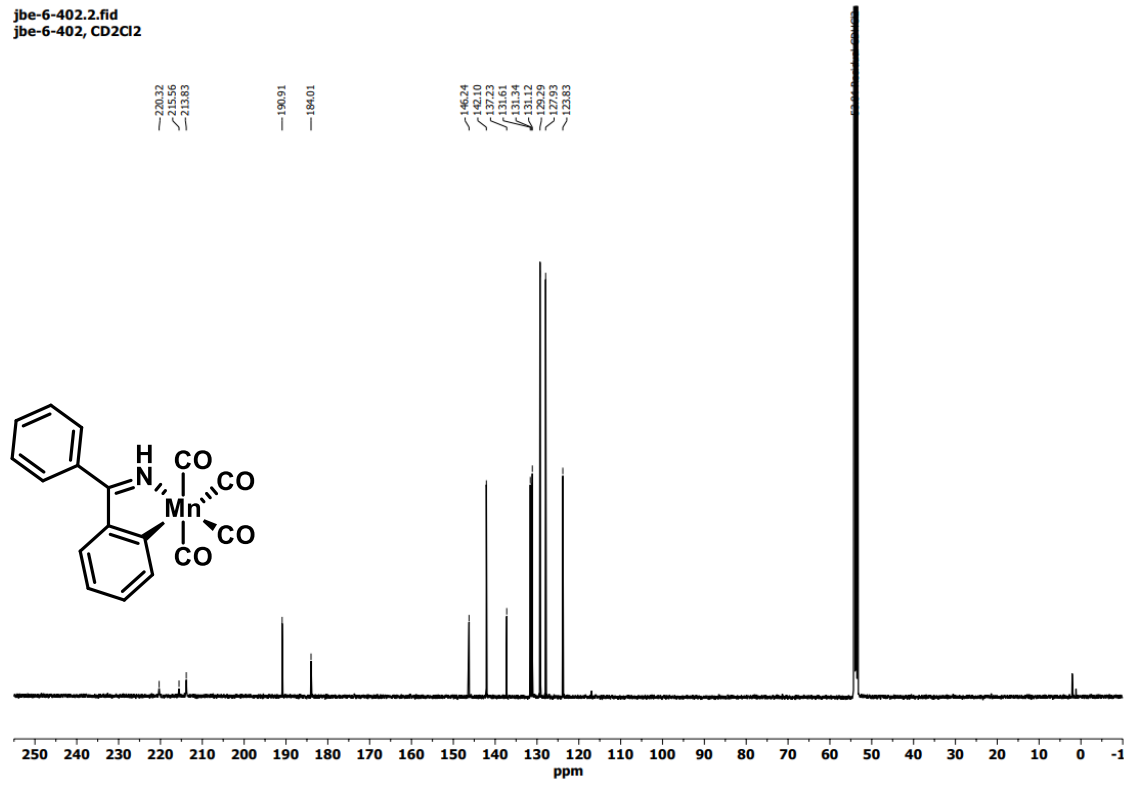

Figure 208. ^{13}C NMR spectrum of compound **182** in deuterated methylene chloride.

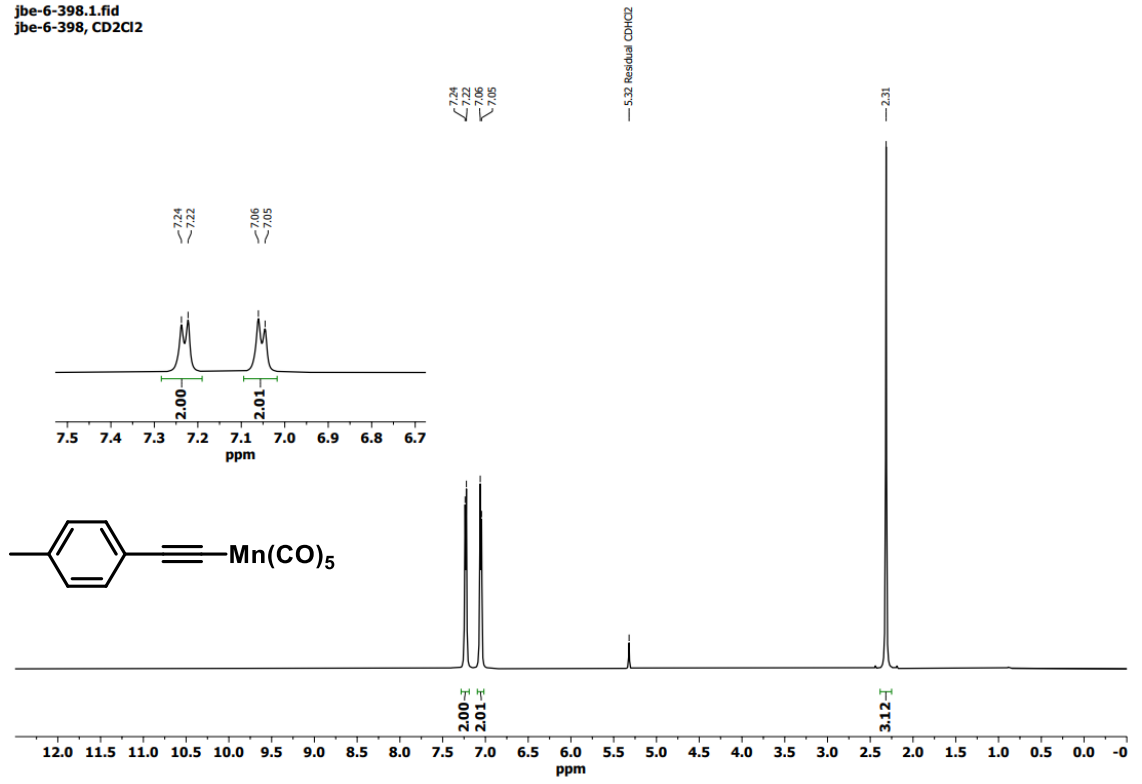

Figure 209. ^{1}H NMR spectrum of compound **223** in deuterated methylene chloride.

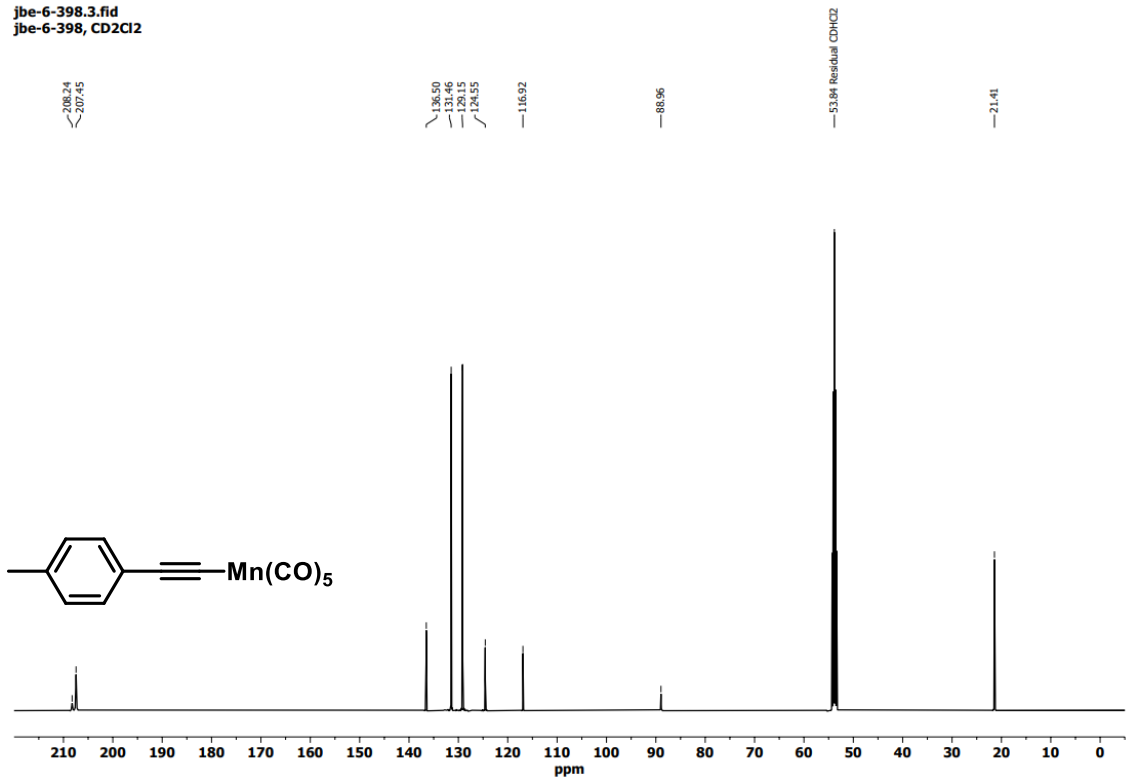

Figure 210. ^{13}C NMR spectrum of compound **223** in deuterated methylene chloride.

6.4 Calibration Plots

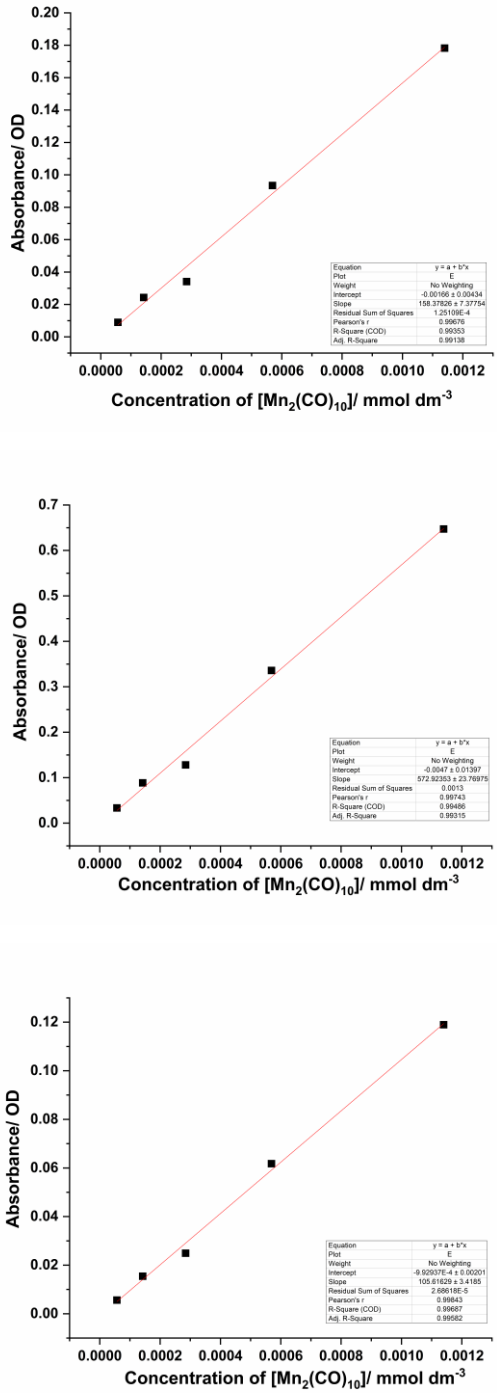

Figure 211. Beer-Lambert plots of $Mn_2(CO)_{10}$ in heptane. Top) 2045 cm^{-1}, Middle) 2014 cm^{-1}, Bottom) 1984 cm^{-1}.

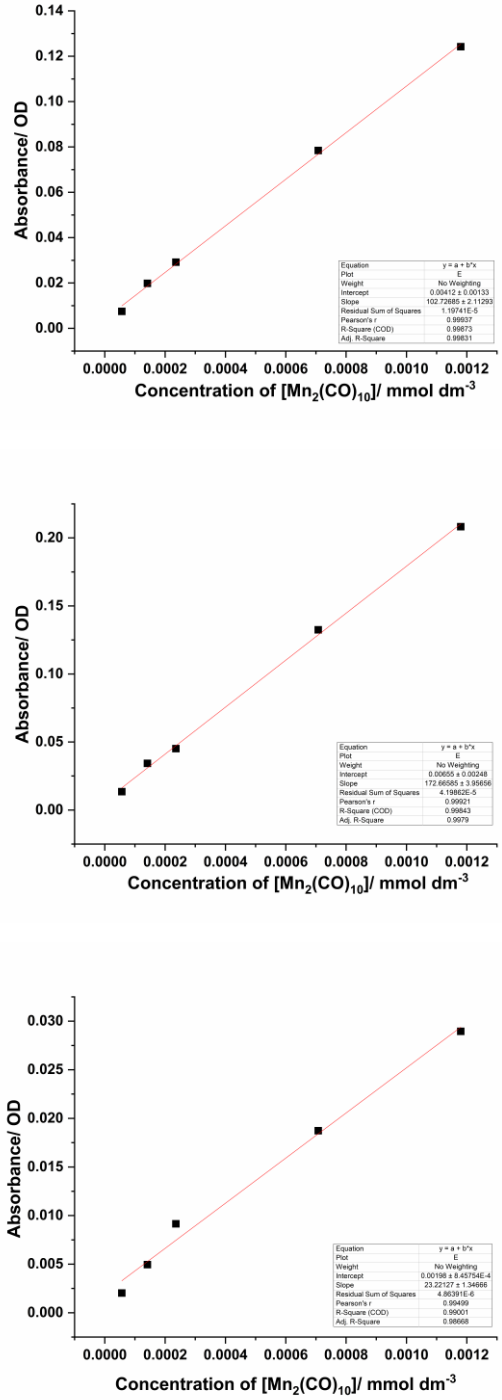

Figure 212. Beer-Lambert plots of $Mn_2(CO)_{10}$ in toluene. Top) 2045 cm^{-1}, Middle) 2014 cm^{-1}, Bottom) 1984 cm^{-1}.

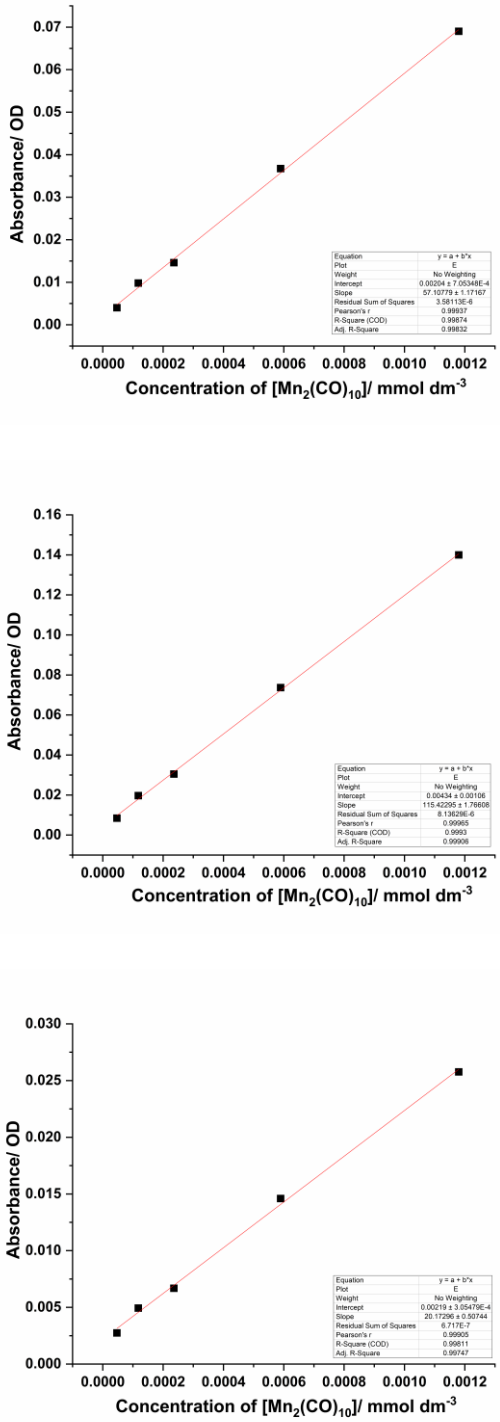

Figure 213. Beer-Lambert plots of $Mn_2(CO)_{10}$ in MeCN. Top) 2045 cm^{-1}, Middle) 2014 cm^{-1}, Bottom) 1984 cm^{-1}.

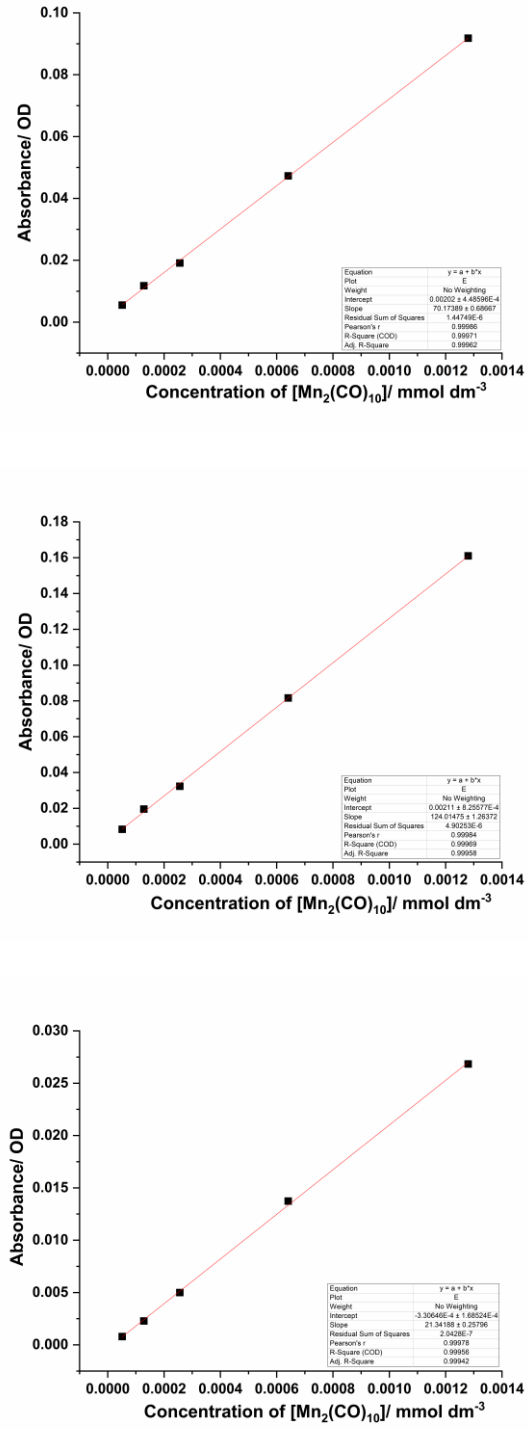

Figure 214. Beer-Lambert plots of $Mn_2(CO)_{10}$ in acetone. Top) 2045 cm^{-1}, Middle) 2014 cm^{-1}, Bottom) 1984 cm^{-1}.

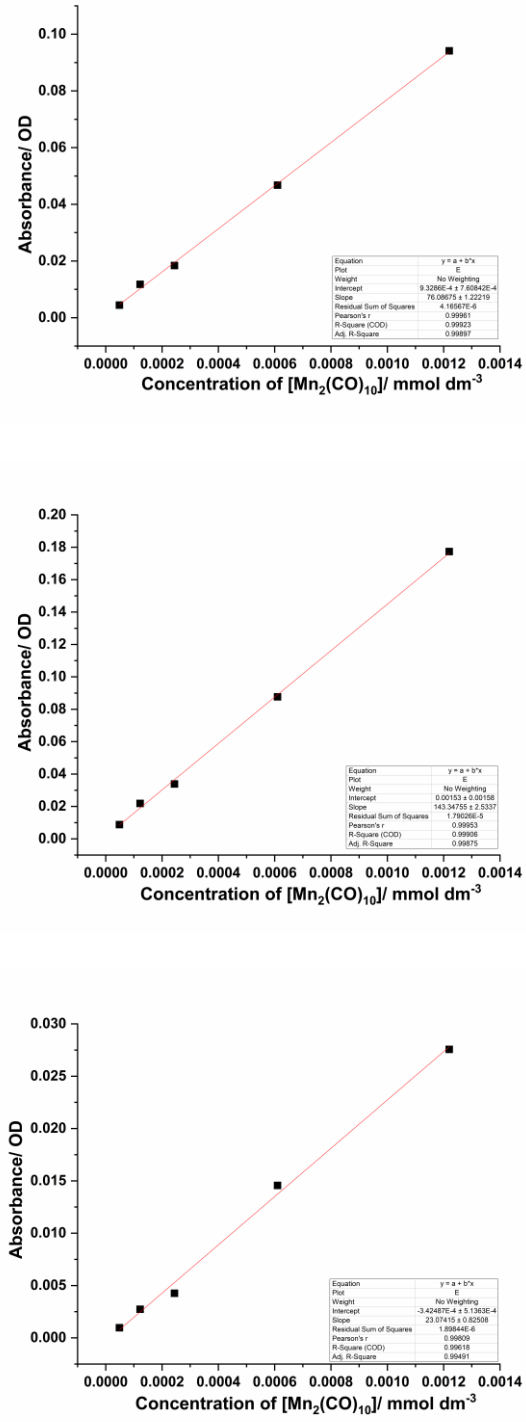

Figure 215. Beer-Lambert plots of $Mn_2(CO)_{10}$ in THF. Top) 2045 cm^{-1}, Middle) 2014 cm^{-1}, Bottom) 1984 cm^{-1}.

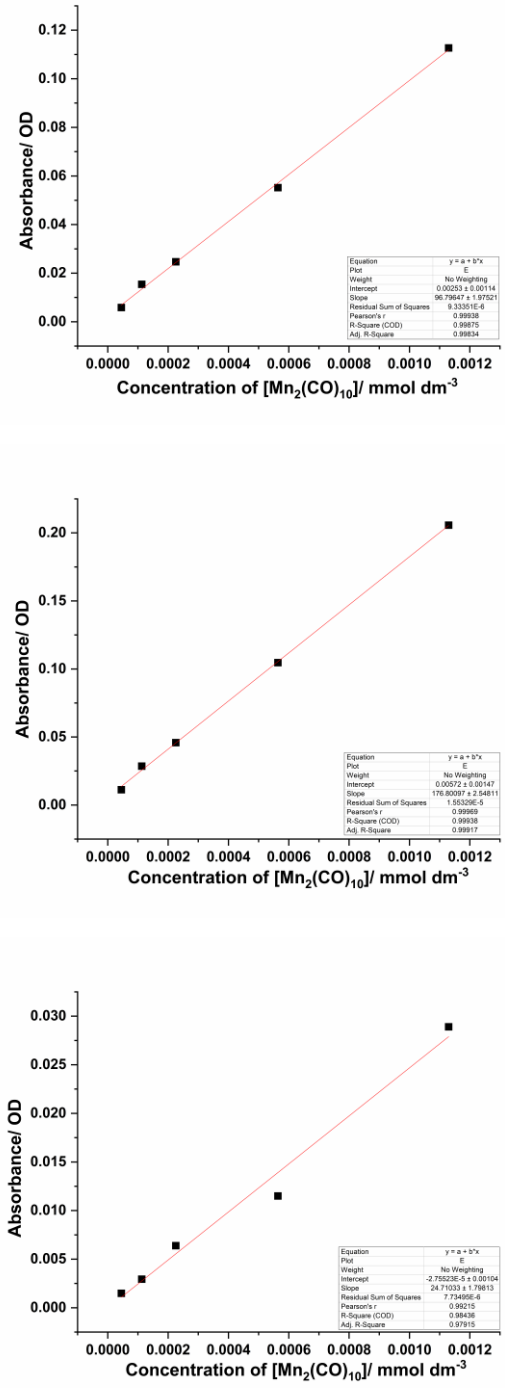

Figure 216. Beer-Lambert plots of $Mn_2(CO)_{10}$ in methylene chloride. Top) 2045 cm^{-1}, Middle) 2014 cm^{-1}, Bottom) 1984 cm^{-1}.

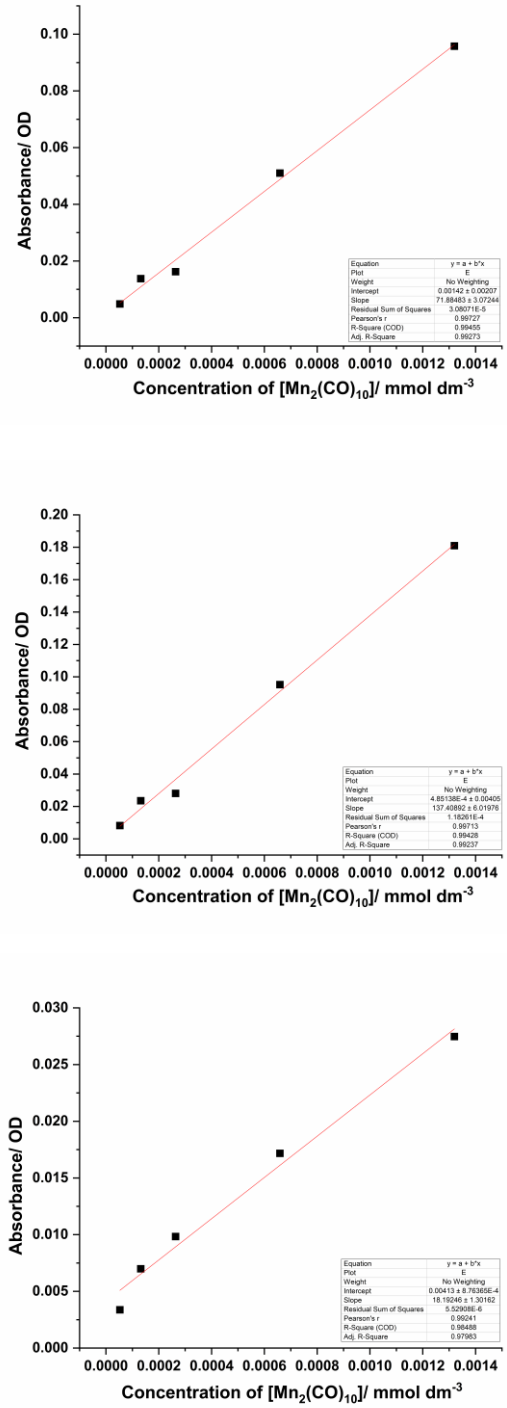

Figure 217. Beer-Lambert plots of $Mn_2(CO)_{10}$ in 1,4-dioxane. Top) 2045 cm^{-1}, Middle) 2014 cm^{-1}, Bottom) 1984 cm^{-1}.

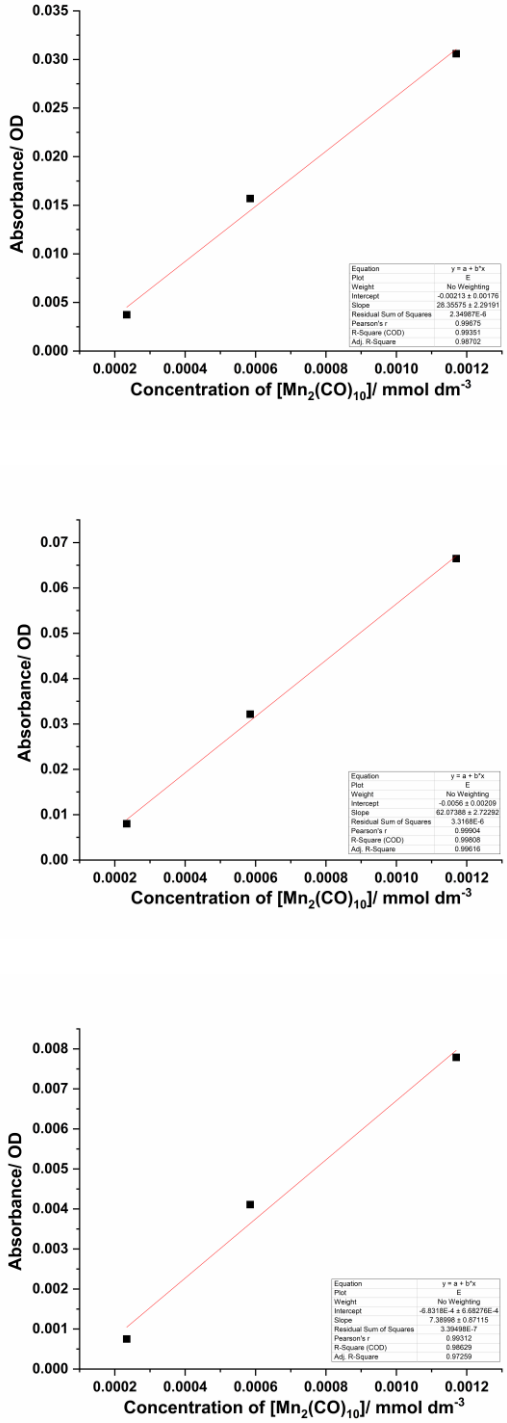

Figure 218. Beer-Lambert plots of $Mn_2(CO)_{10}$ in DMSO. Top) 2045 cm^{-1}, Middle) 2014 cm^{-1}, Bottom) 1984 cm^{-1}.

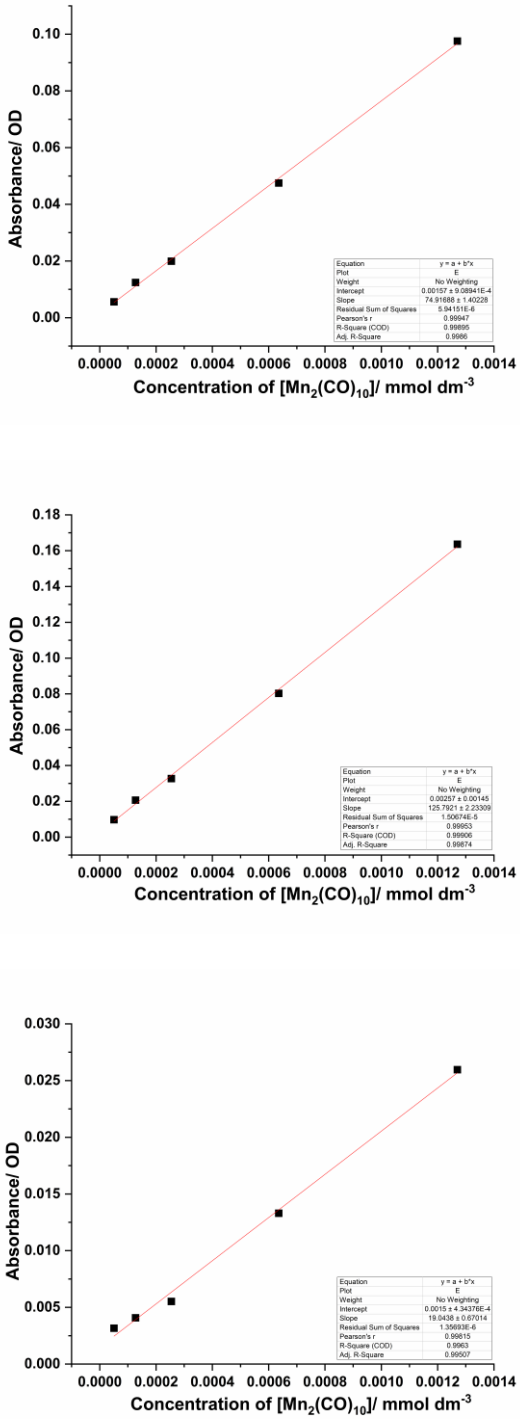

Figure 219. Beer-Lambert plots of $Mn_2(CO)_{10}$ in n-butyl acrylate. Top) 2045 cm^{-1}, Middle) 2014 cm^{-1}, Bottom) 1984 cm^{-1}.

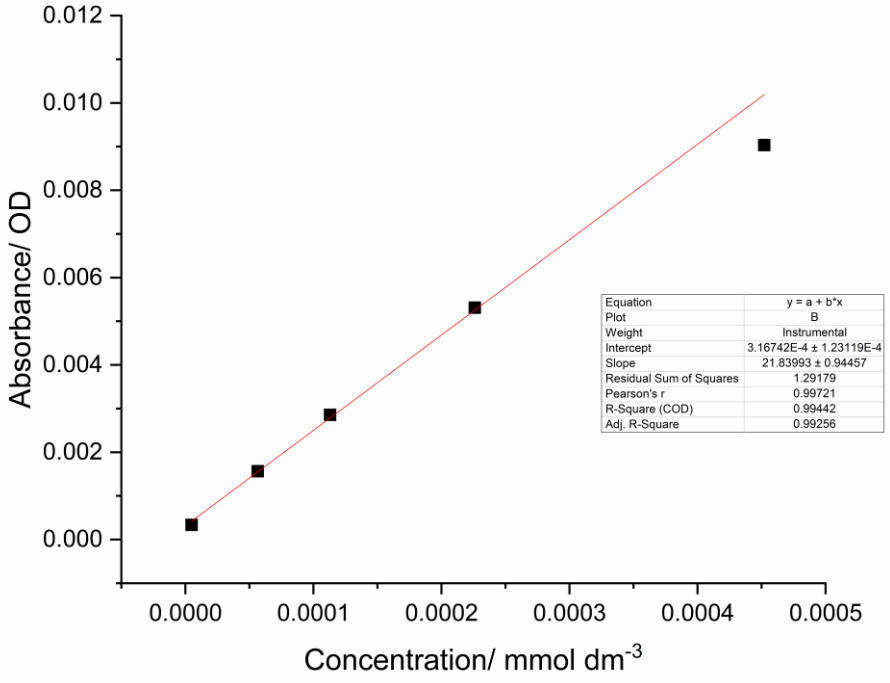

Figure 220. Beer-Lambert plots of compound **158** in heptane at 2074 cm^{-1}.

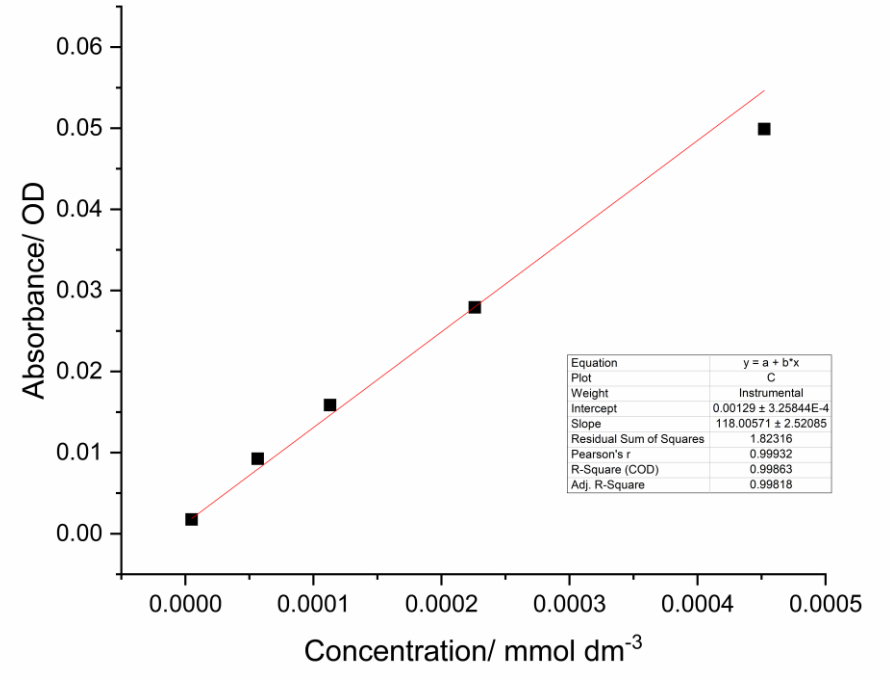

Figure 221. Beer-Lambert plots of compound **158** in heptane at 1990 cm^{-1}.

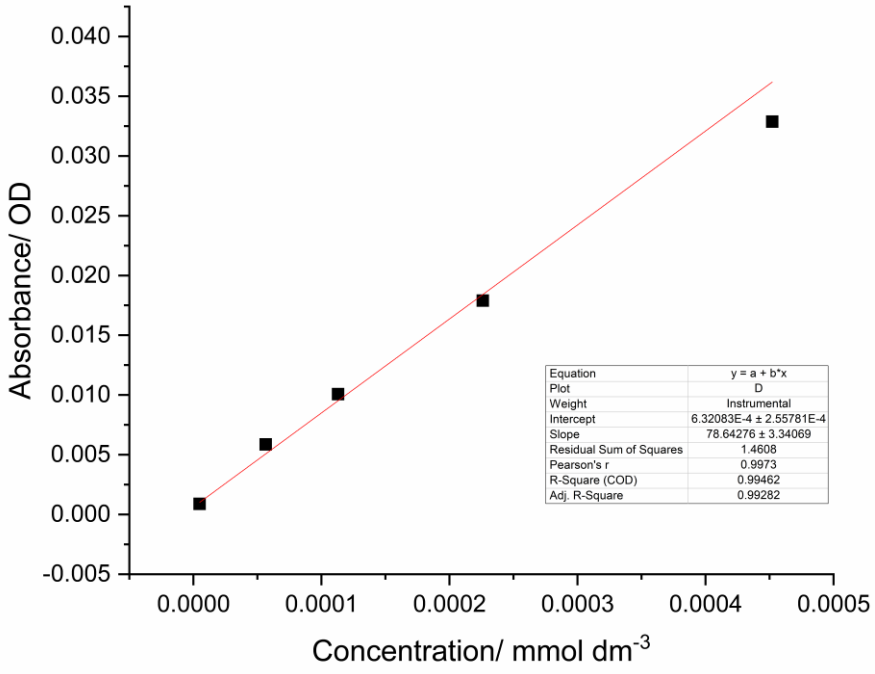

Figure 222. Beer-Lambert plots of compound **158** in heptane at 2080 cm^{-1}.

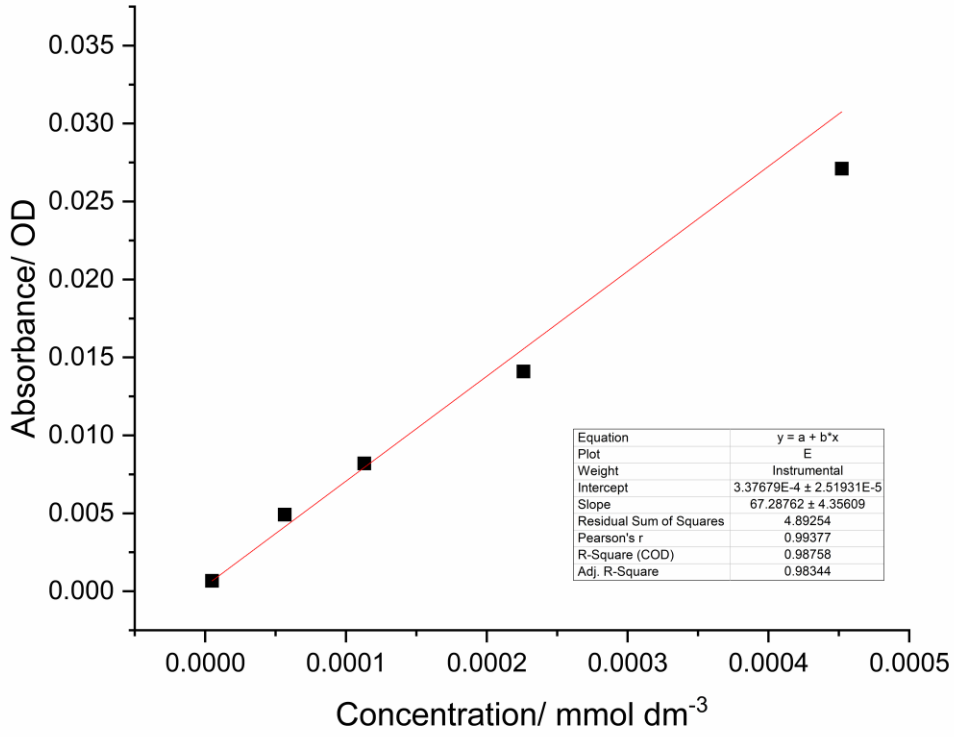

Figure 223. Beer-Lambert plots of compound **158** in heptane at 1940 cm^{-1}.

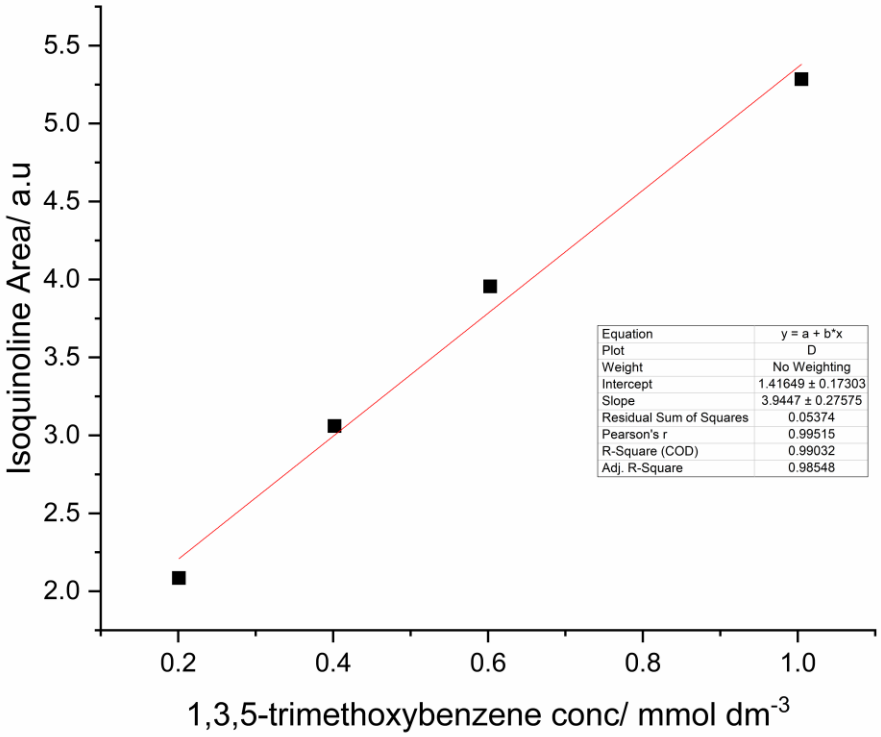

Figure 224. GC calibration plot of isoquinoline **180** using 1,3,5-trimethoxybenzene as an internal standard.

6.5 X-Ray Diffraction Data

Compound 228

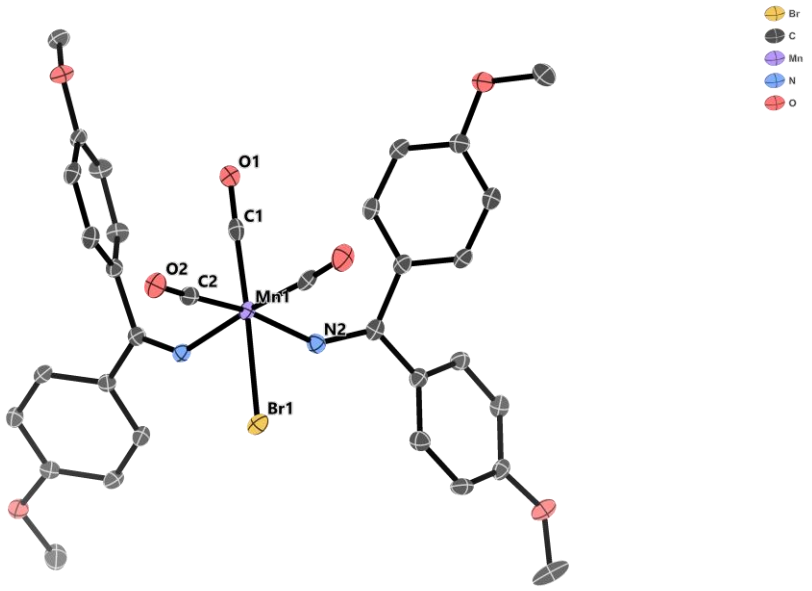

Figure 225. Single crystal X-ray diffraction structure of **228**. Thermal ellipsoids shown with 50% probability and hydrogen atoms removed for clarity. Selected bond lengths (Å): Br1–Mn1: 2.5488(4); C1–Mn1: 1.796(2); C2–Mn1: 1.797(2); C3–Mn1: 1.802(2); N1–Mn1: 2.0566(18); N2–Mn1: 2.0731(19). Selected bond angles (°): O1–C1–Mn1: 174.80(19); N1–Mn1–N2: 85.21(7); N1–Mn1–Br1: 84.17(5); N2–Mn1–Br1: 83.18(5); C1–Mn1–Br1: 176.73(7); C2–Mn1–Br1: 86.72(7); C1–Mn1–N1: 96.01(9); C2–Mn1–N1: 94.79(8); C3–Mn1–N1: 175.46(9).

Table 27. Crystal data and structure refinement for compound **228**.

Identification code	jml1907
Empirical formula	$C_{33}H_{30}BrMnN_2O_7$
Formula weight	701.44
Temperature/K	110.00(10)
Crystal system	monoclinic
Space group	$P2_1/c$
a/Å	10.20445(15)
b/Å	18.1216(3)
c/Å	16.6612(2)
α/°	90
β/°	90.7735(13)
γ/°	90
Volume/Å^3	3080.72(8)
Z	4
ρ_{calc}g/cm^3	1.512
μ/mm^{-1}	5.435
F(000)	1432.0
Crystal size/mm^3	0.134 × 0.114 × 0.058
Radiation	CuKα (λ = 1.54184)
2Θ range for data collection/°	7.208 to 134.146
Index ranges	-11 ≤ h ≤ 12, -21 ≤ k ≤ 16, -19 ≤ l ≤ 19
Reflections collected	11363
Independent reflections	5497 [R_{int} = 0.0255, R_{sigma} = 0.0357]
Data/restraints/parameters	5497/0/410
Goodness-of-fit on F^2	1.028
Final R indexes [I>=2σ (I)]	R_1 = 0.0284, wR_2 = 0.0637
Final R indexes [all data]	R_1 = 0.0326, wR_2 = 0.0663
Largest diff. peak/hole / e Å^{-3}	0.66/-0.35

Compound 216

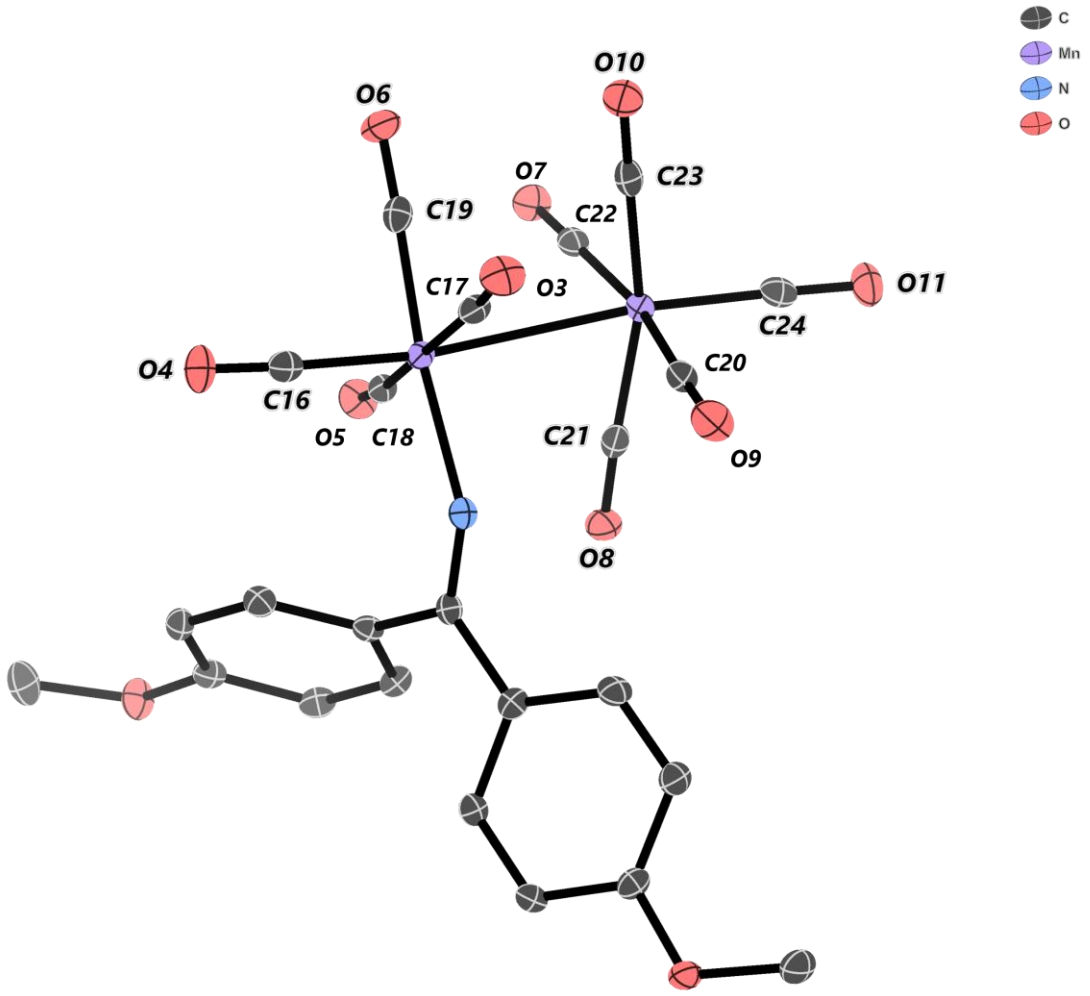

Figure 226. Single crystal X-ray diffraction structure of **216**. Thermal ellipsoids shown with 50% probability and hydrogen atoms removed for clarity. Selected bond lengths (Å): Mn1–Mn2 2.9296(5); Mn2–C22: 1.869(2); Mn2–C24: 1.813(2); Mn1–C16: 1.801(2); Mn1–C17: 1.859(2); Mn1–C18: 1.879(2); Mn1–C19: 1.806(2); Mn1–N1: 2.0608(18). Selected bond angles (°): O7–C22–Mn2: 179.4(2); C20–Mn2–C21: 89.09(10); C20–Mn2–C22: 170.20(10); C20–Mn2–Mn1: 83.34(7); N1–Mn1–Mn2: 91.73(5); N1–Mn1–C16: 94.67(9); N1–Mn1–C19: 174.26; N1–Mn1–C18: 93.28(8).

Table 28. Crystal data and structure refinement for compound **216**.

Identification code	jml21009
Empirical formula	$C_{24}H_{15}Mn_2NO_{11}$
Formula weight	603.25
Temperature/K	110.00(14)
Crystal system	triclinic
Space group	P-1
a/Å	9.0789(5)
b/Å	11.2974(8)
c/Å	12.7130(8)
α/°	110.200(6)
β/°	94.410(5)
γ/°	92.531(5)
Volume/Å^3	1216.63(14)
Z	2
ρ_{calc}g/cm^3	1.647
μ/mm^{-1}	1.102
F(000)	608.0
Crystal size/mm^3	0.41 × 0.292 × 0.224
Radiation	Mo Kα (λ = 0.71073)
2Θ range for data collection/°	7.114 to 58.046
Index ranges	-12 ≤ h ≤ 11, -15 ≤ k ≤ 14, -17 ≤ l ≤ 16
Reflections collected	9897
Independent reflections	5548 [R_{int} = 0.0248, R_{sigma} = 0.0481]
Data/restraints/parameters	5548/0/349
Goodness-of-fit on F^2	1.063
Final R indexes [I>=2σ (I)]	R_1 = 0.0355, wR_2 = 0.0734
Final R indexes [all data]	R_1 = 0.0456, wR_2 = 0.0804
Largest diff. peak/hole / e Å^{-3}	0.44/-0.41

Compound 234

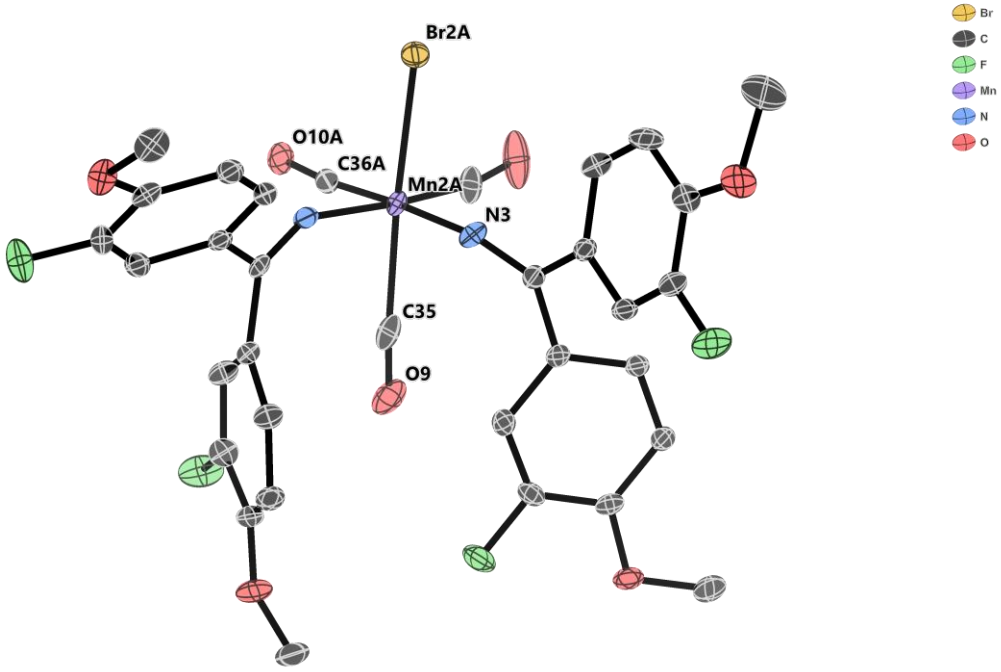

Figure 227. Single crystal X-ray diffraction structure of **234**. Thermal ellipsoids shown with 50% probability and hydrogen atoms removed for clarity. Selected bond lengths (Å): Br1–Mn1: 2.5726(4); C1–Mn1: 1.804(2); C2–Mn1: 1.794(2); C3–Mn1: 1.810(2); N1–Mn1: 2.048(2); N2–Mn1: 2.060(2). Selected bond angles (°): O1–C1–Mn1: 178.0(2); N1–Mn1–N2: 83.39(8); N1–Mn1–Br1: 85.6(6); N2–Mn1–Br1: 80.95(6); C1–Mn1–Br1: 88.97(7); C2–Mn1–Br1: 174.06(8); C1–Mn1–N1: 91.16(9); C2–Mn1–N1: 100.24(9); C3–Mn1–N1: 174.54(10).

Table 29. Crystal data and structure refinement for compound **234**.

Identification code	jml21001
Empirical formula	$C_{34}H_{28}BrCl_2F_4MnN_2O_7$
Formula weight	858.33
Temperature/K	110.00(10)
Crystal system	monoclinic
Space group	$P2_1/n$
a/Å	19.62170(11)
b/Å	17.51016(8)
c/Å	21.66821(11)
α/°	90
β/°	107.9827(6)
γ/°	90
Volume/Å^3	7081.06(7)
Z	8
ρ_{calc}g/cm^3	1.610
μ/mm^{-1}	6.374
F(000)	3456.0
Crystal size/mm^3	0.33 × 0.1 × 0.06
Radiation	Cu Kα (λ = 1.54184)
2Θ range for data collection/°	6.624 to 134.158
Index ranges	-23 ≤ h ≤ 23, -18 ≤ k ≤ 20, -25 ≤ l ≤ 24
Reflections collected	51243
Independent reflections	12632 [R_{int} = 0.0270, R_{sigma} = 0.0231]
Data/restraints/parameters	12632/2/978
Goodness-of-fit on F^2	1.029
Final R indexes [I>=2σ (I)]	R_1 = 0.0318, wR_2 = 0.0786
Final R indexes [all data]	R_1 = 0.0376, wR_2 = 0.0822
Largest diff. peak/hole / e Å^{-3}	0.54/-0.93

* The central core of one of the complexes was disordered. The manganese, bromine and two carbon monoxides were modelled in two positions with refined occupancies of 0.9282:0.0718(8). The ADP of pairs of disordered atoms were constrained to be equal (Mn2 & Mn2a, Br2 & Br2a, C34 & C34A, C36 & C36a, O8 & O8A, O10 & O10A).

One of the dichloromethanes was also disordered and modelled in two positions with refined occupancies of 0.9292:0.0708(14). The C-Cl bond lengths in the minor form were restrained to be 1.745 angstroms. The ADP of two pairs of disordered atoms were constrained to be equal C68 & C68a, Cl4 & Cl4a.

The similarity of the ratios of the complexes and the dichloromethane means that occupancies of the alternative positions are coupled.

Compound 240

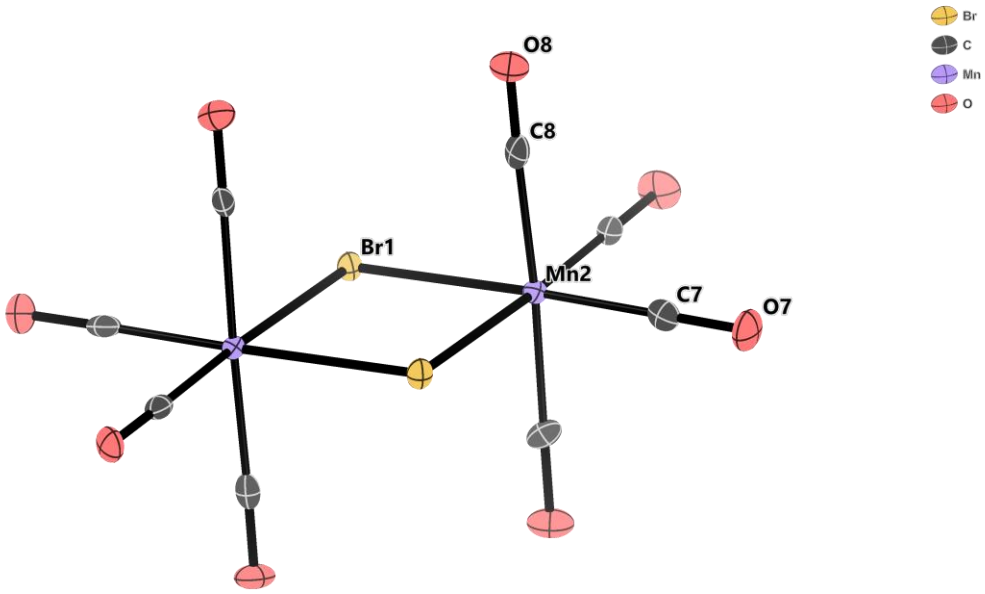

Figure 228. Single crystal X-ray diffraction structure of **240**. Thermal ellipsoids shown with 50% probability and hydrogen atoms removed for clarity. Selected bond lengths (Å): Mn1–Br1: 2.5306(12); Mn2–Br1: 2.5208(12); Mn1–Br2: 2.5305(12); Mn2–Br2: 2.5200(12); C1–Mn1: 1.889(7); C2–Mn1: 18.06(7). Selected bond angles (°): Mn1–Br1–Mn2: 95.48(4); C1–Mn1–C4: 177/7(3); C1–Mn1–C2: 90.4(30); C1–Mn1–Br1: 89.7(2); O1–C1–Mn1: 178.7(6).

Table 30. Crystal data and structure refinement for compound **240**.

Identification code	jml21008
Empirical formula	$Br_2C_8Mn_2O_8$
Formula weight	493.78
Temperature/K	110.00(10)
Crystal system	monoclinic
Space group	$P2_1/c$
a/Å	9.4576(3)
b/Å	11.5772(3)
c/Å	12.6902(3)
α/°	90
β/°	109.197(3)
γ/°	90
Volume/Å^3	1312.22(7)
Z	4
ρ_{calc}g/cm^3	2.499
μ/mm^{-1}	23.152
F(000)	928.0
Crystal size/mm^3	0.161 × 0.12 × 0.064
Radiation	Cu Kα (λ = 1.54184)
2Θ range for data collection/°	9.904 to 134.146
Index ranges	-11 ≤ h ≤ 7, -13 ≤ k ≤ 13, -12 ≤ l ≤ 15
Reflections collected	4872
Independent reflections	2347 [R_{int} = 0.0220, R_{sigma} = 0.0283]
Data/restraints/parameters	2347/0/181
Goodness-of-fit on F^2	1.266
Final R indexes [I>=2σ (I)]	R_1 = 0.0384, wR_2 = 0.1052
Final R indexes [all data]	R_1 = 0.0420, wR_2 = 0.1066
Largest diff. peak/hole / e Å^{-3}	1.03/-1.42

6.6 UV–Visible light filters

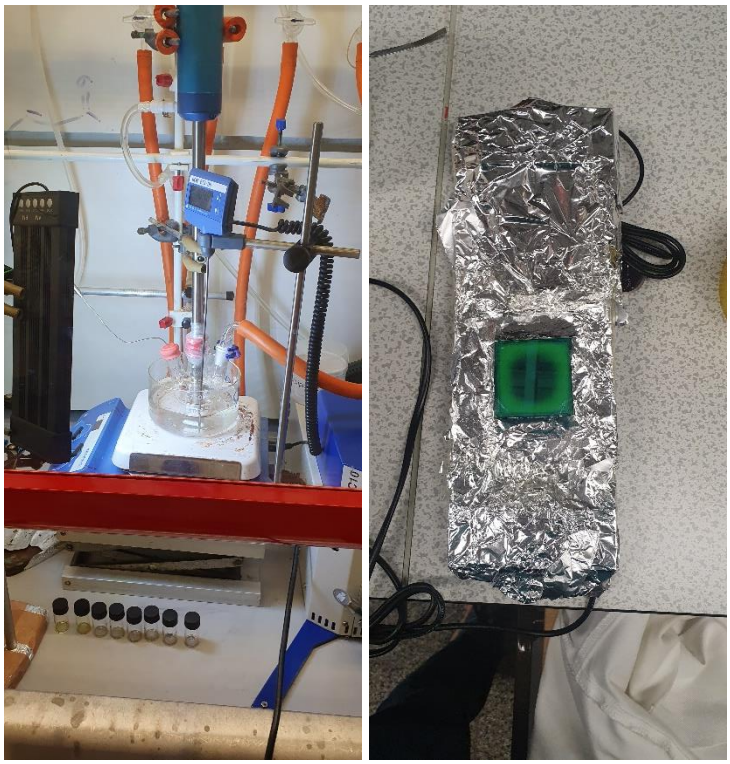

Figure 229. Left: LED array set up for reaction. Right: Foiled LED Array for controlled wavelength experiments.

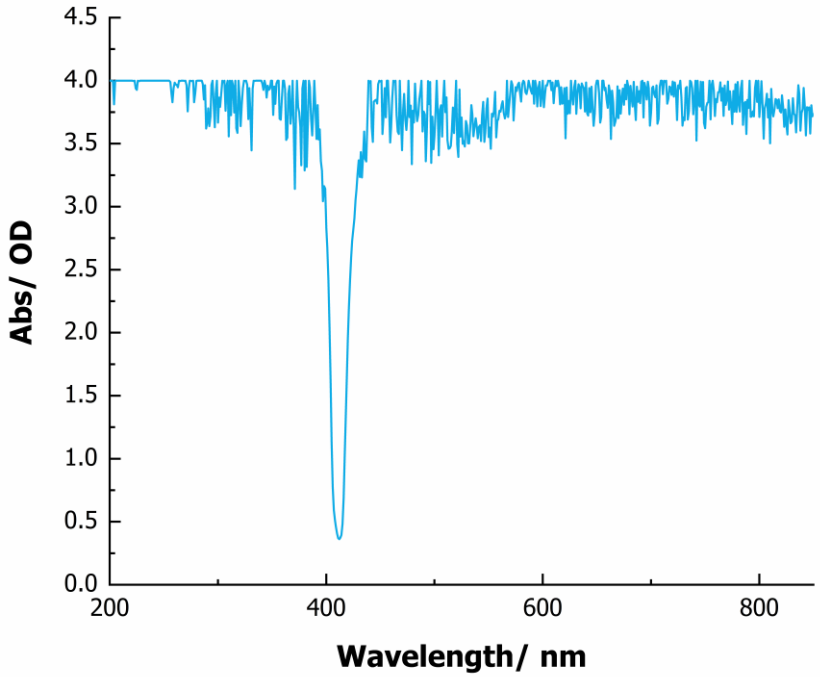

Figure 230. UV–Visible light filter used for 412 nm.

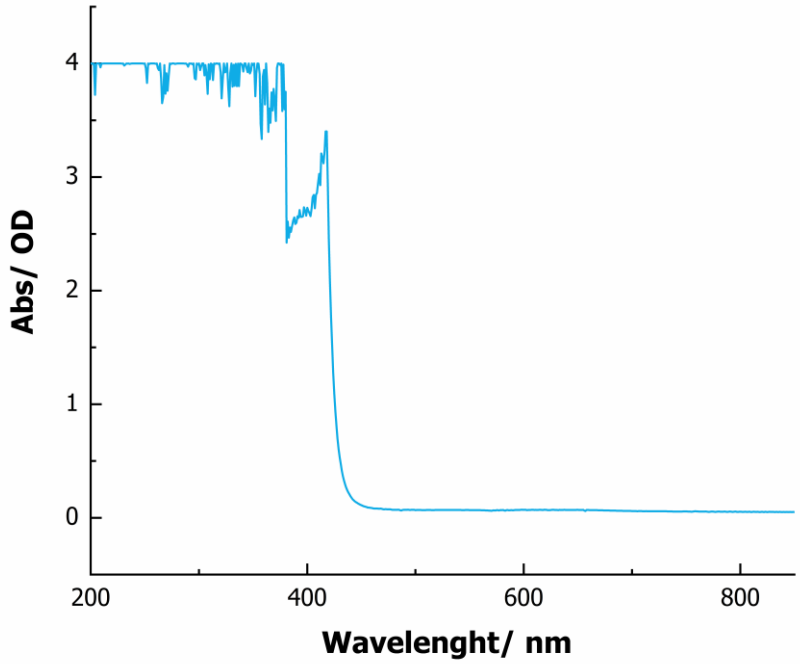

Figure 231. UV–Visible light filter used for 435 nm.

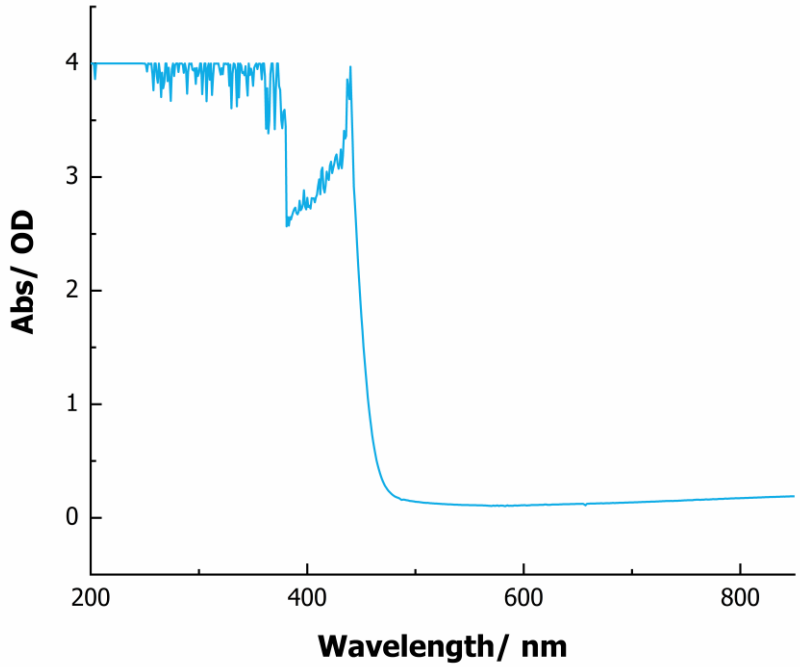

Figure 232. UV–Visible light filter used for 458 nm.

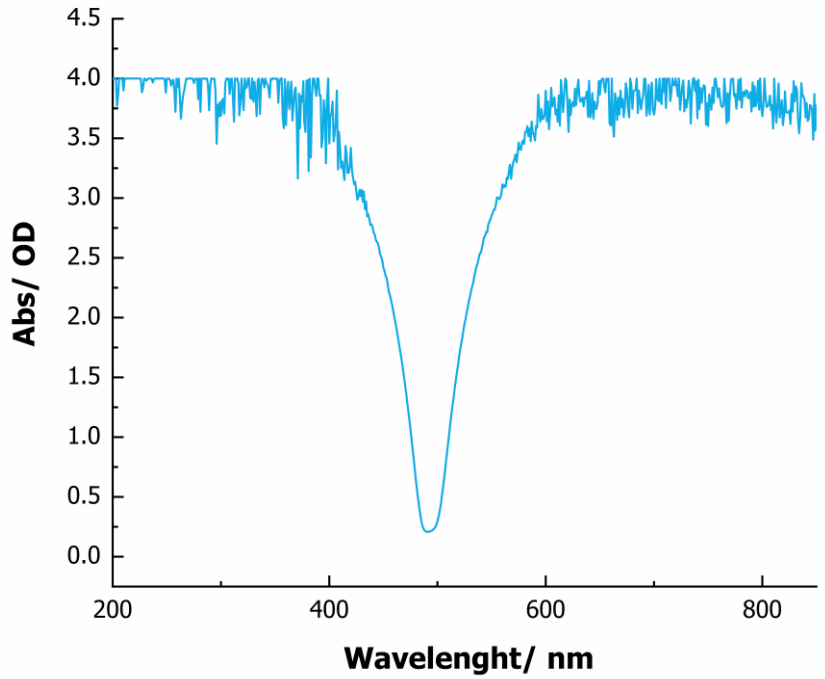

Figure 233. UV–Visible light filter used for 493 nm.

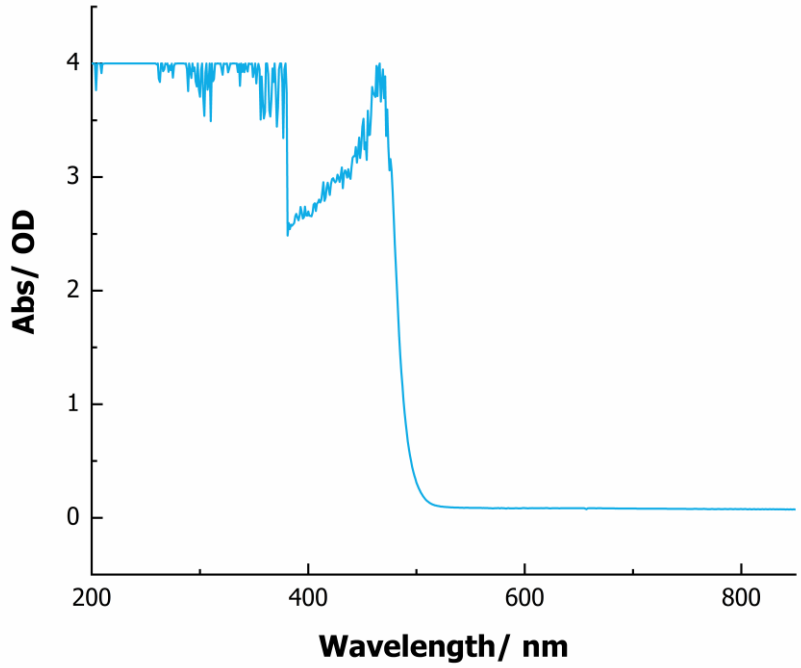

Figure 234. UV–Visible light filter used for 495 nm.

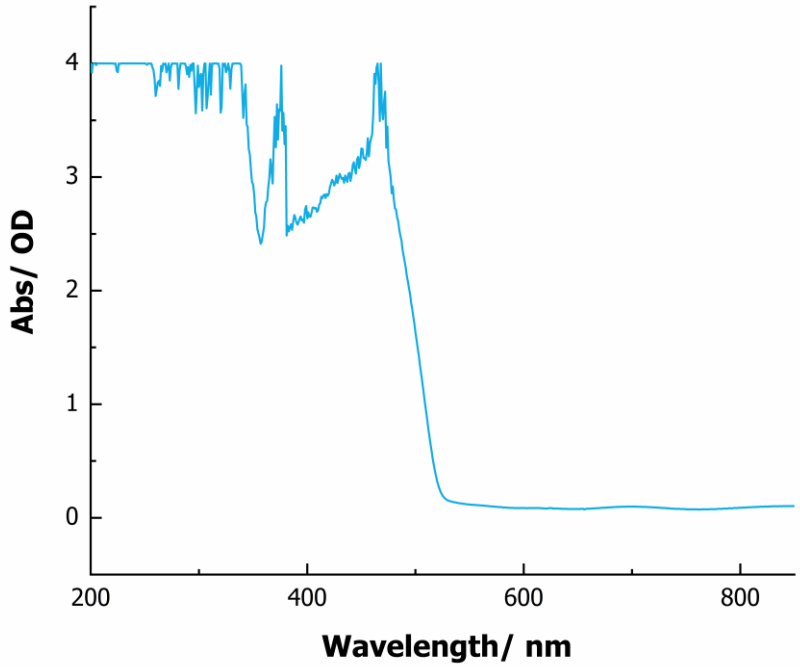

Figure 235. UV–Visible light filter used for 520 nm.

Appendix 1: Published Papers

Chemical Science

ROYAL SOCIETY OF CHEMISTRY

EDGE ARTICLE

View Article Online
View Journal

Cite this: DOI: 10.1039/d2sc02562k

All publication charges for this article have been paid for by the Royal Society of Chemistry

A comprehensive understanding of carbon–carbon bond formation by alkyne migratory insertion into manganacycles†

L. Anders Hammarback, [a] Jonathan B. Eastwood, [a] Thomas J. Burden, [a] Callum J. Pearce,[a] Ian P. Clark,[b] Michael Towrie,[b] Alan Robinson, [c] Ian J. S. Fairlamb *[a] and Jason M. Lynam *[a]

Migratory insertion (MI) is one of the most important processes underpinning the transition metal-catalysed formation of C–C and C–X bonds. In this work, a comprehensive model of MI is presented, based on the direct observation of the states involved in the coupling of alkynes with cyclometallated ligands, augmented with insight from computational chemistry. Time-resolved spectroscopy demonstrates that photolysis of complexes [Mn(C^N)(CO)$_4$] (C^N = cyclometalated ligand) results in ultra-fast dissociation of a CO ligand. Performing the experiment in a toluene solution of an alkyne results in the initial formation of a solvent complex *fac*-[Mn(C^N)(toluene)(CO)$_3$]. Solvent substitution gives an η^2-alkyne complex *fac*-[Mn(C^N)(η^2-R^{1}C$_2$R^2)(CO)$_3$] which undergoes MI of the unsaturated ligand into the Mn–C bond. These data allowed for the dependence of second order rate constants for solvent substitution and first order rate constants for C–C bond formation to be determined. A systematic investigation into the influence of the alkyne and C^N ligand on this process is reported. The experimental data enabled the development of a computational model for the MI reaction which demonstrated that a synergic interaction between the metal and the nascent C–C bond controls both the rate and regiochemical outcome of the reaction. The time-resolved spectroscopic method enabled the observation of a multi-step reaction occurring over 8 orders of magnitude in time, including the formation of solvent complexes, ligand substitution and two sequential C–C bond formation steps.

Received 6th May 2022
Accepted 8th July 2022

DOI: 10.1039/d2sc02562k

rsc.li/chemical-science

Introduction

A comprehensive understanding of the mechanistic processes that underpin catalytic reactions is vital to the rational development of new and improved systems with enhanced performance. Such mechanistic insight underpins the discovery of new synthetic transformations leading to atom- and step-efficient routes for structural modification. However, the observation and quantification of the individual microscopic steps across a catalytic reaction coordinate remains deeply problematic as they are frequently fast, entailing that intermediate species are short-lived and difficult to observe in ensemble 'real' reaction mixtures.[1]

Migratory insertion (MI) is one of the most important fundamental mechanistic processes in transition metal chemistry and catalysis. The term encompasses many transformations and may be generalised as an intramolecular coupling between an unsaturated L-type ligand (*e.g.* CO, alkene or alkyne) and an X-type ligand[2] (*e.g.* hydride, alkyl, aryl, alkenyl alkynyl, alkoxide[3–5] and amido[6]). Specific examples include (1) the combination of carbonyl and hydrocarbyl ligands to give acyl groups, a vital step in the carbonylation of methanol to acetic acid[7] and the Pauson–Khand reaction[8–10] (2) reaction between a metal hydride and an alkene as part of a hydrogenation process[11] and (3) alkene insertion into a metal alkyl complex during polymerisation reactions.[12,13] Processes such as β-hydride elimination and decarbonylation are the microscopic reverse of MI.[14]

MI processes underpin many of the recent synthetic advances in C–H bond functionalisation reactions. Typically, a proximal heteroatom-containing directing group enables selective C–H bond activation, resulting in the formation of a metallacyclic intermediate (Fig. 1a). A subsequent MI reaction with an unsaturated substrate, such as an alkene or alkyne (sometimes referred to as the acceptor molecule) is responsible for the C–C bond formation step. This results in a ring-expansion reaction to give new metallacycles which are key branching points in the reaction. Depending on the conditions employed

[a]Department of Chemistry, University of York, Heslington, York, YO10 5DD, UK. E-mail: ian.fairlamb@york.ac.uk; jason.lynam@york.ac.uk
[b]Central Laser Facility, Research Complex at Harwell, STFC Rutherford Appleton Laboratory, Harwell Campus, Didcot, Oxfordshire, OX11 0QX, UK
[c]Syngenta Crop Protection AG, Münchwilen, Breitenloh 5,4333, Switzerland

† Electronic supplementary information (ESI) available. See https://doi.org/10.1039/d2sc02562k

View Article Online
Chemical Science
Edge Article

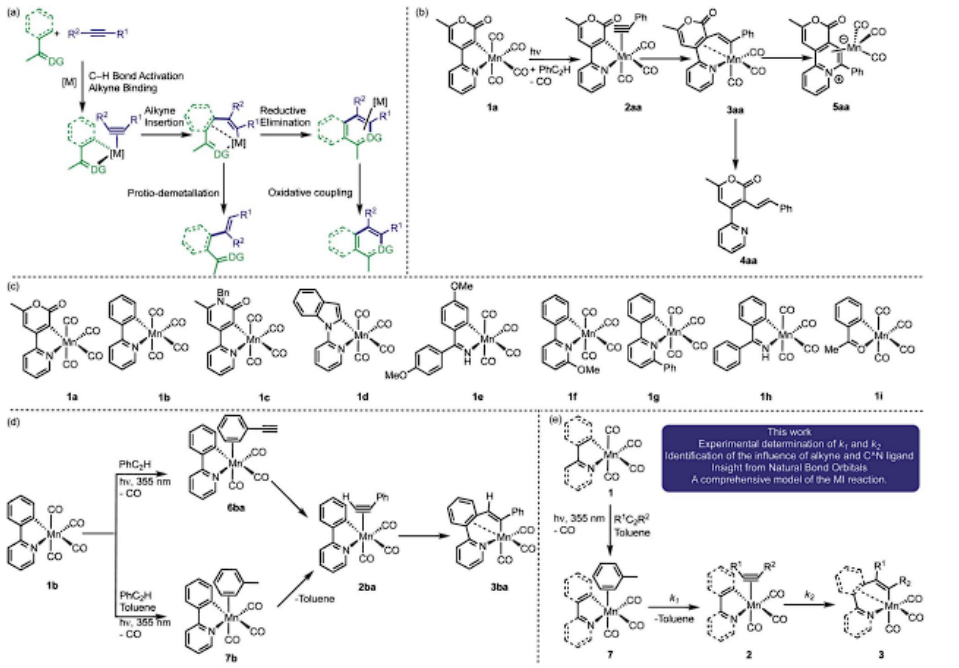

Fig. 1 (a) General mechanistic processes for d^6-metal catalysed C–H bond functionalisation reactions. (b) Previous synthetic work and results from low temperature NMR spectroscopic studies. (c) Complexes used in this study (d) previous insight from TR^MPS. (e) Insight obtained from this work.

and the nature of the catalyst, a range of products from either redox-neutral or oxidative coupling may be obtained (Fig. 1a). There have been significant advances in this area using d^6-metal pre-catalysts based on Mn(I),[15–18] Co(III),[19–23] Ru(II)[24–26] and Rh(III)[27–30] scaffolds.

Model studies have provided insight into MI steps within these catalytic cycles. For example, kinetic studies using cyclometallated Co(η^5-C_5Me_5) complexes have revealed that the rate-controlling process involves loss of a ligand to generate a 16-electron species – alkyne coordination and C–C bond formation are therefore fast under these conditions.[31–34]

Photolysis of the cyclomanganated 2-pyrone complex [Mn(2-pyrone)$(CO)_4$], **1a**, in the presence of PhC_2H, results in CO-dissociation and formation of the 7-membered manganacycle, **3aa**, most likely *via* alkyne complex **2aa** (Fig. 1b).[35] The role of **3aa** as a key intermediate in Mn(I)-catalysed reactions was demonstrated by its ability to undergo protio-demetallation to generate **4aa** or reductive elimination to form **5aa**.

These studies provide important insight into the role of the metallacyclic intermediate, but also demonstrate that many of the intermediates in this process, such as putative alkyne complexes, are short-lived. Although the MI step may not be rate limiting, it plays an important role in controlling the regioselectivity of the reaction. Therefore, being able to directly observe all the states in an MI reaction between a coordinated alkyne with a metallacyclic intermediate would enable an understanding of the factors that control this step in catalysis and more broadly in applied synthesis.

Time-resolved spectroscopy provides a solution to achieve this goal, circumventing the problems with observing specific intermediates in ensemble mixtures. Light can selectivity trigger pre-catalyst activation and a subsequent spectroscopic probe reveals the interactions between the activated catalyst and reaction components. Therefore, the direct observation of catalytic reaction intermediates and their subsequent fate over a range of timescales is possible.[36–38] Our recent application of time-resolved multiple probe spectroscopy (TR^MPS) with infrared detection to complexes **1a–d** (Fig. 1c) demonstrates how this can be applied to study catalytically relevant processes. Photolysis of **1b** in neat PhC_2H results in loss of CO and initial binding of the alkyne through the aryl-substituent to give **6ba** (Fig. 1d).[39] Rearrangement of this complex on a ps timescale then gives **2ba**. The MI reaction to form **3ba** then occurred on a μs timescale. Experiments between **1b** in toluene solutions of

View Article Online
Edge Article Chemical Science

PhC_2H revealed the initial formation of toluene complex, **7b**, indicating that, following CO-loss, initial coordination to the Mn occurs in a statistical fashion (toluene is the most dominant species in the experiment). Substitution of the coordinated toluene by PhC_2H gives **2ba**, followed by formation of **3ba**.

These findings present an opportunity to quantify all of the components of the MI process. It was reasoned that varying the nature of the cyclomanganated ligand in complexes **1** (Fig. 1c) and the substituents on the alkyne would enable the rate constants for the solvent–substitution reaction, k_1, and the C–C bond formation step, k_2, to be determined (Fig. 1e). When coupled with data from computational chemistry, this would provide unique insight into the factors that control the MI reaction. The successful implementation of this strategy is now reported.

Results and discussion

Methodology

In order to gain insight into the factors controlling all of the steps within a MI reaction, the reaction between a range of metallacycles, **1a–i**, and alkynes was investigated using $TR^{M}PS$ with IR detection. Experiments were performed with a pump wavelength of 355 nm and the changes to the vibrational modes in the metal carbonyl region between *ca.* 1850 and 2100 cm^{-1} recorded. The temporal flexibility of the $TR^{M}PS$ experiment was exploited so that processes occurring at pump-probe delays of between 1 ps and 1 ms could be observed.[40,41]

The time-resolved infra-red spectroscopic data are presented as difference spectra with the bands due to species lost on photolysis shown as negative peaks, whereas the subsequent photoproducts are shown as positive features.

Time-resolved infra-red (TR-IR) studies

a. Determination of order of reaction in PhC_2H and Mn complex. The photochemically induced reactions of **1b** and **1e** with PhC_2H were selected as exemplar systems to quantify the rate constants for the MI reaction and determine the order in Mn and alkyne for each step. Using **1e** as an example, photolysis in either neat PhC_2H or in a toluene solution results in the observation of four negative bands corresponding to the ground state IR spectrum of the Mn(I) carbonyl complex. This confirmed that **1e** was lost on irradiation (Fig. 2b and c). In a toluene solution of PhC_2H (Fig. 2c) new bands were observed at 2012 and 1914 cm^{-1} within 5 ps, corresponding to the formation of **7e**. The positions and intensity of the three Mn–CO stretching bands confirming that the complex contains three *fac*-coordinated CO ligands.[42,43] Identical spectra were observed in an experiment performed in the absence of PhC_2H, confirming the assignment as the toluene-coordinated complex.

Over the course of *ca.* 1 μs the bands assigned to **7e** were replaced by three new peaks at 2017, 1950, 1918 cm^{-1}. The shifts to higher wavenumbers are consistent with less π-back-bonding to the CO ligands, as expected with the inclusion of an η^2-bound alkyne (a good π-acceptor) into the coordination sphere of the metal. Therefore, these peaks were assigned to **2ea**. The three bands for **2ea** were then observed to decrease in intensity over the course of *ca.* 10 μs to be replaced by three new peaks at 2006, 1909, 1899 cm^{-1}, which were assigned to metallocycle **3ea** (Fig. 2a).

These observations correspond to the light-induced loss of CO from **1e**, followed by formation of the solvent complex **7e**. Substitution of the Mn-bound toluene by PhC_2H then affords **2ea** and subsequent MI reaction gives **3ea**. That **7e** is the initially formed product demonstrates that the initial binding event is under kinetic control, with solvent molecules being in excess in the reaction.

Analysis of the temporal behaviour of the reactions as a function of [alkyne] allowed for a kinetic analysis of these mechanistic steps. Experiments were performed under pseudo first-order conditions with a large excess of alkyne present.[44] Fits to exponential growth and decay functions allowed for observed first order rate constants (k_{obs}) to be determined as a function of [alkyne] for both transformations **7e** → **2ea** and **2ea** → **3ea**. Plots of k_{obs} *versus* [PhC_2H] (Fig. 2d and e) allowed for the second order rate constant for **7e** → **2ea** (k_1) of $(7.17 \pm 0.26) \times 10^7$ mol^{-1} dm^3 s^{-1} and first order rate constant **2ea** → **3ea** (k_2) $(2.25 \pm 0.16) \times 10^5$ s^{-1} to be determined. Plots of ln k_{1obs} *vs.* ln [PhC_2H] and ln k_2 *vs.* ln [PhC_2H] gave gradients of (0.83 ± 0.04) and (-0.01 ± 0.03), consistent with first and zero-order dependence of each step on the alkyne, respectively (see ESI†).

When the experiment was performed in neat PhC_2H (Fig. 2b) the initially formed photoproduct corresponded to the arene-bound complex **6ea**. Over the course of 100 ps **6ea** isomerised to the **2ea** and then, on a μs timescale, **3ea** was observed to form. Both the band positions of **2ea** and **3ea** and the value of k_2 were identical within 95% confidence limits to those observed in toluene solution, supporting the intramolecular nature of the MI reaction.

Repeating this series of experiments in a toluene solution of PhC_2H with **1b** as Mn-precursor returned an essentially identical series of observations, with $k_1 = (3.74 \pm 0.16) \times 10^7$ mol^{-1} dm^3 s^{-1} and $k_2 = (1.43 \pm 0.03) \times 10^5$ s^{-1}. These results demonstrate that, compared to the cyclomanganated imine complex, **1e**, the rate constant for the substitution of toluene by PhC_2H and for MI were slower.

b. Effects of alkyne substituents and cyclomanganated ligand. A series of experiments were devised to probe the effect of the structure of the alkyne and cyclomanganated ligand on the rates of the solvent substitution and MI reactions. In these experiments an identical concentration of alkyne and manganese complex was used so that the resulting pseudo first order rate constants for the loss of **6**/gain of **2**, $k_{1(obs)}$, were directly comparable between different alkynes and cyclomanganted complexes. As the MI reaction is zero order in alkyne, the first order rate constant for the formation of **3** is equivalent to k_2. The data are collated in Table 1.

Photolysis of toluene solutions of **1b** with alkynes R–4-C_6H_4–C_2H (R = NMe_2, MeO, H, F, CF_3, $MeCO_2$) all resulted in the initial formation of a toluene adduct **7b**. This was followed by substitution of the solvent to give the corresponding alkyne complexes **2b**. The vibrational modes of the CO ligands in

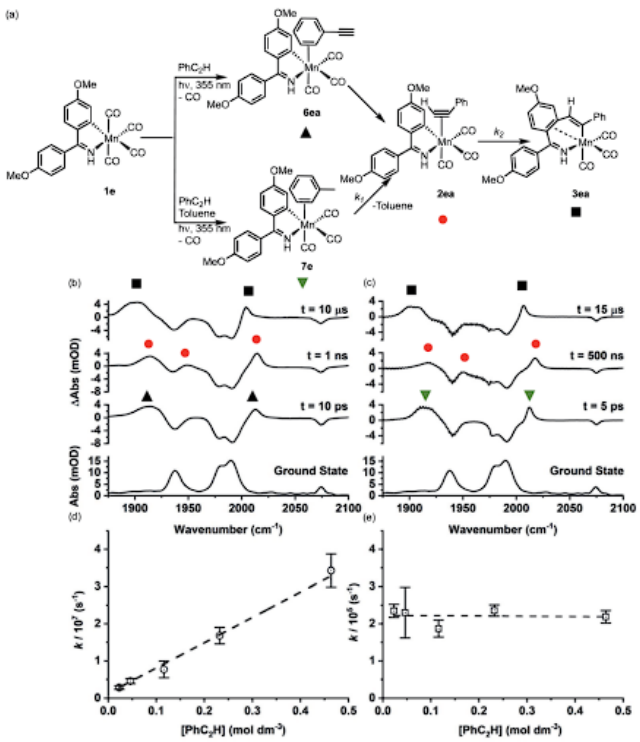

Fig. 2 (a) Reaction scheme showing the structure of intermediates formed on photolysis. (b) Bottom ground state IR spectrum of **1e** in toluene solution, above TRIR data for **1e** in neat PhC_2H recorded at various pump-probe delays. (c) Bottom ground state IR spectrum of **1e** in toluene solution, above TRIR data for **1e** in a toluene solution of PhC_2H recorded at various pump-probe delays. (d) Plot of k_{1obs} *versus* [PhC_2H] determined from experiments of **1e** in a toluene solution of PhC_2H, error bars indicate 95% confidence limits for the rate constants. (e) Plot of k_2 *versus* [PhC_2H] determined from experiments of **1e** in a toluene solution of PhC_2H error bars indicate 95% confidence limits for the rate constants.

complexes **2b** provided insight into the nature of the metal–ligand bonding in these complexes. The frequency of the high-energy symmetric stretch was observed at higher energy when an electron-withdrawing substituted was present on the alkyne (*e.g.* 2014 cm^{-1} for R = CF_3) compared to when an electron donating group was used (*e.g.* 2002 cm^{-1} for R = NMe_2). This is consistent with competition for electron density between the π-acidic alkyne and carbonyl ligands. More electron-rich alkynes are poorer acceptor ligands, resulting in a greater degree of π-backdonation to the Mn-based carbonyl ligands and thus the observed shift to lower energy when R = NMe_2.

This approach also allowed for the effects of different alkynes on solvent substitution and C–C bond formation to be evaluated. On the whole, the values of $k_{1(obs)}$ only showed a small dependence on the nature of the alkyne substrates with the most electron donating substituent being formed at a slower rate than those with electron withdrawing groups. However, k_2 exhibited a much greater variation. For the 4-substituted alkynes, R–4-$C_6H_5C_2H$, k_2 was greatest when an electron withdrawing group was present *e.g.* $(4.86 \pm 1.37) \times 10^5$ s^{-1} for R = CF_3, compared to $(1.11 \pm 0.31) \times 10^5$ s^{-1} for R = NMe_2. The MI reaction of internal alkynes was much slower than their terminal analogues. When compared to PhC_2H, k_2 was approximately half that when PhC_2Ph was used and an order of magnitude slower for the cyclohexyl derivative CyC_2H. Repeating the experiment with $^nBuC_2{}^nBu$ resulted in a different observation. Following the initial formation of **7b**, solvent substitution was observed to give the corresponding alkyne complex as demonstrated by the characteristic bands for this type of complex. However, on the timescale of the experiment (1 ms) no evidence for the subsequent MI reaction was obtained.

These broad trends were also observed when **1e** was used as a substrate. When compared to PhC_2H, the rate constant for MI was considerably slower when PhC_2Ph was employed: (2.25 ±

View Article Online
Edge Article Chemical Science

Table 1 Collated spectroscopic and kinetic parameters

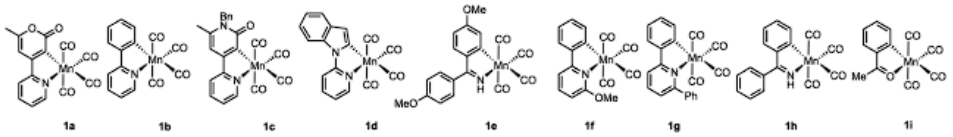

1a 1b 1c 1d 1e 1f 1g 1h 1i

Complex	Alkyne	$\nu_{(CO)}$ complex **2**/cm^{-1}	$\nu_{(CO)}$ complex **3**/cm^{-1}	$k_{1(obs)}/10^6$ s^{-1}	$k_2/10^5$ s^{-1}	Experimental $\Delta G^{\ddagger}_{298}$/kJ mol^{-1}
1a[a]	PhC_2H	2015, 1962, 1923	2008, 1928, 1903	Neat	10.4 ± 1.5	39
1b	PhC_2H	2009, 1944, 1912	2008, 1922, 1899	8.32 ± 3.56	1.43 ± 0.03	44
1b	CyC_2H	2010, 1944, 1908	2006, 1920, 1890	6.30 ± 0.71	0.13 ± 0.01	50
1b[a]	$PhCO_2CH_2C_2H$	2012, 1947, 1909	2001, 1903, 1892	Neat	1.79 ± 0.49	43
1b	PhC_2Ph	2004, 1943, 1912	2003, 1904, 1893	11.95 ± 2.08	0.57 ± 0.06	46
1b	$^nBuC_2{}^nBu$	2006, 1925, 1906	Not observed	4.36 ± 1.00	Not observed	N/A
1b	CF_3–4-C_6H_4–C_2H	2014, 1946, 1918	2012 1925, 1905	11.72 ± 3.30	4.86 ± 1.37	41
1b	F–4-C_6H_4–C_2H	2011, 1942, 1915	2010, 1923, 1900	12.07 ± 5.71	4.10 ± 1.74	41
1b	MeO–4-C_6H_4–C_2H	2008,[b] 1910	2009, 1923, 1898	6.36 ± 3.79	0.91 ± 0.32	45
1b	$MeCO_2$–4-C_6H_4–C_2H	2013, 1894	2011, 1923, 1902	9.95 ± 0.41	4.79 ± 2.90	41
1b	Me_2N–4-C_6H_4–C_2H	2002, 1906, 1884	2007 1921, 1989	5.76 ± 1.33	1.11 ± 0.31	44
1c[a]	PhC_2H	2011, 1916	2002, 1921, 1898	Neat	74.6 ± 12.8	34
1d[a]	PhC_2H	2016, 1931, 1922	2009, 1909	Neat	0.20 ± 0.01	48
1e	PhC_2H	2017, 1950, 1918	2006, 1909, 1899	[c]	2.25 ± 0.16	43
1e	PhC_2H	2014, 1948, 1914	2004, 1906, 1895	Neat	2.36 ± 0.15	43
1e[c]	PhC_2Ph	1997, 1905[b]	1997, 1903, 1893	[d]	0.24 ± 0.01	42
1e	$^nBuC_2{}^nBu$	2009, 1932, 1910	Not observed	61.7 ± 1.7	Not observed	N/A
1f	PhC_2H	2014, 1941, 1906	2012, 1915, 1905	32.5 ± 7.4	1.41 ± 0.05	43
1g	PhC_2H	2012, 1941, 1908	2012, 1915, 1908	55.3 ± 6.5	1.99 ± 0.13	43
1h	PhC_2H	2004, 1914[b]	1991, 1903, 1896	18.0 ± 2.8	4.23 ± 0.18	41
1i	PhC_2H	2023, 1950, 1914	2010, 1906, 1894	5.94 ± 1.01	1.99 ± 0.08	43

[a] Data from ref. 39. [b] One band obscured by bleach. [c] Experiment in heptane solution. [d] Second order rate constant determined to be (2.89 ± 0.14) × 10^9 mmol^{-1} dm^3 s^{-1}. [e] Second order rate constant determined to be (7.17 ± 1.38) × 10^7 mol^{-1} dm^3 s^{-1}.

0.16) × 10^5 s^{-1} and (0.24 ± 0.01) × 10^5 s^{-1} respectively. Due to competition with trace water occurring in toluene, the experiments with PhC_2Ph were performed in heptane solution (water content ≤ 10 ppm). It should be noted that the rate of solvent substitution in heptane is *ca.* two orders of magnitude faster than for toluene, indicating that the former solvent is more weakly bound to the metal. As with **1d**, the corresponding experiment with $^nBuC_2{}^nBu$ resulted in the formation of an η^2-alkyne complex but no evidence for the subsequent MI reaction was obtained.

The effect of the nature of the cyclomanganated ligand on the MI was probed further. This ligand may be considered to consist of a heteroatom-based directing group and the metalated carbon atom which undergoes the MI reaction. Across the series of complexes **1e–1i**, in which the directing group was modified, the MI reaction with PhC_2H in toluene solution exhibited only a relatively small variation in k_2. The greatest rate constant was for **1h** (4.23 ± 0.18) × 10^5 s^{-1}, and the smallest for **1f** (1.41 ± 0.05) × 10^5 s^{-1}. All were similar to those observed for **1b** (1.43 ± 0.03) × 10^5 s^{-1}. However, the data on the pyrone, **1a**, pyridinone, **1c**, and indole, **1d**, complexes, in which the migrating group was changed, showed a greater variation in k_2. The greatest value of k_2 was observed for pyridinone-based **1c** (k_2 = 74.6 ± 12.8 × 10^5 s^{-1}) and the slowest for indole-substituted **1d** (k_2 = 0.20 ± 0.01 × 10^5 s^{-1}), which corresponds to a 373-fold difference in rate constant. These data indicate that, for a given alkyne, it is the primarily the nature of the organic group bound to the manganese which governs the MI reaction and the directing group has little overall effect on this process.

Computational studies

Further insight into the MI reaction was obtained by studying the states involved using Density Functional Theory (see ESI† for full details of the methodology employed). In these calculations, the alkyne complexes, **2**, were taken as the reference state. In the case of unsymmetrically substituted alkynes there are two possible orientations of the alkyne which lead to the MI reaction resulting in 1,2- and 2,1-insertion (Fig. 3a). As the latter process is kinetically preferred (*q.v.*), complexes with the alkyne in the orientation leading to this outcome were used as the reference state.

The MI reactions were modelled for all of the combinations of alkyne and cyclomanganated ligands studied experimentally, for both the 1,2- and 2,1-insertion pathways. In each case a transition state for MI ($\mathbf{TS_{23}}$) was located which, through a dynamic reaction coordinate analysis, was shown to link alkyne complex **2** and metallacycle **3** (Fig. 3a). It was also possible to correlate the experimentally and computationally

View Article Online
Chemical Science
Edge Article

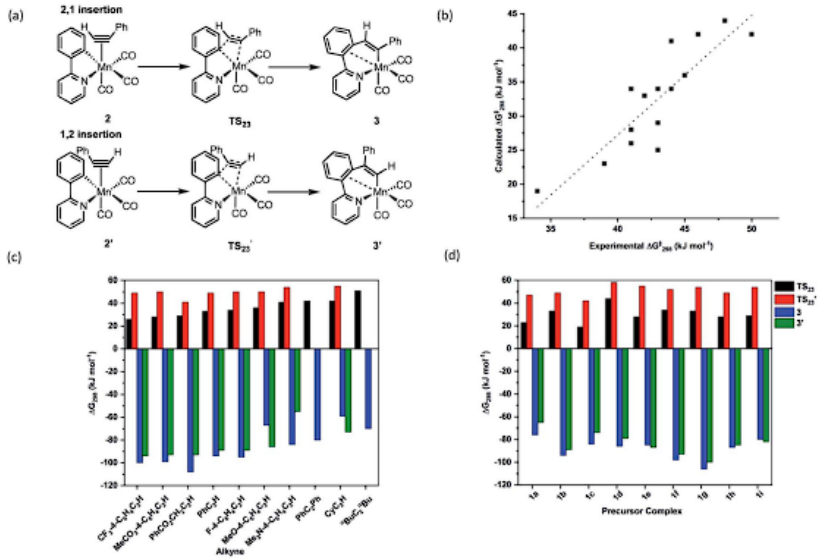

Fig. 3 (a) DFT-calculated pathway for C–C bond formation. (b) Correlation between DFT-calculated and experimentally determined free energies of activation for C–C bond formation, the dotted line is a linear least squares regression ($R^2 = 0.728$). (c) Collated energies showing the effect of different alkynes on the orientation and thermodynamics of insertion into complex **1b**. (d) Collated energies showing the effect of different metallacycles on the orientation and thermodynamics of insertion of PhC_2H.

determined free energies of activation for the insertion reaction. In this case, the experimentally determined first order rate constants (k_2) were converted to Gibbs energies using the Eyring equation. The resulting plot (Fig. 3b) showed a good correlation between the two approaches, demonstrating the computational method was a competent and viable model for this reaction. In addition, the predicted barrier to insertion for $^{n}BuC_2{}^{n}Bu$ was the highest of those calculated, consistent with the fact that no MI reaction was observed in the TRIR experiments with this alkyne.

This analysis demonstrates this is an excellent system to model through computational chemistry as TR^{M}PS has enabled the first order rate constants for the exact elemental step under consideration to be determined.

The calculations provided insight into effects of the different substituents on the rate of the insertion reaction, the orientation of the insertion and ultimately the nature of the C–C bond formation step.

Although the two orientations of the alkyne complex **2** and **2′** were generally found to be at essentially identical energies, the transition states for the 2,1-insertion (black bars, Fig. 3c and d) are found to be uniformly at lower energy than the corresponding 1,2-insertion (red bars). In most cases, the orientation of insertion does not significantly affect the overall thermodynamic change of the insertion process and therefore we propose that the regiochemical outcome of the reaction is kinetically controlled.

Further insight into the nature of the MI reaction was obtained by analysis of the electronic structure of states **2**, **TS$_{23}$** and **3**. An evaluation of the canonical molecular orbitals obtained at the D3-pbe0/def2-TZVPP level of theory revealed that several MOs were involved in C–C bond formation step. Therefore, in order to obtain a chemically intuitive view of the MI reaction, the electronic structure of each state was modelled using the Natural Bond Orbital (NBO) approach.[45] The relevant NBOs involved in the C–C bond formation step for complexes **2ba**, **TS$_{23ba}$** and **3ba** are shown in Fig. 4. The NBOs of the alkyne ligand are π-bonding orbitals 99, 100 and their antibonding counterparts 157 and 158 which all have >90% p-character. Of the two orthogonal sets, orbitals 100 and 158 are directly involved in bonding to the metal, with 100 showing a signification second order perturbation stabilisation ($\Delta E_{ij}^{(2)} = 73.59$ kcal mol^{-1}) reflecting electron donation to a vacant metal-orbital. There is corresponding resonance stabilisation from a filled Mn d-orbital to the antibonding π*-orbital 158 ($\Delta E_{ij}^{(2)} = 24.09$ kcal mol^{-1}) which can be viewed as back-donation in the Dewar–Chatt–Duncanson model. Orbitals 99 and 157 do not show any significant interaction with metal-based orbitals, indicating that the alkyne is best viewed as a formal two-electron donor, consistent with an 18-electron count. The Mn–C bond involved in the MI reaction is described as a carbon-based lone pair (NBO 42), with *ca.* 26% s and 74% p character. The donor interaction to the metal is modelled

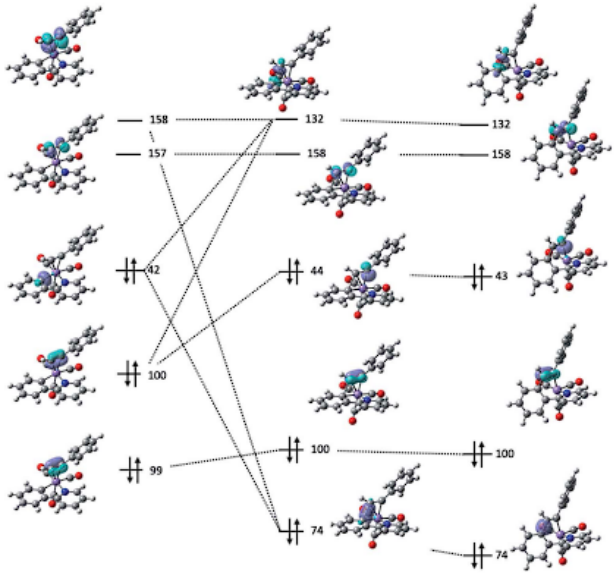

Fig. 4 Key NBOs involved in the migratory insertion process for **2ba** (left) TS_{23ba} (centre) and **3ba** (right).

through resonance stabilisation to an empty M–L anti-bonding orbital ($\Delta E_{ij}^{(2)} = 131.18$ kcal mol^{-1}).

Analysis of the NBOs in $\mathbf{TS_{23ba}}$ revealed the key interactions controlling the C–C bond formation. NBO 74 describes the bonding component of the nascent C–C bond: it has an occupancy of 1.65 electrons and *ca.* 27% s and 73% p character. Examination of the second order perturbation analysis reveals the nature of the metal-assistance in the C–C bond step as NBO 74 acts a donor to a vacant metal orbital (NBO 105, $\Delta E_{ij}^{(2)} =$ 75.02 kcal mol^{-1}, Fig. 5b). This is complemented by back-donation to the corresponding C–C antibonding orbital (NBO 132). This occurs from a filled metal d-orbital (NBO 38) ($\Delta E_{ij}^{(2)} =$ 15.95 kcal mol^{-1}, Fig. 5c) and a hyperconjugative interaction between NBO 132 and the newly-formed Mn–C bond, NBO 44, ($\Delta E_{ij}^{(2)} = 77.13$ kcal mol^{-1}, Fig. 5d). Commensurate with these interactions, the formally C–C antibonding orbital has a population of 0.34 electrons.

Analysis of the NBOs for **3ba** demonstrates that the newly formed C–C bond is composed of a filled bonding orbital (NBO 74, occupancy 1.97 electrons) comprised of overlap between two sp^2-hybridised carbon atoms. The corresponding anti-bonding orbital NBO 132 is essentially vacant (occupancy 0.02 electrons). The newly formed Mn–C bond is described by NBO 43 which is a carbon-based lone pair that is resonance-stabilised by donation to a vacant metal orbital ($\Delta E_{ij}^{(2)} = 146.6$ kcal mol^{-1}). MI reactions result in a formal decrease in electron count (in this case from 18- to 16-electron) and it has been proposed that weak donor interactions between the newly formed metallacycle and the metal help to stabilise the unsaturated nature of the metal.[35] The NBO calculations provide further evidence for this interaction with a small resonance stabilisation between a π-bond on the arene ring and a vacant metal–ligand anti-bonding orbital ($\Delta E_{ij}^{(2)} = 11.89$ kcal mol^{-1}).

Analysis of these NBOs and how they change during the C–C bond formation step provides important mechanistic insight. The formation of $\mathbf{TS_{23ba}}$ is probably best viewed as a combination of NBO 42 (a carbon-based lone pair) with NBO 158 (π*-orbital on the alkyne). Concurrent with this, the formation of NBO 44, which is the carbon-based lone pair responsible for the new Mn–C bond, may be viewed as being derived from NBO 100 (filled p-orbital on the alkyne). Therefore, the two alkyne orbitals engaged in synergic bonding with the Mn are also those involved in the MI process. To provide effective overlap between NBO 42 and NBO 158, it is evident that the alkyne must be aligned with the Mn–C bond in the 2-phenylpyridine, as is observed in both structure **2ba** and transition state structure $\mathbf{TS_{23ba}}$.

The NBO calculations provided insight into how the structural changes to the alkyne and metallacycle within this series of compounds affected the MI reaction. An analysis of the calculated NBOs in states **2**, $\mathbf{TS_{23}}$ and **3** across a range of complexes studied in this work demonstrated that the different substitution patterns only had a notable effect on the donor/acceptor interactions in $\mathbf{TS_{23}}$.

Fig. 5e shows the correlation between the calculated Gibbs energy of activation for the MI reaction based on individual

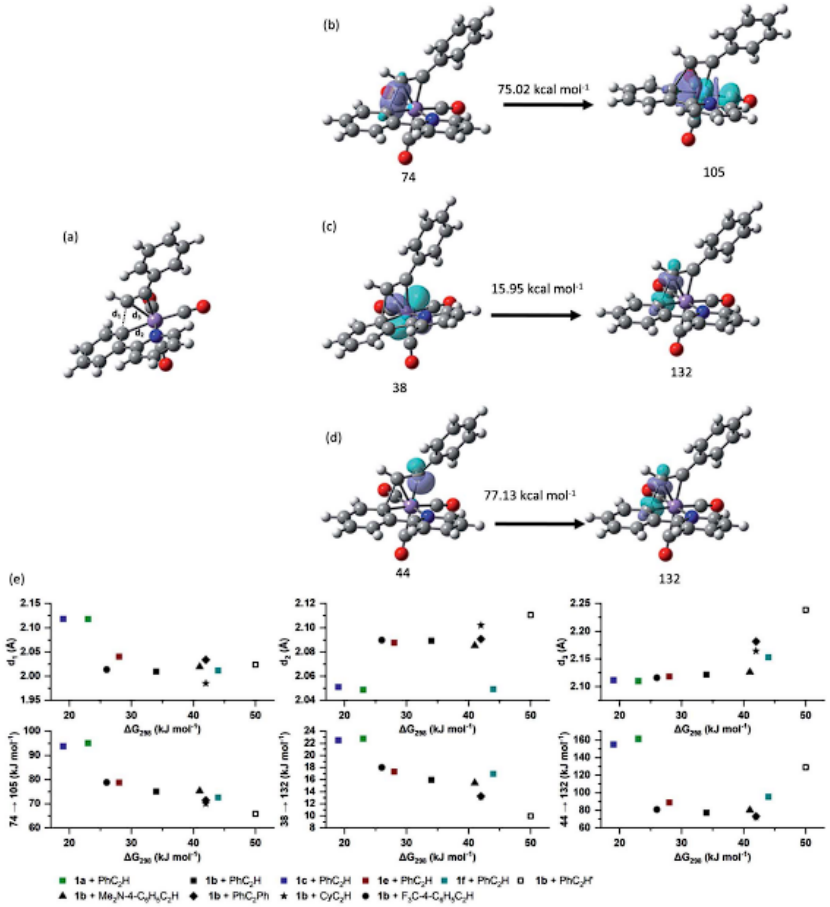

Fig. 5 (a) Structure of TS_{23ba}. (b)–(d) Selected donor–acceptor interactions in TS_{23ba}. The energies given are the second order perturbation energies associated with each interaction. (e) Correlation of computationally derived parameters in TS_{23} with the free energy of activation for the alkyne insertion.

alkyne/metallacycle combinations and the $\Delta E_{ij}^{(2)}$ values for the three donor/acceptor interactions in Fig. 5b–d. Correlations between the bond metrics in the transition state with the Gibbs energy of activation are also shown. These data provide insight into the critical factors controlling the MI reaction. As detailed above, the 2,1-insertion of the alkyne is kinetically favoured over the 1,2-insertion. In the 1,2-transition state the orientation of the alkyne results in longer Mn–C bonds to the alkyne and may be interpreted as greater steric repulsion in the 1,2-insertion transition state. However, the NBO analysis shows that these elongated distances correlate with weaker donor/acceptor interactions between the nascent C–C bond and the metal (black squares *versus* open squares in Fig. 5e). Although this is slightly compensated by a greater C–C hyperconjugative interaction, it is postulated that the strength of these donor/acceptor interactions is the key factor controlling the rate of the MI reaction.

This is further illustrated by comparing the data for PhC_2Ph and CyC_2H. Again, the Mn-alkyne distance are longer than in the PhC_2H case, which results in weaker donor/acceptor interactions. However, for the 2-pyrone and 2-pyridinone manganacycles which show the fastest rates of MI reaction, then the opposite effect is observed, the alkyne and Mn–C bonds are notably shorter and the donor–acceptor interactions much

stronger. Commensurate with this model, the nascent C–C bond is longer in these cases.

Observation of the fate of manganacycle 3ia

As shown in Fig. 1a, manganacycles such as **3** have several potential fates which underpins the synthetic versatility of C–H bond activation reactions promoted by d^6-metal complexes. In the case of complex **3ia**, which is derived from acetophenone, the temporal flexibility of the TR^{M}PS experiment enabled the direct observation of one of these pathways following the MI reaction. Photolysis of **1i** in a toluene solution of PhC_2H resulted in the expected formation of toluene complex **7i** (Fig. 6a), followed by alkyne substitution and insertion to give **2ia** and **3ia** respectively. However, in contrast to the other systems investigated in this study, the peaks in the TRIR spectra for **3ia** were found to subsequently decrease in intensity to be replaced by a new band at 2013 cm^{-1} and a broad feature centred at 1912 cm^{-1} ($k_{obs} = 1.02 \pm 0.03 \times 10^4\ s^{-1}$) which were assigned to **8ia** (Fig. 6b).

The stoichiometric reactions of manganacycles containing ketone-based directing groups may give two different potential outcomes. In the first instance, a formal reductive elimination reaction to give a six-membered ring may occur. In the case of cyclomanganated chalcone derivates this results in the formation of pyranyl complexes.[46,47] This process is analogous to the catalytic oxidative coupling of alkynes with heterocycles and the related formation of **5aa** (Fig. 1b).[25] Alternatively, manganated aromatic ketones have been shown to react with alkynes to give 1*H*-inden-1-ols (Fig. 6d).[48,49] A key step in such a process would be the formation of a five-membered ring and it was envisaged that could occur from **3ia** through nucleophilic attack of the Mn-coordinated carbon atom onto the carbonyl group of the ketone.[46,47] Both of these potential pathways were successfully modelled by DFT (Fig. 6c). In the case of the first pathway, which would afford a six-membered ring, the transition state for C–O bond formation (TS_{39ia}) was located at +17 kJ mol^{-1} with respect to the alkyne complex **2ia** which was taken as the reference state. This corresponds to an energic span of 78 kJ mol^{-1} from **3ia**. The transition state for the formation of the five-membered ring, TS_{38ia} was located at much lower energy (−37 kJ mol^{-1}), a barrier of 24 kJ mol^{-1} from **3ia**.

Complex **8ia** was assigned as the indenoate complex shown in Fig. 6a. This is on the basis that TS_{38ia} is at significantly lower energy than TS_{39ia} and the predicted barrier is 24 kJ mol^{-1}. The predicted scaled IR bands for the metal carbonyl groups predict the experimentally observed blue shift on changing from **3ia** to **8ia**. In the case of the putative formation of **10ia**, a red shift was predicted (see ESI†) which, taken with the larger predicted

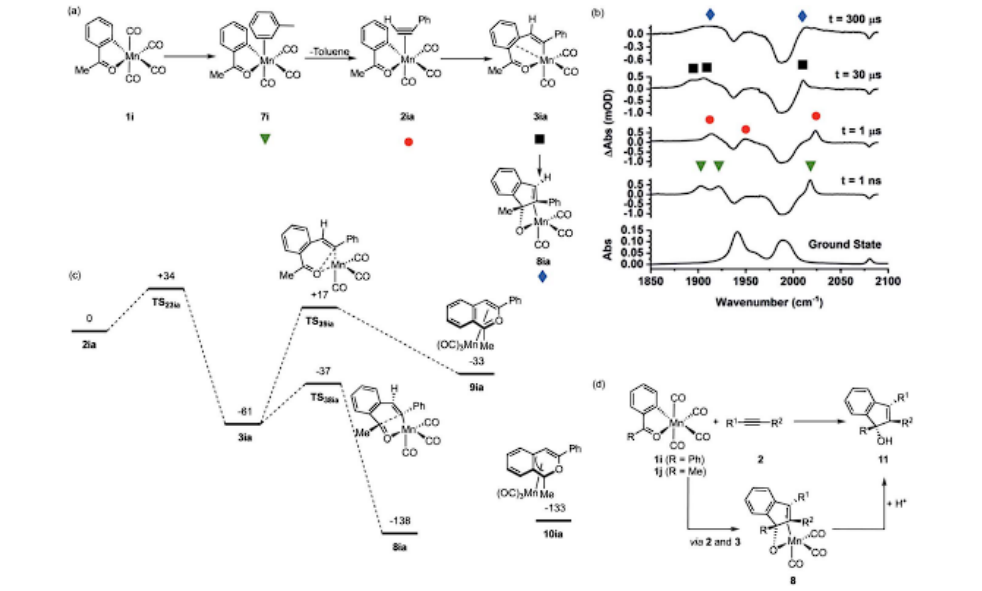

Fig. 6 (a) Reaction scheme showing the structure of intermediates formed on photolysis of **1i** in a toluene solution of PhC_2H. (b) Bottom ground state IR spectrum of **1i** in toluene solution, above TRIR data for **1i** in a toluene solution of PhC_2H recorded at various pump–probe delays. (c) DFT-calculated pathways for Mn-promoted C–C bond formation. Energies are Free Energies at 298 K in kJ mol^{-1} at the D3-pbe0/def2-TZVPP//bp86/SV(P) level with COSMO solvation in toluene. (d) Previously reported Mn-promoted formation of 1*H*-inden-1-ols (top) and the role of intermediate **8** (bottom).

barrier for its formation, excludes assignment to this complex. Additionally, calculations on the related systems which have been shown experimentally to yield the pyranyl complexes indicated that the alternative pathway would be expected (see ESI†).

The observations from this experiment are therefore assigned to the key C–C bond formation steps that underpin the Mn-promoted formation of 1*H*-inden-1-oles (Fig. 6d). Light-induced CO loss from **1i**, is followed by solvent coordination to give **7i**; solvent substitution by the alkyne (**7i** → **2ia**, ns timescale) is followed by insertion (**2ai** → **3ai** 10 μs timescale), with final formation of the five-membered ring (**3ia** → **8ia** 100 μs timescale). In the synthetic work, it is then expected that protonation of **8ia** affords the 1*H*-inden-1-ol (shown as **11** in Fig. 6d).

More widely, these results demonstrate the potential of TR^{M}PS to enable the direct observation of bond-formation steps occurring over several orders of magnitude in time.

Conclusions

The data from this study indicate that the rate and selectivity of the migratory insertion reactions of alkynes into Mn–C bonds is directly controlled by the extent of synergic interactions involving the nascent C–C σ-bond. These interactions are analogous to the more well-known donor/acceptor bonding that underpins the metal-promoted oxidative addition activation pathway of H_2, C–H and related element-hydrogen bonds and it is envisaged that parallel arguments about how metal–ligand interactions influence these reactions can be made in this case.

Previous experimental and computational work have rationalised the regioselectivity of the MI process in terms of both steric[50–52] and/or electronic factors (either orbital coefficients on the alkyne,[53–55] or the relative electron rich/poor nature of the alkyne carbons).[56,57] The steric influence of spectator ligands on the MI process has also been highlighted.[58]

It is proposed that the model presented in this work provides a framework to harmonise all of these arguments. For example, as shown in the case of PhC_2H *vs.* CyC_2H in the current study, an increase in bulk of the alkyne results in a slower rate of ML This is rationalised on the basis of increased metal–ligand bond lengths in the transition states of the more crowded cases and a commensurate decrease in the synergic interaction involving the nascent C–C σ-bond. Electronic factors are also consistent with this model. For example, a more electron deficient alkyne would be expected to increase π-backbonding to the C–C σ-bond accelerating the rate of reaction (as also observed experimentally). In addition, the carbon atom of the alkyne with the greatest orbital coefficient would enable greater metal–ligand interactions in the transition state, again enhancing this synergic interaction.

It is also informative to place the results from this study within the context of catalytic reactions that have been proposed to involve the insertion of an alkyne into a manganacycle. As many of these processes proceed at temperatures >100 °C, then the MI step which occurs on a μs timescale is unlikely to be rate controlling. However, our data support the proposition that the regiochemical outcome (1,2 *vs.* 2,1 alkyne insertion) is kinetically controlled through $\mathbf{TS_{23}}$. A survey of a number of reactions[38,59–64] which relay on this MI reaction show that for terminal alkynes 2,1 insertion is universally observed.[65] This is consistent with the proposed model as the transition state for 1,2-insertion has weaker Mn–C synergic interactions due to a longer d_3 distance (Fig. 5). Examples with unsymmetric internal alkynes only show significant selectivity on insertion when there is a profound difference in substitution pattern (*e.g.*, with MeC_2Ph or EtC_2Ph).[62,63] In these examples, 2,1 insertion dominates presumably due to the same geometric factors which control the insertion of terminal alkynes predominating, enhancing the orbital interactions in $\mathbf{TS_{23}}$.

The approach described in this paper also highlights how spectroscopic measurements can be integrated with computational chemistry to provide unique and important insight into catalytic reaction mechanism. Directly observing processes occurring across a wide range of timescales ensures that previously inaccessible mechanistic insight becomes available.

Data availability

The dataset associated with this article is available at **https://doi.org/10.15124/8ccc891d-15a5-4a79-986b-6d20b3777d59**.

Author contributions

JML and IJSF conceived the experimental programme with input on project direction from AR. The TRIR experiments were performed by LAH, JML, IJSF, JBE, TJB and IPC on instrumentation set-up and built by MT. Manganese compounds were prepared and analysed by LAH, JBE and TJB; JML and CJP performed and analysed the DFT calculations. TRIR data were analysed by JML, LAH, IJSF, JBE, TJB, IPC and MT. JML wrote the paper with input from all authors.

Conflicts of interest

There are no conflicts to declare.

Acknowledgements

We are grateful to Syngenta, the EPSRC and the Department of Chemistry at the University of York (iCASE studentship to LAH EP/N509413/1, studentships for JBE and TJB) as well as the Royal Society of Chemistry (Research Enablement Grant to support JWB) for funding. We thank the STFC for programme access to the ULTRA facility (grant number 1813). The computational work in this project was undertaken on the Viking Cluster, which is a high performance compute facility provided by the University of York. We are grateful for computational support from the University of York High Performance Computing service, Viking and the Research Computing team.

References

1 W. J. Ramsay, N. A. W. Bell, Y. Qing and H. Bayley, *J. Am. Chem. Soc.*, 2018, **140**, 17538–17546.
2 S. Niu and M. B. Hall, *Chem. Rev.*, 2000, **100**, 353–406.

3 J. W. Tye and J. F. Hartwig, *J. Am. Chem. Soc.*, 2009, **131**, 14703–14712.
4 C. P. Richers, S. Roediger, V. Laserna and J. F. Hartwig, *Chem. Sci.*, 2020, **11**, 10449–10456.
5 S. A. Macgregor and G. W. Neave, *Organometallics*, 2003, **22**, 4547–4556.
6 P. S. Hanley and J. F. Hartwig, *Angew. Chem., Int. Ed.*, 2013, **52**, 8510–8525.
7 A. Haynes, P. M. Maitlis, G. E. Morris, G. J. Sunley, H. Adams, P. W. Badger, C. M. Bowers, D. B. Cook, P. I. Elliott, T. Ghaffar, H. Green, T. R. Griffin, M. Payne, J. M. Pearson, M. J. Taylor, P. W. Vickers and R. J. Watt, *J. Am. Chem. Soc.*, 2004, **126**, 2847–2861.
8 B. E. Moulton, A. C. Whitwood, A. K. Duhme-Klair, J. M. Lynam and I. J. S. Fairlamb, *J. Org. Chem.*, 2011, **76**, 5320–5334.
9 P. Magnus and L. M. Principe, *Tetrahedron Lett.*, 1985, **26**, 4851–4854.
10 B. E. Labelle, M. J. Knudsen, M. M. Olmstead, H. Hope, M. D. Yanuck and N. E. Schore, *J. Org. Chem.*, 1985, **50**, 5215–5222.
11 I. D. Gridnev and T. Imamoto, *Acc. Chem. Res.*, 2004, **37**, 633–644.
12 A. Nakamura, S. Ito and K. Nozaki, *Chem. Rev.*, 2009, **109**, 5215–5244.
13 Z. Chen and M. Brookhart, *Acc. Chem. Res.*, 2018, **51**, 1831–1839.
14 D. L. Thorn and R. Hoffmann, *J. Am. Chem. Soc.*, 1978, **100**, 2079–2090.
15 Y. Hu, B. Zhou and C. Wang, *Acc. Chem. Res.*, 2018, **51**, 816–827.
16 W. Liu and L. Ackermann, *ACS Catal.*, 2016, **6**, 3743–3752.
17 L. A. Hammarback, A. Robinson, J. M. Lynam and I. J. S. Fairlamb, *J. Am. Chem. Soc.*, 2019, **141**, 2316–2328.
18 L. A. Hammarback, A. Robinson, J. M. Lynam and I. J. S. Fairlamb, *Chem. Commun.*, 2019, **55**, 3211–3214.
19 M. Moselage, J. Li and L. Ackermann, *ACS Catal.*, 2016, **6**, 498–525.
20 J. Ghorai and P. Anbarasan, *Asian J. Org. Chem.*, 2019, **8**, 430–455.
21 P. G. Chirila and C. J. Whiteoak, *Dalton Trans.*, 2017, **46**, 9721–9739.
22 S. Wang, S. Y. Chen and X. Q. Yu, *Chem. Commun.*, 2017, **53**, 3165–3180.
23 T. Yoshino and S. Matsunaga, *Adv. Synth. Catal.*, 2017, **359**, 1245–1262.
24 M. T. Findlay, P. Domingo-Legarda, G. McArthur, A. Yen and I. Larrosa, *Chem. Sci.*, 2022, **13**, 3335–3362.
25 P. B. Arockiam, C. Bruneau and P. H. Dixneuf, *Chem. Rev.*, 2012, **112**, 5879–5918.
26 C. H. Shan, L. Zhu, L. B. Qu, R. P. Bai and Y. Lan, *Chem. Soc. Rev.*, 2018, **47**, 7552–7576.
27 A. Peneau, C. Guillou and L. Chabaud, *Eur. J. Org. Chem.*, 2018, **2018**, 5777–5794.
28 D. A. Colby, A. S. Tsai, R. G. Bergman and J. A. Ellman, *Acc. Chem. Res.*, 2012, **45**, 814–825.
29 G. Y. Song and X. W. Li, *Acc. Chem. Res.*, 2015, **48**, 1007–1020.
30 X. T. Qi, Y. Z. Li, R. P. Bai and Y. Lan, *Acc. Chem. Res.*, 2017, **50**, 2799–2808.
31 J. Sanjosé-Orduna, D. Gallego, A. Garcia-Roca, E. Martin, J. Benet-Buchholz and M. H. Pérez-Temprano, *Angew. Chem., Int. Ed.*, 2017, **56**, 12137–12141.
32 J. Sanjosé-Orduna, J. M. Sarria Toro and M. H. Pérez-Temprano, *Angew. Chem., Int. Ed.*, 2018, **57**, 11369–11373.
33 J. Sanjosé-Orduna, J. Benet-Buchholz and M. H. Pérez-Temprano, *Inorg. Chem.*, 2019, **58**, 10569–10577.
34 S. Martínez de Salinas, J. Sanjosé-Orduna, C. Odena, S. Barranco, J. Benet-Buchholz and M. H. Pérez-Temprano, *Angew. Chem., Int. Ed.*, 2020, **59**, 6239–6243.
35 N. P. Yahaya, K. M. Appleby, M. Teh, C. Wagner, E. Troschke, J. T. W. Bray, S. B. Duckett, L. A. Hammarback, J. S. Ward, J. Milani, N. E. Pridmore, A. C. Whitwood, J. M. Lynam and I. J. S. Fairlamb, *Angew. Chem., Int. Ed.*, 2016, **55**, 12455–12459.
36 J. D. Firth, L. A. Hammarback, T. J. Burden, J. B. Eastwood, J. R. Donald, C. S. Horbaczewskyj, M. T. McRobie, A. Tramaseur, I. P. Clark, M. Towrie, A. Robinson, J. P. Krieger, J. M. Lynam and I. J. S. Fairlamb, *Chem.–Eur. J.*, 2021, **27**, 3979–3985.
37 L. A. Hammarback, B. J. Aucott, J. T. W. Bray, I. P. Clark, M. Towrie, A. Robinson, I. J. S. Fairlamb and J. M. Lynam, *J. Am. Chem. Soc.*, 2021, **143**, 1356–1364.
38 L. A. Hammarback, A. L. Bishop, C. Jordan, G. Athavan, J. B. Eastwood, T. J. Burden, J. T. W. Bray, F. Clarke, A. Robinson, J. P. Krieger, A. Whitwood, I. P. Clark, M. Towrie, J. M. Lynam and I. J. S. Fairlamb, *ACS Catal.*, 2022, **12**, 1532–1544.
39 L. A. Hammarback, I. P. Clark, I. V. Sazanovich, M. Towrie, A. Robinson, F. Clarke, S. Meyer, I. J. S. Fairlamb and J. M. Lynam, *Nat. Catal.*, 2018, **1**, 830–840.
40 G. M. Greetham, P. Burgos, Q. A. Cao, I. P. Clark, P. S. Codd, R. C. Farrow, M. W. George, M. Kogimtzis, P. Matousek, A. W. Parker, M. R. Pollard, D. A. Robinson, Z. J. Xin and M. Towrie, *Appl. Spectrosc.*, 2010, **64**, 1311–1319.
41 G. M. Greetham, P. M. Donaldson, C. Nation, I. V. Sazanovich, I. P. Clark, D. J. Shaw, A. W. Parker and M. Towrie, *Appl. Spectrosc.*, 2016, **70**, 645–653.
42 B. J. Aucott, A. K. Duhme-Klair, B. E. Moulton, I. P. Clark, I. V. Sazanovich, M. Towrie, L. A. Hammarback, I. J. S. Fairlamb and J. M. Lynam, *Organometallics*, 2019, **38**, 2391–2401.
43 J. B. Eastwood, L. A. Hammarback, M. T. McRobie, I. P. Clark, M. Towrie, I. J. S. Fairlamb and J. M. Lynam, *Dalton Trans.*, 2020, **49**, 5463–5470.
44 The concentration of Mn-based photoproducts in these experiments is *ca.* 5×10^{-5} mol dm^{-3}. See ref. 43.
45 F. Weinhold and C. R. Landis, *Valency and bonding: a natural bond orbital donor-acceptor perspective*, Cambridge University Press, Cambridge, UK, New York, 2005.
46 W. J. Mace, L. Main and B. K. Nicholson, *J. Organomet. Chem.*, 2005, **690**, 3340–3347.
47 W. Tully, L. Main and B. K. Nicholson, *J. Organomet. Chem.*, 1996, **507**, 103–115.

48 L. S. Liebeskind, J. R. Gasdaska, J. S. Mccallum and S. J. Tremont, *J. Org. Chem.*, 1989, **54**, 669–677.
49 N. P. Robinson, L. Main and B. K. Nicholson, *J. Organomet. Chem.*, 1989, **364**, C37–C39.
50 X. K. Zhu, Y. Q. Zheng and J. B. Liu, *J. Phys. Chem. A*, 2021, **125**, 5031–5039.
51 G. P. Huang and P. Liu, *ACS Catal.*, 2016, **6**, 809–820.
52 D. Xing, X. T. Qi, D. Marchant, P. Liu and G. B. Dong, *Angew. Chem., Int. Ed.*, 2019, **58**, 4366–4370.
53 A. G. Algarra, W. B. Cross, D. L. Davies, Q. Khamker, S. A. Macgregor, C. L. McMullin and K. Singh, *J. Org. Chem.*, 2014, **79**, 1954–1970.
54 S. A. Macgregor and E. Wenger, *Organometallics*, 2002, **21**, 1278–1289.
55 A. J. Edwards, S. A. Macgregor, A. D. Rae, E. Wenger and A. C. Willis, *Organometallics*, 2001, **20**, 2864–2877.
56 Y. Li and Z. Y. Lin, *J. Org. Chem.*, 2013, **78**, 11357–11365.
57 W. J. Chen and Z. Y. Lin, *Organometallics*, 2015, **34**, 309–318.
58 X. Zhang, Q. Zhao, J. Q. Fan, D. Z. Chen and J. B. Liu, *Org. Chem. Front.*, 2019, **6**, 618–626.
59 B. Zhou, H. Chen and C. Wang, *J. Am. Chem. Soc.*, 2013, **135**, 1264–1267.
60 R. He, Z.-T. Huang, Q.-Y. Zheng and C. Wang, *Angew. Chem., Int. Ed.*, 2014, **53**, 4950–4953.
61 H. Wang, F. Pesciaioli, J. C. A. Oliveira, S. Warratz and L. Ackermann, *Angew. Chem., Int. Ed.*, 2017, **56**, 15063–15067.
62 C. Wang and M. Rueping, *ChemCatChem*, 2018, **10**, 2681–2685.
63 L. Shi, X. Zhong, H. She, Z. Lei and F. Li, *Chem. Commun.*, 2015, **51**, 7136–7139.
64 X. Yang, X. Jin and C. Wang, *Adv. Synth. Catal.*, 2016, **358**, 2436–2442.
65 To the best of our knowledge the only example of terminal alkyne insertion into a manganacycle which does not exhibit complete 2,1 selectivity involves a cyclometallated triphenylphosphite ligand, see W. J. Grigsby, L. Main and B. K. Nicholson, *Organometallics*, 1993, **12**, 397–407. In this example, the three-dimensional topology of the metallated ligand is markedly different from those studied here, which provides a plausible explanation for the altered selectivity.

Chemistry–A European Journal | Communication
doi.org/10.1002/chem.202004568
Check for updates
Chemistry Europe
European Chemical Societies Publishing

Organometallic Chemistry

Light- and Manganese-Initiated Borylation of Aryl Diazonium Salts: Mechanistic Insight on the Ultrafast Time-Scale Revealed by Time-Resolved Spectroscopic Analysis

James D. Firth,[a] L. Anders Hammarback,[a] Thomas J. Burden,[a] Jonathan B. Eastwood,[a] James R. Donald,[a] Chris S. Horbaczewskyj,[a] Matthew T. McRobie,[a] Adam Tramaseur,[a] Ian P. Clark,[b] Michael Towrie,[b] Alan Robinson,[c] Jean-Philippe Krieger,[c] Jason M. Lynam,*[a] and Ian J. S. Fairlamb*[a]

Abstract: Manganese-mediated borylation of aryl/heteroaryl diazonium salts emerges as a general and versatile synthetic methodology for the synthesis of the corresponding boronate esters. The reaction proved an ideal testing ground for delineating the Mn species responsible for the photochemical reaction processes, that is, involving either Mn radical or Mn cationic species, which is dependent on the presence of a suitably strong oxidant. Our findings are important for a plethora of processes employing Mn-containing carbonyl species as initiators and/or catalysts, which have considerable potential in synthetic applications.

Introduction

Aryl boronates are important building blocks within organic synthesis, without question due to the ubiquity of the Suzuki–Miyaura reaction, which ranks in the top-five most used reactions in target-orientated synthesis,[1] across the pharmaceutical and agrochemical industries.[2,3] The most common methods for their preparation involve either the stoichiometric metalation (to organo-lithium or Grignard reagents) or the Miyaura borylation[4] of aryl halides. The former approach suffers from limited functional group tolerance and the need for anhydrous conditions and controlled reagent addition, whereas the latter requires Pd catalysis. Inexpensive and abundant transition metals including Cu, Ni, Zn and Fe can also be employed.[5,6]

Alternative practical approaches to aryl boronates include C–H activation/borylation, often using earth abundant metals[7,8] and the visible light-induced borylation of aryl radical precursors, including aryl iodides,[9] aryl *N*-hydroxyphthalimido esters,[10] and aryl azo-sulfones.[11] Indeed, aryl diazonium salts have been employed extensively as aryl radical precursors[12–15] due to their relatively low reduction potential and the ease of synthesis from widely available anilines. Photoreduction to the desired aryl radicals can be simply achieved using a photo-initiator, resulting in many reports over the past decade of the photoredox-catalysed arylation of unsaturated systems.[14] For example, Yan and co-workers demonstrated the eosin Y catalysed borylation of aryl diazonium salts to generate aryl pinacol boronates (Scheme 1).[16] In some cases, such processes proceed via photoinitiated radical chain mechanisms, as was observed for arylation with aryl diazonium salts.[17] However, it has been shown that the use of broadband visible light irradiation can lead to the direct photolysis of aryl diazonium salts, generating the aryl boronates via aryl cations.[13,18,19] These findings therefore show that it is critical to understand how the photochemical activation is being executed, under specific conditions, as radical and cationic pathways might be similarly energetically feasible. Furthermore, other research teams have developed non-photoinduced processes for the

[a] Dr. J. D. Firth, Dr. L. A. Hammarback, T. J. Burden, J. B. Eastwood, Dr. J. R. Donald, Dr. C. S. Horbaczewskyj, M. T. McRobie, A. Tramaseur, Dr. J. M. Lynam, Prof. Dr. I. J. S. Fairlamb
Department of Chemistry, University of York
Heslington, York, YO10 5DD (UK)
E-mail: jason.lynam@york.ac.uk
ian.fairlamb@york.ac.uk

[b] Dr. I. P. Clark, Prof. M. Towrie
Central Laser Facility, Research Complex at Harwell
STFC Rutherford Appleton Laboratory, Harwell Campus
Didcot, Oxfordshire, OX11 0QX (UK)

[c] Dr. A. Robinson, Dr. J.-P. Krieger
Syngenta Crop Protection AG, Breitenloh 5, 4333 Münchwilen (Switzerland)

Supporting information and the ORCID identification number(s) for the author(s) of this article can be found under: https://doi.org/10.1002/chem.202004568.

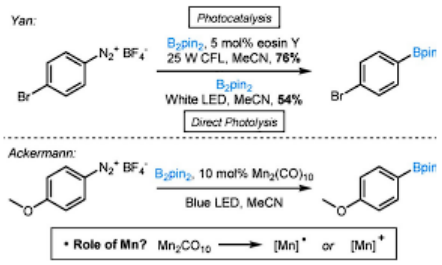

Scheme 1. Light mediated borylation of aryl diazoniums.

Chemistry–A European Journal | Communication doi.org/10.1002/chem.202004568 | Chemistry Europe European Chemical Societies Publishing

synthesis of aryl boronates from aryl diazonium salts,[20–25] including the one-pot diazotization/borylation of anilines,[26–30] proceeding via both radical and cationic intermediates.

A versatile Mn precursor complex, namely dimanganese(0) decacarbonyl, $Mn_2(CO)_{10}$, readily undergoes photo-induced homolysis to generate a manganese-centred radical $[Mn(CO)_5]^•$ (BDE of Mn–Mn bond ≈ 15 kcal mol^{-1}).[31] Facile generation of this reactive species has been employed in several distinctive organic transformations, which often proceed through the abstraction of a halogen from an alkyl halide in reactions involving light.[32–41] Despite this precedent there has been little reported confirming that $Mn_2(CO)_{10}$ generates reactive aryl radicals.[42]

Given our interest in initiating chemical transformations with Mn^I-carbonyl complexes,[43–45] we envisaged that the facile reduction of aryl diazonium salts to aryl radicals could be achieved with Mn_2CO_{10}, leading to generation of aryl pinacol boronates upon treatment with B_2pin_2. Credibility for this proposal comes from Ackermann and co-workers' recent study, with the synthesis of an exemplar aryl boronate (Scheme 1), using $Mn_2(CO)_{10}$ and blue LEDs through a Mn^I-mediated process.[42] We recognized that this single example could be broadened out into a general synthetic methodology, *but* that the reaction manifold allowed us to ask arguably a more fundamentally important question about the involvement of Mn species in a raft of low oxidation state Mn-mediated transformations,[42,46–62] particularly those invoking redox neutral Mn^I species.

It is evident that initiators derived from $Mn_2(CO)_{10}$ could be either radical (Mn^0), cationic (Mn^I) or anionic (Mn^{-I}) in nature. Knowing which species form, particularly under activation by light, and under what reaction conditions, is vitally important in exploiting downstream breakthroughs in synthetic chemistry, particularly with an eye on cascade processes. Answering this question is not straight-forward. However, in recent years we have demonstrated exactly how time-resolved multiple probe spectroscopy (TR^{M}PS) with infrared detection can be used to interrogate reaction steps pertinent to catalysis, from the picosecond to microsecond timescale.[43,63–65] Following photochemical activation of the pre-catalyst, the vibrational modes of the Mn–CO moiety provide the perfect spectroscopic handle for monitoring the accumulation of new species and intermediates as well as their final fate. Thus, in this study we firstly describe the innovation of the Mn-mediated borylation of aryl/heteroaryl diazonium salts into a general synthetic methodology. The reaction proved ideal for generating mechanistic detail and extraordinary insight into the Mn species involved in the photochemical reaction processes, the findings of which are globally important for a plethora of processes employing Mn-containing carbonyl initiators/catalysts.

Results and Discussion

Our investigation began with the borylation of aryl diazonium tetrafluoroborate salt **1a** with B_2pin_2 and $Mn_2(CO)_{10}$ initiator in MeCN, irradiating with a 60 W blue LED lamp (Table 1 and Table S1 in the Supporting Information). Aryl boronate **2a** was formed in quantitative yield and isolated in 96% yield when

Table 1. Optimisation of reaction conditions.[a]

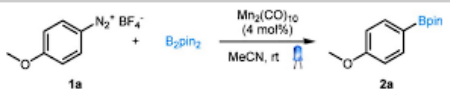

1a 2a

Entry	Deviation from above	Yield of **2a**/%[b]
1	none	100 (96)
2	2% $Mn_2(CO)_{10}$	81
3	1% $Mn_2(CO)_{10}$	44
4	1 equivalent of B_2pin_2	51 (47)
5	without $Mn_2(CO)_{10}$	2
6	without light[c]	3
7	2.5 mL MeCN	96
8	acetone instead of MeCN	100 (85)
9	MeOH instead of MeCN[d]	87
10	THF instead of MeCN	32
11	H_2O instead of MeCN	Trace
12	DMA instead of MeCN[d]	90
13	DMSO instead of MeCN[d]	58

[a] Reaction conditions: **1a** (0.5 mmol), B_2pin_2 (1.5 mmol) and $Mn_2(CO)_{10}$ (4 mol%) in MeCN (0.5 mL) were irradiated with 60W blue LEDs at room temperature under Ar for 2 h. [b] Yield determined by GC using mesitylene (0.25 mmol) as an internal standard. Isolated yield in parentheses. [c] Vial wrapped in foil. [d] 1.0 mL of solvent used.

4 mol% $Mn_2(CO)_{10}$ and 3 equivalents of B_2pin_2 were irradiated in MeCN, for 2 h (Table 1, entry 1). Reducing the stoichiometry of the $Mn_2(CO)_{10}$ or B_2pin_2 resulted in lower yields (Table 1, entries 2–4). Control experiments without either $Mn_2(CO)_{10}$ or light confirmed the essential role of both the former (presumed to be the initiator vide infra) and latter (Table 1, entries 5 and 6). Further reaction optimisation studies showed that reducing reaction concentration by fivefold had a negligible effect on product **2a** yield (96%, Table 1, entry 7) and that acetonitrile was the optimal solvent (Table 1, entries 8–13). We found that use of acetone resulted in full conversion of **1a**, however isolation was complicated by the presence of minor unknown side products. Interestingly, when methanol was used as solvent, gas evolution was observed prior to irradiation, pointing to the involvement of alcohol in the mechanism, perhaps in initiation.[19,25,26]

With optimal reaction conditions in hand, we investigated the robustness and reproducibility of the protocol (for the synthesis of **2a**) using a Glorius sensitivity assessment (Scheme 2, top right, for full details see Supporting Information).[66] This method is a quick means to gain an overview of the reaction condition based sensitivity of a given synthetic method. Our protocol showed little sensitivity to water content, concentration or light intensity and only a moderate sensitivity to the presence of oxygen. Furthermore, the reaction was easily scaled, giving **2a** in 90% yield (2.10 g) on a 10 mmol scale (Scheme 2).

Next, the substrate scope of the transformation was investigated (Scheme 2). The Mn-initiated borylation tolerated ethers giving **2a** (vide supra) and biaryl ether **2b** in excellent yield. Simple alkyl groups were also tolerated giving **2c**–**f** in moderate yield (43–75%). Sterically demanding mesityl and *ortho*-biphenyl substrates gave **2g** and **2h** in 63% and 61% yield, re-

Chemistry–A European Journal | Communication doi.org/10.1002/chem.202004568 | Chemistry Europe

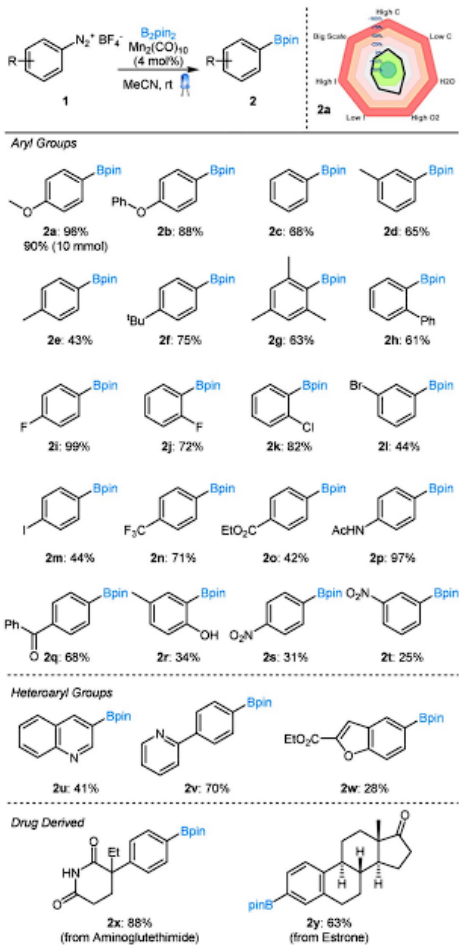

Scheme 2. Borylation of (hetero)aryl diazonium salts **1**.

spectively. Potentially reactive functional groups were also found compatible; halogenated aryl diazonium salts gave borylated haloarenes (**2i–m**) in moderate to excellent yields (44–99%), as well as trifluoromethyl aryl boronate **2n** in 71% yield. Ester (**2o**), amide (**2p**) and ketone (**2q**) functionality were tolerated, as were phenol (**2r**) and nitro groups (**2s** and **2t**), albeit in poorer yields. Furthermore, heteroaryl substituents gave the corresponding pinacol boronates in moderate yield, including quinoline (**2u**), pyridine (**2v**) and benzofuran (**2w**). Pleasingly, more complex drug-derived substrates were accommodated well by the methodology, with boronates **2x** and **2y** being formed in 88% and 63% yield, respectively.

We examined the feasibility of a continuous photo-flow method; irradiating a 0.35 M solution of **1a**, with 4 mol% of initiator $Mn_2(CO)_{10}$ and 3 equivalents of B_2pin_2 for 2.5 h led to a 93% conversion to aryl boronate **2a**. A preliminary mechanistic investigation involving irradiating **1n** in the presence of $Mn_2(CO)_{10}$ and TEMPO indicated that this reaction proceeds via an aryl radical (see Supporting Information for further details).

Mechanistic insight provided by TR^{M}PS

Previous work on the photochemistry of $Mn_2(CO)_{10}$ (summarized in Figure 1) has demonstrated that irradiation at low energy ($\lambda \geq 400$ nm) results in Mn–Mn bond cleavage to give $[Mn(CO)_5]^{\bullet}$.[67] The radical may undergo different fates including (a) dimerization to regenerate $Mn_2(CO)_{10}$ (b) in MeCN strong oxidising agents result in the conversion to 18-electron $[Mn(CO)_5(NCMe)]^+$,[68] and (c) in the absence of an exogenous oxidant, CO-substitution by MeCN affords $[Mn(CO)_3(NCMe)_3][Mn(CO)_5]$. This latter process likely proceeds via 19-electron $[Mn(CO)_3(NCMe)_3]^{\bullet}$ which is then oxidised by $Mn_2(CO)_{10}$ to $[Mn(CO)_3(NCMe)_3][Mn(CO)_5]$, with concomitant formation of $[Mn(CO)_5]^{\bullet}$.[69,70]

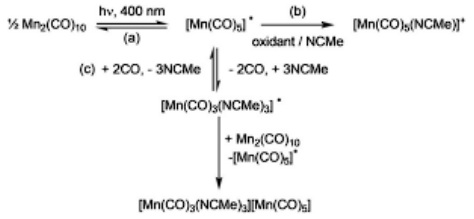

Figure 1. Previously reported fates of photochemically generated $[Mn(CO)_5]^{\bullet}$. (a) Dimerization to reform $Mn_2(CO)_{10}$; (b) oxidation and solvent addition to form $[Mn(CO)_5(NCMe)]^+$; (c) formation of $[Mn(CO)_3(NCMe)_3][Mn(CO)_5]$ corresponding for a formal disproportionation of $Mn_2(CO)_{10}$.

TR^{M}PS was used to gain insight into the mechanistic process underpinning the formation of pinacol boronates **2**. In these experiments, the sample was irradiated with an ultrafast laser pulse ($\lambda = 400$ nm) to activate the $Mn_2(CO)_{10}$. Insight into the nature and dynamic behaviour of the photoproducts was obtained by monitoring the subsequent changes in the infrared spectrum between 1900 and 2100 cm^{-1} with pump-probe delays between 1 ps and 1 ms.[71] The resulting data are shown in Figure 2 and Figure 3 as difference spectra, with negative peaks corresponding to material consumed on photolysis, typically $Mn_2(CO)_{10}$, and positive peaks due to the photoproducts.

Photolysis of $Mn_2(CO)_{10}$ in MeCN solution (ca. 1.36 mmol dm^{-3}) resulted in the formation of $[Mn(CO)_5]^{\bullet}$ in about 100 ps (Figure 2a). As expected, the majority of the Mn-radical recombined to give $Mn_2(CO)_{10}$ as evidenced by the decrease in intensity of the negative bleach bands for the dimer. A single long-lived photoproduct, identified as $[Mn(CO)_3(NCMe)_3]^+$ by comparison to literature data,[72] was formed ($k_{obs} = (1.88 \pm 0.09) \times 10^5$ s^{-1}).

Chemistry–A European Journal | Communication doi.org/10.1002/chem.202004568 | Chemistry Europe

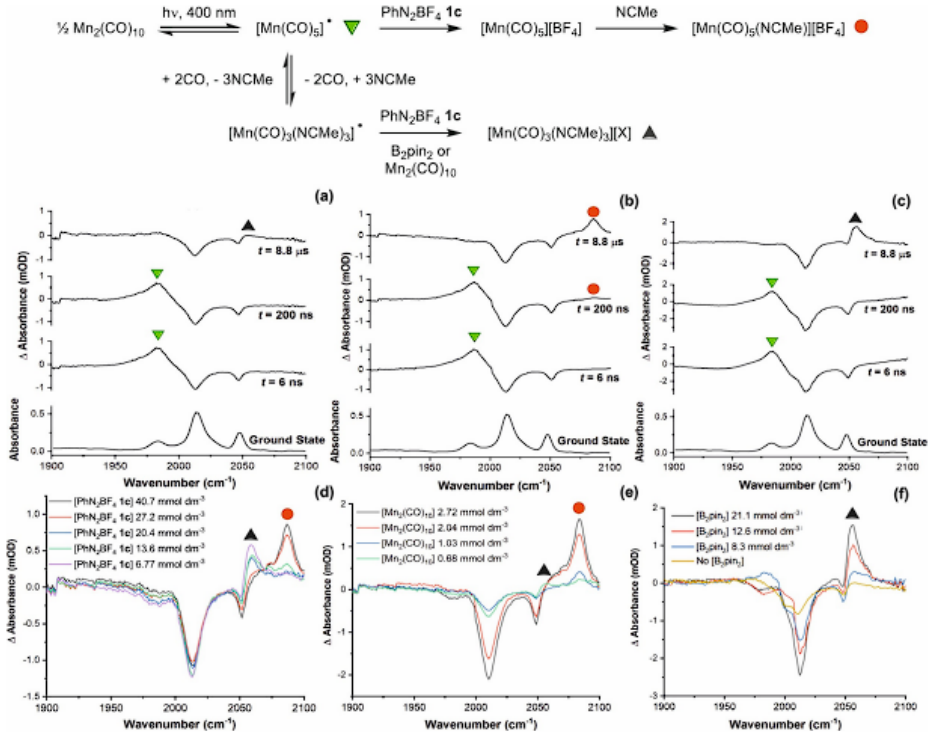

Figure 2. TR^{M}PS-IR data for the reaction between $Mn_2(CO)_{10}$ and PhN_2BF_4 **1c** and/or B_2pin_2. Top: Reaction scheme showing proposed mechanistic pathways. Bottom: TR^{M}PS-IR data in the metal carbonyl region. The *y*-axis shows the change in absorbance (mOD, milli-optical density). The negative peaks correspond to the bleach of the bands for $Mn_2(CO)_{10}$. The positive bands show the growth and change of intermediates. Data were acquired in a sealed flow system under ambient conditions. (a) $Mn_2(CO)_{10}$ (1.36 mmol dm^{-3}) in MeCN (10 mL), (b) $Mn_2(CO)_{10}$ (1.36 mmol dm^{-3}) in MeCN (10 mL) and PhN_2BF_4 **1c** (40.7 mmol dm^{-3}), (c) $Mn_2(CO)_{10}$ (1.36 mmol dm^{-3}) in MeCN (10 mL) and 3.1 equiv B_2pin_2, (d) effect of changing concentration of PhN_2BF_4 **1c** on the extent of the formation of $[Mn(CO)_5(NCMe)]^+$ and $[Mn(CO)_3(NCMe)_3]^+$, spectra recorded after 8.8 µs; (e) effect of changing concentration of $Mn_2(CO)_{10}$ on the extent of the formation of $[Mn(CO)_5(NCMe)]^+$ and $[Mn(CO)_3(NCMe)_3]^+$, spectra recorded after 8.8 µs; (f) effect of changing concentration of B_2pin_2 on the extent of the formation of $[Mn(CO)_3(NCMe)_3]^+$, spectra recorded after 8.8 µs.

Experiments performed in the presence of PhN_2BF_4 **1c** showed concentration-dependent behaviour. At a PhN_2BF_4 **1c** concentration of 40.7 mmol dm^{-3} the initially formed $[Mn(CO)_5]^•$ converted to $[Mn(CO)_5(NCMe)]^+$ (Figure 2b) and evidence for the reformation of $Mn_2(CO)_{10}$ was again obtained. However, experiments performed at lower concentrations of PhN_2BF_4 **1c** afforded $[Mn(CO)_3(NCMe)_3]^+$ as the sole long-lived photoproduct (Figure 2d). Furthermore, experiments performed with PhN_2BF_4 **1c** at high concentrations of $Mn_2(CO)_{10}$ resulted in the formation of $[Mn(CO)_5(NCMe)]^+$ whereas at lower dimer concentrations $[Mn(CO)_3(NCMe)_3]^+$ was formed (Figure 1e).

These data are consistent with the mechanism outlined in Figure 2. At high concentrations, one-electron oxidation of $[Mn(CO)_5]^•$ by the diazonium salt results in the formation $[Mn(CO)_5]^+$, which undergoes rapid solvation to give $[Mn(CO)_5(NCMe)]^+$. Reduction of the diazonium salt results in the formation of phenyl radicals and dinitrogen. In the synthetic reaction the phenyl radicals then react with B_2pin_2 to give **2c**. The irreversible reduction of PhN_2BF_4 **1c** occurs at a potential of −0.16 V (versus SCE in MeCN),[73] given that the corresponding reduction of $[Mn(CO)_5(NCMe)]^+$ has a potential of −0.455 V then this process is clearly thermodynamically viable.[74] At lower concentrations of PhN_2BF_4 **1c** the data are consistent with solvent substitution of $[Mn(CO)_5]^•$ to give $[Mn(CO)_3(NCMe)_3]^•$ and subsequent oxidation by the diazonium salt to give $[Mn(CO)_3(NCMe)_3]^+$ — a viable process as $[Mn(CO)_3(NCMe)_3]^•$ is a strong reducing agent ($E < -3$ V[69]).

At lower concentration conditions, the second order rate of oxidation of $[Mn(CO)_5]^•$ by PhN_2BF_4 **1c** is slower than the rate of solvent substitution and oxidation of $[Mn(CO)_3(NCMe)_3]^•$. This is consistent with the Marcus theory of electron transfer

Chemistry–A European Journal | Communication doi.org/10.1002/chem.202004568 | Chemistry Europe European Chemical Societies Publishing

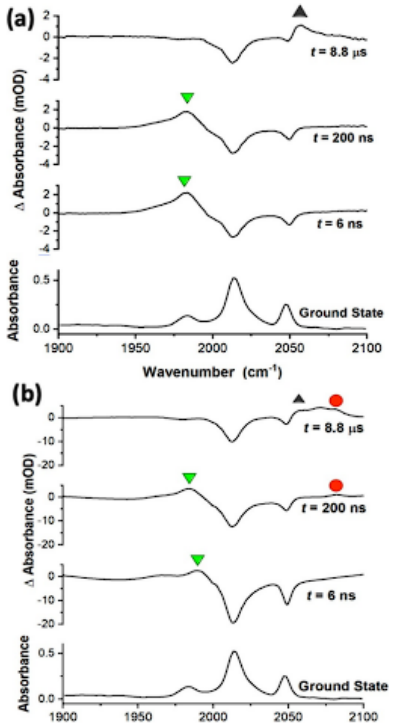

Figure 3. TR^{M}PS-IR data for the reaction between $Mn_2(CO)_{10}$ and PhN_2BF_4 **1c** and B_2pin_2 (a) $Mn_2(CO)_{10}$ (0.1 equiv 0.70 mmol dm^{-3}), and B_2pin_2 (3 equiv, 21.1 mmol dm^{-3}); (b) $Mn_2(CO)_{10}$ (0.04 equiv, 2.29 mmol dm^{-3}) PhN_2BF_4 **1c** (1.7 equiv, 90.6 mmol dm^{-3}) and B_2pin_2 (3 equiv, 156.9 mmol dm^{-3}) in MeCN (10 mL).

which predicts a faster reduction of the diazonium salt by $[Mn(CO)_3(NCMe)_3]^{\bullet}$ than by $[Mn(CO)_5]^{\bullet}$. These data show that PhN_2BF_4 **1c** can be reduced through two different pathways, following the photochemical activation of $Mn_2(CO)_{10}$.

Photolysis of $Mn_2(CO)_{10}$ in the presence of B_2pin_2 resulted in the initial formation of $[Mn(CO)_5]^{\bullet}$ followed by conversion to $[Mn(CO)_3(NCMe)_3]^{+}$ (Figure 2c). Experiments performed at variable concentrations of B_2pin_2 demonstrated that at higher concentrations of B_2pin_2 more $[Mn(CO)_3(NCMe)_3]^{+}$ was formed at the expense of the recovery of $Mn_2(CO)_{10}$. The observation of $[Mn(CO)_3(NCMe)_3]^{+}$ in these experiments is remarkable, for which two explanations are possible. Firstly, the presence of B_2pin_2 increases the rate of solvent substitution at $[Mn(CO)_5]^{\bullet}$ to give greater amounts of $[Mn(CO)_3(NCMe)_3]^{\bullet}$ which is then quenched by $Mn_2(CO)_{10}$ to give $[Mn(CO)_3(NCMe)_3]^{+}$. Secondly, and more plausibly, $[Mn(CO)_3(NCMe)_3]^{\bullet}$ reduces B_2pin_2. The reduction of B_2pin_2 is predicted to occur at a potential of < -3 V[75] supported by the ability of the 19-electron $[Mn(CO)_3(NCMe)_3]^{\bullet}$ species to act as a powerful reducing agent. No evidence was obtained for the known boryl complex, $Mn(CO)_5(Bpin)$ (bands at 2012.06 and 1959.74 cm^{-1}).[76]

In order to gain insight into the mechanistic process which occurred under the reaction conditions used in the development of the synthetic methodology *vide supra*, the TR^{M}PS experiments were performed with $Mn_2(CO)_{10}$ in the presence of both PhN_2BF_4 **1c** and B_2pin_2. When the experiment was performed with a concentration of $Mn_2(CO)_{10}$ used in the previous experiments, but the ratio of reagents used in Table 1, then $[Mn(CO)_3(NCMe)_3]^{+}$ was the dominant product formed from $[Mn(CO)_5]^{\bullet}$ (Figure 3a). A related experiment performed at the same concentration as the synthetic chemistry showed more complicated behavior (Figure 3b) with evidence for the formation of both $[Mn(CO)_3(NCMe)_3]^{+}$ and $[Mn(CO)_5(NCMe)]^{+}$. While an additional unassigned band at 2071 cm^{-1} was also present in this experiment, these results support the conclusion that photochemically generated $[Mn(CO)_5]^{\bullet}$ may either act as reducing agent directly or, following solvent substitution, through $[Mn(CO)_3(NCMe)_3]^{\bullet}$. It is likely that subsequent to initiation, the reaction proceeds through a chain propagation process whereby trapping of the aryl radical results in the formation of a boryl radical anion that can reduce another molecule of aryl diazonium **1**.[15] Of note, even though the reaction is thought to proceed through a chain propagation process, constant irradiation is required due to the facile recombination of $[Mn(CO)_5]^{\bullet}$ to regenerate $Mn_2(CO)_{10}$.

FT-IR analysis of a reaction mixture performed using the conditions in Table 1, entry 1, demonstrated that $[Mn(CO)_5(NCMe)]^{+}$ was the dominant metal carbonyl-containing species at the end of the reaction (see Supporting Information). This is consistent with the primary activation pathway involving reduction of **1c** by $[Mn(CO)_5]^{\bullet}$ and provides an important link between the data obtained by TR^{M}PS and the synthetic chemistry.

Conclusions

In this study we have innovated a robust borylation reaction for aryl/heteroaryl diazonium salts involving $Mn_2(CO)_{10}$ as an initiator. The reaction proved the ideal manifold for state-of-the-art mechanistic work, through a study on the behaviour of the Mn^{I}-carbonyl species utilizing time-resolved multiple probe spectroscopy (TR^{M}PS-IR). This enabled the transient species pertinent to the chemistry and their fates to be mapped out. Our findings indicate that Mn radical species of the type, $[Mn(CO)_5]^{\bullet}$ are formed, which are then susceptible to oxidation at the Mn centre (Figure 4). A clean reaction is seen upon treatment of $[Mn(CO)_5]^{\bullet}$ with high concentrations of PhN_2BF_4 **1c** to give $[Mn(CO)_5(S)]^{+}$ species, where S = CH_3CN (we expect polar aprotic solvents to behave similarly). At lower concentrations of PhN_2BF_4 **1c** $[Mn(CO)_3(S)_3]^{+}$ is generated through oxidation of 19-electron $[Mn(CO)_3(S)_3]^{\bullet}$. In both cases, reduction of the **1c** will result in the generation of aryl radicals which then react with B_2pin_2 to give **2c**. We presume that this results in the concomitant generation of boron-based radicals which propagate the reaction, highlighting the role of the Mn-carbonyl complex as a photo-initiator. In the presence of the

Chemistry–A European Journal | Communication doi.org/10.1002/chem.202004568 | Chemistry Europe European Chemical Societies Publishing

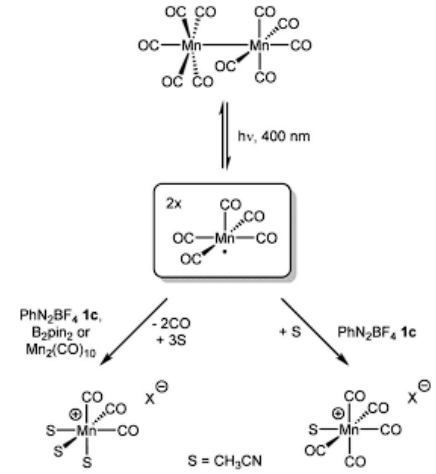

Figure 4. Light activation of $Mn_2(CO)_{10}$ at 400 nm: impact of reaction components on the formation of cationic Mn^I-carbonyl species generated under working reaction conditions.

B_2pin_2 we also see that $[Mn(CO)_3(S)_3]^+$ is formed, indicating that the boronate may also be reduced. While $[Mn(CO)_5(S)]^+$ and $[Mn(CO)_3(S)_3]^+$ are both cationic Mn^I species, the electron-deficiency of the former at Mn will be significant and potentially important when considering downstream reaction chemistries.

Given the promise of light-induced activation of $Mn_2(CO)_{10}$ in synthetic chemistry,[77] our results taken together are important in proposing future mechanistic schemes and taking advantage of the unique reactivity of Mn-carbonyl species. As with C–H bond activation-functionalization catalytic chemistries, the TR^{M}PS-IR approach has proven valuable, as an important mechanistic tool, in mapping out the reactive species that develop from metal carbonyl complexes such as $Mn_2(CO)_{10}$ and determining their roles in synthetic chemistry.

We would like to point readers to a special guest editorial about aryl/heteroaryl diazonium salt cautions and safety considerations.[78]

Acknowledgements

We thank the EPSRC for funding (EP/S009965/1: "A Fully Automated Robotic System for Intelligent Chemical Reaction Screening"), in addition, the EPSRC for an iCASE award involving Syngenta, EP/N509413/1, for funding the PhD studentship to L.A.H. The STFC (access to the ULTRA facility) is gratefully acknowledged for funding, equipment and support. We thank Syngenta and University of York for iCASE funding and studentship to T.J.B and the University of York for a studentship to J.B.E.

Conflict of interest

The authors declare no conflict of interest.

Keywords: manganese · mechanism · photocatalysis · radicals · spectroscopy

[1] D. G. Brown, J. Boström, *J. Med. Chem.* **2016**, *59*, 4443–4458.
[2] C. Torborg, M. Beller, *Adv. Synth. Catal.* **2009**, *351*, 3027–3043.
[3] A. Dumrath, C. Lübbe, M. Beller, *Palladium-Catalyzed Coupling Reactions* (Ed.: Á. Molnár), Wiley-VCH, Weinheim, **2013**, pp. 445–489.
[4] T. Ishiyama, M. Murata, N. Miyaura, *J. Org. Chem.* **1995**, *60*, 7508–7510.
[5] J. W. B. Fyfe, A. J. B. Watson, *Chem* **2017**, *3*, 31–55.
[6] W. K. Chow, O. Y. Yuen, P. Y. Choy, C. M. So, C. P. Lau, W. T. Wong, F. Y. Kwong, *RSC Adv.* **2013**, *3*, 12518–12539.
[7] L. Xu, G. Wang, S. Zhang, H. Wang, L. Wang, L. Liu, J. Jiao, P. Li, *Tetrahedron* **2017**, *73*, 7123–7157.
[8] P. Gandeepan, T. Müller, D. Zell, G. Cera, S. Warratz, L. Ackermann, *Chem. Rev.* **2019**, *119*, 2192–2452.
[9] M. Jiang, H. Yang, H. Fu, *Org. Lett.* **2016**, *18*, 5248–5251.
[10] L. Candish, M. Teders, F. Glorius, *J. Am. Chem. Soc.* **2017**, *139*, 7440–7443.
[11] Y. Xu, X. Yang, H. Fang, *J. Org. Chem.* **2018**, *83*, 12831–12837.
[12] D. P. Hari, B. König, *Angew. Chem. Int. Ed.* **2013**, *52*, 4734–4743; *Angew. Chem.* **2013**, *125*, 4832–4842.
[13] M. Majek, A. Jacobi von Wangelin, *Acc. Chem. Res.* **2016**, *49*, 2316–2327.
[14] I. Ghosh, L. Marzo, A. Das, R. Shaikh, B. König, *Acc. Chem. Res.* **2016**, *49*, 1566–1577.
[15] F. W. Friese, A. Studer, *Chem. Sci.* **2019**, *10*, 8503–8518.
[16] J. Yu, L. Zhang, G. Yan, *Adv. Synth. Catal.* **2012**, *354*, 2625–2628.
[17] A. Tlahuext-Aca, M. N. Hopkinson, B. Sahoo, F. Glorius, *Chem. Sci.* **2016**, *7*, 89–93.
[18] M. Majek, F. Filace, A. J. von Wangelin, *Beilstein J. Org. Chem.* **2014**, *10*, 981–989.
[19] C. Zhu, M. Yamane, *Org. Lett.* **2012**, *14*, 4560–4563.
[20] X. Qi, L.-B. Jiang, C. Zhou, J.-B. Peng, X.-F. Wu, *ChemistryOpen* **2017**, *6*, 345–349.
[21] G. Iakobson, J. Du, A. M. Z. Slawin, P. Beier, *Beilstein J. Org. Chem.* **2015**, *11*, 1494–1502.
[22] X. Qi, H.-P. Li, J.-B. Peng, X.-F. Wu, *Tetrahedron Lett.* **2017**, *58*, 3851–3853.
[23] K. Kubota, Y. Pang, A. Miura, H. Ito, *Science* **2019**, *366*, 1500–1504.
[24] J. Zhang, X. Wang, H. Yu, J. Ye, *Synlett* **2012**, *23*, 1394–1396.
[25] X. Zhang, Z. Zhang, Y. Xie, Y. Jiang, R. Xu, Y. Luo, C. Tao, *J. Chem. Res.* **2018**, *42*, 481–485.
[26] C.-J. Zhao, D. Xue, Z.-H. Jia, C. Wang, J. Xiao, *Synlett* **2014**, *25*, 1431.
[27] F. Mo, Y. Jiang, D. Qiu, Y. Zhang, J. Wang, *Angew. Chem. Int. Ed.* **2010**, *49*, 1846–1849; *Angew. Chem.* **2010**, *122*, 1890–1893.
[28] D. Qiu, L. Jin, Z. Zheng, H. Meng, F. Mo, X. Wang, Y. Zhang, J. Wang, *J. Org. Chem.* **2013**, *78*, 1923–1933.
[29] D. Qiu, Y. Zhang, J. Wang, *Org. Chem. Front.* **2014**, *1*, 422–425.
[30] S. Ahammed, S. Nandi, D. Kundu, B. C. Ranu, *Tetrahedron Lett.* **2016**, *57*, 1551–1554.
[31] Y.-R. Luo, *Comprehensive Handbook of Chemical Bond Energies*, CRC, Boca Raton, **2007**.
[32] H. Liang, Y.-X. Ji, R.-H. Wang, Z.-H. Zhang, B. Zhang, *Org. Lett.* **2019**, *21*, 2750–2754.
[33] P. Nuhant, M. S. Oderinde, J. Genovino, A. Juneau, Y. Gagné, C. Allais, G. M. Chinigo, C. Choi, N. W. Sach, L. Bernier, Y. M. Fobian, M. W. Bundesmann, B. Khunte, M. Frenette, O. O. Fadeyi, *Angew. Chem. Int. Ed.* **2017**, *56*, 15309–15313; *Angew. Chem.* **2017**, *129*, 15511–15515.
[34] G. K. Friestad, J. Qin, *J. Am. Chem. Soc.* **2001**, *123*, 9922–9923.
[35] G. K. Friestad, A. Ji, *Org. Lett.* **2008**, *10*, 2311–2313.
[36] G. K. Friestad, K. Banerjee, *Org. Lett.* **2009**, *11*, 1095–1098.
[37] B. C. Gilbert, C. I. Lindsay, P. T. McGrail, A. F. Parsons, D. T. E. Whittaker, *Synth. Commun.* **1999**, *29*, 2711–2718.
[38] N. Huther, P. T. McGrail, A. F. Parsons, *Eur. J. Org. Chem.* **2004**, 1740–1749.

Chemistry–A European Journal | Communication doi.org/10.1002/chem.202004568 | Chemistry Europe

[39] B. C. Gilbert, W. Kalz, C. I. Lindsay, P. T. McGrail, A. F. Parsons, D. T. E. Whittaker, *J. Chem. Soc. Perkin Trans. 1* **2000**, 1187–1194.
[40] R. S. Herrick, T. R. Herrinton, H. W. Walker, T. L. Brown, *Organometallics* **1985**, *4*, 42–45.
[41] B. C. Gilbert, W. Kalz, C. I. Lindsay, P. T. T. McGrail, A. F. Parsons, D. T. E. E. Whittaker, *Tetrahedron Lett.* **1999**, *40*, 6095–6098.
[42] Y.-F. Liang, R. Steinbock, L. Yang, L. Ackermann, *Angew. Chem. Int. Ed.* **2018**, *57*, 10625–10629; *Angew. Chem.* **2018**, *130*, 10785–10789.
[43] L. A. Hammarback, I. P. Clark, I. V. Sazanovich, M. Towrie, A. Robinson, F. Clarke, S. Meyer, I. J. S. Fairlamb, J. M. Lynam, *Nat. Catal.* **2018**, *1*, 830–840.
[44] L. A. Hammarback, A. Robinson, J. M. Lynam, I. J. S. Fairlamb, *Chem. Commun.* **2019**, *55*, 3211–3214.
[45] L. A. Hammarback, A. Robinson, J. M. Lynam, I. J. S. Fairlamb, *J. Am. Chem. Soc.* **2019**, *141*, 2316–2328.
[46] Y. Hu, B. Zhou, C. Wang, *Acc. Chem. Res.* **2018**, *51*, 816–827.
[47] R. Cano, K. Mackey, G. P. McGlacken, *Catal. Sci. Technol.* **2018**, *8*, 1251–1266.
[48] Y. Hu, B. Zhou, H. Chen, C. Wang, *Angew. Chem. Int. Ed.* **2018**, *57*, 12071–12075; *Angew. Chem.* **2018**, *130*, 12247–12251.
[49] M. Pinto, S. Friães, F. Franco, J. Lloret-Fillol, B. Royo, *ChemCatChem* **2018**, *10*, 2734–2740.
[50] B. Zhou, Y. Hu, T. Liu, C. Wang, *Nat. Commun.* **2017**, *8*, 1169.
[51] H. Wang, F. Pesciaioli, J. C. A. Oliveira, S. Warratz, L. Ackermann, *Angew. Chem. Int. Ed.* **2017**, *56*, 15063–15067; *Angew. Chem.* **2017**, *129*, 15259–15263.
[52] C. Wang, A. Wang, M. Rueping, *Angew. Chem. Int. Ed.* **2017**, *56*, 9935–9938; *Angew. Chem.* **2017**, *129*, 10067–10070.
[53] S.-L. Liu, Y. Li, J.-R. Guo, G.-C. Yang, X.-H. Li, J.-F. Gong, M.-P. Song, *Org. Lett.* **2017**, *19*, 4042–4045.
[54] S. Sueki, Z. Wang, Y. Kuninobu, *Org. Lett.* **2016**, *18*, 304–307.
[55] A. Mukherjee, A. Nerush, G. Leitus, L. J. W. Shimon, Y. Ben David, N. A. Espinosa Jalapa, D. Milstein, *J. Am. Chem. Soc.* **2016**, *138*, 4298–4301.
[56] W. Liu, S. C. Richter, Y. Zhang, L. Ackermann, *Angew. Chem. Int. Ed.* **2016**, *55*, 7747–7750; *Angew. Chem.* **2016**, *128*, 7878–7881.
[57] W. Liu, L. Ackermann, *ACS Catal.* **2016**, *6*, 3743–3752.
[58] B. Zhou, Y. Hu, C. Wang, *Angew. Chem. Int. Ed.* **2015**, *54*, 13659–13663; *Angew. Chem.* **2015**, *127*, 13863–13867.
[59] L. Shi, X. Zhong, H. She, Z. Lei, F. Li, *Chem. Commun.* **2015**, *51*, 7136–7139.
[60] W. Liu, J. Bang, Y. Zhang, L. Ackermann, *Angew. Chem. Int. Ed.* **2015**, *54*, 14137–14140; *Angew. Chem.* **2015**, *127*, 14343–14346.
[61] J. Agarwal, T. W. Shaw, C. J. Stanton, G. F. Majetich, A. B. Bocarsly, H. F. Schaefer, *Angew. Chem. Int. Ed.* **2014**, *53*, 12253; *Angew. Chem.* **2014**, *126*, 5252–5255.
[62] T. E. Rosser, C. D. Windle, E. Reisner, *Angew. Chem. Int. Ed.* **2016**, *55*, 7388–7392; *Angew. Chem.* **2016**, *128*, 7514–7518.
[63] J. B. Eastwood, L. A. Hammarback, M. T. McRobie, I. P. Clark, M. Towrie, I. J. S. Fairlamb, J. M. Lynam, *Dalton Trans.* **2020**, *49*, 5463–5470.
[64] B. J. Aucott, A.-K. Duhme-Klair, B. E. Moulton, I. P. Clark, I. V. Sazanovich, M. Towrie, L. A. Hammarback, I. J. S. Fairlamb, J. M. Lynam, *Organometallics* **2019**, *38*, 2391–2401.
[65] B. J. Aucott, J. B. Eastwood, L. Anders Hammarback, I. P. Clark, I. V. Sazanovich, M. Towrie, I. J. S. Fairlamb, J. M. Lynam, *Dalton Trans.* **2019**, *48*, 16426–16436.
[66] L. Pitzer, F. Schäfers, F. Glorius, *Angew. Chem. Int. Ed.* **2019**, *58*, 8572–8576; *Angew. Chem.* **2019**, *131*, 8660–8664.
[67] D. A. Steinhurst, A. P. Baronavski, J. C. Owrutsky, *Chem. Phys. Lett.* **2002**, *361*, 513–519.
[68] A. F. Hepp, M. S. Wrighton, *J. Am. Chem. Soc.* **1981**, *103*, 1258–1261.
[69] A. E. Stiegman, D. R. Tyler, *Inorg. Chem.* **1984**, *23*, 527–529.
[70] A. E. Stiegman, A. S. Goldman, C. E. Philbin, D. R. Tyler, *Inorg. Chem.* **1986**, *25*, 2976–2979.
[71] G. M. Greetham, D. Sole, I. P. Clark, A. W. Parker, M. R. Pollard, M. Towrie, *Rev. Sci. Instrum.* **2012**, *83*, 103107.
[72] D. Drew, D. J. Darensbourg, M. Y. Darensbourg, *Inorg. Chem.* **1975**, *14*, 1579–1584.
[73] C. P. Andrieux, J. Pinson, *J. Am. Chem. Soc.* **2003**, *125*, 14801–14806.
[74] J. R. Pugh, T. J. Meyer, *J. Am. Chem. Soc.* **1992**, *114*, 3784–3792.
[75] H. Asakawa, K.-H. Lee, K. Furukawa, Z. Lin, M. Yamashita, *Chem. Eur. J.* **2015**, *21*, 4267–4271.
[76] T. J. Mazzacano, N. J. Leon, G. W. Waldhart, N. P. Mankad, *Dalton Trans.* **2017**, *46*, 5518–5521.
[77] L. Wang, J. M. Lear, S. M. Rafferty, S. C. Fosu, D. A. Nagib, *Science* **2018**, *362*, 225–229.
[78] J. D. Firth, I. J. S. Fairlamb, *Org. Lett.* **2020**, *22*, 7057–7059.

Manuscript received: October 14, 2020
Accepted manuscript online: November 1, 2020
Version of record online: January 31, 2021

Dalton Transactions

PAPER

View Article Online
View Journal | View Issue

Cite this: *Dalton Trans.*, 2019, **48**, 16426

Insight into the mechanism of CO-release from trypto-CORM using ultra-fast spectroscopy and computational chemistry†‡

Benjamin J. Aucott, §[a] Jonathan B. Eastwood, §[a] L. Anders Hammarback, §[a] Ian P. Clark,[b] Igor V. Sazanovich,[b] Michael Towrie,[b] Ian J. S. Fairlamb *[a] and Jason M. Lynam *[a]

Photolysis of trypto-CORM, *fac*-[Mn(tryp)(CO)$_3$(NCMe)] (tryp = tryptophanate) at 400 nm results in controlled CO-release which may be utilised to inhibit the growth of *Escherichia coli* (*E. coli*). An investigation into the fundamental processes which underpin the CO-release event is described. Time-dependent density functional theory (TD-DFT) indicates that irradiation at 400 nm results in LMCT from the indole group of the amino acid to orbitals based on the metal as well as the carbonyl and NCMe ligands. Ultrafast time-resolved infra-red spectroscopy (TRIR) demonstrates that in NCMe solution, photolysis (400 nm) results in loss of CO in under 3 ps with the sequential generation of three new states with two carbonyl ligands and a coordinated tryptophanate. The first species is assigned to vibrationally hot ^{3}[Mn(tryp)(CO)$_2$(NCMe)] which undergoes cooling to give the complex in its v = 0 state. This triplet state then undergoes solvation ($\tau \approx 20$ ps) with a concomitant change in spin to give [Mn(tryp)(CO)$_2$(NCMe)$_2$] which persists for the remainder of the experiment (800 μs). These data indicate that following the initial photochemically induced loss of CO, any thermal CO loss is much slower. Related experiments with trypto-CORM in a mixture of DMSO and D_2O gave analogous data, indicating that this process also occurs in the medium used for the evaluation of biological properties.

Received 16th August 2019,
Accepted 14th October 2019

DOI: 10.1039/c9dt03343b

rsc.li/dalton

Introduction

Despite its deserved reputation as a poison, carbon monoxide has been shown to have well-defined beneficial therapeutic effects. CO is produced naturally in mammals, primarily through the physiological degradation of heme, it acts as a signalling molecule and has been shown to protect against ischemic damage and organ graft rejection, it is antibacterial, antimalarial and may act as a vasodilator.[1–3] Although controlled treatment with CO gas may be envisaged as a route to harness these beneficial effects, its lack of selectivity means that alternative delivery methods are needed. This has resulted in the advent of carbon monoxide-releasing molecules (CO-RMs) which are species which liberate CO when subjected to a suitable stimulus.[4–7] The vast majority of CO-RMs are transition metal carbonyl complexes which presumably represents the ability of these elements to readily coordinate CO.[8] Although there are a vast number of metal carbonyl complexes, control over the spatial and temporal delivery of CO remains a challenge. CO-RMs are needed in which the rate, extent and location of CO-release are controlled. This may be achieved by molecules which selectively localise in certain organs[9] or are activated by specific triggers.[10] A number of stimuli have therefore been explored to control the CO-release event, such as activation by enzymes,[11–13] as well as thermal-,[14–18] electrochemical-[19] and magnetic heating-induced release.[20] However, light offers the benefit of temporal and spatial control over the CO-loss event and therefore the photochemical activation of CO-RMs (photoCO-RMs) has been extensively explored.[21–24]

Complexes based on manganese(I) represent the most common class of photoCO-RMs.[25–37] These complexes have antibacterial activity,[25,26,34,35] may be woven into materials and activated with a photosensitiser,[32] or activated by two-photon excitation.[33] We have recently reported the synthesis and antibacterial activity of trypto-CORM (Fig. 1) a manganese-based carbonyl complex with a coordinated tryptophanate ligand.[38]

[a]*Department of Chemistry, University of York, Heslington, York, YO10 5DD, UK. E-mail: ian.fairlamb@york.ac.uk, jason.lynam@york.ac.uk*
[b]*Central Laser Facility, STFC Rutherford Appleton Laboratory, Harwell Campus, Didcot, Oxfordshire, OX11 0QX, UK*

†This manuscript is dedicated to Professor Robin Perutz, an inspirational scientist, colleague and mentor on the occasion of his 70th birthday.

‡Electronic supplementary information (ESI) available: Details xyz coordinates and collated energies for DFT calculations. See DOI: 10.1039/c9dt03343b

§These authors contributed equally.

View Article Online
Dalton Transactions Paper

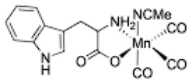

Trypto-CORM

Fig. 1 Structure of trypto-CORM.

Trypto-CORM is able to inhibit the growth of *E. coli* only when exposed to visible (400 nm) light. The behaviour is organism-dependant, for example, trypto-CORM shows some activity against *Neisseria gonorrhoeae* in the dark.[39] Control experiments with leg-haemoglobin (which has an extremely high binding affinity for CO) indicate that this activity is due to the released CO.

An understanding of the pathways that lead to CO loss and the nature of the resulting species has provided important fundamental insight into the structure and bonding of transition metal complexes.[40] For example, Perutz and Turner demonstrated that photolysis of $[Cr(CO)_6]$ in a xenon matrix results in the formation of square-based pyramidal $[Cr(CO)_5]$ with a Cr–Xe interaction.[41] This illustrated the high Lewis acidity of such fragments and provided support for the development of bonding models such as the isolobal analogy. The dynamics of the photochemical loss of CO and subsequent solvation has been explored using time-resolved spectroscopy. Light is employed to photo-dissociate a CO ligand and the structure of the resulting transient intermediates probed using electronic or vibrational spectroscopy.[42–44] Such studies have assisted with the identification of σ-complexes, and informed the understanding of unusual bonding modes in transition metal species.[45–49]

Time-resolved vibrational spectroscopy has been used extensively to probe behaviour in organic solvents, however, there are far fewer reports of this method being applied to study the light-induced loss of CO from photoCO-RMs in more biologically relevant media.[19,36] Such studies, when coupled with a detailed computational understanding of their photochemistry[50] (for example the nature of the electronic transitions and excited state structures which lead to the CO-loss event) will inform the development of new classes of photoCO-RMs.

We have recently employed TRIR spectroscopy to investigate the behaviour of metal complexes *fac*-$[Mn(ppy)(CO)_3(L)]$ (ppy = 2-phenylpyridine, L = ligand) generated by the light-induced dissociation of CO from $[Mn(ppy)(CO)_4]$.[51,52] Complexes based on this scaffold have found uses as CO-RMs[53–55] and in catalysis.[56–59]

These studies have provided insight into the solvation of unsaturated species and the role of these complexes as catalysts for C–H functionalisation. For example, photolysis (355 nm) of $[Mn(ppy)(CO)_4]$ in media such as heptane, toluene, CH_2Cl_2 and ethers results in CO loss in under 1 ps and the generation of solvent complexes *fac*-$[Mn(ppy)(S)(CO)_3]$ (S = solvent).[51] The solvation event is kinetically controlled, for example, in tetrahydrofuran, the solvent initially binds to the manganese through two electrons of a C–H bond which is followed by an ultrafast (ps) rearrangement to the more thermodynamically stable oxygen-bound form.[51] Performing the experiments in the presence of substrates used in the direct C–H functionalisation reactions, such as PhC_2H, allowed for the observation of the resulting π-alkyne complexes and the migratory insertion reaction leading to C–C bond formation.[52]

It was anticipated that related studies using trypto-CORM would provide insight into the nature of the species formed following the light-induced loss of CO. A combined computational (DFT) and experimental (TRIR) study of the light-induced dissociation of CO from trypto-CORM is described herein.

Results and discussion

Vibrational and electronic spectra of trypto-CORM

The ground state infra-red spectrum of trypto-CORM exhibits three bands in the metal carbonyl region in MeOH solution at 2037, 1933 and 1921 cm^{-1}, corresponding to the symmetric and (two) asymmetric stretching modes expected for an octahedral complex with three *fac*-coordinated carbonyl ligands. An additional broader band, assigned to the ester group of the coordinated tryptophan, is observed at 1638 cm^{-1}. This band is red-shifted when compared to the mode in the free amino acid.[38] These strong metal- and organic-carbonyl modes are ideal reporting groups to probe changes in the coordination environment of the manganese following photolysis.

The lowest energy band in the UV-vis spectrum of trypto-CORM in NCMe has a maximum at 360 nm (ε = 1443 mol^{-1} dm^3 cm^{-1}) which tails into the visible region of the spectrum (Fig. 2a).[38] Photolysis of trypto-CORM at 400 nm results in light-induced bleaching of this band and instigates the CO release process.[38] The nature of the transitions which constitute this band were modelled with TD-DFT at the PBE0/DGDZVP/def2tzv level of theory, with implicit solvation in NCMe. The calculations at this level indicate that the lowest energy transition should occur at 431 nm and has a 100% $HOMO_{98} \rightarrow LUMO_{99}$ composition. A less intense feature is predicted at 408 mn (100% $HOMO_{98} \rightarrow LUMO{+}1_{100}$). The HOMO is based on the indole of the tryptophanate ligand whereas the LUMO and LUMO+1 are metal-centred (Fig. 2(b)–(d)). In addition some of the higher energy transitions involve electron density on the ester group of the amino acid ligand (see ESI‡ for complete list) in the occupied orbital. Therefore irradiation at 400 nm is best viewed as resulting in a ligand-to-metal-charge transfer (LMCT).

TRIR spectroscopy on trypto-CORM

The TRIR studies were performed using the LIFEtime system[60] in the ULTRA facility at the Rutherford Appleton Laboratory using the time-resolved multiple-probe spectroscopy (TR^MPS) method.[61] This allows for the acquisition of time-resolved spectra with pump–probe delays between 1 ps and 1 ms. A pump wavelength of 400 nm was employed to simulate the conditions used in the biological experiments.[38]

View Article Online
Paper Dalton Transactions

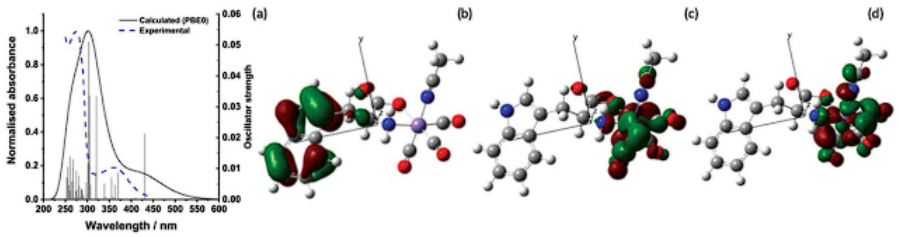

Fig. 2 (a) Experimental and predicted electronic spectra of trypto-CORM (b) $HOMO_{98}$ (c) $LUMO_{99}$ and (d) $LUMO+1_{100}$ calculated at the PBE0/DGDZVP/def2tzv level. Isosurface shown at the 0.04 level.

The initial experiments focussed on understanding the photolysis of trypto-CORM in NCMe solution as it was anticipated that prompt photo-dissociation of CO would result in the formation of a vacant coordination site that would be occupied by the coordinating solvent. The TRIR spectroscopic data are presented as difference spectra with negative bands corresponding to the species which are lost on irradiation and the positive bands due to the photoproducts.

Time-resolved spectra in the region 1780–2100 cm^{-1} (Fig. 3) exhibited strong negative bands corresponding to the ground state spectrum of trypto-CORM. The observation of these ground state bleach (GSB) bands demonstrates that trypto-CORM is lost on photolysis at 400 nm. Analysis of the resulting spectra indicated the formation of three different species. Two, **A** and **B**, were present in spectra recorded with pump–probe delays longer than 3 ps – data recorded with shorter delays were broad and featureless. A spectrum recorded with a pump–probe delay of 10 ps showed the presence of two peaks between 1950 and 1980 cm^{-1} (Fig. 4, top). Gaussian deconvolution (Table 1) of these bands gave band positions of (1964.8 ± 1.5) cm^{-1} and (1976.7 ± 0.6) cm^{-1} assigned to **A** and **B** respectively. A further feature was observed centred at *ca.* 1800 cm^{-1}. This was also successfully deconvoluted into two bands (Fig. 4, bottom) with peak positions of (1813.7 ± 1.7) and (1799.6 ± 3.5) cm^{-1}, assigned to **A** and **B** respectively. These

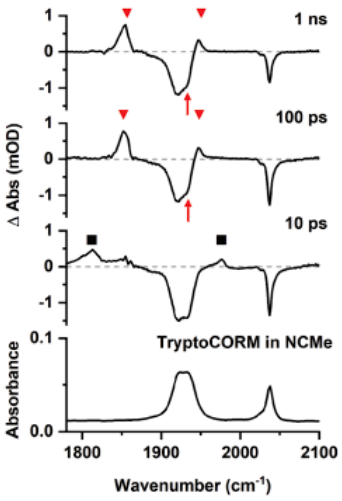

Fig. 3 Bottom IR spectrum of trypto-CORM in NCMe in the region 1780–2100 cm^{-1}. Top time-resolved difference IR spectra for the photolysis (400 nm) of trypto-CORM in NCMe with pump–probe delays of 10 ps, 100 ps, and 1 ns showing bands for A and B (■) and C by (▼). The red arrows show the apparent recovery of the GSB for trypto-CORM.

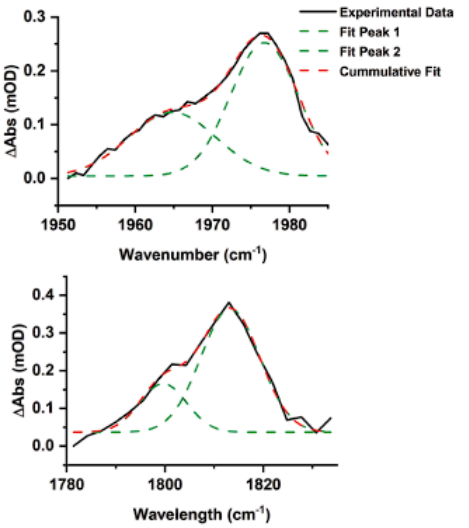

Fig. 4 Gaussian deconvolution of the bands at in the region 1950–1990 cm^{-1} (top, R^2 = 0.986) and 1780–1830 cm^{-1} (bottom, R^2 = 0.970) at 10 ps. Parameters are listed in Table 1.

Table 1 Derived parameters from the Gaussian deconvolution of the bands for complexes A and B at 10 ps

Band position/cm^{-1}	Peak width at half height/cm^{-1}	Integration	Assignment
1976.7 ± 0.6	10.4 ± 0.9	2.74 ± 0.42	**B**
1964.8 ± 1.5	13.4 ± 3.5	1.69 ± 0.62	**A**
1813.7 ± 1.7	14.1 ± 3.3	4.93 ± 1.35	**B**
1799.6 ± 3.5	11.3 ± 6.1	1.55 ± 1.22	**A**

features are at a very low frequency for a metal carbonyl stretching mode.

The presence of two bands is consistent with the photochemically induced loss of a CO ligand from trypto-CORM to give species with two mutually *cis* carbonyl ligands. Analysis of the intensity of the bands with time revealed that **A** had a greater initial concentration than **B**. The change in intensity of **B** with time was fitted to an exponential growth then decay function (τ_{growth} = (2.5 ± 3.9) ps and τ_{decay} = (15.9 ± 3.9) ps, Fig. 5). This was interpreted as initial formation of **A** which then transformed into **B** with a short lifetime. Although it was not possible to obtain a satisfactory fit to first order kinetics for **A**, qualitatively the loss of **A** corresponded with the growth of **B** (see ESI‡).

Over the course of *ca.* 100 ps, the bands for **B** decreased in intensity to be replaced by a peak at 1853 cm^{-1} and a smaller feature at 1947 cm^{-1}: these were assigned to a third photoproduct, **C** (Fig. 3). Inspection of the bands due to the GSB indicated some apparent recovery in intensity of the band due to trypto-CORM at 1933 cm^{-1} (highlighted with an arrow in Fig. 3). It was suspected that this was due to the overlap between the GSB bands for trypto-CORM and a peak for **C**. In order to determine if this was the case, the spectrum of trypto-CORM was subtracted from the difference spectrum recorded with a pump–probe delay of 1 ns. The resulting spectrum (Fig. 6) shows the presence of peak with a band position of 1946 cm^{-1}, leading to the conclusion that **C** was a *cis*-dicarbonyl complex. The growth of **C** proceeded with a statistically identical lifetime to the loss of **B**, τ_{growth} = (20.5 ± 1.1) ps, indicating that **B** → **C**.

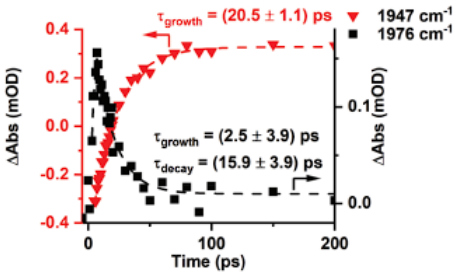

Fig. 5 Change in intensity of the bands due to B (■) and C (▼) with time. Dashed lines show fits against exponential growth/decay (B) and exponential growth (C) kinetics.

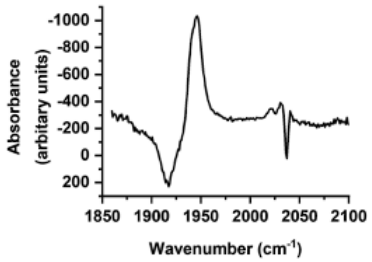

Fig. 6 Difference spectrum in the region 1850–2100 cm^{-1} recorded with a pump–probe delay of 1 ns with ground state bleach signal subtracted.

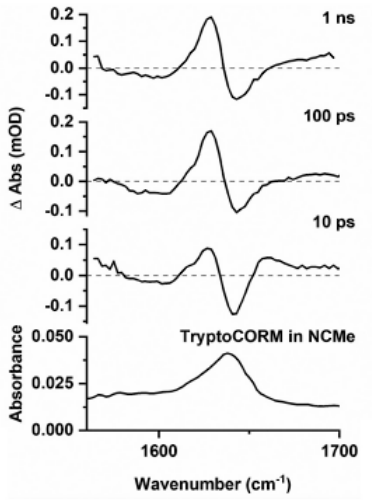

Fig. 7 Bottom IR spectrum of trypto-CORM in NCMe in the region 1560–1700 cm^{-1}. Top time-resolved difference IR spectra for the photolysis (400 nm) of trypto-CORM in NCMe with pump–probe delays of 10 ps, 100 ps, and 1 ns.

Difference spectra recorded in the region 1500–1700 cm^{-1} exhibited a strong GSB at *ca.* 1639 cm^{-1} (Fig. 7), consistent again with the loss of trypto-CORM on photolysis. Bands that could be assigned to the ester group in **A**, **B** and **C** were observed at short (<20 ps) and long (>100 ps) pump–probe delays respectively. The small changes in the band position of the ester mode was taken to indicate that the environment of the tryptophanate ligand had not changed significantly from either the parent trypto-CORM, or between **A**, **B** and **C**.

In order to evaluate the behaviour of trypto-CORM in an aqueous medium, the experiment was repeated in a

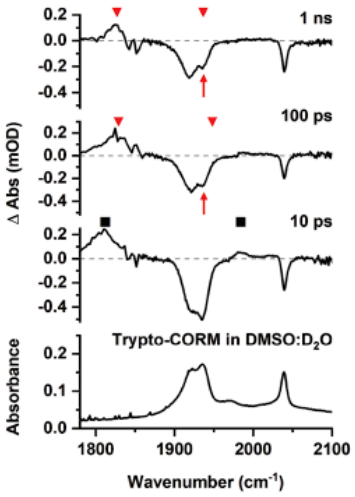

Fig. 8 Bottom IR spectrum of trypto-CORM in DMSO : D_2O (1 : 9 v : v) in the region 1780–2100 cm^{-1}. Top time-resolved difference IR spectra for the photolysis (400 nm) of trypto-CORM in NCMe with pump–probe delays of 10 ps, 100 ps, and 1 ns showing bands for **A** (■) and **C** by (▼). The red arrows show the apparent recover of the GSB for trypto-CORM.

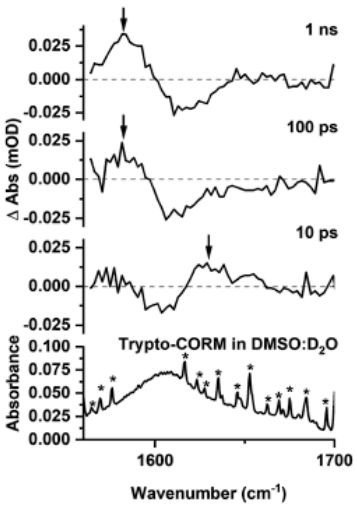

Fig. 9 Bottom IR spectrum of trypto-CORM in DMSO : D_2O (1 : 9 v : v) in the region 1560–1700 cm^{-1}. Top time-resolved difference IR spectra for the photolysis (400 nm) of trypto-CORM in NCMe with pump–probe delays of 10 ps, 100 ps, and 1 ns, band positions marked with an arrow. * indicates bands due to H_2O contamination.

DMSO : D_2O (1 : 9 v : v) solution. The lower solubility of the complex in this medium compared to NCMe entailed that the resulting spectra were less intense. However, it was evident from the resulting data that related processes were occurring in both media. In the region between 1800 and 2100 cm^{-1} bands were observed at 1985 and 1812 cm^{-1} (Fig. 8) which were assigned to the DMSO analogues of **A** and **B**. After 100 ps these bands had been replaced by a new peak at 1826 cm^{-1} and, as was the case for NCMe, the GSB for the trypto-CORM at *ca.* 1935 cm^{-1} had recovered in intensity (Fig. 7, red arrows), indicating a band from a species analogous to **C** overlapping with that from trypto-CORM.

Spectra recorded in the region 1560–1700 cm^{-1} (Fig. 9) were weak, however, it was possible to observe a GSB and that the peaks for transient species present at 10 ps. A band assigned to **C** was present at 1 ns.

These observations demonstrate that the behaviour of trypto-CORM is similar in both media. Given that our previous data had indicated that the NCMe ligand in the complex is thermally labile, it was anticipated that speciation in a DMSO/D_2O mixture was complicated. However, the shifts of the bands in the region 1800–1850 cm^{-1} to lower energy when compared to NCMe suggest that DMSO was coordinated to the metal.[51]

Density functional theory

The TRIR spectroscopy on trypto-CORM had demonstrated the formation of species **A**, **B** and **C**. In order to elucidate the potential structures of these states, a number of trial structures were probed by DFT. Geometries were optimised at the BP86/SV(P) level of theory, vibrational modes and subsequent free energy corrections were also calculated at this level. Single point energies were then calculated on these geometries at the D3BJ-PBE0/def2-TZVPP level with solvent correction using COSMO in NCMe.[62] We have previously used this method on related studies to calculate reaction pathways for C–C bond formation in the coordination sphere of manganese.[51,52] In these cases, there was a linear relationship between the calculated and experimental values for the reaction profiles studied and also between the calculated vibrational modes of the metal carbonyl ligands with those determined by time-resolved infra-red spectroscopy.

The TRIR data had demonstrated that the products must contain two carbonyl ligands. Furthermore, as only small changes were observed in the position of the C=O mode of the coordinated tryptophanate, it was assumed that the binding mode of this ligand did not substantially change on photolysis.

Two general classes of photoproducts were considered on this basis. The first were based on an 18-electron [Mn(tryp)$(CO)_2(NCMe)_2$], [**1**], framework. Four possible isomers (Fig. 10) are possible for this composition. The resulting geometry optimisations predicted, as expected, that all four of the complexes formed pseudo-octahedral geometries. In order to evaluate the relative Gibbs free energies, [**1a**] was taken as the reference state. Complex [**1b**] was found to lie at +14 kJ mol^{-1},

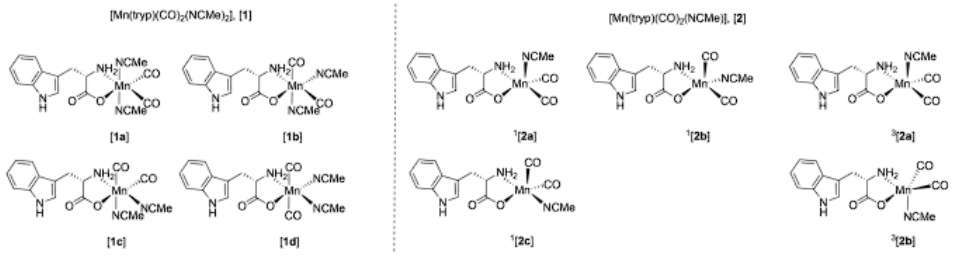

Fig. 10 Potential structures for complexes A and C studied by DFT.

[**1c**] at 3 kJ mol^{-1} whereas [**1d**] with two mutually *trans* carbonyl ligands is at a much higher energy (+74 kJ mol^{-1}).

The second class of potential photoproducts considered were 16-electron complexes [Mn(tryp)(CO)$_2$(NCMe)], [**2**], in which a CO ligand had dissociated leaving a formally vacant coordination site at the metal. Both singlet ^{1}[Mn(tryp)(CO)$_2$(NCMe)], ^{1}[**2**], and triplet ^{3}[Mn(tryp)(CO)$_2$(NCMe)], ^{3}[**2**] spin states were calculated. Three geometric isomers were located for ^{1}[**2**] which possessed geometries intermediate between a trigonal bipyramid and a square-based pyramid with the largest angle in the equatorial plane being *ca.* 150° in all cases. This is in marked contrast to the related 16-electron complex *fac*-[Mn(ppy)(CO)$_3$] which is calculated to have a square-based pyramidal shape (angles in the basal plane 168° and 170°).[51] This species is proposed to be generated from the photochemically induced loss of CO from [Mn(ppy)(CO)$_4$], however, solvation occurs within 1 ps. The difference in geometry between the complexes ^{1}[**2**] and *fac*-[Mn(ppy)(CO)$_3$] may be assigned to the presence of the coordinated ester group in the tryptophante ligand. This is a good π-donor group and may provide electron density for the formally vacant d-orbital in a d^6 16-electron system.[63] The significant shortening of the Mn–O bond length in all three isomers of ^{1}[Mn(tryp)(CO)$_2$(NCMe)] (all less than 1.93 Å) when compared to trypto-CORM (calculated 2.020 Å) and the four isomers of [Mn(tryp)(CO)$_2$(NCMe)$_2$] (all longer than 2 Å) presumably reflect this effect. Complex ^{1}[**2c**], in which the two carbonyl ligands and the oxygen of the tryptophanate ligand occupy the three equatorial sites, is the lowest energy (−17 kJ mol^{-1} relative to ^{1}[**2a**]) of the three isomers investigated.

Two minima were located for ^{3}[Mn(tryp)(CO)$_2$(NCMe)] despite using a number of different starting geometries. These only differ in the orientation of the indole substituent with respect to the NCMe ligand. In ^{3}[**2a**] the indole is on the opposite face to the NCMe, in ^{3}[**2b**] it is on the same face. Despite only a small conformational difference, the DFT calculations indicated a remarkable difference in energy. Complex ^{3}[**2a**] has an energy of −16 kJ mol^{-1} relative to ^{1}[**2a**] whereas ^{3}[**2b**] is at −117 kJ mol^{-1}. A further analysis of the calculations indicated this difference in energy is almost entirely due to the empirical dispersion correction. If this correction is not applied, then the relative energies of the two isomers are −18 kJ mol^{-1} (^{3}[**2a**]) and −8 kJ mol^{-1} (^{3}[**2b**]). This significant dispersion effect is assigned to an interaction between the methyl group of the NCMe ligand and the π-system of the indole which is present in ^{3}[**2b**], but not ^{3}[**2a**]. However, significant care must be taken in the interpretation of such an effect as the current model is only accounting for intramolecular interactions. It is highly likely that the indole in ^{3}[**2a**] (and indeed in all of the other structures examined that do not shown this effect) is interacting with the NCMe solvent in a similar fashion. It is argued that the D3-correction is, in this instance, significantly over stabilising ^{3}[**2b**].

The calculated vibrational modes for the metal carbonyl groups at the BP86/SV(P) level for all the structures explored are presented in Fig. 11. The values have been scaled using the linear empirical relationship from our previous study on related manganese carbonyl complexes.[52] As shown in Fig. 11, using this method also give a good approximation to the experimental values of trypto-CORM.

Structural assignment and mechanistic discussion

The TRIR data indicate that photolysis of trypto-CORM results in the process **A** → **B** → **C**. Focussing firstly on the identity of species **C**, the DFT-predicted bands for complex [**1c**] are the closest match to the experimentally determined values (Fig. 11). The predicted bands for [**1a**] and [**1b**] are similar, but are all at higher energy than [**1c**]. Across all the compounds investigated, the asymmetric stretching mode is predicted to occur at higher energy than the experiment, but for [**1c**] the symmetric stretch is a close match to experiment. Complex [**1d**] can be excluded as the two mutually *trans* carbonyl ligands would entail that the symmetric stretching mode would be at high energy with a very low intensity when compared to the experimental values.

The assignment of the short-lived species observed in the TRIR experiments, **A** and **B**, is more complex. As shown in Table 1, these species show unusually low frequency bands for the asymmetric stretch with a large difference in energy between the two bands, $\Delta\nu$. The fact that only two metal-carbonyl bands are observed for **A** and **B** supports an assignment to complexes containing two mutually *cis* carbonyl ligands. This

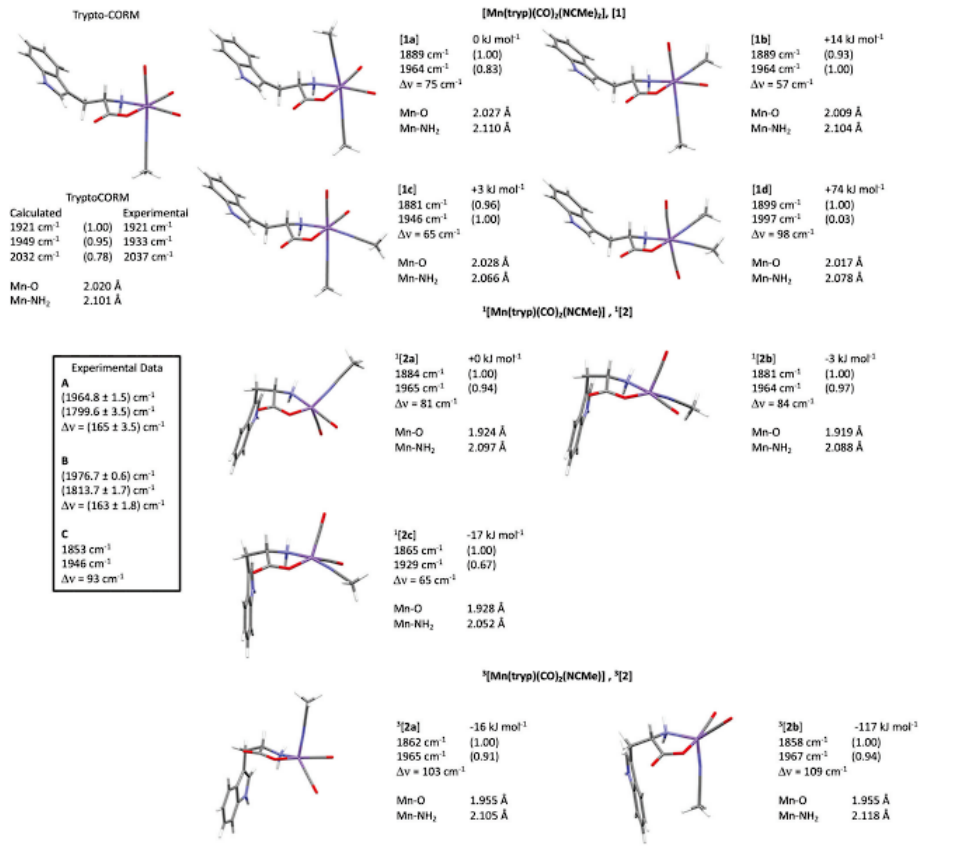

Fig. 11 Calculated structures, scaled infra-red modes for the metal carbonyl stretches (with normalised predicted intensities), relative free energies at 298 K in kJ mol^{-1} and Mn–O and Mn–NH_2 bond lengths, of trypto-CORM and isomers of [1], ^{1}[2] and ^{3}[2] at the D3-PBE0/def2-TZVPP/BP86/SV (P) level of theory. Manganese is shown in purple, carbon grey, hydrogen white, oxygen red and nitrogen blue. The relative energies of complexes [1] are relative to [1a], those for [2] relative to ^{1}[2a]. $\Delta\nu$ refers to the difference in frequency between the two carbonyl modes.

indicates that the CO-loss event must occur in less than 3 ps: the data are not consistent with the formation of a tricarbonyl complex which then undergoes CO loss on a ps timescale to give **C**,¶ as is observed in chromium arene complexes.[64] An examination of the data in Fig. 11 reveals that only the two isomers of ^{3}[2] are predicted to have a large (>100 cm^{-1}) value of $\Delta\nu$. Complexes ^{3}[2] are also predicted to have one of the lowest energy bands for the asymmetric stretching mode. Therefore, states **A** and **B** are both assigned to ^{3}[2c]. One important spectroscopic feature of note is the extremely low frequency of the asymmetric stretch for both **A** and **B**. This is in a region more typical of bridging carbonyl ligands, however, the mass spectrum of trypto-CORM indicates that the complex is monomeric, precluding this assignment.

It is proposed that vibrational cooling is responsible for the process **A** → **B**. As the energy of the photon which results in photodissociation is greater than that needed to break the M–CO bond, ^{3}[2c] is generated in a vibrationally excited state (v > 0).[65] Due to the anharmonic nature of the vibrational

¶We are grateful to a referee who suggested the possibility that complexes **A** and **B** may be singlet excited states of trypto-CORM which then undergo CO loss to give dicarbonyl **C**. This possibility had been discounted on the basis that **A** and **B** exhibit two bands in the difference spectrum (Fig. 3). However, we cannot completely discount the presence of a weak feature obscured by the GSB for trypto-CORM.

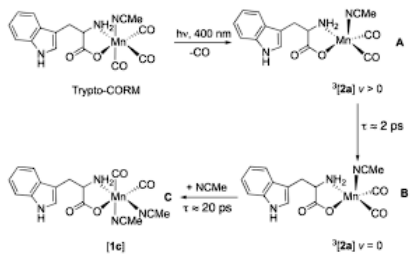

Scheme 1 Proposed mechanism for the photochemically induced loss of CO from trypto-CORM.

energy well, cooling to leads to a blue shift in energy of these modes, as observed for **A** → **B**. Indeed, the difference in frequency between the bands in **A** and **B** (*ca.* 14 cm^{-1}) is consistent with the former being the $\nu = 1 \rightarrow 2$ transition of ^{3}[**2c**], whereas the latter is $\nu = 0 \rightarrow 1$.[66]

A mechanistic picture is proposed, Scheme 1, in which the ultra-fast photodissociation of CO from trypto-CORM results in the formation of ^{3}[**2**] in a vibrationally excited state (**A**) which undergoes cooling to $\nu = 0$ to give **B**. A change in spin with coordination of the solvent gives [**1c**] (**C**). Our calculations indicate that the binding of the solvent to ^{3}[**2**] would be unfavourable as attempts to calculate a triplet spin isomer of [**1**] were unsuccessful. As expected for a d^6 18-electron octahedral complex, ^{3}[**1**] is metal–ligand dissociative and the geometry optimisation resulted in loss of an NCMe ligand with the metal adopting a structure related to ^{3}[**2**]. Hence solvent coordination is predicted to only occur to the single state. The lifetime for the formation of **C** ([**1c**]) is ≈20 ps and solvation of unsaturated d^6 metal complexes by NCMe can occur in 1 ps,[67] hence the change in spin-state is proposed to be rate controlling. Similar behaviour has been reported for photochemically generated ^{3}[$Fe(CO)_4$] and ^{3}[$Co(\eta^5\text{-}C_5H_5)(CO)$].[68] Recent studies on ^{3}[$Mn(\eta^5\text{-}C_5H_5)(CO)_2$] have indicated that the nature of the solvent effects the lifetime of the triplet state which may indicate a solvent-promoted change in spin as an additional mechanistic pathway.[69]

Conclusions

Photolysis of trypto-CORM at 400 nm results in ultrafast CO dissociation and formation of ^{3}[$Mn(tryp)(CO)_2(NCMe)$] in a vibrationally hot state which then undergoes cooling. This triplet state subsequently forms a long-lived species, assigned to *all-cis*-[$Mn(tryp)(CO)_2(NCMe)_2$], [**1c**], with a lifetime of ≈20 ps. This species remains unchanged for the duration of the experiment (800 μs). Previous studies have demonstrated that trypto-CORM is capable of releasing between two and three molecules of CO[38] and these data indicate that any subsequent thermal loss of CO must be slower than 800 μs.

An alternative pathway involving the light-induced loss of NCMe may also be considered. However, loss of the coordinated NCMe in the same solvent would, on re-coordination, regenerate trypto-CORM. If such a process is occurring then it must take place in under 3 ps as no evidence for a tricarbonyl photoproduct, [$Mn(tryp)(CO)_3$], was obtained in this study.

The experiments demonstrate that TRIR spectroscopy, coupled with DFT, can provide detailed information about the nature of the ultra-fast processes underpinning photochemical CO-release, including in model systems for an aqueous environment.

Experimental

Trypto-CORM was prepared a described previously.[38] Time-resolved infra-red spectra were recorded on the LIFEtime instrument in the ULTRA facility at the Rutherford Appleton. Details of the experiment have been described previously,[60] however, in brief, the pump source was the output of a Yb:KGW amplifier providing 15 W, 260 fs pulses at 1030 nm with a 100 kHz repetition rate (Pharos). This was used to drive a BBO-based 515 nm pumped optical parametric amplifier (OPA) to deliver pulses at 400 nm. The pump beam was collimated, travelled over a computer programmable 0–16 ns optical delay (1200 mm long, double pass), and focused onto the sample. The pump energy at the sample was attenuated down to 500 nJ and focused down to a 120 × 120 μm^2 spot. The probe source was the output of a Yb:KGW amplifier providing 6 W, 180 fs pulses at 1030 nm with a 100 kHz repetition rate (Pharos). This drove two 3 W BBO/KTA based OPAs. The two Pharos sources share a common 80 MHz oscillator to allow for pump–probe delay steps of 12.5 ns. The probe beam was split to provide probe and reference pulses. To go beyond pump–probe delays of 12.5 ns, subsequent seed pulses were selected from the 80 MHz oscillator. Data were collected using pump–probe delays ranging from 1 ps to 988.5 μs. The probe beams were collimated, synchronised by a fixed optical delay, and focused by a gold parabolic mirror onto the sample. The three beams were overlapped on the sample using a 50 μm pinhole. The probe beams were measured by two separate 128-element detectors. To cover the full spectroscopic window required, data from a number of different detector positions were combined to generate the required spectra.

For the experiments in NCMe, trypto-CORM *ca.* 30 mg was dissolved in 20 ml anhydrous NCMe and placed in a Duran flask. The experiments in DMSO/D_2O were performed by dissolving *ca.* 13 mg of trypto-CORM in 2 ml DMSO before adding D_2O to make the total volume 20 ml. The solutions were then flowed through a Harrick cell fitted with a 100 μm Teflon spacer using a peristaltic pump for the duration of the experiment.

Data were initially visualised in the ULTRA View version 2 software,[70] where baseline-correction was undertaken. The resulting spectra were then exported as comma-separated values files into Origin 2019.[71] The spectra in the metal carbonyl region were calibrated against the GSB of an authentic

sample of trypto-CORM allowing for detector pixels to be allocated to specific frequencies. The region between 1860 and 1500 cm^{-1} was calibrated against a 190 μm polystyrene standard. Kinetic data were analysed using the *expdec* and *expgrowdec* functions in Origin 2019 and errors are presented as 95% confidence limits. Subtraction of the GSB from the difference spectrum in Fig. 5 was performed by scaling the difference spectrum and a spectrum of authentic trypto-CORM recorded in NCMe on an FTIR instrument to the peak at 2013 cm^{-1}. The subtraction was then performed using the *Subtract Reference Data* feature in Origin 2019.

DFT calculations were performed using the TURBOMOLE V6.4 package using the resolution of identity (RI) approximation.[72–78] Initial optimisations were performed at the (RI-)BP86/SV(P) level, followed by frequency calculations at the same level. All minima were confirmed as such by the absence of imaginary frequencies. Single-point calculations on the (RI-)BP86/SV(P) optimised geometries were performed using the hybrid PBE0 functional and the flexible def2-TZVPP basis set. The (RI-)PBE0/def2-TZVPP SCF energies were corrected for their zero-point energies, thermal energies and entropies (obtained from the (RI-)BP86/SV(P)-level frequency calculations). Vibrational frequencies were scaled using the empirical relationship developed in our previous work [$\nu_{expt} = (\nu_{calc} - 561.7)/0.7369$].[52] No symmetry constraints were applied during optimisations. Triplet states were optimised using a spin unrestricted formalism. Solvent corrections were applied with the COSMO[62] dielectric continuum model and dispersion effects modelled with Grimme's D3 method.[79,80] Energies, *xyz* coordinates and the first 50 lines of the vibrational spectra are presented in the electronic ESI.‡

Additional TD-DFT calculations were performed using the Gaussian 16 Rev. A.03 Win64[81] at the PBE0/DGDZVP/def2tzv level, with NCMe as the implicit solvent using CPCM. The first 10 states calculated are collated in the ESI.‡

Conflicts of interest

There are no conflicts to declare.

Acknowledgements

We are grateful to the EPSRC (studentship to B. J. A., EP/M506680/1 an iCASE award with Syngenta, EP/N509413/1 studentship to L. A. H. and for the computational equipment used in this study, grants EP/H011455/1 and EP/K031589/1) the STFC (programme access to the ULTRA facility grant 1813) and the University of York (studentship to J. B. E.) for funding.

Notes and references

1 R. Motterlini and L. E. Otterbein, *Nat. Rev. Drug Discovery*, 2010, **9**, 728–743.
2 R. Foresti, M. G. Bani-Hani and R. Motterlini, *Intensive Care Med.*, 2008, **34**, 649–658.
3 F. Zobi, *Future Med. Chem.*, 2013, **5**, 175–188.
4 R. Alberto and R. Motterlini, *Dalton Trans.*, 2007, 1651–1660.
5 T. R. Johnson, B. E. Mann, J. E. Clark, R. Foresti, C. J. Green and R. Motterlini, *Angew. Chem., Int. Ed.*, 2003, **42**, 3722–3729.
6 J. E. Clark, P. Naughton, S. Shurey, C. J. Green, T. R. Johnson, B. E. Mann, R. Foresti and R. Motterlini, *Circ. Res.*, 2003, **93**, e2–e8.
7 R. Motterlini, J. E. Clark, R. Foresti, P. Sarathchandra, B. E. Mann and C. J. Green, *Circ. Res.*, 2002, **90**, E17–E24.
8 I. J. S. Fairlamb and J. M. Lynam, in *Advances in Bioorganometallic Chemistry*, ed. T. Hirao and T. Moriuchi, Elsevier, 2019, pp. 137–154.
9 A. R. Marques, L. Kromer, D. J. Gallo, N. Penacho, S. S. Rodrigues, J. D. Seixas, G. J. L. Bernardes, P. M. Reis, S. L. Otterbein, R. A. Ruggieri, A. S. G. Goncalves, A. M. L. Goncalves, M. N. De Matos, I. Bento, L. E. Otterbein, W. A. Blattler and C. C. Romao, *Organometallics*, 2012, **31**, 5810–5822.
10 X. Ji, K. Damera, Y. Zheng, B. Yu, L. E. Otterbein and B. Wang, *J. Pharm. Sci.*, 2016, **105**, 406–416.
11 S. Romanski, E. Stamellou, J. T. Jaraba, D. Storz, B. K. Krämer, M. Hafner, S. Amslinger, H. G. Schmalz and B. A. Yard, *Free Radical Biol. Med.*, 2013, **65**, 78–88.
12 S. Romanski, B. Kraus, M. Guttentag, W. Schlundt, H. Rucker, A. Adler, J.-M. Neudorfl, R. Alberto, S. Amslinger and H.-G. Schmalz, *Dalton Trans.*, 2012, **41**, 13862–13875.
13 S. Romanski, B. Kraus, U. Schatzschneider, J.-M. Neudörfl, S. Amslinger and H.-G. Schmalz, *Angew. Chem., Int. Ed.*, 2011, **50**, 2392–2396.
14 I. J. S. Fairlamb, A. K. Duhme-Klair, J. M. Lynam, B. E. Moulton, C. T. O'Brien, P. Sawle, J. Hammad and R. Motterlini, *Bioorg. Med. Chem. Lett.*, 2006, **16**, 995–998.
15 I. J. S. Fairlamb, J. M. Lynam, B. E. Moulton, I. E. Taylor, A. K. Duhme-Klair, P. Sawle and R. Motterlini, *Dalton Trans.*, 2007, 3603–3605.
16 A. J. Atkin, S. Williams, P. Sawle, R. Motterlini, J. M. Lynam, I. J. S. Fairlamb, A. J. Atkin, S. Williams, P. Sawle, R. Motterlini, J. M. Lynam and I. J. S. Fairlamb, *Dalton Trans.*, 2009, **38**, 3653–3656.
17 W.-Q. Zhang, A. J. Atkin, R. J. Thatcher, A. C. Whitwood, I. J. S. Fairlamb and J. M. Lynam, *Dalton Trans.*, 2009, **38**, 4351–4358.
18 W.-Q. Zhang, A. C. Whitwood, I. J. S. Fairlamb and J. M. Lynam, *Inorg. Chem.*, 2010, **49**, 8941–8952.
19 S. McMahon, S. Amirjalayer, W. J. Buma, Y. Halpin, C. Long, A. D. Rooney, S. Woutersen and M. T. Pryce, *Dalton Trans.*, 2015, **44**, 15424–15434.
20 P. C. Kunz, H. Meyer, J. Barthel, S. Sollazzo, A. M. Schmidt and C. Janiak, *Chem. Commun.*, 2013, **49**, 4896–4898.
21 M. A. Wright and J. A. Wright, *Dalton Trans.*, 2016, **45**, 6801–6811.

22 I. Chakraborty, S. J. Carrington and P. K. Mascharak, *Acc. Chem. Res.*, 2014, **47**, 2603–2611.
23 U. Schatzschneider, *Inorg. Chim. Acta*, 2011, **374**, 19–23.
24 P. C. Ford, *Coord. Chem. Rev.*, 2018, **376**, 548–564.
25 M. Tinajero-Trejo, N. Rana, C. Nagel, H. E. Jesse, T. W. Smith, L. K. Wareham, M. Hippler, U. Schatzschneider and R. K. Poole, *Antioxid. Redox Signal.*, 2016, **24**, 765–780.
26 C. Nagel, S. McLean, R. K. Poole, H. Braunschweig, T. Kramer and U. Schatzschneider, *Dalton Trans.*, 2014, **43**, 9986–9997.
27 H. Pfeiffer, T. Sowik and U. Schatzschneider, *J. Organomet. Chem.*, 2013, **734**, 17–24.
28 P. Govender, S. Pai, U. Schatzschneider and G. S. Smith, *Inorg. Chem.*, 2013, **52**, 5470–5478.
29 S. J. Carrington, I. Chakraborty and P. K. Mascharak, *Chem. Commun.*, 2013, **49**, 11254–11256.
30 F. Mohr, J. Niesel, U. Schatzschneider and C. W. Lehmann, *Z. Anorg. Allg. Chem.*, 2012, **638**, 543–546.
31 J. Niesel, A. Pinto, H. W. Peindy, N.'D. K. Merz, I. Ott, R. Gust and U. Schatzschneider, *Chem. Commun.*, 2008, 1798–1800.
32 S. H. C. Askes, G. U. Reddy, R. Wyrwa, S. Bonnet and A. Schiller, *J. Am. Chem. Soc.*, 2017, **139**, 15292–15295.
33 Q. Jiang, Y. Xia, J. Barrett, A. Mikhailovsky, G. Wu, D. Wang, P. Shi and P. C. Ford, *Inorg. Chem.*, 2019, **58**, 11066–11075.
34 N. Rana, H. E. Jesse, M. Tinajero-Trejo, J. A. Butler, J. D. Tarlit, M. L. U. zur Muhlen, C. Nagel, U. Schatzschneider and R. K. Poole, *Microbiology*, 2017, **163**, 1477–1489.
35 J. Betts, C. Nagel, U. Schatzschneider, R. Poole and R. M. La Ragione, *PLoS One*, 2017, **12**, e186359.
36 W. Huber, R. Linder, J. Niesel, U. Schatzschneider, B. Spingler and P. C. Kunz, *Eur. J. Inorg. Chem.*, 2012, **2012**, 3140–3146.
37 E. Kottelat, A. Ruggi and F. Zobi, *Dalton Trans.*, 2016, **45**, 6920–6927.
38 J. S. Ward, J. M. Lynam, J. Moir and I. J. S. Fairlamb, *Chem. – Eur. J.*, 2014, **20**, 15061.
39 J. S. Ward, R. Morgan, J. M. Lynam, I. J. S. Fairlamb and J. W. B. Moir, *MedChemComm*, 2017, **8**, 346–352.
40 R. N. Perutz, O. Torres and A. Vlcek, in *Comprehensive Inorganic Chemistry II*, Elsevier Press, 2013, vol. 8, pp. 229–253.
41 R. N. Perutz and J. J. Turner, *J. Am. Chem. Soc.*, 1975, **97**, 4791–4800.
42 J. A. Calladine, S. B. Duckett, M. W. George, S. L. Matthews, R. N. Perutz, O. Torres and Q. V. Khuong, *J. Am. Chem. Soc.*, 2011, **133**, 2303–2310.
43 O. Torres, J. A. Calladine, S. B. Duckett, M. W. George and R. N. Perutz, *Chem. Sci.*, 2015, **6**, 418–424.
44 J. M. Butler, M. W. George, J. R. Schoonover, D. M. Dattelbaum and T. J. Meyer, *Coord. Chem. Rev.*, 2007, **251**, 492–514.
45 A. J. Cowan and M. W. George, *Coord. Chem. Rev.*, 2008, **252**, 2504–2511.
46 O. Torres, J. A. Calladine, S. B. Duckett, M. W. George and R. N. Perutz, *Chem. Sci.*, 2015, **6**, 418–424.
47 J. Guan, A. Wriglesworth, X. Z. Sun, E. N. Brothers, S. D. Zarić, M. E. Evans, W. D. Jones, M. Towrie, M. B. Hall and M. W. George, *J. Am. Chem. Soc.*, 2018, **140**, 1842–1854.
48 J. A. Calladine, S. B. Duckett, M. W. George, S. L. Matthews, R. N. Perutz, O. Torres and K. Q. Vuong, *J. Am. Chem. Soc.*, 2011, **133**, 2303–2310.
49 S. A. Bartlett, N. A. Besley, A. J. Dent, S. Diaz-Moreno, J. Evans, M. L. Hamilton, M. W. D. Hanson-Heine, R. Horvath, V. Manici, X.-Z. Sun, M. Towrie, L. Wu, X. Zhang and M. W. George, *J. Am. Chem. Soc.*, 2019, **141**, 11471–11480.
50 M. Fumanal, Y. Harabuchi, E. Gindensperger, S. Maeda and C. Daniel, *J. Comput. Chem.*, 2019, **40**, 72–81.
51 B. J. Aucott, A.-K. Duhme-Klair, B. E. Moulton, I. P. Clark, I. V. Sazanovich, M. Towrie, L. A. Hammarback, I. J. S. Fairlamb and J. M. Lynam, *Organometallics*, 2019, **38**, 2391–2401.
52 L. A. Hammarback, I. P. Clark, I. V. Sazanovich, M. Towrie, A. Robinson, F. Clarke, S. Meyer, I. J. S. Fairlamb and J. M. Lynam, *Nat. Catal.*, 2018, **1**, 830–840.
53 J. S. Ward, J. T. W. Bray, B. J. Aucott, C. Wagner, N. E. Pridmore, A. C. Whitwood, J. W. B. Moir, J. M. Lynam and I. J. S. Fairlamb, *Eur. J. Inorg. Chem.*, 2016, 5044–5051.
54 J. S. Ward, J. M. Lynam, J. W. B. Moir, D. E. Sanin, A. P. Mountford and I. J. S. Fairlamb, *Dalton Trans.*, 2012, **41**, 10514–10517.
55 B. J. Aucott, J. S. Ward, S. G. Andrew, J. Milani, A. C. Whitwood, J. M. Lynam, A. Parkin and I. J. S. Fairlamb, *Inorg. Chem.*, 2017, **56**, 5431–5440.
56 N. P. Yahaya, K. M. Appleby, M. Teh, C. Wagner, E. Troschke, J. T. W. Bray, S. B. Duckett, L. A. Hammarback, J. S. Ward, J. Milani, N. E. Pridmore, A. C. Whitwood, J. M. Lynam and I. J. S. Fairlamb, *Angew. Chem., Int. Ed.*, 2016, **55**, 12455–12459.
57 Y. Hu, B. Zhou and C. Wang, *Acc. Chem. Res.*, 2018, **51**, 816–827.
58 L. A. Hammarback, A. Robinson, J. M. Lynam and I. J. S. Fairlamb, *Chem. Commun.*, 2019, **55**, 3211–3214.
59 L. A. Hammarback, A. Robinson, J. M. Lynam and I. J. S. Fairlamb, *J. Am. Chem. Soc.*, 2019, **141**, 2316–2328.
60 G. M. Greetham, P. M. Donaldson, C. Nation, I. V. Sazanovich, I. P. Clark, D. J. Shaw, A. W. Parker and M. Towrie, *Appl. Spectrosc.*, 2016, **70**, 645–653.
61 G. M. Greetham, D. Sole, I. P. Clark, A. W. Parker, M. R. Pollard and M. Towrie, *Rev. Sci. Instrum.*, 2012, **83**, 103107.
62 A. Klamt and G. Schuurmann, *J. Chem. Soc., Perkin Trans. 2*, 1993, 799–805.
63 J. F. Riehl, Y. Jean, O. Eisenstein and M. Pelissier, *Organometallics*, 1992, **11**, 729–737.
64 I. P. Clark, M. W. George, G. M. Greetham, E. C. Harvey, C. Long, J. C. Manton, H. McArdle and M. T. Pryce, *J. Phys. Chem. A*, 2012, **116**, 962–969.
65 J. E. Shanoski, C. K. Payne, M. F. Kling, E. A. Glascoe and C. B. Harris, *Organometallics*, 2005, **24**, 1852–1859.

66 T. P. Dougherty and E. J. Heilweil, *J. Chem. Phys.*, 1994, **100**, 4006–4009.
67 L. Zhu, S. Saha, Y. Wang, D. A. Keszler and C. Fang, *J. Phys. Chem. B*, 2016, **120**, 13161–13168.
68 J. P. Lomont, S. C. Nguyen and C. B. Harris, *Acc. Chem. Res.*, 2014, **47**, 1634–1642.
69 X. Wu, Z. Liu, T. S. Murphey, X. Z. Sun, M. W. D. Hanson-Heine, M. Towrie, J. N. Harvey and M. W. George, *Faraday Discuss.*, 2019, DOI: 10.1039/C9FD00067D.
70 M. R. Pollard and G. M. Greetham, *ULTRA View Data Analysis*, STFC.
71 *OriginPro*, OriginLab Corporation, Northampton, MA, USA, 2019.
72 R. Ahlrichs, M. Bär, M. Häser, H. Horn and C. Kölmel, *Chem. Phys. Lett.*, 1989, **162**, 165–169.
73 K. Eichkorn, O. Treutler, H. Öhm, M. Häser and R. Ahlrichs, *Chem. Phys. Lett.*, 1995, **240**, 283–290.
74 O. Treutler and R. Ahlrichs, *J. Chem. Phys.*, 1995, **102**, 346–354.
75 K. Eichkorn, F. Weigend, O. Treutler and R. Ahlrichs, *Theor. Chem. Acc.*, 1997, **97**, 119–124.
76 M. von Arnim and R. Ahlrichs, *J. Chem. Phys.*, 1999, **111**, 9183–9190.
77 P. Deglmann, F. Furche and R. Ahlrichs, *Chem. Phys. Lett.*, 2002, **362**, 511–518.
78 P. Deglmann, K. May, F. Furche and R. Ahlrichs, *Chem. Phys. Lett.*, 2004, **384**, 103–107.
79 S. Grimme, J. Antony, S. Ehrlich and H. Krieg, *J. Chem. Phys.*, 2010, **132**, 154104.
80 S. Grimme, S. Ehrlich and L. Goerigk, *J. Comput. Chem.*, 2011, **32**, 1456–1465.
81 M. J. Frisch, G. W. Trucks, H. B. Schlegel, G. E. Scuseria, M. A. Robb, J. R. Cheeseman, G. Scalmani, V. Barone, G. A. Petersson, H. Nakatsuji, X. Li, M. Caricato, A. V. Marenich, J. Bloino, B. G. Janesko, R. Gomperts, B. Mennucci, H. P. Hratchian, J. V. Ortiz, A. F. Izmaylov, J. L. Sonnenberg, D. Williams-Young, F. Ding, F. Lipparini, F. Egidi, J. Goings, B. Peng, A. Petrone, T. Henderson, D. Ranasinghe, V. G. Zakrzewski, J. Gao, N. Rega, G. Zheng, W. Liang, M. Hada, M. Ehara, K. Toyota, R. Fukuda, J. Hasegawa, M. Ishida, T. Nakajima, Y. Honda, O. Kitao, H. Nakai, T. Vreven, K. Throssell, J. A. Montgomery Jr., J. E. Peralta, F. Ogliaro, M. J. Bearpark, J. J. Heyd, E. N. Brothers, K. N. Kudin, V. N. Staroverov, T. A. Keith, R. Kobayashi, J. Normand, K. Raghavachari, A. P. Rendell, J. C. Burant, S. S. Iyengar, J. Tomasi, M. Cossi, J. M. Millam, M. Klene, C. Adamo, R. Cammi, J. W. Ochterski, R. L. Martin, K. Morokuma, O. Farkas, J. B. Foresman and D. J. Fox, *Gaussian 16 Rev. A.03*, Wallingford, CT.

Dalton Transactions

ROYAL SOCIETY OF CHEMISTRY

PAPER

View Article Online
View Journal | View Issue

Cite this: *Dalton Trans.*, 2020, **49**, 5463

Time-resolved infra-red spectroscopy reveals competitive water and dinitrogen coordination to a manganese(I) carbonyl complex†

Jonathan B. Eastwood, [a] L. Anders Hammarback, [a] Matthew T. McRobie, [a] Ian P. Clark, [b] Michael Towrie, [b] Ian. J. S. Fairlamb *[a] and Jason M. Lynam *[a]

Received 24th December 2019,
Accepted 23rd March 2020

DOI: 10.1039/c9dt04878b

rsc.li/dalton

Time-resolved infra-red (TRIR) spectroscopy has been used to demonstrate that photolysis of [Mn(C^N)(CO)$_4$] (C^N = bis-(4-methoxyphenyl)methanimine) in heptane solution results in ultra-fast CO dissociation and ultimate formation of a rare Mn-containing dinitrogen complex *fac*-[Mn(C^N)(CO)$_3$(N$_2$)] with a diagnostic stretching mode for a terminal-bound N≡N ligand at 2249 cm^{-1}. An isotopic shift to 2174 cm^{-1} was observed when the reaction was performed under ^{15}N$_2$ and the band was not present when the experiment was undertaken under an atmosphere of argon, reinforcing this assignment. An intermediate solvent complex *fac*-[Mn(C^N)(CO)$_3$(heptane)] was identified which is formed in less than 2 ps, indicating that CO-release occurs on an ultra-fast timescale. The heptane ligand is labile and is readily displaced by both N$_2$ and water to give *fac*-[Mn(C^N)(CO)$_3$(N$_2$)] and *fac*-[Mn(C^N)(CO)$_3$(OH$_2$)] respectively. The *fac*-[Mn(C^N)(CO)$_3$(heptane)] framework showed a significant affinity for N$_2$, as performing the reaction under air produced significant amounts of *fac*-[Mn(C^N)(CO)$_3$(N$_2$)]. Kinetic analysis reveals that the substitution of heptane by N$_2$ (k = (1.028 ± 0.004) × 10^9 mol^{-1} dm^3 s^{-1}), and H$_2$O is competitive on fast (<1 μs) time scales. The binding of water is reversible and, under an atmosphere of N$_2$, some *fac*-[Mn(C^N)(CO)$_3$(OH$_2$)] converts to *fac*-[Mn(C^N)(CO)$_3$(N$_2$)].

Introduction

Coordination of dinitrogen to transition metals plays an important role in N$_2$ fixation. Binding enhances the reactivity of the coordinated ligand, ameliorating the low kinetic reactivity dictated by the strong N≡N bond.[1] In addition there has been recent interest in the transition metal-catalysed use of ammonia as an energy carrier and the ruthenium-catalysed conversion of NH$_3$ to N$_2$ has recently been reported.[2] Moreover, this process also relies on the ultimate formation of a dinitrogen complex. It is therefore unsurprising that there have been concerted and detailed studies of the synthesis and reactivity of transition metal dinitrogen complexes. Inspired by the active site of the nitrogenase enzyme, there has been a particular focus on dinitrogen complexes of Group 6 metals and molecular species able to catalytically convert N$_2$ to NH$_3$ have been reported.[3] There are also many examples of dinitrogen complexes from Groups 4, 5 and 8 which have provided insight into the different binding modes that N$_2$ may exhibit.[1]

Remarkably, there are only a handful of examples of N$_2$ complexes of the Group 7 metals.[3,4] Indeed the limited examples of manganese dinitrogen complexes are primarily based on two structural frameworks (Fig. 1). One such framework is *trans*-[Mn(P–P)$_2$XY] (P–P = chelating phosphorus ligand). For example, Kubas demonstrated that reaction of N$_2$ with *trans*-[Mn(CO)(dppe)$_2$][BAr′$_4$] (dppe = 1,2-bis-(diphenylphosphino)ethane, Ar′ = C$_6$H$_3$-(3,5-CF$_3$)$_2$), in which the formally 16-e Mn-centre is stabilised by two C–H agostic interactions, results in the formation of [Mn(CO)(N$_2$)(dppe)$_2$][BAr′$_4$].[5] The related complex *trans*-[MnH(N$_2$)(dmpe)$_2$] (dmpe = 1,2-bis-(dimethylphosphino)ethane) may be prepared from the thermal reaction of *trans*-[MnH$_3$(dmpe)$_2$] with N$_2$.[6]

The second series of compounds are based on a half-sandwich motif. The archetype of this series, [Mn(η^5-C$_5$H$_5$)(CO)$_2$(N$_2$)], was originally prepared by oxidation of [Mn(η^5-C$_5$H$_5$)(CO)$_2$(N$_2$H$_4$)] with hydrogen peroxide,[7] although displacement of the THF ligand in [Mn(η^5-C$_5$H$_5$)(CO)$_2$(THF)] by N$_2$ may also be used as a route to this complex.[8] The photochemically induced replacement of CO by N$_2$ has been shown to be an effective route to this class of compounds: irradiation of

[a]*Department of Chemistry, University of York, Heslington, York, YO10 5DD, UK. E-mail: ian.fairlamb@york.ac.uk, jason.lynam@york.ac.uk*
[b]*Central Laser Facility, STFC Rutherford Appleton Laboratory, Harwell Campus, Didcot, Oxfordshire, OX11 0QX, UK*

†Electronic supplementary information (ESI) available: Additional TRIR spectra and collated *xyz* coordinates, energies and vibrational modes from the DFT calculations. See DOI: 10.1039/c9dt04878b

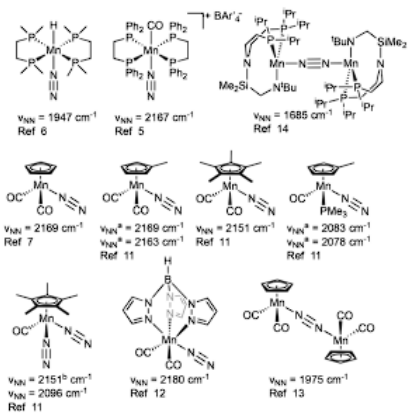

Fig. 1 Examples of known manganese dinitrogen compounds with NN vibrational mode frequencies, (a) band split due to rotamers, (b) tentative assignment due to band overlap.

$[Mn(\eta^5\text{-}C_5H_5)(CO)_3]$ under N_2 results in CO loss and formation of $[Mn(\eta^5\text{-}C_5H_5)(CO)_2(N_2)]$.[9,10] This method may be extended to a number of related derivatives. For example George and Poliakoff have shown that photolysis of $[Mn(\eta^5\text{-}C_5R_4Me)(CO)_2L]$ (R = H, Me; L = CO, $PMe_{3-x}Ph$ x = 0–3) in supercritical fluids in the presence of dinitrogen may be used to prepare complexes $[Mn(\eta^5\text{-}C_5R_4Me)(CO)(N_2)L]$: evidence for the formation of $[Mn(\eta^5\text{-}C_5Me_5)(CO)(N_2)_2]$ was obtained.[11] Similarly photolysis of $[Mn(Tp)(CO)_3]$ (Tp = hydrido-tris-(1-pyrazolyl) borate) in cyclohexane/$HSiEt_3$ solution under N_2 results in CO dissociation and formation of $[Mn(Tp)(CO)_2(N_2)]$.[12] The dinitrogen-bridged dimer $[\{Mn(\eta^5\text{-}C_5H_5)(CO)_2\}_2(N_2)]$ may be prepared from the reaction of $[Mn(\eta^5\text{-}C_5H_5)(CO)_2(THF)]$ with N_2CHCF_3.[13] An example of P_2N_2-based complex with a bridging N_2 ligand has also been reported.[14]

Given the current interest in using manganese carbonyl complexes as catalysts for organic transformations,[15–20] the observation of new manganese dinitrogen complexes could offer potential for the future development of pathways for nitrogen fixation. We have recently employed time-resolved infra-red spectroscopy to demonstrate that photolysis of $[Mn(ppy)(CO)_4]$ (ppy = 2-phenylpyridine) results in ultra-fast loss of a CO ligand and formation of species $[Mn(ppy)(CO)_3S]$ within 1 ps, where S is the solvent medium employed.[21] If S is a substrate for Mn-catalysed C–H functionalisation, such as an alkyne or an activated alkene, then subsequent C–C bond formation may be observed.[16] It was reasoned that if a suitably weakly bound solvent, such as a hydrocarbon, were employed then this could be displaced by a molecule of dinitrogen. TRIR has been used to identify dinitrogen complexes formed by displacement of a coordinated hydrocarbon ligand for a number of different metal complexes and to quantify the rates of substitution.[22] In a similar vein, George has demonstrated that using perfluorinated solvents as weakly bound token ligands even allows for the coordination of Xe to photochemically generated $[W(CO)_5]$[23] and $[Mn(\eta^5\text{-}C_5H_5)(CO)_2]$ fragments.[24]

The implementation of this approach to form a mixed manganese carbonyl/dinitrogen complex is now reported. Instead of the 2-phenylpyridine-substituted complex, the related species $[Mn(C^N)(CO)_4]$, [1], was employed as it was anticipated that the more sterically demanding cyclometallated imine ligand might favour the coordination of linear N_2 to the metal.

Results and discussion

The photochemical dissociation of CO from $[Mn(C^N)(CO)_4]$, [1], was studied at the ULTRA facility, Rutherford Appleton Laboratory, using the time-resolved multiple probe (TR^MPS) method. By virtue of using synchronised pump- and probe-lasers, TR^MPS permits photo-induced events occurring from 1 ps–800 μs to be observed. A pump wavelength of 355 nm was employed and the changes to the bands in the region 1850–2300 cm^{-1} of the infra-red spectrum used to probe the changes to the metal following irradiation. The resulting data are displayed as difference spectra with negative peaks corresponding to bands lost on irradiation and positive peaks to the photoproducts.

Ultra-fast photochemically initiated behaviour of [1]

Photolysis of [1] in heptane solution under an atmosphere of dinitrogen results in the formation of intense negative peaks corresponding to the ground state bleach of the complex. These were present at the shortest pump–probe delays employed. At very short pump–probe delays (<2 ps) the positive peaks were broad, but then sharpened with a lifetime of (7.8 ± 0.4) ps and moved to higher energy to give three new bands with approximately equal intensity at 1918, 1924 and 2024 cm^{-1} (Fig. 2). These data are consistent with the ultra-fast loss of a carbonyl ligand and the formation of a complex *fac*-$[Mn(C^N)(heptane)(CO)_3]$, [2]. Specifically, the band positions and intensity are typical of a species with three facially co-ordinated carbonyl ligands – a complex with a meridional arrangement would exhibit a different pattern of bands (both in terms of energy and intensities).[21,25]

The sharpening and shift in band position at short-pump probe delays is consistent with vibrational cooling.[26,27] As the pump laser energy is greater than that required to dissociate a CO ligand, the resulting photoproducts are formed in a vibrationally excited state which then relaxes to the v = 0 level. The anharmonic nature of the vibrational energy well results in the commensurate shift to higher energy on relaxtion. In the spectra recorded between 1 and 150 ps (Fig. 2b and c) a feature at lower energy than the bands for [2] was observed, which decays with a lifetime, τ, of (26.4 ± 0.8) ps. This was assigned to [2] in $v > 0$ vibrational energy levels. The observed shift of *ca.* 14 cm^{-1} from the longer-lived bands for [2] (assigned to the $v = 0 \rightarrow 1$ transition) support this hypothesis.[26] In addition,

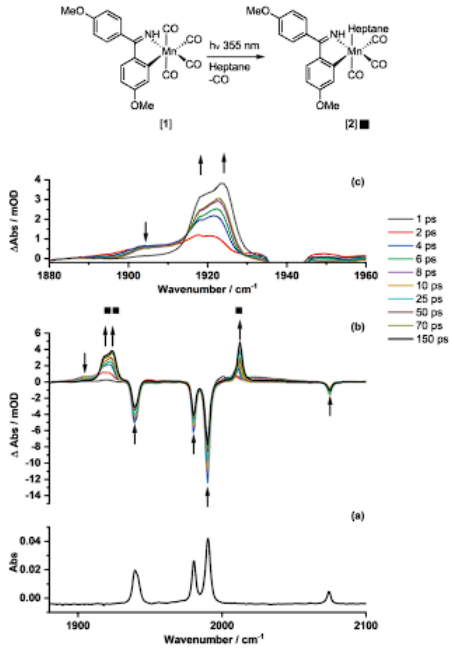

Fig. 2 (a) Ground state spectrum of [1] in heptane (b) TRIR spectra of [1] in heptane solution recorded with selected pump–probe delays between 1 and 150 ps. Black squares show the bands for [2] and arrows indicate the change in intensity of the peaks (c) Expansion of the region between 1880 and 1960 cm^{-1}, showing positive features only.

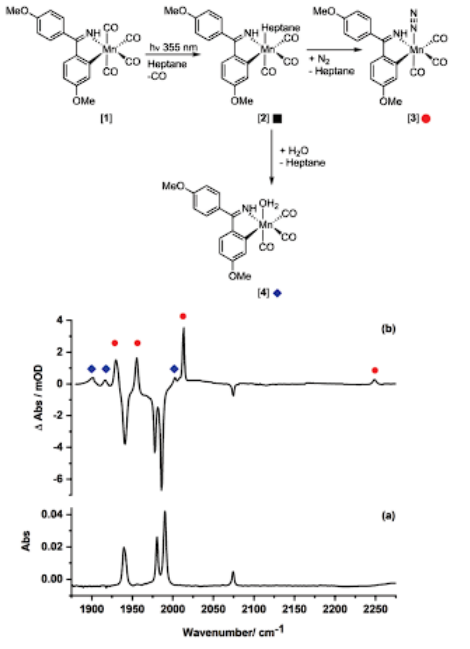

Fig. 3 (a) Ground state IR spectrum of [1] in heptane solution. (b) TRIR spectrum of [1] in heptane under N_2 with a pump–probe delay of 500 ns showing the formation of [3], red circles, and [4] blue diamonds. The bands between 1875 and 2100 cm^{-1} are assigned to CO stretching modes, whereas the peak at 2249 cm^{-1} is assigned to the N≡N vibration.

the ground state bleach bands for [1] became less negative at a similar rate, τ = (26.7 ± 2.6) ps, consistent with vibrational cooling of excited [1].[28]

At very short pump–probe delays (<10 ps) broad bands at *ca.* 1949 and 2027 cm^{-1} (Fig. S9†) provided evidence for a further short-lived species being generated on photolysis. On the basis of the related behaviour exhibited by $[Cr(bpy)(CO)_4]$[25] (bpy = 2,2′-bipyrdyl) and $[Mn(ppy)(CO)_4]$[21] this species was assigned to ^{3}[1] which decayed to ground state [1].

Identification of a Mn(I) dinitrogen complex

Over the course of *ca.* 20 ns, the bands for [2] decreased in intensity to be replaced by one major and one minor species, [3] and [4] respectively (Fig. 3). Complex [3] exhibited bands at 1929, 1955 and 2013 cm^{-1} notably blue-shifted from the heptane complex. The intensity of these features was again consistent with the formation of a facially coordinated tricarbonyl complex although the blue-shift in the band positions relative to [1] implied that that a π-acceptor ligand had coordinated to the metal, resulting in less π-backbonding to the three remaining carbonyl ligands.

It was suspected that the formation of [3] represented the displacement of the weakly coordinated heptane molecule in [2] by dinitrogen to give *fac*-$[Mn(C^N)(CO)_3(N_2)]$. This was supported by the observation of a band at 2249 cm^{-1}, which was assigned to the N≡N stretching mode of the complex (Fig. 3). This band is at higher energy than in the related mononuclear manganese N_2 complexes (Fig. 1) and is only shifted by 81 cm^{-1} from the Raman band in $^{14}N_2$ (2330 cm^{-1}).[29] This may represent the fact that the π-accepting dinitrogen and carbonyl ligands are mutually *trans* in [3].

In order to fully secure this assignment, two further experiments were undertaken. Firstly, the reaction was performed under an atmosphere of $^{15}N_2$ (Fig. 4c). In this case, the bands in the metal carbonyl region assigned to [3] were unchanged compared to the reaction performed at natural isotopic abundance, however the N≡N stretching mode shifted to 2174 cm^{-1}. This is consistent with the isotopic shift to 2173 cm^{-1} predicted for the $^{15}N{\equiv}^{15}N$ mode on the basis of a harmonic oscillator model. Secondly, when the experiment was performed under an atmosphere of argon, complex [3] was

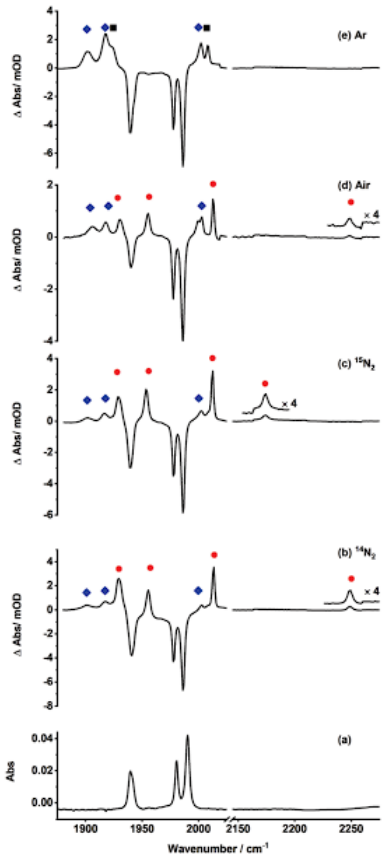

Fig. 4 (a) Ground state IR spectrum of [1] in heptane solution. (b) TRIR spectrum of [1] in heptane recorded under an atmosphere of N_2 (c) TRIR spectrum of [1] in heptane recorded under an atmosphere of $^{15}N_2$. (d) TRIR spectrum of [1] in heptane recorded under an atmosphere of air (b) TRIR spectrum of [1] in heptane recorded under an atmosphere of argon. All spectra were recorded with a pump–probe delay of 500 ns. Complex [2] is labelled with black squares, [3] red circles and [4] blue diamonds. The peak for the ground state bleach at 2074 cm^{-1} omitted for clarity.

not observed although [4] was present (Fig. 4e). Therefore, the experimental data support the assignment of [3] as *fac*-[Mn(C^N)(CO)$_3$(N$_2$)].

Insight into the nature of [4] came from a reaction in which a single drop of water was added to an experiment performed under a nitrogen atmosphere. In this case, the proportion of [4] formed relative to [3] increased significantly (see ESI†). It was therefore proposed that [4] is *fac*-[Mn(C^N)(CO)$_3$(OH$_2$)] in which trace amounts of water displace the heptane ligand. Similar observations have been made on photolysis of [W(CO)$_6$][30] and [Mn(ppy)(CO)$_4$][21] in hydrocarbon solution. In these experiments, [4] underwent further reactions to give a number of new carbonyl-containing products (see ESI†). We have tentatively assigned this process to the formation of hydroxy-bridged Mn carbonyl clusters, similar to those observed on catalysis deactivation during C–H functionalisation reactions.[18]

Nitrogen binding to the putative *fac*-[Mn(C^N)(CO)$_3$] fragment is highly selective. Photolysis of [1] under an atmosphere of air again led to the bands for the dinitrogen complex [3] dominating the difference spectrum, with [4] being observed as the only other significant product (Fig. 4d). No evidence of deleterious oxidation and/or the formation of a dioxygen or carbon dioxide adduct was obtained. Qualitatively, this may represent the fact that the formation of [3] from [1] corresponds to the substitution of isoelectronic CO and N_2 ligands.

DFT calculations

In order to obtain a quantitative view of this process, the energetics of a series of ligand substitutions reactions were calculated using density functional theory at the D3(BJ)-PBE0/def2-TZVPP//BP86/SV(P) level of theory with COSMO solvation in heptane. The isodesmic substitution of the heptane complex, [2] was taken as the reference state for the calculations and the resulting energies are shown in Table 1.

The calculations demonstrate that heptane is a far poorer ligand than water, dinitrogen and carbon monoxide. Water

Table 1 Calculated energy differences for the substitution of heptane by CO, N_2 and H_2O at the D3(BJ)-PBE0/def2-TZVPP//BP86/SV(P) level of theory with COSMO solvation in heptane. ΔE corresponds to the zero-point energy-corrected SCF energy change, ΔG_{298} includes corrections for the chemical potential (calculated at the BP86/SV(P) level)

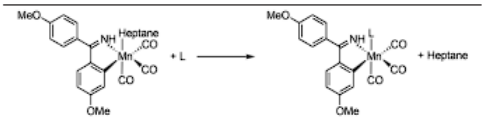

Entry	L	Product complex	Experimental ν(CO)[a]/cm^{-1}	ΔE/kJ mol^{-1}	ΔG_{298}/kJ mol^{-1}
1	CO	[1]	1940 (1934) 1980 (1967) 1990 (1969) 1974 (2066)	−113	−116
2	Heptane	[2]	1918 (1895) 1924 (1915) 2024 (1999)	0	0
3	N_2	[3]	1929 (1929) 1955 (1956) 2013 (2017)	−29	−33
4	H_2O	[4]	1900 (1902) 1913 (1911) 2012 (1998)	−23	−28

[a] Calculated values at the BP86/SV(P) level in brackets, these have been scaled using an empirical correction factor.[16]

View Article Online
Dalton Transactions Paper

and nitrogen have similar binding constants to the manganese and therefore the coordination of these two ligands should be competitive. The calculations indicated that the binding of nitrogen had a small thermodynamic preference when compared to water ($\Delta\Delta G_{298} = -5$ kJ mol^{-1}), although such a small difference must be treated with caution. Carbon monoxide is predicted to coordinate far more strongly to the manganese than either N_2 or H_2O.

Further insight into the influence of the different ligands coordinated to the *fac*-[Mn(C^N)(CO)$_3$] fragment was obtained by examining the bond metrics within the calculated structures (Table 2). Comparison of carbonyl, [1], and dinitrogen, [3], complexes confirms that the N_2 ligand is a poorer π-acceptor than CO as the M–C bond, *a*, (for the CO ligand *trans* to the CO and N_2 ligands) is shorter in the case of [3]. The calculated N–N bond length (1.125 Å) only shows a small elongation when compared to the dinitrogen (gas phase experimental value 1.0977 Å,[31] calculated at BP86/SV(P) 1.112 Å), but is consistent with the corresponding bond length in *trans*-[MnH(N_2)(dmpe)$_2$], 1.127(7) Å.[6] However, the Mn–N bond length in [3] is predicted to be longer (1.907 Å) than in the dmpe-containing complex (1.817(5) Å). This presumably reflects the fact that the N_2 is *trans* to an another π-accepting ligand despite in *trans*-[MnH(N_2)(dmpe)$_2$] the dinitrogen being opposite to a hydride ligand.

The calculated geometry of the heptane complex, [2], provides additional information about the binding of this ligand to the manganese. The DFT-predicted structure demonstrates that the hydrogen of the C–H bond is more closely coordinated to the metal than the carbon (Mn–H 1.997 Å, Mn–C 2.871 Å) and the Mn–H–C bond angle is 130.9°. This behaviour has been observed in the solid-state structure of alkane complexes and indicates that the heptane is best defined as η^1 σ-alkane using the nomenclature of Macgregor and Weller.[32] Structures were investigated in which the heptane was bound to the manganese through C–H interactions at each of the four unique carbon atoms. The predicted IR spectra for each complex were identical and, in line with our previous work on [Mn(ppy)(CO)$_3$(heptane)],[21] the energetics of binding to these different sites has a significant dependence on the DFT method employed (see ESI† for details). Consequently it was not possible to determine which site(s) of the heptane ligand bind to the metal. Examination of the Mn–C and C–O bond lengths within the carbonyl ligands of [2] (*a*–*f* Table 2) indicates that the carbonyl ligands are more tightly held in this complex than in any of the species investigated: the Mn–C bond *trans* to the heptane ligand, Mn–C_a, is the shortest of the all species investigated. In addition, the bond lengths between the two metal-atoms of the cyclometallated ligand in [2] are shorter than in the other complexes investigated (Mn–C_g 2.049 Å, Mn–N_h 2.015 Å). These latter structural effects may be viewed as the donor groups having a stronger interaction with the metal when a poor ligand (in this case heptane) is bound to the metal.

Kinetic profile of the formation of [3] and [4] from [2]

The kinetic profile for the conversion of [2] to [3] and [4] is shown in Fig. 5. Inspection of the data indicated that [2] appeared to convert into both [3] and [4] over the course of *ca.* 500 ns. Then, over approximately 1 μs, the amount of [3] increased further with commensurate loss of [4]. In order to

Table 2 Structures and calculated bond lengths in Å at the BP86/SV(P) level for complexes [1], [2], [3] and [4]

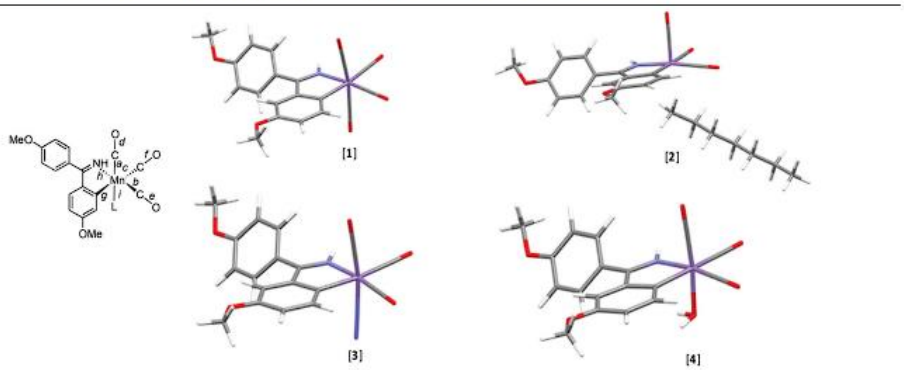

Complex	Mn–C_a	Mn–C_b	Mn–C_c	C–O_d	C–O_e	C–O_f	*Mn–C_g*	*Mn–N_h*	*Mn–L_i*
[1]	1.841	1.801	1.822	1.160	1.166	1.165	2.078	2.036	1.840
[2]	1.759	1.792	1.824	1.168	1.170	1.169	2.049	2.015	1.997
[3]	1.808	1.803	1.829	1.162	1.166	1.166	2.073	2.035	1.907[a]
[4]	1.772	1.794	1.824	1.169	1.169	1.169	2.058	2.021	2.173

[a] N–N bond length = 1.125 Å.

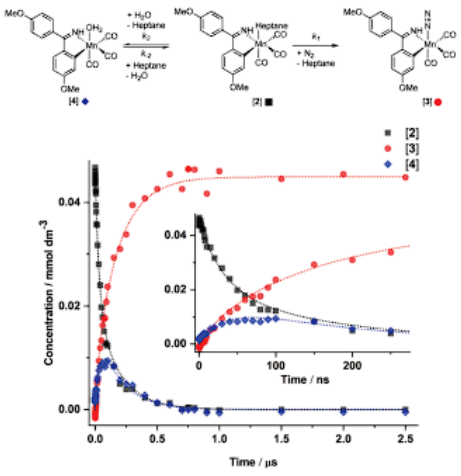

Fig. 5 Top kinetic model for the formation of [4] and subsequent reaction to form Mn clusters. Bottom kinetic profile for the loss of [2] and formation of [4]. The dotted lines show the fit to the kinetic model with parameters $[Mn]_0 = 4.49 \times 10^{-5}$ mol dm^{-3}, $[H_2O]_0 = (6.24 \pm 0.14)$ mmol dm^{-3}, $k_1 = (1.028 \pm 0.004) \times 10^9$ mol^{-1} dm^3 s^{-1}, $k_2 = (1.54 \pm 0.02) \times 10^9$ mol^{-1} dm^3 s^{-1}, $k_{-2} = (1.63 \pm 0.03) \times 10^7$ mol^{-1} dm^3 s^{-1}, $[N_2] = 9.54$ mmol dm^{-3}. Inset shows the behaviour and fit up to 270 ns.

quantify the processes which underpin this behaviour, the data were fitted to a series of kinetic models using the COPASI software.[33] Care must be taken in the construction of kinetic models based on TRIR data, especially when bimolecular pathways may be involved. Specifically, it is not possible to determine the absorption coefficients of the bands for short-lived intermediates and therefore the absorption values in the difference spectra cannot be converted to absolute concentration values. In order to address this, the absorption coefficients for the four vibrational modes of [1] were measured. The intensity of the bleach band at 1980 cm^{-1} in the difference spectrum (recorded with a pump–probe delay of 50 ps) was then used to determine the concentration of [1] lost on irradiation. This was defined as $[\mathbf{Mn}]_0$ as at this time point it was argued that all of the [1] which had been consumed on photolysis had been converted to [2], and that the concentration of the heptane complex at this point was also equivalent to $[\mathbf{Mn}]_0$. As the complexes [2], [3] and [4] are all based on the same *fac*-[Mn(C^N)(CO)$_3$(S)] framework, it was assumed that the absorption coefficients of the high-energy symmetric stretching modes would be similar, and that $[\mathbf{2}]_t + [\mathbf{3}]_t + [\mathbf{4}]_t = [\mathbf{Mn}]_0$, where $[\mathbf{X}]_t$ is the concentration of a given complex at time t. Therefore, the change in absorbance of each species with time could be converted into changes in concentration.

A number of models were simulated and the best fit to the experimental data is shown in Fig. 5. In this model, the substitution of heptane by nitrogen is irreversible with a second order rate constant, $k_1 = (1.028 \pm 0.004) \times 10^9$ mol^{-1} dm^3 s^{-1} (based on the concentration of N_2 in heptane at 1 atmosphere and 25 °C being 9.54 mmol dm^{-3}).[34] This is a very fast reaction, approaching the diffusion controlled rate limit in heptane solution calculated to be 2.35×10^{10} mol^{-1} dm^3 s^{-1} at 20 °C (ref. 35) and may simply represent how weakly the hydrocarbon is bound to the manganese. Extrapolation of the second order rate constant for the substitution of heptane by water is more problematic as the rate of this process will depend on the rate constant k_2 and the (unknown) concentration of water in the sample. However, it was assumed that value of k_2 would be similar to k_1. Both k_2 and [H_2O] were iterated in independent fits to the kinetic model which then converged on values of $k_2 = (1.54 \pm 0.02) \times 10^9$ mol^{-1} dm^3 s^{-1}, $k_{-2} = (1.63 \pm 0.03) \times 10^7$ mol^{-1} dm^3 s^{-1} and $[H_2O]_0 = (6.24 \pm 0.14)$ mmol dm^{-3}.[36]

These data represent a picture where the substitution of heptane by either water or nitrogen is extremely rapid and the subsequent establishment of an equilibrium position between [3] and [4] occurs on a longer timescale. There are two further mechanistic points to highlight. Firstly, no evidence for the existence for the formally 16-electron complexes *fac*-[Mn(C^N)(CO)$_3$] or *fac*-[Mn(ppy)(CO)$_3$] has been obtained in any TRIR experiments which implies they have a lifetime of less than 1 ps.[21] It is argued that such species would be highly Lewis acidic and in the condensed phase solvation is extremely rapid following photochemical CO-loss. It is therefore difficult to argue that the substitution of heptane is formally a dissociative pathway. Secondly, models in which [4] converted directly to [3] did not give satisfactory fits to the experimental data, ruling this out as a potential mechanistic pathway. In any event, the data illustrate that [3] is thermodynamically more stable than [4].

Conclusions

The selective formation of a rare manganese dinitrogen complex has been observed on photo-induced CO-dissociation from [Mn(C^N)(CO)$_4$] in heptane solution. The kinetic data present a mechanistic picture in which substitution at the initially formed heptane complex, *fac*-[Mn(C^N)(CO)$_3$(heptane)], occurs close to the diffusion controlled limit and therefore the proportion of dinitrogen and water complexes obtained is controlled by the relative concentration of the two substrates. An equilibrium position is obtained on a microsecond timescale and indicates that the dinitrogen complex is more stable than the aqua complex. This situation is also predicted by the DFT calculations, although the energetic difference is very small. These results demonstrate that it is possible to access dinitrogen complexes containing reactive cyclometallated ligands and may offer a new potential pathway for N_2 fixation.

Experimental

Complex [1] was prepared as described previously.[37] Heptane (anhydrous, stored and handled under N_2) and $^{15}N_2$ were sup-

plied by Sigma Aldrich. Time-resolved infra-red spectra were recorded on the LIFEtime instrument in the ULTRA facility at the Rutherford Appleton Laboratories.[38] The pump source was the output of a Yb:KGW amplifier providing 15 W, 260 fs pulses at 1030 nm with a 100 kHz repetition rate (Pharos). This was used to drive a BBO-based 515 nm pumped optical parametric amplifier (OPA) to deliver pulses at 355 nm. The pump beam was collimated, travelled over a computer programmable 0–16 ns optical delay (1200 mm long, double pass), and focused onto the sample. The pump energy at the sample was attenuated down to 500 nJ and focused down to a 120 × 120 μm^2 spot. The probe source was the output of a Yb:KGW amplifier providing 6 W, 180 fs pulses at 1030 nm with a 100 kHz repetition rate (Pharos). This drove two 3 W BBO/KTA based OPAs. The two Pharos sources share a common 80 MHz oscillator to allow for pump–probe delay steps of 12.5 ns. The probe beam was split to provide probe and reference pulses. To go beyond pump–probe delays of 12.5 ns, subsequent seed pulses were selected from the 80 MHz oscillator. Data were collected using pump–probe delays ranging from 1 ps to 988.5 μs. The probe beams were collimated, synchronised by a fixed optical delay, and focused by a gold parabolic mirror onto the sample. The three beams were overlapped on the sample using a 50 μm pinhole. The probe beams were measured by two separate 128-element detectors. To cover the full spectroscopic window required, data from different detector positions were combined to generate the required spectra.

Solutions of [**1**] were prepared in heptane (typically 16.5 mg of [**1**] in 20 ml heptane) in a thick-walled Duran flask. Samples under N_2, $^{15}N_2$ and Ar were prepared by sparging these solutions for *ca.* 20 min whilst flowing (peristaltic pump) through a Harrick cell fitted with a 100 μm Teflon spacer. The samples where then sealed, light excluded (either by covering in aluminium foil or employing an amberised flask) and transferred to the LIFEtime instrument. To ensure that the photoproducts were not themselves irradiated, data were acquired while continuously flowing and rastering the sample.

Data were initially visualised in the ULTRA View version 2 software,[39] where baseline-correction was undertaken. The resulting spectra were then exported as comma-separated variable files into Origin2019.[40] The spectra were calibrated against samples of polystyrene (200 μm thick) and 1,4-dioxane.

Kinetic analysis was performed in COPASI. Absorbance data were converted to concentration by using the bleach band at 1980 cm^{-1} to determine total concentration of manganese, $[\mathbf{Mn}]_0$, following photolysis at a pump–probe delay of 50 ps. Absorbance data were then scaled so that $[\mathbf{2}]_t + [\mathbf{3}]_t + [\mathbf{4}]_t = [\mathbf{Mn}]_0$. These data were then imported into COPASI and used to iterate against the parameters k_1, k_2, k_{-2} and, independently, against $[H_2O]_0$. The resulting data are quoted with 95% confidence limits.

DFT calculations were performed using the TURBOMOLE V6.4 package using the resolution of identity (RI) approximation.[41–47] Initial optimisations were performed at the (RI-)BP86/SV(P) level, followed by frequency calculations at the same level. All minima were confirmed as such by the absence of imaginary frequencies. Single-point calculations on the (RI-)BP86/SV(P) optimised geometries were performed using the hybrid PBE0 functional and the def2-TZVPP basis set. The (RI-)PBE0/def2-TZVPP SCF energies were corrected for their zero-point energies, thermal energies and entropies (obtained from the (RI-)BP86/SV(P)-level frequency calculations). No symmetry constraints were applied during optimisations. Solvent corrections were applied with the COSMO[48] dielectric continuum model and dispersion effects modelled with Grimme's D3 method.[49,50] Energies, *xyz* coordinates and the first 50 lines of the vibrational spectra are presented in the ESI.†

Conflicts of interest

There are no conflicts to declare.

Acknowledgements

We are grateful to the EPSRC (iCASE award with Syngenta, EP/N509413/1 studentship to L. A. H. and for the computational equipment used in this study, grants EP/H011455/1 and EP/K031589/1) the STFC (programme access to the ULTRA facility grant 1813) and the University of York (studentship to J. B. E.) for funding.

Notes and references

1 Y. Tanabe and Y. Nishibayashi, Overviews of the Preparation and Reactivity of Transition Metal–Dinitrogen Complexes, in *Transition Metal-Dinitrogen Complexes*, Wiley-VCH, Weinheim, 2019, ISBN: 978-3-527-34425-3.
2 K. Nakajima, H. Toda, K. Sakata and Y. Nishibayashi, *Nat. Chem.*, 2019, **11**, 702–709.
3 N. Khoenkhoen, B. de Bruin, J. N. H. Reek and W. I. Dzik, *Eur. J. Inorg. Chem.*, 2015, **2015**, 567–598.
4 E. A. Ison, Toward N-N Bond Cleavage: Synthesis and Reactivity of Group 7 Dinitrogen Complexes, in *Transition Metal-Dinitrogen Complexes*, Wiley-VCH, Weinheim, 2019, ISBN: 978-3-527-34425-3.
5 W. A. King, X.-L. Luo, B. L. Scott, G. J. Kubas and K. W. Zilm, *J. Am. Chem. Soc.*, 1996, **118**, 6782–6783.
6 C. Perthuisot, M. Fan and W. D. Jones, *Organometallics*, 1992, **11**, 3622–3629.
7 D. Sellmann, *Angew. Chem., Int. Ed. Engl.*, 1971, **10**, 919–919.
8 D. Sellmann, *Angew. Chem., Int. Ed. Engl.*, 1972, **11**, 534–534.
9 S. M. Howdle and M. Poliakoff, *J. Chem. Soc., Chem. Commun.*, 1989, 1099–1101.
10 Y. Zheng, W. Wang, J. Lin, Y. She and K. Fu, *J. Phys. Chem.*, 1992, **96**, 9821–9827.
11 J. A. Banister, M. W. George, S. Grubert, S. M. Howdle, M. Jobling, F. P. A. Johnson, S. L. Morrison, M. Poliakoff,

U. Schubert and J. R. Westwell, *J. Organomet. Chem.*, 1994, **484**, 129–135.
12 B. H. G. Swennenhuis, R. Poland, N. J. DeYonker, C. E. Webster, D. J. Darensbourg and A. A. Bengali, *Organometallics*, 2011, **30**, 3054–3063.
13 M. L. Ziegler, K. Weidenhammer, H. Zeiner, P. S. Skell and W. A. Herrmann, *Angew. Chem., Int. Ed. Engl.*, 1976, **15**, 695–696.
14 W. A. Chomitz and J. Arnold, *Chem. Commun.*, 2007, 4797–4799.
15 Y. Hu, B. Zhou and C. Wang, *Acc. Chem. Res.*, 2018, **51**, 816–827.
16 L. A. Hammarback, I. P. Clark, I. V. Sazanovich, M. Towrie, A. Robinson, F. Clarke, S. Meyer, I. J. S. Fairlamb and J. M. Lynam, *Nat. Catal.*, 2018, **1**, 830–840.
17 L. A. Hammarback, A. Robinson, J. M. Lynam and I. J. S. Fairlamb, *Chem. Commun.*, 2019, **55**, 3211–3214.
18 L. A. Hammarback, A. Robinson, J. M. Lynam and I. J. S. Fairlamb, *J. Am. Chem. Soc.*, 2019, **141**, 2316–2328.
19 N. P. Yahaya, K. M. Appleby, M. Teh, C. Wagner, E. Troschke, J. T. W. Bray, S. B. Duckett, L. A. Hammarback, J. S. Ward, J. Milani, N. E. Pridmore, A. C. Whitwood, J. M. Lynam and I. J. S. Fairlamb, *Angew. Chem., Int. Ed.*, 2016, **55**, 12455–12459.
20 W. Liu and L. Ackermann, *ACS Catal.*, 2016, **6**, 3743–3752.
21 B. J. Aucott, A.-K. Duhme-Klair, B. E. Moulton, I. P. Clark, I. V. Sazanovich, M. Towrie, L. A. Hammarback, I. J. S. Fairlamb and J. M. Lynam, *Organometallics*, 2019, **38**, 2391–2401.
22 D. C. Grills, K.-W. Huang, J. T. Muckerman and E. Fujita, *Coord. Chem. Rev.*, 2006, **250**, 1681–1695.
23 S. A. Bartlett, N. A. Besley, A. J. Dent, S. Diaz-Moreno, J. Evans, M. L. Hamilton, M. W. D. Hanson-Heine, R. Horvath, V. Manici, X.-Z. Sun, M. Towrie, L. Wu, X. Zhang and M. W. George, *J. Am. Chem. Soc.*, 2019, **141**, 11471–11480.
24 X. Wu, Z. Liu, T. S. Murphey, X. Z. Sun, M. W. D. Hanson-Heine, M. Towrie, J. N. Harvey and M. W. George, *Faraday Discuss.*, 2019, **220**, 86–104.
25 I. R. Farrell, P. Matousek, M. Towrie, A. W. Parker, D. C. Grills, M. W. George and A. Vlček, *Inorg. Chem.*, 2002, **41**, 4318–4323.
26 B. J. Aucott, J. B. Eastwood, L. A. Hammarback, I. P. Clark, I. V. Sazanovich, M. Towrie, I. J. S. Fairlamb and J. M. Lynam, *Dalton Trans.*, 2019, **48**, 16426–16436.
27 T. P. Dougherty and E. J. Heilweil, *J. Chem. Phys.*, 1994, **100**, 4006–4009.
28 T. Lian, S. E. Bromberg, M. C. Asplund, H. Yang and C. B. Harris, *J. Phys. Chem.*, 1996, **100**, 11994–12001.
29 J. Bendtsen and F. Rasmussen, *J. Raman Spectrosc.*, 2000, **31**, 433–438.
30 G. M. Greetham, D. Sole, I. P. Clark, A. W. Parker, M. R. Pollard and M. Towrie, *Rev. Sci. Instrum.*, 2012, **83**, 103107.
31 R. J. L. Roy, Y. Huang and C. Jary, *J. Chem. Phys.*, 2006, **125**, 164310.
32 A. J. Martínez-Martínez, B. E. Tegner, A. I. McKay, A. J. Bukvic, N. H. Rees, G. J. Tizzard, S. J. Coles, M. R. Warren, S. A. Macgregor and A. S. Weller, *J. Am. Chem. Soc.*, 2018, **140**, 14958–14970.
33 S. Hoops, S. Sahle, R. Gauges, C. Lee, J. Pahle, N. Simus, M. Singhal, L. Xu, P. Mendes and U. Kummer, *Bioinformatics*, 2006, **22**, 3067–3074.
34 F. P. A. Johnson, M. W. George, V. N. Bagratashvili, L. N. Vereshchagina and M. Poliakoff, *Mendeleev Commun.*, 1991, **1**, 26–28.
35 Calculated with a value for the diffusion constant, D_0, of 3.10×10^{-5} cm^2 s^{-1}. See: J. W. Moore and R. M. Wellek, *J. Chem. Eng. Data*, 1974, **19**, 136.
36 The heptane used was anhydrous grade with ≤0.001% water.
37 R. He, Z.-T. Huang, Q.-Y. Zheng and C. Wang, *Angew. Chem., Int. Ed.*, 2014, **53**, 4950–4953.
38 G. M. Greetham, P. M. Donaldson, C. Nation, I. V. Sazanovich, I. P. Clark, D. J. Shaw, A. W. Parker and M. Towrie, *Appl. Spectrosc.*, 2016, **70**, 645–653.
39 M. R. Pollard and G. M. Greetham, *ULTRA View Data Analysis*, STFC.
40 *OriginPro*, OriginLab Corporation, Northampton, MA, USA, 2019.
41 R. Ahlrichs, M. Bär, M. Häser, H. Horn and C. Kölmel, *Chem. Phys. Lett.*, 1989, **162**, 165–169.
42 K. Eichkorn, O. Treutler, H. Öhm, M. Häser and R. Ahlrichs, *Chem. Phys. Lett.*, 1995, **240**, 283–290.
43 O. Treutler and R. Ahlrichs, *J. Chem. Phys.*, 1995, **102**, 346–354.
44 K. Eichkorn, F. Weigend, O. Treutler and R. Ahlrichs, *Theor. Chem. Acc.*, 1997, **97**, 119–124.
45 M. von Arnim and R. Ahlrichs, *J. Chem. Phys.*, 1999, **111**, 9183–9190.
46 P. Deglmann, F. Furche and R. Ahlrichs, *Chem. Phys. Lett.*, 2002, **362**, 511–518.
47 P. Deglmann, K. May, F. Furche and R. Ahlrichs, *Chem. Phys. Lett.*, 2004, **384**, 103–107.
48 A. Klamt and G. Schuurmann, *J. Chem. Soc., Perkin Trans. 2*, 1993, 799–805.
49 S. Grimme, J. Antony, S. Ehrlich and H. Krieg, *J. Chem. Phys.*, 2010, **132**, 154104.
50 S. Grimme, S. Ehrlich and L. Goerigk, *J. Comput. Chem.*, 2011, **32**, 1456–1465.

ACS Catalysis

pubs.acs.org/acscatalysis Research Article

Manganese-Mediated C−H Bond Activation of Fluorinated Aromatics and the *ortho*-Fluorine Effect: Kinetic Analysis by *In Situ* Infrared Spectroscopic Analysis and Time-Resolved Methods

L. Anders Hammarback, Amy L. Bishop, Christina Jordan, Gayathri Athavan, Jonathan B. Eastwood, Thomas J. Burden, Joshua T. W. Bray, Francis Clarke, Alan Robinson, Jean-Philippe Krieger, Adrian Whitwood, Ian P. Clark, Michael Towrie, Jason M. Lynam,* and Ian J. S. Fairlamb*

Cite This: ACS Catal. 2022, 12, 1532−1544 Read Online

ACCESS | Metrics & More | Article Recommendations | Supporting Information

ABSTRACT: Insights into the factors controlling the site selectivity of transition metal-catalyzed C−H bond functionalization reactions are vital to their successful implementation in the synthesis of complex target molecules. The introduction of fluorine atoms into substrates has the potential to deliver this selectivity. In this study, we employ spectroscopic and computational methods to demonstrate how the "*ortho*-fluorine effect" influences the kinetic and thermodynamic control of C−H bond activation in manganese(I)-mediated reactions. The C−H bond activation of fluorinated *N*,*N*-dimethylbenzylamines and fluorinated 2-phenylpyridines by benzyl manganese(I) pentacarbonyl $BnMn(CO)_5$ leads to the formation of cyclomanganated tetracarbonyl complexes (**2a−b** and **4a−e**), which all exhibit C−H bond activation *ortho*-to-fluorine. Corroboration of the experimental findings with density functional theory methods confirms that a kinetically controlled irreversible σ-complex-assisted metathesis mechanism is operative in these reactions. The addition of benzoic acid results in a mechanistic switch, so that cyclomanganation proceeds through a reversible AMLA-6 mechanism (kinetically and thermodynamically controlled). These stoichiometric findings are critical to catalysis, particularly subsequent insertion of a suitable acceptor substrate into the C−Mn bond of the regioisomeric cyclomanganated tetracarbonyl complex intermediates. The employment of time-resolved infrared spectroscopic analysis allowed for correlation of the rates of terminal acetylene insertion into the C−Mn bond with the relative thermodynamic stability of the regioisomeric complexes. Thus, more stable manganacycles, imparted by an *ortho*-fluorine substituent, exhibit a slower rate of terminal acetylene insertion, whereas a *para*-fluorine atom accelerates this step. A critical factor in governing C−H bond site selectivity under catalytic conditions is the generation of the regioisomeric cyclomanganated intermediates, rather than their subsequent reactivity toward alkyne insertion.

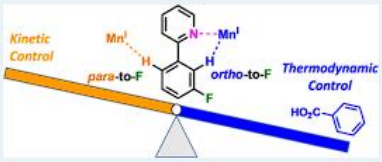

KEYWORDS: *C−H bond activation, catalysis, manganese, site selectivity, alkynes, pyridines*

INTRODUCTION

The transition metal-mediated functionalization of carbon−hydrogen (C−H) bonds is an important method for structural elaboration. Controlling the regioselectivity of such processes ensures that a specific C−H bond within a substrate of interest is activated, especially when the reactions are applied to the synthesis of complex target molecules.[1] A common solution to controlling the regiochemical outcome of the reaction is to employ Lewis basic-directing groups, which control the coordination of the substrate to a transition metal, ensuring site-specific C−H bond activation.[2] Alternative strategies, without the use of metal-directing groups, can influence regioselectivity and provide an alternative route to control chemical synthesis.[3]

The unique properties of the fluorine atom offer interesting opportunities to alter the inherent regioselectivity in C−H bond activation. Fluorinated aromatic (organic) systems often show an increased preference for metal-mediated activation of aromatic C−H bonds *ortho* with respect to fluorine substituents, and this effect is commonly referred to as the "*ortho*-fluorine effect".[4] The *ortho*-fluorine effect has been observed for many transition metal-mediated transformations, both with[5] and without[6] supplementary directing groups.

There is currently no clear mechanistic consensus on the origin of the *ortho*-fluorine effect, and the proposals often change with the reaction system. Studies by Eisenstein, Clot, and Perutz have shown that the C−M bond strength was

Received: November 29, 2021
Revised: December 28, 2021
Published: January 11, 2022

https://doi.org/10.1021/acscatal.1c05477
ACS Catal. 2022, 12, 1532−1544

Scheme 1. Cyclometallation Examples where there is a Regiochemical Choice Impacted by Fluorine Substituents in C−H Bond Activation and Functionalization Processes

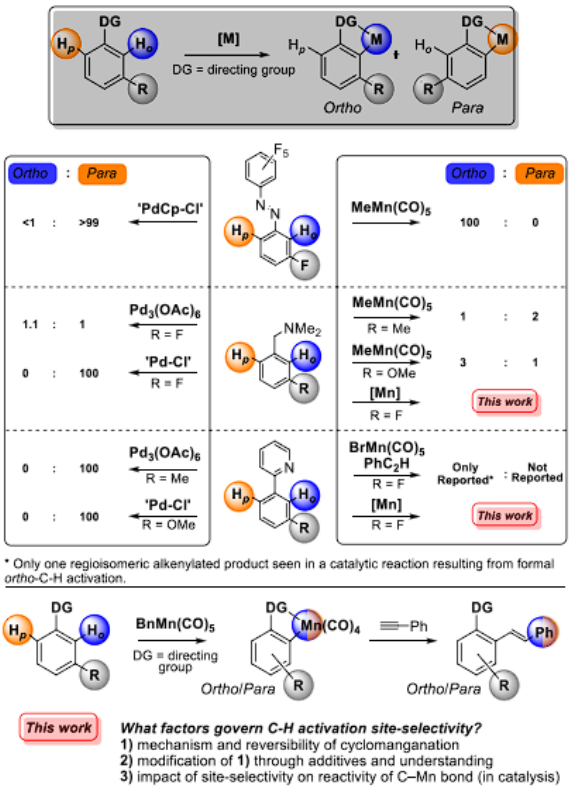

stronger *ortho* to the fluorine substituent in a series of *ortho*-selective transition metal-mediated (M = Re, Rh, Ir, Ni, Pt, Ta, and W) C−H bond activation of fluorobenzenes.[6a−c] In the C−H bond cyclometallation (M = Rh and Ir) of *meta*-substituted 1-phenylpyrazoles, Davies and Macgregor found no correlation between the observed *ortho*/*para*-selectivity and the C−M bond lengths of the resulting metallacycles.[5a] Eisenstein and Perutz have also reported, for Pd-mediated C−H bond arylation of fluorobenzenes, that the observed *ortho*-preference arises from a lower activation barrier for C−H bond activation.[6d]

In our previous study with Perutz on Pd-mediated C−H bond activation of fluorinated benzylamines (Scheme 1), we showed that the starting Pd complex, and thus the mechanism of C−H activation, had a major impact on the resulting regioselectivity.[5d] Li_2PdCl_4 (S_EAr) exhibited complete *para*-selectivity, while $Pd_3(OAc)_6$ (CMD/AMLA-6) yielded close to the same amount of both regioisomers. Davies and Macgregor additionally revealed that the extent of an inherent *ortho*-preference in the direct C−H bond cyclometallation (M = Rh and Ir) of *meta*-fluorinated 1-phenylpyrazoles depended on whether the reaction was under kinetic or thermodynamic control.[5a] The same effect has also been reported by Jones and Perutz in the Rh-mediated C−H bond activation of fluorobenzenes, where the kinetic and thermodynamic products could be generated depending on reaction temperature.[6e]

There are few studies probing the nature of fluorine-induced regioselectivity in 3d-metal-catalyzed C−H bond functionalization reactions. One notable exception is the report by Chirik and co-workers on the borylation of fluorinated arenes by a cobalt pincer complex, which demonstrated that the Co−C bond was exceptionally sensitive to *ortho*-fluorine incorporation and provided a thermodynamic driving force for the observed catalytic selectivity.[7] This increased sensitivity offers the potential for 3d-metals to have a greater intrinsic selectivity for C−H bond activation on the introduction of fluorine into a given substrate.

Manganese carbonyl complexes are of considerable current interest due to their applications in redox-neutral catalytic processes for C−H bond functionalization.[8] Following Chen and Wang's "breakthrough" study in 2013 on Mn(I)-mediated

https://doi.org/10.1021/acscatal.1c05477
ACS Catal. 2022, 12, 1532−1544

Scheme 2. Cyclomanganation of Fluorinated Benzylamines and 2-Phenylpyridines

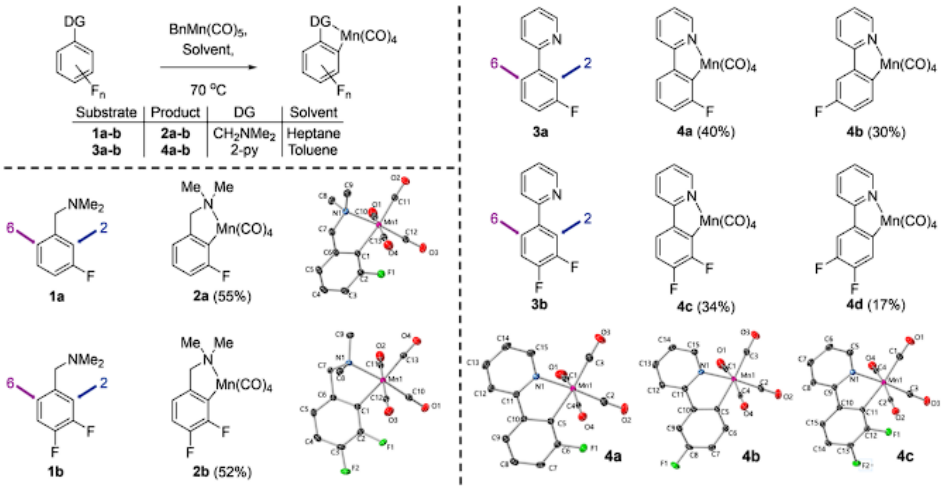

C−H bond alkenylation of 2-phenylpyridines,[9] these species have demonstrated a significant potential and versatility as Earth-abundant metal catalysts for applied chemical synthesis.[10] The catalytic chemistry is founded in the stoichiometric organometallic chemistry of manganese, which has been studied for >40 years and has included extensive work on directed cyclomanganation of aromatic C−H bonds[11,12] and subsequent reactivity of the resulting manganacycles.[12,13]

Manganese carbonyl complexes have been utilized in the study of fluorine-induced regioselectivity. For example, in 1978, Bruce reported an apparent *ortho*-fluorine effect in the Mn-mediated C−H bond activation of fluorinated azobenzene derivatives, generating exclusively the *ortho*-complex.[5b] Liebeskind found a relatively strong *ortho*-preference in the C−H bond cyclomanganation of *meta*-fluorinated acetophenones (4.5:1, *ortho*/*para*), where other substituents exhibited weaker *ortho*-selectivity (OMe, 2.1:1, *ortho*/*para*) to selective formation of the *para*-complex (Me, CF_3, and CN).[13a] An *ortho*-fluorine effect has also been reported in Mn(I)-mediated alkenylation of 2-phenylpyridines, where only the C−H bond functionalization *ortho* to fluorine was seen for *meta*-fluorinated 2-phenylpyridine.[9]

In a recent series of studies, we have described how mechanistic studies on reactions catalyzed by Mn(I) carbonyl complexes can provide unique insights into transition metal-mediated bond activation and formation pathways.[14] Combining complementary information from time-resolved infrared spectroscopy on a picosecond to microsecond (ps to μs) timescale, with measurements by NMR and *in situ* IR analysis on *in operando* reactions and calculations using density functional theory (DFT), has enabled obtaining a comprehensive picture of the steps, underpinning C−C bond formation, catalyst activation, and deactivation pathways. This approach also allowed for the first experimental observation of the steps, underpinning the concerted metalation deprotonation (CMD) reaction to be directly observed.[15]

These methods offer an opportunity to rationalize the kinetic and thermodynamic control exerted by the incorporation of fluorine into substrates for Mn-catalyzed C−H bond functionalization.

Herein, we describe the *ortho*-selective C−H bond metalation of *meta*-fluorinated benzylamine and 2-phenylpyridine derivatives, where we aim to

- Measure the extent of the fluorine-induced regioselectivity in relevant aromatic systems.
- Assess the origin of the *ortho*-fluorine effect in a 3d-metal system through understanding of the reaction mechanism and the properties affecting activation of C−H bonds, including the role of additives.

RESULTS AND DISCUSSION

Two sets of substrates were selected to investigate the nature of the *ortho*-fluorine effect in cyclomanganation reactions. *Meta*-fluorinated benzylamines were chosen, as they enable comparison with other Mn(I)-mediated reaction systems using different substituents (Me and OMe),[5c] as well as our previously reported results on the corresponding cyclopalladation processes.[5d] The reaction can react to form the C−Mn bond at either the 2 or 6 position of the arene (Scheme 2), which will be referred to as *ortho* and *para*, respectively, that is, *ortho* or *para* to the substituent (i.e., the directing group). Due to the extensive use of 2-phenylpyridines in Mn(I)-catalyzed C−H bond functionalization[8,9,12,16] and our previous mechanistic studies into these reaction systems,[14,15,17] the cyclomanganation of fluorinated 2-phenylpyridines **3a** and **3b** was investigated (Scheme 2). Related studies on ligands with a pyrrolidine directing group are reported in the Supporting Information.

The cyclomanganation of monofluorinated benzylamine derivative **1a** was performed using $BnMn(CO)_5$ as the manganese precursor in hexane at reflux for 16 h (Scheme 2). The ^{19}F NMR spectrum of the crude reaction mixture

https://doi.org/10.1021/acscatal.1c05477
ACS Catal. 2022, 12, 1532−1544

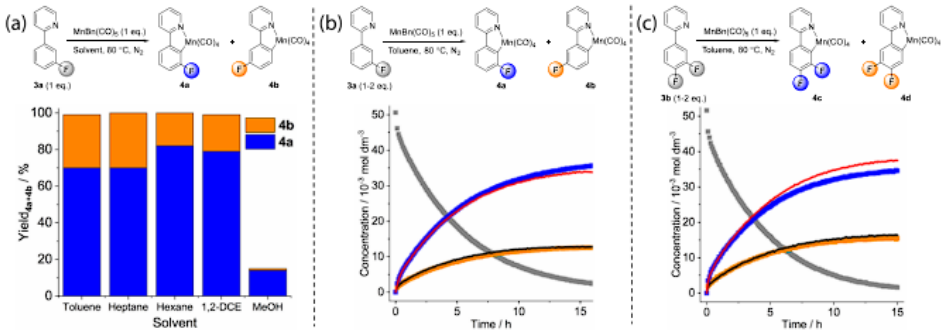

Figure 1. (a) Solvent screen for the cyclomanganation of **3a**. (b) *In situ* ^{19}F NMR study of the cyclomanganation of **3a** using $C_6H_5CF_3$ as an internal standard. Key: blue/red lines = **4a** using 1.0 (blue) and 1.5 equiv (red) **3a** and orange/black lines = **4b** using 1.0 (orange) and 1.5 eq. (black) **3a**. (c) *In situ* ^{19}F NMR study of the cyclomanganation of **3b**. Key: blue/red lines = **4c** using 1.0 (blue) and 1.5 equiv (red) **3b** and orange/black lines = **4d** using 1.0 (orange) and 2.0 equiv (black) **3b**.

revealed that only one regioisomer of the manganacycles was generated in substantial quantities, with the minor regioisomer only being present in trace amounts (<1%). Following purification (55% yield of isolated material) and subsequent characterization, it was determined that the major regioisomer in the reaction was *ortho*-complex **2a**. Single-crystal X-ray diffraction (XRD) analysis was utilized to provide further support for the structural assignment. Thus, the reaction exhibited similar *ortho*-preference as reported for the cyclomanganation of fluorinated azobenzenes.[5b] Repeating the cyclomanganation on difluorinated derivative **1b** yielded *ortho*-complex **2b** as the major product (99:1, *ortho*/*para*). The yield of the reaction (52%) was also comparable to **1a**, showing that the additional fluorine substituent had a limited effect on both the selectivity and efficiency of the reaction.

The alkyl substituents on the amine proved to have a limited impact on the reaction, as when the dimethylamino group was altered to a pyrrolidine ring, the reaction again generated the *ortho*-complexes as the major product in comparable yields (see Supporting Information). However, the extent of the *ortho*-preference was reduced marginally to 93:7, *ortho*/*para*, for the monofluorinated derivative. The cyclomanganation of *meta*-fluorinated 2-phenylpyridine **3a** was performed using the same manganese precursor, $BnMn(CO)_5$, in toluene at 80 °C for 16 h. The crude ^{19}F NMR spectrum revealed complete consumption of **3a** and the presence of two new fluorine-containing species. Following purification, both the *ortho*- (**4a**, 40%) and *para*-isomers (**4b**, 30%) of the manganacycle were characterized. Due to difficulties in the separation of the regioisomeric complexes, the ratio of the isolated material does not reflect the true ratio of the reaction (see further details below). Nevertheless, the relatively large quantities of *para*-complex **4b** presented a marked difference in reactivity and selectivity as compared to the benzylamines and other *ortho*-selective directing groups. The extensive formation of the *para*-complex was mirrored in the cyclomanganation of difluorinated 2-phenylpyridine **3b**, yielding both the *ortho*- (**4c**, 34%) and *para*-complexes (**4d**, 17%).

Single-crystal XRD analysis for manganese(I) complexes **4a**−**c** (see Supporting Information) showed no significant difference in the C_{Ar}−Mn bond lengths between the two regioisomers [**4a** = 2.0557(18) Å and **4b** = 2.0510(17) Å], consistent with Davies and Macgregor's study on *ortho*/*para*-cyclometallated (M = Rh and Ir) 1-phenylpyrazoles.[5a] This finding suggested that the relative strength of the C−Mn bond was not responsible for the observed regioselectivity. In addition, the Mn−CO bond lengths and relative bond angles were also similar between the two regioisomers. The two species additionally exhibited similar IR spectra, with only minor shifts in the metal carbonyl bands [**4a** = 2077, 1992 (br), and 1934 cm^{-1} and **4b** = 2081, 1995 (br), and 1942 cm^{-1} in CH_2Cl_2 at room temperature]. The C_{Ar}−Mn bond length was not altered when adding another fluorine substituent (**4c** = 2.0501(12) Å) and no significant change could be found in the other relevant bond lengths and bond angles.

***In Situ* ^{19}F NMR Reaction Monitoring.** The unusually small *ortho*-selectivity for the 2-phenylpyridine derivatives **3a** and **3b** warranted further investigation to determine the rationale behind the lower selectivity and to understand the difference in reactivity when other directing groups, such as the benzylamines, were employed.

Initially, to determine if any effects had arisen from the reaction solvent, a solvent screen was completed for the cyclomanganation of **3a** (Figure 1a). The reactions were performed at 80 °C for 16 h, after which the crude material was analyzed by ^{19}F NMR spectroscopic analysis. Both high boiling point hydrocarbon solvents, toluene and heptane, exhibited complete consumption of **3a** and a similar *ortho*/*para* ratio of 7:3 (**4a**/**4b**). Changing to a lower boiling point solvent in hexane led to reduced formation of *para*-complex **4b** (4.6:1, **4a**/**4b**), though still affording complete consumption of **3a**. A similar reactivity and *ortho*/*para* ratio (4:1) was obtained when the cyclomanganation was performed in 1,2-dichloroethane (1,2-DCE).

A major change in reactivity was observed with MeOH and extensive manganese degradation was noted, with only minor quantities of the manganacycles generated with a strong preference for *ortho*-complex **4a** (14:1, **4a**/**4b**). Toluene was selected as the reaction solvent for the subsequent studies due to the high efficiency of the reaction and relatively large amount of *para*-complex **4b** that was formed. The reaction kinetics of the cyclomanganation reaction in toluene at 80 °C using monofluorinated substrate **3a** were monitored using *in situ* ^{19}F NMR spectroscopic analysis (Figure 1b). The clear

https://doi.org/10.1021/acscatal.1c05477
ACS Catal. 2022, 12, 1532−1544

difference in the chemical shift between the regioisomers (**4a** = −86.3 ppm and **4b** = −121.4 ppm) allowed for the reaction profile for each product to be obtained. The *ortho*/*para* ratio of 2.9:1 remained constant throughout the reaction, and no significant degradation or interconversion between the species could be observed following the completion of the reaction. The observed rate of formation of both products (k_{4a} = 5.1 ± 0.6 10^{-5} s^{-1} and k_{4b} = 5.6 ± 0.1 10^{-5} s^{-1}, Table 1) was near identical to the loss of the starting material (k_{3a} = 5.20 ± 0.07 10^{-5} s^{-1}), which is expected for parallel reaction pathways in such systems.[18]

Table 1. Observed Rate Constants for the Formation of *ortho*-Complexes 4a and 4c

entry	substrate (equiv)	$k_{ortho}/10^{-5}$ s^{-1}	o/p selectivity
1	**3a** (1)	5.1 ± 0.6	2.9
2	**3a** (1.5)	5.2 ± 0.1	2.6
3	**3a** (1)[a]	9.3 ± 0.5	2.2
4	**3b** (1)	5.9 ± 0.1	2.3
5	**3b** (2)	5.9 ± 0.1	2.5
6	**3a** (1)[b]	10.1 ± 0.1	17

[a]2 equiv of $BnMn(CO)_5$. [b]0.1 equiv $PhCO_2H$ added (entry 6, highlighted to show the acid effect).

The lack of interconversion between **4a** and **4b** indicated an irreversible reaction mechanism, which could be affected by the addition of excess **3a**. Thus, the reaction was repeated using 1.5 equiv of **3a** relative to $MnBn(CO)_5$ (Figure 1b). The reaction profile and regioselectivity (2.6:1, **4a**/**4b**) were near identical to the reaction with 1 equiv (2.9:1, **4a**/**4b**), suggesting a zero-order dependence in **3a** on the reaction and that **3a** did not impact the reversibility of the reaction. Consequently, the apparent irreversibility of the reaction inferred that the regioselectivity was kinetically determined and provided an explanation for the observed selectivity between the two regioisomeric complexes even with near identical C−Mn bond lengths.

When the reaction was repeated using two equivalents of $BnMn(CO)_5$ (see Supporting Information), the observed rate constant almost doubled (k_{4a} = 9.3 ± 0.5 × 10^{-5} s^{-1}), while the *ortho*/*para* ratio remained similar (2.2:1, **4a**/**4b**). This increase in the rate of reaction suggested a first-order dependence of manganese in the reaction, likely derived from the initial loss of a CO ligand as being rate-limiting.

The cyclomanganation of **3b** (Figure 1c) exhibited a similar kinetic trace to **3a**, with a minor shift in the *ortho*/*para* ratio (2.3:1). Again, no significant interconversion could be observed at longer times following the completion of the reaction, even after 40 h (see Supporting Information). Repeating the reaction with excess **3b** (2 equiv) again yielded a similar reaction profile.

Effect of Acid Additives. We have previously shown that carboxylic acid additives have a marked effect on the efficacy of Mn(I)-catalyzed C−H bond functionalization reactions,[17c] enabling ligand liberation from cyclomanganated 2-phenylpyridines.[15] Hence, it was hypothesized that the addition of an acid would enable a reversible reaction mechanism for C−H bond activation through a protodemetallation pathway, in a similar vein to that observed for a half-sandwich Rh complex reported by Jones and co-workers.[19] The addition of a carboxylic acid additive could potentially result in a mechanistic shift for cyclomanganation from σ-complex-assisted metathesis (σ-CAM) to a CMD/AMLA-6 mechanism.[17]

The cyclomanganation of **3a** with added benzoic acid (0.1 equiv) resulted in a substantially different reaction profile (Figure 2a), with *ortho*-complex **4a** formed in a large excess

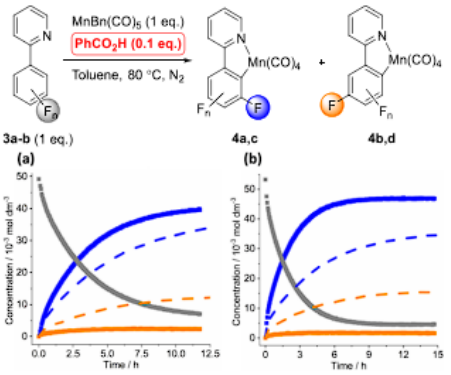

Figure 2. Cyclomanganation of fluorinated 2-phenylpyridine derivatives **3a**−**b** with the addition of $PhCO_2H$ (0.1 equiv) and the kinetic trace obtained by *in situ* ^{19}F NMR spectroscopy using $C_6H_5CF_3$ as an internal standard. Key: dotted line = without additive and squares = with $PhCO_2H$ added. (a) Kinetic trace for the reaction using **3a**. (b) Kinetic trace for the reaction using **3b**.

over **4b** (17:1). At no point during the reaction did the concentration of **4b** reach a significant level in comparison to **4a**. Unreacted **3a** (14%) was observed in the solution at the end of the reaction, yielding a final **3a**/**4a**/**4b** ratio of 3:17:1. The addition of benzoic acid (0.1 equiv) to the cyclomanganation of **3b** (Figure 2b) resulted in an increased selective reaction to afford the *ortho*-complex **4c** preferentially over **4d** (29:1 ratio). A small amount of **3b** remained in solution (3%), following the completion of the reaction, but in lower quantities than for the monofluorinated derivative.

The addition of benzoic acid to the cyclomanganation reactions increased the rate of the reaction [k_{4a} = 5.20 ± 0.07 × 10^{-5} s^{-1} without additives and k_{4a} = 1.01 ± 0.01 × 10^{-4} s^{-1} with 0.1 equiv (Table 1). Benzoic acid added], consistent with a shift to a CMD/AMLA-6 mechanism. Performing the experiments at a range of acid concentrations (0.05−0.20 equiv) led to a linear increase in the observed rate of C−Mn bond formation (see Supporting Information). The plot of $\ln(k_{4a})$ versus time yielded a surprising reaction order in acid of 0.44 ± 0.02, which likely stems from the operation of both σ-CAM and CMD/AMLA-6 mechanisms under the reaction conditions.

To further probe the effect of the acid additive, *para*-complex **4b** was heated in toluene and monitored by *in situ* ^{19}F NMR spectroscopic analysis (Figure 3). The reaction showed no conversion to either **3a** or **4a** within the first 4.25 h, which is consistent with an irreversible reaction mechanism and reveals the high thermal stability associated with these manganacycles. The addition of benzoic acid (0.5 equiv) was followed by the rapid depletion of the resonance for **4b** and liberation of **3a** (67%) by protonation of the Mn−C bond and formation of **4a** (31%). Interestingly, **3a** was observed to form,

https://doi.org/10.1021/acscatal.1c05477
ACS Catal. 2022, 12, 1532−1544

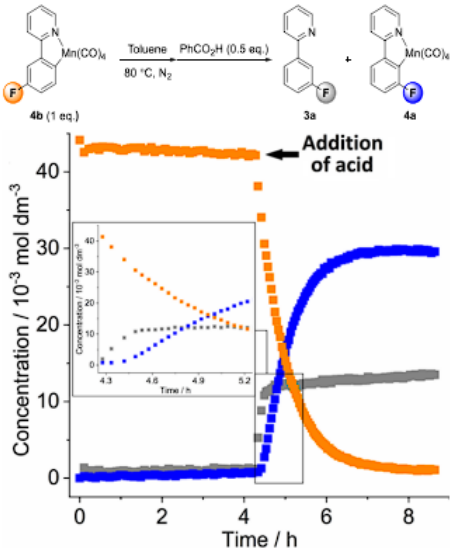

Figure 3. *In situ* ^{19}F NMR spectroscopic monitoring of the heating of **4b** at 80 °C in toluene before the addition of $PhCO_2H$ (0.5 equiv) after 4.25 h.

reaching a steady level, prior to the generation of the *ortho*-complex **4a**. This indicates the presence of an intermolecular mechanism for interconversion of the two regioisomeric products. The relatively large amount of acid added explains why a protonated compound **3a** is formed under the reaction conditions.

To assess the intra- versus intermolecular nature of the regioisomer interconversion (**4b** → **4a**), a competition experiment between *para*-fluorinated 2-phenylpyridine **3c** and **3a** was performed and monitored using *in situ* ^{19}F NMR spectroscopy (Figure 4). Initially, **3a** was cyclomanganated without any additives; thereafter, **3c** (0.6 equiv) and benzoic acid (0.5 equiv) were added to the reaction (addition 1). *Meta*-complex **4e** was observed following this addition, suggesting the presence of an intermolecular reaction mechanism. The formation of **4e** was at the expense of both **4a** and **4b**, giving rise to a relative product ratio of 2.6:1 (**4a**/**4e**). Only a minor quantity of *para*-complex **4b** (3%) was present in the solution, and uncoordinated ligand **3a** was generated in the reaction because of the disappearance of **4a** and **4b**. A further 3.7 equiv of **3c** were added (addition 2) to the reaction following stabilization of the kinetic traces, leading to **4e** becoming the dominant manganacycle in a 2.7-fold excess over **4a** (0.375:1 **4a**/**4e**). **4b** only remained in trace quantities at the end of the experiment. The ratio between **3a** and **3c** (bound and free ligand) was 1.8:1 after addition 1, which changed to 0.235:1 following addition 2. The data support an CMD/AMLA-6 intramolecular protonation reaction, which is then followed by an intermolecular exchange between free and coordinated 2-phenylpyridine ligands.

The distribution between the different complexes under these reversible reaction conditions should be determined by

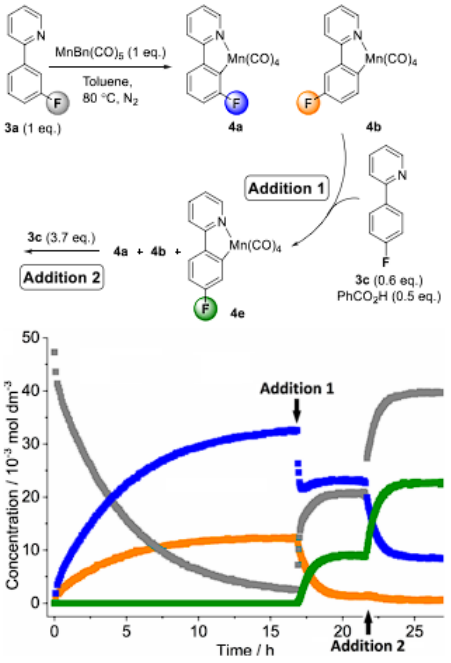

Figure 4. *In situ* ^{19}F NMR spectroscopic study, over the course of the cyclomanganation of **3a** at 80 °C in toluene, with the addition of $PhCO_2H$ (0.5 equiv) and **3c** (0.6 + 3.7 equiv) after 17 and 21.5 h.

their relative thermodynamic stability. Thus, by comparing the quantity of each complex with the total amount of the corresponding 2-phenylpyridine derivative in solution, it was determined that *ortho*-complex **4a** was 1.4−1.6 times more stable than *meta*-complex **4e**. Due to the small amounts of *para*-complex **4b** in solution, a value for the relative stability of this complex could not be obtained. However, **4b** was clearly the least stable complex. The relative stability of the regioisomeric complexes can be summarized as **4a** > **4e** > **4b** (*ortho* > *meta* > *para*).

Time-Resolved Multiple Probe Spectroscopy Monitoring of C−C Bond Formation. Having established the relative kinetic and thermodynamic preference in the C−H bond activation *in operando*, we sought to examine the influence of the fluorine atom in the organic ligand on further reactivity of the regioisomeric manganacycles. Time-resolved multiple probe spectroscopy (TR^MPS) allows for the observation of light-induced events on picosecond to millisecond timescales. We have successfully employed this technique in studying several Mn(I)-mediated systems in recent years,[14,15,20] including solvent interactions following CO-loss[20a] and C−C bond formation with alkynes and other unsaturated substrates.[14] We thus identified TR^MPS-IR as a suitable technique to further explore the stability and reactivity of the regioisomeric manganacycles. TR^MPS-IR is a pump−probe method in which a laser pulse (λ = 355 nm) induces the CO loss from the Mn center and a subsequent IR pulse allows

https://doi.org/10.1021/acscatal.1c05477
ACS Catal. 2022, 12, 1532−1544

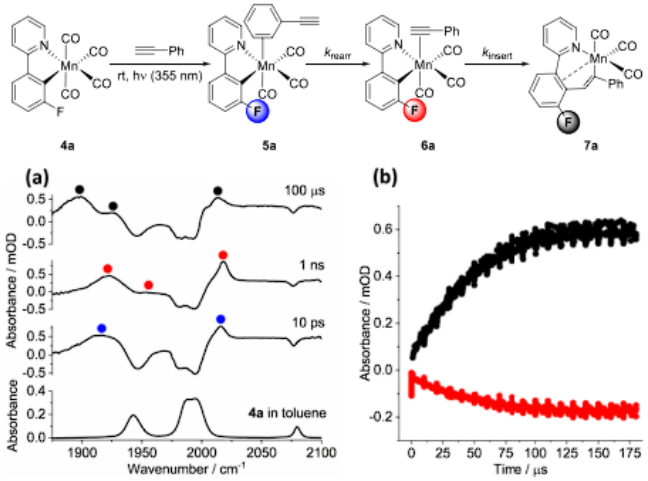

Figure 5. Reaction scheme and TR^{M}PS data for the 355 nm irradiation of **4a** in neat PhC_2H. (a) Ground-state IR spectra of **4a** and IR spectrum over time of the reaction solution. (b) Kinetic trace for the C−C bond formation step. Red shows the growth and loss of the alkyne complex **6a**, and black shows the growth of **7a**.

for the vibrational spectra of the resulting photoproducts to be obtained. The position and intensity of the band due to the remaining CO ligand provide information about the speciation and dynamic behavior following irradiation. We decided to utilize the alkyne insertion chemistry previously studied[14] as a probe for a potential kinetic *ortho*-fluorine effect in the C−C bond formation event. Changes in the rate of insertion of a substrate into the C−Mn bond should be indicative of any effects caused by the presence of fluorine.

Initially, *ortho*-complex **4a** was dissolved in neat PhC_2H and subsequently irradiated (λ = 355 nm), while monitored using TR^{M}PS-IR. The experiment used pump−probe delays between 1 ps to 800 μs and spectral detection in the region 1850−2100 cm^{-1}. The resulting data are presented as difference spectra (Figure 5), where positive peaks correspond to the generated photoproducts and negative peaks to the ground state spectrum of **4a**, following consumption by photolysis. The spectroscopic features and band locations for the various species mirrored those observed for the nonfluorinated derivatives (Table 2).[14] Light-induced loss of CO is evident at the shortest pump−probe delays employed (1 ps), and an arene-bound PhC_2H complex **5a** (1915 and 2016 cm^{-1}) was observed, which was assigned on the basis of our previous work.[14] After 1 ns, the bands due to **5a** had been replaced by those for alkyne-coordinated complex **6a** (1923, 1955, and 2018 cm^{-1}). Evidence for the subsequent insertion of the alkyne into the C−Mn bond to form 7-membered complex **7a** was obtained through the bands at 1897, 1924, and 2013 cm^{-1}. A minor unknown species (2002 cm^{-1}) also formed in the reaction concomitantly with **7a**, though in minor quantities, which did not seem to affect the formation of **7a**.

Essentially, identical data were obtained for the respective C−C bond forming events for the other manganacycles (**4b**−**4e**), with only minor changes in band position (see Supporting Information) being observed. However, the presence of the fluorine substituents was found to have a distinct impact on the rate of formation of compound class **7** (Table 1). When the 2-phenylpyridine ligand contained an *ortho*-fluorine substituent, the rate constant for the insertion of the alkyne into the Mn−C bond was reduced (e.g., for *ortho*-derivative **7a** k_{insert} = 2.21 ± 0.04 × 10^4 s^{-1}; for the nonfluorinated derivative k_{insert} = 1.35 ± 0.09 × 10^5 s^{-1}.[14] The addition of a second fluorine in **4c** and **4d** lowered the observed rate constant by factors of 6.1 and 3.1, respectively, compared to the mono-fluorinated derivatives (**4a** and **4b**).

The location of the fluorine substituents on the arene strongly influenced the observed rate constant for C−C bond formation: *para*-complex **4b** (k_{insert} = 5.7 ± 0.2 × 10^4 s^{-1}) reacted faster than *ortho*-complex **4a** (k_{insert} = 2.21 ± 0.04 × 10^4 s^{-1}). The rate constant obtained for *meta*-complex **4e** was located at an intermediate value when compared to the other two regioisomers (k_{insert} = 3.5 ± 0.1 × 10^4 s^{-1}) and thus generated a relative reaction trend of **4b** > **4e** > **4a** (k_{insert}: *para* > *meta* > *ortho*), which in turn mirrored the relative thermodynamic stability of the complex determined *vide supra*. These results unambiguously demonstrate the influence of the fluorine substituent on the rate of carbon−carbon bond formation with the coordination sphere of Mn(I) compounds.

Catalytic Reaction Conditions. To gain further understanding of the influence of the fluorine substituents on the regioselectivity in catalytically relevant systems, we studied the Mn(I)-mediated C−H bond alkenylation of the fluorinated 2-phenylpyridines. Mn(I)-catalyzed alkenylation processes have been extensively studied,[8,9,12,14,17] and we have previously determined a full mechanism for this reaction.[17a] Chen and Wang reported the *ortho*-alkenylated 2-phenylpyridine **8a** as the sole reaction product when **3a** was used as a substrate[9] and thus suggest that the cyclomanganation steps may be reversible under the reaction conditions. However, when we performed the reaction between PhC_2H (1 equiv) and **3a** (2 equiv) at 80

https://doi.org/10.1021/acscatal.1c05477
ACS Catal. 2022, 12, 1532−1544

Table 2. TR^{M}PS Data and Rate Constants for the C−C Bond Formation Step in the Photolysis of the Manganacycles in Neat PhC_2H[a]

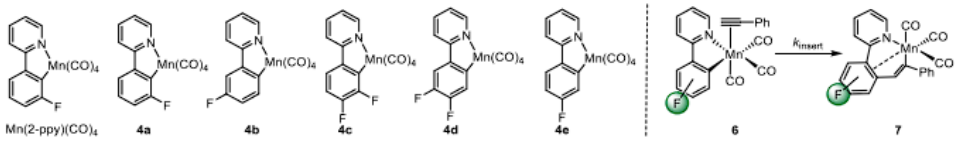

Mn(2-ppy)(CO)$_4$ **4a** **4b** **4c** **4d** **4e** **6** **7**

entry	compound	6/cm^{-1}		7/cm^{-1}		$k_{insert}/10^4$ s^{-1}	$\Delta G^{\ddagger}_{298.15}$/kJ mol^{-1} exp	$\Delta G^{\ddagger}_{298.15}$/kJ mol^{-1} calc	$\Delta G^{\circ}_{298.15}$/kJ mol^{-1} calc
1	Mn(2-ppy) (CO)$_4$	2009	2010	2008	2003	13.5 ± 0.9	44	29	−91
		1944	1941	1922	1925				
		1912		1899					
		1915		1893					
2	4a	2018	2018	2013	2005	2.21 ± 0.04	48	37	−83
		1955	1950	1924	1925				
		1923		1897					
		1922		1895					
3	4b	2013	2012	2011	2033	5.7 ± 0.2	46	35	−94
		1948	1942	1920	1925				
		1912		1897					
		1917		1895					
4	4c	2020	2020	2021	2006	0.86 ± 0.01[b]	51	43	−75
		1968	1952	1925	1927				
		1925		1897					
		1923		1896					
5	4d	2015	2013	2013	2005	1.86 ± 0.05	49	39	−88
		1953	1944	1921	1926				
		1917		1895					
		1918		1896					
6	4e	2014	2013	2012	2003	3.5 ± 0.1	47	37	−90
		1950	1944	1923	1926				
		1916		1898					
		1918		1896					

[a]Scaled DFT-predicted vibrational modes are shown in italics. $\Delta G^{\ddagger}_{298.15}{}^{calc}$ is equivalent to the energy of TS_{67} (Scheme 4) and $\Delta G^{\circ}_{298.15}{}^{calc}$ is the energy of 7. In both cases, the energy of the respective complex **6** is taken as the reference energy. All energies are free energies at 298.15 K at the D3(BJ)-pbe0/def2-TZVPP//bp86/SV(P) level of theory. [b]Data treated with a six-point smoothing function.

Scheme 3. Mn(I)-Catalyzed Alkenylation of 3a Using PhC_2H

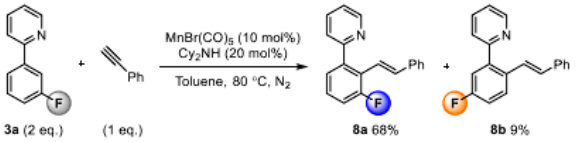

3a (2 eq.) (1 eq.) **8a** 68% **8b** 9%

°C in toluene, using Cy_2NH (20 mol %) as the base additive and $BrMn(CO)_5$ as the precatalyst (Scheme 3), we isolated and characterized both the *ortho*- (**8a**, 68%) and *para*-alkenylated (**8b**, 9%) derivatives. The small quantities of **8b** generated in combination with change of solvent and reaction vessel may help explain the discrepancies in the observed product ratio between our and Chen and Wang's work.[9]

When benzylamine **1a** was exposed to the alkenylation conditions, no alkene product was generated, only the starting material was observed, and no other products were observed in the crude ^{1}H and ^{19}F NMR spectra.

The strong and distinct IR-spectroscopic reporter ligands on the manganese allowed for the *in situ* monitoring of changes in metal carbonyl peaks under the catalytic conditions, and thus, a new Mn-species was generated, using a Mettler-Toledo ReactIR instrument with the Si probe. We combined the *in situ* IR monitoring with *ex situ* ^{19}F NMR spectroscopy to obtain kinetic profiles, enabling distinction between different regioisomeric products and complexes with a 2-phenylpyridine moiety.

Several new manganese carbonyl species were observed to form during the reaction between PhC_2H (1 equiv) and **3a** (2 equiv) at 80 °C in toluene solution, using Cy_2NH (20 mol %) as the base additive and $MnBr(CO)_5$ as the precatalyst (Figure 6a). The precatalyst had been consumed within the first few minutes of the reaction and replaced by a new species (**7a′**, 1943, 1987, and 2071 cm^{-1}). The new species was assigned as the tetracarbonyl derivative of the seven-membered insertion complex **7a** due to its similarity to the nonfluorinated derivative, which we have previously characterized and

https://doi.org/10.1021/acscatal.1c05477
ACS Catal. 2022, 12, 1532−1544

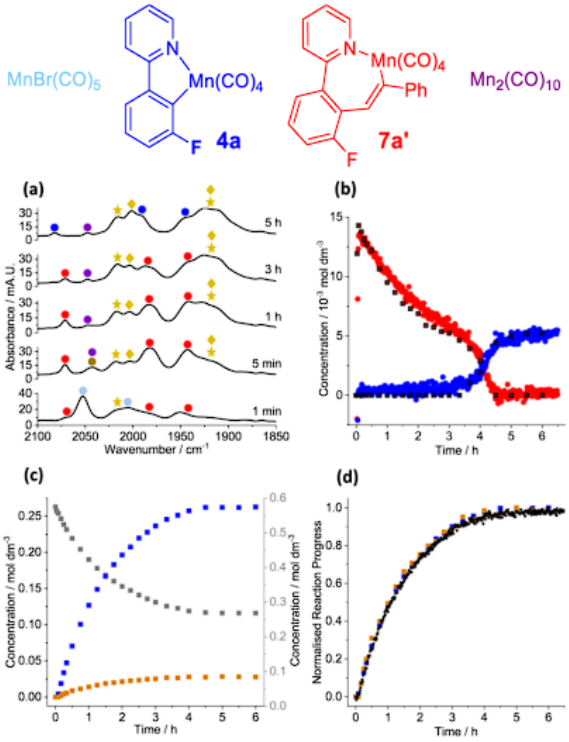

Figure 6. *In situ* IR and *ex situ* ^{19}F NMR spectroscopic monitoring of the alkenylation of **3a** (2 equiv) using PhC_2H (1 equiv), Cy_2NH (20 mol %), $MnBr(CO)_5$ (10 mol %), and *n*-Bu_2O. Key: see structures given above and the gold star/diamonds represent manganese degradation complexes.

shown to be the catalyst resting state.[17a] **7a′** displayed a single signal in the ^{19}F NMR spectra (−115 ppm), which exhibited the same kinetic profile as obtained from the *in situ* IR spectroscopy (Figure 6b). A ^{19}F NMR signal corresponding to *para*-derivative **7b′** was not found, suggesting that the *para*-complex is more active toward proton transfer. The concentration of **7a′** depleted slowly as the organic product formed; reaction completion was noted when no PhC_2H was left in solution. The remaining **7a′** was then rapidly consumed and replaced by *ortho*-complex **4a** *via* one of the available protonation pathways. *Para*-complex **4b** was not observed in the ^{19}F NMR spectra and highlighted a significant *ortho*-preference in the subsequent cyclomanganation step promoted by the excess 2-phenylpyridine in solution. It should be noted that the mechanism involving PhC_2H acting as the acid may yield a different observed selectivity during the cyclomanganation step.[17a]

Manganese degradation complexes, such as Mn clusters, were observed forming in the reaction in a similar fashion as observed in the nonfluorinated system.[17a] The exact structural identity of these Mn clusters has not successfully been determined. A band at 2047 cm^{-1} was tentatively assigned as $Mn_2(CO)_{10}$, which we have previously observed under catalytic conditions,[17c] though the extensive spectral overlap did not allow for observation of the other spectroscopic bands corresponding to this species.

The kinetic profiles obtained by ^{19}F NMR spectroscopy (Figure 6c) showed that *ortho*-derivative **8a** was generated in nine times excess over *para*-derivative **8b**. The shape of the curves was similar to that of the cyclomanganation reaction without acid additives (Figure 1b), though with a larger *ortho*-preference, suggesting an intrinsic formation of the organic products. This was further supported by the comparison between the normalized reaction profiles and an IR deformation band (970 cm^{-1}) corresponding to the alkene products (Figure 6d). The identical shape of the normalized reaction profiles demonstrates that the product ratio remained constant throughout the reaction and was not determined by secondary isomerization processes.

Therefore, the selectivity was likely set by the cyclomanganation step within the catalytic cycles, as the C−C formation step favors the generation of *para*-product **8b**. It was also possible that the protonation step would define the selectivity, but the lack of observation of the seven-membered catalyst resting state **7b′** likely means that the protonation was either favored for the *para*-isomer or similar between the two regioisomers.

https://doi.org/10.1021/acscatal.1c05477
ACS Catal. 2022, 12, 1532−1544

Computational Work. Insights into how the incorporation of fluorine into the 2-phenylpyridine ligands affected both the kinetic and thermodynamics of complex formation were obtained using DFT methods. The geometry of the complexes was optimized at the bp86/SV(P) level of theory and was used in subsequent single-point energy calculations at the D3(BJ)-pbe0/def2-TZVPP level. Thermal corrections (298.15 K) from the bp86/SV(P) level were then applied to obtain Gibbs free energies. This has proved to be a robust method to probe the chemistry of Mn-carbonyl compounds.[14,15,17,20]

A series of isodesmic reactions were modeled (Scheme 4a) to assess the thermodynamic effect of fluorine incorporation in the ligands. In this case, the change in Gibbs energy for substituting the parent 2-phenylpyridine by a range of fluorine-containing analogues (**3a**−**k**) was calculated.[21] Some general trends may be drawn from these data. First, there is a thermodynamic preference for cyclomanganation at sites with an *ortho*-fluorine (**3a** and **3b**, blue arrows, **3f**, **3g**, **3i**−**k**, Scheme 4b), which results in a *ca.* 10 kJ mol^{-1} stabilization compared to the hydrogen-substituted analogue. Second, there is a small *meta*-fluorine effect, which provides additional stabilization (e.g., **3g** and **3h**). Third, the introduction of a *para*-fluorine (e.g., **3a** purple arrow, **3h**) does not appear to affect the overall stability. Although some of these changes in energy are relatively small, they are consistent across this series, and also, the corresponding benzylamine analogues show an identical trend (see Supporting Information).

The experimental data indicate that the reaction of $MnBn(CO)_5$ with **3a** shows only a small, kinetically controlled, *ortho*-fluorine effect with a **4a**:**4b** ratio of 7:3 in toluene solution. Insights into this process was obtained by modeling the two regioisomeric C−H bond activation pathways for **3a** by $MnBn(CO)_5$ (Scheme 4c). The computational model was based on coordination of **3a** to a "$MnBn(CO)_3$" fragment through nitrogen of the pyridyl directing group and a C−H agostic interaction.[22] Two isomeric states **9a** (taken as the reference state) and **9b** were identified that differed only in the site of the agostic interaction. The C−H bond activation proceeds through $\mathbf{TS_{9\text{-}10}}$ in which the hydrogen atom is transferred to the benzyl ligand through a σ-CAM-type mechanism.

In both cases, the barrier for this process is low, indicating that the mode of C−H bond activation is facile and would not be rate-controlling. The energetic span for the formation of cyclomanganated complexes **10a** and **10b** is greater for **9b** (30 kJ mol^{-1}) compared to that for **9a** (22 kJ mol^{-1}) (assuming that **9a** and **9b** do not interconvert through a lower energy pathway), indicating a marginal kinetic preference for the formation of the *ortho*-fluorinated species. As with the calculations on the isodesmic reactions, **10a** containing an *ortho*-fluorine was located at lower energy than the *para*derivative **10b** (−60 kJ mol^{-1} vs −50 kJ mol^{-1}).

The insertion of PhC_2H into the Mn−C bond of **6** was also evaluated using DFT methods, again giving good agreement with the experiment outcomes (Table 2). In this case, the calculations indicated that the incorporation of fluorine into any position of the cyclomanganated phenyl ring increased the energy of the respective $\mathbf{TS_{6\text{-}7}}$ (Scheme 4d) (and thus $\Delta G^{\ddagger}_{298.15}{}^{calc}$) compared to the nonfluorinated analogue. The predicted change in free energies of the activation span is 14 kJ mol^{-1} and so care must be taken in their interpretation. Of note, there is essentially a linear correlation between the DFT-predicted barriers and those determined experimentally through time-resolved infrared spectroscopy. This supports the interpretation that the incorporation of an *ortho*-fluorine atom decreases the rate of insertion. In addition, the substrates with the lowest rate of insertion also have the least negative calculated $\Delta G^{\circ}_{298.15}{}^{calc}$ (i.e., the relative energy of **7** when

Scheme 4. (a) Isodesmic Reaction Used to Probe the Effect of Fluorine Incorporation Into 2-Phenylpyridine Ligands. (b) Calculated Free Energy Changes at 298.15 K for the Reaction Shown in (a). The Arrow Shows the Site of Cyclomanganation. (c) Reaction Profile for the Intramolecular C−H Bond Activation at Mn Through a σ-CAM Mechanism. (d) Calculated Pathway for the Insertion of PhC_2H Into Mn−C Bonds. Collated Data are in Table 2. All Energies are Free Energies in kJ mol^{-1}at 298.15 K at the D3(BJ)-pbe0/def2-TZVPP//bp86/SV(P) Level of Theory

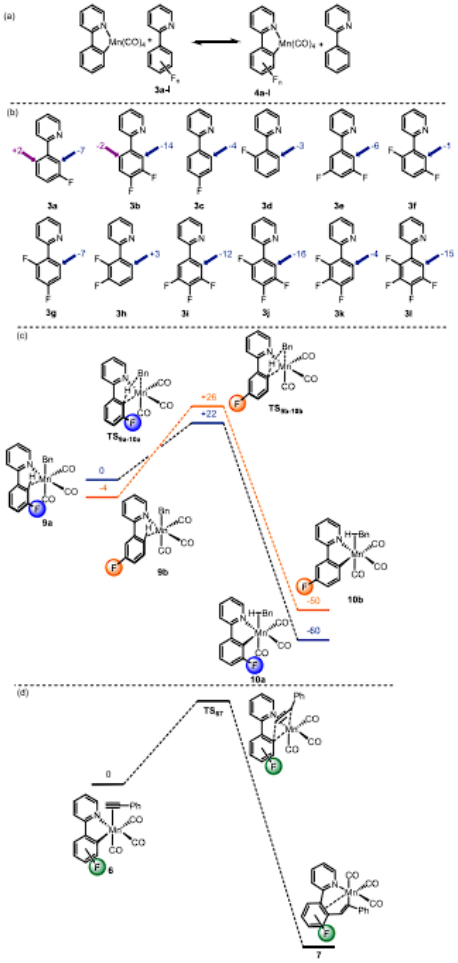

https://doi.org/10.1021/acscatal.1c05477
ACS Catal. 2022, 12, 1532−1544

compared to **6**). This may be interpreted as a further manifestation of the *ortho*-fluorine effect. In the case of complexes such as **4a** and **4c**, the formation of the respective complexes **7** results in the loss of a cyclomanganated atom with an *ortho*-fluorine, resulting in a lower thermodynamic driving force for the reaction. This may be viewed as the *ortho*-fluorine stabilizing **6**, resulting in a higher kinetic barrier to insertion. If the insertion reaction is best viewed as an intramolecular nucleophilic attack on the coordinated alkyne, the presence of the *ortho*-fluorine may result in the phenyl group being a poorer nucleophile.

CONCLUSIONS

Controlling the site selectively of C−H bond activation in complex substrates is key to unlocking the potential of direct C−H bond functionalization methods. As recently highlighted by Davies and Macgregor, to draw robust mechanistic conclusions, it is vital to understand if the selectivity of such a process is under kinetic or thermodynamic control.[6a,e] Through this study, we have revealed the presence and varying strength of the *ortho*-fluorine effect in catalytically-competent Mn(I)-mediated C−H bond activation reactions of fluorinated arenes. The irreversible reaction mechanism, and thus kinetically determined selectivity, under the standard reaction conditions afforded the *ortho*-complex of the benzylamine derivatives in near complete selectivity (**1a** and **1b**), while the *para*-complexes were more prevalent for the 2-phenylpyridine-directed examples (**3a** and **3b**). With the addition of benzoic acid, the mechanism could be altered to a reversible CMD/AMLA-6 mode of C−H bond activation and thereby ensuring the selectivity is determined thermodynamically. The relative thermodynamic stability determined by experimental and computational methods revealed an *ortho* > *meta* > *para* stability trend, which was the reverse of that observed for their reactivity toward C−C bond formation (*para* > *meta* > *ortho*), that is, alkyne insertion into the C−Mn bond, as studied by $TR^{M}PS$. In combination with the single-crystal XRD analysis, it was determined that the inherent reactivity of the manganese-(I) carbonyl complexes stems from their relative thermodynamic stability rather than other processes, such as their relative C−Mn bond strength.

The knowledge obtained was translated into the study of Mn(I)-catalyzed C−H bond alkenylation of 2-phenylpyridines, where the minor *para*-isomer **8b** was identified for the first time forming in minor amounts. The preference for *ortho*-isomer **8a** in the reaction was set by the cyclomanganation step within the catalytic cycles rather than by the *para*-favored C−C bond formation of the protonation step within the catalytic cycles. The outcome points to this being the most important step within the reaction mechanism if reactivity is to be altered to afford different regioselectivities or more efficient catalytic processes, that is, lower Mn catalyst loadings.

ASSOCIATED CONTENT

Supporting Information

The Supporting Information is available free of charge at https://pubs.acs.org/doi/10.1021/acscatal.1c05477.

Experimental procedures used, details of kinetic studies including time-resolved IR spectroscopic studies, and computational studies using DFT methods (PDF)

CIF files for the single crystal X-ray diffraction structures of **2a**, **2b**, **2d**, **4a**, **4b** and **4c** (CIF)

checkCIF/PLATON report (PDF)

AUTHOR INFORMATION

Corresponding Authors

Jason M. Lynam − *Department of Chemistry, University of York, York YO10 5DD, United Kingdom;* orcid.org/0000-0003-0103-9479; Email: jason.lynam@york.ac.uk

Ian J. S. Fairlamb − *Department of Chemistry, University of York, York YO10 5DD, United Kingdom;* orcid.org/0000-0002-7555-2761; Email: ian.fairlamb@york.ac.uk

Authors

L. Anders Hammarback − *Department of Chemistry, University of York, York YO10 5DD, United Kingdom*

Amy L. Bishop − *Department of Chemistry, University of York, York YO10 5DD, United Kingdom*

Christina Jordan − *Department of Chemistry, University of York, York YO10 5DD, United Kingdom*

Gayathri Athavan − *Department of Chemistry, University of York, York YO10 5DD, United Kingdom*

Jonathan B. Eastwood − *Department of Chemistry, University of York, York YO10 5DD, United Kingdom*

Thomas J. Burden − *Department of Chemistry, University of York, York YO10 5DD, United Kingdom*

Joshua T. W. Bray − *Department of Chemistry, University of York, York YO10 5DD, United Kingdom*

Francis Clarke − *Department of Chemistry, University of York, York YO10 5DD, United Kingdom*

Alan Robinson − *Syngenta Crop Protection AG, Basel 4332, Switzerland;* orcid.org/0000-0002-2499-7373

Jean-Philippe Krieger − *Syngenta Crop Protection AG, Basel 4333, Switzerland*

Adrian Whitwood − *Department of Chemistry, University of York, York YO10 5DD, United Kingdom;* orcid.org/0000-0002-5132-5468

Ian P. Clark − *Central Laser Facility, STFC Rutherford Appleton Laboratory, Didcot, Oxfordshire OX11 0QX, United Kingdom*

Michael Towrie − *Central Laser Facility, STFC Rutherford Appleton Laboratory, Didcot, Oxfordshire OX11 0QX, United Kingdom*

Complete contact information is available at: https://pubs.acs.org/10.1021/acscatal.1c05477

Notes

The authors declare no competing financial interest.

ACKNOWLEDGMENTS

We are grateful to Dr. Jessica Milani for assistance with the synthesis of the fluorinated amine starting materials. We thank Professors Robin N. Perutz, Paul H. Walton, and Andrew S. Weller (York) for discussion of our findings. We are grateful to the ERASUMS exchange scheme for funding C.J. and the Wild fund for supporting a PhD scholarship for G.A. Syngenta and EPSRC are thanked for funding an iCASE PhD studentship for L.A.H. We acknowledge EPSRC grants (EP/H011455, EP/K031589/1, and EP/N509413/1).

REFERENCES

(1) (a) Kalläne, S. I.; Braun, T. Catalytic Borylation of SCF_3-Functionalized Arenes by Rhodium(I) Boryl Complexes: Regioselective C−H Activation at the *ortho*-Position. *Angew. Chem., Int. Ed.* **2014**, *53*, 9311−9315. (b) Carr, K. J. T.; Davies, D. L.; Macgregor, S.

https://doi.org/10.1021/acscatal.1c05477
ACS Catal. 2022, 12, 1532−1544

A.; Singh, K.; Villa-Marcos, B. Metal Control of Selectivity in Acetate-assisted C−H Bond Activation: An Experimental and Computational Study of Heterocyclic, Vinylic and Phenylic C(sp^2)−H Bonds at Ir and Rh. *Chem. Sci.* **2014**, *5*, 2340−2346. (c) Ciana, C.-L.; Phipps, R. J.; Brandt, J. R.; Meyer, F.-M.; Gaunt, M. J. A Highly *para*-Selective Copper(II)-Catalyzed Direct Arylation of Aniline and Phenol Derivatives. *Angew. Chem., Int. Ed.* **2011**, *50*, 458−462. (d) Hartwig, J. F.; Larsen, M. A. Undirected, Homogeneous C−H Bond Functionalization: Challenges and Opportunities. *ACS Cent. Sci.* **2016**, *2*, 281−292.

(2) (a) Sambiagio, C.; Schönbauer, D.; Blieck, R.; Dao-Huy, T.; Pototschnig, G.; Schaaf, P.; Wiesinger, T.; Zia, M. F.; Wencel-Delord, J.; Besset, T.; Maes, B. U. W.; Schnürch, M. A Comprehensive Overview of Directing Groups Applied in Metal-Catalysed C−H Functionalisation Chemistry. *Chem. Soc. Rev.* **2018**, *47*, 6603−6743. (b) Tang, R.-Y.; Li, G.; Yu, J.-Q. Conformation-Induced Remote *meta*-C−H Activation of Amines. *Nature* **2014**, *507*, 215−220. (c) Kuhl, N.; Hopkinson, M. N.; Wencel-Delord, J.; Glorius, F. Beyond Directing Groups: Transition-Metal-Catalyzed C−H Activation of Simple Arenes. *Angew. Chem., Int. Ed.* **2012**, *51*, 10236−10254.

(3) Ribas, X. *C−H and C−X Bond Functionalization: Transition Metal Mediation*; The Royal Society of Chemistry, 2013.

(4) Clot, E.; Eisenstein, O.; Jasim, N.; Macgregor, S. A.; McGrady, J. E.; Perutz, R. N. C−F and C−H Bond Activation of Fluorobenzenes and Fluoropyridines at Transition Metal Centers: How Fluorine Tips the Scales. *Acc. Chem. Res.* **2011**, *44*, 333−348.

(5) (a) Alharis, R. A.; McMullin, C. L.; Davies, D. L.; Singh, K.; Macgregor, S. A. The Importance of Kinetic and Thermodynamic Control when Assessing Mechanisms of Carboxylate-Assisted C−H Activation. *J. Am. Chem. Soc.* **2019**, *141*, 8896−8906. (b) Bruce, M. I.; Goodall, B. L.; Stone, F. G. A. Cyclometallation reactions. Part 17. Comparative Studies of the Manganation and Palladation of Some Substituted Azobenzenes. *J. Chem. Soc., Dalton Trans.* **1978**, 687−694. (c) Liebeskind, L. S.; Gasdaska, J. R.; McCallum, J. S.; Tremont, S. J. *Ortho*-Functionalization of Aromatic Ketones via Manganation. A Synthesis of Indenols. *J. Org. Chem.* **1989**, *54*, 669−677. (d) Milani, J.; Pridmore, N. E.; Whitwood, A. C.; Fairlamb, I. J. S.; Perutz, R. N. The Role of Fluorine Substituents in the Regioselectivity of Intramolecular C−H Bond Functionalization of Benzylamines at Palladium(II). *Organometallics* **2015**, *34*, 4376−4386. (e) Alharis, R. A.; McMullin, C. L.; Davies, D. L.; Singh, K.; Macgregor, S. A. Understanding Electronic Effects on Carboxylate-Assisted C−H Activation at Ruthenium: The Importance of Kinetic and Thermodynamic Control. *Faraday Discuss.* **2019**, *220*, 386−403.

(6) (a) Clot, E.; Besora, M.; Maseras, F.; Mégret, C.; Eisenstein, O.; Oelckers, B.; Perutz, R. N. Bond Energy M−C/H−C Correlations: Dual Theoretical and Experimental Approach to the Sensitivity of M−C Bond Strength to Substituents. *Chem. Commun.* **2003**, 490−491. (b) Clot, E.; Oelckers, B.; Klahn, A. H.; Eisenstein, O.; Perutz, R. N. cis−trans Isomerisation of $CpRe(CO)_2(H)(Ar_F)$ ($Ar_F = C_6F_nH_{5-n}$; n = 0−5) is the Rate Determining Step in C−H Activation of Fluoroarenes: a DFT Study. *Dalton Trans.* **2003**, 4065−4074. (c) Clot, E.; Mégret, C.; Eisenstein, O.; Perutz, R. N. Exceptional Sensitivity of Metal-Aryl Bond Energies to *ortho*-Fluorine Substituents: Influence of the Metal, the Coordination Sphere, and the Spectator Ligands on M-C/H-C Bond Energy Correlations. *J. Am. Chem. Soc.* **2009**, *131*, 7817−7827. (d) Guihaumé, J.; Clot, E.; Eisenstein, O.; Perutz, R. N. Importance of Palladium−Carbon Bond Energies in Direct Arylation of Polyfluorinated Benzenes. *Dalton Trans.* **2010**, *39*, 10510−10519. (e) Lafrance, M.; Rowley, C. N.; Woo, T. K.; Fagnou, K. Catalytic Intermolecular Direct Arylation of Perfluorobenzenes. *J. Am. Chem. Soc.* **2006**, *128*, 8754−8756. (f) Selmeczy, A. D.; Jones, W. D.; Partridge, M. G.; Perutz, R. N. Selectivity in the Activation of Fluorinated Aromatic Hydrocarbons by Rhodium Complexes $[(C_5H_5)Rh(PMe_3)]$ and $[(C_5Me_5)Rh(PMe_3)]$. *Organometallics* **1994**, *13*, 522−532. (g) He, M.; Soulé, J.-F.; Doucet, H. Synthesis of (Poly)fluorobiphenyls through Metal-catalyzed C-H Bond Activation/Arylation of (Poly)fluorobenzene Derivatives. *ChemCatChem* **2014**, *6*, 1824−1859.

(7) Pabst, T. P.; Obligacion, J. V.; Rochette, É.; Pappas, I.; Chirik, P. J. Cobalt-atalyzed Borylation of Fluorinated Arenes: Thermodynamic Control of C(sp^2)-H Oxidative Addition Results in *ortho*-to-Fluorine Selectivity. *J. Am. Chem. Soc.* **2019**, *141*, 15378−15389.

(8) Reviews: (a) Liu, W.; Ackermann, L. Manganese-Catalyzed C−H Activation. *ACS Catal.* **2016**, *6*, 3743−3752. (b) Cano, R.; Mackey, K.; McGlacken, G. P. Recent Advances in Manganese-Catalysed C−H Activation: Scope and Mechanism. *Catal. Sci. Technol.* **2018**, *8*, 1251−1266. (c) Hu, Y.; Zhou, B.; Wang, C. Inert C−H Bond Transformation Enabled by Organometallic Manganese Catalysis. *Acc. Chem. Res.* **2018**, *51*, 816−827.

(9) Zhou, B.; Chen, H.; Wang, C. Mn-Catalyzed Aromatic C−H Alkenylation with Terminal Alkynes. *J. Am. Chem. Soc.* **2013**, *135*, 1264−1267.

(10) For selected reviews concerning earth abundant catalysis in general, see: (a) Su, B.; Cao, Z.-C.; Shi, Z.-J. Exploration of Earth-Abundant Transition Metals (Fe, Co, and Ni) as Catalysts in Unreactive Chemical Bond Activations. *Acc. Chem. Res.* **2015**, *48*, 886−896. (b) Bedford, R. B. How Low Does Iron Go? Chasing the Active Species in Fe-Catalyzed Cross-Coupling Reactions. *Acc. Chem. Res.* **2015**, *48*, 1485−1493. (c) Wang, D.; Astruc, D. The Recent Development of Efficient Earth-Abundant Transition-Metal Nanocatalysts. *Chem. Soc. Rev.* **2017**, *46*, 816−854. (d) Albrecht, M.; Bedford, R.; Plietker, B. Catalytic and Organometallic Chemistry of Earth-Abundant Metals. *Organometallics* **2014**, *33*, 5619−5621. (e) Webster, R. L. β-Diketiminate Complexes of the First Row Transition Metals: Applications in Catalysis. *Dalton Trans.* **2017**, *46*, 4483−4498. (f) Kitanosono, T.; Masuda, K.; Xu, P.; Kobayashi, S. Catalytic Organic Reactions in Water toward Sustainable Society. *Chem. Rev.* **2018**, *118*, 679−746.

(11) (a) Bruce, M. I.; Iqbal, M. Z.; Stone, F. G. A. *Ortho*-Metalation reactions. Part I. Reactions of Azobenzene with Some Metal Carbonyl Complexes of Sub-groups VI, VII, and VIII. *J. Chem. Soc. A* **1970**, 3204−3209. (b) Bruce, M. I.; Goodall, B. L.; Iqbal, M. Z.; Stone, F. G. A.; Doedens, R. J.; Little, R. G. *Ortho*-Metallation of Benzylideneaniline: Structure of $C_6H_5N{:}CH{\cdot}C_6H_4Mn(CO)_4$. *J. Chem. Soc. D* **1971**, *0*, 1595−1596. (c) McKinney, R. J.; Firestein, G.; Kaesz, H. D. Metalation Reaction. VII. Metalation of Aromatic Ketones and Anthraquinone with Methylmanganese and Methylrhenium Carbonyl Complexes. *Inorg. Chem.* **1975**, *14*, 2057−2061. (d) Bruce, M.; Goodall, B.; Matsuda, I. Cyclometallation Reactions. XIII. Reactions of Phenyl-substituted Heterocyclic Nitrogen-donor Ligands. *Aust. J. Chem.* **1975**, *28*, 1259−1264. (e) Robinson, N. P.; Main, L.; Nicholson, B. K. *Ortho*-manganated Arenes in Synthesis: V. *Ortho*-manganation of N-acyl Heteroaromatics, Benzamides and Substituted Benzaldehydes. Crystal Structure of (η^2-O,C-1-acetyl-2-indolyl)-tetracarbonylmanganese. *J. Organomet. Chem.* **1988**, *349*, 209−218. (f) Pfeffer, M.; Urriolabeitia, E. P.; Fischer, J. Effects of *ortho*-Substituents in the Synthesis and Stability of Cyclomanganated Benzylamine Derivatives. X-ray Crystal Structure of Mn-$\{C_6H_2(OCH_3)_2$-4,6-CH_2NMe_2-2$\}(CO)_4$. *Inorg. Chem.* **1995**, *34*, 643−650.

(12) Wang, C. Manganese-Mediated C−C Bond Formation via C−H Activation: From Stoichiometry to Catalysis. *Synlett* **2013**, *24*, 1606−1613.

(13) (a) Liebeskind, L. S.; Gasdaska, J. R.; McCallum, J. S.; Tremont, S. J. *Ortho*-functionalization of Aromatic Ketones via Manganation. A Synthesis of Indenols. *J. Org. Chem.* **1989**, *54*, 669−677. (b) Cambie, R. C.; Metzler, M. R.; Rutledge, P. S.; Woodgate, P. D. Cyclomanganation of Diterpenoids; Functionalization of C14. *J. Organomet. Chem.* **1990**, *381*, C26−C30. (c) Tully, W.; Main, L.; Nicholson, B. K. Preparation of Cyclomanganated Chalcones and Their Reactions with Methyl Acrylate and Other α, β-Unsaturated Carbonyl Compounds. *J. Organomet. Chem.* **1995**, *503*, 75−92. (d) Depree, G. J.; Main, L.; Nicholson, B. K. Some Insertion Reactions of the Mn−C Bond of Cyclomanganated Triphenylphosphine Chalcogenides. *J. Organomet. Chem.* **1998**, *551*, 281−291. (e) Depree, G. J.; Main, L.; Nicholson, B. K.; Robinson, N. P.; Jameson, G. B. Synthesis and Alkyne-coupling Chemistry of

https://doi.org/10.1021/acscatal.1c05477
ACS Catal. 2022, 12, 1532−1544

Cyclomanganated 1- and 3-Acetylindoles, 3-Formylindole and Analogues. *J. Organomet. Chem.* **2006**, *691*, 667−679.
(14) Hammarback, L. A.; Clark, I. P.; Sazanovich, I. V.; Towrie, M.; Robinson, A.; Clarke, F.; Meyer, S.; Fairlamb, I. J. S.; Lynam, J. M. Mapping Out the Key Carbon−Carbon Bond-Forming Steps in Mn-Catalysed C−H Functionalisation. *Nat. Catal.* **2018**, *1*, 830−840.
(15) Hammarback, L. A.; Aucott, B. J.; Bray, J. T. W.; Clark, I. P.; Towrie, M.; Robinson, A.; Fairlamb, I. J. S.; Lynam, J. M. Direct Observation of the Microscopic Reverse of the Ubiquitous Concerted Metalation Deprotonation Step in C−H Bond Activation Catalysis. *J. Am. Chem. Soc.* **2021**, *143*, 1356−1364.
(16) (a) Zhou, B.; Ma, P.; Chen, H.; Wang, C. Amine-Accelerated Manganese-Catalyzed Aromatic C−H Conjugate Addition to α,β-Unsaturated Carbonyls. *Chem. Commun.* **2014**, *50*, 14558−14561. (b) Zhou, B.; Hu, Y.; Wang, C. Manganese-Catalyzed Direct Nucleophilic C(sp^2)−H Addition to Aldehydes and Nitriles. *Angew. Chem., Int. Ed.* **2015**, *54*, 13659−13663.
(17) (a) Hammarback, L. A.; Robinson, A.; Lynam, J. M.; Fairlamb, I. J. S. Mechanistic Insight into Catalytic Redox-Neutral C−H Bond Activation Involving Manganese(I) Carbonyls: Catalyst Activation, Turnover, and Deactivation Pathways Reveal an Intricate Network of Steps. *J. Am. Chem. Soc.* **2019**, *141*, 2316−2328. (b) Yahaya, N. P.; Appleby, K. M.; Teh, M.; Wagner, C.; Troschke, E.; Bray, J. T. W.; Duckett, S. B.; Hammarback, L. A.; Ward, J. S.; Milani, J.; Pridmore, N. E.; Whitwood, A. C.; Lynam, J. M.; Fairlamb, I. J. S. Manganese(I)-Catalyzed C−H Activation: The Key Role of a 7-Membered Manganacycle in H-Transfer and Reductive Elimination. *Angew. Chem. Int. Ed.* **2016**, *55*, 12455−12459. (c) Hammarback, L. A.; Robinson, A.; Lynam, J. M.; Fairlamb, I. J. S. Delineating the Critical Role of Acid Additives in Mn-Catalysed C−H Bond Functionalisation Processes. *Chem. Commun* **2019**, *55*, 3211−3214.
(18) Hartwig, J. F. *Organotransition Metal Chemistry*; University Science Books, 2010.
(19) VanderWeide, A. I.; Brennessel, W. W.; Jones, W. D. Reversible Concerted Metalation−Deprotonation C−H Bond Activation by $[Cp^*RhCl_2]_2$. *J. Org. Chem.* **2019**, *84*, 12960−12965.
(20) (a) Aucott, B. J.; Duhme-Klair, A.-K.; Moulton, B. E.; Clark, I. P.; Sazanovich, I. V.; Towrie, M.; Hammarback, L. A.; Fairlamb, I. J. S.; Lynam, J. M. Manganese Carbonyl Compounds Reveal Ultrafast Metal-Solvent Interactions. *Organometallics* **2019**, *38*, 2391−2401. (b) Aucott, B. J.; Eastwood, J. B.; Anders Hammarback, L.; Clark, I. P.; Sazanovich, I. V.; Towrie, M.; Fairlamb, I. J. S.; Lynam, J. M. Insight into the Mechanism of CO-Release from Trypto-CORM Using Ultra-fast Spectroscopy and Computational Chemistry. *Dalton Trans.* **2019**, *48*, 16426−16436. (c) Eastwood, J. B.; Hammarback, L. A.; McRobie, M. T.; Clark, I. P.; Towrie, M.; Fairlamb, I. J. S.; Lynam, J. M. Time-resolved Infra-red Spectroscopy Reveals Competitive Water and Dinitrogen Coordination to a Manganese(I) Carbonyl Complex. *Dalton Trans.* **2020**, *49*, 5463−5470.
(21) In the case of monodentate ligands, the thermodynamic ortho-flourine effect is often quantified by determining changes to bond dissociation enthalpies. In this case, using this approach would involve either the cleavage of both Mn−N and Mn−C bonds of the bidendate ligands or, if just the Mn−C bond was broken, the formation of a diradical. Given the problems with both approaches, the isodesmic reaction model will give a more robust insight into the effect of fluorine incorporation, at least in this case.
(22) An alternative pathway in which C−H bond activation occurs at a "$MnBn(CO)_4$" was also located, see Supporting Information. In this case, **3a**, was coordinated through the pyridyl nitrogen and did not exhibit an agostic interaction. The transition state for C−H bond activation was found to be at much higher energy than that proceeding the σ-CAM mechanism in Figure 7c.

https://doi.org/10.1021/acscatal.1c05477
ACS Catal. 2022, 12, 1532−1544

Appendix 2: TRIR Data

400 nm Pump Wavelength Data

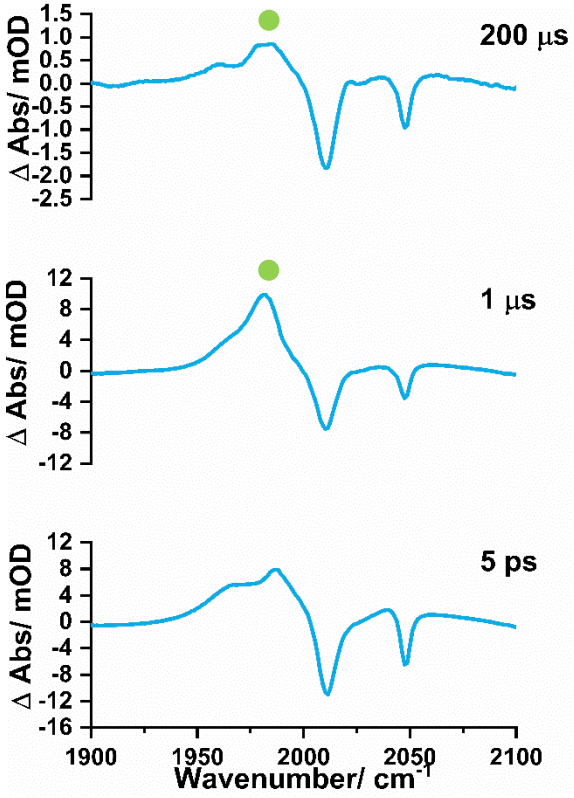

Figure 236. TRIR spectra of $[Mn_2(CO)_{10}]$ in anhydrous THF solution exciting with a 400 nm pump wavelength under an atmosphere of N_2 at selected pump-probe delays. **241** denoted by denoted by green circles.

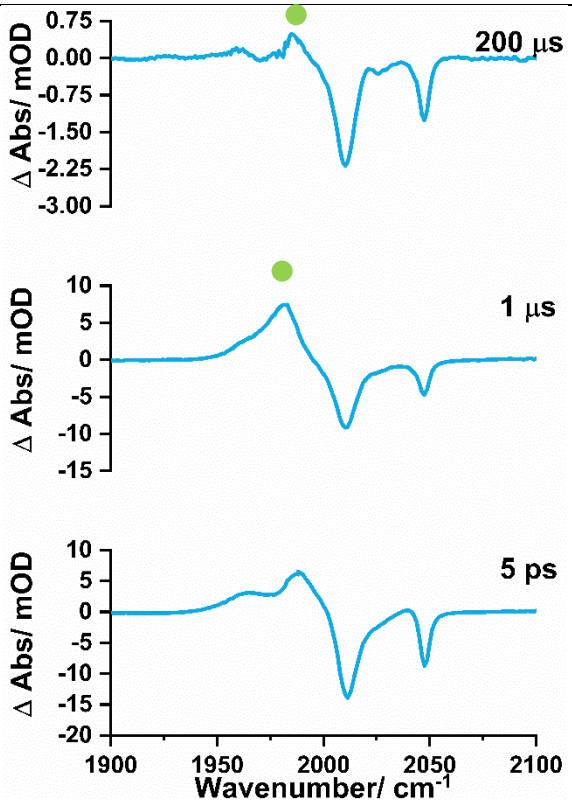

Figure 237. TRIR spectra of $[Mn_2(CO)_{10}]$ in anhydrous 1,4-dioxane solution exciting with a 400 nm pump wavelength under an atmosphere of N_2 at selected pump-probe delays. **241** denoted by denoted by green circles.

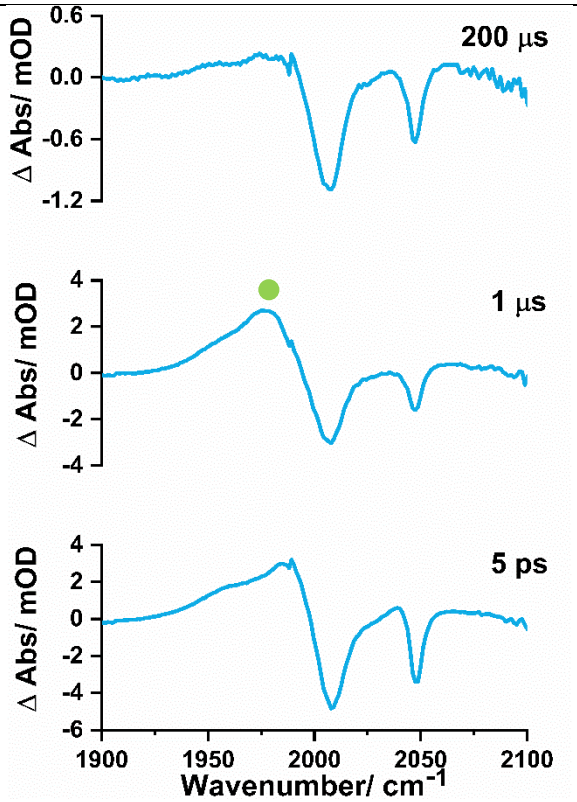

Figure 238. TRIR spectra of $[Mn_2(CO)_{10}]$ in anhydrous DMSO solution exciting with a 400 nm pump wavelength under an atmosphere of N_2 at selected pump-probe delays. **241** denoted by denoted by green circles.

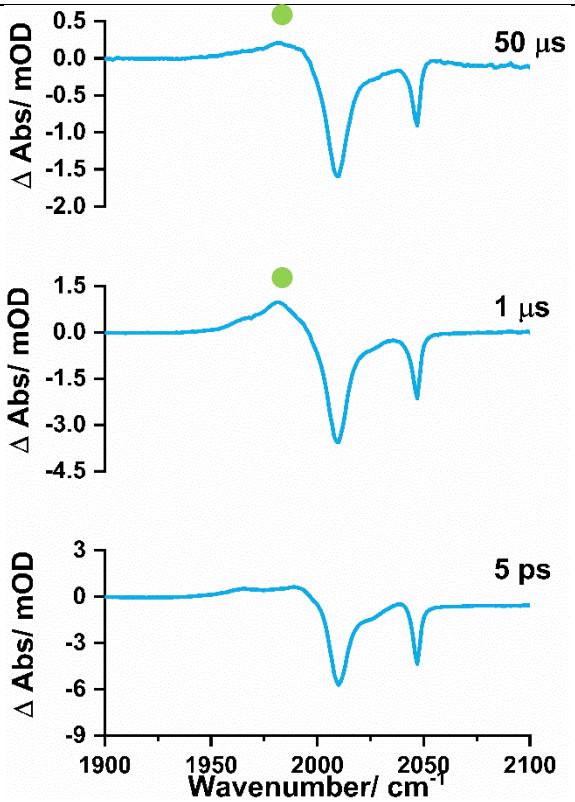

Figure 239. TRIR spectra of $[Mn_2(CO)_{10}]$ in anhydrous styrene solution exciting with a 400 nm pump wavelength under an atmosphere of N_2 at selected pump-probe delays. **241** denoted by denoted by green circles.

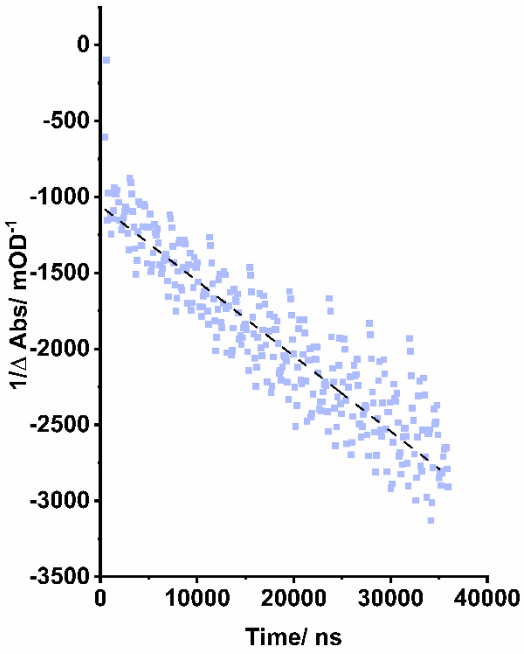

Figure 240. Plot of time (x axis) versus 1/ Δ absorption (y axis) to determine the second order rate constant for the recovery of the ground state bleach of $[Mn_2(CO)_{10}]$ at 2046 cm^{-1} in anhydrous toluene solution from Figure 152.

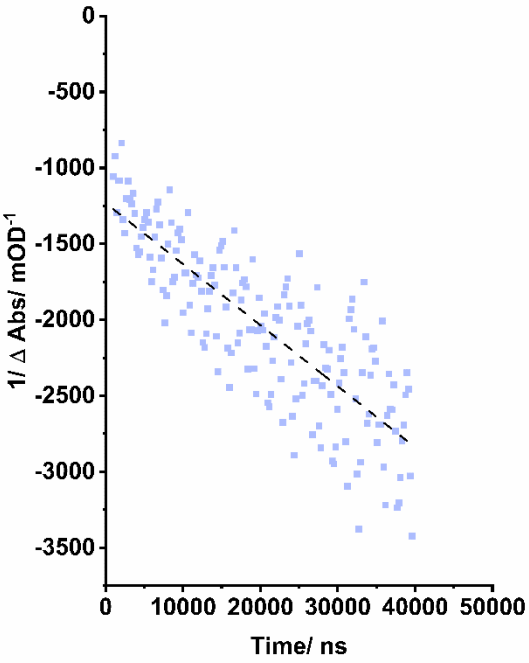

Figure 241. Plot of time (x axis) versus 1/ Δ absorption (y axis) to determine the second order rate constant for the recovery of the ground state bleach of $[Mn_2(CO)_{10}]$ at 2046 cm^{-1} in anhydrous acetonitrile solution from Figure 153.

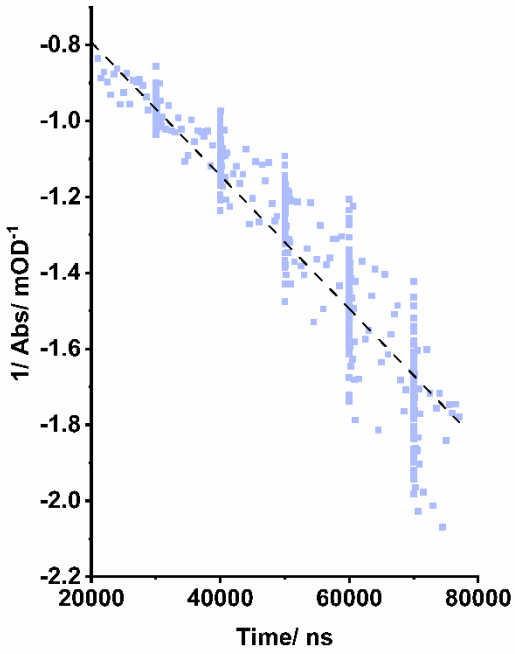

Figure 242. Plot of time (x axis) versus 1/ Δ absorption (y axis) to determine the second order rate constant for the recovery of the ground state bleach of $[Mn_2(CO)_{10}]$ at 2046 cm^{-1} in anhydrous THF solution from Figure 236.

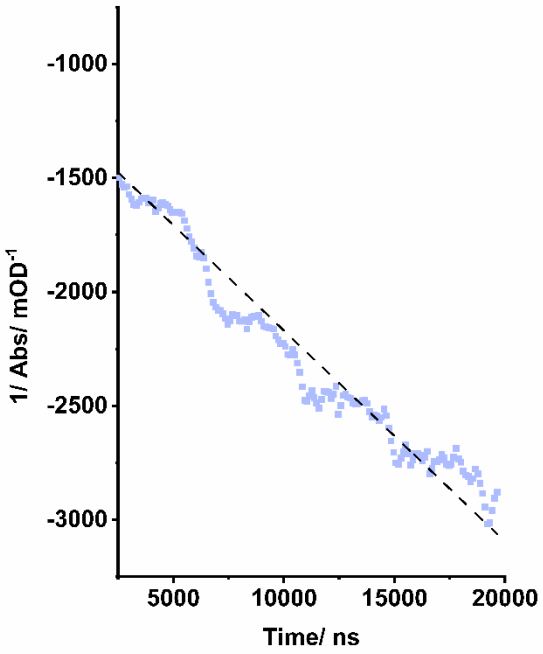

Figure 243. Plot of time (x axis) versus 1/ Δ absorption (y axis) to determine the second order rate constant for the recovery of the ground state bleach of $[Mn_2(CO)_{10}]$ at 2046 cm^{-1} in anhydrous 1,4-dioxane solution from Figure 237.

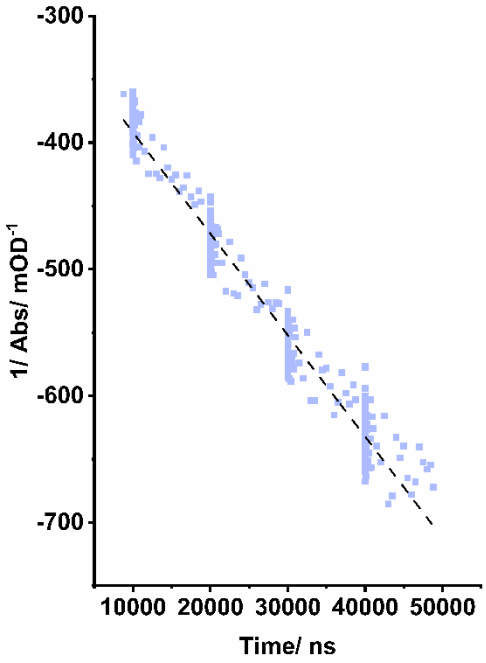

Figure 244. Plot of time (x axis) versus 1/ Δ absorption (y axis) to determine the second order rate constant for the recovery of the ground state bleach of $[Mn_2(CO)_{10}]$ at 2046 cm^{-1} in anhydrous DMSO solution from Figure 238.

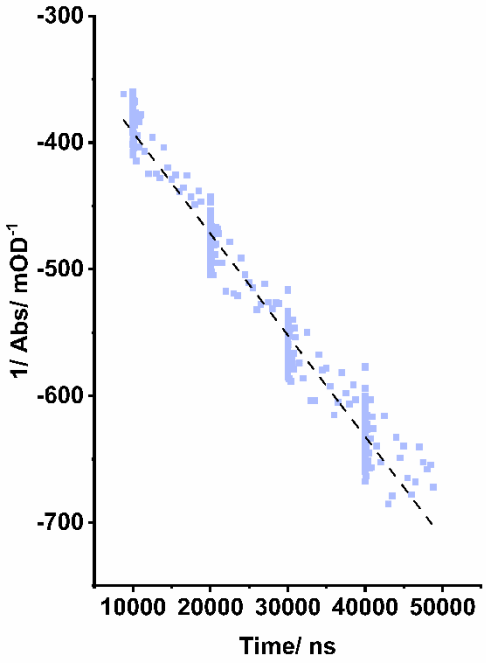

Figure 245. Plot of time (x axis) versus 1/ Δ absorption (y axis) to determine the second order rate constant for the recovery of the ground state bleach of $[Mn_2(CO)_{10}]$ at 2046 cm^{-1} in anhydrous styrene solution Figure 239.

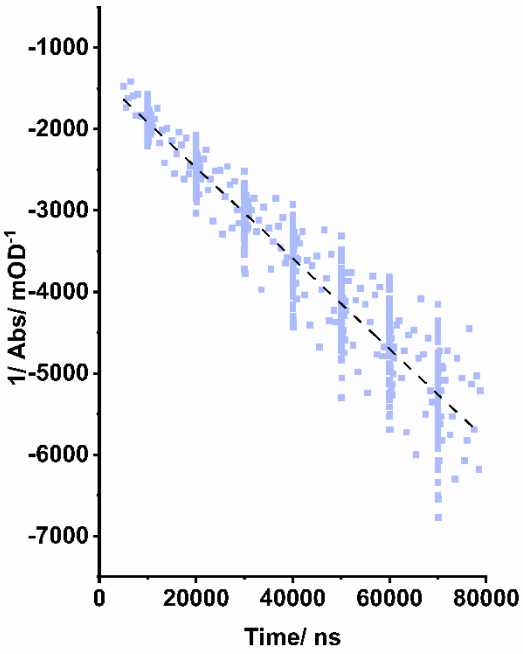

Figure 246. Plot of time (x axis) versus 1/ Δ absorption (y axis) to determine the second order rate constant for the recovery of the ground state bleach of $[Mn_2(CO)_{10}]$ at 2046 cm^{-1} in anhydrous cyclohexane solution.

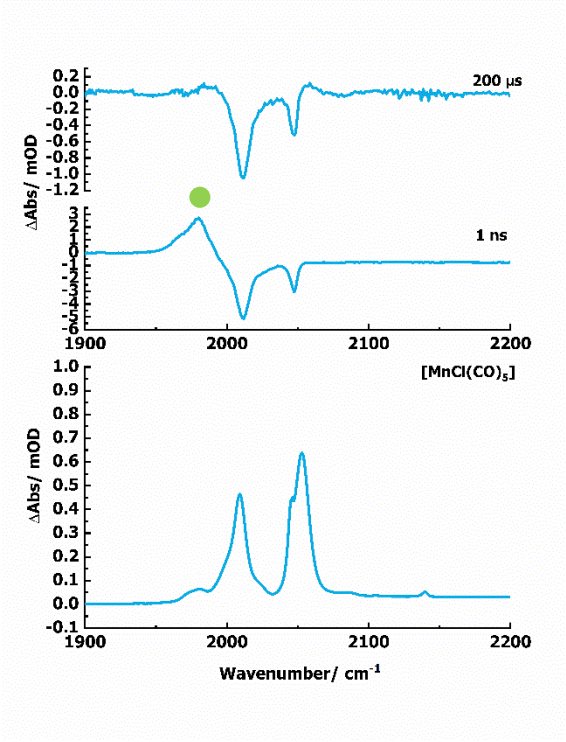

Figure 247. Top: TRIR spectra of $[Mn_2(CO)_{10}]$ in anhydrous chlorobenzene solution exciting with a 400 nm pump wavelength under an atmosphere of N_2 at selected pump-probe delays. **241** denoted by denoted by green circles. Bottom: FTIR spectrum of $[MnCl(CO)_5]$ in chlorobenzene solution.

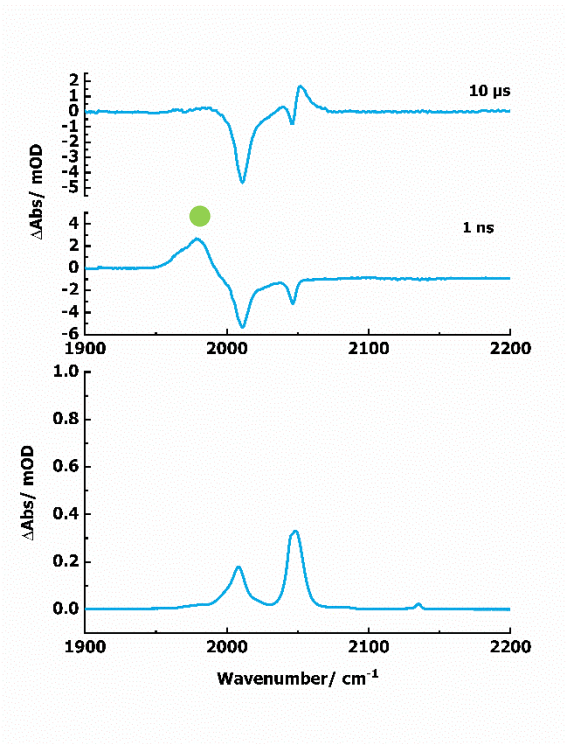

Figure 248. Top: TRIR spectra of $[Mn_2(CO)_{10}]$ in anhydrous bromobenzene solution exciting with a 400 nm pump wavelength under an atmosphere of N_2 at selected pump-probe delays. **241** denoted by denoted by green circles. Bottom: FTIR spectrum of $[MnBr(CO)_5]$ in brombenzene solution.

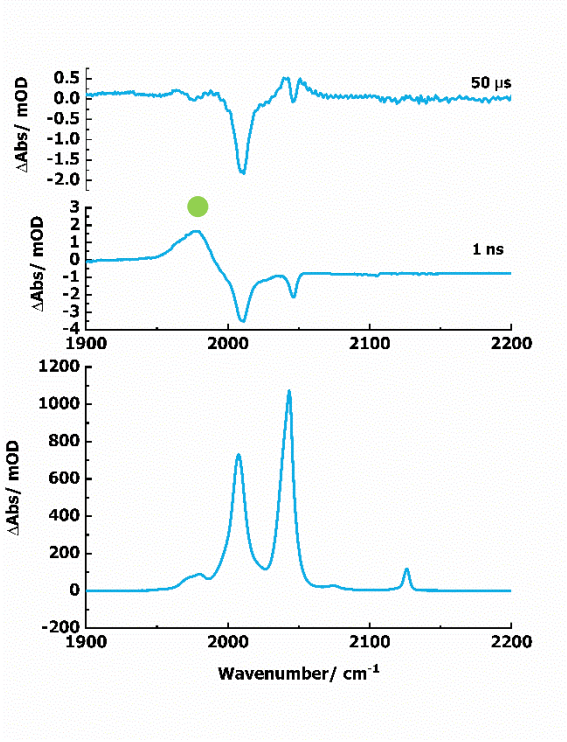

Figure 249. Top: TRIR spectra of $[Mn_2(CO)_{10}]$ in anhydrous iodobenzene solution exciting with a 400 nm pump wavelength under an atmosphere of N_2 at selected pump-probe delays. **241** denoted by denoted by green circles. Bottom: FTIR specrum of $[MnI(CO)_5]$ in iodobenzene solution.

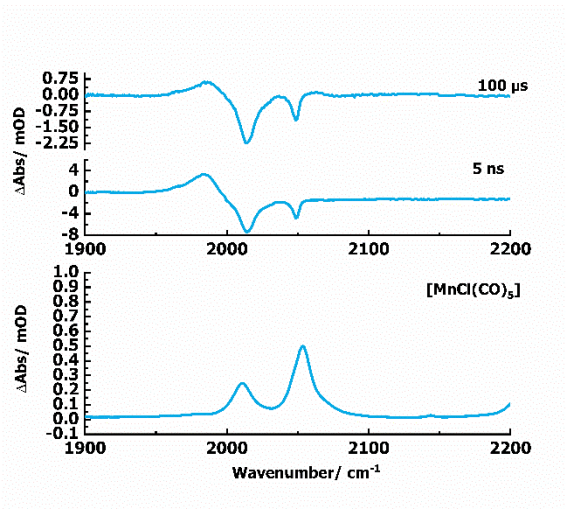

Figure 250. Top: TRIR spectra of $[Mn_2(CO)_{10}]$ in anhydrous chloroform solution exciting with a 400 nm pump wavelength under an atmosphere of N_2 at selected pump-probe delays. **241** denoted by denoted by green circles. Bottom: FTIR spectrum of $[MnCl(CO)_5]$ in chloroform solution.

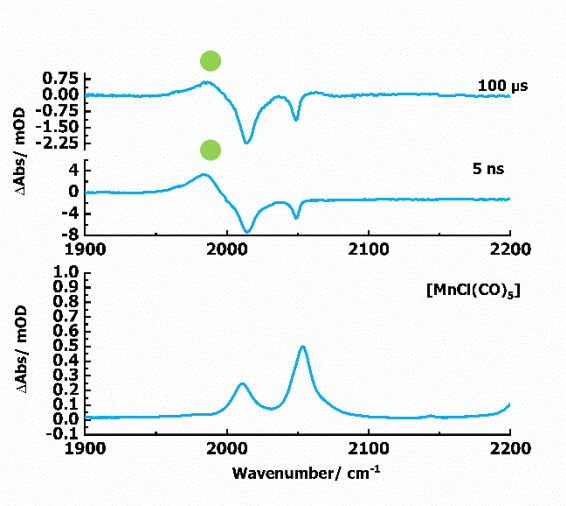

Figure 251. Top: TRIR spectra of $[Mn_2(CO)_{10}]$ in anhydrous chlorohexane solution exciting with a 400 nm pump wavelength under an atmosphere of N_2 at selected pump-probe delays. **241** denoted by denoted by green circles. Bottom: FTIR spectrum of $[MnCl(CO)_5]$ in chlorohexane solution.

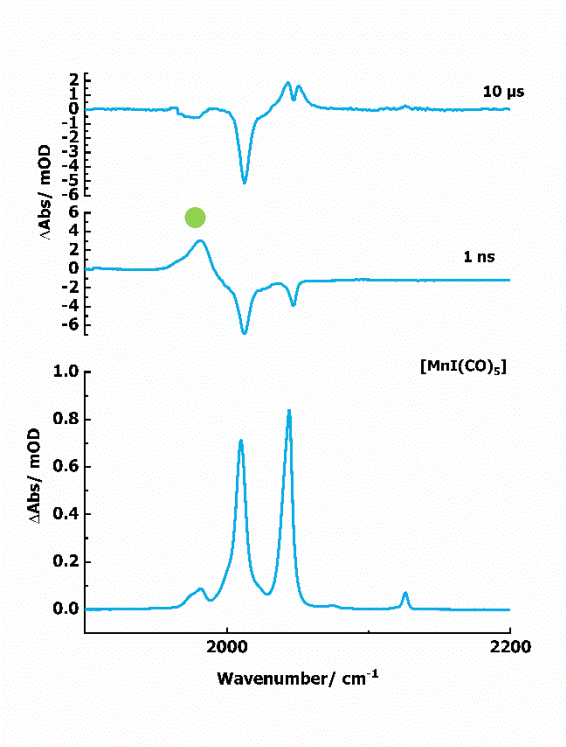

Figure 252. Top: TRIR spectra of $[Mn_2(CO)_{10}]$ in anhydrous iodohexane solution exciting with a 400 nm pump wavelength under an atmosphere of N_2 at selected pump-probe delays. **241** denoted by denoted by green circles. Bottom: FTIR spectrum of $[MnI(CO)_5]$ in iodohexane soltuion.

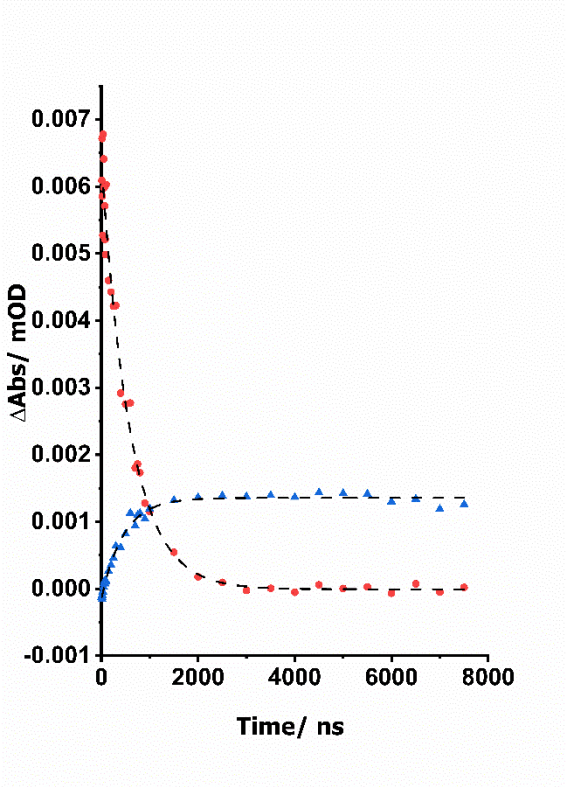

Figure 253. Kinetics for halide abstraction in anhydrous ethyl 4-Iodobenzoate solution. $[Mn_2(CO)_{10}]$ in ethyl 4-iodobenzene solution under an atmosphere of N_2 excited with a pump wavelength of 400 nm.

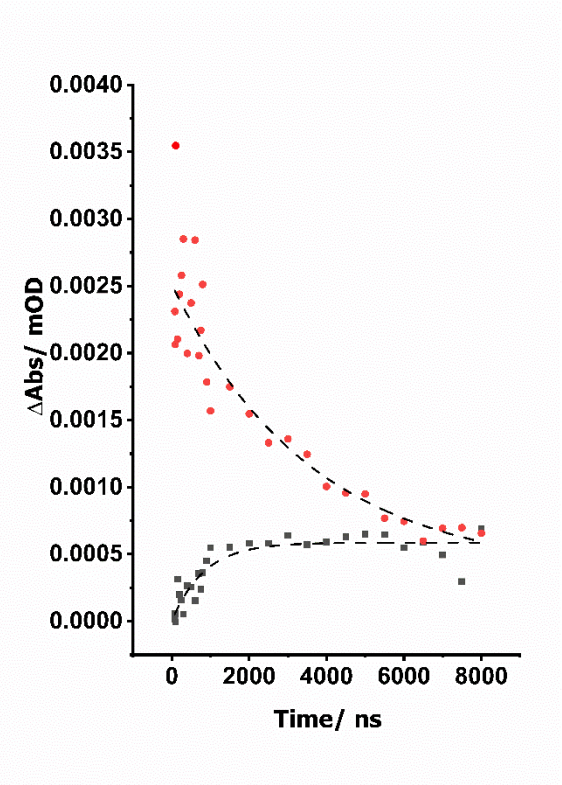

Figure 254. Kinetics for halide abstraction in anhydrous ethyl 4-bromobenzoate solution. $[Mn_2(CO)_{10}]$ in ethyl 4-bromobenzene solution under an atmosphere of N_2 excited with a pump wavelength of 400 nm.

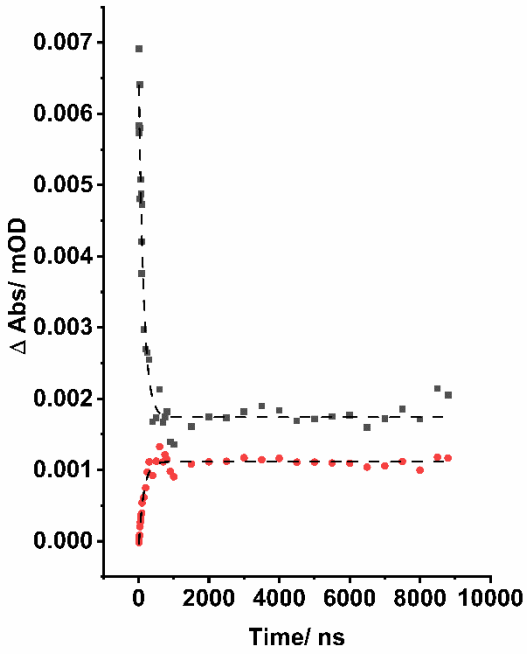

Figure 255. Kinetics for halide abstraction in anhydrous ethyl 4-chlorobenzoate solution. $[Mn_2(CO)_{10}]$ in ethyl 4-chlorobenzene solution under an atmosphere of N_2 excited with a pump wavelength of 400 nm.

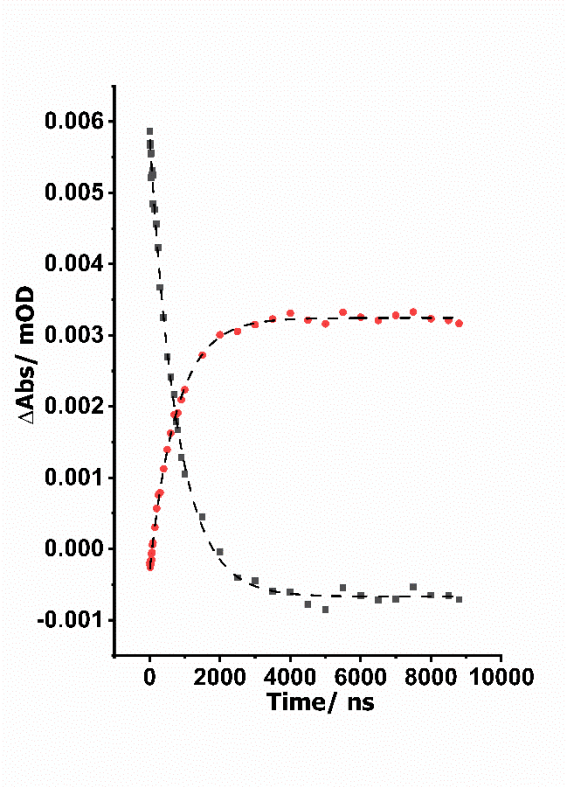

Figure 256. Kinetics for halide abstraction in anhydrous bromohexane solution. $[Mn_2(CO)_{10}]$ in bromohexane solution under an atmosphere of N_2 excited with a pump wavelength of 400 nm.

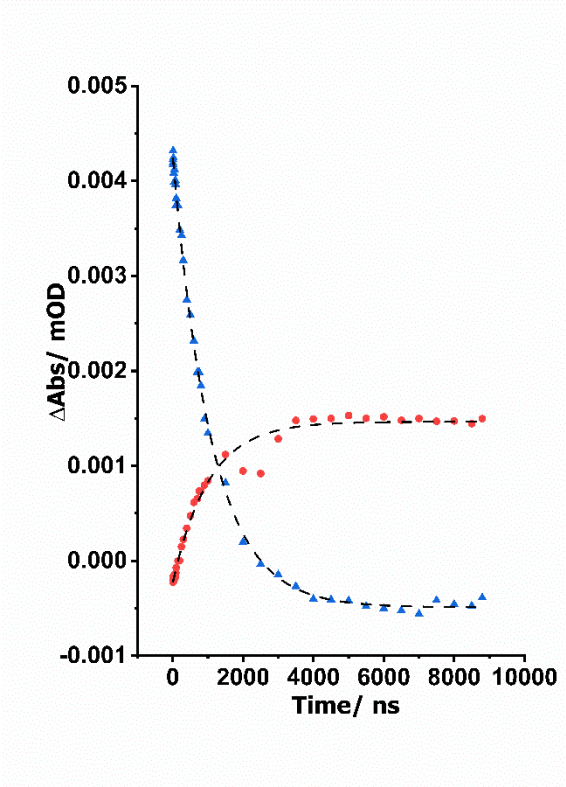

Figure 257. Kinetics for halide abstraction in anhydrous iodohexane solution. $[Mn_2(CO)_{10}]$ in 4-iodohexane solution under an atmosphere of N_2 excited with a pump wavelength of 400 nm.

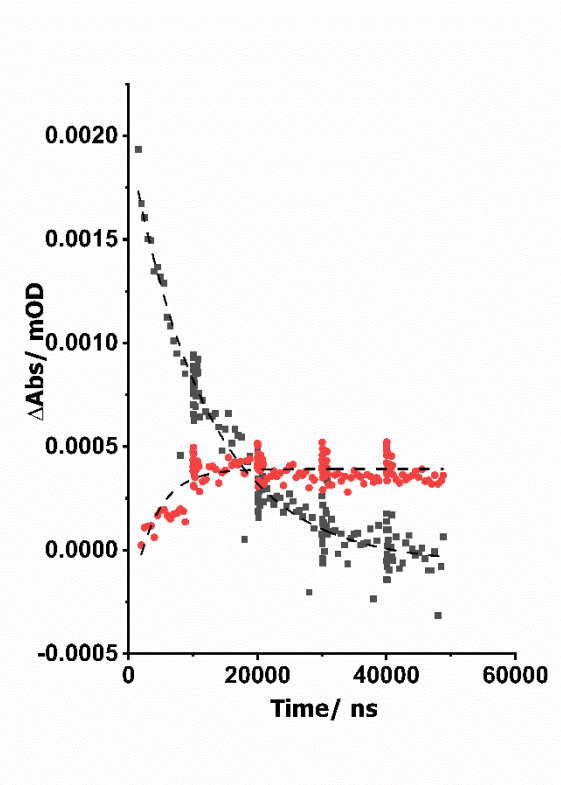

Figure 258. Kinetics for halide abstraction in anhydrous iodobenzene solution. $[Mn_2(CO)_{10}]$ in iodobenzene solution under an atmosphere of N_2 excited with a pump wavelength of 400 nm.

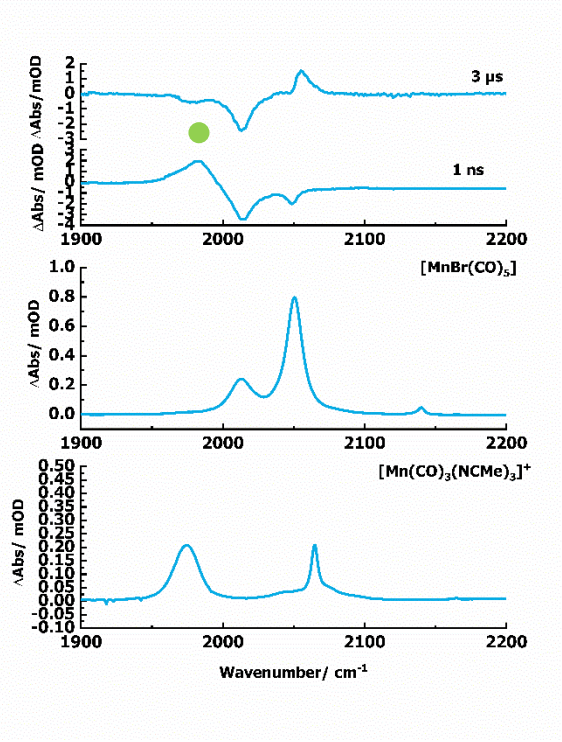

Figure 259. Top: TRIR spectra of $[Mn_2(CO)_{10}]$ in 0.2 mL anhydrous bromobenzene and 9.8 mL anhydrous acetonitrile solution exciting with a 400 nm pump wavelength under an atmosphere of N_2 at selected pump-probe delays. **241** denoted by denoted by green circles. Middle: FTIR spectrum of $[MnBr(CO)_5]$ in acetonitrile solution. Bottom: FTIR spectrum of $[MnBr(CO)_5]$ in acetonitrile solution.

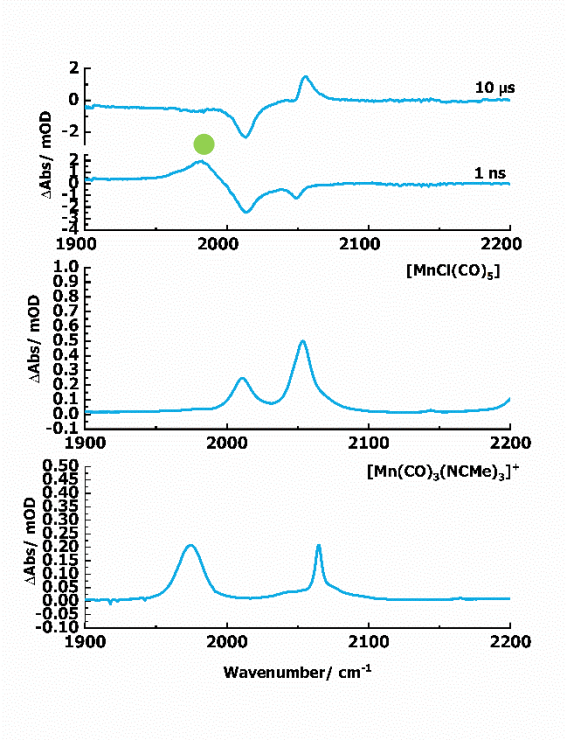

Figure 260. Top: TRIR spectra of $[Mn_2(CO)_{10}]$ in 0.2 mL anhydrous chlorobenzene and 9.8 mL anhydrous acetonitrile solution exciting with a 400 nm pump wavelength under an atmosphere of N_2 at selected pump-probe delays. **241** denoted by denoted by green circles. Middle: FTIR spectrum of $[MnCl(CO)_5]$ in acetonitrile solution. Bottom: FTIR spectrum of $[MnCl(CO)_5]$ in acetonitrile solution.

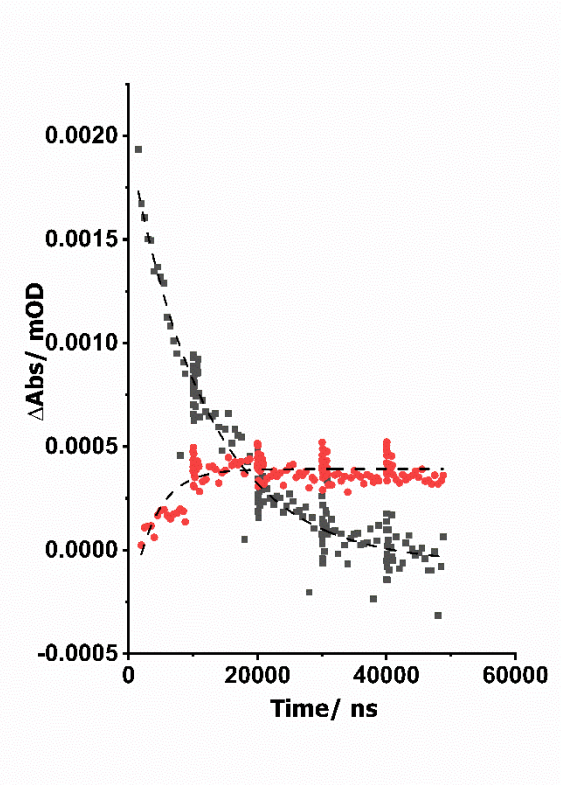

Figure 261. Kinetics for reactivity of **214** in 0.2 mL of anhydrous bromobenzene and 9.8 mL anhydrous acetonitrile solution. $[Mn_2(CO)_{10}]$ in 98% acetonitrile, 2% bromobenzene solution under an atmosphere of N_2 excited with a pump wavelength of 400 nm.

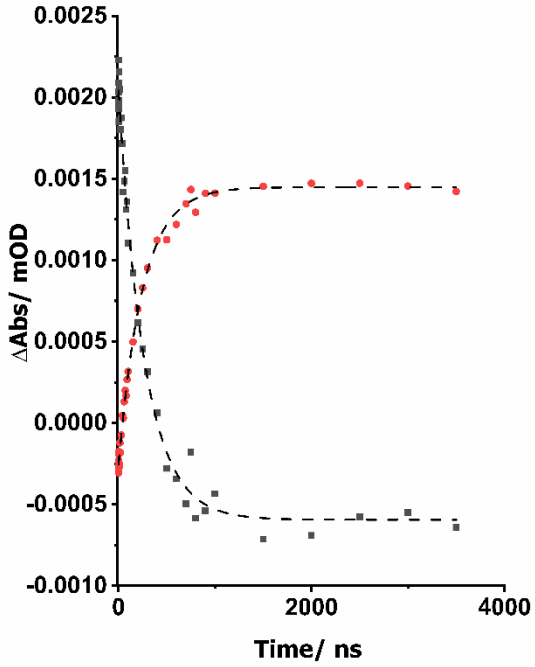

Figure 262. Kinetics for reactivity of **214** in 0.2 mL of anhydrous chlorobenzene and 9.8 mL anhydrous acetonitrile solution. $[Mn_2(CO)_{10}]$ in 98% acetonitrile, 2% chlorobenzene solution under an atmosphere of N_2 excited with a pump wavelength of 400 nm.

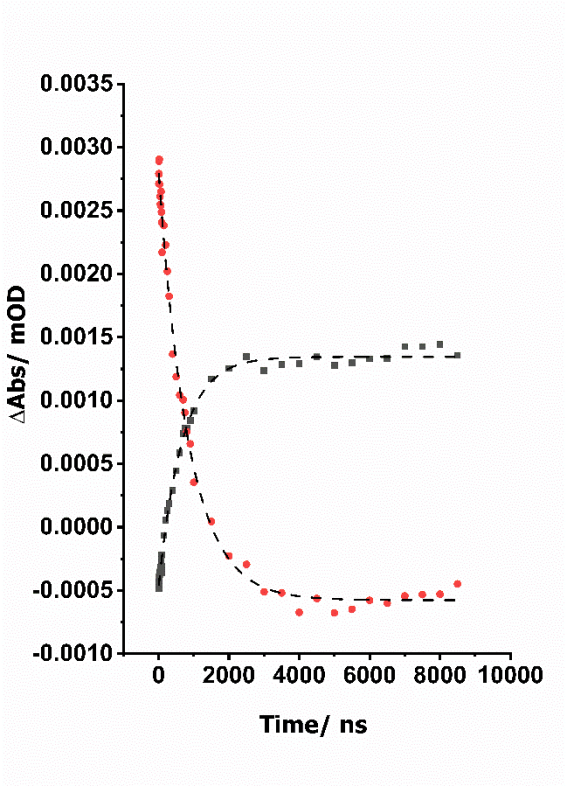

Figure 263. Kinetics for reactivity of **214** in 0.2 mL of anhydrous chloroform and 9.8 mL anhydrous acetonitrile solution. $[Mn_2(CO)_{10}]$ in 98% acetonitrile, 2% chloroform solution under an atmosphere of N_2 excited with a pump wavelength of 400 nm.

355 nm Pump Wavelength Data

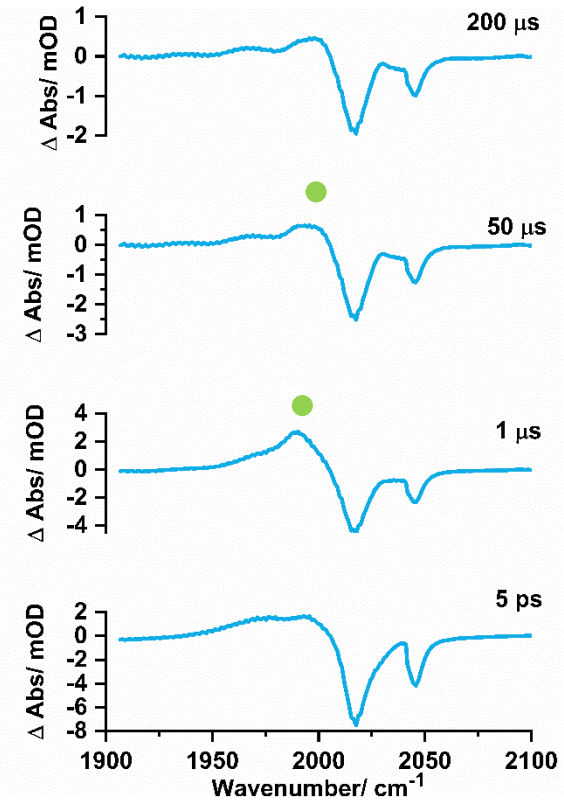

Figure 264. TRIR spectra of $[Mn_2(CO)_{10}]$ in anhydrous *n*-heptane solution exciting with a 355 nm pump wavelength under an atmosphere of N_2 at selected pump-probe delays. **241** denoted by denoted by green circles.

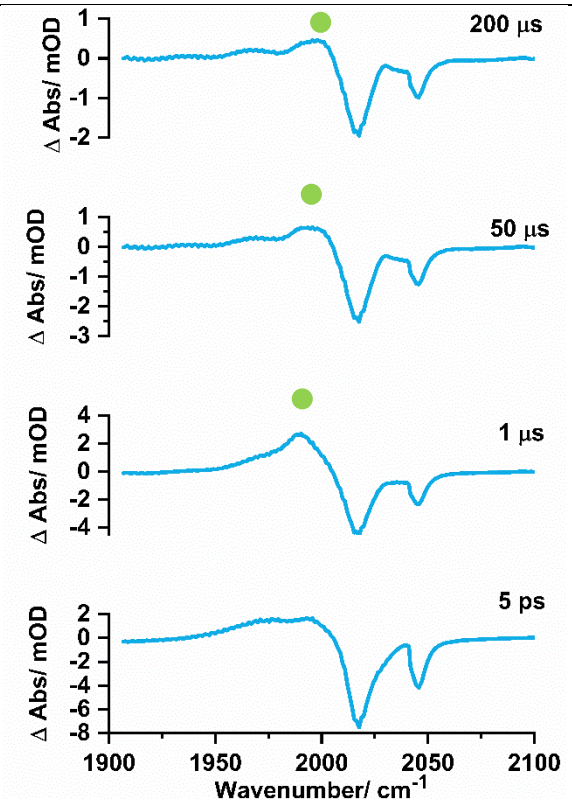

Figure 265. TRIR spectra of $[Mn_2(CO)_{10}]$ in anhydrous acetonitrile solution exciting with a 355 nm pump wavelength under an atmosphere of N_2 at selected pump-probe delays. **241** denoted by denoted by green circles.

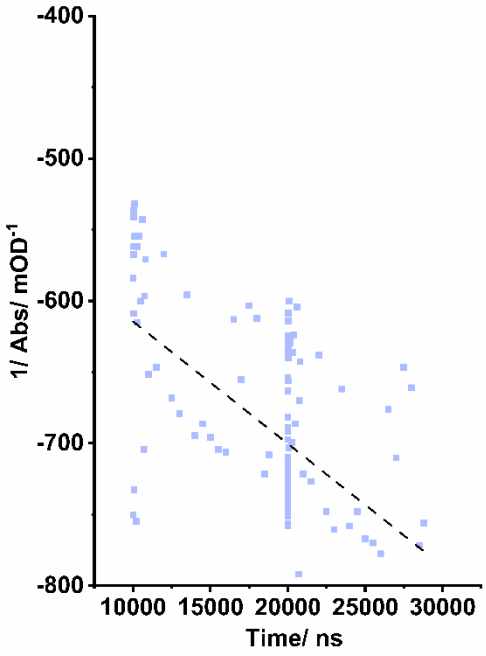

Figure 266. Plot of time (x axis) versus 1/ Δ absorption (y axis) to determine the second order rate constant for the recovery of the ground state bleach of $[Mn_2(CO)_{10}]$ at 2046 cm^{-1} in anhydrous acetonitrile solution.

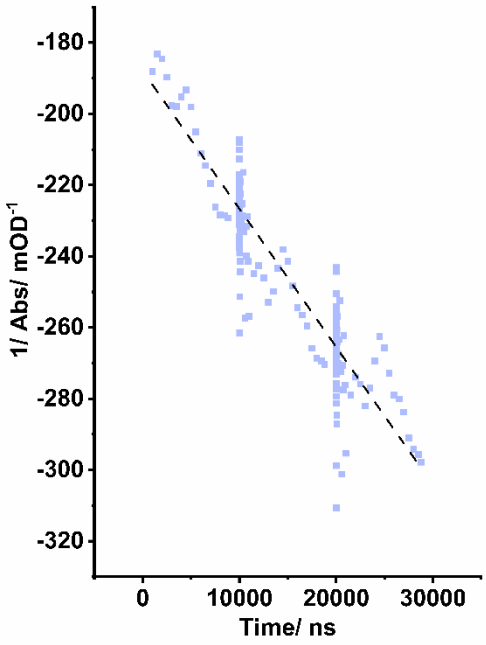

Figure 267. Plot of time (x axis) versus 1/ Δ absorption (y axis) to determine the second order rate constant for the recovery of the ground state bleach of $[Mn_2(CO)_{10}]$ at 2046 cm^{-1} in anhydrous *n*-heptane solution.

Abbreviations

Ac	acetyl
Ar	arene
Atm	atmosphere
ATR	attenuated total reflectance
Bn	benzyl
b.p.	boiling point
Bu	butyl
C	Celsius
Ca.	*circa*
CLF	Central Laser Facility
CMD	concerted metalation deprotonation
Cy	cyclohexyl
Cp	cyclopentadienyl
Cp’	methylyclopentadienyl
DFT	density functional theory
DMSO	dimethylsulphoxide
ESI	electrospray ionisation
Et	ethyl
Equiv.	equivalent
fac	*facial*
FT	Fourier transform
GC	gas chromatography
h	hours
Hz	hertz

i-	*iso*
IR	infrared
k	rate constant
L	ligand
LIFDI	liquid introduced field desorption ionisation
Lit.	literature
m-	*meta*
Me	methyl
mer	*meridional*
MHz	megahertz
mOD	milli optical density
MS	mass spectrometry
NHC	*N*-heterocyclic carbene
Mw	molecular weight
N/A	not applicable
NCMe	acetonitrile
NMR	nuclear magnetic resonance
o-	*ortho*
OPA	optical parametric amplifier
OTf	triflate
p-	*para*
Ph	phenyl
pin	pinacolato
PMP	paramethoxyphenyl
ppm	parts per million

Pr	propyl
ppy	2-phenylpyridine
RAL	Rutherford Appleton Laboratory
R_f	retention factor
rt	room temperature
S	solvent
t-	*tertiary*
TA	transient absorption
THF	tetrahydrofuran
TLC	thin layer chromatography
Tol	tolyl
TRIR	time-resolved infrared
TR^MPS	time-resolved multiple probe spectroscopy
UV	ultraviolet
vaccuo	vacuum
Vis	visible

References

[1] R. Cano, K. Mackey, G. P. McGlacken, *Catal. Sci. Technol.* **2018**, *8*, 1251–1266.

[2] C. Wang, *Synlett* **2013**, *24*, 1606–1613.

[3] J. F. Hartwig, *J. Am. Chem. Soc.* **2016**, *138*, 2–24.

[4] G. Rouquet, N. Chatani, *Angew. Chem. Int. Ed.* **2013**, *52*, 11726–11743.

[5] S. Murahashi, *J. Am. Chem. Soc.* **1955**, *77*, 6403–6404.

[6] T. W. Lyons, M. S. Sanford, *Chem. Rev.* **2010**, *110*, 1147–1169.

[7] L. Ackermann, R. Vicente, A. R. Kapdi, *Angew. Chem. Int. Ed.* **2009**, *48*, 9792–9826.

[8] N. V. Tzouras, I. K. Stamatopoulos, A. T. Papastavrou, A. A. Liori, G. C. Vougioukalakis, *Coord. Chem. Rev.* **2017**, *343*, 25–138.

[9] J. R. Carney, B. R. Dillon, S. P. Thomas, *European J. Org. Chem.* **2016**, 3912–3929.

[10] I. Bauer, H. Knolker, *Chem. Rev.* **2015**, *115*, 3170–3387.

[11] S. Bhunia, G. G. Pawar, S. V. Kumar, Y. Jiang, *Angew. Chem. Int. Ed.* **2017**, *56*, 16136–16179.

[12] S. Z. Tasker, E. A. Standley, T. F. Jamison, *Nature* **2014**, *509*, 299–309.

[13] G. Pototschnig, N. Maulide, M. Schn, *Eur. J. Chem.* **2017**, *23*, 9206–9232.

[14] J. P. Kleiman, M. Dubeck, *J. Am. Chem. Soc.* **1961**, *85*, 1961–1962.

[15] J. A. Labinger, J. E. Bercaw, *Nature* **2002**, *417*, 507–514.

[16] D. T. Hurd, G. W. Sentell, F. J. Norton, *J. Am. Chem. Soc.* **1949**, *1723*, 1899.

[17] K. N. Anisimov, A. A. Ioganson, N. E. Kolobova, *Russ. Chem. Rev.* **1968**, *37*, 184–197.

[18] W. Hieber, G. Wagner, *Zeitschrift für Naturforsch. B* **1957**, *12*, 478–479.

[19] W. Hieber, G. Wagner, *Justus Liebigs Ann. Chem.* **1958**, *618*, 24–30.

[20] M. Bruce, M. Z. Iqbal, F. G. A. Stone, *J. Chem. Soc.* **1970**, 3204–3209.

[21] R. F. Heck, *J. Am. Chem. Soc.* **1967**, *90*, 313–317.

[22] M. Bruce, *Angew. Chem. Int. Ed. Engl.* **1977**, *16*, 73–86.

[23] R. L. Bennett, M. I. Bruce, F. G. A. Stone, *J. Organomet. Chem.* **1975**, *94*, 65–74.

[24] A. Suarez, J. Manuel, V. Maria, T. Pereira, E. Gayoso, *J. Organomet. Chem.* **1987**, *335*, 359–363.

[25] W. Tully, L. Main, B. K. Nicholson, *J. Organomet. Chem.* **2005**, *690*, 3348–3356.

[26] N. P. Robinson, G. J. Depree, R. W. De Wit, L. Main, B. K. Nicholson, *J. Organomet. Chem.* **2005**, *690*, 3827–3837.

[27] N. P. Robinson, L. Main, B. K. Nicholson, *J. Organomet. Chem.* **1988**, *349*, 209–218.

[28] G. J. Depree, L. Main, B. K. Nicholson, *J. Organomet. Chem.* **1998**, *551*, 281–291.

[29] W. J. Grigsby, L. Main, B. K. Nicholson, *Bull. Chem. Soc. Jpn.* **1990**, *63*, 649–651.

[30] L. A. Hammarback, I. P. Clark, I. V Sazanovich, M. Towrie, A. Robinson, F. Clarke, S. Meyer, I. J. S. Fairlamb, J. M. Lynam, *Nat. Catal.* **2018**, *1*, 830–840.

[31] P. Gandeepan, T. Müller, D. Zell, G. Cera, S. Warratz, L. Ackermann, *Chem. Rev.* **2019**, *119*, 2192–2452.

[32] L. H. P. Gommans, L. Main, B. K. Nicholson, *Chem. Commun.* **1987**, 761–762.

[33] R. C. Cambie, M. R. Metzler, P. S. Rutledge, P. D. Woodgate, *J. Organomet. Chem.* **1990**, *381*, 26–30.

[34] R. C. Cambie, M. R. Metzler, P. S. Rutledge, P. D. Woodgate, *J. Organomet. Chem.* **1990**, *398*, 24–26.

[35] L. S. Liebeskind, J. R. Gasdaska, J. S. McCallum, S. J. Tremont, *J. Org. Chem.* **1989**, *54*, 669–677.

[36] S. Onaka, N. Furuichi, Y. Tatematsu, *Bull. Chem. Soc. Jpn.* **1987**, *60*, 2280–2282.

[37] N. P. Robinson, L. Main, B. K. Nicholson, *J. Organomet. Chem.* **1989**, *364*, 37–39.

[38] W. J. Grigsby, L. Main, B. K. Nicholson, *Organometallics* **1993**, *12*, 397–407.

[39] W. Tully, L. Main, B. K. Nicholson, *J. Organomet. Chem.* **2001**, *633*, 162–172.

[40] W. Tully, L. Main, B. K. Nicholson, *J. Organomet. Chem.* **1996**, *507*, 103–115.

[41] W. Liu, L. Ackermann, *ACS Catal.* **2016**, *6*, 3743–3752.

[42] Y. Hu, B. Zhou, C. Wang, *Acc. Chem. Res.* **2018**, *51*, 816–827.

[43] A. Suárez, F. Faraldo, J. M. Vila, H. Adams, A. Fernández, M. López-Torres, J. J. Fernández, *J. Organomet. Chem.* **2002**, *656*, 270–273.

[44] N. P. Yahaya, K. M. Appleby, M. Teh, C. Wagner, E. Troschke, J. T. W. Bray, S. B. Duckett, L. A. Hammarback, J. S. Ward, J. Milani, N. E. Pridmore, A. C. Whitwood, J. M. Lynam, I. J. S. Fairlamb, *Angew. Chem. Int. Ed.* **2016**, *55*, 12455–12459.

[45] Y. Kuninobu, Y. Nishina, T. Takeuchi, K. Takai, *Angew. Chem. Int. Ed.* **2007**, *46*, 6518–6520.

[46] B. Zhou, H. Chen, C. Wang, *J. Am. Chem. Soc.* **2013**, *135*, 1264–1267.

[47] J. Roger, A. L. Gottumukkala, H. Doucet, *ChemCatChem* **2010**, *2*, 20–40.

[48] W. Liu, J. Bang, Y. Zhang, L. Ackermann, *Angew. Chem. Int. Ed.* **2015**, *54*, 14137–14140.

[49] L. Shi, X. Zhong, H. She, Z. Lei, F. Li, *Chem. Commun.* **2015**, *51*, 7136–7139.

[50] Q. Lu, S. Greßies, F. J. R. Klauck, F. Glorius, *Angew. Chem. Int. Ed.* **2017**, *56*, 6660–6664.

[51] L. A. Hammarback, A. Robinson, J. M. Lynam, I. J. S. Fairlamb, *J. Am. Chem. Soc.* **2019**, *141*, 2316–2328.

[52] Y. F. Liang, L. Massignan, W. Liu, L. Ackermann, *Eur. J. Chem.* **2016**, *22*, 14856–14859.

[53] S. Wu, Q. Yang, Q. Hu, Y. Wang, L. Chen, H. Zhang, L. Wu, J. Li, *Org. Chem. Front.* **2018**, *5*, 2852–2855.

[54] S. H. Cai, L. Ye, D. X. Wang, Y. Q. Wang, L. J. Lai, C. Zhu, C. Feng, T. P. Loh, *Chem. Commun.* **2017**, *53*, 8731–8734.

[55] Z. Ruan, N. Sauermann, E. Manoni, L. Ackermann, *Angew. Chem. Int. Ed.* **2017**, *56*, 3172–3176.

[56] C. Wang, A. Wang, M. Rueping, *Angew. Chem. Int. Ed.* **2017**, *56*, 9935–9938.

[57] S. Y. Chen, X. L. Han, J. Q. Wu, Q. Li, Y. Chen, H. Wang, *Angew. Chem. Int. Ed.* **2017**,

56, 9939–9943.

[58] Y. Liang, L. Massignan, L. Ackermann, *ChemCatChem* **2018**, *10*, 2768–2772.

[59] S. L. Liu, Y. Li, J. R. Guo, G. C. Yang, X. H. Li, J. F. Gong, M. P. Song, *Org. Lett.* **2017**, *19*, 4042–4045.

[60] R. He, Z.-T. Huang, Q.-Y. Zheng, C. Wang, *Angew. Chem. Int. Ed.* **2014**, *53*, 4950–4953.

[61] W. Liu, D. Zell, M. John, L. Ackermann, *Angew. Chem. Int. Ed.* **2015**, *54*, 4092–4096.

[62] Q. Lu, S. Greßies, S. Cembellín, F. J. R. Klauck, C. G. Daniliuc, F. Glorius, *Angew. Chem. Int. Ed.* **2017**, *56*, 12778–12782.

[63] X. Kong, B. Xu, *Tetrahedron Lett.* **2020**, *61*, 151521.

[64] T. Liu, Y. Hu, Y. Yang, C. Wang, *CCS Chem.* **2020**, *3*, 749–757.

[65] S. Sueki, Z. Wang, Y. Kuninobu, *Org. Lett.* **2016**, *18*, 304–307.

[66] J. Huo, Y. Yang, C. Wang, *Org. Lett.* **2021**, *23*, 3384–3388.

[67] X. Kong, B. Xu, *Tetrahedron Lett.* **2020**, *61*, 151521.

[68] Y. Hu, C. Wang, *Sci. China Chem.* **2016**, *59*, 1301–1305.

[69] Y. F. Liang, R. Steinbock, L. Yang, L. Ackermann, *Angew. Chem. Int. Ed.* **2018**, *57*, 10625–10629.

[70] J. D. Firth, L. A. Hammarback, T. J. Burden, J. B. Eastwood, J. R. Donald, C. S. Horbaczewskyj, M. T. McRobie, A. Tramaseur, I. P. Clark, M. Towrie, A. Robinson, J. P. Krieger, J. M. Lynam, I. J. S. Fairlamb, *Eur. J. Chem.* **2021**, *27*, 3979–3985.

[71] M. Ciftci, M. A. Tasdelen, Y. Yagci, *Polym. Int.* **2016**, *65*, 1001–1014.

[72] K. Koumura, K. Satoh, M. Kamigaito, *Polym. J.* **2009**, *41*, 595–603.

[73] L. I. B. Haines, A. J. Poe, *Nature* **1967**, *215*, 699–701.

[74] A. D. Asandei, O. I. Adebolu, C. P. Simpson, *J. Am. Chem. Soc.* **2012**, *134*, 6080–6083.

[75] C. H. Bamford, C. A. Finch, *Trans. Faraday Soc* **1963**, *59*, 540–547.

[76] N. Huther, P. T. McGrail, A. F. Parsons, *European J. Org. Chem.* **2004**, 1740–1749.

[77] C. H. Bamford, S. U. Mullik, *Polymer* **1976**, *17*, 225–230.

[78] Z. Yan, X. A. Yuan, Y. Zhao, C. Zhu, J. Xie, *Angew. Chem. Int. Ed.* **2018**, *57*, 12906–12910.

[79] Y. Pang, G. Liu, C. Huang, X. Yuan, W. Li, J. Xie, *Angew. Chemie* **2020**, *132*, 12889–12894.

[80] D. Wang, Y. He, H. Dai, C. Huang, X. A. Yuan, J. Xie, *Chinese J. Chem.* **2020**, *38*, 1497–1502.

[81] D. Wang, J. Dong, W. Fan, X. A. Yuan, J. Han, J. Xie, *Angew. Chem. Int. Ed.* **2020**, *59*, 1–6.

[82] R. R. Behera, R. Ghosh, S. Panda, S. Khamari, B. Bagh, *Org. Lett.* **2020**, *22*, 3642–3648.

[83] K. Azouzi, A. Bruneau-Voisine, L. Vendier, J. B. Sortais, S. Bastin, *Catal. Commun.* **2020**, *142*, 106040.

[84] A. Jana, K. Das, A. Kundu, P. R. Thorve, D. Adhikari, B. Maji, *ACS Catal.* **2020**, *10*, 2615–2626.

[85] K. Azouzi, D. A. Valyaev, S. Bastin, J. B. Sortais, *Curr. Opin. Green Sustain. Chem.* **2021**, *31*, 100511.

[86] M. Schlagbauer, F. Kallmeier, T. Irrgang, R. Kempe, *Angew. Chem. Int. Ed.* **2019**, *131*, 1–7.

[87] K. Ganguli, A. Mandal, B. Sarkar, S. Kundu, *Tetrahedron* **2020**, *76*, 1–6.

[88] R. Van Putten, G. A. Filonenko, A. Gonzalez De Castro, C. Liu, M. Weber, C. Müller, L. Lefort, E. Pidko, *Organometallics* **2019**, *38*, 3187–3196.

[89] J. J. Turner, J. K. Burdett, R. N. Perutz, M. Poliakoff, *pure Appl. Chem.* **1977**, *49*, 271–285.

[90] J. Víchová, F. Hartl, A. Vlcek, *J. Am. Chem. Soc.* **1992**, *4*, 10903–10910.

[91] I. R. Farrell, P. Matousek, M. Towrie, A. W. Parker, D. C. Grills, M. W. George, A. Vlček, *Inorg. Chem.* **2002**, *41*, 4318–4323.

[92] G. M. Greetham, D. Sole, I. P. Clark, A. W. Parker, M. R. Pollard, M. Towrie, *Rev. Sci. Instrum.* **2012**, *83*, 103107.

[93] G. M. Greetham, P. M. Donaldson, C. Nation, I. V. Sazanovich, I. P. Clark, D. J. Shaw, A. W. Parker, M. Towrie, *Appl. Spectrosc.* **2016**, *70*, 645–653.

[94] L. A. Hammarback, B. J. Aucott, J. T. W. Bray, I. P. Clark, M. Towrie, A. Robinson, I. J. S. Fairlamb, J. M. Lynam, *J. Am. Chem. Soc.* **2021**, *143*, 1356–1364.

[95] B. J. Aucott, J. B. Eastwood, L. A. Hammarback, I. P. Clark, I. V Sazanovich, M. Towrie, J. S. Fairlamb, J. M. Lynam, *Dalt. Trans.* **2019**, *48*, 16426–16436.

[96] B. J. Aucott, A. K. Duhme-Klair, B. E. Moulton, I. P. Clark, I. V. Sazanovich, M. Towrie, L. A. Hammarback, I. J. S. Fairlamb, J. M. Lynam, *Organometallics* **2019**, *38*, 2391–2401.

[97] T. L. Snoeck, F. Grevels, D. J. Stufkens, A. Vlček, *Inorganica Chim. Acta* **1998**, *278*, 83–90.

[98] T. Lian, S. E. Bromberg, M. C. Asplund, H. Yang, C. B. Harris, *J. Phys. Chem.* **1996**, *100*, 11994–12001.

[99] R. N. Perutz, J. J. Turner, *J. Organomet. Chem.* **1975**, *97*, 4791–4800.

[100] J. W. Moore, R. M. Wellek, *J. Chem. Eng. Data* **1974**, *19*, 136–140.

[101] J. Polak, B. C. Lu, *Can. J. Chem.* **1973**, *51*, 4018–4023.

[102] Y. Wang, Y. Gong, X. Zheng, M. Zhou, *Chem. Phys. Lett.* **2006**, *431*, 13–18.

[103] N. Khoenkhoen, B. De Bruin, J. N. H. Reek, W. I. Dzik, *Eur. J. Inorg. Chem.* **2015**, *2015*, 567–598.

[104] J. a Banister, M. W. George, S. Grubert, S. M. Howdle, M. Jobling, F. P. a Johnson, S. L. Morrison, M. Poliakoff, U. S. I, J. R. West-well, *J. Organomet. Chem.* **1994**, *484*, 129–135.

[105] D. J. Darensbourg, D. Madrid, *Inorg. Chem.* **1974**, *13*, 1532–1534.

[106] W. A. King, X. L. Luo, B. L. Scott, G. J. Kubas, K. W. Zilm, *J. Am. Chem. Soc.* **1996**, *118*, 6782–6783.

[107] C. Perthuisot, M. Fan, W. D. Jones, *Organometallics* **1992**, *11*, 3622–3629.

[108] J. B. Eastwood, L. A. Hammarback, M. T. McRobie, I. P. Clark, M. Towrie, I. J. S. Fairlamb, J. M. Lynam, *Dalt. Trans.* **2020**, *49*, 5463–5470.

[109] G. I. Childs, C. S. Colley, J. Dyer, D. C. Grills, X. Z. Sun, J. Yang, M. W. George, *J. Chem. Soc. Dalt. Trans.* **2000**, *2*, 1901–1906.

[110] A. J. Cowan, P. Portius, H. K. Kawanami, O. S. Jina, D. C. Grills, X. Z. Sun, J. McMaster, M. W. George, *Proc. Natl. Acad. Sci. U. S. A.* **2007**, *104*, 6933–6938.

[111] R. Battino, T. Rettich, T. Tominaga, *J. Phys. Chem. ref. Data* **1984**, *13*, 567–597.

[112] T. Aneeja, M. Neetha, C. M. A. Afsina, G. Anilkumar, *Catal. Sci. Technol.* **2021**, *11*, 444–458.

[113] Y. Kuninobu, S. Sueki, N. Kaplaneris, L. Ackermann, *Manganese Catalysis*, The Royal Society Of Chemistry, **2021**.

[114] L. Anders Hammarback, A. Robinson, J. M. Lynam, I. J. S. Fairlamb, *Chem. Commun.* **2019**, *55*, 3211–3214.

[115] X. C. Huang, X. H. Yang, R. J. Song, J. H. Li, *J. Org. Chem.* **2014**, *79*, 1025–1031.

[116] C. Kornhaaß, J. Li, L. Ackermann, *J. Org. Chem.* **2012**, *77*, 9190–9198.

[117] T. Gerfaud, L. Neuville, J. Zhu, *Angew. Chem. Int. Ed.* **2009**, *48*, 572–577.

[118] R. Alajarín, C. Burgos, *Modern Heterocyclic Chemistry*, Wiley-VCH, Weinheim, **2011**.

[119] Y. Yoshida, T. Kurahashi, S. Matsubara, *Chem. Lett.* **2011**, *40*, 1140–1142.

[120] L. Peng, Y. C. Gao, *Synth. React. Inorg. Met. Chem.* **2004**, *34*, 1181–1190.

[121] L. A. Hammarback, J. B. Eastwood, T. J. Burden, C. J. Pearce, I. P. Clark, M. Towrie, A. Robinson, I. J. S. Fairlamb, J. M. Lynam, *Chem. Sci.* **2022**, *13*, 9902–9913.

[122] M. Wrighton, *Chem. Rev.* **1974**, *74*, 401–430.

[123] T. J. Meyer, J. V Caspar, *Chem. Rev.* **1985**, *85*, 187–218.

[124] D. R. Bidinosti, N. S. McIntyre, *Chem. Commun.* **1966**, *15*, 555.

[125] E. O. Fischer, E. Offhaus, J. Muller, D. Nothe, *Chem. Ber* **1972**, *105*, 3027.

[126] S. A. Hallock, A. Wojcicki, *J. Organomet. Chem* **1973**, *54*, 27.

[127] C. L. Kwan, J. K. Kochi, *J. Organomet. Chem* **1975**, *101*, 9.

[128] S. A. Fieldhouse, B. W. Fullam, G. W. Neilson, M. C. R. Symons, *J. Chem. Soc. D* **1974**, 567.

[129] A. Hudson, M. F. Lappert, B. K. Nicholson, *J. Organomet. Chem* **1975**, *92*, 11.

[130] J. A. Howard, J. R. Morton, K. F. Preston, *Chem. Phys. Lett.* **1981**, *83*, 81–83.

[131] S. P. Church, M. Poliakoff, J. A. Timney, J. J. Turner, *J. Am. Chem. Soc.* **1981**, *103*, 7515–7520.

[132] R. A. Levenson, H. B. Gray, G. P. Ceasar, *J. Am. Chem. Soc.* **1970**, *12*, 3653–3658.

[133] J. L. Hughey, C. P. Anderson, T. J. Meyer, *J. Org. Chem.* **1977**, *125*, 49–52.

[134] W. L. Waltz, O. Hackelberg, L. M. Dorfman, A. Wojcicki, *J. Am. Chem. Soc.* **1978**, *100*, 7259–7264.

[135] H. Huber, E. P. Kündig, G. A. Ozin, A. J. Poe, *J. Am. Chem. Soc.* **1975**, *97*, 308–314.

[136] J. Z. Zhang, C. B. Harris, *J. Chem. Phys.* **1991**, *95*, 4024–4032.

[137] T. Kobayashi, H. Ohtani, H. Noda, H. Yamazaki, S. Teratani, K. Yasufuku, *Organometallics* **1986**, *5*, 110–113.

[138] J. C. Owrutsky, A. P. Baronavski, *J. Chem. Phys.* **1996**, *2*, 9864–9873.

[139] S. P. Church, H. Hermann, F. Grevels, K. Schaff, *J. Chem. Soc, Chem. Commun.* **1984**, 785–786.

[140] I. Fairlamb, J. D. Firth, L. A. Hammarback, T. J. Burden, J. B. Eastwood, J. R. Donald, C. S. Horbaczewskyj, M. T. McRobie, A. Tramaseur, I. P. Clark, M. Towrie, A. Robinson, J.-P. Krieger, J. M. Lynam, *Chem. – A Eur. J.* **2021**, *27*, 3979–3985.

[141] T. A. Seder, S. P. Church, E. Weitz, *J. Am. Chem. Soc.* **1986**, *108*, 7518–7524.

[142] R. A. Levenson, H. B. Gray, *J. Am. Chem. Soc.* **1975**, *21*, 6042–6047.

[143] H. Yesaka, S. Nagakura, T. Kobayashi, K. Yasufuku, *J. Am. Chem. Soc.* **1983**, *105*, 6249–6252.

[144] L. J. Rothberg, N. J. Cooper, K. S. Peters, V. Vaida, *J. Am. Chem. Soc.* **1982**, *104*, 3536–3537.

[145] A. F. Hepp, M. S. Wrighton, *J. Am. Chem. Soc.* **1983**, *105*, 5934–5935.

[146] I. R. Dunkin, P. Harter, C. J. Shields, *J. Am. Chem. Soc.* **1984**, *106*, 7248–7249.

[147] T. A. Seder, S. P. Church, E. Weitz, **1986**, *108*, 1084–1086.

[148] D. A. Prinslow, V. Vaida, *J. Am. Chem. Soc.* **1987**, *109*, 5097–5100.

[149] D. A. Steinhurst, A. P. Baronavski, J. C. Owrutsky, *Chem. Phys. Lett.* **2002**, *361*, 513–519.

[150] A. Waldman, S. Ruhman, S. Shaik, G. N. Sastry, *Chem. Phys. Lett.* **1994**, *230*, 110–116.

[151] S. Kyu Kim, S. Pedersen, A. H. Zewail, *Chem. Phys. Lett.* **1995**, *233*, 500–508.

[152] D. Drew, D. J. Darensbourg, M. Y. Darensbourg, *Inorg. Chem.* **1974**, *14*, 1579–1584.

[153] H. Cho, K. Hong, M. L. Strader, J. H. Lee, R. W. Schoenlein, N. Huse, T. K. Kim, *Inorg. Chem.* **2016**, *55*, 5895–5903.

[154] C. Reichardt, T. Welton, in *Solvents Solvent Eff. Org. Chem.*, John Wiley & Sons, Ltd, **2010**, pp. 7–64.

[155] D. M. Thompson, M. Bengough, M. C. Baird, *Organometallics* **2002**, *21*, 4762–4770.

[156] V. Riera, J. Gimeno, M. Laguna, M. P. Gamasa, *J. Chem. Soc. D* **1979**, *6*, 996–1002.

[157] Y.-R. Luo, *Comprehensive Handbook of Chemical Bond Energies*, Taylor & Francis Group, Baton Rouge, **2007**.

[158] A. E. Stiegman, D. R. Tyler, *Inorg. Chem.* **1984**, *23*, 527–529.

[159] W. Liu, S. C. Richter, Y. Zhang, L. Ackermann, *Angew. Chem. Int. Ed.* **2016**, *55*, 7747–7750.

[160] T. Jia, C. Wang, *ChemCatChem* **2019**, *11*, 5292–5295.

[161] W. C. Still, M. Kahn, A. Mitra, *J. Org. Chem.* **1978**, *43*, 2923–2925.

[162] O. v Dolomanov, L. J. Bourhis, R. J. Gildea, J. A. K. Howard, H. Puschmann, *Appl. Crystt* **2009**, *42*, 339–341.

[163] G. M. Sheldrick, *Acta Crystallogr.* **2015**, *A71*, 3–8.

[164] G. M. Sheldrick, *Acta Crystallogr.* **2015**, *C71*, 3–8.

[165] P. Deglmann, F. Furche, R. Ahlrichs, *Chem. Phys. Lett.* **2002**, *362*, 511–518.

[166] P. Deglmann, K. May, F. Furche, R. Ahlrichs, *Chem. Phys. Lett.* **2004**, *384*, 103–107.

[167] M. Von Arnim, R. Ahlrichs, *J. Chem. Phys.* **1999**, *111*, 9183–9190.

[168] K. Eichkorn, F. Weigend, O. Treutler, R. Ahlrichs, *Theor. Chem. Acc.* **1997**, *97*, 119–124.

[169] O. Treutler, R. Ahlrichs, *J. Chem. Phys.* **1995**, *102*, 346–354.

[170] R. Ahlrichs, M. Bär, M. Häser, H. Horn, C. Kölmel, *Chem. Phys. Lett.* **1989**, *162*, 165–169.

[171] K. Eichkorn, O. Treutler, H. Öhm, M. Häser, R. Ahlrichs, *Chem. Phys. Lett.* **1995**, *242*, 652–660.

[172] A. Klamt, G. Schüürmann, *J. Chem. Soc. Perkin Trans. 2* **1993**, 799–805.

[173] A. Allouche, *J. Comput. Chem.* **2012**, *32*, 174–182.

[174] S. Grimme, J. Antony, S. Ehrlich, H. Krieg, *J. Chem. Phys.* **2010**, *132*, DOI 10.1063/1.3382344.

[175] S. P. Schmidt, W. C. Trogler, F. Basolo, *J. Am. Chem. Soc.* **1984**, *106*, 1308–1313.

[176] R. A. Motterlini, B. E. Mann, A. Scapens, David, *Therapeutic Delivery of Carbon Monoxide*, **2010**, 2010/0105770 A1.

[177] Y. K. Chung, P. G. Williard, D. A. Sweigart, *Organometallics* **1982**, *1*, 1053–1056.